Quansheng Zhang · Shengbo Eben Li
Kun Deng

Automotive Air Conditioning

Optimization, Control and Diagnosis

Springer

Automotive Air Conditioning

Quansheng Zhang • Shengbo Eben Li
Kun Deng

Automotive Air Conditioning

Optimization, Control and Diagnosis

With contributions from

Marcello Canova, Chang Duan, J.T.B.A. Kessels, Qian Jiang, Sisi Li, Stefano Marelli, Simona Onori, Pierluigi Pisu, Stephanie Stockar, Tiezhi Sun, P.P.J. van den Bosch, Pengchuan Wang, Fen Wu, Shaobing Xu, Chengzhi Yuan, David Yuill, Xiaoxue Zhang

Springer

Quansheng Zhang
Center for Automotive Research
The Ohio State University
Columbus, OH, USA

Kun Deng
Coordinated Science Laboratory
University of Illinois at Urbana-Champaign
Urbana, IL, USA

Shengbo Eben Li
State Key Lab of Automotive
Safety and Energy
Department of Automotive Engineering
Tsinghua University
Beijing, China

ISBN 978-3-319-33589-6 ISBN 978-3-319-33590-2 (eBook)
DOI 10.1007/978-3-319-33590-2

Library of Congress Control Number: 2016939397

Printed on acid-free paper

This Springer imprint is published by Springer Nature
The registered company is Springer International Publishing AG Switzerland

Preface

Many engineering applications are based on vapor compression cycle, a complex thermodynamic process that cannot be directly described by low-order differential equations (ODEs). Such systems have been studied extensively from the viewpoint of numerical simulation. However, the optimization, control, and fault diagnosis of such systems is a relatively new subject, which has been developing steadily over the last decades, inspired partially by research advances in the modeling methodology of moving-boundary method.

This book presents, in a unified framework, recent results on the output tracking, energy optimization, and fault diagnosis for the air conditioning system used on on-road vehicles. The intent is not to include all of the developments on this subject but, through a focused exposition, to introduce the reader to the tools and methods that we can employ to improve the current control strategies on product system. A second objective is to document the occurrence and significance of model-based optimization and control in automotive air conditioning system, a large class of applications that have received limited attention in the existing literature, in contrast to building heating, ventilation, and air conditioning (HVAC) system.

The book is intended primarily as a reference for engineers interested in optimization and control of thermofluid system and the mathematical modeling of engineering applications.

More specifically, the book focuses on typical layout of automotive air conditioning system. The book is organized into four sections. Part I focuses on control-oriented model development. Chapter 1 introduces the traditional modeling approach of the thermodynamics of heat exchangers in a passenger compartment. Chapter 2 exemplifies the model development process of an industrial project for automotive air conditioning system in heavy-duty trucks. Chapter 3 details the model order reduction method used in building HVAC system that might shed light on the difficulty of deriving low-order control-oriented models. Part II focuses on control design for output tracking of cooling capacity and superheat temperature, two critical requirements on system performance. Chapter 4 presents the recent development of robust control of parameter-varying model, a promising framework that could be used to describe the air conditioning system dynamics at different

cooling loads. Chapter 5 utilizes the H infinity synthesis technique to design local controller ensuring the trajectories of the two outputs tracked. Chapter 6 utilizes the mu synthesis technique to improve the tracking performance when both parameter and system uncertainties exist. Chapter 7 details the theory of mean-field control that is proved to improve building HVAC efficiency significantly. Chapter 8 details a specific optimal control theory for constrained nonlinear systems. Both theories have promising applications in the problem of output tracking in automotive air conditioning system. Part III focuses on the problem of electrified vehicle energy management when the air conditioning load is considered. Chapter 9 presents the recent development of energy management strategy for hybrid electric vehicles when multiple-objective conflict and trade-off are required. Chapter 10 utilizes embedded method to design optimal operation sequence for mechanical clutch connecting the crankshaft and compressor in vehicles with conventional powertrain. Chapter 11 utilizes hybrid minimum principle to design the optimal operation sequence when phase change material is stored in an evaporator. Chapter 12 details controllers for cruising control of hybridized powertrain. Part IV focuses on the fault diagnosis of automotive air conditioning system. Chapter 13 presents the recent development of fault detection and isolation methods, as well as their applications to vehicle systems. Chapter 14 utilizes H infinity filter to detect and isolate a variety of fault types, such as actuator fault, sensor fault, and parameter fault. Chapter 15 evaluates the performance of automated fault detection and diagnosis tools developed for building HVAC system.

I am grateful to Marcello Canova, my advisor in the Department of Mechanical and Aerospace Engineering at the Ohio State University, for having created a stimulating atmosphere of academic excellence, within which the research that led to this book was performed over my graduate study. I am also indebted to John Kessels from DAF Trucks, Professor P.P.J. van den Bosch from Eindhoven University of Technology, Professor Chang Duan from Prairie View A&M University, Professor Fen Wu from North Carolina State University, Professor Simona Onori from Clemson University, Professor Pierluigi Pisu from Clemson University, and Professor David Yuill from the University of Nebraska.

I would like to express my gratitude to my parents Hechuan Zhang and Xiuying Zhang for their affection and unquestioning support. The presence of my wife Marina Neklepaeva beside me made the completion of this book all the more gratifying.

Bloomfield Hills, MI, USA Quansheng Zhang
March 8, 2016

Contents

Part I
Model Development

Chapter 1
CFD-Based Modeling of Heat Transfer in a Passenger Compartment

Tiezhi Sun, Qian Jiang, and Pengchuan Wang

Abstract The thermal characteristic of automobile air conditions is very important to improve comfort. The efficient heating, ventilating, and air conditioning (HVAC) systems for automotive applications have determined a great impulse in the research to predict the thermal performance. Limitations of the measurement data and reduction in design cycles have driven the demand for numerical simulation. Computational fluid dynamics (CFD) is an effective technology by providing valuable data which experimental methods cannot measure. This chapter presents the basic numerical theory and method of CFD for heat transfer in passenger compartment.

Keywords Computational fluid dynamics • 3D modeling • Passenger compartment

1.1 Introduction

Thermal comfort is one of the most important factors of comfort inside the passenger compartment. Limitations of the measurement data and reduction in design cycles have driven the demand for numerical simulations. The rapid development of the computational fluid dynamics (CFD) technique has become an attractive way to analyze the fluid flows and thermal characteristics of passenger compartments.

During the past few decades, some efforts have been made to study the fluid flows and the passenger compartment's comfort. Han et al. [1] conducted the simulation on compartment cooling by solving the reynolds-averaged navier-stokes

T. Sun (✉)
School of Naval Architecture, Dalian University of Technology, Dalian 116024, China
e-mail: sun.tiezhi.hit@gmail.com

Q. Jiang
Center for Advanced Life Cycle Engineering, University of Maryland,
College Park, MD 20740, USA
e-mail: qjiang@umd.edu

P. Wang
University of Michigan, Ann Arbor, MI 48109, USA
e-mail: pechwang@umich.edu

Q. Zhang et al., *Automotive Air Conditioning*, DOI 10.1007/978-3-319-33590-2_1

equations and energy equation, they found that overall flow information such as the propagation of cold air fronts, turbulent jet penetration and buoyance-included recirculating flows. Wan et al. [2] calculated the contaminant concentration and air flow in a passenger vehicle, they selected the best solutions to find the most comfortable indoor climate with respect to temperature and contaminant concentration. Currle [3] calculated the flow field and temperature distribution in a passenger compartment by using the commercial CFD program STAR-CD, they optimized the ventilation of the front and rear legroom. Brown et al. [4] presented a new transient passenger thermal comfort model, the advantage of this mode was that it can accurately predict the human thermal sensation response during transient vehicle warm-up and cooldown conditions. Kataoka et al. [5] predicted the thermal comfort in an automobile with numerical simulation, the flow field and temperature distribution were solved with a grid system based on many small cubic elements. Hsieh et al. [6] analyzed the 3-D heat transfer and fluid flow of air over a radiator and engine compartment. The effects of different inlet airflow angles of the grill and bumper were investigated in detail. Ivanescu et al. [7] simulated the distribution of the temperature and the air flow fields of passengers' compartment starting from the body's energy balance, they found that thermal comfort was reached faster in the case where the air flow rate was bigger, but keeping the same air temperature. Singh et al. [8] studied the effect of dynamic vents, they found that faster cooling of the cabin and maintaining a uniform temperature distribution inside the cabin is possible at a particular vent angle. Shafie et al. [9] investigated the effects of using different ventilation setups on the air flow velocity and temperature distributions inside a passenger bus, the results of CFD simulations show that the displacement ventilation setup resulted in more uniform distribution of air flow velocity and air temperature inside the passenger compartment.

The purpose of this study is to present the basic theory and numerical methods of fluid flows in passenger compartment. In the following presentation, the governing equations will first be introduced, followed by the turbulence model. Then mesh and discretization methods are presented. In addition, the accuracy and convergence of numerical simulation are discussed.

1.2 Governing Equations

In order to simulate fluid flow and heat transfer in a passenger compartment, it is necessary to describe the associate physics in mathematical terms. The set of governing equations consists of the mass, momentum and energy equations. These equations are presented as follows.

1.2.1 The Mass Conservation Equation

The law of mass conservation states that mass cannot be created in a fluid system, nor can it disappear from one. For unsteady compressible flows, the mass equation can be written as follows:

$$\frac{\partial \rho}{\partial t} + \nabla \cdot \left(\rho \overrightarrow{V} \right) = 0 \tag{1.1}$$

where ρ is the density, $\overrightarrow{V}$ denotes the velocity.

For a Cartesian coordinates system, it becomes

$$\frac{\partial \rho}{\partial t} + \frac{\partial}{\partial x}(\rho u) + \frac{\partial}{\partial y}(\rho v) + \frac{\partial}{\partial z}(\rho w) = 0 \tag{1.2}$$

where u, v, and w are the velocity components in the x, y, and z directions, respectively.

For incompressible flows density has a known constant value. Hence, Eq. (1.2) can be written as

$$\frac{\partial}{\partial x}(\rho u) + \frac{\partial}{\partial y}(\rho v) + \frac{\partial}{\partial z}(\rho w) = 0 \tag{1.3}$$

1.2.2 The Momentum Equation

According to the Newton's second law, the momentum equations in x, y, and z directions can be expressed as:

$$\rho \frac{Du}{Dt} = \frac{\partial (-p + \tau_{xx})}{\partial x} + \frac{\partial \tau_{yx}}{\partial y} + \frac{\partial_{zx}}{\partial z} + S_{Mx} \tag{1.4}$$

$$\rho \frac{Dv}{Dt} = \frac{\partial \tau_{xy}}{\partial x} + \frac{\partial \left(-p + \tau_{yy}\right)}{\partial y} + \frac{\partial_{zy}}{\partial z} + S_{My} \tag{1.5}$$

$$\rho \frac{Dw}{Dt} = \frac{\partial \tau_{xz}}{\partial x} + \frac{\partial_{yz}}{\partial y} + \frac{\partial (-p + \tau_{zz})}{\partial z} + S_{Mz} \tag{1.6}$$

where p is a compressive stress, τ_{xx}, τ_{yy}, and τ_{zz} are normal stresses. τ_{xy}, τ_{xz} are shear stresses. For example, τ_{xy} is the stress in the y-direction on x-plane. S_M is a source term.

1.2.3 The Energy Equation

The energy equation is based on the first law of thermodynamics, which implies sum of the net added heat to a system and the net work done on it equally increases the system energy. The general form of this equation is

$$\rho\left[\frac{\partial h}{\partial t}+\nabla\cdot\left(h\overrightarrow{V}\right)\right]=-\frac{Dp}{Dt}+\nabla\cdot(k\nabla T)+\phi \tag{1.7}$$

where h is the specific enthalpy which is related to specific internal energy; ϕ is the dissipation function representing the work done against viscous forces; and k is the thermal conductivity.

1.3 Turbulence Models

The fluid flow in the passenger compartment can be considered as incompressible turbulent flow. The choice of an appropriate turbulence model influences the computational results and the required computation resource, because not every model can predict precisely unsteady flow. CFD offers a user-friendly platform with a range of flow models which can be used individually as per the requirement of the end result. Turbulent flows could be solved using several different approaches. The main approaches of turbulence modeling include Reynolds average Navier–Stokes (RANS) models, large Eddy simulation (LES), and direct numerical simulation (DNS).

Figure 1.1 shows the prediction methods of these three approaches. The DNS and LES approaches resolve shorter length scales than RANS. However they have a demand of much greater computer power than those models applying RANS method. RANS models offer the most economic approach for computing complex turbulent industrial flows, the classical models based on the RANS equations are discussed in the next section.

1.3.1 K-Epsilon Turbulence Model

The $k-\varepsilon$ model has become one of the most widely used turbulence models. Reasonable accuracy, robustness, and economy for a wide range of turbulent flows explain its popularity in general flow and heat transfer simulations. The original model was initially proposed by Launder and Spalding [11]. For the standard $k-\varepsilon$ turbulence model, the turbulence kinetic energy k and dissipation rate ε are obtained by the following equations:

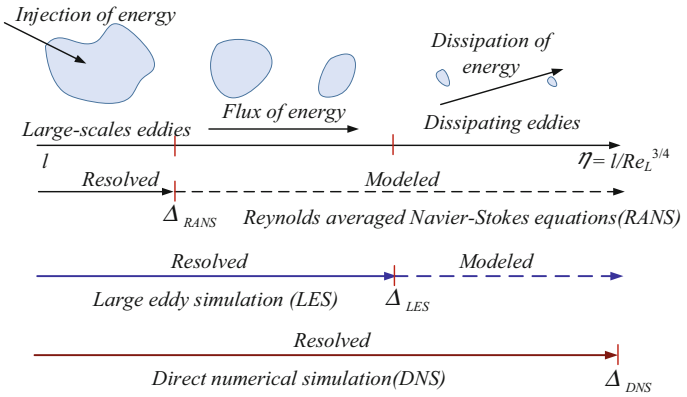

Fig. 1.1 Prediction methods of DNS, LES, and RANS approaches [10]

$$\frac{\partial(\rho k)}{\partial t}+\frac{\partial\left(\rho k u_j\right)}{\partial x_j}=\frac{\partial}{\partial x_j}\left[\left(\mu+\frac{\mu_t}{\sigma_k}\right)\frac{\partial k}{\partial x_j}\right]+G_k+G_b-\rho\varepsilon-Y_M+S_k \quad (1.8)$$

$$\frac{\partial(\rho\varepsilon)}{\partial t}+\frac{\partial\left(\rho\varepsilon u_j\right)}{\partial x_j}=\frac{\partial}{\partial x_j}\left[\left(\mu+\frac{\mu_t}{\sigma_\varepsilon}\right)\frac{\partial\varepsilon}{\partial x_j}\right]+C_{1\varepsilon}\frac{\varepsilon}{k}\left(G_k+G_{3\varepsilon}G_b\right)-C_{2\varepsilon}\rho\frac{\varepsilon^2}{k}+S_\varepsilon \quad (1.9)$$

where G_k represents the generation of turbulent kinetic energy arises due to mean velocity gradients, G_k is the generation of turbulent kinetic energy that arises due to buoyancy. S_k and S_ε are source terms defined by the user. The constant coefficients are given with $C_{\varepsilon 1}=1.44$, $C_{\varepsilon 2}=1.92$, $\sigma_k=1.0$, $\sigma_\varepsilon=1.2$, $C_\mu=0.09$, σ_k, and σ_ε, respectively, with the turbulence kinetic energy and dissipation rate corresponding to the Prandtl number.

The turbulence eddy viscosity is defined as:

$$\mu_t=C_\mu\rho_m\frac{k^2}{\varepsilon} \quad (1.10)$$

where C_μ is a constant.

1.3.2 SST Turbulence Model

The shear stress transport (SST) turbulence model was developed by Menter using the k-epsilon model and k-omega model [12]. The blending function triggers the k-epsilon model in areas away from the surface, and triggers the standard k-omega model near wall regions. These features of the SST model make it perform more

accurate prediction for the flow separation problem under the condition of adverse pressure gradient. The transport equations for turbulence kinetic energy k and specific dissipation rate ω are given by:

$$\frac{\partial(\rho k)}{\partial t} + \frac{\partial}{\partial x_j}(\rho u_i k) = \frac{\partial}{x_j}\left[\left(\mu + \frac{\mu_t}{\sigma_k}\right)\frac{\partial k}{\partial x_j}\right] + \tilde{G}_k - Y_k + S_k \tag{1.11}$$

$$\frac{\partial(\rho\omega)}{\partial t} + \frac{\partial}{\partial x_j}(\rho u_i \omega) = \frac{\partial}{\partial x_j}\left[\left(\mu + \frac{\mu_t}{\sigma_\omega}\right)\frac{\partial \omega}{\partial x_j}\right] + G_\omega - Y_\omega + D_\omega + S_\omega \tag{1.12}$$

where $\tilde{G}_k$ is the generation of turbulence kinetic energy that arises due to mean velocity gradients. Y_k and Y_ω represent the dissipation of k and ω due to turbulence. S_k and S_ω are source terms defined by the user

The term for production of turbulence kinetic energy, $\tilde{G}_k$, is defined as:

$$\tilde{G}_k = \min\left(G_k, 10\rho\beta^* k\omega\right) \tag{1.13}$$

The turbulent viscosity is given by:

$$\mu_t = \frac{\rho k}{\omega}\frac{1}{\max\left[\frac{1}{\alpha}, \frac{SF_2}{\alpha_1 \omega}\right]} \tag{1.14}$$

where S is the strain rate magnitude. The turbulent Prandtl numbers which were constant in standard model are shown below and incorporate the blending functions F_1 and F_2. The blending functions are given by:

$$\sigma_k = \frac{1}{F_1/\sigma_{k,1} + (1 - F_1)/\sigma_{k,2}} \tag{1.15}$$

$$\sigma_\omega = \frac{1}{F_1/\sigma_{\omega,1} + (1 - F_1)/\sigma_{\omega,2}} \tag{1.16}$$

1.4 Numerical Methods

1.4.1 Mesh Terminology and Types

Mesh generation is usually considered as the most time consuming and important part of CFD analysis. The computational domain is discretized by meshing and gridding. Element or cell is the fundamental unit of the mesh. The mesh terminology shown in Fig. 1.2 is used to describe our meshes. A cell is surrounded by faces, which connected through nodes or vertices, and the face is a surface surrounded by edges.

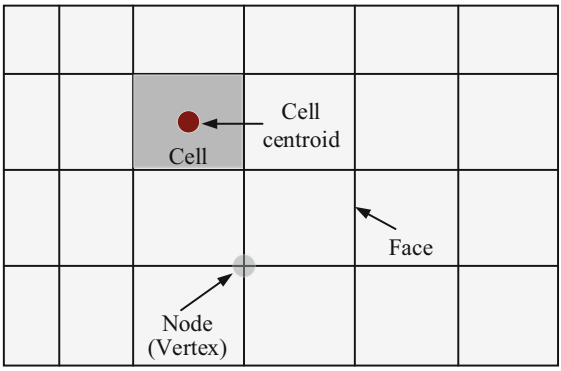

Fig. 1.2 Mesh terminology

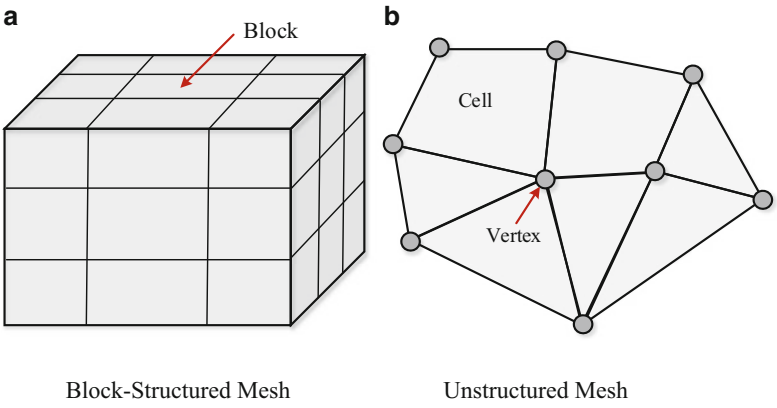

Fig. 1.3 Typical mesh. (**a**) Block-structured mesh. (**b**) Unstructured mesh

Mesh generation is very important for the accuracy of the numerical solution. A typical mesh is shown in Fig. 1.3. Figure 1.3a shows a block-structured mesh, here, the mesh is divided into blocks, and the mesh within each block is structured. Methods for generating high quality structured meshes for hexahedra have existed for a long time, but are widely used in simple or regular geometries. As CFD is becoming more widely used for analyzing industrial flows, unstructured meshes are becoming advanced to deal with complex geometries. Figure 1.3b shows an unstructured mesh. Here, each vertex is connected to an arbitrary number of neighbor vertices. Unstructured grid generation usually takes less time structured grid generation. However, structured grid can generate quickly when the geometry is based on a previously existing geometry with a structured grid.

Figure 1.4 shows an example of mesh generation for a passenger compartment. The advantage of unstructured grid methods is that they are generated automatically and, therefore, require little user time.

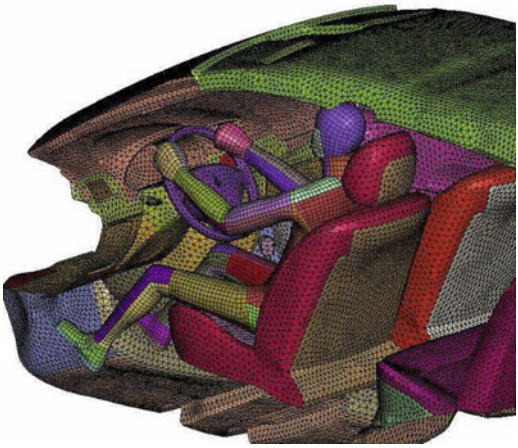

Fig. 1.4 Mesh generation in passenger compartment [7]

1.4.2 Discretization Methods

In the numerical solutions technique, there are several CFD numerical solutions that have been developed in the discretization of governing equations. The CFD discretization method can be classified into three branches, namely finite difference method (FDM), finite element method (FEM), and finite volume method (FVM). The differences between them are the way in which the flow variables are approximated and the discretization processes are done.

FDMs approximate the derivatives in the governing differential equation using truncated Taylor series expansions. Through FDMs, the partial derivatives of governing (PED) are replaced with finite, algebraic difference quotients at the corresponding nodes. However, FDM is not as convenient as FEM or FVM for it requires the definition of complex conditions.

FEM is one of the most frequently used methods by engineering sciences of fluid mechanics and thermodynamic to describe the behavior of physical systems in the form of partial differential equations. FEM uses the simple piecewise functions valid on elements to describe the local variations of unknown flow variables. However, compared to FDM and FVM, it is not widely applied.

The FVM is the numerical algorithm calculation process involving the use of finite volume cells, i.e., small volume surrounding each node point on a mesh. The volume integrals in a partial differential equation that contains a divergence term are converted to surface integrals, using the divergence theorem. The FVMs are mainly employed for numerical solution of problems in fluid mechanics. The main CFD code packages using the FVM approach involve Fluent, CFX, Phoenics, Star-CD, Flow 3D, etc. FVE is currently the most suitable method for the CFD process as it enjoys an advantage in memory use and speed for very large problems, source term dominated flows, and turbulence flows.

1.5 Accuracy and Convergence

Accuracy is related to the difference between the numerical solution and the exact solution. Actually, in most cases, we do not know the exact solution. Numerical solutions of fluid flow and heat transfer problems are only approximate solutions. Numerical solutions always include three kinds of errors: modeling errors, discretization errors, and iteration errors. In the first kind, the errors are defined as the difference between the actual solution and the exact flows. They are usually influenced by the assumptions made in deriving the transport equations for the variables, and they also introduced by simplifying the domain geometry, boundary conditions. The discretization errors are defined as the difference between the t solution of the algebraic system of equations and the solution of the conservation equations. Iteration errors are usually called convergence errors, which are defined as the iterative and exact solutions.

Generally speaking, convergence is typically represented by the diminishing residuals of the numerical solution and is the achievement of a limiting behavior in the solution of the equations. Typically, the basic criteria of residual values and solution imbalances should be satisfied for CFD analysis. The residual is one of the most important criterions of an iterative solution's convergence, as it directly quantifies the error in the numerical solution of the solved equations. CFD analysis is solving conservation equations of mass, momentum, energy, etc., we must try our best to obtain a good solution does indeed conserve these quantities.

1.6 Summary

In this chapter, a brief review of the numerical theory and method for heat transfer in the air conditioning system was presented. A number of literature related to the passenger compartment's comfort have been presented. The basic governing equations and numerical solution procedure were discussed. The k-epsilon turbulence model and the SST turbulence model are widely used in the numerical simulation. Unstructured grid generation is usually selected to be used in the passenger compartment as it can handle complex geometries. The FVM is currently the most suitable method for the CFD process as it enjoys an advantage in memory use and speed for very large problems, source term dominated flows, and turbulence flows. The accuracy and convergence properties should be concerned when we use the numerical method to solve the differential equations.

References

1. T. Han, Three-dimensional Navier–Stokes simulation for passenger compartment cooling. Int. J. Veh. Des. **10**(2), 175–186 (1989)
2. J.W. Wan, J. Van der Kooi, Influence of the position of supply and exhaust openings on comfort in a passenger vehicle. Int. J. Veh. Des. **12**(5–6), 588–597 (1991)
3. J. Currle, Numerical simulation of the flow in a passenger compartment and evaluation of the thermal comfort of the occupants. SAE Technical Paper No. 970529 (1997)
4. J.S. Brown, B.W. Jones, A new transient passenger thermal comfort model. SAE Technical Paper No. 970528 (1997)
5. T. Kataoka, Y. Nakamura, Prediction of thermal sensation based on simulation of temperature distribution in a vehicle cabin. Heat Transfer Asian Res. **30**(3), 195–212 (2001)
6. C.-T. Hsieh, J.-Y. Jang, 3-D thermal-hydraulic analysis for airflow over a radiator and engine room. Int. J. Automot. Technol. **8**(5), 659–666 (2007)
7. M. Ivanescu, C.A. Neascu, I. Tabascu, Studies of the thermal comfort inside of the passenger compartment using the numerical simulation. International Congress Motor Vehicles and Motors, October 7–9, Kragujevac, Serbia (2010)
8. O.P. Singh et al., Effect of dynamic vents on the thermal comfort of a passenger car. J. Mech. Eng. **61**(10), 561–570 (2015)
9. N.E.A. Shafie, H.M. Kamar, N. Kamsah, Effects of ventilation setups on air flow velocity and temperature fields in bus passenger compartment. Jurnal Teknologi **77**(30), 49–53 (2015)
10. J. Sodja, *Turbulence Models in CFD* (University of Ljubljana, Ljubljana, 2007), pp. 1–18
11. B.E. Launder, D.B. Spalding, The numerical computation of turbulent flows. Comput. Methods Appl. Mech. Eng. **3**(2), 269–289 (1974)
12. F.R. Menter, Two-equation eddy-viscosity turbulence models for engineering applications. AIAA J. **32**(8), 1598–1605 (1994)

Chapter 2
Model Development for Air Conditioning System in Heavy Duty Trucks

J.T.B.A. Kessels and P.P.J. van den Bosch

Abstract This chapter presents a modelling approach for the air conditioning (AC) system in heavy duty trucks. The presented model entails two major elements: a mechanical compressor model and a thermal AC model. The compressor model describes the massflow of the refrigerant as well as the mechanical power requested from the combustion engine. The thermal AC model predicts how ambient air flow cools down when it passes the AC system. This model also includes the latent heat emerging from water condensation. Both elements of the model have been validated with experimental data. The compressor parameters follow from hardware-in-the-loop experiments where the AC compressor is measured under various load profiles. Validation of the thermal AC model is done by climate chamber testing with a DAF XF heavy duty truck on a roller dynamometer.

Keywords Lumped-parameter modeling • Air conditioning system • Automotive

2.1 Introduction

Heavy duty long haul trucks are typically equipped with an air conditioning (airco) system to offer a comfortable cabin climate to the driver. The airco system fulfills two elementary functions: cooling down the cabin temperature (when the ambient temperature is too high) and dehumidifying the air (in rainy conditions or winter weather). Both functions request mechanical power which is ultimately delivered by the internal combustion engine (ICE). This chapter presents a modeling approach for the mechanical power consumption of the airco compressor. Furthermore, it also presents a model for the thermal behavior of the airflow when it is cooled down by the airco system. These models can be used to develop advanced control strategies for improving the energy efficiency of the airco system, see, for example, [4, 5].

J.T.B.A. Kessels (✉)
DAF Trucks N.V., Vehicle Control Department, Eindhoven, The Netherlands
e-mail: John.Kessels@daftrucks.com

P.P.J. van den Bosch
Eindhoven University of Technology, Control Systems - Department of Electrical Engineering
e-mail: P.P.J.v.d.Bosch@tue.nl

Q. Zhang et al., *Automotive Air Conditioning*, DOI 10.1007/978-3-319-33590-2_2

Fig. 2.1 DAF XF prototype truck developed in CONVENIENT project

More specifically, an energy management strategy can incorporate these models to optimize the power demand of the airco system such that:

- the airflow towards the cabin receives exactly enough cooling power to establish the desired temperature and humidity for the driver;
- regenerative braking energy is stored in the thermal buffer capacity of the airco system.

This research is carried out within the EU collaborative project CONVENIENT[1] (Complete Vehicle Energy-saving Technologies for Heavy-Trucks, [2]). In this project a suite of technologies is developed to maximize the fuel economy of long haul trucks. In total three prototype trucks are developed to demonstrate these technologies. DAF Trucks N.V. is responsible for the development of the DAF XF tractor with semi-trailer, suitable for long haul applications, see Fig. 2.1. For this prototype truck with hybrid electric powertrain, smart auxiliaries are developed by means of a Smart Vehicle Powernet control concept [7]. The airco system of the truck is one of the auxiliaries considered in the Smart Vehicle Powernet. This chapter describes the underlying airco model for developing the Smart Vehicle Powernet [7].

[1]This work has received funding from the European Union's Seventh Framework Programme for research, technological development, and demonstration under grant agreement no [312314].

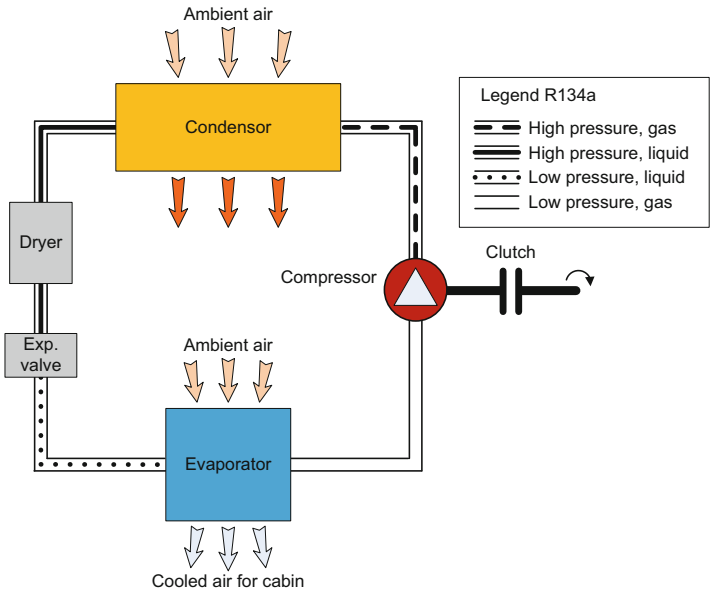

Fig. 2.2 Overview of air conditioning system in heavy duty truck

2.2 System Overview

The basic principles of an air conditioning system are explained by thermodynamics, see, for example, [1]. A schematic overview of the air conditioning system in the truck is depicted in Fig. 2.2. This system circulates refrigerant R134a using the following hardware:

- Compressor: The compressor increases the pressure of the refrigerant. The compressor is belt driven and receives power from the ICE. A mechanical clutch is installed to (dis-)connect the compressor (from)/to the belt.
- Condensor: The condensor operates as a heat exchanger. It cools down the high pressure refrigerant and releases its heat to the airflow through the condensor. Cooling down the refrigerant leads to condensation of the refrigerant. The condensor is placed in the engine bay directly behind the grill to receive sufficient airflow.
- Expansion valve: The expansion valve releases the refrigerant towards the evaporator. This is a sensitive task because the influx should be balanced with the heat exchanged in the evaporator. Only gaseous refrigerant is allowed to leave the evaporator. Therefore the expansion valve monitors the refrigerant output from the evaporator to decide if more/less refrigerant has to flow into the evaporator.
- Evaporator: The evaporator is mounted in the Heating Ventilation and Air Conditioning (HVAC) system. The evaporator exchanges heat between the refrigerant

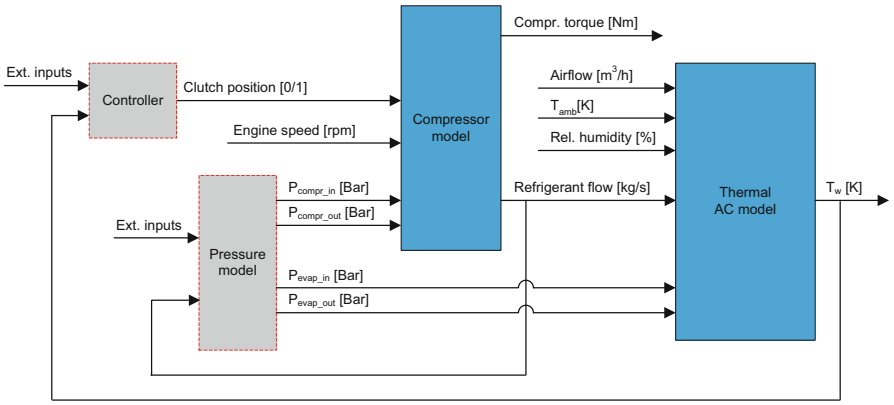

Fig. 2.3 Cascade model structure for AC system

and the airflow which is used for cabin heating and ventilation. Refrigerant that flows through the evaporator absorbs heat from the airflow. The airflow cools down (and possibly also dehumidifies) and the refrigerant expands from liquid to gaseous phase. The airflow is directed further to the cabin for climate control.

The model developed in this work for the air conditioning system consists of two parts:

- Compressor model: A mechanical model for the compressor is constructed. This model translates mechanical power (delivered by the ICE) into cooling power (delivered to the refrigerant).
- Thermal AC model: This model describes the thermodynamic behavior of the air conditioning (AC) system. The main focus of this model is to describe the heat transfer in the evaporator. The evaporator is located in the HVAC system. The refrigerant in the evaporator will absorb heat from the air that flows through the HVAC. The main output from this model is an estimate of the temperature of the airflow downstream the evaporator.

Both models can be connected in a cascade structure, as visualized in Fig. 2.3. The underlying idea is to construct a simulation environment which is suitable for developing advanced HVAC controls. The output from the thermal AC model is used to evaluate driver comfort, whereas the compressor torque yields insight in the power demand of the airco system. A missing element in the model is the pressure model. This is planned for future research, but the interested reader could examine [10] for an example in passenger car application.

2.3 Compressor Model

The compressor model is based on two key parameters: volumetric efficiency and isentropic efficiency. The volumetric efficiency will be used to estimate the flow of the refrigerant through the compressor. The isentropic efficiency is used to estimate the mechanical power demand of the compressor. Both parameters have been measured by the supplier of the compressor on a hardware-in-the-loop (HIL) test bench for various pressure levels.

2.3.1 Calculation of Refrigerant Flow

The volumetric efficiency η_{vol} [-] is defined as the ratio of the actual measured flow ϕ_a [m^3/s] (measured at the suction side of the compressor at a certain pressure) and the theoretical flow ϕ_t [m^3/s]

$$\eta_{\text{vol}} = \frac{\phi_a}{\phi_t} \tag{2.1}$$

The theoretical flow ϕ_t [m^3/s] of a compressor can be calculated by multiplying its displacement volume V_p [m^3] with its rotational velocity N [rpm]

$$\phi_t = \frac{N}{60} V_p \tag{2.2}$$

Given the density ρ [kg/m^3] of the refrigerant at the suction side of the compressor, the actual refrigerant massflow $\dot{m}_R$ [kg/s] is calculated as

$$\dot{m}_R = \rho\, \phi_a = \rho\, \eta_{\text{vol}} \frac{N}{60} V_p \tag{2.3}$$

2.3.2 Calculation of Compressor Power

The enthalpy of the refrigerant changes when it passes the compressor. This enthalpy change is used to define the isentropic efficiency. Considering an isentropic compressor, the theoretical work W_{isen} [J] done by the compressor is defined as

$$W_{\text{isen}} = -\int_{p_s}^{p_d} V dp \tag{2.4}$$

where refrigerant is compressed from pressure p_s [Pa] to p_d [Pa] (i.e., from the compressor suction side to the discharge side). The analytical solution for this integral is well known from literature, see, e.g., [9]

$$W_{\text{isen}} = \frac{\gamma}{\gamma - 1} m_R \, R_R \, T_s \left[\left(\frac{p_d}{p_s} \right)^{\frac{\gamma-1}{\gamma}} - 1 \right] \tag{2.5}$$

with T_s [K] the temperature of the refrigerant at the suction side of the compressor. $\gamma = 1.2$ [-] is the heat capacity ratio; R_R [J kg^{-1} K^{-1}] is the specific gas constant of the refrigerant and m_R [kg/mol] is the molecular weight of the refrigerant.

The isentropic efficiency η_{isen} [-] is defined as the ratio between the isentropic compressor work and the actual compressor work

$$\eta_{\text{isen}} = \frac{W_{\text{isen}}}{W_{\text{actual}}} \tag{2.6}$$

Given the isentropic efficiency, the actual mechanical energy demand from the compressor is calculated

$$W_{\text{actual}} = \frac{1}{\eta_{\text{isen}}} \frac{\gamma}{\gamma - 1} m_R \, R_R \, T_s \left[\left(\frac{p_d}{p_s} \right)^{\frac{\gamma-1}{\gamma}} - 1 \right] \tag{2.7}$$

The mechanical compressor power P_{AC} [W] follows by replacing the refrigerant weight with the massflow from (2.3). This substitution holds for steady state conditions and results in

$$P_{\text{AC}} = \frac{1}{\eta_{\text{isen}}} \frac{\gamma}{\gamma - 1} \dot{m}_R \, R_R \, T_s \left[\left(\frac{p_d}{p_s} \right)^{\frac{\gamma-1}{\gamma}} - 1 \right] \tag{2.8}$$

Finally, the compressor torque τ_{AC} [Nm] is calculated with help of the rotational speed N [rpm]

$$\tau_{\text{AC}} = P_{\text{AC}} \frac{60}{2\pi \, N} \tag{2.9}$$

2.4 Thermal AC Model

The thermal AC model describes the transfer from AC cooling power into cold air out of the HVAC. The evaporator in the HVAC takes a central role here. Based on first principles of conduction and convection, its thermal behavior will be derived. There should be noted, however, that the humidity of the ambient air also plays an

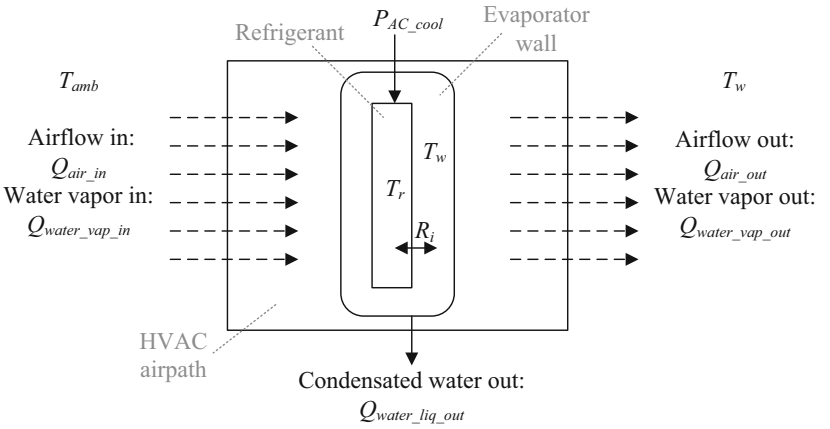

Fig. 2.4 Thermal AC model

important role. After all, cold air can hold less water so cooling down ambient air in the HVAC easily results in condensation of water. This water drops out of the HVAC and incorporates the so-called latent heat which needs to be taken into account too.

2.4.1 Thermal Model Structure

The basic thermal model structure is depicted in Fig. 2.4. It is decided to model the heat exchanger of the evaporator as a lumped thermal mass with temperature T_w [K] (which refers to the wall temperature of the evaporator). Besides the temperature of the evaporator, the thermal model incorporates also the temperature of the refrigerant inside the evaporator: T_r [K]. The model injects cooling power $P_{\text{Ac\_cool}}$ [W] directly in the refrigerant. Furthermore, a thermal resistance R_i [K/W] is introduced to model the heat transfer Q_{w2r} [W] from evaporator to refrigerant

$$Q_{w2r} = \frac{T_w - T_r}{R_i} \tag{2.10}$$

Altogether, the thermal AC model resembles two thermal buffers

$$\begin{aligned} C_w \dot{T}_w = {} & Q_{\text{air\_in}} + Q_{\text{water\_vap\_in}} - Q_{\text{air\_out}} - Q_{\text{water\_vap\_out}} \\ & + Q_{\text{latent}} - Q_{w2r} \end{aligned} \tag{2.11}$$

$$C_r \dot{T}_r = Q_{w2r} - P_{\text{AC\_cool}} \tag{2.12}$$

with C_w [J/K] and C_r [J/K] the lumped heat capacity of the evaporator and refrigerant, respectively. The other terms will be described in the text below.

Ambient air with temperature T_{amb} [K] enters the HVAC with flow ϕ_{air} [m^3/s], specific heat $c_{\text{air}} = 1005\,\text{J/kg K}$, and density $\rho_{\text{air}} = 1.25\,\text{kg/m}^3$. This leads to the heatflow $Q_{\text{air\_in}}$ [W]

$$Q_{\text{air\_in}} = \rho_{\text{air}}\, c_{\text{air}}\, \phi_{\text{air}}\, T_{\text{amb}} \tag{2.13}$$

It is noted that the coefficients in (2.13) correspond to dry air. According to the relative humidity, however, the airflow will be a mixture of air and water vapor. This water vapor will result into an additional influx $Q_{\text{water\_vap\_in}}$ [W] for the HVAC

$$Q_{\text{water\_vap\_in}} = c_{\text{water\_vap}}\, \phi_{\text{air}}\, X_{\text{air\_in}}\, T_{\text{amb}} \tag{2.14}$$

with $c_{\text{water\_vap}}$ [J/kg K] the specific heat of water vapor and $X_{\text{air\_in}}$ [kg/m^3] the absolute humidity of ambient air. Further details on the calculation of $X_{\text{air\_in}}$ will be provided in Sect. 2.4.2.

The airflow through the HVAC flows through the evaporator and cools down. It is assumed that the air temperature downstream the evaporator equals the wall temperature of the evaporator defined as T_w [K]. The corresponding heatflow $Q_{\text{air\_out}}$ [W] of output air (dry) is equal to

$$Q_{\text{air\_out}} = \rho_{\text{air}}\, c_{\text{air}}\, \phi_{\text{air}}\, T_w \tag{2.15}$$

Similar as with the air–water mixture for the input flow, the heatflow corresponding to the water vapor leaving the HVAC is modeled as $Q_{\text{water\_vap\_out}}$ [W]

$$Q_{\text{water\_vap\_out}} = c_{\text{water\_vap}}\, \phi_{\text{air}}\, X_{\text{air\_out}}\, T_{\text{w}} \tag{2.16}$$

with $X_{\text{air\_out}}$ [kg/m^3] the absolute humidity of the airflow leaving the HVAC. Note that this absolute humidity is equal or lower than the humidity of the input air. This is a side effect of cooling down the airflow. The underlying model equations for $X_{\text{air\_in}}$ and $X_{\text{air\_out}}$ will be provided in Sect. 2.4.2. A lower output humidity results in water condensation. Water droplets will flow out of the HVAC. The corresponding heatflow from liquid water leaving the HVAC is defined as $Q_{\text{water\_liq\_out}}$ [W]

$$Q_{\text{water\_liq\_out}} = c_{\text{water\_liq}}\, \phi_{\text{air}}\, (X_{\text{air\_in}} - X_{\text{air\_out}})\, T_w \tag{2.17}$$

with $c_{\text{water\_liq}}$ [J/kg K] the specific heat of liquid water. Condensation of water vapor results in substantial heat. This so-called latent heat is also taken into account by means of Q_{latent} [W]

$$Q_{\text{latent}} = H_{\text{vap}}\, \phi_{\text{air}}\, (X_{\text{air\_in}} - X_{\text{air\_out}}) \tag{2.18}$$

with $H_{\text{vap}} = 2257\text{e}3\,\text{J/kg}$ the specific heat of vaporization of water.

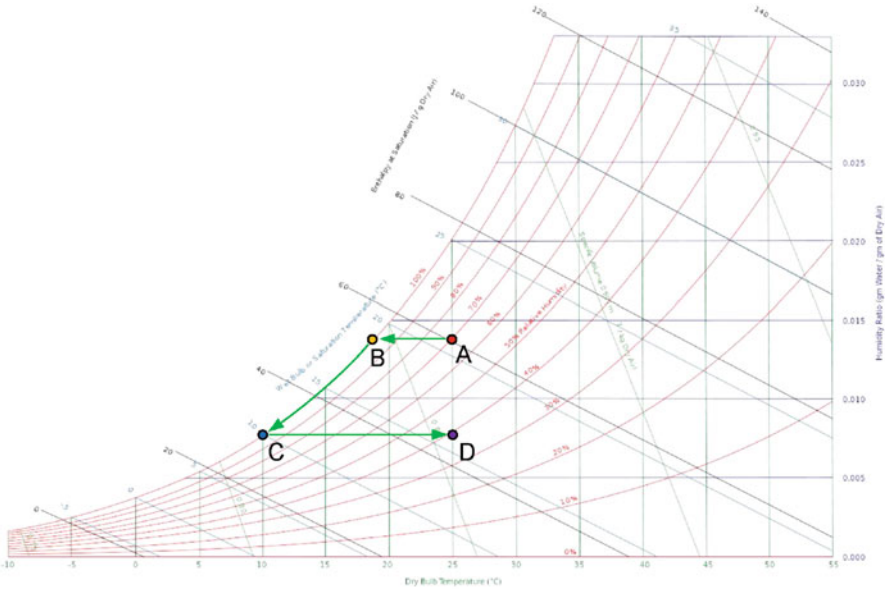

Fig. 2.5 Psychrometric chart with visualization how air dehumidifies in HVAC

2.4.2 Air Humidity and Latent Heat

One aspect of an air conditioning system is that it cools down the air towards the cabin. A second aspect of the air conditioning system is that it also reduces the humidity of the air. This is because cold air cannot hold as much water vapor as warm air. How the model calculates the amount of water condensation in the HVAC, as well as the related heatflow Q_{latent}, is described in this section.

The psychrometric chart in Fig. 2.5 visualizes how the relative humidity changes under variation of temperature. As an illustrative example, consider a warm but rainy day with ambient temperature $T_{\text{amb}} = 25\,^{\circ}\text{C}$ and relative humidity $\text{RH} = 70\,\%$ (point A). By cooling down, the relative humidity increases up to $\text{RH} = 100\,\%$ when reaching temperature $T = 19\,^{\circ}\text{C}$ (point B). Remark: point B is called dewpoint because below this point, the air cannot contain more water vapor. Cooling down further will result in water condensation. Suppose that the air is further cooled down to $T = 10\,^{\circ}\text{C}$ (point C). When this air is re-heated back to $T = 25\,^{\circ}\text{C}$, the relative humidity becomes approx. $\text{RH} = 40\,\%$ (point D), which is substantially lower than the original humidity (point A) and helps preventing a foggy windscreen.

The report from Vaisala [6] is used as starting point for collecting the model equations for humidity conversion. The relative humidity RH [%] of air is defined as the ratio of the water vapor pressure P_w [Pa] to the saturation water vapor pressure P_{ws} [Pa]

$$\text{RH} = \frac{P_w}{P_{ws}} \times 100 \tag{2.19}$$

The saturation water vapor pressure P_{ws} typically relates to the situation where the air reaches RH $= 100\,\%$. The following approximation is proposed in [6]

$$P_{ws} = A \times 10^{\left(\frac{(T-273.15)\ m}{(T-273.15)+T_n}\right)} \tag{2.20}$$

with temperature T [K] and constants $A = 611.6$, $m = 7.591$, and $T_n = 240.7$ taken from [6]. The substitution of (2.20) in (2.19) allows to calculate P_w under the condition that RH is known.

From P_w the absolute humidity is calculated. The absolute humidity AH [g/m^3] is defined as the mass of water vapor in a volume of 1 m^3 and calculated by [6]

$$\mathrm{AH} = \frac{C \times P_w}{T} \tag{2.21}$$

with constant $C = 2.167\,\mathrm{gK/J}$ and T [K] the air temperature. Calculation of AH is done for point A and point C

$$\mathrm{AH}_A = \frac{C \times P_w(T_A, \mathrm{RH}_A)}{T_A} \tag{2.22}$$

$$\mathrm{AH}_C = \frac{C \times P_w(T_C, \mathrm{RH}_C)}{T_C} \tag{2.23}$$

with $T_A = T_{\mathrm{amb}}$ and RH_A measured from ambient air. The wall temperature from (2.11) is used for $T_C = T_w$ and $\mathrm{RH}_C = 100\,\%$.

The difference between AH_A and AH_C defines the amount of water condensation. Returning back to the Eqs. (2.14)–(2.18) the following substitution is done for the absolute humidity

$$X_{\mathrm{air\_in}} = \mathrm{AH}_A \,/\, 10^3 \quad \text{and} \quad X_{\mathrm{air\_out}} = \mathrm{AH}_C \,/\, 10^3 \tag{2.24}$$

2.5 Model Validation

Experiments are done to collect measurement data for model validation. The experiments fall apart into two parts:

- HIL compressor measurements: A HIL test setup is used to characterize the model parameters of an isolated AC compressor. The preferred items to be measured are the pressure, temperature, and flow of the refrigerant when entering/leaving the compressor. Also the compressor speed and torque is measured to determine its mechanical power.
- Rollerdyno measurements: A climate chamber with heavy duty roller dynamometer is used to estimate the model parameters of the complete AC system. A picture of the climate chamber test setup (with DAF XF EuroVI truck) is shown in Fig. 2.6.

Fig. 2.6 Validation of AC system with DAF test truck in climate chamber

The pressure and the temperature of the refrigerant are measured at six locations: compressor in/out, condensor in/out, expansion valve in, and evaporator out. The torque and speed of the compressor are measured to determine its mechanical power. The temperature of the airflow is measured before and after the evaporator as well as the condensor. Different experiments are done with ambient conditions: $10 \leq T_{\text{amb}} \leq 30\,^{\circ}\text{C}$; $50 \leq \text{RH} \leq 70\,\%$.

2.5.1 Validation of Compressor Model

The compressor measurements with the HIL test setup offer insight into the volumetric efficiency η_{vol} and the compressor efficiency η_{isen}. Both parameters are measured and stored in a look-up-table as function of compressor speed and charge/discharge ratio. Validation of the compressor torque in (2.9) is done with help of the rollerdyno measurements in the climate chamber. From the measurement data, the following information is used:

- Speed: The speed of the ICE is available and will be used to determine the AC compressor speed (by means of a fixed ratio determined by the pulley).

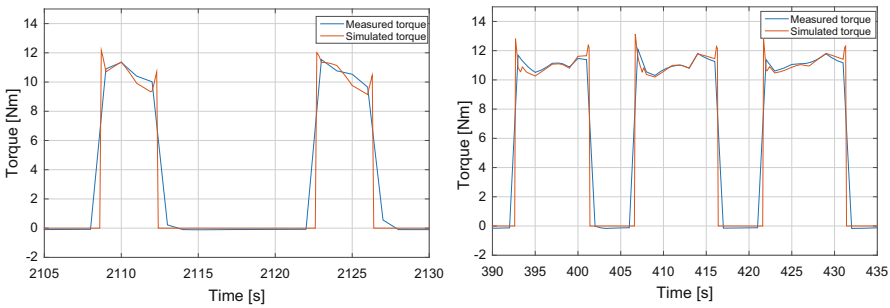

Fig. 2.7 Validation of compressor torque: $T_{\text{amb}} = 25\,^{\circ}\text{C}$ (*left*) and $T_{\text{amb}} = 30\,^{\circ}\text{C}$ (*right*)

- Torque: A dedicated torque sensor is installed to measure the torque of the AC compressor.
- Pressure: Two pressure sensors are applied to measure the charge and discharge pressure of the compressor.

The compressor torque from (2.9) is plotted against measurement data in Fig. 2.7. Two different use cases are considered for the compressor torque: the left picture shows the situation with ambient temperature 25 °C; the right picture shows the situation with ambient temperature 30 °C. The model achieves the best accuracy when the compressor clutch is completely closed (error smaller than 10 %). Less accuracy is achieved during closing and opening of the clutch. This is because the model does not take into account slipping of the clutch.

2.5.2 *Validation of Thermal AC Model*

This section describes the validation of the thermal AC model as derived in Sect. 2.4. A comparison will be made between the air temperature downstream the evaporator and the temperature T_w estimated by the model (2.11). Before the model validation can start, first an explanation is needed about the measured temperatures in the HVAC.

During the rollerdyno experiments, the temperature downstream the evaporator is measured with nine temperature sensors. These sensors are all mounted on the back-wall of the evaporator, distributed on a 3×3 grid. This allows to measure the temperature behind the evaporator at nine different locations in the air channel. For one experiment ($T_{\text{amb}} = 25\,^{\circ}\text{C}$) these sensor measurements are visualized in Fig. 2.8. It is observed that the air temperature behind the evaporator does not respect a homogenous distribution. For validation of (2.11) only one temperature profile can be used. It is decided to use the temperature sensor with comes closest to the average temperature of all nine sensors.

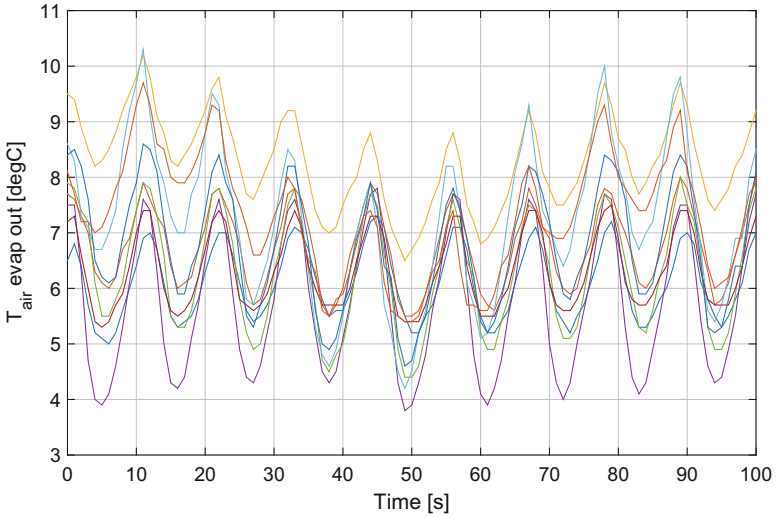

Fig. 2.8 Measured air temperature downstream evaporator; nine sensors measure temperature distribution over air channel

The next step will be the identification of the model parameters. The rollerdyno experiments are used to identify the model parameters from the thermal equations (2.10)–(2.12). The parameters which will be identified are the heat capacities C_w and C_r and the thermal resistance R_i. The experiment that has been selected to identify these parameters entails a low ambient temperature and low humidity. This ensures that water condensation is avoided in the HVAC and its impact on the heat balance from (2.11) can be neglected (i.e., $Q_{\text{water\_liq\_out}} = 0$ and $Q_{\text{latent}} = 0$). The identification toolbox from *Matlab* is used to find the parameters of interest. In particular, a gray-box identification is done by constructing an Output-Error OE model structure. The *Matlab* function *Idgrey* is finally used to calculate C_w, C_r, and R_i.

Now that the model parameters are identified, the final validation of the thermal model is done. Recall that in this work a pressure model is lacking for the refrigerant R134a. To overcome this problem, the cooling input power $P_{\text{AC\_cool}}$ in (2.12) is calculated from the enthalpy change in the evaporator, see also [3]. With help of the experimental data, the following approximation has been chosen:

$$P_{\text{AC\_cool}} \approx (h_{\text{evap\_in}} - h_{\text{evap\_out}})\, \dot{m}_{\text{R134a}} \tag{2.25}$$

where $\dot{m}_{\text{R134a}}$ is determined by Eq. (2.3) from the compressor model. The pressure sensors, which are installed before the expansion valve and after the evaporator, are used to estimate the enthalpy $h_{\text{evap\_in}}$ [J/kg] and $h_{\text{evap\_out}}$ [J/kg], respectively. Conversion from pressure to enthalpy is done according to the standard pressure-enthalpy diagrams available from literature. In Fig. 2.9 this conversion is visualized

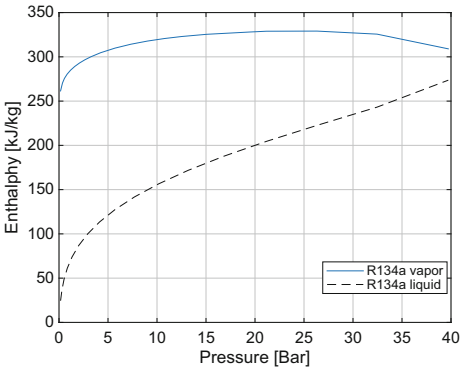

Fig. 2.9 Static relation between pressure and enthalpy for R134a

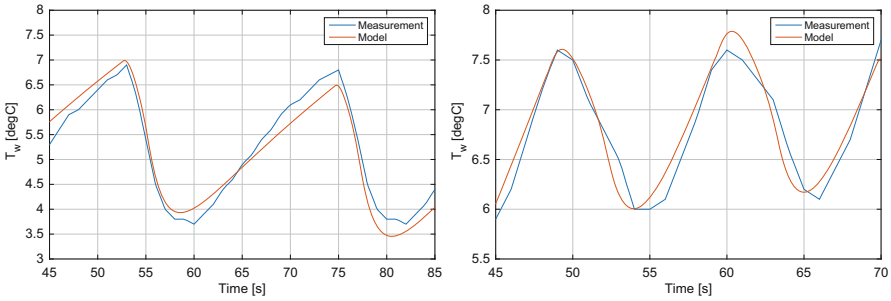

Fig. 2.10 Validation of evaporator wall temperature: $T_{\text{amb}} = 15\,^{\circ}\text{C}$ (*left*) and $T_{\text{amb}} = 25\,^{\circ}\text{C}$ (*right*)

for refrigerant R134a (data taken from [8]). The refrigerant is assumed to be in liquid phase before the expansion valve, whereas after the evaporator the refrigerant must be in gas form. This way, $h_{\text{evap\_in}}$ relies on the liquid graph and $h_{\text{evap\_out}}$ uses the vapor graph.

The final validation of the thermal AC model is done with experiments at a higher temperature to include the verification of the latent heat model. In particular, the experiments with ambient temperature 15 and 25 °C are selected to show the validation results in Fig. 2.10. One can observe that the temperature cycles between fixed boundaries. The exact behavior of these cycles relates to the on/off strategy of the compressor clutch. The compressor clutch strategy, however, is not investigated in this work. Nonetheless, a higher ambient temperature results in a higher load for the AC system and the cycle frequency goes up.

Figure 2.10 also reveals that the AC model, in particular Eq. (2.11), is able to predict the temperature downstream the evaporator. During the on-time of the compressor (where the temperature decreases) as well as during the off-time (where the temperature increases) the model achieves an error smaller than 0.5 °C.

There should be noted that the accuracy of T_w highly depends on the accuracy of the cooling input $P_{\text{AC\_cool}}$. A mismatch in cooling power defined in (2.12) results in drift for the estimated temperature T_w.

2.6 Concluding Remarks

This chapter develops a model for the airco system in heavy duty long haul trucks. Two aspects of the airco model are considered in detail:

- Compressor model: The airco system requests mechanical power, ultimately delivered by the diesel engine of the truck. The compressor model calculates the mechanical power for the situation that the compressor clutch is closed. This model also predicts the massflow of the refrigerant through the compressor, which is used to determine the cooling power in the thermal part of the airco model.
- Thermal AC model: Ambient air cools down when it passes the evaporator. This part of the model estimates the airflow temperature directly behind the evaporator. The model also estimates the humidity of the output air, as well as the amount of water condensation.

Both elements of the model are verified by means of experimental validation. A HIL test-setup is used to collect specific measurement data of the compressor: the volumetric efficiency and the isentropic efficiency. Next, a DAF XF prototype truck is placed in a climate chamber on a roller dynamometer. Experiments at different ambient conditions are done to validate the model. A comparison between the measurement data and the model outputs learns that the following accuracy is established:

- Compressor model: The compressor torque is calculated within 10 % of the measured torque signal. Slipping of the compressor clutch is not considered. During transient situations (i.e., when the clutch closes/opens and the compressor switches on/off) the model looses validity.
- Thermal AC model: The temperature of the airflow leaving the evaporator resembles the measurement data. The temperature of the model deviates less than 0.5 K from the measurement data (considering various ambient conditions).

Future research for this airco model should address the development of a pressure model. Once the model includes a pressure model for the refrigerant, it can be used to develop advanced energy management strategies.

References

1. C.P. Arora, *Thermodynamics* (McGraw-Hill Education (India) Pvt Limited, Bangalore, 2001)
2. Complete vehicle energy-saving technologies for heavy-trucks (CONVENIENT), (2016), www.convenient-project.eu
3. S.P. Datta, P.K. Das, S. Mukhopadhyay, Effect of refrigerant charge, compressor speed and air flow through the evaporator on the performance of an automotive air conditioning system, in *Proceedings of the 15th International Refrigeration and Air Conditioning Conference*, Purdue, 14–17 July 2014

4. W.O. Forrest, M.S. Bhatti, Energy efficient automotive air conditioning system, in *SAE 2002 World Congress*, Detroit, Michigan, 4–7 March 2002. SAE Technical Paper 2002-01-0229
5. M. Fritz, F. Gauterin, M. Frey, J. Wessling, E. Wohlfarth, R. Oberfell, An approach to develop energy efficient operation strategies and derivation of requirements for vehicle subsystems using the vehicle air conditioning system as an example, in *SAE 2013 World Congress & Exhibition*, Detroit, Michigan, 2013. SAE Technical Paper 2013-01-0568
6. Humidity conversion formulas - calculation formulas for humidity, Technical Report, Vaisala Oyj, Helsinki, Finland, 2013
7. J.T.B.A. Kessels, J.H.M. Martens, P.P.J. van den Bosch, W.H.A. Hendrix, Smart vehicle powernet enabling complete vehicle energy management, in *Proceedings of the IEEE Vehicle Power and Propulsion Conference (VPPC)*, Seoul, Korea, October 2012, pp. 938–943
8. Pressure - enthalpy diagram 134a, Technical Report, INEOS Fluor, Cheshire, 2001
9. S.R. Turns, *Thermodynamics: Concepts and Applications* (Cambridge University Press, Cambridge, 2006)
10. Q. Zhang, M. Canova, Modeling and output feedback control of automotive air conditioning system. Int. J. Refrig. **58**, 207–218 (2015)

Chapter 3
Aggregation-Based Thermal Model Reduction

Kun Deng, Shengbo Eben Li, Sisi Li, and Zhaojian Li

Abstract In this chapter, we propose an aggregation-based model reduction method for nonlinear building thermal models. The full-order model, which is already a lumped-parameter approximation, quickly grows in state-space dimension as the number of zones increases. An advantage of the proposed method, apart from being applicable to the nonlinear thermal models, is that the reduced model obtained has the same structure and physical intuition as the original model. The key to the methodology is an analogy between a continuous-time Markov chain and the linear part of the thermal dynamics. A recently developed aggregation-based method of Markov chains is employed to aggregate the large state space of the full-order model into a smaller one. Simulations are provided to illustrate tradeoffs between modeling error and computation time.

Keywords Model order reduction • Air conditioning system • Building

3.1 Introduction

A typical heating, ventilation, and air conditioning (HVAC) system consists of AHUs, supply ducts, and terminal boxes. The air handling unit (AHU) supplies

K. Deng
Coordinated Science Laboratory, University of Illinois at Urbana-Champaign, Urbana, IL 61801, USA
e-mail: kundeng2@illinois.edu

S.E. Li (✉)
State Key Laboratory of Automotive Safety and Energy, Department of Automotive Engineering, Tsinghua University, Beijing 10084, China
e-mail: lishbo@tsinghua.edu.cn

S. Li
Department of Mathematics and Computer Sciences, Mercy College, Dobbs Ferry, NY 10522, USA
e-mail: sli8@mercy.edu

Z. Li
Department of Aerospace Engineering, University of Michigan, Ann Arbor, 48105, USA
e-mail: zhaojli@umich.edu

Q. Zhang et al., *Automotive Air Conditioning*, DOI 10.1007/978-3-319-33590-2_3

conditioned air to terminal boxes at the so-called leaving-air temperature and humidity. Each terminal box delivers air to one or more zones. Using reheat coil, the supply air temperature can be increased beyond the AHU leaving temperature. In a variable-air-volume (VAV) system, the terminal box can vary the supply air mass flow rate through dampers. A controller at each terminal box can be used to maintain the temperature of a zone at a specified value by controlling the mass flow rate of air supplied to the zone. The dynamics of the building with its HVAC system includes AHU dynamics and the zone thermal dynamics.

Interests in methods for controlling building HVAC systems to reduce their energy usage or cost have been on the increase in recent years; particularly in advanced model-based approaches such as model predictive control (MPC) [1–3]. Accurate models of building zone temperature evolution are required for advanced control algorithms with the computational complexity taking into account. This is because the model complexity is a major issue for implementing the optimization-based control schemes, particularly if the optimization is to be performed with a day-long prediction horizon to take advantage of slow thermal responses of buildings as well as daily variations in environment and energy prices [2]. The focus of this chapter is on model reduction of multi-zone building thermal dynamics.

A thermal resistor–capacitor (RC) network model is used to construct dynamic models of multi-zone buildings with nodes representing zones or internal surface points. Due to the nonlinear nature of model, the number of available techniques for model reduction is limited. Balanced truncation methods for nonlinear systems use controllability and observability energy functions of a system to find the reduced realizations [4–6]. Lall et al. in [7] use empirical Gramians to determine the importance of a particular subspace in terms of its contribution to the input–output behavior. These energy functions or empirical Gramians, however, are difficult to compute in practice [8]. Moreover, the reduced models generated by truncation methods do not retain the physical intuition of the full model, i.e., truncated states of the reduced model usually have no physical meanings.

In this chapter, we propose an *aggregation-based* model reduction method that preserves the RC-network structure of the nonlinear building thermal model. This is achieved by obtaining super-nodes via aggregation of building nodes. The aggregation-based approach proposed in this chapter is based on model reduction method of Markov chains that has recently been developed in [9]. The main idea here is to connect the linear part of building thermal model to a continuous-time Markov chain (CTMC), and apply the aggregation method of Markov chains to systematically find optimal coordination of aggregation and the optimal linear dynamics. The nonlinear model part is then aggregated accordingly based on the same optimal coordination. The major advantage of the proposed aggregation-based method compared to truncation-based methods is the *structure-preserving* property in the sense that the reduced model is still an RC-network with parameters and nodes maintaining the same physical meaning as the full building model. The other advantage is that it does not suffer from the computational difficulties of empirical Gramians or energy functions.

This chapter extends the aggregation method proposed in [10] to a more realistic nonlinear building thermal model, and assesses the performance and computational complexity of reduced-order models through numerical simulations. The aggregation-based method proposed here is related to model reduction techniques for grey-box models [11, 12], where the model structure and parameters are obtained through the physical insights. The aggregated building model can be thought as a grey-box model and coordination of aggregation specifies the model structure. The aggregation-based method described here can also be used to create zoning approximations for building models by combining zones together [13]. In a very recent work [14], a Koopman operator approach is proposed to systematically create zoning approximation for buildings, where the dominant modes of thermal behavior are extracted from the building simulations. Then modes information is used to combine multiple zones into single zones. The major difference is that our method is directly based on the knowledge of building descriptions, while the method in [14] is mainly based on data from building simulations.

The rest of the chapter is organized as follows. In Sect. 3.2, the full-order model is described and the model reduction problem is stated. In Sect. 3.3, the Markov chain analogy of the building thermal dynamics is presented. In Sect. 3.4, the aggregation-based methodology is applied to reduce the building thermal model. In Sect. 3.5, theoretical results are illustrated by numerical simulations. The conclusions appear in Sect. 3.6.

3.2 Full-Order Building Thermal Model

The focus of this chapter is on model reduction of the building zone thermal dynamics, which suffer more of modeling complexity than the AHU dynamics [10]. As a result, the AHU dynamics are replaced by static gains in this chapter without significant loss of accuracy. A lumped-parameter model of resistances and capacitances is constructed to describe the thermal dynamics of a multi-zone building, with current and voltage being analogous to heat flow and temperature, respectively. We only consider the interzone conductive heat transfer but ignore the convective heat transfer that occurs through the open windows, doors, and hallways. The 3R2C models of surface elements (e.g., walls, windows, ceilings, and floors) are inter-connected to construct an *RC-network model* for building thermal dynamics [15]. The set $\mathcal{V} := \{1, \ldots, n+1\}$ denotes the set of nodes of the network. The nodes are assumed to be re-indexed so that the first N nodes correspond to $1, \ldots, N$ physical zones, and the next $(n - N)$ nodes correspond to the points internal to the surfaces that appear due to the 3R2C models. The last $(n + 1)$th node corresponds to the outside.

For each node $i \in \mathcal{V}$, the associated temperature and thermal capacitance are denoted as T_i and C_i, respectively. Let $\mathcal{E}$ denote the set of all edges of the RC-network, where edges represent pathways for conductive heat transports. For any nodes $i, j \in \mathcal{E}$, the thermal resistance between i and j is represented as a

lumped parameter R_{ij}, with $R_{ji} = R_{ij}$ by convention. The inputs to the building model are summarized here: $\dot{m}_i^{\text{in}}$ denotes the mass flow rate of the supply air, $\dot{Q}_i^r$ denotes the heat gain due to reheating that may occur at the VAV box, $\dot{Q}_i^{\text{int}}$ denotes the internal heat gain (i.e., the rate of heat generated by occupants, equipments, lights, etc.), and $\dot{Q}_i^{\text{ext}}$ denotes the external heat gain (i.e., the rate of solar radiation). It is assumed that (1) the values of C_i and R_{ij} are known parameters obtained based on building structures and materials, (2) the supply air temperature T^s is assumed to be a constant here, and (3) the (estimation of) the outside temperature T_o and the heat gains $\dot{Q}^r, \dot{Q}^{\text{int}}, \dot{Q}^{\text{ext}}$ are available based on historical data, weather forecast, and sensor measurements.

In the following, a compact state-space representation is presented for building thermal dynamics. To establish a Markov chain analogy in the next section, the outside temperature is also taken as a "virtual state" T_{n+1} to the building system. We assign a very large "virtual capacitance" to the outside node: $C_{n+1} \gg C_i$, for $i = 1, \ldots, n$. Letting $C_{n+1} \to \infty$, the dynamic equations are derived from the energy balance laws:

$$\frac{dT}{dt} = AT + L(T, U, \dot{Q}) \tag{3.1}$$

where the state vector $T := [T_1, \ldots, T_{n+1}]^T$, the control vector $U := [\dot{m}_1^{\text{in}}, \ldots, \dot{m}_N^{\text{in}}, 0, \ldots, 0]^T$, and the heat gain vector $\dot{Q} := [\dot{Q}_1, \ldots, \dot{Q}_N, 0, \ldots, 0]^T$. The *transition rate matrix* A is an $(n+1) \times (n+1)$ matrix with entries given by

$$A_{ij} := \begin{cases} 0, & \text{if } j \neq i,\ (i,j) \notin \mathcal{E} \\ 1/(C_i R_{ij}), & \text{if } j \neq i,\ (i,j) \in \mathcal{E} \\ -\sum_{k \neq i} A_{ik}, & \text{if } j = i,\ (i,j) \in \mathcal{E} \end{cases} \tag{3.2}$$

and the nonlinear function:

$$\begin{cases} L_i(T, U, \dot{Q}) = \dfrac{C_{pa} U_i (T^s - T_i) + \dot{Q}_i}{C_i}, & i = 1, \ldots, N \\ L_i(T, U, \dot{Q}) = 0, & i = N+1, \ldots, n \\ L_i(T, U, \dot{Q}) = \eta, & i = n+1 \end{cases}$$

where $\eta(t) \in \mathbb{R}$ is chosen such that $\eta(t) = \dot{T}_o(t)$.

3.3 Markov Chain Analogy and Aggregation

In this section, it is shown that the linear part of the building thermal model (3.1) is analogous to a *continuous-time Markov chain*. The *linear dynamics* of the building thermal model (3.1) are given by:

$$\frac{dT}{dt} = AT. \tag{3.3}$$

Due to the special structure of the matrix A [see (3.2)], the linear thermal model (3.3) is *conservative*. Specifically, a scalar-valued function $V(t) := \sum_{i\in\mathcal{V}} C_i T_i(t)$ is conserved for all time, i.e., $\frac{dV}{dt}(t) = 0$ for all $t \geq 0$. We denote $V_0 := V(0) = \sum_{i\in\mathcal{V}} C_i T_i(0)$ as the *invariant quantity* of the linear thermal model (3.3).

3.3.1 Analogy to a Markov Chain

Based upon the conservative property of the linear thermal model (3.3), define the *thermal distribution* as a row vector, denoted by f, where

$$f_i = \frac{C_i}{V_0} T_i, \quad i \in \mathcal{V}.$$

Note that $\sum_{i\in\mathcal{V}} f_i(t) \equiv 1$ for all $t \geq 0$.

On differentiating f_i with respect to t, and using (3.3),

$$\frac{df_i}{dt} = \frac{C_i}{V_0}\frac{dT_i}{dt} = \sum_{j\in\mathcal{V}} A_{ij}\frac{C_i}{V_0} T_j. \tag{3.4}$$

By substituting (3.2) in (3.4), we have

$$\begin{aligned}\frac{df_i}{dt} &= A_{ii}\frac{C_i}{V_0} T_i + \sum_{j\neq i} \frac{1}{C_i R_{ij}}\frac{C_i}{V_0} T_j \\ &= A_{ii}\frac{C_i}{V_0} T_i + \sum_{j\neq i} \frac{1}{C_j R_{ji}}\frac{C_j}{V_0} T_j \qquad (3.5) \\ &= \sum_{j\in\mathcal{V}} f_j A_{ji} \qquad (3.6)\end{aligned}$$

where the fact that $R_{ij} = R_{ji}$ is used in deriving the equality (3.5). Using matrix notation for representing (3.6), we obtain the dynamics of the thermal distribution and its solution

$$\frac{df}{dt} = fA \qquad \Rightarrow \qquad f(t) = f(0)e^{At}, \quad \forall t \geq 0.$$

The Markov chain analogy is now clear. Note that each row sum of A is zero, its diagonal entries are negative, and its non-diagonal entries are non-negative (see (3.2)). Thus, the transition rate matrix A is the *infinitesimal generator* of a *transition semigroup* $\{e^{At}\}_{t\geq 0}$: For any $t, s \geq 0$, (1) $e^{A0} = I$, (2) e^{At} is a stochastic

matrix (that is, e^{At} is a non-negative matrix whose row sums are equal to one), and (3) $e^{A(t+s)} = e^{At}e^{As}$.

Consider now a CTMC $\{X(t)\}_{t\geq 0}$ on the state space $\mathcal{V}$ with the transition semigroup $\{e^{At}\}_{t\geq 0}$ [16]. Let $g(t)$ denote the *probability distribution* at time t, i.e.,

$$g_i(t) = \Pr(X(t) = i), \quad i \in \mathcal{V}.$$

Using the transition semigroup property, we have

$$g_i(t) = \sum_{j\in\mathcal{V}} \Pr(X(0) = j)\Pr(X(t) = i \mid X(0 = j)) = \sum_{j\in\mathcal{V}} g_j(0)(e^{At})_{ji}.$$

If $f(0)$ is the initial distribution of $\{X(t)\}_{t\geq 0}$, i.e., $g(0) = f(0)$, then

$$g(t) = g(0)e^{At} = f(0)e^{At} = f(t). \tag{3.7}$$

Thus, starting from the same initial distribution, the probability distribution of the CTMC $\{X(t)\}_{t\geq 0}$ is equal to the thermal distribution of the linear thermal model (3.3). For more details on CTMC, we refer the reader to [16, 17] and the references therein.

For any ergodic Markov chain, there exists a unique *stationary distribution* π (obtained as a solution to $\pi A = 0$), whereby starting from any initial distribution

$$\lim_{t\to\infty} g(t) = \pi.$$

For linear thermal model (3.3), the associated Markov chain is shown to be ergodic in [10], and the stationary distribution is given by:

$$\pi_i = \frac{C_i}{\sum_{j\in\mathcal{V}} C_j}, \quad i \in \mathcal{V}. \tag{3.8}$$

3.3.2 Discretization of the Continuous-Time Markov Chain

In practice, it is more convenient to work with discrete-time Markov chains (DTMC) instead of CTMC. The DTMC $\{X(k\Delta t)\}_{k\geq 0}$ is obtained by discretizing the CTMC $\{X(t)\}_{t\geq 0}$ with a step-size Δt. Let $\xi(k)$ denote the probability distribution of the DTMC at kth time step, i.e., $\xi_i(k) = \Pr(X(k\Delta t) = i)$ for $i \in \mathcal{V}$. Using (3.7),

$$\xi(k) = \xi(0)P^k(\Delta t), \quad k \geq 0$$

where the *transition matrix* is defined as

$$P(\Delta t) := e^{A\Delta t}. \tag{3.9}$$

For any $t \geq 0$, there exists an integer $k \geq 0$ such that $k\Delta t \leq t < (k+1)\Delta t$ and $e^{At} \approx e^{Ak\Delta t}$ for small enough Δt. Thus the CTMC $\{X(t)\}_{t\geq 0}$ with the transition semigroup $\{e^{At}\}_{t\geq 0}$ is approximated by the DTMC $\{X(k\Delta t)\}_{k\geq 0}$ with the transition matrix $P(\Delta t)$ as $\Delta t \to 0$. One can verify that π given in (3.8) is also the stationary distribution of the DTMC, i.e., $\lim_{k\to\infty} \xi(k) = \pi$.

3.3.3 Aggregation of Markov Chain

Let (π, P) denote a DTMC defined on the state space $\mathcal{V} = \{1, \ldots, n+1\}$ with the transition matrix P and the stationary distribution π. The model reduction problem is to find an optimal aggregated Markov chain, denoted by $(\bar{\pi}, \bar{P})$, defined on the state space $\bar{\mathcal{V}} = \{1, \ldots, m+1\}$, where $m \leq n$, such that the KL divergence rate $R_\phi(P\|\bar{P})$ between two Markov chains is minimized.

The *m-partition problem* is to find a partition function $\phi : \mathcal{V} \mapsto \bar{\mathcal{V}}$ and an aggregated transition matrix $\bar{P}$ that solves the following optimization problem:

$$\begin{aligned} &\min_{\phi,\bar{P}} R_\phi(P\|\bar{P}) \\ &\text{s.t. } \bar{P}\mathbf{1} = \mathbf{1},\ \bar{P} \geq 0. \end{aligned}$$

As shown in Theorem 2 of [9], for a fixed (whether optimal or not) partition function ϕ, the optimal aggregated Markov chain $(\bar{\pi}(\phi), \bar{P}(\phi))$ is given by:

$$\bar{P}_{kl}(\phi) = \frac{\sum_{i\in\phi^{-1}(k)} \sum_{j\in\phi^{-1}(l)} \pi_i P_{ij}}{\sum_{i\in\phi^{-1}(k)} \pi_i}, \quad k, l \in \bar{\mathcal{V}} \tag{3.10}$$

where the stationary distribution of $\bar{P}(\phi)$ is given by

$$\bar{\pi}_k(\phi) = \sum_{i\in\phi^{-1}(k)} \pi_i, \quad k \in \bar{\mathcal{V}}. \tag{3.11}$$

As a result, the m-partition problem reduces to finding only an *optimal partition function* $\phi^* : \mathcal{V} \to \bar{\mathcal{V}}$ such that

$$\phi^* \in \arg\min_{\phi} R_\phi(P\|\bar{P}(\phi)). \tag{3.12}$$

It is shown in [9] that solving the optimization problem (3.12) exactly is difficult for $m > 2$, but a sub-optimal solution for $m = 2$ can be easily computed. This leads to a sub-optimal solution for arbitrary $m \geq 2$ through the *recursive bi-partition algorithm* [9].

3.3.4 Analogy to Thermal Dynamics

Based on the Markov chain analogy for the linear thermal dynamics (see Sect. 3.3.1), the model reduction framework for Markov chains is extended to building thermal models:

- *Metric for comparing thermal distributions*: The KL divergence is employed as a metric to compare two thermal distributions f and g defined on the same building node set $\mathcal{V}$:

$$D(f\|g) = \sum_{i\in\mathcal{V}} f_i \log(f_i/g_i).$$

  For the model reduction problem, it is of interest to compare two thermal distributions defined on building graphs of different cardinalities. Let f and $\bar{f}$ denote two thermal distributions defined on $\mathcal{V}$ and $\bar{\mathcal{V}}$, respectively. The low-dimensional distribution $\bar{f}$ is lifted to a high-dimensional distribution $\hat{f}$ defined on $\mathcal{V}$ by using partition function ϕ and lifting distribution μ:

$$\hat{f}_i^{(\mu)}(\phi) = \frac{\mu_i}{\sum_{k\in\psi(i)}\mu_k}\bar{f}_{\phi(i)}, \quad i \in \mathcal{V}. \tag{3.13}$$

  The lifting may be viewed as a linear transformation that conserves the total heat. The KL metric is then used to compare the two thermal distributions f and $\hat{f}$ on the same node set $\mathcal{V}$.
- *Metric for comparing thermal models*: The KL divergence rate is used as a measure to compare two building thermal models. In particular, suppose full-order model is simulated starting from an initial distribution $f(0)$. Denote the resulting trajectory of the thermal distribution as $\{f(k\Delta t)\}_{0\le k\le N}$. Now, suppose the reduced-order model is also simulated starting from the initial distribution

$$\bar{f}_l(0) = \sum_{i\in\phi^{-1}(l)} f_i(0), \quad l \in \bar{\mathcal{V}}.$$

  Denote the resulting trajectory of thermal distribution as $\{\bar{f}(k\Delta t)\}_{0\le k\le N}$, which evolves over reduced graph $\bar{\mathcal{V}}$. The trajectory $\{\bar{f}(k\Delta t)\}_{0\le k\le N}$ is lifted to the full building graph by using (3.13), and denoted by $\{\hat{f}(k\Delta t)\}_{0\le k\le N}$. The KL divergence rate between full- and reduced-order models is given by,

$$\frac{1}{N}\sum_{k=1}^{N} D(f(k\Delta t)\|\hat{f}(k\Delta t)). \tag{3.14}$$

  Thus, the KL divergence rate is a measure of average distance between trajectories generated from simulating two thermal models.

- *Bi-partition*: An optimal bi-partition of a given model produces a 2-state reduced-order model that is closest to the full-order model in the sense of distance (3.14). Since the distance is a time average, discrepancies between two models at the slow(est) time-scales contribute more to the error compared to the fast transients. The choice of metric thus leads to a 2-state model that approximates the full-order model on the slowest time-scale.
- *Recursive bi-partition*: The recursive application of bi-partition algorithm produces a reduced-order model that progressively captures multiple time-scales in the problem. The first bi-partition results in splitting of the graph into two clusters, and a 2-state model that captures the slowest time-scale. The next bi-partition further splits one of the two clusters so as to capture the slowest time-scale in that cluster, and so on. In effect after m-applications of the algorithm, the reduced-order model describes the m slowest time-scales of the full-order model.

3.4 Aggregated Building Thermal Model

In this section, the aggregation methodology is applied to obtain a reduced-order model for building thermal model (3.1). We first describe the reduced-order model for the linear part of the building thermal model (3.1), and then the reduced-order model for the nonlinear part of (3.1).

3.4.1 Aggregated Linear Thermal Dynamics

For the linear thermal model (3.3), the goal is to aggregate the node set $\mathcal{V} = \{1, \ldots, n+1\}$ into a smaller super-node set $\bar{\mathcal{V}} = \{1, \ldots, m+1\}$ where $m \leq n$. For each super-node $k \in \bar{\mathcal{V}}$, we introduce the super-temperature $\bar{T}_k$, super-capacitance $\bar{C}_k$, and super-resistance $\bar{R}_{kl}$. For a given partition function ϕ, the reduced-order model for (3.3) has the form:

$$\frac{d\bar{T}}{dt} = \bar{A}(\phi)\bar{T}, \tag{3.15}$$

where $\bar{T} = [\bar{T}_1, \ldots, \bar{T}_{m+1}]^T$ denotes the super-temperature vector, and $\bar{A}(\phi)$ denotes the $(m+1) \times (m+1)$ super-transition-rate matrix. The Markov chain analogy also works for the reduced-order model with the associated transition semigroup $\{e^{\bar{A}(\phi)t}\}_{t\geq 0}$. Discretizing with a small step-size Δt, one obtains the transition matrix for the aggregated Markov chain defined on $\bar{\mathcal{V}}$:

$$\bar{P}(\Delta t) := e^{\bar{A}(\phi)\Delta t}.$$

Recall that the transition matrix for the DTMC associated with the full-order linear thermal dynamics is denoted by $P(\Delta t)$ (see (3.9)). The goal is to choose $\bar{A}(\phi)$ so that the aggregated Markov chain with the transition matrix $\bar{P}(\Delta t)$ optimally approximates the original Markov chain with the transition matrix $P(\Delta t)$. The aggregation method described in Sect. 3.3.3 is employed to determine the formula for the optimal aggregated transition matrix $\bar{A}(\phi)$. According to (3.10), the formula for the optimal aggregated Markov transition matrix is given by:

$$\bar{P}_{kl}(\Delta t) = \frac{\sum_{i\in\phi^{-1}(k)} \sum_{j\in\phi^{-1}(l)} \pi_i P_{ij}(\Delta t)}{\sum_{i\in\phi^{-1}(k)} \pi_i}, \quad k, l \in \bar{\mathcal{V}}. \tag{3.16}$$

By expressing $P(\Delta t)$ and $\bar{P}(\Delta t)$ in the form

$$\begin{aligned} P(\Delta t) &= I + A\Delta t + O(\Delta t^2), \\ \bar{P}(\Delta t) &= I + \bar{A}(\phi)\Delta t + O(\Delta t^2), \end{aligned}$$

the equation (3.16) becomes

$$\begin{aligned} \mathbb{1}_{\{k=l\}} + \bar{A}_{kl}(\phi)\Delta t + O(\Delta t^2) &= \frac{\sum_{i\in\phi^{-1}(k)} \sum_{j\in\phi^{-1}(l)} \pi_i (\mathbb{1}_{\{i=j\}} + A_{ij}\Delta t + O(\Delta t^2))}{\sum_{i\in\phi^{-1}(k)} \pi_i} \\ &= \mathbb{1}_{\{k=l\}} + \frac{\sum_{i\in\phi^{-1}(k)} \sum_{j\in\phi^{-1}(l)} \pi_i A_{ij}}{\sum_{i\in\phi^{-1}(k)} \pi_i} \Delta t + O(\Delta t^2). \end{aligned} \tag{3.17}$$

By matching terms on both sides of (3.17), we obtain the formula for the optimal super-transition-rate matrix

$$\bar{A}_{kl}(\phi) = \frac{\sum_{i\in\phi^{-1}(k)} \sum_{j\in\phi^{-1}(l)} \pi_i A_{ij}}{\sum_{i\in\phi^{-1}(k)} \pi_i}, \quad k, l \in \bar{\mathcal{V}}. \tag{3.18}$$

By substituting (3.2) and (3.8) into (3.18), one can verify that $\bar{A}(\phi)$ is indeed a *transition-rate matrix* for any partition function ϕ, i.e., the row sums of $\bar{A}(\phi)$ are zeros, diagonal entries are negative, and non-diagonal entries are non-negative:

$$\begin{cases} \bar{A}_{kl}(\phi) = \dfrac{\sum_{i\in\phi^{-1}(k)} \sum_{j\in\phi^{-1}(l)} 1/R_{ij}}{\sum_{i\in\phi^{-1}(k)} C_i}, & k \neq l \in \bar{\mathcal{V}} \\ \bar{A}_{kk}(\phi) = -\sum_{l\neq k} \bar{A}_{kl}(\phi), & k \in \bar{\mathcal{V}} \end{cases} \tag{3.19}$$

The super-capacitances and super-resistances can also be expressed in terms of C_i and R_{ij}:

- According to (3.8), the stationary distribution of the aggregated Markov chain has the form:

$$\bar{\pi}_k(\phi) = \frac{\bar{C}_k(\phi)}{\sum_{l\in\bar{\mathcal{V}}} \bar{C}_l(\phi)}, \quad k \in \bar{\mathcal{V}} \tag{3.20}$$

  where $\bar{C}_k(\phi)$ denotes the *super-capacitances* for the kth node. By substituting (3.8) into (3.11), we obtain formula for the optimal stationary distribution:

$$\bar{\pi}_k(\phi) = \sum_{i\in\phi^{-1}(k)} \pi_i = \frac{\sum_{i\in\phi^{-1}(k)} C_i}{\sum_{l\in\bar{\mathcal{V}}} \sum_{j\in\phi^{-1}(l)} C_j}, \quad k \in \bar{\mathcal{V}}. \tag{3.21}$$

  By comparing (3.20) and (3.21), we obtain the formulae for the super-capacitances:

$$\bar{C}_k(\phi) = \sum_{i\in\phi^{-1}(k)} C_i, \quad k \in \bar{\mathcal{V}}. \tag{3.22}$$

- By using (3.19) and (3.22), we obtain the formulae for the *super-resistances*:

$$\bar{R}_{kl}(\phi) = \frac{1}{\bar{C}_k(\phi)\bar{A}_{kl}(\phi)} = \frac{1}{\sum_{i\in\phi^{-1}(k)} \sum_{j\in\phi^{-1}(l)} 1/R_{ij}}, \quad k \neq l \in \bar{\mathcal{V}}. \tag{3.23}$$

Thus, the reduced-order linear model (3.15) corresponds to a reduced RC-network with super-capacitances and super-resistances given by (3.22) and (3.23), respectively. The super-capacitance $\bar{C}_k(\phi)$, given in (3.22), is the equivalent capacitance of parallel configuration of all capacitors in the kth partition. Similarly, the super-resistance $\bar{R}_{kl}(\phi)$ given in (3.23) is the equivalent resistance of parallel configuration of all resistors connecting the kth partition and the lth partition. These observations also serve to provide an intuitive justification of the aggregation approach.

Similar to the full-order model (3.1), the reduced-order model (3.15) is also *conservative* because of the fact that $\bar{A}(\phi)$ is a super-transition-rate matrix. The invariant quantity for the reduced-order model is given by

$$\bar{V}_0 := \sum_{k\in\bar{\mathcal{V}}} \bar{C}_k \bar{T}_k(0).$$

If one chooses the initial condition for the reduced-order model (3.15) as

$$\bar{T}_k(0) = \sum_{i\in\phi^{-1}(k)} (C_i/\bar{C}_k(\phi))T_i(0), \quad k \in \bar{\mathcal{V}}, \tag{3.24}$$

then

$$\bar{V}_0 = \sum_{k\in\bar{\mathcal{V}}} \sum_{i\in\phi^{-1}(k)} C_i T_i(0) = \sum_{i\in\mathcal{V}} C_i T_i(0) = V_0.$$

This implies that the invariant quantity of the linear thermal dynamics is unchanged after the aggregation. The *aggregated thermal distribution* is defined as

$$\bar{f}_k = \frac{\bar{C}_k}{\bar{V}_0}\bar{T}_k, \quad k \in \bar{\mathcal{V}}. \tag{3.25}$$

Recall that we introduce the lifting technique to compare the low- and high-dimensional distributions. The *lifted thermal distribution* is defined as

$$\hat{f}_i = \frac{C_i}{V_0}\hat{T}_i, \quad i \in \mathcal{V} \tag{3.26}$$

where $\hat{T}_i$ is called the *lifted temperature* for the node i. Using (3.13) and choosing the lifting distribution as $\mu = \pi$, we obtain

$$\hat{f}_i = \frac{\pi_i}{\sum_{j\in\psi(i)}\pi_j}\bar{f}_{\phi(i)}. \tag{3.27}$$

Substituting (3.8) and (3.25) into (3.27), we have

$$\hat{f}_i = \frac{C_i}{\sum_{j\in\psi(i)} C_j}\frac{\bar{C}_{\phi(i)}}{\bar{V}_0}\bar{T}_{\phi(i)} = \frac{C_i}{V_0}\bar{T}_{\phi(i)} \tag{3.28}$$

where we use the fact that $\bar{C}_{\phi(i)} = \sum_{j\in\psi(i)} C_j$ and $\bar{V}_0 = V_0$. By comparing (3.26) and (3.28), we have the explicit expression for the lifted temperature

$$\widehat{T}_i = \bar{T}_{\phi(i)}, \quad i \in \mathcal{V}.$$

Note that the lifted temperature $\widehat{T}_i$ of the node i is indeed a temperature quantity for the corresponding aggregated node $\phi(i)$. Thus, we can compare the full and reduced-order models by directly comparing T_i and $\bar{T}_{\phi(i)}$ for each node i.

3.4.2 Aggregated Building Thermal Model

Recall that the outside node is taken as a virtual $(n+1)$th node in the full-order building thermal model (3.1), and the outside temperature is denoted as T_{n+1}. We also take the outside node as a virtual $(m+1)$th node in the reduced-order model and we denote its temperature as $\bar{T}_{m+1}$. That is, for any given partition function ϕ, the building node set $\{1,\ldots,n\}$ is aggregated into the super-node set $\{1,\ldots,m\}$,

and the $(n+1)$th outside node has a one-to-one correspondence to the $(m+1)$th super-node.

Due to the current source interpretation of nonlinear thermal dynamics $L(T, U, Q)$, the current sources connecting to the same group of the aggregated nodes are directly added up to form a super-current source for the corresponding super-node:

- For $k = 1, \ldots, m$, the aggregated nonlinear thermal dynamics is given by:

$$\begin{aligned}\widetilde{L}_k(T, U, \dot{Q}) &= \sum_{i \in \phi^{-1}(k)} C_i L_i(T, U, Q)/\bar{C}_k(\phi) \\ &= (C_{pa}(T^s \bar{U}_k(\phi) - \widetilde{W}_k(\phi)) + \dot{\bar{Q}}_k(\phi))/\bar{C}_k(\phi) \end{aligned} \tag{3.29}$$

  where

$$\bar{U}_k(\phi) := \sum_{i \in \phi^{-1}(k)} U_i, \quad \dot{\bar{Q}}_k(\phi) := \sum_{i \in \phi^{-1}(k)} \dot{Q}_i, \quad \widetilde{W}_k(\phi) := \sum_{i \in \phi^{-1}(k)} U_i T_i. \tag{3.30}$$

- For $k = m+1$, the aggregated nonlinear thermal dynamics is given by:

$$\widetilde{L}_{m+1}(T, U, \dot{Q}) = \eta$$

  where $\eta(t) = \dot{T}_o(t)$ and $T_o(t)$ denotes the outside temperature. The construction here is to make sure $\bar{T}_{m+1}(t) = T_o(t)$ for all $t \geq 0$ in the reduced-order model (3.32) described later.

Since U and Q are external inputs to the full-order model, we can also take $\bar{U}(\phi)$ and $\dot{\bar{Q}}(\phi)$ defined in (3.30) as the super-inputs to the reduced-order model. One problem is that the term $\widetilde{W}(\phi)$ defined in (3.30) depends on T, which is the state vector of the full-order model. We use $\bar{T}_k$ (the temperature of the kth super-node) to approximate T_i (the temperature of the ith node that belongs to the kth group) in $\widetilde{W}_k(\phi)$:

$$\bar{W}_k(\phi) := \sum_{i \in \phi^{-1}(k)} U_i \bar{T}_k = \bar{U}_k(\phi)\bar{T}_k, \quad k = 1, \ldots, m.$$

Replacing $\widetilde{W}_k(\phi)$ by $\bar{W}_k(\phi)$ in (3.29), we approximate $\widetilde{L}_k(T, U, \dot{Q})$ by

$$\bar{L}_k(\bar{T}, \bar{U}(\phi), \dot{\bar{Q}}(\phi)) = \left(C_{pa}\bar{U}_k(\phi)(T^s - \bar{T}_k) + \dot{\bar{Q}}_k(\phi)\right)/\bar{C}_k(\phi) \tag{3.31}$$

for $k = 1, \ldots, m$ and $\bar{L}_{m+1}(\bar{T}, \bar{U}(\phi), \dot{\bar{Q}}(\phi)) = \eta$. Note that the aggregated nonlinear thermal dynamics in (3.31) only depends on super-quantities for the reduced-order model.

By combining the aggregated linear thermal dynamics (3.15) with the aggregated nonlinear thermal (3.31), we obtain the state-space representation of the reduced-order building thermal model:

$$\frac{d\bar{T}}{dt} = \bar{A}(\phi)\bar{T} + \bar{L}(\bar{T}, \bar{U}(\phi), \dot{\bar{Q}}(\phi)). \tag{3.32}$$

The model reduction method proposed in this chapter preserves the RC-network structure of the original building model, that is, the reduced-order model (3.32) is still an RC-network defined with super-nodes with super-edges connecting these super-nodes. According to state-space representation (3.32), the aggregated building thermal dynamics can be also expressed by the following coupled differential equations: For each $k = 1, \ldots, m$,

$$\bar{C}_k(\phi)\frac{d\bar{T}_k}{dt}(t) = \sum_{l \in \bar{\mathcal{N}}_k} (\bar{T}_l(t) - \bar{T}_k(t))/\bar{R}_{kl}(\phi) + \dot{\bar{Q}}_k(\phi)(t) + \Delta\bar{H}_k(\phi)(t) \tag{3.33}$$

where $\bar{T}_k$ is the temperature of the kth super-node, $\bar{\mathcal{N}}_k \subset \bar{\mathcal{V}}$ denotes the set of neighbors of the kth super-node, $\dot{\bar{Q}}_k(\phi)$ denotes the heat gain for the kth super-node, and the ventilation heat exchange $\Delta\bar{H}_k(\phi)$ for the kth super-node is given by

$$\Delta\bar{H}_k(\phi)(t) = C_{pa}\dot{\bar{m}}_k^{\text{in}}(\phi)(t)(T^s - \bar{T}_k(t))$$

with the mass flow rate entering the kth super-node given by $\dot{\bar{m}}_k^{\text{in}}(\phi) = \sum_{i \in \phi^{-1}(k)} \dot{m}_i^{\text{in}}$. The initial condition of the reduced-order model (3.33) is chosen as (3.24).

The reduced-order model so far depends on the choice of the partition function ϕ. The sub-optimal partition function ϕ^* is obtained by using the recursive bi-partition algorithm. However, one can also directly choose a sub-optimal ϕ^* based on physical intuition (e.g., floor plans in a multi-zone building), or some other kinds of expert-based heuristics.

3.5 Simulation and Discussion

3.5.1 Simulation Setup

In this section, we apply the aggregation-based model reduction method to the downstream part of the four-zone building HVAC system shown in Fig. 3.1, where each zone is serviced by a single terminal box. The layout of the four-zone building is shown in Fig. 3.1a. Each of the four rooms/zones has an equal floor area of 5×5 m and each wall is 3 m tall, which provides a volumetric area of 75 m^3 for each room. Room 1 has a small window (5 m^2) on the north facing wall, whereas rooms 2 and 4 have larger windows (7 m^2 each) on the east facing wall. Room 3 does not have a window.

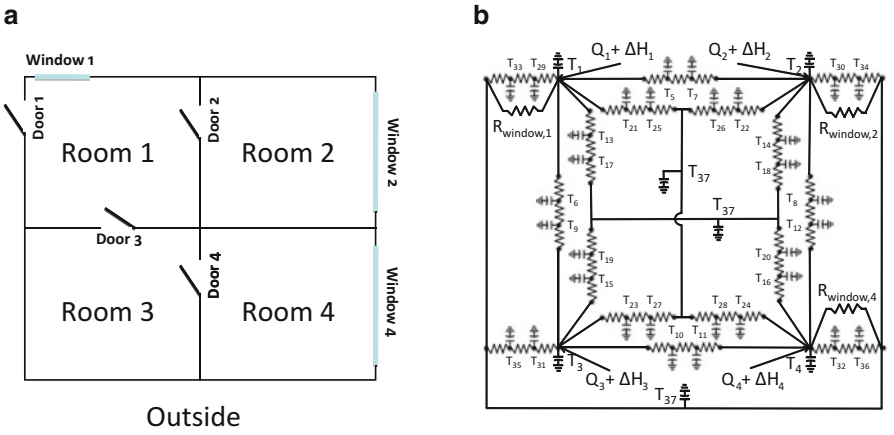

Fig. 3.1 (**a**) The layout of the four-zone building of the HVAC system, and (**b**) its RC-network representation

The HVAC system used for simulation is designed to supply maximal mass flow rate of 0.25 kg/s per room. The supplied air temperature is fixed at $T^s = 12.8\,°\text{C}$. Here we assume that there is no return air and 100% of the outside air is sent to the AHU. The number of occupants in each room is uniformly generated as a random integer between 0 and 4. Outside temperature and outside solar radiation data is obtained for a summer day (05/24/1996) of Gainesville, FL [18]. Numerical results presented here are simulated using ode45 function in Matlab for 24 hours with the time step-size chosen as 10 min. All temperatures are initialized at 24 °C, respectively. The mass flow rates entering four zones are given by $\dot{m}_1^{\text{in}} = 0.15\,\text{kg/sec}$, and $\dot{m}_2^{\text{in}} = \dot{m}_3^{\text{in}} = \dot{m}_4^{\text{in}} = 0\,\text{kg/sec}$. There are two inputs: outside temperature T_0 and the heat gains $\dot{Q}_i$.

3.5.2 *Recursive Bi-partition of Building Graph*

The RC-network representation of the four-zone building is shown in Fig. 3.1b. There are total 36 building nodes plus 1 outside node for the model of this four-zone building: 4 zone nodes $\{1, \ldots, 4\}$, 8 internal-wall nodes $\{5, \ldots, 12\}$, 8 internal-floor nodes $\{13, \ldots, 20\}$, 8 internal-ceiling nodes $\{21, \ldots, 28\}$, 8 external wall nodes $\{29, \ldots, 36\}$, and 1 outside node $\{37\}$. Each node is assigned with a thermal capacitance, and two adjacent nodes are connected with a thermal resistance. The windows are modeled as single resistors since they have relatively little capacitance. The values of capacitances and resistances used for simulation are obtained from commercially available software Carrier Hourly Analysis Program [19]. The outside node is assumed to have a very large capacitance $C_{37} = 10^{10}\,\text{KJ}/(\text{m}^2\text{K})$.

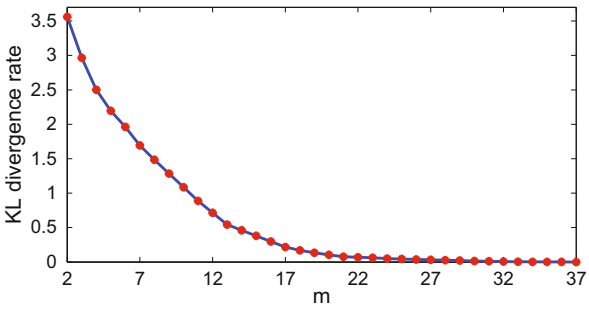

Fig. 3.2 Modeling error (KL divergence rate) in aggregating the linear thermal dynamics vs. number of partitions

The recursive bi-partition algorithm is used to find sub-optimal partitions of the building graph based on the analysis of the linear thermal dynamics. The first iteration of the algorithm divides the node set into two groups: the first group contains all building nodes: $\{1, 2, \ldots, 36\}$, and the second group contains only the outside node: $\{37\}$. Such a 2-partition result makes sense since it captures the slowest time-scale of building thermal dynamics.

The second iteration of the algorithm leads to a 3-partition, which divides the nodes into three groups: the first group consists of all (zone, wall, ceiling, window, and floor) nodes associated with the room 3, the second group contains all other building nodes associated with the rooms $1, 2, 4$, and the third group contains only the outside node: $\{37\}$. Compared with the 3-partition results, the 4-partition identifies a new group containing all nodes associated with room 1. For the 5-partition, the algorithm returns five groups of nodes with clear physical intuition: group i contains all nodes corresponding to room i, for $i = 1, \ldots, 4$, and group 5 consists of the single outside node $\{37\}$! For $m > 5$, the m-partition further partitions the nodes associated with individual rooms. The largest possible m is 37, which corresponds to no reduction in model order.

Recall that the KL divergence rate (3.14) is used as a measure of the modeling error for aggregating the linear thermal dynamics. Figure 3.2 depicts the KL divergence rate with respect to the number of partitions m for $2 \leq m \leq 37$. We observe from Fig. 3.2 that the modeling error monotonically decreases to the zero as the number of partitions increases to the dimension of the full-order model, and that there is little additional improvement beyond a model order of around 18. Although the KL divergence rate is only applicable to the linear part of the model, one can still use it as a conservative guideline for the reduction of the nonlinear model. In that case, we can guess that for good prediction accuracy, the reduced-order model should have about 18 states. This is verified by simulations we report next.

3.5.3 Simulation of Full- and Reduced-Order Models

The full-order model (3.1) is used to describe the full building thermal dynamics, with 36 building nodes plus 1 outside node. The multiple partition results obtained in Sect. 3.5.2 are used to construct the reduced-order models through aggregation of building nodes into groups, where each group of nodes is represented by a super-node. For $k = 1, \ldots, 36$, the kth-order reduced model (3.32) is used to describe the reduced building thermal dynamics with k super-nodes plus 1 outside node. For comparison, we lift the reduced model to one with 36 building nodes plus 1 outside node (see Sect. 3.4.1 for more details), which allows direct comparison between the temperature of a zone predicted by the full- and reduced-order models.

All simulations reported here are open-loop simulations: the same mass flow rates ($\dot{m}_1^{\text{in}} = 0.15\,\text{kg/sec}$ and $\dot{m}_2^{\text{in}} = \dot{m}_3^{\text{in}} = \dot{m}_4^{\text{in}} = 0\,\text{kg/sec}$) are used as inputs in conducting simulations for both full and reduced-order models. Note that the inputs are aggregated accordingly to obtain the super-inputs for the reduced-order model (see Sect. 3.4.2 for more details). To test the goodness of the reduced-order models, we compare the four zone temperatures simulated by the full- and reduced-order models. When simulated by the full-order model, the temperature of room i is denoted by T_i. When simulated by the reduced-order model, the lifted temperature

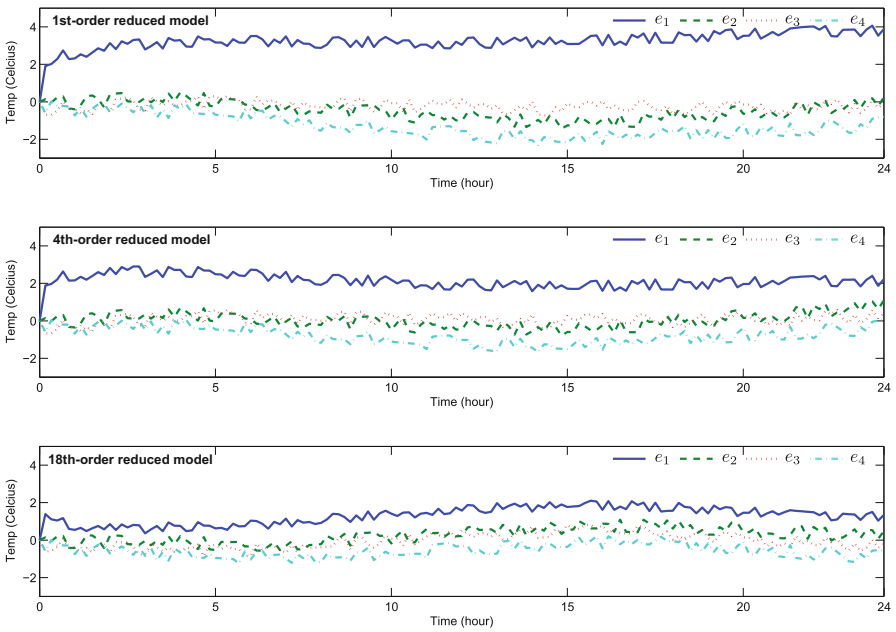

Fig. 3.3 Four zone temperature simulation errors are given by $e_i = \widehat{T}_i - T_i$ for $i = 1, \ldots, 4$, where T_i is the temperature simulated by the full-order model and $\widehat{T}_i$ is the lifted temperature simulated by the (1st-order, 4th-order, and 18th-order) reduced models

of room i is denoted by $\widehat{T}_i$ (see Sect. 3.4.1 for more details). The ith zone temperature prediction error is denoted by $e_i = \widehat{T}_i - T_i$.

Figure 3.3 shows the temperature prediction errors corresponding to reduced-order models with varying degree of reduction: (1) 1st-order reduced model (1 super-node corresponding to all building nodes), (2) 4th-order reduced model (4 super-nodes corresponding to 4 groups of nodes associated with 4 zones), and (3) 18th-order reduced model. Note that a kth-order reduced model corresponds to the $(k+1)$-partition described in Sect. 3.5.2 with k super-building nodes and 1 outside node.

We observe from Fig. 3.3 that, as expected, prediction errors decrease as the order of the reduced model increases. In addition, the conjecture based on KL divergence rate that the 18th-order model will have predictions close to that of the full-order model turns out to be true. In the 18th-order model, the prediction error for the zone with the maximum error (zone 1 here) has a mean of 1.30 °C and standard deviation of 0.46 °C.

We also observe from the Fig. 3.3 that *except for zone 1*, temperature prediction with even the fourth-order model (middle plot), which represents a ninefold reduction in model order, is quite accurate, where the prediction error for the zone with the maximum error (zone 4 here) has a mean of −0.77 °C and the standard deviation of 0.44 °C. However, the mean and standard deviation of prediction error for zone 1 with the fourth-order model are 2.14 °C and 0.37 °C, which is much larger. Thus, large reduction in the model order is not likely to be useful for control design and analysis studies. However, we expect such low order models to be still useful in preliminary building and HVAC system design studies.

The higher error in the temperature prediction of zone 1 could be due to the method's inability to accurately approximate enthalpy dynamics due to the ventilation (note that zone 1 is the only one with the ventilation), or due to the error introduced in lifting the reduced model to a full-order model for purposes of comparison. Future work will examine these factors in greater detail.

The computation time for executing the Matlab simulation code increases as the order of the reduced model increases. For the case considered in this chapter, the computation times for simulation are 6.829, 6.988, 7.623, 349.86 s for the 1st-order, 4th-order, 18th-order, and full 36th-order models, respectively. In practice, one can make a tradeoff between the accuracy and complexity of the reduced-order model by choosing an appropriate order of the reduced model.

3.5.4 Simulation of Super-Zone Models

In a building with a large number of zones, one may want to further reduce the number of zones as well. The aggregation method presented in this chapter can also be used to reduce a large number of zones into as few super-zones as a practitioner wants.

If zone nodes are aggregated into a smaller number of super-zone nodes, there does not exist one-to-one correspondence between a zone node to a single super-zone node. We can't directly compare the zone temperature for the full-order model with the super-zone temperature for the reduced-order model. To compare the full- and reduced-order models, we adopt the following method. Recall that the exogenous inputs for the reduced model can be computed from the exogenous inputs for the full model as described in (3.30), irrespective of what the order of the reduced model is. We do this only for the outside temperature and heat gains for the rooms. The mass flow rate inputs of the reduced model are computed as follows. The desired temperature for the kth super-zone is chosen to be the following linear combination of the desired temperatures all zones of the kth group:

$$\bar{T}_k^{\text{set}}(t) = \sum_{i \in \phi^{-1}(k)} (C_i / \bar{C}_k(\phi)) T_i^{\text{set}}(t).$$

This choice is made to take into account the difference in the heat capacity of the zones, which lead to different energy requirements from the air conditioning system. The same PI controller that was used to compute the mass flow rate for each of the zones in the full-order model is now applied to each super-zone. We then compare the mass flow rates obtained for a super-zone in the reduced-order model with the sum of the mass flow rates for the corresponding zones in the full-order model.

For the four-room building considered here, we aggregate the four zone nodes into three super-zone-nodes: The first super-zone node corresponding to the first zone node, the second super-zone node corresponding to the third zone node, and the third super-zone node corresponding to the aggregation of the second and fourth zone nodes. Then, by fixing the partition assignments for the zone nodes, we can further aggregate the building internal nodes into super-internal-nodes using the recursive bi-partition algorithm.

As before, we consider two reduced-order models: (1) with 18 super-nodes (3 super-zone nodes plus 15 super-internal nodes) and (2) with 24 super-nodes (3 super-zone nodes plus 21 super-internal nodes). By applying the PI controller, we

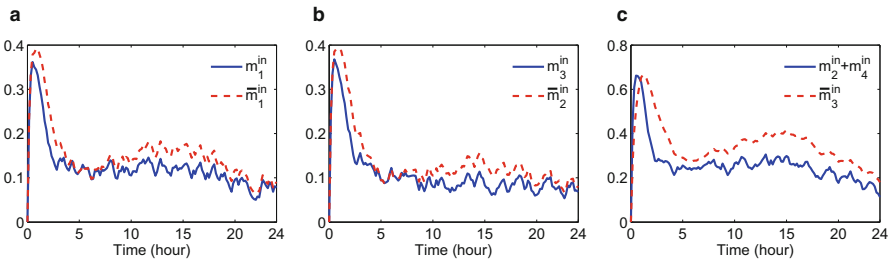

Fig. 3.4 Comparison results of mass flow rates (kg/sec) for (**a**) zone-1 compared with super-zone-1, (**b**) zone-3 compared with super-zone-2, and (**c**) zone-2 and zone-4 compared with super-zone-3, between the full-order model and the reduced 18th-order model

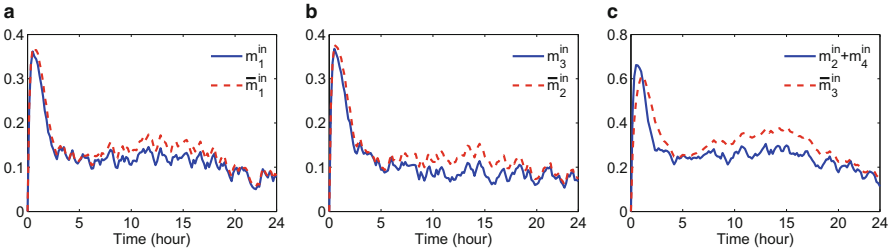

Fig. 3.5 Comparison results of mass flow rates (kg/sec) for (**a**) zone-1 compared with super-zone-1, (**b**) zone-3 compared with super-zone-2, and (**c**) zone-2 and zone-4 compared with super-zone-3, between the full-order model and the reduced 24th-order model

find that all zone or super-zone temperatures track the desired temperatures well for both full- and reduced-order models. We omit the temperature plots here since these are similar to plots shown in the last section. The mass flow rates obtained from the PI controllers for full- and reduced-order models are shown in Fig. 3.4 (for the 18th-order model) and Fig. 3.5 (for the 24th-order model). We observe that:

- For $k = 1, 2, 3$, the mass flow rate $\dot{\bar{m}}_k$ for the kth super-zone corresponds well to the sum of mass flow rates of all zones in the kth group. Since the mass flow rate is the important indicator of the power consumption of the building, the reduced-order model can be used to estimate the power consumption with less complexity.
- The prediction errors of mass flow rates for the 24th-order model is smaller than those for the 18th-order model. In practice, one can make a tradeoff between the accuracy and complexity of the reduced-order model.

3.6 Conclusions and Future Directions

We proposed a method to reduce the order of a multi-zone building thermal model via aggregation of states. We first establish a Markov chain analogy to the linear part of the building model. A recently developed Markov aggregation method is then applied to obtain the optimal aggregation of the state space. Extension of the aggregation method to the nonlinear part of the model is carried out by aggregating inputs accordingly into the super-inputs. A key advantage of the proposed method is that the reduced model is still an RC-network model with the same structure as the original model but with less number of nodes and less parametric information. This makes the reduced model useful not only for simulation and analysis but also for building design iterations.

References

1. F. Oldewurtel, A. Parisio, C. Jones, M. Morari, D. Gyalistras, M. Gwerder, V. Stauch, B. Lehmann, K. Wirth, Energy efficient building climate control using stochastic model predictive control and weather predictions, in *American Control Conference*, July 2010, pp. 5100–5105
2. Y. Ma, G. Anderson, F. Borrelli, A distributed predictive control approach to building temperature regulation, in *Proceedings of American Control Conference*, San Francisco, CA, 2011, pp. 2089–2094
3. S. Goyal, H. Ingley, P. Barooah, Zone-level control algorithms based on occupancy information for energy efficient buildings, in *American Control Conference*, June 2012, pp. 3063–3068
4. J. Scherpen, Balancing for nonlinear systems. Syst. Control Lett. **21**(2), 143–153 (1993)
5. J. Hahn, T.F. Edgar, An improved method for nonlinear model reduction using balancing of empirical Gramians. Comput. Chem. Eng. **26**(10), 1379–1397 (2002)
6. I.J. Couchman, E.C. Kerrigan, C. Bohm, Model reduction of homogeneous-in-the-state bilinear systems with input constraints. Automatica **47**(4), 761–768 (2011)
7. S. Lall, J. Marsden, S. Glavaski, A subspace approach to balanced truncation for model reduction of nonlinear control systems. J. Robust Nonlinear Control **12**. 519–526 (2002)
8. S. Goyal, P. Barooah, A method for model-reduction of nonlinear building thermal dynamics. Energy Build. **47**, 332–340 (2012). Available: http://dx.doi.org/10.1016/j.enbuild.2011.12.005 [Online]
9. K. Deng, P.G. Mehta, S.P. Meyn, Optimal Kullback-Leibler aggregation via the spectral theory of Markov chains. IEEE Trans. Automatic Control **56**(12), 2793–2808 (2011)
10. K. Deng, P. Barooah, P.G. Mehta, S. Meyn, Building thermal model reduction via aggregation of states, in *Proceedings of American Control Conference*, Baltimore, MD, Jun 2010, pp. 5118–5123
11. J.E. Braun, N. Chaturvedi, An inverse gray-box model for transient building load prediction. HVAC&R Res. **8**(1), 73–99 (2002)
12. R. Romijn, L. Ozkan, S. Weiland, J. Ludlage, W. Marquardt, A grey-box modeling approach for the reduction of nonlinear systems. J. Process Control **18**, 906–914 (2008)
13. F. Alghimlas, Building load simulation and validation of an office building, in *Second International Conference for Enhanced Building Operations*, October 2002
14. M. Georgescu, B. Eisenhower, I. Mezic, Creating zoning approximations to building energy models using the Koopman operator, in *Proceedings of IBPSA-USA's SimBuild 2012 Conference*, Madison, Wisconsin, 2012
15. M.M. Gouda, S. Danaher, C. Underwood, Building thermal model reduction using nonlinear constrained optimization. Build. Environ. **37**(12), 1255–1265 (2002)
16. D.W. Stroock, *An Introduction to Markov Processes*. Graduate Texts in Mathematics, vol. 230 (Springer, New York, 2005)
17. D. Revuz, *Markov Chains*. North-Holland Mathematical Library, vol. 11, 2nd edn. (Elsevier/North-Holland, New York, Amsterdam, 1984)
18. National solar radiation data base (NSRDB), 2005, Available: http://rredc.nrel.gov/solar/old_data/nsrdb/1991-2005/tmy3/ [Online]
19. Carrier Corporation, *HAP Quick Reference Guide* (Carrier Corporation, Farmington, CT, 2003)

Part II
Control

Chapter 4
Robust $\mathscr{H}_\infty$ Switching Control of Polytopic Parameter-Varying Systems via Dynamic Output Feedback

Chengzhi Yuan, Chang Duan, and Fen Wu

Abstract The problem of designing a globally optimal robust output-feedback controller for time-varying polytopic uncertain systems is a well-known non-convex optimization problem. In this paper, new sufficient conditions for robust $\mathscr{H}_\infty$ output-feedback control synthesis are proposed in terms of a special type of bilinear matrix inequalities (BMIs), which can be solved effectively using linear matrix inequality (LMI) optimization plus a line search. In order to reduce the conservatism of robust output-feedback control methods based on single quadratic Lyapunov function, we utilize multiple Lyapunov functions. The associated robust output-feedback controller is constructed as a switching-type full-order dynamic output-feedback controller, consisting of a family of linear subcontrollers and a min-switching logic. The proposed approach features the important property of computational efficiency with stringent performance. Its effectiveness and advantages have been demonstrated through numerical studies.

Keywords Parameter-varying system • Switched control • Robust control

4.1 Introduction

During the past decades, a great deal of attention was devoted to the study of systems with time-varying parametric uncertainties, due to their theoretical importance in control theory and widespread applications in practical engineering problems. Both issues of stability and control design for these types of systems have been examined extensively in the literature (see, e.g., [1–5] and the references therein). A typical robust control strategy is to construct a single linear time-invariant (LTI) controller

C. Yuan (✉) • F. Wu
Department of Mechanical and Aerospace Engineering, North Carolina State University, Raleigh, NC, USA
e-mail: cyuan2@ncsu.edu; fwu@eos.ncsu.edu

C. Duan
Department of Mechanical Engineering, Prairie View A&M University, Prairie View, TX, USA
e-mail: chduan@pvamu.edu

Q. Zhang et al., *Automotive Air Conditioning*, DOI 10.1007/978-3-319-33590-2_4

for norm-bounded uncertain systems using a single quadratic Lyapunov function [4, 6]. Some classical works along this line are worth to be mentioned. Different tools for both robustness analysis and controller design for systems subject to structured uncertainties can be found in [4, 7–9], while [2, 10–12] considered similar problems for systems with unstructured uncertainties. One potential drawback of these classical methods lies in the conservatism due to the use of a single quadratic Lyapunov function. In recent years, more advanced robust control approaches were proposed to achieve better controlled performance. In particular, originated from the pioneering works [13, 14], different switching-type robust controllers have been proposed for various systems with different types of uncertainties, such as [15, 16] on linear fractional transformation (LFT) systems and [7, 17] for polytopic uncertain systems, both of which utilized the multiple Lyapunov function technique from the switching control context [18]. A comprehensive review of the literature on robust control of uncertain systems, including some recent results from either deterministic or probabilistic perspective, can be found in [5].

Different from the state-feedback control case, the problem of designing a robust output-feedback controller for linear uncertain systems is known to be difficult. The main source of difficulty stems from the non-convex nature of the problem itself. Specifically, the associated robust control synthesis problem is typically represented as a bilinear matrix inequality (BMI) optimization problem for most design objectives. This type of non-convex optimization problems is NP-hard, even under the single quadratic Lyapunov function framework (see, e.g., [4, 6, 19–21]). Various approaches have been reported to tackle the non-convexity issue. Some rely on heuristic optimization algorithms to attain a locally optimal solution [19, 22], which could be very involved and time-consuming; some resort to certain mathematical relaxations to arrive at a convex synthesis condition but of more conservatism [20]. As such, developing an effective robust output-feedback control synthesis framework that simultaneously renders stringent performance and computational efficacy is urgently desirable but still remains as an open problem.

In this paper, we propose a new robust switching output-feedback (RSOF) control scheme for a class of polytopic parameter-varying uncertain systems. Different from the classical robust output-feedback control techniques, the proposed RSOF controller consists of a family of full-order dynamic LTI subcontrollers and a min-switching logic that governs the switching among them, which therefore results in a switched closed-loop system with time-varying polytopic uncertainties. The basic idea applied here for switching stability analysis and controller design is borrowed from the switching control literature (see, for instance, [17, 18, 23–28]). In particular, motivated by the methodologies from [17] on switched state-feedback control of polytopic uncertain systems, [29] on asynchronous switching output-feedback controller synthesis, and [30] on stabilization of switched linear systems via min-switching control, we will first derive the analysis conditions for robust $\mathscr{H}_\infty$ stability of the resulting switched closed loop by using piecewise switched Lyapunov functions. Then, based on the analysis conditions, the associated robust switching control synthesis problem is formulated as a special type of BMIs, which can be solved effectively in terms of LMIs plus a line search. The proposed

switching control design scheme advances existing methods for robust output-feedback control synthesis in two important ways: better achievable controlled performance in terms of $\mathscr{H}_\infty$ criterion due to the adoption of piecewise switched Lyapunov functions; reduced computational complexity by solving a convex LMI-based optimization coupled with a single line search. Numerical examples are given to illustrate the effectiveness and advantages of the proposed design approach.

The rest of the paper is organized as follows. The problem statement and the form of RSOF controller are presented in Sect. 4.2. Sections 4.3 and 4.4 contain the main results of this paper including the robust analysis and control synthesis conditions, respectively. Simulation results are provided in Sect. 4.5. Conclusions are finally drawn in Sect. 4.6.

Notation $\mathbb{R}$ stands for the set of real numbers and $\mathbb{R}_+$ for the positive real numbers. The set of non-negative integers is denoted by $\mathbb{N}_+$. $\mathbb{R}^{m\times n}$ is the set of real $m \times n$ matrices, and $\mathbb{R}^n$ represents the set of real $n \times 1$ vectors. The transpose of a real matrix M is denoted by M^T. The Hermitian operator $He\{\cdot\}$ is defined as $He\{M\} = M + M^T$ for real matrices. The identity matrix of any dimension is denoted by I. $\mathbb{S}^n$ and $\mathbb{S}^n_+$ are used to denote the set of real symmetric $n \times n$ matrices and positive definite matrices, respectively. If $M \in \mathbb{S}^n$, then $M > 0$ ($M \geq 0$) indicates that M is a positive definite (positive semi-definite) matrix and $M < 0$ ($M \leq 0$) denotes a negative definite (negative semi-definite) matrix. A block diagonal matrix with matrices $X_1, X_2, \ldots, X_p$ on its main diagonal is denoted by $diag\{X_1, X_2, \ldots, X_p\}$. Furthermore, we use the symbol $\star$ in LMIs to denote entries that follow from symmetry. For $x \in \mathbb{R}^n$, its norm is defined as $\|x\| := (x^T x)^{1/2}$. The space of square integrable functions is denoted by $\mathscr{L}_2$, that is, for any $u \in \mathscr{L}_2$, $\|u\|_2 := \left(\int_0^\infty u^T(t)u(t)dt\right)^{1/2} < \infty$. For two integers $k_1 < k_2$, we denote $\mathbf{I}[k_1, k_2] = \{k_1, k_1 + 1, \ldots, k_2\}$. The set of Metzler matrices $\mathscr{M}$ consists of all matrices $\Pi \in \mathbb{R}^{N\times N}$ with elements π_{ji}, such that $\pi_{ji} \geq 0$ for all $i, j \in \mathbf{I}[1, N]$ with $i \neq j$ and $\sum_{j=1}^N \pi_{ji} = 0$ for all $i \in \mathbf{I}[1, N]$.

4.2 Problem Statement

Consider the following linear system with uncertain time-varying parameters:

$$\begin{bmatrix} \dot{x}_p(t) \\ e(t) \\ y(t) \end{bmatrix} = \begin{bmatrix} A_p(\xi(t)) & B_{p1}(\xi(t)) & B_{p2}(\xi(t)) \\ C_{p1}(\xi(t)) & D_{p11}(\xi(t)) & D_{p12}(\xi(t)) \\ C_{p2}(\xi(t)) & D_{p21}(\xi(t)) & D_{p22}(\xi(t)) \end{bmatrix} \begin{bmatrix} x_p(t) \\ d(t) \\ u(t) \end{bmatrix} \tag{4.1}$$

where the vectors $x_p \in \mathbb{R}^{n_x}, u \in \mathbb{R}^{n_u}, d \in \mathbb{R}^{n_d}, y \in \mathbb{R}^{n_y}$, and $e \in \mathbb{R}^{n_e}$ denote the plant state, control input, exogenous disturbance, measurement output, and error (performance) output, respectively. The system matrices are uncertain and time-varying, they are given by the convex combination

$$\begin{bmatrix} A_p(\xi(t)) & B_{p1}(\xi(t)) & B_{p2}(\xi(t)) \\ C_{p1}(\xi(t)) & D_{p11}(\xi(t)) & D_{p12}(\xi(t)) \\ C_{p2}(\xi(t)) & D_{p21}(\xi(t)) & D_{p22}(\xi(t)) \end{bmatrix} = \sum_{i=1}^{N_p} \xi_i(t) \begin{bmatrix} A_{p,i} & B_{p1,i} & B_{p2,i} \\ C_{p1,i} & D_{p11,i} & D_{p12,i} \\ C_{p2,i} & D_{p21,i} & D_{p22,i} \end{bmatrix} \tag{4.2}$$

where the constant matrices at the polytope vertex, i.e., $(A_{p,i}, B_{p1,i}, B_{p2,i}, C_{p1,i}, D_{p11,i}, D_{p12,i}, C_{p2,i}, D_{p21,i}, D_{p22,i})$ for all $i \in \mathbf{I}[1, N_p]$, are known for controller design. The vector $\xi(t) := [\xi_1(t) \ \ldots \ \xi_{N_p}(t)]^T \in \mathbb{R}^{N_p}$ represents the time-varying parametric uncertainty which is not measurable in real time, and belongs to the unitary simplex Λ defined by

$$\Lambda = \left\{ \lambda \in \mathbb{R}^{N_p} : \sum_{i=1}^{N_p} \lambda_i = 1, \ \lambda_i \geq 0, \ \forall i \in \mathbf{I}[1, N_p] \right\} \tag{4.3}$$

To ease the notation and whenever the context is clear, the explicit time dependence of vector $\xi(t) \in \Lambda$ will be dropped. Furthermore, for simplicity of presentation, we have the following assumptions regarding system (4.1):

Assumption 1. *$(A_{p,i}, B_{p2,i}, C_{p2,i})$ is stabilizable and detectable for any $i \in \mathbf{I}[1, N_p]$.*

Assumption 2. *Matrices $(B_{p2,i}, C_{p2,i}, D_{p12,i}) = (B_{p2}, C_{p2}, D_{p12})$ are constant matrices, and $D_{p22,i} = 0$ for all $i \in \mathbf{I}[1, N_p]$.*

We stress that these two assumptions are made without losing any generality. Assumption 1 is necessary to guarantee the existence of an output-feedback stabilizing controller from y to u for each subsystem of (4.1) on the polytope vertices. In the second assumption, $D_{p22,i} = 0$ can be relaxed using the well-known loop transformation technique [4], while the assumptions on matrices $(B_{p2,i}, C_{p2,i}, D_{p12,i})$ can also be satisfied by adding stable pre- and post-filters to the input and output channels, respectively [31]. An illustrative example will be given in Sect. 4.5 (Example 1) to show how to satisfy this assumption.

Keeping in mind that the time-varying uncertainty $\xi \in \Lambda$ is not available for feedback control use, the objective of this work is to design an RSOF control law such that the overall closed-loop system is asymptotically stable and achieves certain performance level from the disturbance d to the error output e for all uncertain parameter $\xi \in \Lambda$.

To fulfill this objective, we will construct the following dynamic RSOF controller:

$$\begin{bmatrix} \dot{x}_c(t) \\ u(t) \end{bmatrix} = \begin{bmatrix} A_{c,\sigma(x_c(t))} & B_{c,\sigma(x_c(t))} \\ C_{c,\sigma(x_c(t))} & D_{c,\sigma(x_c(t))} \end{bmatrix} \begin{bmatrix} x_c(t) \\ y(t) \end{bmatrix} \tag{4.4}$$

where $x_c \in \mathbb{R}^{n_c}$ is the controller state with its dimension n_c to be determined. $\sigma(x_c(t))$ is a switching rule of controller that selects a particular sequence of LTI subcontrollers among N_p available ones defined by $(A_{c,j}, B_{c,j}, C_{c,j}, D_{c,j})$ with $j \in \mathbf{I}[1, N_p]$. Its value is determined by the min-switching strategy as shown in

Fig. 4.1, where j_q is the current active controller index, and $x_{cl} := [x_p^T \; x_c^T]^T$. Matrices $P_{j_q} \in \mathbb{S}_+^{n_x+n_c}$ are positive definite. The matrices P_j together with matrices $(A_{c,j}, B_{c,j}, C_{c,j}, D_{c,j})$ $(\forall j \in \mathbf{I}[1, N_p])$ of compatible dimensions are subject to design.

The closed-loop system formed by interconnecting the controlled plant (4.1) and the RSOF controller (4.4) can be written in the following switched polytopic form:

$$\begin{bmatrix} \dot{x}_{cl}(t) \\ e(t) \end{bmatrix} = \begin{bmatrix} A_{cl,\xi\sigma} & B_{cl,\xi\sigma} \\ C_{cl,\xi\sigma} & D_{cl,\xi\sigma} \end{bmatrix} \begin{bmatrix} x_{cl}(t) \\ d(t) \end{bmatrix} \tag{4.5}$$

where $x_{cl} = [x_p^T \; x_c^T]^T$ and

$$\begin{aligned} A_{cl,\xi\sigma} &= \begin{bmatrix} A_p(\xi) + B_{p2}D_{c,\sigma}C_{p2} & B_{p2}C_{c,\sigma} \\ B_{c,\sigma}C_{p2} & A_{c,\sigma} \end{bmatrix}, \\ B_{cl,\xi\sigma} &= \begin{bmatrix} B_{p1}(\xi) + B_{p2}D_{c,\sigma}D_{p21}(\xi) \\ B_{c,\sigma}D_{p21}(\xi) \end{bmatrix}, \\ C_{cl,\xi\sigma} &= \begin{bmatrix} C_{p1}(\xi) + D_{p12}D_{c,\sigma}C_{p2} & D_{p12}C_{c,\sigma} \end{bmatrix}, \\ D_{cl,\xi\sigma} &= D_{p11}(\xi) + D_{p12}D_{c,\sigma}D_{p21}(\xi). \end{aligned}$$

Moreover, we define for all $i, j \in \mathbf{I}[1, N_p]$,

$$A_{cl,ij} = \begin{bmatrix} A_{p,i} + B_{p2}D_{c,j}C_{p2} & B_{p2}C_{c,j} \\ B_{c,j}C_{p2} & A_{c,j} \end{bmatrix}, \quad B_{cl,ij} = \begin{bmatrix} B_{p1,i} + B_{p2}D_{c,j}D_{p21,i} \\ B_{c,j}D_{p21,i} \end{bmatrix}$$

$$C_{cl,ij} = \begin{bmatrix} C_{p1,i} + D_{p12}D_{c,j}C_{p2} & D_{p12}C_{c,j} \end{bmatrix}, \quad D_{cl,ij} = D_{p11,i} + D_{p12}D_{c,j}D_{p21,i}.$$

Then, we have

$$A_{cl,\xi j} = \sum_{i=1}^{N_p} \xi_i A_{cl,ij}, \quad B_{cl,\xi j} = \sum_{i=1}^{N_p} \xi_i B_{cl,ij},$$

$$C_{cl,\xi j} = \sum_{i=1}^{N_p} \xi_i C_{cl,ij}, \quad D_{cl,\xi j} = \sum_{i=1}^{N_p} \xi_i D_{cl,ij}.$$

for all $j \in \mathbf{I}[1, N_p]$.

In this paper, the robust $\mathscr{H}_\infty$ control problem will be considered. More precise descriptions about this problem is given as follows:

Problem 4.1. Given the uncertain system (4.1). The robust $\mathscr{H}_\infty$ control design objective is to determine matrices $(A_{c,j}, B_{c,j}, C_{c,j}, D_{c,j}, P_j)$ subject to (4.4) and the switching strategy in Fig. 4.1, such that the switched closed-loop system in (4.5) is robustly asymptotically stable and achieves a minimal worst-case $\mathscr{H}_\infty$ norm γ_∞ defined by

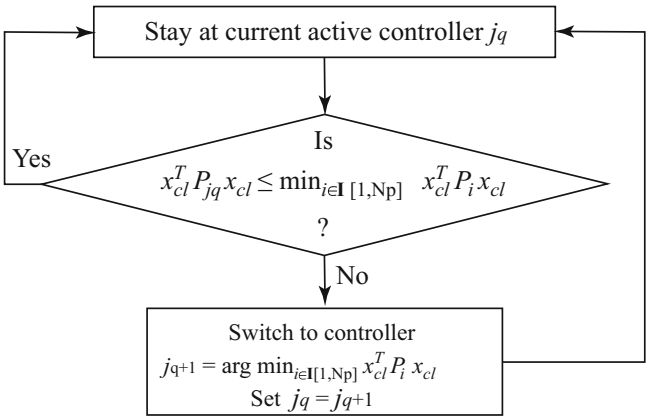

Fig. 4.1 Min-switching strategy

$$\max_{\xi\in\Lambda} \sup_{\|d\|_2\neq 0} \frac{\|e\|_2}{\|d\|_2} < \gamma_\infty. \tag{4.6}$$

With respect to the $\mathscr{H}_\infty$ control problem, the following sections will be devoted to studying the robust stability property of the switched closed-loop system (4.5) under the min-switching logic in Fig. 4.1, and subsequently deriving computationally tractable conditions for the RSOF controller synthesis.

4.3 Robust Analysis via Min-Switching

In this section, we will first present the analysis conditions for robust $\mathscr{H}_\infty$ performance of the time-varying switched polytopic system (4.5) by using multiple quadratic Lyapunov functions and parameter-dependent Metzler matrix [23]. Specifically, we will utilize the parameter-dependent Metzler matrix $\Pi(\xi) : \Lambda \to \mathbb{R}^{N_p\times N_p}$ with elements given by

$$\pi_{ij}(\xi) := \begin{cases} \tau_j\xi_i, & i \neq j \\ \tau_j(\xi_j - 1), & i = j \end{cases} \tag{4.7}$$

where $\tau_j \geq 0$ for all $j \in \mathbf{I}[1, N_p]$. It can be easily verified through the same arguments as in [23] that $\Pi(\xi) \in \mathscr{M}$ for all $\xi \in \Lambda$.

Then, we have the following theorem summarize the $\mathscr{H}_\infty$ analysis conditions:

Theorem 4.1. *Given a scalar $\gamma_\infty \in \mathbb{R}_+$, the RSOF controller (4.4) with the min-switching strategy as shown in Fig. 4.1 globally asymptotically stabilizes the time-varying polytopic uncertain system (4.1) and renders an $\mathscr{H}_\infty$ performance level less*

than γ_∞, if there exist matrices $P_j \in \mathbb{S}_+^{n_x+n_c}$, and scalars $\tau_j \geq 0$ such that

$$\begin{bmatrix} He\{P_j A_{cl,ij}\} + \tau_j(P_i - P_j) & \star & \star \\ B_{cl,ij}^T P_j & -\gamma_\infty^2 I & \star \\ C_{cl,ij} & D_{cl,ij} & -I \end{bmatrix} < 0 \tag{4.8}$$

hold for all $i, j \in \mathbf{I}[1, N_p]$.

Proof. Consider the closed-loop system (4.5), we define the following piecewise Lyapunov function:

$$V(x_{cl}) := x_{cl}^T P_{j_q} x_{cl} \tag{4.9}$$

where $P_{j_q} \in \mathbb{S}_+^{n_x+n_c}$ and $j_q \in \mathbf{I}[1, N_p]$ are the current active subcontroller index determined by the min-switching strategy in Fig. 4.1. Then, multiplying ξ_i to both sides of inequality (4.8) and summing up from $i = 1$ to $i = N_p$, it yields

$$\begin{bmatrix} He\{P_j A_{cl,\xi j}\} + \tau_j \sum_{i=1}^{N_p} \xi_i(P_i - P_j) & \star & \star \\ B_{cl,\xi j}^T P_j & -\gamma_\infty^2 I & \star \\ C_{cl,\xi j} & D_{cl,\xi j} & -I \end{bmatrix} < 0 \tag{4.10}$$

We first examine the stability property for the closed-loop system (4.5) with $d \equiv 0$. In light of the definition in (4.7), the min-switching strategy in Fig. 4.1, and since $\tau_j, \xi_i \geq 0$ ($\forall i, j \in \mathbf{I}[1, N_p]$), we have

$$\tau_{j_q} \sum_{i=1}^{N_p} \xi_i x_{cl}^T (P_i - P_{j_q}) x_{cl} = \sum_{i=1}^{N_p} \pi_{ij_q}(\xi) x_{cl}^T P_i x_{cl} \geq \sum_{i=1}^{N_p} \pi_{ij_q}(\xi) x_{cl}^T P_{j_q} x_{cl} = 0 \tag{4.11}$$

Therefore, the $(1, 1)$ element of condition (4.10) ensures

$$\dot{V}(x_{cl}) = x_{cl}^T (A_{cl,\xi j_q}^T P_{j_q} + P_{j_q} A_{cl,\xi j_q}) x_{cl} < 0$$

for $x_{cl} \neq 0$. Let t_q^- denote the time when the controller switched out from j_qth subcontroller and t_q^+ be the time when the controller switched to the next subcontroller. Then, at t_q^-, condition $x_{cl}^T P_{j_q} x_{cl} \leq \min_{i \in \mathbf{I}[1,N_p]} x_{cl}^T P_i x_{cl}$ must be violated, that is,

$$\min_{i \in \mathbf{I}[1,N_p]} x_{cl}^T(t_q^-) P_i x_{cl}(t_q^-) < x_{cl}^T(t_q^-) P_{j_q} x_{cl}(t_q^-)$$

Since the min-switching strategy determines $j_{q+1} = \arg\min_{i \in \mathbf{I}[1,N_p]} x_{cl}^T P_i x_{cl}$, that is,

$$x_{cl}^T(t_q^+) P_{j_{q+1}} x_{cl}(t_q^+) = \min_{i \in \mathbf{I}[1,N_p]} x_{cl}^T(t_q^-) P_i x_{cl}(t_q^-)$$

Then, we have $x_{cl}^T(t_q^+)P_{j_{q+1}}x_{cl}(t_q^+) < x_{cl}^T(t_q^-)P_{j_q}x_{cl}^T(t_q^-)$, which implies $V(x_{cl}(t_q^+)) < V(x_{cl}(t_q^-))$, and $V(x_{cl})$ thus satisfies the monotonically non-increasing condition. According to the Theorem 2.3 in [32], the switched system (4.5) is globally asymptotically stable.

Now, we examine the closed-loop $\mathscr{H}_\infty$ performance. Through Schur complement, condition (4.10) with (4.11) gives

$$\begin{bmatrix} He\{P_jA_{cl,\xi j}\} & \star \\ B_{cl,\xi j}^T P_j & -\gamma_\infty^2 I \end{bmatrix} + \begin{bmatrix} C_{cl,\xi j}^T \\ D_{cl,\xi j}^T \end{bmatrix} \begin{bmatrix} C_{cl,\xi j} & D_{cl,\xi j} \end{bmatrix} < 0$$

Multiplying $[x_{cl}^T \ d^T]$ from the left of the above condition and its transpose to the right, it yields

$$\dot{V}(x_{cl}) + e^T e - \gamma_\infty^2 d^T d < 0$$

Integrating both sides of the above condition from $t = 0$ to ∞ and taking into account that under zero initial condition $V(x_{cl}(0)) = 0$ and $V(x_{cl}(\infty)) \geq 0$, we can conclude that $\|e\|_2 < \gamma_\infty \|d\|_2$.

Remark 4.1. Compared with classical results on robust stability analysis of linear parameter-varying (LPV) systems [4], we have adopted a piecewise switched Lyapunov function instead of using a single quadratic Lyapunov function, which is motivated from the context of switching control [18, 23]. The resulting conditions Theorem 4.1 for $\mathscr{H}_\infty$ control improve classical results in the sense that quadratic stability of each system matrix $A_{cl,ij}$ with $i, j \in \mathbf{I}[1, N_p]$ and $i \neq j$ is not necessarily required to guarantee feasibility.

4.4 RSOF Controller Synthesis

Based on the analysis results in the previous section, we are in the position to study the $\mathscr{H}_\infty$ control synthesis problem for the RSOF controller (4.4). The RSOF control synthesis problem requires the determination of the coefficient matrices $(A_{c,j}, B_{c,j}, C_{c,j}, D_{c,j})$ in the controller dynamics (4.4) and P_j with respect to the min-switching strategy in Fig. 4.1, for all $j \in \mathbf{I}[1, N_p]$. However, since the plant state x_p is not always available for feedback control use, and in order to make the switching logic in Fig. 4.1 implementable, we will specify the Lyapunov matrices with a prescribed structure so as to structurally incorporate switching rules that depend only on available information, i.e.,

$$P_j = \begin{bmatrix} S & N \\ N^T & X_j \end{bmatrix}, \tag{4.12}$$

where $S \in \mathbb{S}_+^{n_x}, N \in \mathbb{R}^{n_x \times n_c}$, and $X_j \in \mathbb{S}_+^{n_c}$, for all $j \in \mathbf{I}[1, N_p]$. We aim to derive computationally tractable conditions, such that all these controller coefficient matrices can be jointly synthesized through convex optimization. To this end, we first introduce the following lemma, which is useful in the subsequent derivation for our main results.

Lemma 4.1. *Given a symmetric matrix Υ_0 and matrices Υ_1, Υ_2 with compatible dimensions, condition $\Upsilon_0 + \begin{bmatrix} 0 & \star \\ \Upsilon_2^T \Upsilon_1 & 0 \end{bmatrix} < 0$ holds if and only if the following condition holds for some positive number ϵ.*

$$\begin{bmatrix} \Upsilon_0 - \begin{bmatrix} \epsilon \Upsilon_1^T \Upsilon_1 & \star \\ 0 & \frac{1}{\epsilon} \Upsilon_2^T \Upsilon_2 \end{bmatrix} & \star \\ \begin{bmatrix} \epsilon \Upsilon_1 & \Upsilon_2 \end{bmatrix} & -\epsilon I \end{bmatrix} < 0 \tag{4.13}$$

Proof. Through Schur complement, condition (4.13) is equivalent to

$$\Upsilon_0 - \begin{bmatrix} \epsilon \Upsilon_1^T \Upsilon_1 & \star \\ 0 & \frac{1}{\epsilon} \Upsilon_2^T \Upsilon_2 \end{bmatrix} + \begin{bmatrix} \epsilon \Upsilon_1^T \Upsilon_1 & \star \\ \Upsilon_2^T \Upsilon_1 & \frac{1}{\epsilon} \Upsilon_2^T \Upsilon_2 \end{bmatrix} = \Upsilon_0 + \begin{bmatrix} 0 & \star \\ \Upsilon_2^T \Upsilon_1 & 0 \end{bmatrix} < 0.$$

Then, using this lemma and the analysis results in Theorem 4.1, we have the following theorem solve the robust $\mathscr{H}_\infty$ control synthesis problem in terms of matrix inequalities.

Theorem 4.2. *Given tunable scalars $\tau_j \geq 0$, if there exist positive definite matrices $R_j, \hat{S} \in \mathbb{S}_+^{n_x}$, symmetric matrices $T_{ij} \in \mathbb{S}^{n_x}$, rectangular matrices $\hat{A}_{c,j} \in \mathbb{R}^{n_x \times n_x}, \hat{B}_{c,j} \in \mathbb{R}^{n_x \times n_y}, \hat{C}_{c,j} \in \mathbb{R}^{n_u \times n_x}, \hat{D}_{c,j} \in \mathbb{R}^{n_u \times n_y}$, and positive scalars $\hat{\epsilon}, \hat{\gamma}_\infty \in \mathbb{R}_+$ such that for all $i, j \in \mathbf{I}[1, N_p]$, the following conditions hold:*

$$\begin{bmatrix} He\{A_{p,i} R_j + B_{p2} \hat{C}_{c,j}\} + \tau_j T_{ij} - 2R_j + \hat{\epsilon} I & \star \\ \hat{A}_{c,j} + \hat{\epsilon} A_{p,i}^T + C_{p2}^T \hat{D}_{c,j}^T B_{p2}^T & He\{\hat{S} A_{p,j} + \hat{B}_{c,j} C_{p2}\} + \hat{\epsilon} I \\ \hat{\epsilon} B_{p1,i}^T + D_{p21,i}^T \hat{D}_{c,j}^T B_{p2}^T & B_{p1,i}^T \hat{S} + D_{p21,i}^T \hat{B}_{c,j}^T \\ C_{p1,i} R_j + D_{p12} \hat{C}_{c,j} & \hat{\epsilon} C_{p1,i} + D_{p12} \hat{D}_{c,j} C_{p2} \\ R_j & (A_{p,i} - A_{p,j})^T \hat{S} \end{bmatrix}$$

$$\begin{bmatrix} \star & \star & \star \\ \star & \star & \star \\ -\hat{\gamma}_\infty^2 I & \star & \star \\ \hat{\epsilon} D_{p11,i} + D_{p12} \hat{D}_{c,j} D_{p21,i} & -I & \star \\ 0 & 0 & -\hat{\epsilon} I \end{bmatrix} < 0, \tag{4.14}$$

$$\begin{bmatrix} T_{ij} + R_j & \star & \star \\ R_j & R_i & \star \\ \hat{\epsilon} I & \hat{\epsilon} I & \hat{S} \end{bmatrix} \geq 0, \quad \begin{bmatrix} R_j & \star \\ \hat{\epsilon} I & \hat{S} \end{bmatrix} > 0. \tag{4.15}$$

Then, the time-varying polytopic uncertain system (4.1) is globally asymptotically stabilized by the RSOF controller (4.4) of order $n_c = n_x$, and the closed-loop $\mathscr{H}_\infty$ performance level is less than $\gamma_\infty = \frac{\hat{\gamma}_\infty}{\hat{\epsilon}}$ under the min-switching strategy with the condition in Fig. 4.1 replaced by

$$x_c^T X_j x_c \leq \min_{i \in \mathbf{I}[1,N_p]} x_c^T X_i x_c, \tag{4.16}$$

where $X_j = -N^T R_j M_j^{-T}$, $M_j N^T = I - R_j S$, and $S = \frac{1}{\hat{\epsilon}^2}\hat{S}$. Furthermore, the coefficient matrices of the RSOF controller are given by

$$\begin{bmatrix} A_{c,j} & B_{c,j} \\ C_{c,j} & D_{c,j} \end{bmatrix} = \begin{bmatrix} \hat{\epsilon}N & \hat{\epsilon}SB_{p2} \\ 0 & I \end{bmatrix}^{-1} \begin{bmatrix} \hat{A}_{c,j} - \hat{\epsilon}SA_{p,j}R_j & \hat{B}_{c,j} \\ \hat{C}_{c,j} & \hat{D}_{c,j} \end{bmatrix} \begin{bmatrix} M_j^T & 0 \\ C_{p2}R_j & \hat{\epsilon}I \end{bmatrix}^{-1}. \tag{4.17}$$

for all $j \in \mathbf{I}[1, N_p]$.

Proof. According to Theorem 4.1, and using the partitions in (4.12), we define for all $j \in \mathbf{I}[1, N_p]$,

$$Z_{1,j} = \begin{bmatrix} R_j & I \\ M_j^T & 0 \end{bmatrix}, \quad Z_2 = \begin{bmatrix} I & S \\ 0 & N^T \end{bmatrix}, \tag{4.18}$$

such that $P_j Z_{1,j} = Z_2$ and $M_j N^T = I - R_j S$, which implies $X_j = -N^T R_j M_j^{-T}$. Moreover, we specify

$$\tilde{Z}_{1,j} = \begin{bmatrix} R_j & \hat{\epsilon}I \\ M_j^T & 0 \end{bmatrix}, \quad \hat{Z}_2 = \begin{bmatrix} I & \hat{\epsilon}S \\ 0 & \hat{\epsilon}N^T \end{bmatrix}, \tag{4.19}$$

which gives $P_j \tilde{Z}_{1,j} = \hat{Z}_2$. The definition of $\hat{\epsilon} > 0$ will be given later. Based on condition (4.15), it can be verified that $\tilde{Z}_{1,j}^T P_j \tilde{Z}_{1,j} = \begin{bmatrix} R_j & \hat{\epsilon}I \\ \hat{\epsilon}I & \hat{S} \end{bmatrix} > 0$, in turn, $P_j > 0$ as $\tilde{Z}_{1,j}$ is nonsingular.

Then, by performing congruence transformation with matrix $diag\{\tilde{Z}_{1,j}, \hat{\epsilon}I, I\}$ on condition (4.8), we obtain the following results:

$$\begin{aligned} \tilde{Z}_{1,j}^T P_j A_{cl,ij} \tilde{Z}_{1,j} = \hat{Z}_2^T A_{cl,ij} \tilde{Z}_{1,j} &= \begin{bmatrix} A_{p,i}R_j + B_{p2}\hat{C}_{c,j} & \hat{\epsilon}A_{p,i} + B_{p2}\hat{D}_{c,j}C_{p2} \\ \hat{A}_{c,j} + \hat{\epsilon}S(A_{p,i} - A_{p,j})R_j & \hat{S}A_{p,i} + \hat{B}_{c,j}C_{p2} \end{bmatrix}, \\ \hat{\epsilon} B_{cl,ij}^T P_j \tilde{Z}_{1,j} = \hat{\epsilon} B_{cl,ij}^T \hat{Z}_2 &= \begin{bmatrix} \hat{\epsilon}B_{p1,i}^T + D_{p21,i}^T \hat{D}_{c,j}^T B_{p2}^T & B_{p1,i}^T \hat{S} + D_{p21,i}^T \hat{B}_{c,j}^T \end{bmatrix}, \\ C_{cl,ij}\tilde{Z}_{1,j} &= \begin{bmatrix} C_{p1,i}R_j + D_{p12}\hat{C}_{c,j} & \hat{\epsilon}C_{p1} + D_{p12}\hat{D}_{c,j}C_{p2} \end{bmatrix}, \\ \hat{\epsilon}^2 \gamma_\infty^2 &= \hat{\gamma}_\infty^2, \end{aligned} \tag{4.20}$$

where

$$\begin{aligned}
\hat{A}_{c,j} &= \hat{\epsilon}SA_{p,j}R_j + \hat{\epsilon}SB_{p2}D_{c,j}C_{p2}R_j + \hat{\epsilon}NB_{c,j}C_{p2}R_j + \hat{\epsilon}SB_{p2}C_{c,j}M_j^T + \hat{\epsilon}NA_{c,j}M_j^T,\\
\hat{B}_{c,j} &= \hat{S}B_{p2}D_{c,j} + \hat{\epsilon}^2NB_{c,j},\\
\hat{C}_{c,j} &= D_{c,j}C_{p2}R_j + C_{c,j}M_j^T,\\
\hat{D}_{c,j} &= \hat{\epsilon}D_{c,j}, \quad \hat{S} = \hat{\epsilon}^2S.
\end{aligned} \tag{4.21}$$

On the other hand, we have

$$\tilde{Z}_{1,j}^T(P_i - P_j)\tilde{Z}_{1,j} = \tilde{Z}_{1,j}^T\begin{bmatrix}0 & 0\\ 0 & X_i - X_j\end{bmatrix}\tilde{Z}_{1,j} = \begin{bmatrix}M_j(X_i - X_j)M_j^T & 0\\ 0 & 0\end{bmatrix}$$

Since $M_jN^T = I - R_jS$, it can be shown that $X_j = N^T(S - R_j^{-1})^{-1}N > 0$. Using the matrix inversion lemma [4], and through algebraic manipulations, we obtain

$$M_j(X_i - X_j)M_j^T = S^{-1} - R_j + (R_j - S^{-1})(R_i - S^{-1})^{-1}(R_j - S^{-1}). \tag{4.22}$$

Moreover, through Schur complement, condition (4.15) implies

$$T_{ij} \geq S^{-1} - R_j + (R_j - S^{-1})(R_i - S^{-1})^{-1}(R_j - S^{-1})$$

which together with (4.22) concludes that $\tau_j\left(M_j(X_i - X_j)M_j^T\right) \leq \tau_jT_{ij}$. Therefore, after the congruence transformation, condition (4.15) can be deduced. Moreover, condition (4.8) becomes

$$\Upsilon_0 + \begin{bmatrix}0 & 0\\ \begin{bmatrix}\hat{\epsilon}S(A_{p,i} - A_{p,j})\\ 0\end{bmatrix} & R_j\ 0\end{bmatrix} < 0. \tag{4.23}$$

where

$$\Upsilon_0 := \begin{bmatrix}
He\{A_{p,i}R_j + B_{p2}\hat{C}_{c,j}\} + \tau_jT_{ij} & \star & \star & \star\\
\hat{A}_{c,j} + \hat{\epsilon}A_{p,i}^T + C_{p2}^T\hat{D}_{c,j}^TB_{p2}^T & He\{\hat{S}A_{p,i} + \hat{B}_{c,j}C_{p2}\} & \star & \star\\
\hat{\epsilon}B_{p1,i}^T + D_{p21,i}^T\hat{D}_{c,j}^TB_{p2}^T & B_{p1,i}^T\hat{S} + D_{p21,i}^T\hat{B}_{c,j}^T & -\hat{\gamma}_\infty^2I & \star\\
C_{p1,i}R_j + D_{p12}\hat{C}_{c,j} & \hat{\epsilon}C_{p1,i} + D_{p12}\hat{D}_{c,j}C_{p2} & \hat{\epsilon}D_{p11,i} + D_{p12}\hat{D}_{c,j}D_{p21,i} & -I
\end{bmatrix}$$

Then, by setting $\Upsilon_1 = R_j, \Upsilon_2 = \left[\hat{\epsilon}(A_{p,i} - A_{p,j})^TS\ 0\right]$, invoking Lemma 4.1, to guarantee the satisfaction of condition (4.23), it is equivalent to have the following

condition for some positive number $\epsilon = \frac{1}{\hat{\epsilon}}$,

$$\begin{bmatrix} \left\{ \begin{matrix} He\{A_{p,i}R_j + B_{p2}\hat{C}_{c,j}\} \\ +\tau_j T_{ij} - \epsilon R_j R_j \end{matrix} \right\} & \star \\ \hat{A}_{c,j} + \hat{\epsilon}A_{p,i}^T + C_{p2}^T \hat{D}_{c,j}^T B_{p2}^T & \left\{ \begin{matrix} He\{\hat{S}A_{p,i} + \hat{B}_{c,j}C_{p2}\} \\ -\hat{\epsilon}^3 S(A_{p,i} - A_{p,j})(A_{p,i} - A_{p,j})^T S \end{matrix} \right\} \\ \hat{\epsilon}B_{p1,i}^T + D_{p21,i}^T \hat{D}_{c,j}^T B_{p2}^T & B_{p1,i}^T \hat{S} + D_{p21,i}^T \hat{B}_{c,j}^T \\ C_{p1,i}R_j + D_{p12}\hat{C}_{c,j} & \hat{\epsilon}C_{p1,i} + D_{p12}\hat{D}_{c,j}C_{p2} \\ \epsilon R_j & \hat{\epsilon}(A_{p,i} - A_{p,j})^T S \end{bmatrix}$$

$$\begin{bmatrix} \star & \star & \star \\ \star & \star & \star \\ -\hat{\gamma}_\infty^2 I & \star & \star \\ \hat{\epsilon}D_{p11,i} + D_{p12}\hat{D}_{c,j}D_{p21,i} & -I & \star \\ 0 & 0 & -\epsilon I \end{bmatrix} < 0,$$

Consequently, perform congruence transformation with matrix $diag\{I, I, I, \hat{\epsilon}I\}$ on the above condition, and based on the fact that $-Z^T W^{-1} Z \leq -Z^T - Z + W$ holds for any pair of $W > 0$ and Z, we have $-\epsilon R_j R_j \leq -2R_j + \hat{\epsilon}I$ and $-\hat{\epsilon}^3 S(A_{p,i} - A_{p,j})(A_{p,i} - A_{p,j})^T S \leq -He\{\hat{S}(A_{p,i} - A_{p,j})\} + \hat{\epsilon}I$. This yields exactly condition (4.14). Moreover, the controller formula (4.17) can be verified by inverting the relations in (4.21).

Due to the product of scalar variables τ_j and matrix variables T_{ij}, condition (4.14) in Theorem 4.2 is non-convex by nature. For this special type of BMIs, one can resort to LMI optimization technique coupled with a multi-dimensional search over the scalar variables. When the number of N_p is large, a possible way to reduce computational cost of the synthesis problem is by enforcing $\tau_j = \tau \geq 0$ for all $j \in \mathbf{I}[1, N_p]$. Although the resulting conditions are more conservative, they can be solved relatively easier via LMI optimization with a single line search parameter. The following corollary formally presents this result for the robust $\mathscr{H}_\infty$ control problem.

Corollary 4.1. *Given a tunable scalar $\tau \geq 0$, the result of Theorem 4.2 remains valid whenever inequalities (4.14) are replaced by*

$$\begin{bmatrix} He\{A_{p,i}R_j + B_{p2}\hat{C}_{c,j}\} + \tau T_{ij} - 2R_j + \hat{\epsilon}I & \star \\ \hat{A}_{c,j} + \hat{\epsilon}A_{p,i}^T + C_{p2}^T \hat{D}_{c,j}^T B_{p2}^T & He\{\hat{S}A_{p,j} + \hat{B}_{c,j}C_{p2}\} + \hat{\epsilon}I \\ \hat{\epsilon}B_{p1,i}^T + D_{p21,i}^T \hat{D}_{c,j}^T B_{p2}^T & B_{p1,i}^T \hat{S} + D_{p21,i}^T \hat{B}_{c,j}^T \\ C_{p1,i}R_j + D_{p12}\hat{C}_{c,j} & \hat{\epsilon}C_{p1,i} + D_{p12}\hat{D}_{c,j}C_{p2} \\ R_j & (A_{p,i} - A_{p,j})^T \hat{S} \end{bmatrix}$$

$$\begin{bmatrix} \star & \star & \star \\ \star & \star & \star \\ -\hat{\gamma}_\infty^2 I & \star & \star \\ \hat{\epsilon} D_{p11,i} + D_{p12}\hat{D}_{c,j} D_{p21,i} & -I & \star \\ 0 & 0 & -\hat{\epsilon} I \end{bmatrix} < 0. \tag{4.24}$$

for all $i, j \in \mathbf{I}[1, N_p]$.

The results of Theorem 4.2 and Corollary 4.1 then can be used to pose the following optimization problem for the robust $\mathscr{H}_\infty$ control problem, such that the RSOF controller that renders the closed loop a suboptimal $\mathscr{H}_\infty$ performance level can be designed. As mentioned above, this type of optimization problem can be solved through a line search over τ with LMIs.

$$\begin{aligned} \min_{R_j, \hat{S}, T_{ij}, \hat{A}_{c,j}, \hat{B}_{c,j}, \hat{C}_{c,j}, \hat{D}_{c,j}, \hat{\epsilon}, \tau, \ \forall i,j \in \mathbf{I}[1,N_p]} \quad & \hat{\gamma}_\infty^2 \\ \text{s.t.} \quad & (4.15) \text{ and } (4.24). \end{aligned} \tag{4.25}$$

4.5 Numerical Examples

In this section, two examples will be used to illustrate the design procedure and effectiveness of the proposed RSOF control scheme. The first example aims to design a robust output-feedback $\mathscr{H}_\infty$ controller for a system with sensor outages. Moreover, it will be demonstrated via the second example that the proposed design scheme based on using a piecewise switched Lyapunov function is indeed capable of rendering a better $\mathscr{L}_2$-gain performance for the closed-loop system than that obtained under the single quadratic Lyapunov function framework.

Example 1. Consider a fourth order two-input two-output system subject to sensor outages, which is borrowed from [33] and also considered in [20]. The system can be described as the following polytopic uncertain system:

$$G: \begin{cases} \dot{x}(t) = Ax(t) + B_1 d(t) + B_2 u(t) \\ e(t) = C_1 x(t) + D_{11} d(t) + D_{12} u(t) \\ y(t) = C_2(\xi(t)) x(t) + D_{21} d(t) \end{cases} \tag{4.26}$$

where

$$\begin{bmatrix} A & B_1 & B_2 \\ C_1 & D_{11} & D_{12} \\ C_2(\xi) & D_{21} & 0 \end{bmatrix} = \left[\begin{array}{cccc|c:cc} -2 & 1 & 1 & 1 & 1 & 0 & 0 \\ 3 & 0 & 0 & 2 & 0 & 1 & 0 \\ -1 & 0 & -2 & -3 & 1 & 0 & 0 \\ -2 & -1 & 2 & -1 & 0 & 0 & 1 \\ \hline 1 & 0 & -1 & 0 & 0 & 0 & 0 \\ \hdashline c_1 & 0 & 0 & 0 & 0 & 0 & 0 \\ 0 & 0 & c_2 & 0 & 0 & 0 & 0 \end{array}\right]$$

where two unknown parameters c_1 and c_2 both take values from $\{0, 1\}$. Specifically, $c_i = 0$ with $i = 1, 2$ indicates the ith measurement experiences an outage. We assume as in [33] and [20] that there always exists at least one measurement working for feedback control use, i.e., c_1 and c_2 will not be simultaneously equal to zero. This will results in a polytope of $N_p = 3$ vertices with

$$C_{2,1} = \begin{bmatrix} 0 & 0 & 0 & 0 \\ 0 & 0 & 1 & 0 \end{bmatrix}, \quad C_{2,2} = \begin{bmatrix} 1 & 0 & 0 & 0 \\ 0 & 0 & 0 & 0 \end{bmatrix}, \quad C_{2,3} = \begin{bmatrix} 1 & 0 & 0 & 0 \\ 0 & 0 & 1 & 0 \end{bmatrix}. \tag{4.27}$$

To apply the proposed RSOF control scheme to solve the $\mathscr{H}_\infty$ control problem, we observe that the output matrix $C_2(\xi)$ does not satisfy Assumption 2. Nevertheless, following the methodology from [31], the original plant can be transformed to a new system that fits into the proposed design framework by concatenating a stable LTI filter to the measurement channel (as depicted in Fig. 4.2). The state-space model of the LTI filter is chosen as

$$G_y : \begin{bmatrix} \dot{x}_y \\ \tilde{y} \end{bmatrix} = \begin{bmatrix} A_y & B_y \\ C_y & 0 \end{bmatrix} \begin{bmatrix} x_y \\ y \end{bmatrix},$$

where $x_y \in \mathbb{R}^{n_a}$ is the filter state, and $\tilde{y} \in \mathbb{R}^{n_y}$ is the filtered output that will serve as the controller input. Then, the resulting augmented system can be written in the form of (4.1) with

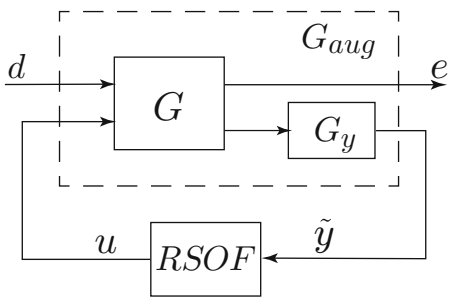

Fig. 4.2 Augmented system structure (Example 1)

$$G_{aug}: \begin{cases} A_{p,i} = \begin{bmatrix} A & 0 \\ B_y C_{2,i} & A_y \end{bmatrix}, \quad B_{p1} = \begin{bmatrix} B_1 \\ B_y D_{21} \end{bmatrix}, \quad B_{p2} = \begin{bmatrix} B_2 \\ 0 \end{bmatrix}, \\ C_{p1} = \begin{bmatrix} C_1 & 0 \end{bmatrix}, \quad D_{p11} = D_{11}, \quad D_{p12} = D_{12}, \\ C_{p2} = \begin{bmatrix} 0 & C_y \end{bmatrix}, \quad D_{p21} = 0, \quad D_{p22} = 0. \end{cases} \tag{4.28}$$

For controller synthesis, we specify the filter with

$$\begin{bmatrix} A_y & B_y \\ C_y & 0 \end{bmatrix} = \begin{bmatrix} -100I_2 & I_2 \\ 100I_2 & 0 \end{bmatrix}$$

Therefore, based on the augmented system data, we solve the optimization problem (4.25) to yield a suboptimal value of $\gamma_\infty = 1.7415$, which significantly improves those obtained by using the methods in [33] and [20] for all scenarios discussed therein (see Tables 1 and 2 in [20]). Furthermore, the corresponding RSOF controller in the form of (4.4) contains three subcontrollers with the order $n_c = 4 + 2 = 6$.

With the synthesized RSOF controller, we run the time-domain simulation by applying a pulse disturbance input of magnitude 1 starting from $t = 0$ and ending at $t = 1$ sec The closed-loop responses, including four plant states (Fig. 4.3a), the uncertain time-varying vector $\xi(t)$ (Fig. 4.3b), two control inputs (Fig. 4.3c), and the controller switching signals (Fig. 4.3d), are presented. According to (4.27), in Fig. 4.3b, $\xi(t) = [1\ 0\ 0]^T$ corresponds to the case of sensor failure on y_1, while $\xi(t) = [0\ 1\ 0]^T$ is with respect to the case when the second output y_2 fails. As can be seen, for this simulation study, only one output measurement is available at each time instant. Nevertheless, from Fig. 4.3a, c, it is observed that in spite of the sensor outages, the designed RSOF controller is still capable of stabilizing the overall closed-loop system with reasonable control input efforts.

Example 2. This example aims to further demonstrate the effectiveness and advantages of the proposed switching control scheme based on piecewise switched Lyapunov functions. We consider a two-disk $\mathscr{H}_\infty$ control problem as discussed in [34]. The uncertain dynamics of the two-disk model is given in the following form:

$$T_\rho: \begin{bmatrix} \dot{x}_1(t) \\ \dot{x}_2(t) \\ \dot{x}_3(t) \\ \dot{x}_4(t) \\ y(t) \end{bmatrix} = \begin{bmatrix} 0 & 0 & 1 & 0 & 0 & 0 & 0 \\ 0 & 0 & 0 & 1 & 0 & 0 & 0 \\ \rho_1(t) - \frac{k}{M_1} & -\frac{k}{M_1} & -\frac{b}{M_1} & 0 & \frac{1}{M_1} & \frac{0.1}{M_1} & 0 \\ -\frac{k}{M_2} & \rho_2(t) - \frac{k}{M_2} & 0 & -\frac{b}{M_2} & 0 & 0 & \frac{0.1}{M_2} \\ 0 & 1 & 0 & 0 & 0 & 0 & 0 \end{bmatrix} \begin{bmatrix} x_1(t) \\ x_2(t) \\ x_3(t) \\ x_4(t) \\ u(t) \\ d_1(t) \\ d_2(t) \end{bmatrix}$$

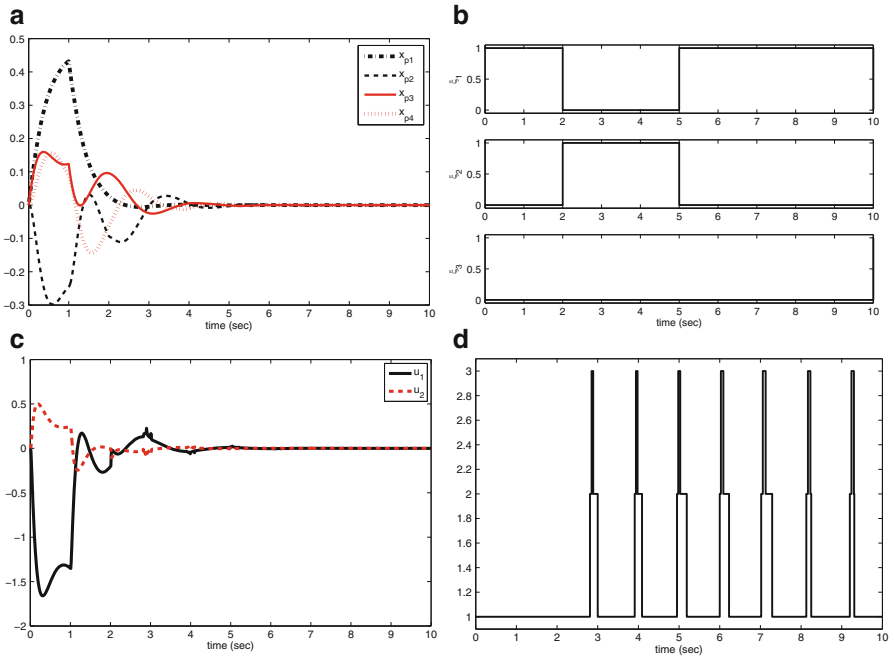

Fig. 4.3 $\mathscr{H}_\infty$ RSOF control (Example 1). (**a**) Plant states, (**b**) uncertain parameter $\xi(t)$, (**c**) control input, (**d**) switching signal

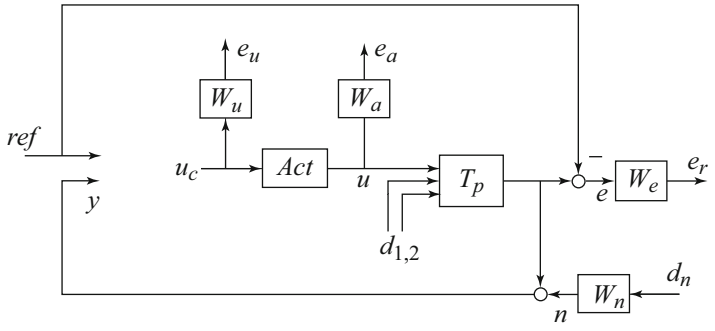

Fig. 4.4 Weighted open-loop plant interconnection of the two-disk problem [34] (Example 2)

with $M_1 = 1, M_2 = 0.5, b = 1, k = 200$ and two uncertain parameters $\rho_1(t) \in [0, 9]$, $\rho_2(t) \in [0, 25]$ yielding a polytope of $N_p = 4$ vertices. For robust $\mathscr{H}_\infty$ control synthesis, we adopt the same performance weighting functions as in [34] to form a weighted open-loop plant as depicted in Fig. 4.4, where the weighting functions are specified as

$$W_e(s) = \frac{0.3s + 1.2}{s + 0.04}, \quad W_u(s) = \frac{s + 0.1}{0.01s + 125},$$
$$W_a(s) = 0.00001, \quad W_n(s) = \frac{s + 0.4}{0.01s + 400}.$$

The actuator dynamics is assumed to be $Act(s) = \frac{1}{0.01s+1}$.

Based on such a system setup, we solve the optimization problem (4.25) with $\tau = 1$. The RSOF control synthesis yields a suboptimal $\mathscr{L}_2$ gain $\gamma_\infty = 1.1139$. To demonstrate the effectiveness of the proposed RSOF control approach, this result is compared with that obtained by using μ-type synthesis method [4, 6]. Specifically, a robust controller consisting of a single LTI output-feedback control law is designed by using a single quadratic Lyapunov function. It should be pointed out that the robust output-feedback control synthesis problem is known to be non-convex. For fairness of comparison, we utilize a global optimization technique, namely the Branch and Bound algorithm [22], to yield a globally optimal solution. After extensive search over the solution space, we are able to obtain the corresponding global optima as $\gamma_\infty = 1.55$, which is larger than our result by 28.14%. The gain of performance can be attributed to the adoption of piecewise switched Lyapunov functions in the proposed design framework. Further comparisons are conducted through time-domain simulations. The closed-loop system responses with a step reference input by using, respectively, the single LTI controller and the proposed RSOF controller are plotted in Fig. 4.5. As can be seen from Fig. 4.5a, consistent with the calculated $\mathscr{H}_\infty$ norm, the RSOF controller indeed outperforms the LTI controller with less overshoot, faster settling time, less steady-state error, as well as less control efforts (see Fig. 4.5b) during the transient period.

4.6 Conclusions

A new RSOF control scheme has been proposed for a class of linear systems with time-varying polytopic uncertainties. The proposed RSOF controller is constructed in a switching fashion, which consists of a set of linear dynamic output-feedback controllers and a switching rule (namely the min-switching strategy) that governs the switching among them. The novelty of the proposed control design scheme lies in that: (1) no online measurements of the uncertain time-varying parameters are required for controller implementation; (2) the robust control synthesis conditions are cast as a special type of BMIs, which can be solved via LMI optimization plus a line search; (3) owing to the use of piecewise switched Lyapunov functions, better controlled performance can be achieved comparing with those obtained by using a single quadratic Lyapunov function. The effectiveness and advantages of the proposed control design scheme have been demonstrated through numerical studies.

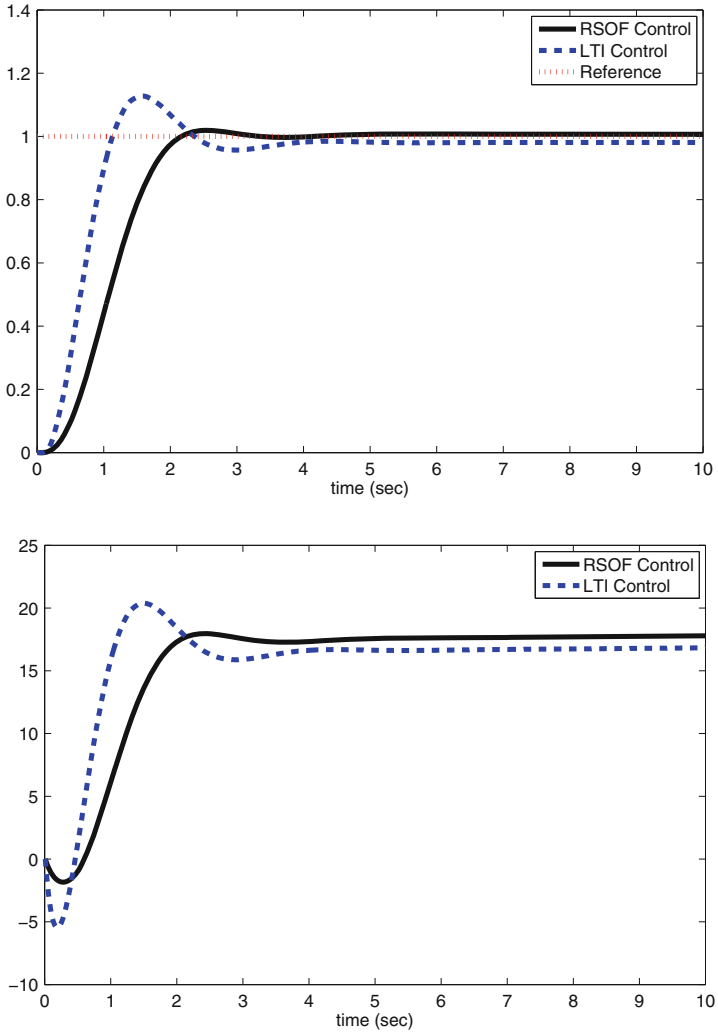

Fig. 4.5 Step response of the two-disk system (Example 2). (**a**) Tracking output, (**b**) control input

References

1. K. Zhou, P.P. Khargonekar, Robust stabilization of linear systems with norm-bounded time-varying uncertainty. Syst. Control Lett. **10**, 17–20 (1988)
2. L. Xie, C.E. de Souza, Robust $\mathscr{H}_\infty$ control for linear systems with norm-bounded time-varying uncertainty. IEEE Trans. Autom. Control **37**, 1188–1191 (1992)
3. A. Packard, J. Doyle, The complex structured singular value. Automatica **29**(1) 71–109 (1993)
4. K. Zhou, J.C. Doyle, K. Glover, *Robust and Optimal Control* (Englewood Cliffs, NJ: Prentice Hall, 1996)

5. I.R. Petersen, R. Tempo, Robust control of uncertain systems: classical results and recent developments. Automatica **50** 1315–1335 (2014)
6. S. Boyd, L.E. Ghaoui, E. Feron, V. Balakrishnan, *Linear Matrix Inequalities in System and Control Theory* (SIAM, Philadelphia, PA, 2004)
7. C. Yuan, F. Wu, C. Duan, Robust switching output feedback control of discrete-time linear polytopic uncertain systems, in *Proceedings of the 34th Chinese Control Conference, Hangzhou, China*, July 2015, pp. 2973–2978
8. B. Barmish, *New Tools for Robustness of Linear Systems* (MacMillan, New York, 1994)
9. A. Megretski, A. Rantzer, System analysis via integral quadratic constraints. IEEE Trans. Autom. Control **42**(6), 819–830 (1997)
10. G.E. Dullerud, F. Paganini, *A Course in Robust Control Theory: A Convex Approach* (Springer, New York, 2000)
11. P. Gahinet, P. Apkarian, A linear matrix inequality approach to $\mathscr{H}_\infty$ control. Int. J. Robust Nonlinear Control **4**, 421–448 (1994)
12. C. Scherer, P. Gahinet, M. Chilali, Multiobjective output-feedback control via LMI optimization. IEEE Trans. Autom. Control **42**(7), 896–911 (1997)
13. J.P. Hespanha, D. Liberzon, A.S. Morse, Overcoming the limitations of adaptive control by means of logic-based switching, Syst. Control Lett. **49**, 49–65 (2003)
14. J.P. Hespanha, D. Liberzon, A.S. Morse, Hysteresis-based switching algorithms for supervisory control of uncertain systems. Automatica **39**, 263–272 (2003)
15. J.C. Geromel, G.S. Deaecto, Switched state feedback control for continuous-time uncertain systems. Automatica **45**, 593–597 (2009)
16. C. Yuan, F. Wu, Robust $\mathscr{H}_2$ and $\mathscr{H}_\infty$ switched feedforward control of uncertain LFT systems. Int. J. Robust Nonlinear Control (2015). doi: 10.1002/rnc.3380
17. G.S. Deaecto, J.C. Geromel, $\mathscr{H}_\infty$ state feedback switched control for discrete time-varying polytopic systems. Int. J. Control **86**(4), 591–598 (2013)
18. D. Liberzon, *Switching in Systems and Control* (Birkhauser, Boston, MA, 2003)
19. S. Kanev, C. Scherer, M. Verhaegen, B.D. Schutter, Robust output-feedback controller design via local BMI optimization. Automatica **40**, 1115–1127 (2004)
20. J.C. Geromel, R.H. Korogui, J. Bernussou, $\mathscr{H}_2$ and $\mathscr{H}_\infty$ robust output feedback control for continuous time polytopic systems, IET Control Theory Appl. **1**(5), 1541–1549 (2007)
21. G.H. Yang, D. Ye, Robust $\mathscr{H}_\infty$ dynamic output feedback control for linear time-varying uncertain systems via switching-type controllers. IET Control Theory Appl. **4**(1), 89–99 (2010)
22. V. Balakrishnan, S. Boyd, S. Balemi, Branch and bound algorithm for computing the minimum stability degree of parameter-dependent linear systems. Int. J. Robust Nonlinear Control. **1**, 295–317 (1991)
23. G.S. Deaecto, J.C. Geromel, J. Daafouz, Switched state-feedback control for continuous time-varying polytopic systems. Int. J. Control. **84**(9), 1500–1508 (2011)
24. C. Yuan, F. Wu, Robust control of switched linear systems via min of quadratics, in *ASME Conference Dynamic System and Control*, Palo Alto, CA, Oct 2013, Paper No. DSCC2013-3715
25. R.A. DeCarlo, M.S. Branicky, S. Pettersson, B. Lennartson, Perspectives and results on the stability and stabilizability of hybrid systems. Proc. IEEE **88**(7) (2000)
26. C. Yuan, F. Wu, Hybrid control for switched linear systems with average dwell time. IEEE Trans. Autom. Control **60**(1), 240–245 (2015)
27. C. Yuan, F. Wu, Switching control of linear systems subject to asymmetric actuator saturation. Int. J. Control **88**(1), 204–215 (2015)
28. C. Yuan, C. Duan, F. Wu, Almost output regulation of discrete-time switched linear systems, *Proceedings of the American Control Conference*, Chicago, IL, 2015, pp. 4042–4047
29. C. Yuan, F. Wu, Asynchronous switching output feedback control of discrete-time switched linear systems. Int. J. Control **88**(9), 1–9 (2015)
30. C. Duan, F. Wu, Analysis and control of switched linear systems via modified Lyapunov-Metzler inequalities. Int. J. Robust Nonlinear Control. **24**, 276–294 (2014)
31. W. Xie, Improved $\mathscr{L}_2$ gain performance controller synthesis for Takagi-Sugeno fuzzy system, IEEE Trans. Fuzzy Syst. **16**(5), 1142–1150 (2008)

32. M.S. Branicky, Multiple Lyapunov functions and other analysis tools for switched and hybrid systems. IEEE Trans. Autom. Control **43**(4), 475–482 (1998)
33. R.J. Veillette, J.V. Medanic, W.R. Perkins, Design of reliable control systems, IEEE Trans. Autom. Control **37**(3) 290–304 (1992)
34. F. Wu, Control of linear parameter varying systems, Ph.D. Dissertation, University of California, Berkeley, 1995

Chapter 5
Output Feedback Control of Automotive Air Conditioning System Using H_∞ Technique

Quansheng Zhang and Marcello Canova

Abstract This chapter presents an application of robust control theory to an automotive air conditioning (A/C) system. A control-oriented model built using moving-boundary method is validated against experimental data collected on a vehicle chassis dynamometer, at constant engine speeds as well as on driving cycles. Next, an H_∞ controller is synthesized by formulating an optimization problem whose solution requires appropriate weighting functions selection. Singular perturbation method is utilized to remove states associated with fast dynamics in both model and controller. Both full-order and reduced-order H_∞ controllers are verified by simulation results obtained using the nonlinear A/C system model. It is demonstrated that the designed controller is capable of tracking the reference output trajectories while rejecting disturbances introduced on the boundary conditions of the heat exchangers. Furthermore, a preliminary study is performed to reveal the opportunity of designing a gain-scheduled H_∞ controller for global output tracking.

Keywords Air conditioning system • H infinity synthesis • Moving-boundary method • Automotive • Singular perturbation method

5.1 Introduction

The automotive industry is striving to improve fuel economy in vehicles, under considerable pressures dictated by the increasing fuel prices, and the mandates to reduce CO_2 emissions globally. Several engineering solutions have been introduced to production in the past years to improve the energy conversion efficiency of the powertrain components, such as the engine and transmission [1]. Substantial improvements can also be achieved through the use of advanced control techniques, for instance, to optimize the use of the A/C system based on the engine and

Reprinted from Zhang and Canova (2015), with permission from Elsevier.

Q. Zhang (✉) • M. Canova
Center for Automotive Research, The Ohio State University, 930 Kinnear Road, Columbus, OH 43212, USA
e-mail: zhang.777@osu.edu

Q. Zhang et al., *Automotive Air Conditioning*, DOI 10.1007/978-3-319-33590-2_5

drivetrain operations [2]. Reducing the impact of automotive air conditioning systems on vehicle fuel consumption is a challenging control problem, which could be addressed by adopting supervisory energy management strategies (overseeing the system operations and optimizing the power consumption without affecting the cabin comfort), as well as low-level feedback control schemes for tracking targeted set-points.

Generally, applications of control theory to A/C systems and refrigeration systems involve the formulation of a tracking control problem for the evaporator pressure and superheat temperature [3, 4]. In details, the superheat temperature should be maintained higher than a specific threshold to avoid liquid refrigerant flowing into the compressor. At the same time, the evaporator pressure should be controlled to a desired target to carefully balance the ability of the heat exchanger to extract heat from the cabin air without reaching the moisture freezing point. Although the control inputs are different depending on the actuator configurations, the controllers should track the two controlled outputs and reject disturbances to the A/C loop caused by varying flow rates and air temperature at the condenser and evaporator [5, 6].

The modeling of the dynamics of the A/C system with accuracy and computational efficiency is critical to the design of robust model-based control algorithms. However, modeling the system dynamics requires accurate characterization of phase change processes, as the working fluids absorb and reject heat in the evaporator and condenser. The most common approach to control-oriented modeling of heat exchangers for refrigeration cycles is based on the moving-boundary method (MBM) [7–12]. An A/C system model based on the MBM characterizes the pressure and enthalpy dynamics in the evaporator and condenser starting from a detailed description of the phase transitions within the heat exchangers.

In order to reduce the difficulty of performing control design when using the aforementioned models, a common approach is to start from low-order, linear models obtained from the NDAEs through system identification or model order reduction [13]. For instance, [14] presents a discrete-time state variable model for indirect adaptive control recursively identified using a multi-input multi-output (MIMO) parameter estimation algorithm. A linear quadratic regulator (LQR) was then implemented for reference tracking and disturbance rejection. A local model network based on Youla parameterization was developed in [3], and Lyapunov-based methods were used to stabilize a tracking controller with respect to different local linear models. Similarly, a low-order nonlinear evaporator model was developed for backstepping design of a nonlinear adaptive controller [15]. A model predictive control (MPC) algorithm was applied to compute an optimal command profile of each actuator by formulating a multiple criterion including cycle efficiency and technological constraints [16], based on a low-order nonlinear model of a vapor compression cycle proposed in [17]. A linear-quadratic Gaussian(LQG) controller was designed together with a state observer of the Kalman filter type for controlling the evaporator feeding and for matching the cooling capacity [18]. Recently, advanced techniques tackling model uncertainty and external disturbances are preliminary investigated, such as sliding mode control [19] and robust control [4].

One important aspect in control design for A/C systems and refrigeration systems is related to robustness, which is critical to ensure the ability of the controller to reject model uncertainties introduced by the system identification and disturbances on the boundary conditions to the heat exchangers. Mitigating the influence of model uncertainties and disturbances on tracking performance is a problem typically solved in the framework of robust control. In the automotive field, robust control has been demonstrated for several practical applications, e.g., boost pressure control in turbocharged diesel engines [20, 21]. On the other hand, there is a lack of systematic studies on the application of robust control theory to the control design of A/C systems and compression refrigeration systems [5, 22].

Therefore, this chapter presents a robust control design for output tracking and disturbance rejection of the A/C system. Section 5.2 explains the modeling approach based on the MBM, and the resulted model is calibrated and validated against experimental data collected on a vehicle chassis dynamometer in Sect. 5.3. An overview of control objective formulation and H_∞ synthesis procedure is given in Sect. 5.4. The design process is detailed in Sect. 5.5 with validations on the nonlinear MBM A/C model.

5.2 Automotive A/C System Description

For this study, the production air conditioning system of a Minivan, whose plant diagram is shown in Fig. 5.1, was instrumented to allow for experimental characterization. In particular, two ball valves were inserted to isolate the lines feeding the rear evaporator, hence simplifying the characterization of the circuit. Two pressure transducers and two thermocouples were then positioned at the suction and discharge side of the compressor. The clutch current was also measured through an inductive sensor. Additional thermocouples (not shown in figure) were finally inserted to measure the temperature of the air at the inlet of the evaporator and condenser. The air flow velocity was controlled by varying the PWM signal of the

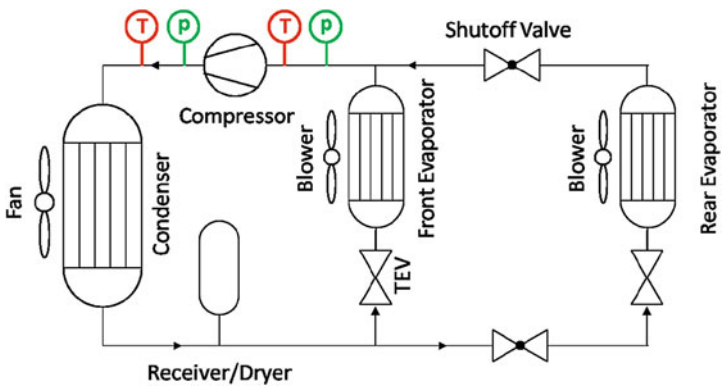

Fig. 5.1 Schematic of the air conditioning system in the experimental setup

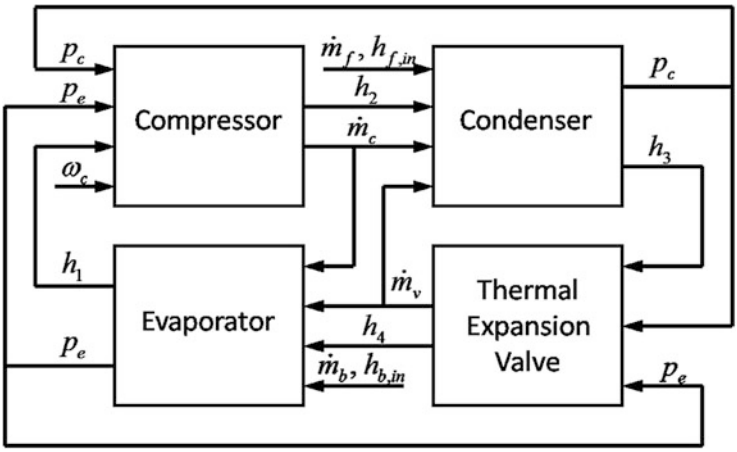

Fig. 5.2 Block diagram of the A/C system model

fan and blower, and measured by a Pitot tube. The test vehicle was instrumented with an ETAS ES1000 system interfaced with the ECU to allow for acquisition of engine torque and speed, and to control the radiator fan and cabin blower. Finally, the vehicle was installed on a chassis dynamometer, allowing for the characterization of the system at steady state conditions or during driving cycles.

The vehicle air conditioning system model follows the plant layout and includes four primary components, namely evaporator, compressor, condenser, and expansion valve. A causality diagram of the complete model is shown in Fig. 5.2, and illustrates how the physical variables, such as enthalpy, mass flow rate, and pressure, are exchanged by the four components. In general, the heat exchangers set the pressures of the system, while the compressor and expansion valve determine the mass flow rates at the evaporator and condenser. The model structure and equations for each component will be described in detail sequentially.

The compressor and expansion valve are generally modeled as static components, in consideration that their transient response is typically much faster than the heat exchangers. The compressor model is based on [23], where the outputs are computed starting from the characteristic maps provided by the manufacturer. The mass flow rate $\dot{m}_c$ and outlet enthalpy h_2 of the compressor are defined, respectively, as:

$$\dot{m}_c = \eta_v V_d \rho_1 \omega_c, \qquad h_2 = \frac{h_{2s} - h_1}{\eta_s} + h_1 \tag{5.1}$$

where V_d is the compressor displacement, ρ_1, h_1 the refrigerant density and enthalpy at the compressor inlet, ω_c the compressor speed, and $h_{2s} - h_1$ is the isentropic enthalpy difference. The volumetric efficiency η_v and isentropic efficiency η_s of the compressor are modeled as algebraic nonlinear functions of the pressure ratio $PR = p_2/p_1$ and the dimensionless Mach index Z, which accounts for the effects of the compressor speed [23, 24]. Figure 5.3 shows the predicted volumetric and isentropic efficiency predicted by the model, overlapped by the manufacturer data.

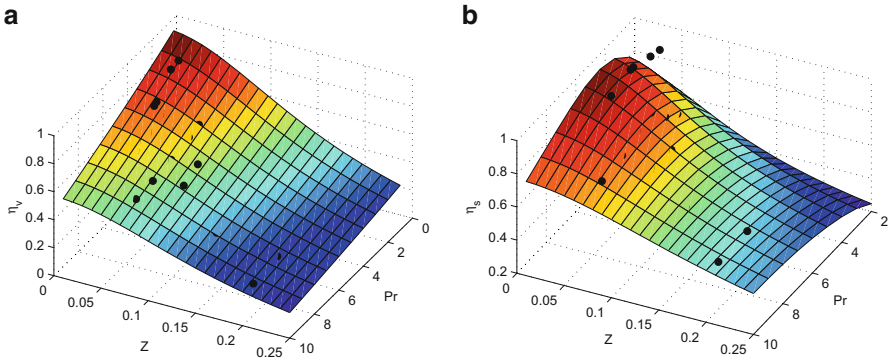

Fig. 5.3 Performance maps of the A/C compressor. (**a**) Volumetric efficiency, (**b**) Isentropic efficiency

The thermostatic expansion valve (TEV) is modeled by the orifice equation for incompressible fluids:

$$\dot{m}_v = C_{d,v} A_v \sqrt{2\rho_3 (p_3 - p_4)} \tag{5.2}$$

where A_v is the valve curtain area and C_v is the discharge coefficient. The outlet enthalpy is obtained by assuming an ideal throttling process, hence $h_4 = h_3$.

The dynamics of heat exchangers where the fluid undergoes phase changes have been generally modeled in the MBM framework [8, 12, 25], where the refrigerant inside the heat exchanger is lumped according to its phase (liquid, superheated vapor, or two-phase), and the boundary position between two adjacent lumping regions is dynamically moving. In short, MBM is used to derive a control-oriented model, whose differential equations are detailed in [26] and not given here for brevity.

5.3 Model Calibration and Validation

The evaporator and condenser models are physically based, hence they require specification of the main geometric parameters, thermodynamic properties of the working fluids (R134a and air), and heat transfer coefficients. The geometric parameters were obtained from drawings provided by the heat exchangers manufacturers, while the refrigerant properties were imported into the models from the thermodynamic tables (available with commercial software, such as REFPROP). During the calibration phase of the model, specific correlations for single- and two-phase flow in microchannels have been adopted from literature to determine the heat transfer coefficients for the refrigerant. In the single phase regions, the heat transfer correlation includes two parts [27]. For evaporation, the correlation

proposed in [28] combines the nucleating boiling and convective boiling effects, $\alpha_{tp} = S\alpha_{nb} + F\alpha_{sp}$. For condensation, the correlation given by Koyama et al. [29] combines the influences of the forced convection Nu_F and gravity controlled convection Nu_B using an asymptotic expression $Nu = (Nu_F^2 + Nu_B^2)^{1/2}$. On the external air side, specific heat transfer coefficients are defined for compact heat exchangers with louvers and fins, as noted by Chang and Wang [30] and Kim and Bullard [31].

In order to compensate for modeling errors and uncertainties in the heat transfer coefficients correlations, a calibration was conducted on the complete A/C system model, leveraging upon the available experimental setup. Specifically, the calibration was limited to applying multipliers correcting the values of the heat transfer coefficients predicted by the empirical correlations found in literature.

Experimental data were collected on the test vehicle located in a thermally controlled chassis dynamometer room, so that the air flow rate and temperature at the evaporator and condenser could be controlled to constant and known values. For each tested condition, the vehicle was operated at constant speed (corresponding to engine speed of 700 rpm (idle), 1500, and 2500 rpm), and the air conditioning system was activated, letting the A/C system control operating the compressor clutch. The model was calibrated using the data collected during the test at 1500 rpm, and verified for the other two conditions. The model parameters (heat transfer multipliers) were calibrated by minimizing a cost function that accounts for the RMS error between the measured condenser and evaporator pressure, and the model prediction. Note that the calibration was focused on matching the model response when the A/C system is fully active, thereby neglecting the startup and shutdown phase. Figure 5.4 compares the pressures at the two heat exchangers and the evaporator exit temperature predicted by the model with the corresponding experimental data for the test conducted at 700 rpm (idle speed). As shown in Fig. 5.4a, b, the model appears to accurately predict the system behavior, in particular capturing the dynamics induced on the condenser and evaporator pressures by the compressor clutch cycling operations. The simulations for 1500 and 2500 rpm are not shown here for brevity.

A further verification of the A/C system model is conducted with reference to the SC03 air conditioning cycle, which is a test conducted under highly dynamic conditions. The vehicle speed trace for this regulatory driving cycle is shown in Fig. 5.5a. The cycle represents a 3.6 miles route during which the A/C system is active. Figure 5.5 compares the outputs of the model with the corresponding experimental data. During the SC03 test, the compressor speed (related to the engine speed) changes considerably, causing significant variations in the refrigerant flow rate that affect the pressure dynamics in the heat exchangers. This is particularly evident by observing the fluctuations of the condenser pressure, as shown in Fig. 5.5b. The model captures the dynamics induced by the compressor speed and the on–off cycling of the clutch.

Finally, Table 5.1 summarizes the RMS error for all the calibration and validation cases considered. Note that the average pressure in the heat exchangers is set to different values based on the engine speed. The condenser pressure error is

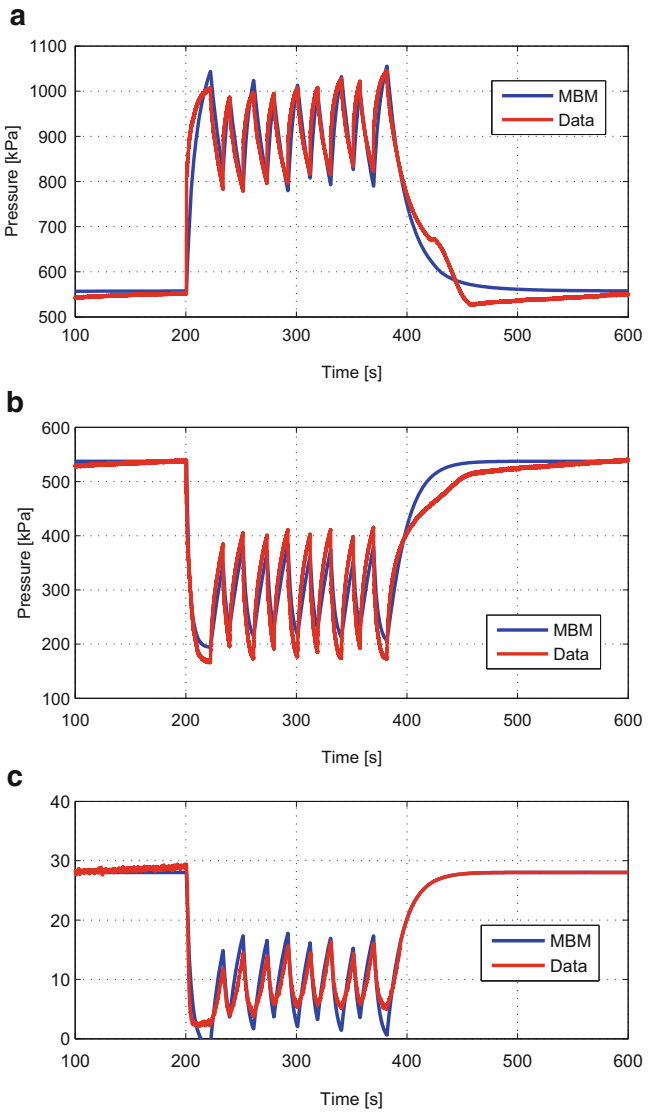

Fig. 5.4 Comparison of experimental data and model prediction ($N = 700$ rpm). (**a**) Condenser pressure, (**b**) Evaporator pressure, (**c**) Evaporator exit temperature

within 6 % of its average value, and the evaporator pressure error is around 8 %. Their relative accuracy can be improved by adding weighting factors into the RMS definition. Nevertheless, the model appears quite accurate in capturing the pressure dynamics at the condenser and evaporator, which are essential for predicting the compressor power consumption.

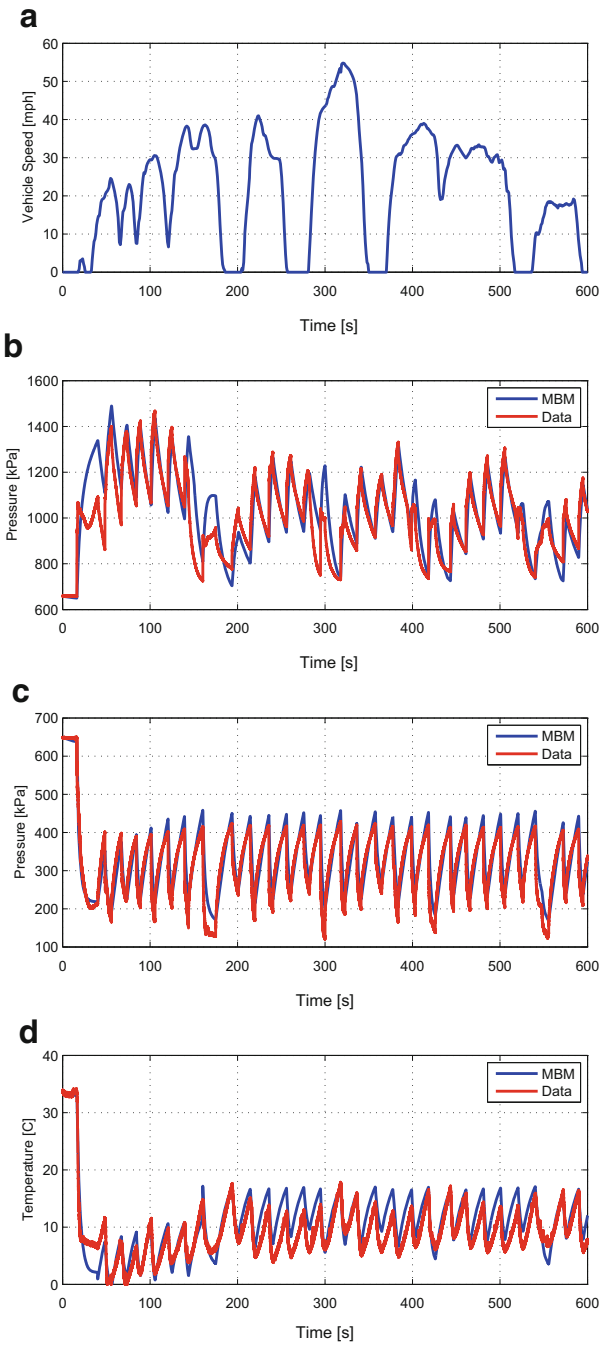

Fig. 5.5 Verification of MBM model for the SC03 driving cycle. (**a**) Vehicle speed profile, (**b**) Condenser pressure, (**c**) Evaporator pressure, (**d**) Evaporator exit temperature

Table 5.1 Pressure errors between measurement and prediction (in kPa)

	MBM model	
Engine speed	Condenser pressure	Evaporator pressure
700 rpm	44.1 (7.3 %)	32.6 (5.5 %)
1500 rpm	50.6 (8.4 %)	29.6 (4.9 %)
2000 rpm	56.4 (8.4 %)	30.6 (5.1 %)
SC 03 Cycle	63.5 (10.6 %)	38.6 (6.4 %)

5.4 Control Design Overview

Before delving into the design process, it is beneficial to justify the choice of the synthesis technique, namely H_∞ synthesis.

5.4.1 Control Objective

The control problem is a multi-objective optimization problem. Physically, it requires a vapor compression cycle not only to provide a cooling capacity for regulating the cabin temperature, but also to ensure a desirable energy conversion efficiency. The controller designed for a chiller system in [16] was used as a baseline controller, where a multi-objective optimization problem was formulated using a weighted sum of quadratic partial criteria, namely deviations from the desired refrigerating capacity, the reciprocal of coefficient of performance (COP), and a smooth command profile. Meanwhile, the superheat temperature is independently dealt by a PID controller actuating the valve. The water flow rate at the evaporator is treated as a disturbance during chiller partial optimization.

In the aforementioned formulation, although MPC, as an advanced control technique, was adopted to solve the online optimization problem, it still belongs to rudimental single-input-single output (SISO) control technique, because the superheat temperature is regulated only by the expansion valve opening, independent of compressor speed. The strong coupling in the system, as quantified in [32] using relative gain array (RGA), needs the application of advanced MIMO control techniques.

There, a variety of forthcoming control designs in the areas related to vapor compression cycles formulate the optimization problem as an optimal LQR design [18], by casting the objective function into

$$J = \int_0^\infty \left[y^T(t) \cdot Q \cdot y(t) + u^T(t) \cdot R \cdot u(t) \right] dt \tag{5.3}$$

where the weighting matrices Q and R are constant real and symmetric. Q is assumed to be positive semi-definite and R as positive definite. y include all the outputs and u all the inputs. Hence, the outcome of solving the above formulation

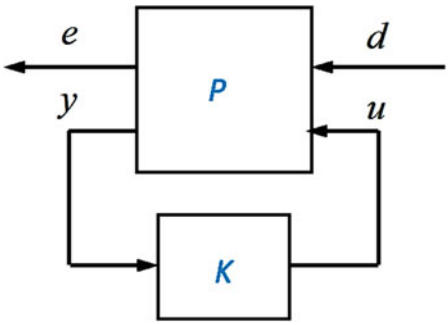

Fig. 5.6 Plant and controller in H_2 and H_∞ synthesis

using Riccati equations is a MIMO controller. Some variants are noticed between the LQR controller and the baseline controller: (1) the requirement of cooling capacity is converted into the deviation from the desired evaporator pressure, because in majority of the time, the refrigerant circuit, instead of the cabin module, is of interest; (2) the COP constraint is equivalent to the threshold of superheat temperature, because a monotonic relationship between COP and superheat temperature exists according to an analysis in [5, 6].

A stochastic implementation of LQR in noisy condition is known as a LQG regulator, and the latter technique, in robust control theory, is equivalent to an H_2 optimization problem. The H_2 control problem is to find a proper, real rational controller K that stabilizes plant P internally and the minimizes the H_2 norm of the transfer function T_{de} between the disturbance d and the controlled output e, as shown in Fig. 5.6. According to a counterexample from [33], there are no guaranteed stability margins for an H_2 controller. However, significant external disturbances exist on the air sides of heat exchangers of an automotive A/C system, which might cause unstable closed-loop performance if a LQG controller, or an H_2 controller, is implemented. For example, the condenser in the A/C loop is installed in parallel to the radiator in the engine cooling system in order to share a radiator fan mounted in the right front of a vehicle, which is electrically driven mainly for the purpose of regulating a desirable engine temperature. Although it is a controllable input to the engine cooling system, the radiator fan is an uncontrollable external disturbance entering the A/C system through the condenser. Moreover, the evaporator blower is controlled either manually by a driver or automatically by an intelligent cabin control module, both of which are dependent on the air temperature dynamics in the cabin but independent on the refrigerant dynamics. Therefore, a robust control with guaranteed stability margin, such as an H_∞ controller, is indispensable to a local controller specifically developed for the A/C loop.

5.4.2 H_∞ Synthesis Background

Using the same interconnection in Fig. 5.6, the H_∞ synthesis is to find a controller K such that the closed-loop system is asymptotically stable and the H_∞ norm of the transfer function between the disturbance ω and controlled output z, $\|T_{\omega z}\|_\infty$, is as small as possible [34]. Note that H_∞ norm is used instead of H_2 norm; besides, output feedback is considered instead of state feedback on the form $u = Kx$.

The H_∞ synthesis framework is compatible with the multi-objective optimization problem proposed in [16, 17], as it enables the controller output z to incorporate all the partial criteria listed. For instance, the deviation from desirable cooling capacity, or deviation from desirable evaporator pressure, can be expressed a pressure error term and treated as an element of z vector. Similarly, the efficiency constrain, or the superheat temperature limit, can be expressed as a term characterizing the deviation from superheat set-point and stored into another element. The framework also grants the flexibility of adding the energy consumption of the compressor, or the amplitude of the control input, into the z vector. The influence of external disturbances on the air side of the heat exchangers can be tailored into the ω vector to fit the framework. Therefore, the H_∞ synthesis framework is capable of describing the multi-objective optimization problem as well as LQG/H_2 techniques.

The solution for system matrices of the H_∞ controller resorts to the help of the *Bounded Real Lemma*, which states: *T is internally asymptotically stable and satisfies $\|T_{\omega z}\|_\infty < \gamma$ is and only if the largest singular value of D is less than γ, and there exists a positive definite matrix $X = X^T$ such that either the condition in Riccati equation or the one in linear matrix inequality (LMI) is satisfied*

1. Riccati equation condition

$$XA + A^T X + XB_{cl}R^{-1}B_{cl}^T X + C_{cl}^T(I + D_{cl}R^{-1}D_{cl}^T) = 0 \tag{5.4}$$

2. LMI condition

$$\begin{bmatrix} XA_{cl} + A_{cl}X & XB_{cl} & C_{cl}^T \\ B_{cl}^T X & -\gamma I & D_{cl}^T \\ C_{cl} & D_{cl} & -\gamma I \end{bmatrix} < 0 \tag{5.5}$$

where $A_{cl}, B_{cl}, C_{cl}, D_{cl}$ are system matrices of the closed-loop system, $A = (A_{cl} + B_{cl}R^{-1}D_{cl}^T C_{cl})$, and $R = \gamma^2 I - D_{cl}^T D_{cl}$.

The controller system matrices (A_c, B_c, C_c, D_c) are embedded in the closed-loop system matrices. In the full-order controller case, it is possible to extract the controller system matrices explicitly by splitting the conditions into two Riccati equations and LMIs, respectively.

5.5 Design Process

In the A/C system, the robust H_∞ controller shown in Fig. 5.7 is designed to track prescribed trajectories of two output variables, namely the pressure difference Δp between the condenser and the evaporator, and the superheat temperature SH at the evaporator. The reference values for the tracked variables are indicated with Δp_r and SH_r, respectively. At the same time, the controller should reject disturbances caused by air mass flow rate at the condenser, $\dot{m}_{\mathrm{ca}}$, and the evaporator, $\dot{m}_{\mathrm{ea}}$. Because there are no sensors mounted on vehicles for the two variables, the two disturbances are not measurable. They typically vary considerably in operation, due to the presence of fans and blowers, and the relative wind speed when the vehicle is in motion. In addition, noise n_1 and n_2 is present in the measured signals of measured superheat temperature SH and pressure difference Δp.

5.5.1 *Full-Order H_∞ Controller Design*

The controlled output vector z and the disturbance vector ω in the A/C loop are clarified as follows.

The six elements in the output vector z to be minimized are selected as

$$\left[e_{\Delta p}\ e_{\mathrm{SH}}\ N_{\mathrm{cmp}}\ \alpha\ \Delta p\ \mathrm{SH}\right]^T \tag{5.6}$$

, and the reasons of choosing each variable are given below:

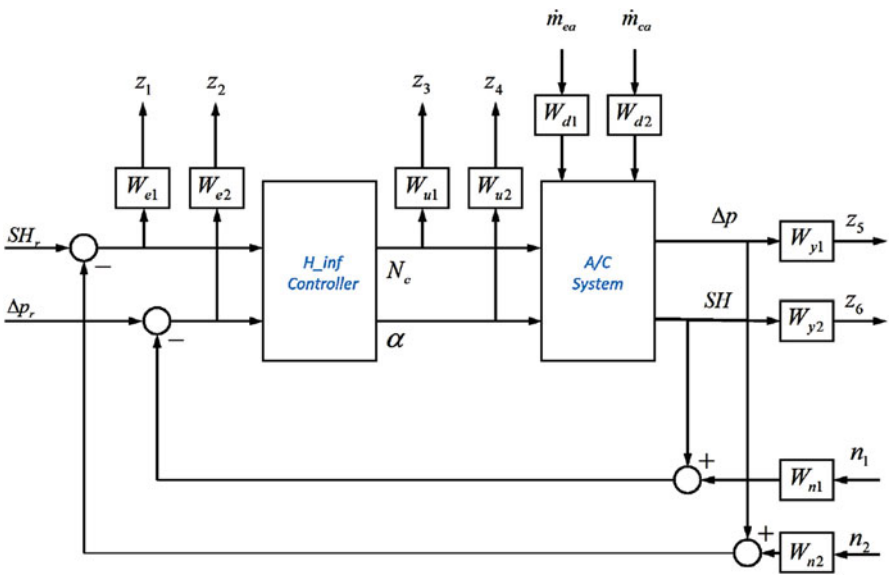

Fig. 5.7 Typical A/C configuration

- the errors $e_{\Delta p} = \Delta p_r - \Delta p$ and $e_{\mathrm{SH}} = \mathrm{SH}_r - \mathrm{SH}$ on the output evaporator pressure and superheat should be minimized to achieve good tracking performance;
- the compressor rotation speed N_{cmp} and the valve opening α should be varied as little as possible, resulting in less deviation from the nominal operating point of the A/C system and minimum control effort;
- the fluctuations in the pressure difference Δp and superheat temperature SH during transients should be limited to ensure stability of the A/C system model.

Since the H_∞ controller design focuses on the frequency domain responses, weighting functions are added for improving the closed-loop performance. In particular, two weighting functions (W_e, W_y) are used to shape the control input and output:

- Weighting for static performance of the closed-loop system, W_e,

$$W_e = \frac{K_e}{s + \epsilon} \tag{5.7}$$

- Weighting for limiting the system bandwidth and tracking performance, W_y,

$$W_y = \frac{K_y s}{\epsilon s + \omega_y} \tag{5.8}$$

After adding the weighting functions, the closed-loop output vector z is defined as:

$$z_1 = W_{e1} e_1 = \frac{K_{e1}}{s + \epsilon_{e1}} (\Delta p_r - \Delta p) \tag{5.9}$$

$$z_2 = W_{e2} e_2 = \frac{K_{e2}}{s + \epsilon_{e2}} (\zeta_{e1,r} - \zeta_{e1}) \tag{5.10}$$

$$z_3 = W_{u1} u_1 = N_{\mathrm{cmp}} \tag{5.11}$$

$$z_4 = W_{u2} u_2 = \alpha \tag{5.12}$$

$$z_5 = W_{y1} y_1 = \frac{K_{y1} s}{\epsilon_{y1} s + \omega_{y1}} \Delta p \tag{5.13}$$

$$z_6 = W_{y2} y_2 = \frac{K_{y2} s}{\epsilon_{y2} s + \omega_{y2}} \zeta_{e1} \tag{5.14}$$

where the parameters of the weighting functions are selected as $K_{e1} = 200, K_{e2} = 100, \epsilon_{e1} = 400, \epsilon_{e2} = 800, K_{y1} = K_{y2} = 1, \epsilon_{y1} = \epsilon_{y2} = 0.1, \omega_{y1} = \omega_{y2} = 1$ [33].

The reference pressure difference Δp_r and superheat temperature SH_r are time-varying and regarded as additional disturbances besides the unknown disturbances $\dot{m}_{\mathrm{ca}}$ and $\dot{m}_{\mathrm{ea}}$, as well as the noises. Therefore, the disturbance vector is defined as:

$$\omega = [\Delta \dot{m}_{\mathrm{ea}}, \Delta \dot{m}_{\mathrm{ca}}, \Delta p_r, \mathrm{SH}_r, n_1, n_2] \tag{5.15}$$

After defining the output vector and disturbance vector, the augmented state space equation of the A/C model is represented by:

$$\begin{cases} \dot{x}_a(t) = A_a x_a(t) + B_{a,\omega}\omega(t) + B_{a,u}u(t) \\ z(t) = C_{a,z}x_a(t) + 0_{6\times 6}\omega(t) + D_{a,z}u(t) \\ y(t) = C_{a,y}x_a(t) + D_{a,y}\omega(t) + 0_{2\times 2}u(t) \end{cases} \tag{5.16}$$

where the input u, disturbance ω, controlled output z, and measured output y have already been defined above, and the state vector of the augmented model now includes the states of the MBM A/C model as well as parts of the output vector, or $x_a = \begin{bmatrix} x & z_1 & z_2 & z_5 & z_6 \end{bmatrix}^T$.

The rank conditions are satisfied by choosing appropriate structure of the disturbance and output vector [33]. The controller K_{yu} is derived by solving Riccati equations associated with the augmented system matrices according to methods provided in [35].

5.5.2 Model and Controller Order Reduction

The dynamics A/C system possess different time scales due to the difference response time of mass transport and heat transfer. For instance, two different time scales exist in the heat exchanger models for the tube wall and the refrigerant, because of the different orders of heat transfer coefficients at the air side and refrigerant side [13, 17]. Hence, it is desirable to exploit the possibility of order reduction. The underlying principle is the singular perturbation theory, which substituting fast dynamics by its equivalence. However, the descriptor form of A/C model cannot be used directly for singular perturbation method as it is not in standard form. Instead, the A/C model is transformed into a specific form, on which the theory also works as proved in [36, 37]. Specifically, if the time-factor exists on the right-hand side of the system dynamical equations as follows:

$$\begin{cases} \dot{x} = f(x) + g(x)u + \frac{1}{\epsilon}b(x)k(x0 \\ y = h(x_s, x_f) \end{cases} \tag{5.17}$$

the above can be converted into the stand singular perturbed form

$$\begin{cases} \dot{x}_s = g_s(x_s, x_f, u, \epsilon) \\ \epsilon\dot{x}_f = g_f(x_s, x_f, u, \epsilon) \\ y = h(x_s, x_f) \end{cases} \tag{5.18}$$

through an ϵ independent nonlinear coordinate change $T(x)$, if and only if

1. $L_b k(x)$ is nonsingular.
2. the distribution $b(x) = \text{span}b_1(x), \ldots, b_p(x)$ is involutive.

The coordinate change T(x) is a nonlinear transformation

$$\begin{bmatrix} x_s \\ x_f \end{bmatrix} = T(x) = \begin{bmatrix} \phi(x) \\ k(x) \end{bmatrix} \tag{5.19}$$

where $\phi(x)$ is found to meet $L_{b(x)\phi(x)} = 0$.

The above theory was applied to the model order reduction of the evaporator model in [19] by choosing the scaling factor as the reciprocal of the heat transfer coefficient of the refrigeration side of the two-phase region, $k(x)$ as the temperature difference between the refrigerant and the wall at the two-phase region, as well as $b(x)$ the terms left in the term of heat transfer rate.

$$\begin{aligned} \tfrac{1}{\epsilon} &= \alpha_{i1} \\ b(x) &= \pi D_o L_{e1} \\ k(x) &= T_{w1} - T_{r1} \end{aligned} \tag{5.20}$$

The transformation described by $\phi(x)$ is a function of $Z(x)$ matrix as solved in [19]. Based on the above choice of state transformation, two necessary conditions are satisfied. In the standard form, the fast dynamics is represented by the temperature difference. To this extent, it is found the two temperatures, namely wall temperature T_{w1} and refrigerant temperature T_{r1} at two-phase region, are close to each other. The above analysis arises from the fact that the heat transfer coefficient of refrigerant in the two-phase region is significantly larger than for the other regions (superheated and subcooled).

5.5.3 Simulation Results

The H_∞ control design presented above was applied to the nonlinear MBM and verified in simulation at different operating conditions. The results and analysis address the ability of the controller to minimize the tracking errors, z_1 and z_2, in presence of time-varying reference signals Δp_r and SH_r, while rejecting disturbances in the air velocities $\dot{m}_{\mathrm{ca}}$ and $\dot{m}_{\mathrm{ea}}$

In particular, two scenarios are considered. Firstly, the reference pressure is varied by imposing step changes, while the reference superheat temperature is maintained constant as shown in Fig. 5.8. The simulation results show that the H_∞ controller is effective in matching the evaporator pressure to the reference value. The actual pressure and superheat temperature both achieve the target set-points after the initial transient. In Fig. 5.8, the steady state errors between the reference output and actual output are very small and the transition time is less than 50 s. During the transient, the superheat temperature is always higher than 10 C, hence the evaporator

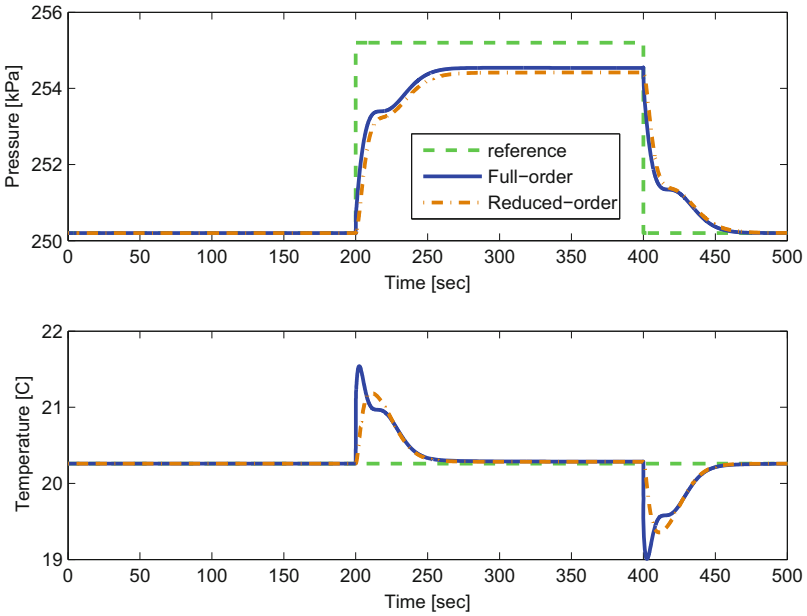

Fig. 5.8 System outputs during pressure tracking

outlet temperature is in vapor phase all the time. Besides, the compressor rotation speed N_c and valve opening percentage α are within the range of 20 % deviations.

Secondly, a disturbance rejection test is conducted to evaluate the ability of the H_∞ control to mitigate the effects of changes in the evaporator air velocity. The disturbance shown is added before and after the step change of the reference pressure signal. When the disturbance signal is added into the case of evaporator pressure tracking (Fig. 5.8), the simulation results of the reference outputs are shown in Fig. 5.9. As expected, the ripples caused by the disturbance are compensated by actuator modulations.

In both Figs. 5.8 and 5.9, the full-order controller and the reduced-order controller achieve the objectives of output tracking and disturbance rejection. Besides mathematical complexity, the main difference between the two controllers occurs during transient. Specifically, the influence of the fast dynamics in the closed-loop system with the reduced-order controller is not as significant as the one with the full-order controller. This conclusion is also supported by a frequency analysis of closed-loop system responses, namely from the reference pressure P_{er} and the reference superheat temperature SH_r to the actual pressure P_e and the actual superheat temperature SH. In Fig. 5.10, both controllers achieve the same steady state performance from the fact that the static gain from the reference signal to the corresponding actual variable is one, and the cross static gain is negligible. The main difference exists at high frequency region, meaning that discrepancy occurs between the performances of two controllers during transient in time domain.

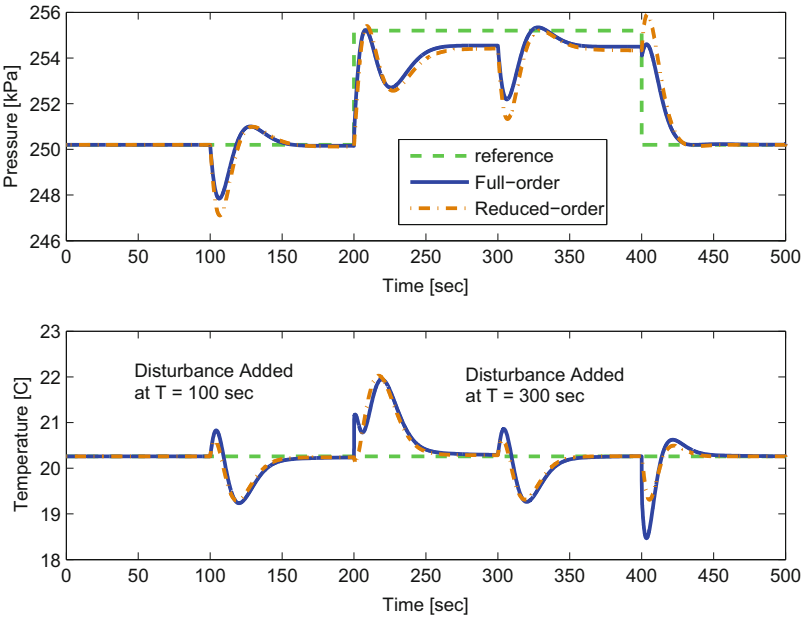

Fig. 5.9 System outputs during disturbance rejection

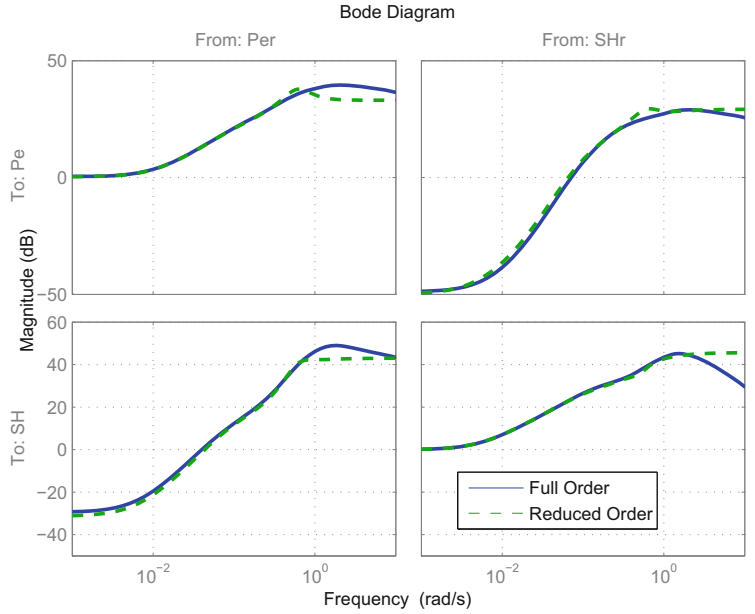

Fig. 5.10 Performance comparison of the full-order and reduced-order closed-loop systems

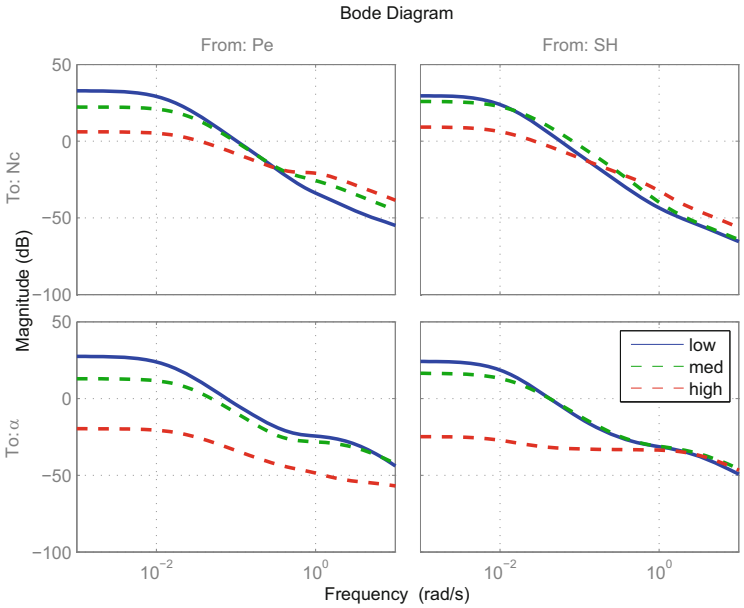

Fig. 5.11 Controller variation due to different cooling loads

Although the above design H_∞ controller is proved to realize the objective of output tracking and disturbance rejection locally, it is difficult to expand the feasible working region of a single H_∞ controller globally. In fact, in order to achieve the same level of closed-loop performances, the H_∞ controllers designed at different cooling loads have significant dynamics variations. Three scenarios corresponding to low, medium, and high cooling loads are considered, and the open-loop responses of the resulted H_∞ controllers are plotted in Fig. 5.11. Clearly, the gains at low frequency region change at different cooling loads, indicating the demand of a gain-scheduled H_∞ controller.

In this work, a simple interpolation approach is adopted to adaptively change the H_∞ controller at different working point. The simple gain-scheduled H_∞ controller is also validated using the above two scenarios, namely output tracking without/with external disturbances. Figure 5.12 shows a global output tracking over the entire working region. The reference evaporator pressure, starting from medium cooling load, switches to low cooling load first and back to high cooling load finally. Due to the fast responses of the controller over evaporator pressure, the actual evaporator pressure almost overlaps the reference values. On the other hand, the actual superheat temperature shows noticeable transitions as the cooling load changes, and its maximum deviation is always within the safety threshold.

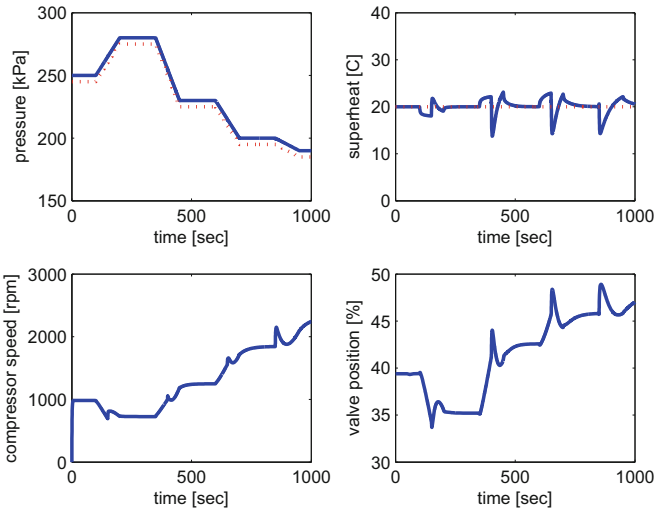

Fig. 5.12 System inputs and outputs during global tracking without disturbance

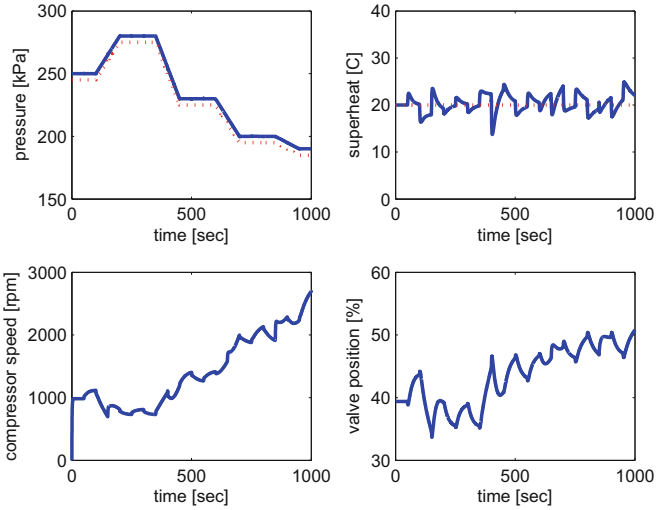

Fig. 5.13 System inputs and outputs during global tracking with disturbance added

In order to demonstrate the robustness of the designed controller over external disturbance. The variation of the air mass flow rate at the evaporator exterior surface is modeled as a pulse with period 100 s and width 50 s. Figure 5.13 shows the tracking performance over the same reference signals after disturbances are added into the nonlinear A/C model. As expected, the controller designed is proved to maintain its capability of tracking the evaporator pressure very well. Due to the existence of external disturbance, the variation of the actual superheat temperature

becomes more frequently than before, but still within the safety threshold. Therefore, it is demonstrated that tracking and robustness are both achieved over the entire working region.

Appendix

LTI A/C Model

The MBM A/C is linearized at multiple working points with different cooling loads on the A/C system. The linear system matrices, as proved in [4], are related to matrices in the original descriptor system by:

$$A := Z(x_o)^{-1} \left.\frac{\partial f}{\partial x}\right|_{x_o,u_o}$$
$$B := Z(x_o)^{-1} \left.\frac{\partial f}{\partial u}\right|_{x_o,u_o} \tag{5.21}$$

The LTI plant at design point is given by

$$A = \begin{pmatrix} -28.12 & 195 & 1.821 & -2.226 & 6.144 \\ 0.1828 & -1.364 & 0 & 0 & 0 \\ 0.0025 & 0 & -0.0733 & 0.02245 & 0 \\ -1.823 & 0.04938 & 20.83 & -25.45 & -56.36 \\ 0.2378 & -1.864 & 0.02361 & -0.02886 & -0.1698 \end{pmatrix}$$

$$B = \begin{pmatrix} -0.2037 & 134.7 & 0 \\ 0 & 0 & 0.2767 \\ 0 & 0 & 0.1106 \\ -0.221 & 53.26 & 0 \\ -0.00264 & 10.88 & 0 \end{pmatrix}$$

$$C = \begin{pmatrix} 1 & 0\,0 & 0 & 0 \\ -0.1121 & 0\,0 & 1.144 & 0 \end{pmatrix} \tag{5.22}$$

Full-Order and Reduced-Order Controller

The resulted full-order H_∞ controller is given as follows:

$$A_K = \begin{pmatrix} 2549 & 4.427e5 & 1.701e5 & 485.1 & -5.583e4 & -5561 & -1.013e4 & -48.84 & -2909 & 1.117e5 \\ 0.1743 & -1.364 & 0 & -4.037e-4 & 0 & 0 & 0 & 0 & 0 & 0.05534 \\ 2.548e-3 & 0 & -0.07325 & 0.01155 & 0 & 0 & 0 & 0 & 0 & 0.02213 \\ 1011 & 1.74e5 & 6.688e4 & 166.1 & -2.201e4 & -2186 & -3982 & -20.56 & -1150 & 4.391e4 \\ 208.9 & 3.583e4 & 1.377e4 & 39.45 & -4521 & -450.2 & -820.2 & -3.821 & -234.9 & 9044 \\ 0 & 0 & 0 & 0 & 0 & -0.01 & 0 & 0 & 0 & 0 \\ 0 & 0 & 0 & 0 & 0 & 0 & -0.001 & 0 & 0 & 0 \\ 4.083e4 & 7.008e6 & 2.692e6 & 7718 & -8.832e5 & -8.806e4 & -1.604e5 & -842.8 & -812.1 & 1.769e6 \\ 7.86e4 & 1.35e7 & 5.187e6 & 1.486e4 & -1.703e6 & -1.696e5 & -3.089e5 & -1430 & -9.843e4 & 3.406e6 \\ -0.02367 & 0 & 0 & -4.199e-3 & 0 & 0 & 0 & 0 & 0 & -0.25 \end{pmatrix}$$

$$B_K = \begin{pmatrix} -0.4261 & 0.01531 \\ -0.06253 & -0.002588 \\ -0.007535 & -0.06985 \\ -0.02836 & -0.02514 \\ 0.02427 & 0.08724 \\ 7.324 & 0 \\ 0 & 7.324 \\ 0 & 0 \\ 0 & 0 \\ -0.1765 & -0.02692 \end{pmatrix}$$

$$C_K = \begin{pmatrix} 5.444 & 934.3 & 359 & 1.029 & -117.8 & -11.74 & -21.38 & 1.221 \\ 2.62 & 449.9 & 172.9 & 0.4955 & -56.76 & -5.653 & -10.3 & -0.04765 & -2.946 & 113.5 \end{pmatrix} \tag{5.23}$$

The resulted reduced-order H_∞ controller is given as follows:

$$A_R = \begin{pmatrix} -0.001084 & 0.0009316 & -7.376e-5 \\ 0.001646 & -0.01216 & -0.06382 \\ 0.006088 & -0.01624 & -0.4687 \end{pmatrix}$$

$$B_R = \begin{pmatrix} 5.804 & 58.52 \\ -56.15 & 5.281 \\ -3.346 & 0.1396 \end{pmatrix}$$

$$C_R = \begin{pmatrix} -0.1279 & 0.09375 & 1.537 \\ -4.558e-5 & 3.618e-5 & 0.000733 \end{pmatrix}$$

$$D_R = \begin{pmatrix} 0.1662 & -2.14 \\ 0.00039 & -0.007264 \end{pmatrix} \tag{5.24}$$

References

1. F. Chiara, M. Canova, A review of energy consumption, management and recovery in automotive systems with considerations on future trends. Proc. Inst. Mech. Eng. Part D J. Automob. Eng. June 1, **227**, 914–936 (2013)
2. T. Harrison, Air conditioning system utilizing vehicle waste energy. SAE Technical Paper No. 2009-01-0543
3. B. Rasmussen, A. Alleyne, Gain scheduled control of an air conditioning system using the youla parameterization. IEEE Trans. Control Syst, Technol. **18**(5), 1216–1225 (2010)
4. Q. Zhang, L. Fiorentini, M. Canova, H robust control of an automotive air conditioning system, in *American Control Conference (ACC)* (IEEE, 2014), pp. 5675–5680
5. J.-L. Lin, T.-J. Yeh, Modeling, identification and control of air-conditioning systems. Int. J. Refrig. **30**(2), 209–220 (2007)
6. T.-J. Yeh, Y.-J. Chen, W.-Y. Hwang, J.-L. Lin, Incorporating fan control into air-conditioning systems to improve energy efficiency and transient response. Appl. Therm. Eng. **29**(10), 1955–1964 (2009)
7. X.-D. He, S. Liu, H.H. Asada, Modeling of vapor compression cycles for multivariable feedback control of HVAC systems. J. Dyn. Syst. Meas. Control **119**(2), 183–191 (1997)
8. X. He, S. Liu, H. Asada, H. Itoh, Multivariable control of vapor compression systems. HVAC&R Res. **4**(3), 205–230 (1998)
9. M. Willatzen, N. Pettit, L. Ploug-Sørensen, A general dynamic simulation model for evaporators and condensers in refrigeration. part i: moving-boundary formulation of two-phase flows with heat exchange. Int. J. Refrig. **21**(5), 398–403 (1998)
10. N. Pettit, M. Willatzen, L. Ploug-Sørensen, A general dynamic simulation model for evaporators and condensers in refrigeration. part ii: simulation and control of an evaporator. Int. J. Refrig. **21**(5), 404–414 (1998)
11. T. McKinley, A. Alleyne, An advanced nonlinear switched heat exchanger model for vapor compression cycles using the moving-boundary method. Int. J. Refrig. **31**(7), 1253–1264 (2008)
12. B. Li, A. Alleyne, A dynamic model of a vapor compression cycle with shut-down and start-up operations. Int. J. Refrig. **33**(3), 538–552 (2010)
13. J. Jensen, Dynamic modeling of thermo-fluid systems. Ph.D. Thesis, Technical University of Denmark, Department of Energy Engineering (2003)
14. R. Shah, B.P Rasmussen, A. Alleyne, Application of a multivariable adaptive control strategy to automotive air conditioning systems. Int. J. Adapt. Control Signal Process. **18**(2), 199–221 (2004)
15. H. Rasmussen, L.F.S. Larsen, Non-linear and adaptive control of a refrigeration system. IET Control Theory Appl. **5**(2), 364–378 (2011)
16. D. Leducq, J. Guilpart, G. Trystram, Non-linear predictive control of a vapour compression cycle. Int. J. Refrig. **29**(5), 761–772 (2006)
17. D. Leducq, J. Guilpart, G. Trystram, Low order dynamic model of a vapor compression cycle for process control design. J. Food Process Eng. **26**(1), 67–91 (2003)
18. L.C. Schurt, C.J. Hermes, A.T. Neto, A model-driven multivariable controller for vapor compression refrigeration systems. Int. J. Refrig. **32**(7), 1672–1682 (2009)
19. Q. Zhang, M. Canova, G. Rizzoni, Sliding mode control of an automotive air conditioning system, in *American Control Conference* (IEEE, 2013), pp. 5748–5753
20. M. Jung, K. Glover, Calibratable linear parameter-varying control of a turbocharged diesel engine. IEEE Trans. Control Syst. Technol. **14**(1), 45–62 (2006)
21. X. Wei, L. del Re, Gain scheduled h8 control for air path systems of diesel engines using LPV techniques. IEEE Trans. Control Syst. Technol. **15**(3), 406–415 (2007)
22. S. Daly, *Automotive Air Conditioning and Climate Control Systems* (Butterworth-Heinemann, Oxford, 2006)

23. T. Scott, S. Sundaram, Robust compressor model for ac system simulation. SAE Technical Paper 2007-01-0596
24. V. Chlumsky, *Reciprocating and Rotary Compressors* (E & F Spon Ltd., London, 1965)
25. J. MacArthur, E. Grald, Unsteady compressible two-phase flow model for predicting cyclic heat pump performance and a comparison with experimental data. Int. J. Refrig. **12**(1), 29–41 (1989)
26. Q. Zhang, Modeling, energy optimization and control of vapor compression refrigeration systems for automotive applications. Ph.D. Thesis, The Ohio State University (2014)
27. M. Steinke, S. Kandlikar, Single-phase liquid heat transfer in microchannels, in *International Conference on Microchannels and Minichannels* (2005)
28. W. Zhang, T. Hibiki, K. Mishima, Correlation for flow boiling heat transfer in mini-channels. Int. J. Heat Mass Transf. **47**(26), 5749–5763 (2004)
29. S. Koyama, K. Kuwahara, K. Nakashita, K. Yamamoto, An experimental study on condensation of refrigerant r134a in a multi-port extruded tube. Int. J. Refrig. **26**(4), 425–432 (2003)
30. Y. Chang, C. Wang, A generalized heat transfer correlation for louver fin geometry. Int. J. Heat Mass Transf. **40**(3), 533–544 (1997)
31. M. Kim, C. Bullard, Air-side thermal hydraulic performance of multi-louvered fin aluminum heat exchangers. Int. J. Refrig. **25**(3), 390–400 (2002)
32. X.-D. He, S. Liu, H.H. Asada, Modeling of vapor compression cycles for multivariable feedback control of HVAC systems. J. Dyn. Syst. Meas. Control **119**(2), 183–191 (1997)
33. K. Zhou, J.C. Doyle, *Essentials of Robust Control*, vol. 104 (Prentice Hall, Upper Saddle River, 1998)
34. J.C. Doyle, K. Glover, P.P. Khargonekar, B.A. Francis, State-space solutions to standard h_2 and h_∞ control problems. IEEE Trans. Autom. Control **34**(8), 831–847 (1989)
35. B. Francis, J. Helton, G. Zames, H-optimal feedback controllers for linear multivariable systems. IEEE Trans. Autom. Control **29**(10), 888–900 (1984)
36. W. Marquardt, Nonlinear model reduction for optimization based control of transient chemical processes, in Proc. CPC VI, ser. AIChE Symposium Series, **98**(326), 30–60 (2001)
37. A. Kumar, P. Christofides, P. Daoutidis, Singular perturbation modeling of nonlinear processes with nonexplicit time-scale multiplicity. Chem. Eng. Sci. **53**(8), 1491–1504 (1998)
38. Q. Zhang, M. Canova, Modeling and output feedback control of automotive air conditioning system. Int. J. Refrig. **58**, 207–218 (2015)

Chapter 6
Improving Tracking Performance of Automotive Air Conditioning System via μ Synthesis

Quansheng Zhang and Marcello Canova

Abstract In order to improve the performances of air conditioning systems, it is desirable to track time-varying trajectories generated by optimization algorithms, which H_∞ synthesis techniques have been proved to successfully solve. However, the control-oriented models of vapor compressor cycles used for algorithm development, even if built from first-principles, suffer from model uncertainties introduced by modeling assumptions, calibration inaccuracies, and linearization errors. The differences between the actual plant and the control-oriented model, mainly in the form of unmodeled dynamics and parameter uncertainty, undermine the stable margin as well as the performance of the closed-loop system with H_∞ controllers. In order to solve the problem, the concept of the structured singular value μ is used to analyze the influences of model uncertainties on robust stability and robust performance. Based on μ analysis results, μ synthesis techniques, compared to H_∞ methods, achieve better stability and performance margins over the same set of uncertainties. Furthermore, simulation results show that the μ controller achieves better performances of output tracking and disturbance rejection than the H_∞ controller for the automotive air conditioning system studied.

Keywords μ Synthesis • Robust control • Automotive • Air conditioning system

Nomenclature

a	Air
c	Condenser
cmp	Compressor
e	Evaporator
g	Gas
h	Enthalp

Reprinted from Zhang and Canova (2015), with permission from Elsevier.

Q. Zhang (✉)
Center for Automotive Research, The Ohio State University, 930 Kinnear Road, Columbus, OH 43212, USA
e-mail: zhang.777@osu.edu

Q. Zhang et al., *Automotive Air Conditioning*, DOI 10.1007/978-3-319-33590-2_6

l	Liquid
$\dot{m}$	Mass flow rate
N	Compressor speed
p	Pressure
$\dot{Q}$	Heat transfer rate
SC	Subcooled
SH	Superheated
T	Temperature
TP	Two phase
v	Valve
α	Valve position
γ	Void fraction
δ	Uncertainty
ρ	Density
ζ	Normalized phase region length
μ	Structured singular value

6.1 Introduction

In automotive air conditioning (A/C) system, the industry usually uses PID controllers to maintain system performance, requiring significant calibration efforts on gain tuning. In contrast, model-based control methods might be applied in order to explore the opportunity for system optimization through coordinated control of available actuators. Generally, the application of control theory to the A/C system involves the formulation of a tracking control problem for the evaporator pressure and the superheat temperature [1]. To enable the use of the model-based control method, a dynamic model of the A/C system with limited complexity is necessary to accurately predict the pressure and the enthalpy change in the evaporator and condenser. Specifically, the moving boundary method (MBM) is the most popular technique to model the pressure dynamics in the heat exchangers in presence of refrigerant phase change [2, 3].

In order to reduce the difficulty of performing control design when using the aforementioned models in the form of high-order nonlinear differential and algebraic equations (NDAEs), a general approach is to start from low-order, linear models obtained through system identification or model order reduction [4, 5]. For instance, [6] presents a discrete-time state-space model for indirect adaptive control that is recursively identified using a multi-input multi-output (MIMO) parameter estimation algorithm. A linear quadratic regulator (LQR) was then implemented for reference tracking and disturbance rejection. A local model network based on Youla parameterization was developed in [1], and a Lyapunov-based method was used to stabilize a tracking controller with respect to different local linear models. Similarly, a low-order nonlinear evaporator model was developed for backstepping design of a nonlinear adaptive controller [7]. Recently, advanced control methods have been

preliminarily applied to the output tracking problem of the automotive A/C system, such as sliding mode control (SMC) [8] and H_∞ control [9].

Besides the requirement on tracking performance of evaporator pressure and superheat temperature, another important aspect in control design for the A/C system is the controller's robustness to model uncertainties. Due to the simplification of the two-phase flow occurring in the heat exchanger, modeling and calibration of the MBM A/C model inevitably introduce uncertainties in the form of parameter uncertainty (volume uncertainty and heat transfer coefficient uncertainty), as well as unmodeled dynamics (mean void fraction uncertainty and actuator uncertainty). All the aforementioned model uncertainties are hardly touched in previous work. For instance, the LQR/LQG controller in [6] performs perfect only when the linear model matches the real plant after the fast convergence of the parameter estimation algorithm. The MIMO approach in [1] is proved to robust stable to certain varying rate of the schedule variables, excluding the influences of model uncertainties.

Mitigating the influences of parameter uncertainty and unmodeled dynamics on tracking performance of the closed-loop A/C system is a problem typically solved in the framework of robust control, such as H_∞ control in [10, 11] and μ synthesis in [12–14]. In the automotive field, robust control has been demonstrated for several practical applications, in particular turbocharged diesel engines [15–17]. However, it lacks a systematic study on the application of robust control theory to the control design of the A/C system. In the HVAC field, robust control has been demonstrated for the air path of a building HVAC system [18], while the refrigerant dynamics in the heat exchangers is not fully exploited. To this extent, it presents an application of a μ analysis and synthesis to an automotive A/C system, with the objective of tracking desired superheat temperature and evaporator pressure, as well as rejecting disturbances due to unknown time-varying boundaries conditions at the air side of the condenser and evaporator.

This chapter is organized as follows. Section 6.2 briefly describes the MBM A/C model and the H_∞ controller designed without uncertainties considered. Section 6.3 models a variety of uncertainties that might exist in A/C system, and evaluate the performance of the closed-loop A/C system with the H_∞ controller when uncertainties emerge. Then, a μ synthesis is performed in Sect. 6.4 to find a controller without severe performance deterioration under uncertainties.

6.2 A/C Model and H_∞ Control

In this section, the mathematical equations describing the dynamics of the automotive A/C system are presented, whose calibration procedure and validation test are available in [19]. Since the interest is in control algorithm development, the input–output relationship and the thermodynamic states of the MBM A/C model are focused in order to achieve a high-level representation. A benchmark controller is designed following the framework of H_∞ synthesis, which requires an augmentation of the control-oriented model with additional external disturbances and performance criteria. The tedious mathematical solution for control design is available in [19] as well.

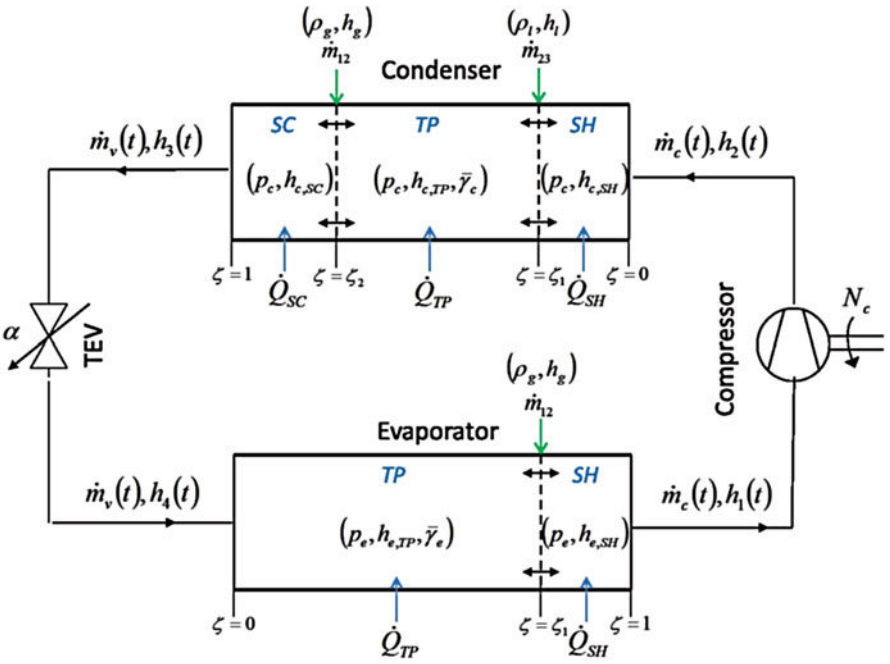

Fig. 6.1 Layout of the A/C system

6.2.1 A/C System Modeling

The refrigerant loop of an automotive A/C system includes a fixed-displacement rotary piston compressor, a condenser with a fan, a receiver/drier, an evaporator with a blower, and a thermal expansion valve. The interconnection of the four primary components (evaporator, compressor, condenser, and expansion valve) is illustrated in Fig. 6.1. The vapor compression cycle removes heat from the air flowing into the cabin through the evaporator, as the refrigerant evaporates from two-phase (TP) status into superheated (SH) status, and rejects heat to the air flowing through the condenser, as the refrigerant condenses from superheated (SH) status into subcooled (SC) status through two-phase (TP) status. In a well-established modeling framework, the compressor and valve are modeled as static components. The dynamics related to the heat and mass transfer inside the heat exchangers are described using the MBM method [2, 3], where Reynolds transport theorem describing the mass and energy conservation for transient one-dimensional flow is applied to each phase region of the condenser and evaporator with boundary conditions and refrigerant properties specified in Fig. 6.1. The detailed derivations [19] are omitted here for brevity and only the final mathematical equations describing system dynamics are summarized.

In compressor, the mass flow rate $\dot{m}_c$ and outlet enthalpy h_2 are defined, respectively, as:

$$\dot{m}_c = \eta_v V_d \rho_1 \omega_c, \quad h_2 = \frac{h_{2s} - h_1}{\eta_s} + h_1 \tag{6.1}$$

where V_d is the compressor displacement, ρ_1, h_1 the refrigerant density and enthalpy at the compressor inlet, ω_c the compressor speed, and $h_{2s} - h_1$ is the isentropic enthalpy difference. The first control input is the compressor rotation speed N_c in the unit of rpm.

The mass flow rate through the expansion valve is modeled by the orifice flow equation, approximated by assuming constant fluid density:

$$m_v = C_{d,v} A_v \sqrt{2\rho_3 (p_e - p_r)} \tag{6.2}$$

where A_v is the valve curtain area and C_v is the discharge coefficient. The outlet enthalpy is typically found by assuming an ideal throttling process, hence $h_4 = h_3$. The second control input is the valve position α in percentage, determining the effective flow area of the valve.

The mass and energy balance equations for the two-phase region and superheated region of the evaporator are given directly in Eqs. (6.3a, 6.3b) and (6.4a, 6.4b), respectively. In these differential equations, the left hands represent the variation of independent states of the refrigerant, and the right hands the exchanges of mass and energy at the inlet and outlet of individual phase region, as well as the heat transfer along the wall of corresponding region. The terms multiplying the state variations depend on the refrigerant inherent thermodynamic properties, hence are state-dependent.

$$\left(\frac{\rho_{e,\mathrm{TP}} - \rho_g}{\rho_{e,\mathrm{TP}}}\right)\frac{d\zeta_1}{dt} + \frac{1}{\rho_{e,\mathrm{TP}}}\frac{\partial \rho_{e,\mathrm{TP}}}{\partial p_e}\frac{dp_e}{dt}\cdot\zeta_1 + \frac{1}{\rho_{e,\mathrm{TP}}}\frac{\partial \rho_{e,\mathrm{TP}}}{\partial \overline{\gamma}_e}\frac{d\overline{\gamma}_e}{dt}\cdot\zeta_1 = \frac{\dot{m}_v}{\rho_{e,\mathrm{TP}} V_e} - \frac{\dot{m}_{12}}{\rho_{e,\mathrm{TP}} V_e} \tag{6.3a}$$

$$\begin{aligned} &\frac{\rho_g\left(h_{e,\mathrm{TP}} - h_g\right)}{\rho_{e,\mathrm{TP}}}\frac{d\zeta_1}{dt} + \left(\frac{\partial h_{e,\mathrm{TP}}}{\partial p_e} - \frac{1}{\rho_{e,\mathrm{TP}}}\right)\frac{dp_e}{dt}\cdot\zeta_1 + \frac{\partial h_{e,\mathrm{TP}}}{\partial \overline{\gamma}_e}\frac{d\overline{\gamma}_e}{dt}\cdot\zeta_1 \\ &= \frac{\dot{m}_v}{\rho_{e,\mathrm{TP}} V_e}\left(h_4 - h_{e,\mathrm{TP}}\right) - \frac{\dot{m}_{12}}{\rho_{e,\mathrm{TP}} V_e}\left(h_g - h_{e,\mathrm{TP}}\right) + \frac{\dot{Q}_{\mathrm{TP}}}{\rho_{e,\mathrm{TP}} V} \end{aligned} \tag{6.3b}$$

$$\begin{aligned} -\left(\frac{\rho_{e,\mathrm{SH}} - \rho_g}{\rho_{e,\mathrm{SH}}}\right)\frac{d\zeta_1}{dt} + \frac{1}{\rho_{e,\mathrm{SHP}}}\frac{\partial \rho_{e,\mathrm{SH}}}{\partial p_e}\frac{dp_e}{dt}\cdot(1-\zeta_1) + \frac{1}{\rho_{e,\mathrm{SH}}}\frac{\partial \rho_{e,\mathrm{SH}}}{\partial h_{e,\mathrm{SH}}}\frac{dh_{e,\mathrm{SH}}}{dt}\cdot(1-\zeta_1) \\ = \frac{\dot{m}_{12}}{\rho_{e,\mathrm{SH}} V_e} - \frac{\dot{m}_c}{\rho_{e,\mathrm{SH}} V_e} \end{aligned} \tag{6.4a}$$

$$\begin{aligned} &-\frac{\rho_g\left(h_g - h_{e,\mathrm{SH}}\right)}{\rho_{e,\mathrm{SH}}}\frac{d\zeta_1}{dt} + \frac{1}{\rho_{e,\mathrm{SH}}}\frac{dp_e}{dt}\cdot(1-\zeta_1) - \frac{dh_{e\mathrm{SH}}}{dt}\cdot(1-\zeta_1) \\ &= \frac{\dot{m}_{12}}{\rho_{e,\mathrm{SH}} V_e}\left(h_g - h_{e,\mathrm{SH}}\right) - \frac{\dot{m}_c}{\rho_{e,\mathrm{SH}} V_e}\left(h_1 - h_{e,\mathrm{SH}}\right) + \frac{\dot{Q}_{\mathrm{SH}}}{\rho_{e,\mathrm{SH}} V_e} \end{aligned} \tag{6.4b}$$

The mass and energy balances for the subcooled, two-phase, and superheated region of the condenser are similar to these of the evaporator. Besides, the wall temperatures, which are not uniform along the tube, are modeled as first order systems. None of these differential equations are presented here for brevity. The MBM A/C model after integrating all the component models is in the descriptor form,

$$\begin{aligned} Z(x)\dot{x} &= f(x, u, v) \\ y &= g(x) \end{aligned} \tag{6.5}$$

Because the A/C system performance is mainly related to the variables in the evaporator model, the following discussion focuses on the evaporator model in descriptor form. The inputs are the compressor rotation speed and expansion valve opening percentage, $\left[N_c \ \alpha \right]^T$. The boundary conditions are the variables describing the air side of the heat exchangers, and could be treated as unknown disturbances, $d = \dot{m}_{\text{ea}}$. The state vector describing the evaporator status includes five states as: $x_e = \left[\zeta_{e1} \ p_e \ h_{e2} \ T_{e1w} \ T_{e2w} \right]^T$. Finally, the outputs are the pressures and superheat temperature, $y = \left[p_e \ \text{SH} \right]^T$. The Z matrix and f vector are complex expressions of refrigerant properties, heat transfer coefficients, and geometric parameters. The MBM A/C model has been calibrated and validated using experimental data in both nominal steady state and drive cycle, according to the procedure outlined in [19]. The inputs and outputs of the MBM A/C model is illustrated in Fig. 6.2.

The MBM A/C model is linearized at multiple working points with different cooling loads on the A/C system, ranging from low to medium and to high. The cooling load is regulated by changing the inlet air temperature of the evaporator. For consistency, the superheat temperature is kept around 200 °C by cooperation of the compressor speed N_c and expansion valve position α; however, the evaporator pressure P_e is allowed to vary according to the cooling load as a gain scheduling parameter. Specifically, the boundary conditions, controlled inputs, and steady-state refrigeration states are summarized in Table 6.1.

The system matrices of the linearized A/C model corresponding to the medium cooling load are

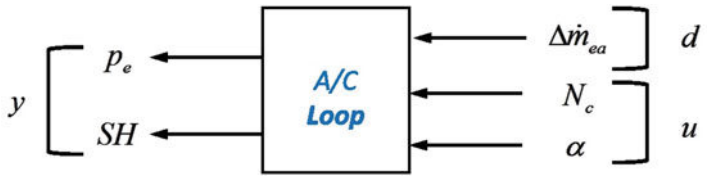

Fig. 6.2 A/C system inputs and outputs

Table 6.1 A/C operating points

$\dot{Q}_a$	T_a (°C)	N_c (rpm)	α (%)	P_e (kpa)
Low	25	450	25	302.2
Medium	30	1000	40	251.2
High	40	2500	55	204.6

$$
\begin{aligned}
A &= \begin{bmatrix} -28.12 & 195 & 1.821 & -2.226 & 6.144 \\ 0.1828 & -1.364 & 0 & 0 & 0 \\ 0.0025 & 0 & -0.0733 & 0.02245 & 0 \\ -1.823 & 0.04938 & 20.83 & -25.45 & -56.36 \\ 0.2378 & -1.864 & 0.02361 & -0.02886 & -0.1698 \end{bmatrix} \\
B &= \begin{bmatrix} -0.2037 & 134.7 & 0 \\ 0 & 0 & 0.2767 \\ 0 & 0 & 0.1106 \\ -0.221 & 53.26 & 0 \\ -0.00264 & 10.88 & 0 \end{bmatrix} \\
c &= \begin{bmatrix} 1 & 0 & 0 & 0 & 0 \\ -0.1121 & 0 & 0 & 1.144 & 0 \end{bmatrix}
\end{aligned} \tag{6.6}
$$

which, as proved in [9], are related to matrices in the original descriptor system by:

$$
A := Z(x_0)^{-1} \left.\frac{\partial f}{\partial x}\right|_{x_0,u_0} \qquad B := Z(x_0)^{-1} \left.\frac{\partial f}{\partial u}\right|_{x_0,u_0} \tag{6.7}
$$

6.2.2 H_∞ Synthesis

For the MIMO A/C model shown in Fig. 6.2, a widely investigated problem is to track prescribed trajectories of two output variables, namely the evaporator pressure p_e and the superheat temperature SH. Meanwhile, the controller should reject disturbances caused by air mass flow rate at the evaporator, $\dot{m}_{\text{ea}}$, which is not measurable and unknown on vehicles. Among a variety of control methods, H_∞ control has been firstly proposed in [9] and proved to successfully realize the control objectives. In robust control theory, H_∞ synthesis is to find a controller K for a plant model P such that the closed-loop system is asymptotically stable and the H_∞ norm of the transfer function between the disturbance d and the controlled output e, $\|T_{de}\|_\infty$, is as small as possible [10], as shown in Fig. 6.3.

In order to fit the H_∞ synthesis framework, the performance criteria e and unknown disturbances d in Fig. 6.3 should be clarified for automotive A/C systems, resulting in the entries of the augmented vectors listed sequentially in Fig. 6.4. Mathematically, the six elements in the vector of weighted performance criterion are selected as

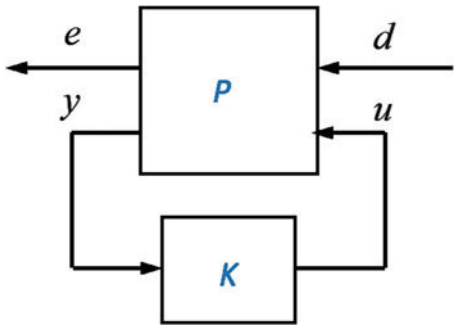

Fig. 6.3 General H_∞ control scheme

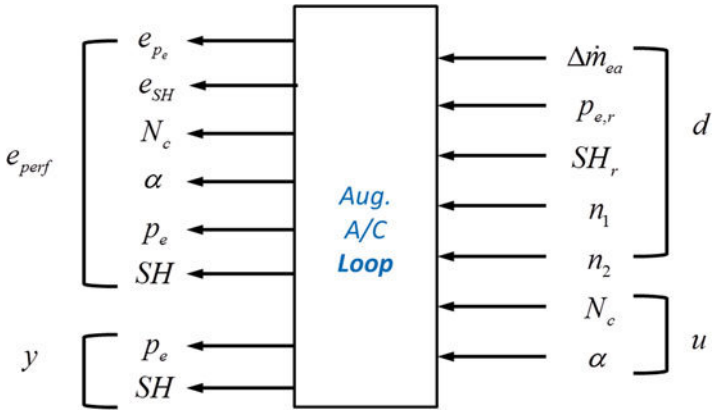

Fig. 6.4 A/C System H_∞ control scheme

$$\left[e_{p_e}\ e_{\mathrm{SH}}\ N_{\mathrm{cmp}}\ \alpha\ p_e\ \mathrm{SH} \right]^T \tag{6.8}$$

where $e_{p_e} = p_e, r - p_e$ and $e_{\mathrm{SH}} = \mathrm{SH}_r - \mathrm{SH}$ are errors on the output evaporator pressure and superheat temperature, N_{cmp} the compressor rotation speed and α the valve opening percentage, p_e evaporator pressure and SH superheat temperature. The weighting functions are selected following the suggestions in [20] and their specific mathematical forms and parameters are given in [9].

The reference evaporator pressure p_r and superheat temperature SH_r are time-varying and regarded as additional disturbances besides the unknown disturbances $\dot{m}_{\mathrm{ea}}$, as well as the noises. Therefore, the disturbance vector is defined as:

$$\left[\Delta\dot{m}_{\mathrm{ea}}\ p_{e,r}\ \mathrm{SH}_r\ n_1\ n_2 \right]^T \tag{6.9}$$

The original A/C model in state-space form is augmented with the output vector and disturbance vector defined, and an H_∞ controller is found by solving linear matrix inequalities (LMIs) associated with the augmented system according to methods provided in [11]. The above design procedure is detailed in previous work

in [19], where simulation results are provided to support the validity of the controller during output tracking and disturbance rejection. The full-order H_∞ controller has the same number of states as the augmented A/C model. After analyzing the "energy" of individual state, the first three states dominate the main dynamics in the system. Hence, the final H_∞ controller after model order reduction [19] is given below:

$$
\begin{aligned}
A_{C1} &= \begin{bmatrix} -0.001084 & 0.0000316 & -7.376 \times 10^{-5} \\ 0.001646 & -0.01216 & -0.06382 \\ 0.006088 & -0.01624 & -0.4687 \end{bmatrix} \\
B_{C1} &= \begin{bmatrix} 5.804 & 58.52 \\ -56.15 & 5.281 \\ -3.346 & 0.1396 \end{bmatrix} \\
C_{C1} &= \begin{bmatrix} -0.1270 & 0.00375 & 1.537 \\ -4.558 \times 10^{-5} & 3.618 \times 10^{-5} & 0.0007333 \end{bmatrix} \\
D_{C1} &= \begin{bmatrix} 0.1662 & -2.14 \\ 0.00030 & -0.007264 \end{bmatrix}
\end{aligned} \tag{6.10}
$$

6.3 Robust Analysis of H_∞ Controller

In automotive A/C system, the existence of parameter uncertainties and unmodeled dynamics affect the closed-loop stability and performance. The synthesis process of a controller over a plant with uncertainty is different from an H_∞ synthesis based on a plant without uncertainty. When model uncertainties emerge, the robust stability and robust performance of the closed-loop system with an H_∞ controller are not satisfied. Hence, it is desirable to pursue an advanced control technique named μ synthesis targeted for plants with uncertainties.

Ideally, an implementable algorithm is expected to ensure system stable as well as maintain performance requirements when uncertainties are noticeable. Mathematically, a controller K is supposed to achieve both stability and performance under uncertainty Δ for a plant P as shown in Fig. 6.5, where the plant P is an open-loop interconnection that contains all of the known elements including the nominal plant model in Fig. 6.2 and weighted performance criteria in Fig. 6.4. Specifically, three types of inputs enter P: perturbation outputs z, disturbances d, and control u. Three sets of outputs are generated: perturbation inputs ω, errors e, and measurements y. The Δ block is the uncertain element parameterizing all the assumed model uncertainty in the problem.

In this section, the focus is to illustrate the internal structure of the Δ block in Fig. 6.5. Those blocks representing parameter uncertainties and unmodeled dynamics are inserted into the simulator of the MBM A/C model developed, over

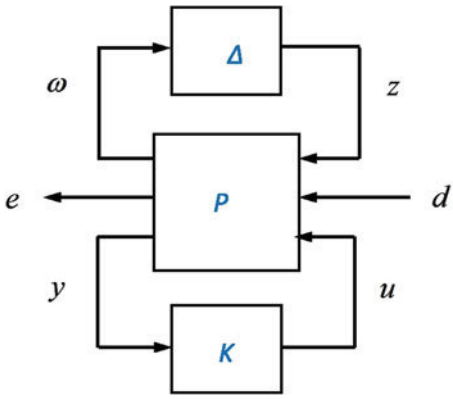

Fig. 6.5 General μ synthesis scheme

which the robust stability and robust performance of the H_∞ controller are verified in both frequency domain and time domain.

6.3.1 Uncertainty Implementation

The model used for control design is inevitably different from the actual dynamics of the plant due to practical factors categorized into unmodeled dynamics and parameter uncertainty. For example, the sources of modeling uncertainty in a vapor compression system might exist in compressor volumetric efficiency and isentropic efficiency, valve discharge coefficient, pipe pressure and heat losses, and the total refrigerant charge in the A/C loop. However, a thorough study of the above uncertainties is not practical, because a sequential identification of individual uncertainty is not an easy task, and the solution process is mathematically intractable as the number of the uncertainties increases. For current investigation, the model uncertainties that are closely related to the model type adopted (MBM A/C model) are of interest, namely parameter uncertainties of the volume of the heat exchanger and the heat transfer coefficients, as well as unmodeled dynamics of mean void fractions and compressor mass flow rates, all of which are generated when some fundamental assumptions are adopted to facilitate development of MBM A/C model.

Before exploring the generation mechanism of considered model uncertainties, an overview of their implementations in an MBM A/C model might be helpful. Since the MBM A/C model is in descriptor form as discussed, its implementation in Matlab/Simulink, at the highest level, is structured as in Fig. 6.6. The actuator inputs u are converted into thermodynamic properties (mainly mass flow rates) that are fed into the right-hand sides of the differential equations of the MBM A/C model, $f(x, u, v)$. The system matrix $Z(x)$ is built by looking up thermodynamic properties (density and enthalpy) given current system state x. The integral of the ratio of the

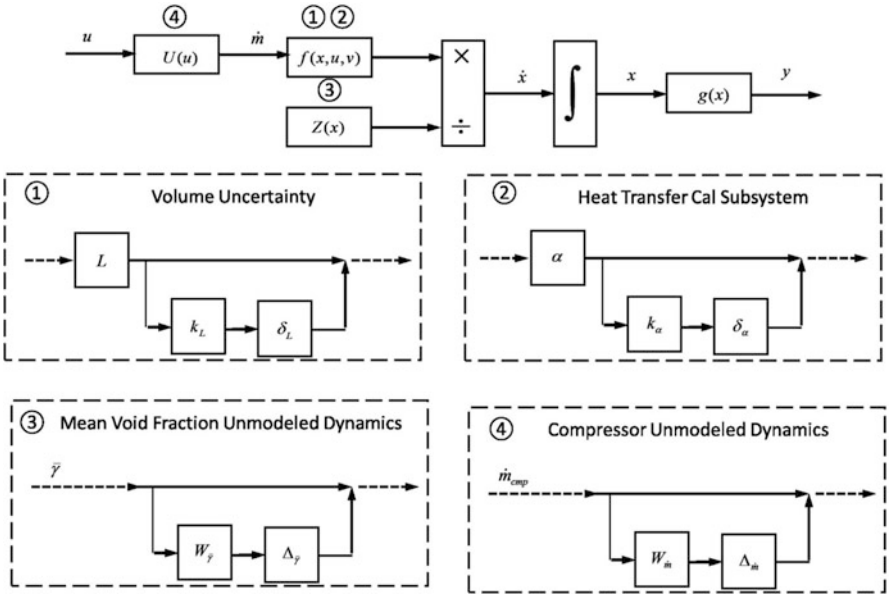

Fig. 6.6 Implementation of parameter uncertainty and unmodeled dynamics in simulator

f vector over Z matrix generates the current state x, which is used to calculate the output y algebraically. The two parameter uncertainties and two unmodeled dynamics are implemented sequentially in corresponding locations of the simulator, as labeled in the bottom four blocks in Fig. 6.6. For parameter uncertainty, an uncertain unit scalar block δ with amplitude k is added in parallel to parameter gain; for unmodeled dynamics, an uncertain unit system block Δ with frequency distribution $W(s)$ is added in parallel to the main signal path. Because both the parameter uncertainty and unmodeled dynamics are at the lowest level, those blocks linked to them are omitted in Fig. 6.6 for brevity. However, all model uncertainties change local dynamics that further affects global dynamics of the MBM A/C model.

Now, the generation mechanisms of the two parameter uncertainties and the two unmodeled dynamics are explained sequentially by analyzing the main assumptions adopted by the methodology of the MBM modeling approach.

A fundamental assumption at the beginning of the modeling process is to treat a heat exchanger as a fictitious long horizontal tube whose thermal mass, heat transfer area, and mass flux are equivalent to the actual component. This simplification neglects the axial conduction, thermal resistance, etc. [6]. Although the equivalent tube length is calculated to guarantee the volumes before and after the assumption are fixed, the modeling assumption inevitably introduces discrepancy between the estimated and "actual" equivalent length. The conclusion still holds for micro-channel heat exchangers, where the equivalent long horizontal single pass tube is

assumed to have a reduced mass flow rate by a factor of $1/n$, where n is the number of parallel-passes. Besides, relevant physical parameters, such as heat exchanger mass and air-flow cross-sectional area, are reduced by the same factor [3]. This simplification further neglects refrigerant maldistribution due to the parallel-passes as well as the headers of the heat exchangers. In both scenarios, a parameter uncertainty is added to the volume of the heat exchanger, $L = z \times P + \Delta(L)$.

During the calibration phase of the model, specific correlations for single and two-phase flow in micro-channels have been adopted from literature to determine the heat transfer coefficients for the refrigerant. In the single phase regions, the heat transfer correlation includes two parts [21]. For evaporation, the correlation proposed in [22] combines the nucleating boiling and convective boiling effects, $\alpha_{\text{tp}} = S\alpha_{\text{nb}} + F\alpha_{\text{sp}}$. For condensation, the correlation given by [23] combines the influences of the forced convection Nu_F and gravity controlled convection Nu_B using an asymptotic expression $\text{Nu} = \left(\text{Nu}_F^2 + \text{Nu}_B^2\right)^{1/2}$. On the external air side, specific heat transfer coefficients are defined for compact heat exchangers with louvers and fins, as noted by [24, 25]. The above heat transfer correlations are obtained by fitting experimental data of massive heat exchangers with a variety of geometries (e.g., tube or micro-channel diameter) and flow conditions (e.g., turbulent or laminar flow). Although the heat transfer multipliers scaling the heat transfer coefficients are capable of matching actual system responses with guaranteed accuracy, its accuracy deteriorates when the plants are not uniform. A common situation is that at leat 10 % deviation exits for two-phase correlations due to the liquid-laminar and gas-turbulent flow. A rigorous treatment of parameter uncertainties in all these correlations is to specify uncertainty bounds for each correlation, leading to a sophisticated high-order uncertainty vector. Instead, a practical approach is to lump all the uncertainties together into the heat transfer coefficients of the two-phase region on refrigerant side that dominates the process of heat transfer and refrigerant dynamics. To this extent, the actual heat transfer coefficient is bounded, $\alpha_{e,\text{act}} = \alpha_{e,\text{cor}} + \Delta\alpha$.

Mean void fraction uncertainty is inherent in the modeling of two-phase flow in the heat exchanger. The mean void fraction is dependent on not only the current refrigerant pressure, but also the inlet and outlet refrigerant quality, namely $\overline{\gamma} = f(P, x_{\text{in}}, x_{\text{out}})$. A specific correlation arises from the averaging of local void fraction distribution. For instance, a distribution of local void fraction over vapor quality is in the form of

$$\gamma(x, P) = \left[1 + \alpha_0 \left(\frac{1-x}{x}\right)^{\alpha_1} \left(\frac{\rho_g}{\rho_f}\right)^{\alpha_2} \left(\frac{\mu_f}{\mu_g}\right)^{\alpha_3}\right]^{-1} \tag{6.11}$$

where α_i are fitting parameters. The mean void fraction is an integral of local void fraction along the two-phase region of the heat exchanger. The dependency of vapor quality on location might be any appropriate relationship, and one simple treatment is linear [26]. The specific form of local void fraction distribution assumes two-phase flow in equilibrium; besides, the linear mapping between vapor quality

and location is an idealized simplification. Hence, both assumptions introduce uncertainty if the dependence of void fraction on pressure is modeled, especially when mode switching occurs during A/C system starting-up and shutting-down.

In previous work, the treatment of mean void fraction is either assuming it a constant or allowing it varying according to the corresponding heat exchanger pressure, both of which introduce uncertainty. For instance, the flow in two-phase region can be further divided into different regimes (bubble flow, slug flow, churn flow, etc.). The complicated phenomenon is averaged by a variety of mean void fraction correlations simply correlating mean void fraction with the pressure under equilibrium-flow assumption which implicitly neglecting the time lag between the two dynamics of mean void fraction and pressure. During the large transition, a first order approximation is made in [3] to help tuning the changing rates of the actual mean void fraction $\overline{\gamma}$ with respect to the ideal mean void fraction $\overline{\gamma}_{\text{tot}}$

$$\frac{\delta\overline{\gamma}_{\text{tot}}}{dp}\frac{dp}{dt} = \frac{d\overline{\gamma}}{dt} = K\left(\overline{\gamma} - \overline{\gamma}_{\text{tot}}\right) \tag{6.12}$$

So far, it is difficult to identify the errors introduced by the choice of local void fraction correlation, the linear mapping between two-phase spatial location and corresponding refrigerant quality, as well as the lag between the actual and ideal mean void fraction. To this extent, a unified approach is adopted to treat all the above errors into multiplicative unmodeled dynamics,

$$M\left(G, W_u\right) := \left\{\tilde{G} : \left|\frac{\tilde{G}\left(j\omega\right) - G\left(j\omega\right)}{G\left(j\omega\right)}\right| \leq \left|W_u\left(j\omega\right)\right|\right\} \tag{6.13}$$

where $G(s)$ is the nominal A/C model and W_u is a multiplicative uncertainty weighting functions.

Finally, the assumption of static compressor model might also introduce uncertainty if its dynamics affects the response speed of the vapor compression cycle. For instance, a first order dynamic is added to the refrigerant circulating across the compressor into the overall refrigeration loop,

$$\dot{m}_{\text{cmp}} = \frac{\dot{m}_{\text{cmp,static}} - \dot{m}_{\text{cmp}}}{\tau} \tag{6.14}$$

where the time constant τ is chosen to be 40 s [3]. Therefore, it is reasonable to add an unmodeled compressor dynamics into the actuator model of the automotive A/C system.

6.3.2 Uncertainty Analysis

Theoretically, the ratio of output variations over uncertainties variations is dependent on working points as well as plant structure. Hence, a unified approach of characterizing these uncertainties is desirable. The corresponding uncertainty structure Δ is not a simple stack of all the above uncertainties but depends on their definition sequence. Defining the structure of Δ involves specifying three thins: the type of each block, the total number of blocks, and their dimensions. From the above analysis of parameter uncertainty and unmodeled dynamics, there are two types of blocks: repeated scalar and full blocks for two parameter uncertainties and two first order unmodeled dynamics, respectively. Hence, the structure of Δ for the automotive A/C system is the form of

$$\Delta = \left[\text{diag}\left(\delta_1\ \delta_2\ A_1\ A_2\right) : \delta_i \in C, A_j \in C^{1\times 1}\right] \tag{6.15}$$

Linear fraction transformations (LFTs), a powerful and flexible approach to represent uncertainty in matrices and systems, is used to pull out the uncertainties in Fig. 6.6 systematically [20]. Let M be a complex matrix partitioned as

$$M = \begin{bmatrix} M_{11}\ M_{12} \\ M_{21}\ M_{22} \end{bmatrix} \tag{6.16}$$

and let Δl and Δu be two other complex matrices. Then a lower LFT with respect to Δ_l is formally defined as the map $F_l(M, \Delta_l) := M_{11} + M_{12}\Delta_l(I - M_{22}\Delta_l)^{-1}M_{21}$; an upper LFT with respect to Δ_u as $F_u(M, \Delta_u) := M_{22} + M_{21}\Delta_u(I - M_{11}\Delta_u)^{-1}M_{12}$. A useful interpretation of an LFT is that it has a nominal mapping, M_{11}, and is perturbed by Δ, with a prior knowledge as to how the perturbation affects the nominal map. In order to write the plant P into an LFT in terms of Δ, it is required to label the inputs and outputs of the δ's as y's and u's, respectively, and write z and y's in terms of ω and u's with all δ's taken out [20]. Figure 6.7 illustrates these extra entries connected to the uncertainty block (or perturbation) after the pulling-out process.

The influences of model uncertainties on system performance are of interest. A comprehensive quantitative study of the sensitivities of the A/C system outputs, namely evaporator pressure and superheat temperature, over parameter uncertainties, and unmodeled dyanmcis, has been performed in [27], where these model uncertainties are treated as unknown faults to detect. An alternative method of sensitivity study is to analytically differentiate the outputs over the model uncertainties using the MBM A/C model, which is mathematically formidable given the fact of strong nonlinearities and high-orders. Thus, a qualitative study is performed here to identify the main contributors of variations of response time and static gains.

After implementation of parameter uncertainty in the nonlinear MBM A/C model, its open-loop responses are shown in Fig. 6.8 by sampling the uncertainty

parameters with postive/negative one-tenth parameter uncertainties. From the different rising and setting times of the step response profiles, parameters uncertainties are found mainly affect the response time of the A/C system.

After implementation of unmodeled dynamics in the nonlinear MBM A/C model, its open-loop responses are shown in Fig. 6.9 by sampling the uncertainty parameters with postive/negative one-tenth unmodeled dynamics. From the different static gains, rising and setting times of the step response profiles, unmodeled dynamics is found affect both the amplitude and response time of the A/C system.

6.3.3 Robust Stability and Robust Performance

After the uncertain plant model P, structured uncertainty Δ and the H_∞ controller in Fig. 6.5 have been specified, two criteria are of interest: robust stability test and robust performance test, because they reveal the properties of the controller in frequency domain.

Robust stability test refers to whether the closed-system is stable under uncertainties. From Fig. 6.5, the plant P and the controller K are grouped through lower LFT, $M := F_l(M, K)$, as indicated in Fig. 6.10a. Herein, the new system matrix M is built by connecting an uncertain system P with a feedback controller K. Since the structure of the perturbation matrix Δ has already been defined in Eq. (6.15), the size of perturbations to which the system is robustly stable is only dependent on certain kind of property of system matrix M.

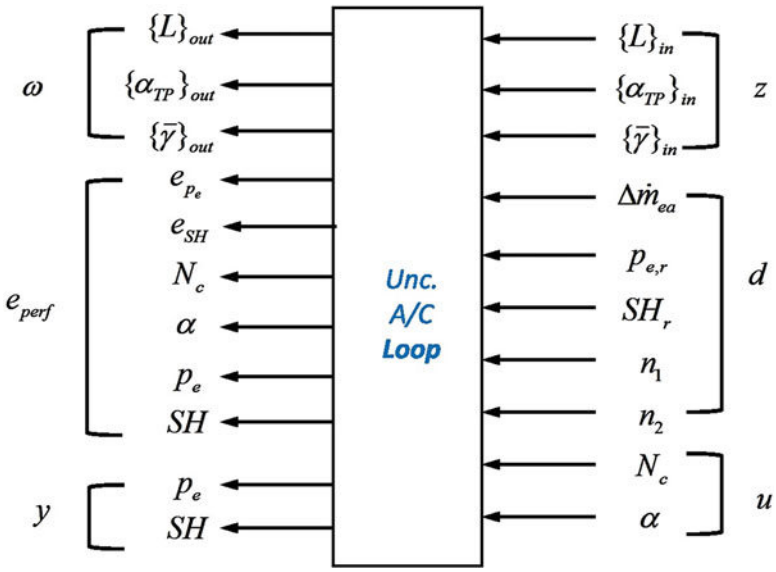

Fig. 6.7 A/C system μ synthesis scheme

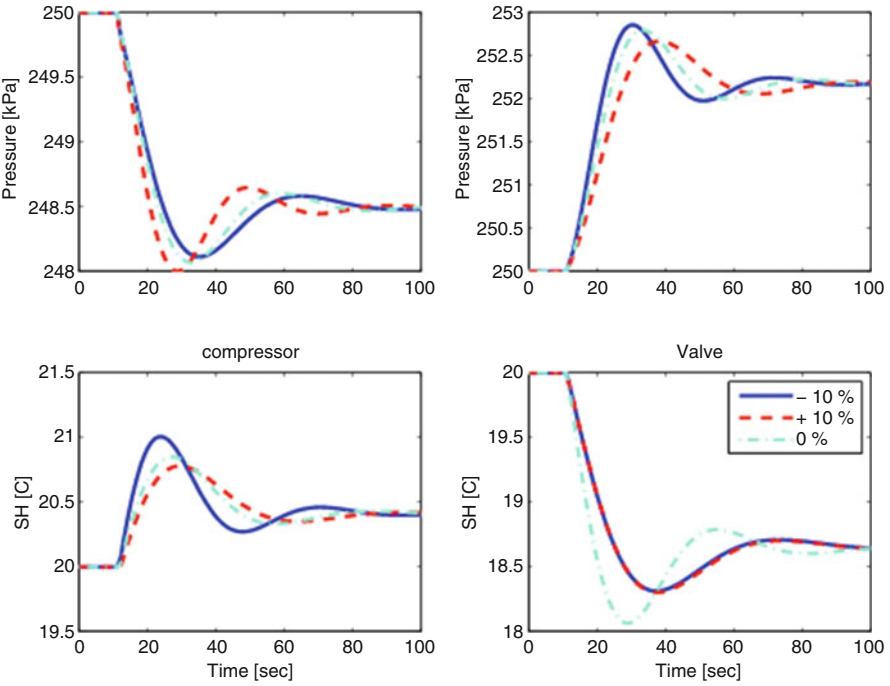

Fig. 6.8 Responses of uncertain A/C system to parameter uncertainty

Robust performance test refers to whether the output performance is satisfied under uncertainties. A good performance of MIMO control system is characterized using H_∞ norms of the weighted closed-loop transfer function T from disturbance d to performance variables e, noted as $T := F_u(M, \Delta)$ through upper linear fractional transformation. A transfer function T is small, which is equivalent to the fact that the performance is good, if and only if T can tolerate all possible stable feedback perturbation ΔF without leading to instability, as shown in Fig. 6.10b. Hence, a robust performance test could be determined using a robust stability test by introducing a fictitious uncertainty block across the disturbance/error channels.

$$A_P = \begin{bmatrix} A & 0 \\ 0 & A_F \end{bmatrix} \tag{6.17}$$

As indicated in above discussions, in order to analyze the robust stability and robust performance of uncertainty system, certain kind property of the uncertain closed-loop M corresponding to a specific uncertain structure Δ should be defined. In [20], a matrix function, denoted by $\mu(\cdot)$ and named structured singular value, is defined as

$$\mu_A(M) := \frac{1}{\min\{\sigma(\Delta) : \det(I - M\Delta) = 0\}} \tag{6.18}$$

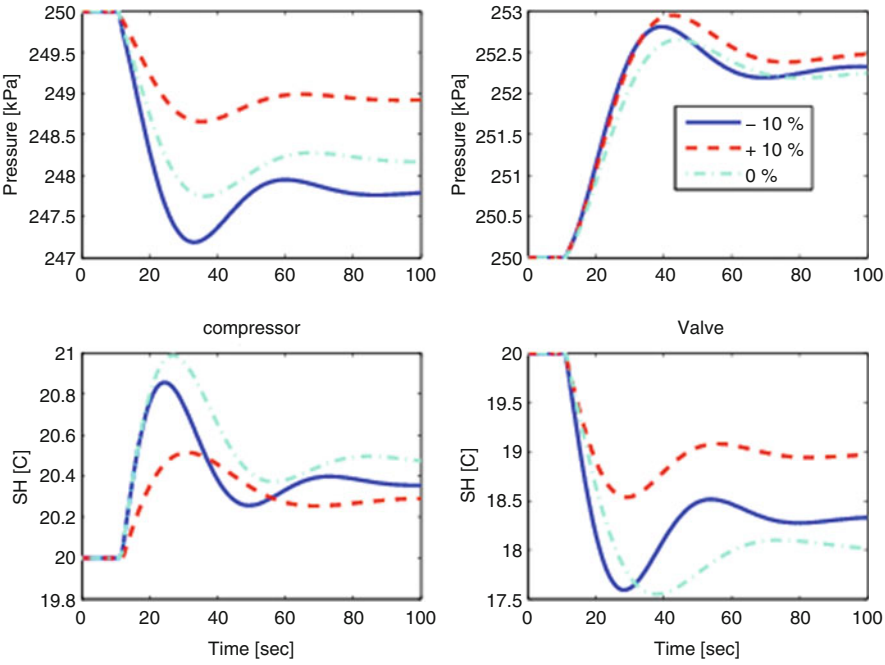

Fig. 6.9 Responses of uncertain A/C system to unmodeled dynamics

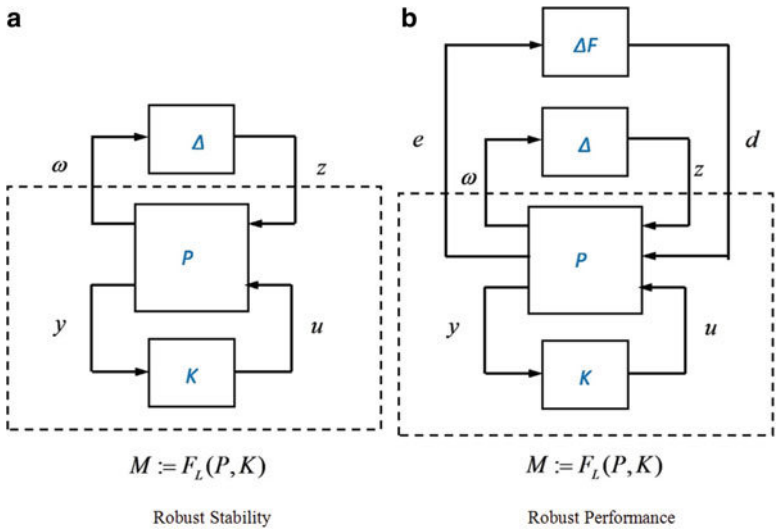

Fig. 6.10 Test schemes. (**a**) Robust stability. (**b**) Robust performance

An intuitive interpretation of the definition of structured singular value is that $\mu\Delta(M)$ is a measure of the smallest structured Δ that causes instability. In general, there is no direct computation method of structured singular value. However, an inequality can assist numerical software calculating lower and upper bounds of structured singular value over the frequency of interest [20].

The definition of structured singular value allows to formulate the two criteria of testing robust stability and robust performance.

Robust stability: let $\beta > 0$. The closed-loop is well posed and internally stable for all $\Delta(\cdot) \in M(A)$ with $\|\Delta\|_\infty \leq \frac{1}{\beta}$ if and only if $\sup_{\omega \in R} \mu_{A_F}\left[M_p(j\omega)\right] \leq \beta$.

Robust performance: let $\beta > 0$. For all $\Delta(\cdot) \in M(A)$ with $\|\Delta\|_\infty \leq \frac{1}{\beta}$, the cloop is well posed, internaly stable, and $\left\|F_u\left(M_p, \Delta\right)\right\|_\infty < \beta$ if and only if $\sup_{\omega \in R} \mu_{A_F}\left[M_p(j\omega)\right] \leq \beta$.

Note that for the discussion of robust stability and robust performance afterwards, a default setting is chosen, $\beta = 1$. In other words, if $\beta < 1$, the criterionis satisfied; otherwise, it is unsatisfied.

The robust stability and robust performance of the closed-loop A/C system with the H_∞ controller designed are shown in Fig. 6.11a, b, respectively. From Fig. 6.11a, the upper and lower bounds of the structured singular value representing robust stability is very close. The peak is about 0.51 and occurs at $\omega = 0.175$ rad/s. Hence, stability is guaranteed for all perturbations with appropriate structure, and $\max_\omega \sigma\left[\Delta(j\omega)\right] < 1 \approx 1.96$. Figure 6.11b, the upper and lower bounds of the structured singular value representing robust performance has discrepancy at low frequency domain. The peak value of both lower and upper bounds is about 1.95. In other words, for every perturbation $\Delta = 1.95\left[\text{diag}\left(\delta 1, \delta 2, \Delta 1, \Delta 2\right)\right]$ satisfying $\max_\omega \sigma\left[\Delta(j\omega)\right] < 1$, the stability is guaranteed and FU $(M, \Delta) \leq 1.95$. Moreover, there is a perturbation $\Delta = [\text{diag}(\delta 1, \delta 2, \Delta 1, \Delta 2)]$ satisfying $\max_\omega \sigma\left[\Delta(j\omega)\right] \approx 1/1.95 < 1$, such that FU $(M, \Delta) \approx 1.95 > 1$, implying that robust performance is not quite achieved.

6.3.4 *Reference Tracking and Disturbance Rejection*

Using uncertain A/C plant models selected from uncertainty structure with 3 %, 6 %, 10 % deviations from the nominal plant, the inefficiency of achieving robust performance becomes prominent from responses of the closed-loop system to reference evaporator pressure and superheat temperature, especially when disturbances arising from the evaporator air side are added. The tracking performance of evaporator pressure and superheat temperature is shown in Fig. 6.12a, b, respectively. Starting from a nominal working point around $(P_e, \text{SH}) = (250\ \text{kPa}, 20\ ^\circ\text{C})$ corresponding to a medium cooling load, step changes are added at 10 s into the reference evaporator pressure (5 kPa) and reference superheat (5 °C), respectively. Although different overshoot, rising time and setting time exist, the actual responses of all uncertain closed-loop A/C models are proved to track the step-up changes of the reference

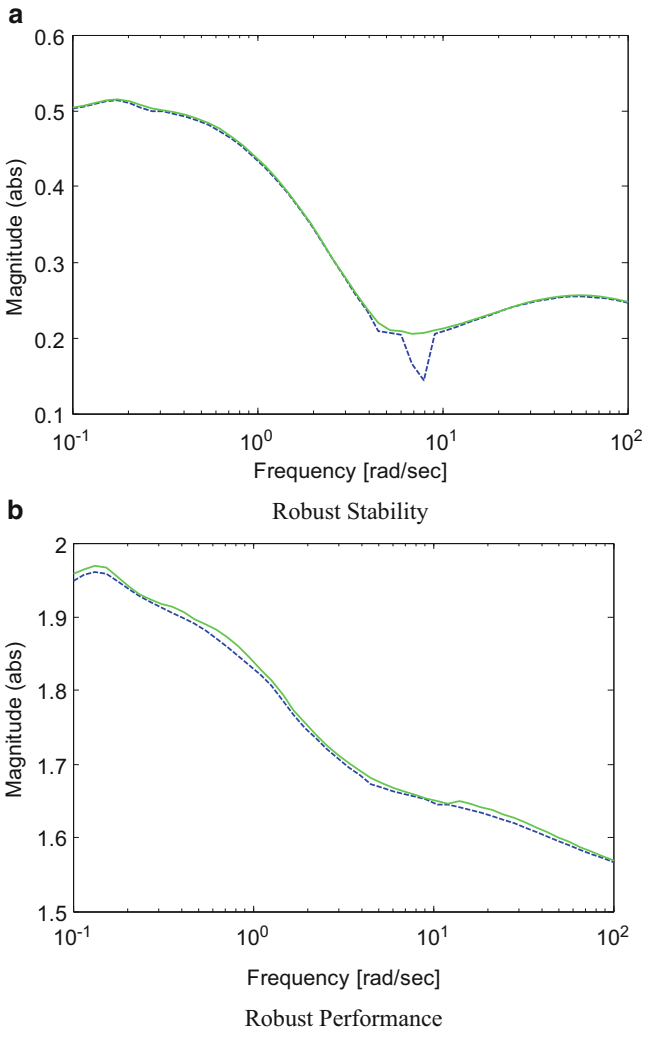

Fig. 6.11 Analysis of closed-loop A/C system with H_∞ controller. (**a**) Robust stability. (**b**) Robust performance

signals as expected, indicating robust stability is guaranteed. The performance deterioration is distributed evenly for individual tracking objective. Comparing Fig. 6.12a to Fig. 6.12b, the differences among the responses of sampled uncertain A/C system to superheat temperature are not as significant as these to evaporator pressure.

The inconsistency of closed-loop responses becomes even worse when tracking performance is evaluated under disturbances, when a 5 % variation is added into the evaporator air side at 10 s and removed after 50 s. The disturbance

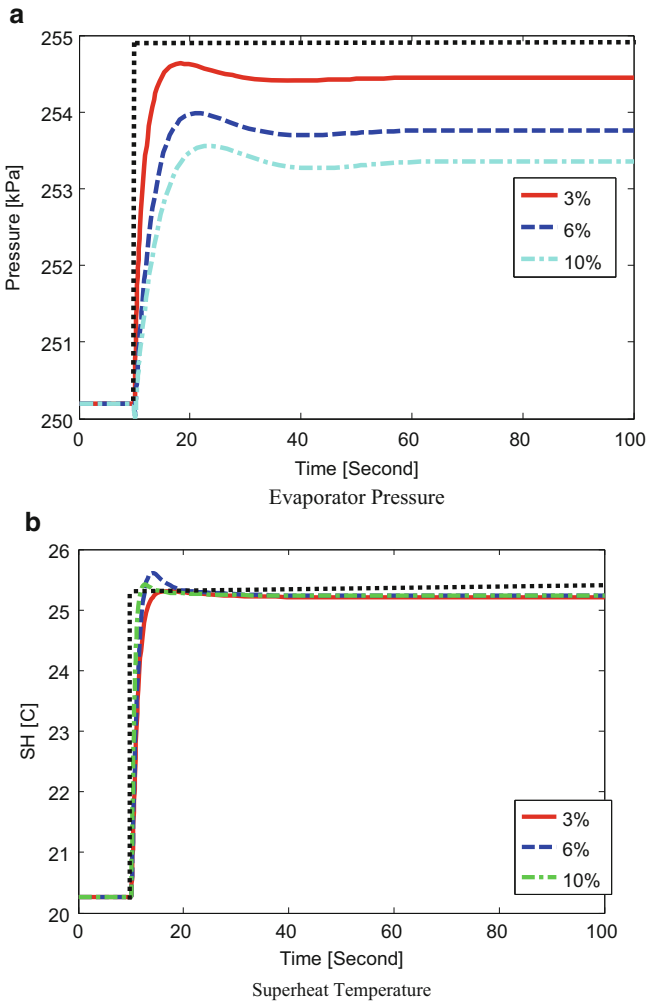

Fig. 6.12 Tracking performance of H_∞ controller under uncertainty. (**a**) Evaporator pressure. (**b**) Superheat temperature

rejection of the actual evaporator pressure and superheat temperature are shown in Fig. 6.13a, b. From both figures, the actual two outputs are finally maintained around the nominal working point (P_e, SH) = (250 kPa, 20 °C) after transition, as suggested by the H_∞ controller design requirements. However, the overshoot of the two actual outputs of sampled uncertain A/C models varies significantly, namely 1–4 kPa for evaporator pressure and 0.5−3 °C for superheat temperature. Hence, the performance deterioration is more significantly demonstrated using simulation under the scenario of disturbance rejection, compared to reference tracking.

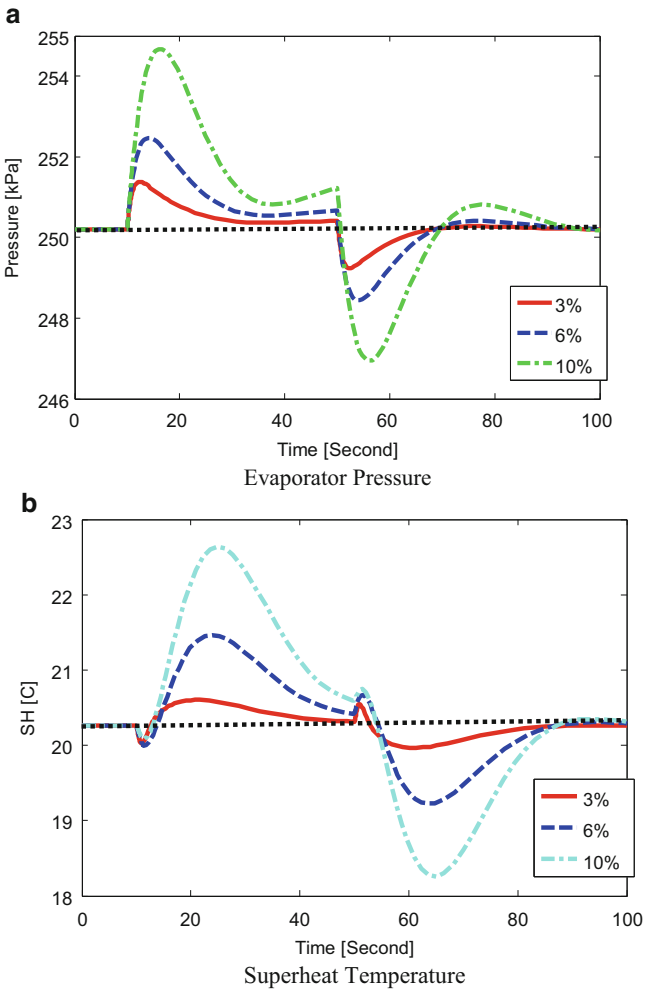

Fig. 6.13 Disturbance rejection of H_∞ controller under uncertainty. (**a**) Evaporator pressure. (**b**) Superheat temperature

6.4 μ Synthesis

From the simulation results of the closed-loop A/C system with an H_∞ controller, the designed controller K is not capable of achieving both stability and performance under uncertainty Δ for a plant P in Fig. 6.5. In order to develop a controller providing improved reference tracking and disturbance rejection for A/C plant with uncertainty, an advanced control technique, μ synthesis, is adopted, whose theoretical foundation is built upon the analysis of robust stability and robust performance discussed before.

6.4.1 Robust Stability and Robust Performance

Literally, the goal of μ synthesis is to ensure the performance of all sampled uncertain models uniform. Mathematically, it minimizes over all stabilizing controllers K, the peak value of $\mu\Delta(\cdot)$ of the closed-loop transfer function $F_L(P, K)$. More formally,

$$\min_{K} \max_{\omega} \mu_{\Delta} \left[F_L (P, K) (j\omega) \right] \tag{6.19}$$

where the uncertainty is consistent with the one defined in Eq. (6.17) consisting of both actual uncertainty and fictitious uncertainty. For tractability of the μ synthesis problem, it is necessary to replace $\mu\Delta$ $(\cdot)$ with its upper bound. After some mathematical iterations, the final optimization problem becomes

$$\min_{K} \min_{\widehat{D}_s \in D_{\Delta}} \left\| \widehat{D} F_L (P, K) \widehat{D}^{-1} \right\|_{\infty} \tag{6.20}$$

where D_{Δ} is a real-rational, stable, and minimum-phase transfer function. This optimization is currently solved using an iterative approach by finding optimal solution when D and K are fixed sequentially. The detail of D–K iteration is given in [20].

The calculated μ controller has more than 20 states, and the first three states contain the majority of "energy" compared to the rest. Hence, balanced model order reduction technique is applied to find a low-order μ controller described as

$$\begin{aligned} A_{\mu} &= \begin{bmatrix} -0.011634 & -0.05728 & -0.0289 \\ -0.01911 & -1.247 & -0.8841 \\ -0.005893 & -0.8549 & -0.7394 \end{bmatrix} \\ B_{C1} &= \begin{bmatrix} 0.601 & 4.429 \\ 10.03 & 2.679 \\ 5.583 & 0.4171 \end{bmatrix} \\ C_{C1} &= \begin{bmatrix} -4.482 & -11.26 & -5.598 \\ -0.001746 & -0.001392 & 0.003263 \end{bmatrix} \end{aligned} \tag{6.21}$$

The robust stability and robust performance of the closed-loop A/C system with μ controller integrated are shown in Fig. 6.14a, b, respectively. From Fig. 6.14a, the upper and lower bounds of the structured singular value representing robust stability is very close, too. The peak is about 0.82 and occurs at $\omega = 0.15$ rad/s, which is higher than the one of the H_{∞} controller. Hence, stability is guaranteed for all perturbations with appropriate structure. Hence, the robust stability margin of the μ controller is less than the one of the H_{∞} controller. Figure 6.14b, the upper and lower bounds of the structured singular value representing robust performance has discrepancy over the entire frequency domain. The peak value of both lower

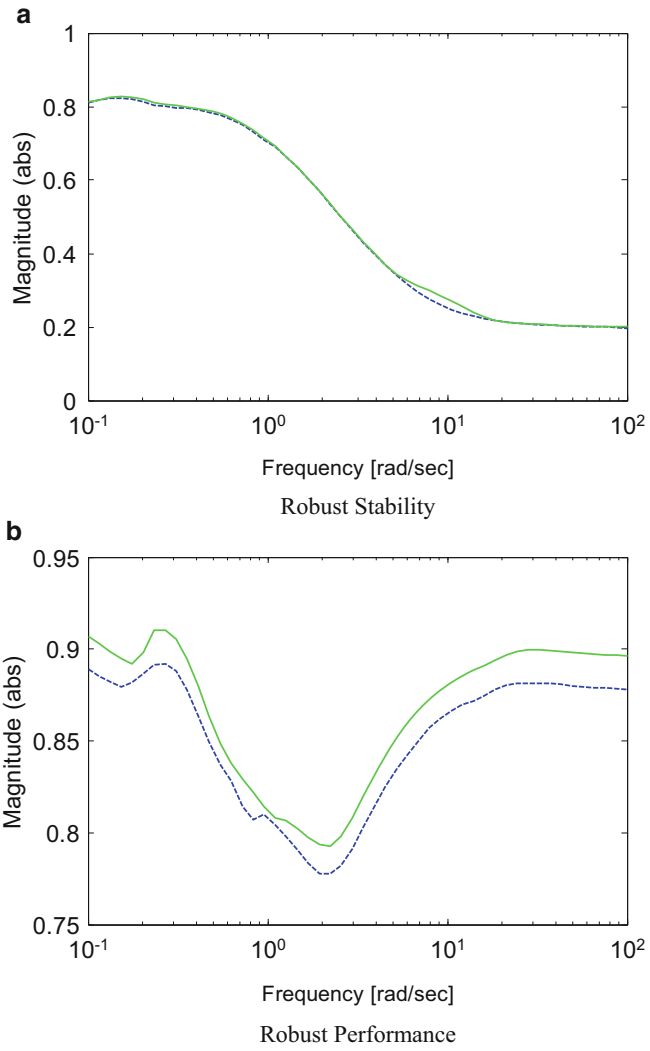

Fig. 6.14 Analysis of closed-loop A/C system with μ controller. (**a**) Robust stability. (**b**) Robust performance

and upper bounds is about 0.91. In other words, for every perturbation $\Delta = [\text{diag}\,(\delta 1, \delta 2, \Delta 1, \Delta 2)]$ satisfying the stability is guaranteed and $\text{FU}\,(M, \Delta) \leq 0.91$. Moreover, there is a perturbation $\Delta = [\text{diag}\,(\delta 1, \delta 2, \Delta 1, \Delta 2)]$ satisfying such that $\text{FU}\,(M, \Delta) \approx 0.91 < 1$, implying that the requirement of robust performance is satisfied.

6.4.2 *Reference Tracking and Disturbance Rejection*

Integrating the designed μ controller with the uncertain A/C plant models selected from uncertainty structure with 3 %, 6 %, 10 % deviations from the nominal plant, we will prove the capability of the controller in achieving robust performance from the responses of the closed-loop system to the changes of the reference evaporator pressure and superheat temperature, especially when disturbances arising from the evaporator air side are added. The tracking performance of evaporator pressure and superheat temperature is shown in Fig. 6.15a, b, respectively. With the same nominal

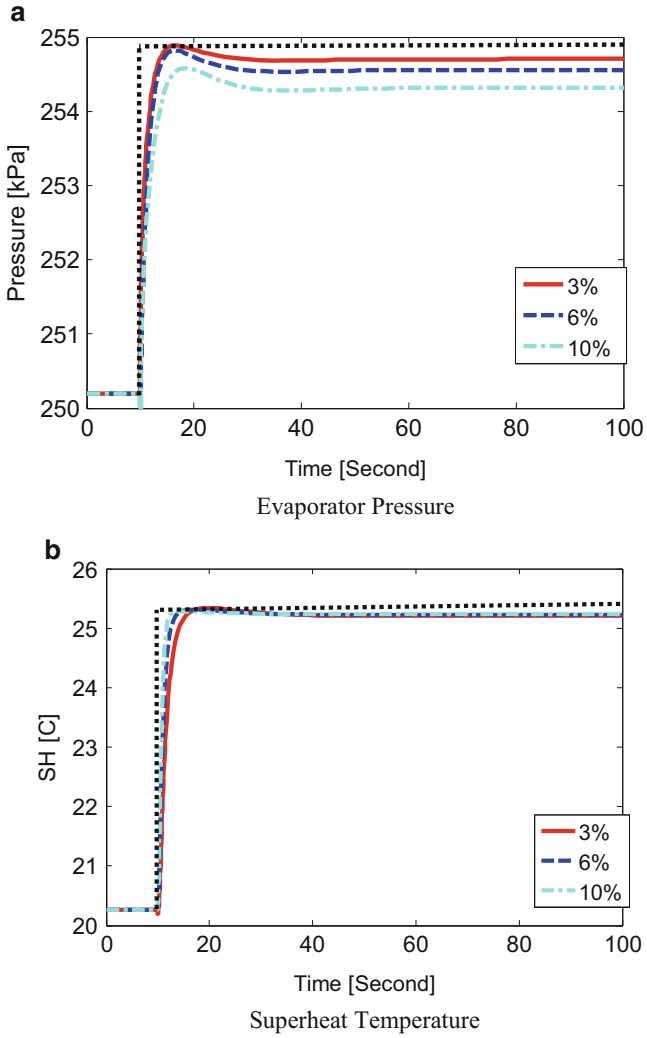

Fig. 6.15 Tracking performance of μ controller under uncertainty. (**a**) Evaporator pressure. (**b**) Superheat temperature

working point and step signals as before, the actual responses of all uncertain closed-loop A/C models are proved to track the step-up changes of the reference signals as expected, indicating robust stability is guaranteed. The tracking performances, such as overshoot, rising time and setting time, are improved from the fact that the deviation amplitude of these responses of sampled uncertain A/C system to reference evaporator pressure in Fig. 6.15a is reduced by half compared to those in Fig. 6.12a. Similar conclusion could be drawn from the comparison between responses to reference superheat temperature in Fig. 6.15b and these in Fig. 6.12b, though the reduction of deviation amplitude is not very obvious.

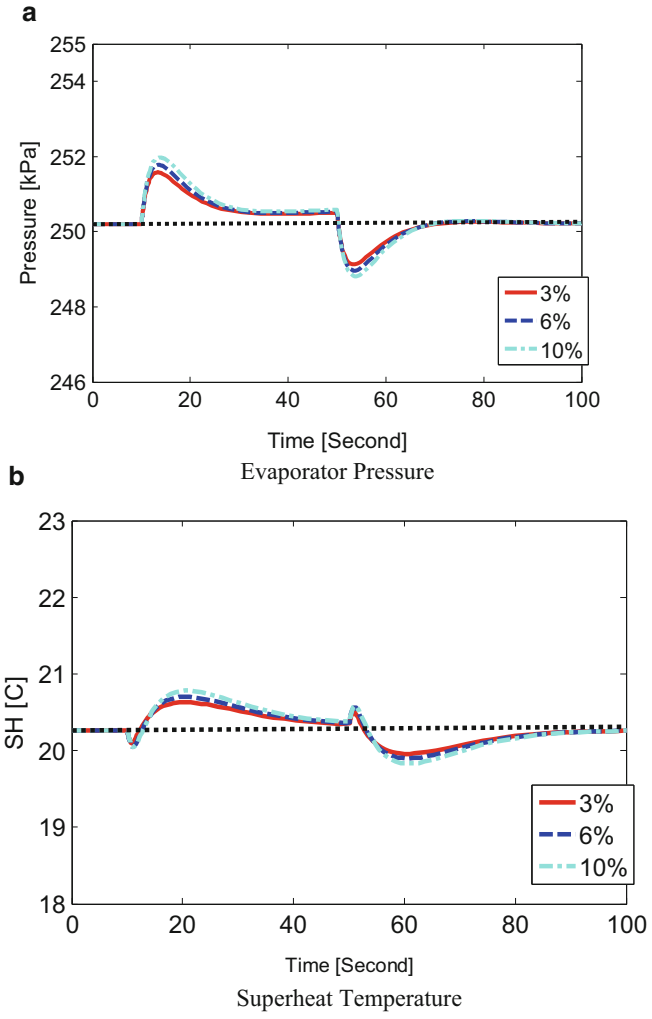

Fig. 6.16 Disturbance rejection of μ controller under uncertainty. (**a**) Evaporator pressure. (**b**) Superheat temperature

The consistency of closed-loop responses becomes much better when tracking performance is evaluated under the same disturbances as before. The disturbance rejection of the actual evaporator pressure and superheat temperature is shown in Fig. 6.16a, b. From both figures, the actual two outputs are finally maintained around the nominal working point after transient, as suggested by the μ controller design requirements. However, the performance criteria, such as overshoot, rising time and setting time, of both actual outputs of sampled uncertain A/C models are very consistent, compared to the significant variation in Fig. 6.13a, due to the fact the stability performance margin of the μ controller is much larger than the one of H_∞ controller.

References

1. B. Rasmussen, A. Alleyne, Gain scheduled control of an air conditioning system using the Youla parameterization. IEEE Trans. Control Syst. Technol. **18**(5), 1216–1225 (2010)
2. X.-D. He, S. Liu, H.H. Asada, Modeling of vapor compression cycles for multivariable feedback control of HVAC systems. J. Dyn. Syst. Meas. Control. **119**(2), 183–191 (1997)
3. B. Li, A. Alleyne, A dynamic model of a vapor compression cycle with shut-down and start-up operations. Int. J. Refrig. **33**(3), 538–552 (2010)
4. Q. Zhang, M. Canova, Lumped-parameter modeling of an automotive air conditioning system for energy optimization and management. In *ASME 2013 Dynamic Systems and Control Conference* (American Society of Mechanical Engineers, 2013), pp. V001T04A003–V001T04A003, http://proceedings.asmedigitalcollection.asme.org/proceeding.aspx?articleid=1841102
5. J. Jensen, Dynamic modeling of thermo-fluid systems. Ph.D. Dissertation, Department of Energy Engineering, Technical University of Denmark, 2003
6. R. Shah, B.P. Rasmussen, A. Alleyne, Application of a multivariable adaptive control strategy to automotive air conditioning systems. Int. J. Adapt. Control Signal Process **18**(2), 199–221 (2004)
7. H. Rasmussen, L.F.S. Larsen, Non-linear and adaptive control of a refrigeration system. IET Control Theory Appl. **5**(2), 364–378 (2011)
8. Q. Zhang, M. Canova, G. Rizzoni, Sliding mode control of an automotive air conditioning system. *American Control Conference*. IEEE, 2013, pp. 5748–5753
9. Q. Zhang, M. Canova, G. Rizzoni, Robust control of an automotive air conditioning system. *American Control Conference*. IEEE, 2014, pp. 5748–5753
10. J.C. Doyle, K. Glover, P.P. Khargonekar, B.A. Francis, State-space solutions to standard h_2 and H_∞ control problems. IEEE Trans. Autom. Control **34**(8), 831–847 (1989)
11. B. Francis, J. Helton, G. Zames, H-optimal feedback controllers for linear multivariable systems. IEEE Trans. Autom. Control **29**(10), 888–900 (1984)
12. A. Packard, J. Doyle, The complex structured singular value. Automatica **29**(1), 71–109 (1993)
13. G.J. Balas, J.C. Doyle, K. Glover, A. Packard, R. Smith, *μ-Analysis and Synthesis Toolbox* (MUSYN and MathWorks, Natick, MA, 1993)
14. P. Gahinet, A. Nemirovskii, A.J. Laub, M. Chilali, The LMI control toolbox. *IEEE Conference on Decision and Control*, vol. 2, Institute of Electrical Engineers Inc. (IEE), 1994, pp. 2038–2038
15. M. Jung, K. Glover, Calibratable linear parameter-varying control of a turbocharged diesel engine. IEEE Trans. Control Syst. Technol. **14**(1), 45–62 (2006)
16. X. Wei, L. del Re, Gain scheduled H_∞ control for air path systems of diesel engines using LPV techniques. IEEE Trans. Control Syst. Technol. **15**(3), 406–415 (2007)

17. M. Lee, M. Sunwoo, Modelling and H_∞ control of diesel engine boost pressure using a linear parameter varying technique. Proc. Inst. Mech. Eng. D J. Automob. Eng. **226**(2), 210–224 (2012)
18. M. Anderson, M. Buehner, P. Young, D. Hittle, C. Anderson, J. Tu, D. Hodgson, Mimo robust control for HVAC systems. IEEE Trans. Control Syst. Technol. **16**(3), 475–483 (2008)
19. Q. Zhang, M. Canova, Modeling and output feedback control of automotive air conditioning systems. Accepted by International Journal of Refrigeration, 2014
20. K. Zhou, J.C. Doyle, *Essentials of Robust Control*, vol. 104 (Prentice Hall, Upper Saddle River, NJ, 1998)
21. M. Steinke, S. Kandlikar, Single-phase liquid heat transfer in microchannels. *International Conference on Microchannels and Minichannels*, 2005
22. W. Zhang, T. Hibiki, K. Mishima, Correlation for flow boiling heat transfer in mini-channels. Int. J. Heat Mass Transf. **47**(26), 5749–5763 (2004)
23. S. Koyama, K. Kuwahara, K. Nakashita, K. Yamamoto, An experimental study on condensation of refrigerant r134a in a multi-port extruded tube. Int. J. Refrig. **26**(4), 425–432 (2003)
24. Y. Chang, C. Wang, A generalized heat transfer correlation for Iouver fin geometry. Int. J. Heat Mass Transf. **40**(3), 533–544 (1997)
25. M. Kim, C. Bullard, Air-side thermal hydraulic performance of multi-louvered fin aluminum heat exchangers. Int. J. Refrig. **25**(3), 390–400 (2002)
26. T. McKinley, A. Alleyne, An advanced nonlinear switched heat exchanger model for vapor compression cycles using the moving-boundary method. Int. J. Refrig. **31**(7), 1253–1264 (2008)
27. M.C. Keir, A.G. Alleyne, Dynamic modeling, control, and fault detection in vapor compression systems. Air Conditioning and Refrigeration Center, College of Engineering, University of Illinois at Urbana-Champaign, Tech. Rep., 2006
28. Q. Zhang, M. Canova, Improving tracking performance of automotive air conditioning system via μ synthesis. Sci. Technol. Built Environ. **21**(4), 448–461 (2015)

Chapter 7
Mean-Field Control for Improving Energy Efficiency

Sisi Li, Shengbo Eben Li, and Kun Deng

Abstract In this chapter, we describe a mean-field control method to improve energy efficiency for operating the heating, ventilation, and air conditioning (HVAC) systems. To illustrate the idea of this method, we consider a distributed set-point temperature regulation problem for building HVAC systems. With a large number of zones in large buildings, the problem becomes intractable with standard control approaches due to the large state space dimension of the dynamic model. To mitigate complexity, we apply the mean-field control approach to large-scale control problems in buildings. The mean-field here represents the *net effect* of the entire building envelope on any individual zone. Rather than solving the large-scale centralized problem, we explore distributed game-theoretic solution approaches that work by optimizing with respect to the mean-field. The methodology is illustrated with a numerical example in a simulation environment.

Keywords Temperature control • Air conditioning system • Building

7.1 Introduction

Buildings are one of the primary consumers of energy. In the USA, buildings are responsible for 30 % of energy consumption, and 71 % of electricity consumption, while accounting for 33 % of CO_2 emissions [1]. A large amount of the energy consumed in buildings is wasted. A major reason for this wastage is *inefficiencies*

S. Li
Department of Mathematics and Computer Sciences, Mercy College,
Dobbs Ferry, NY 10522, USA
e-mail: sli8@mercy.edu

S.E. Li
State Key Laboratory of Automotive Safety and Energy, Department of Automotive Engineering,
Tsinghua University, Beijing, 10084, China
e-mail: lishbo@tsinghua.edu.cn

K. Deng (✉)
Coordinated Science Laboratory, University of Illinois at Urbana-Champaign,
Urbana, IL 61801, USA
e-mail: kundeng2@illinois.edu

Q. Zhang et al., *Automotive Air Conditioning*, DOI 10.1007/978-3-319-33590-2_7

in the building technologies, particularly in operating the heating, ventilation, and air conditioning (HVAC) systems. According to a study commissioned by the US Department of Energy, the current building systems are only 20–30 % efficient in energy usage [2]. These inefficiencies are in turn caused by the manner in which HVAC systems are currently operated. The temperature in each zone is controlled by a local controller, without regards to the effect that other zones may have on it or the effect it may have on others. Substantial improvement may be possible if inter-zone interactions are taken into account in designing control laws for individual zones.

In fact, there is a growing interest in optimal control methods to minimize building-wide energy consumption based on dynamic models [3–7]. Such control techniques require a model of the transient thermal dynamics of the building that relates the control signals to the space temperature of each zone. A challenge in developing such techniques is the *complexity* of the underlying models due to large dimension of state space and a large number of control objectives. A model based on the first-principles will be a large set of coupled PDEs, which is intractable in general. Even the so-called reduced-order models that rely on a lumped resistor–capacitor analogy of walls and windows lead to models with large state space. Such a reduced order model for a medium-size commercial building with about 100 zones will have a state dimension close to 1000 [8].

In this chapter, we describe a *decentralized* optimal control strategy for the zones of a multi-zone building where model complexity is mitigated by using a two pronged approach. First, we use recently developed aggregation-based model reduction techniques [9] to construct a reduced-order model of the multi-zone building's thermal dynamics. Second, we use the mean-field intuition from statistical mechanics so that the effect of other zones on a particular zone is captured through a *mean-field* model [10]. Then the whole model (even the reduced model) does not have to be used in computing the controls for short-time scales.

By using the mean-field idea, we cast the control problem as a game, whereby each zone has its own control objective modeled as set-point tracking of the local (zonal) temperature. In general, the control problem quickly becomes intractable for even a moderate number of competing objectives. In order to mitigate complexity, we employ the Nash certainty equivalence (NCE) principle to obtain a mean-field description [11]. The mean-field here represents the *net effect* of the entire building envelope on any individual zone. A local optimal zonal control is designed based on the local model of thermal dynamics and its interaction with the building via the mean-field (mass influence). A consistency relationship is used to enforce the mean-field in a self-consistent manner. The methodology is shown to yield distributed control laws that can easily be implemented on large-scale problems.

We compare the performance of the proposed controller with that of a PI controller. Controllers currently used in commercial buildings use a combination of discrete logic and PID type controllers. Simulations show that the proposed scheme achieves comparable temperature tracking performance while reducing energy consumption by reducing the mass-flow rates entering the zones. The outline of this chapter is as follows: In Sect. 7.2, we describe the baseline and reduced models of building thermal dynamics. In Sect. 7.3, the mean-field control methodology is

described for the building temperature regulation problem. In Sect. 7.4, we describe the mean-field control for linearized building model. The simulation results and comparisons with PI control appear in Sect. 7.5.

7.2 Building Thermal Model

7.2.1 Configuration of HVAC System

A typical multi-zone HVAC system used in modern buildings is the variable-air-volume (VAV) system. Such a system supplies air at a constant temperature. The airflow to the zones is controlled based on room thermal load requirements. Figure 7.1 depicts the configuration of a four-zone building equipped with a VAV system: Upstream, an air handling unit (AHU) conditions air by passing it across the cooling coil. A series of ducts is used to supply the cold and dry air to VAV boxes for each of the downstream zones. Each VAV box contains a local controller, tasked with maintaining the zone temperature at a specified value, by controlling the mass flow rate of air supplied to the zone using dampers. The total air flow rate of the entire system therefore varies with time. Zonal controllers at VAV boxes may also apply "reheat" (adding heat) or "pre-cooling" (removing heat) to the conditioned air before supplying it to the zone.

7.2.2 Baseline Building Thermal Model

A building thermal model is constructed by combining elemental models of conductive interaction between two zones separated by a solid surface (e.g., walls, windows, ceilings, and floors). A lumped parameter model of conduction across a surface is assumed to be an RC-network, with current and voltage being analogs of heat flow and temperature [12].

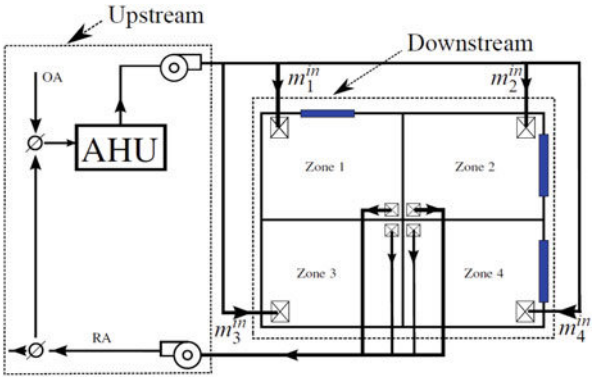

Fig. 7.1 The configuration of a four-zone building HVAC system

The resulting model can be described by an *undirected graph* $G = (\mathcal{V}_0, \mathcal{E})$, where $\mathcal{V}_0 := \{0\} \cup \mathcal{V}$ denotes the set of *nodes* of the graph. The node $\{0\}$ denotes the outside and the set $\mathcal{V} := \{1, \ldots, n\}$ denotes the building nodes. The nodes are so indexed that the first N nodes of $\mathcal{V}$ correspond to the zones $1, \ldots, N$, and these are called the *zone nodes*. The next $(n - N)$ nodes of $\mathcal{V}$ correspond to the internal points of the surfaces. These are called the *internal nodes*. An edge (i, j) exists between nodes i and j if there is a resistance connecting them directly. The set $\mathcal{E} \subset \mathcal{V}_0 \times \mathcal{V}_0$ is the set of all *edges*. Therefore each edge (i, j) has an associated *thermal resistance* $R_{ij} \in \mathbb{R}_+$. Since the graph is undirected, $R_{ji} = R_{ij}$ by convention. Each node $i \in \mathcal{V}$ has an associated thermal capacitance C_i.

The states and inputs of the building thermal model are summarized below:

$$\text{States} : T_1, \ldots, T_N, T_{N+1}, \ldots, T_n$$

$$\text{Inputs} : T_0, T^s; \dot{m}_i^{\text{in}}, \dot{Q}_i^r, \dot{Q}_i^{\text{int}}, \dot{Q}_i^{\text{ext}}, i = 1, \ldots, N$$

where $T_1, \ldots, T_N$ denote the space temperature of the zones, $T_{N+1}, \ldots, T_n$ denotes the temperature of the points internal to the surface elements, T_0 denotes the outside temperature, T^s denotes the temperature of the air supplied by the AHU, $\dot{m}_i^{\text{in}}$ denotes the mass-flow rate of the supply air entering the ith zone, $\dot{Q}_i^r$ denotes the rate of heat due to reheat, $\dot{Q}_i^{\text{int}}$ denotes the rate of heat generated by occupants, equipments, and lights in the ith zone, and $\dot{Q}_i^{\text{ext}}$ denotes the rate of solar radiation entering the ith zone.

The supplied air temperature T^s is usually constant for a VAV system, at least of short intervals of time. All other inputs are time varying. In this chapter, we assume that (estimates of) the outside temperature T_0 and the heat gains $\dot{Q}_i^r, \dot{Q}_i^{\text{int}}, \dot{Q}_i^{\text{ext}}$ are available based on historical data, weather predictions, and various sensors.

The thermal dynamics of a multi-zone building, described by a graph G, is represented by the following coupled differential equations: for each $i \in \mathcal{V}$,

$$C_i \dot{T}_i(t) = \dot{Q}_i(t) + \Delta H_i(t) + \sum_{j \in \mathcal{N}_i} (T_j(t) - T_i(t))/R_{ij} \tag{7.1}$$

where $\mathcal{N}_i := \{j \in \mathcal{V}_0 : j \neq i, (i, j) \in \mathcal{E}\}$ denotes the set of *neighbors* of the node i. The *heat gain* $\dot{Q}_i$ is the rate of thermal energy entering the node i from external sources, other than ventilation air and conduction from neighboring nodes:

$$\begin{aligned} \dot{Q}_i(t) &= \dot{Q}_i^r(t) + \dot{Q}_i^{\text{int}}(t) + \dot{Q}_i^{\text{ext}}(t), && i = 1, \ldots, N \\ \dot{Q}_i(t) &= 0, && i = N + 1, \ldots, n. \end{aligned}$$

The *ventilation heat exchange* ΔH_i is the rate of thermal energy entering the node i due to ventilation:

$$\begin{aligned} \Delta H_i(t) &= C_{\text{pa}} \dot{m}_i^{\text{in}}(t)(T^s - T_i(t)), && i = 1, \ldots, N \\ \Delta H_i(t) &= 0, && i = N + 1, \ldots, n \end{aligned}$$

where C_{pa} is the specific heat capacitance of the supplied air at constant pressure. In the following, we also call the mass-flow rate $\dot{m}^{\text{in}}$ as the control input u to building, i.e., $u_i = \dot{m}_i^{\text{in}}$ for $i = 1, \ldots, N$.

The coupled ordinary differential equation model (7.1) is *bilinear* in T and $\dot{m}^{\text{in}}$. In practice, we can measure the zone temperatures, which are usually treated as the output of the building thermal model. The model (7.1) can be expressed equivalently using a state space representation:

$$\begin{aligned} \dot{T} &= AT + B(T)u + d \\ Y &= KT \end{aligned} \tag{7.2}$$

where the temperature vector $T := [T_1, \ldots, T_n]'$, the control vector $u := [\dot{m}_1^{\text{in}}, \ldots, \dot{m}_N^{\text{in}}]'$, the output vector $Y := [Y_1, \ldots, Y_N]'$, and the load vector $d := [d_1, \ldots, d_N, 0, \ldots, 0]'$ where for $i = 1, \ldots, N$,

$$d_i := \begin{cases} (T_0/R_{i0} + Q_i)/C_i, & \text{if } (i,0) \in \mathcal{E} \\ Q_i/C_i, & \text{if } (i,0) \notin \mathcal{E}. \end{cases}$$

The matrix $A \in \mathbb{R}^{n \times n}$ is given by

$$A_{ij} := \begin{cases} 0, & \text{if } j \neq i,\ (i,j) \notin \mathcal{E} \\ 1/(C_i R_{ij}), & \text{if } j \neq i,\ (i,j) \in \mathcal{E} \\ -\sum_{k \neq i} A_{ik}, & \text{if } j = i,\ (i,j) \in \mathcal{E}. \end{cases} \tag{7.3}$$

The matrix $B(T) \in \mathbb{R}^{n \times N}$ is defined as

$$B_{ij}(T) := \begin{cases} C_{\text{pa}}(T^s - T_i)/C_i, & \text{if } i = j = 1, \ldots, N \\ 0, & \text{otherwise.} \end{cases}$$

The matrix $K \in \mathbb{R}^{N \times n}$ is given by

$$K = [I_{N \times N} \quad 0_{N \times (n-N)}].$$

We assume that the pair $(A, B(T))$ is controllable for any $T \geq 0$, and the pair (A, K) is observable.

7.2.3 *Reduced Building Thermal Model*

For a building with N zones, the number of states for the baseline model (7.1) is of the order of $7N$, usually much more [8]. A medium-sized commercial building may have around 100 zones and a larger one could have several hundreds. The dimension

of the building model can thus be quite large. In this section, we describe a reduced-order building thermal model by using an aggregation technique [9]. The reduced models will be used in Sect. 7.3 to develop the mean-field control strategies.

To obtain the reduced model, we aggregate a subset of nodes into *super-nodes*. Mathematically, suppose we want to reduce the state space dimension from n to m, where $m \leq n$ is the (user-specified) number of super-nodes. The first step is to determine a *partition function* $\phi : \mathcal{V} \to \bar{\mathcal{V}}$, where $\bar{\mathcal{V}} := \{1, \ldots, m\}$ such that ϕ is onto but possibly many-to-one. The elements of $\bar{\mathcal{V}}$ are the super-nodes, and for every $k \in \bar{\mathcal{V}}$, the node set $\phi^{-1}(k) \subset \mathcal{V}$ includes the nodes in the baseline model that are aggregated into the kth super-node. Similar to the baseline model, we let $\{0\}$ denote the outside node and define the set $\bar{\mathcal{V}}_0 := \{0\} \cup \bar{\mathcal{V}}$.

Given a fixed m-partition function ϕ, we introduce the following quantities for the reduced model:

- The *super-capacitance* of the kth partition is the combination of all capacitances of the nodes in kth partition:

$$\bar{C}_k^{(\phi)} := \sum_{i \in \phi^{-1}(k)} C_i, \quad k \in \bar{\mathcal{V}}.$$

- The *super-resistance* between kth and lth partitions is the parallel-equivalence of all resistances connecting the nodes between two partitions:

$$\bar{R}_{kl}^{(\phi)} := \frac{1}{\sum_{i \in \phi^{-1}(k)} \sum_{j \in \phi^{-1}(l)} 1/R_{ij}}, \quad k \neq l \in \bar{\mathcal{V}}.$$

- The *super-load* of the kth partition is the combination of all thermal loads for the zones in the kth partition:

$$\dot{\bar{Q}}_k^{(\phi)}(t) := \sum_{i \in \phi^{-1}(k)} \dot{Q}_i(t), \quad k \in \bar{\mathcal{V}}.$$

The reduced-order model is also an RC-network defined on super-nodes with super-edges connecting these super-nodes. Its thermal dynamics is represented by the following coupled differential equations: for each $k \in \bar{\mathcal{V}}$,

$$\begin{aligned} \bar{C}_k^{(\phi)} \dot{\bar{T}}_k(t) = \; & \dot{\bar{Q}}_k^{(\phi)}(t) + \Delta \bar{H}_k^{(\phi)}(t) \\ & + \sum_{l \in \bar{\mathcal{N}}_k} (\bar{T}_l(t) - \bar{T}_k(t)) / \bar{R}_{kl}^{(\phi)} \end{aligned} \tag{7.4}$$

where $\bar{T}_k$ is the temperature of the kth super-node, $\bar{\mathcal{N}}_k \subset \bar{\mathcal{V}}_0$ denotes the set of neighbors of the kth super-node, and the ventilation heat exchange for the kth super-node is given by

$$\Delta \bar{H}_k^{(\phi)}(t) := \sum_{i \in \phi^{-1}(k) \cap \{1,\ldots,N\}} \Delta H_i(t)$$
$$= \sum_{i \in \phi^{-1}(k) \cap \{1,\ldots,N\}} C_{\text{pa}} \dot{m}_i^{\text{in}}(t)(T^s - T_i(t)).$$

The initial condition of the reduced model (7.4) at initial time t_0 is defined as

$$\bar{T}_k(t_0) = \sum_{i \in \phi^{-1}(k)} (C_i / \bar{C}_k^{(\phi)}) T_i(t_0), \quad k \in \bar{\mathcal{V}}.$$

Note that the reduced model (7.4) requires for its inputs: the mass-flow rate $\dot{m}_i^{\text{in}}$ and the zone temperature T_i for $i = 1, \ldots, N$. These are assumed to be available, or are measured.

We can represent the reduced model (7.4) using the state space representation:

$$\dot{\bar{T}} = \bar{A}^{(\phi)} \bar{T} + \bar{B}^{(\phi)}(T, u) + \dot{\bar{Q}}^{(\phi)} \tag{7.5}$$

where $\bar{T} := [\bar{T}_1, \ldots, \bar{T}_m]'$ denotes the super-temperature vector, the terms $\bar{A}^{(\phi)}$ and $\bar{B}^{(\phi)}$ are defined accordingly.

The reduced model described so far depends on the choice of the partition function ϕ. We should note that any m-partition function ϕ induces a reduced model with m super-states. In [9], we proposed a recursive bi-partition algorithm to search for the sub-optimal m-partition function ϕ^*. However, one can also directly choose a sub-optimal ϕ^* based on physical intuition (e.g., floors in a multi-zone building), or some kind of expert-based heuristics. The goodness of the reduced model (7.4) with ϕ^* can be verified in practice. In this chapter, we will not discuss the algorithms for choosing the optimal partition function ϕ^*. In the following, we assume that ϕ^* has already properly specified, and we mainly focus on how to design optimal control laws by taking advantage of the reduced building model.

Example 1 (Reduced Model with One Super-Node). For the reduced model (7.4), one may pick any number of super-nodes (less than n) to reduce the complexity. In the extreme case, with $m = 1$, we only have one super-node to represent the entire building thermal dynamics. The thermal dynamics of this single super-node is represented by the following differential equation:

$$\bar{C}\dot{\bar{T}}(t) = \dot{\bar{Q}}(t) + \Delta \bar{H}(t) + (T_0 - \bar{T}(t))/\bar{R}_0 \tag{7.6}$$

where two super-quantities are defined as

$$\bar{C} := \sum_{i=1}^{n} C_i, \quad \bar{R}_0 := \frac{1}{\sum_{i \in \mathcal{N}_0} 1/R_{i0}},$$

and two super-inputs are given by

$$\dot{\bar{Q}}(t) = \sum_{i=1}^{N} \dot{Q}_i(t), \quad \Delta\bar{H}(t) = C_{\text{pa}} \sum_{i=1}^{N} \dot{m}_i^{\text{in}}(t)(T^s - T_i(t)).$$

The initial condition of (7.6) is given by

$$\bar{T}(t_0) = \sum_{i=1}^{n} (C_i/\bar{C}) T_i(t_0).$$

The single super-node model described by (7.6) is an extremely simplified version of the building thermal dynamics described by (7.1). The dynamics are very slow due to the very large capacitance $\bar{C}$. The input of (7.6) requires the combination of mass flow rates of all zones. In this chapter, we use the reduced model (7.6) to describe the *mass-behavior of the building*.

7.3 Mean-Field Control

In this section, we propose a distributed control law wherein each zone regulates its own temperature by only using the information of the local zone temperature and the mass-behavior of building system. The idea is that the local control of zone temperature is fast dynamics, while the mass-behavior of building is slow dynamics. In short-time scales, each zone designs the local optimal controller based on its own temperature, its own temperature set-point, and the super-temperature obtained from the reduced building model (7.4), but ignores the thermal interaction from all other building nodes. In long-time scales, the resulting control of all zone will collectively affect the mass-behavior of building system. See Fig. 7.2 for a conceptual illustration of the mean-field control idea.

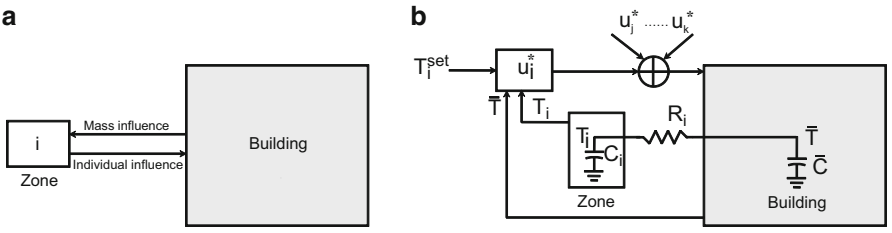

Fig. 7.2 Conceptual illustration of mean-field control: (**a**) individual (zone) playing with mass (whole building); (**b**) mean-field control diagram, where the whole building thermal dynamics is represented by a reduced model with one super-node

We consider N zones, each with its local set-point tracking control objective. The dynamics of the ith zone is given by

$$\dot{T}_i = l_i^\circ(T_i; T_{-i}) + b_i(T_i)u_i + d_i \tag{7.7}$$

where

$$l_i^\circ(T_i; T_{-i}) := -\sum_{j\in\mathcal{N}_i}(T_i - T_j)/(C_i R_{ij}),$$

$$b_i(T_i) := C_{\text{pa}}(T^s - T_i)/C_i, \quad d_i := \dot{Q}_i/C_i,$$

with $T_{-i} := (T_j)_{j\neq i}$. The control problem for the ith zone is to minimize the finite-horizon cost function

$$J_i^\circ(u_i; u_{-i}) = \int_{t_0}^{t_1} c(T_i, u_i)dt \tag{7.8}$$

where

$$c(T_i, u_i) := \frac{1}{2}\Delta T_i^2 + \frac{1}{2}ru_i^2 \tag{7.9}$$

with the tracking error $\Delta T_i := T_i - T_i^{\text{set}}$, and a given scalar $r > 0$ as control penalty. A *Nash equilibrium* in control policies is given by $\{u_i^*\}_{i=1}^N$ such that u_i^* minimizes $J_i^\circ(u_i; u_{-i}^*)$ for $i = 1, \ldots, N$.

We denote $R_i := (\sum_{j\in\mathcal{N}_i} 1/R_{ij})^{-1}$ and define the time constant for the ith zone as $\tau_i := C_i R_i$. The individual zones are distinguished by their initial conditions $T_i(0)$, set-point T_i^{set}, loads d_i, and the time constants τ_i. We introduce a parameter $\omega := (T(0), T^{\text{set}}, \tau, d)$, and consider a large number N of zones, where ω is sampled from a given distribution $\rho(\omega)$. For each zone i, the parameter ω_i is assumed to be i.i.d., with common distribution $\omega_i \sim \rho(\omega)$.

We seek a control solution that is decentralized and of the following form: for each $i \in \mathcal{V}$ and $t_0 \le t \le t_1$, the control input $u_i(t)$ depends only on *local information* $\{T_i(s) : t_0 \le s \le t\}$, and perhaps some *aggregate information*. This amounts to a dynamic game, whose exact solution is infeasible for large N.

Instead we construct an approximation of the form described in [13]. This approximation is based on the aggregated models described in Sect. 7.2.3 with the following steps:

(i) We identify a small number of super-nodes that describe the slow evolution of the thermal dynamics of the building. To simplify the introduction of the mean-field control method, we consider here only the simplest case: we use a single super-node to represent the entire building. The aggregated model (7.6) is used to describe the evolution of the super-temperature.

(ii) We consider an approximation of the interaction between a single zone and the entire building. Motivated by the consideration of the physics of thermal interactions (large time constants for interactions) and the separable nature of the control objectives (e.g., (7.8)), we consider an approximation based on replacing $T_{-i}(t)$ by $F(t)$, a known function of time. In particular, $l_i^\circ(T_i(t); T_{-i}(t))$ in (7.7) is replaced by

$$\bar{l}_i(T_i(t); F(t)) := -\frac{T_i(t) - F(t)}{\tau_i}.$$

Comparison of l_i° and $\bar{l}_i$ suggests the following approximation:

$$F(t) \approx \bar{T}(t). \tag{7.10}$$

(iii) For the local model (7.7) with $l_i^\circ(T_i; T_{-i})$ replaced by $\bar{l}_i(T_i; F)$, the game reduces to decentralized optimal control problems. The individual zones are "oblivious" to the state of the entire system and make their control decisions based only on local state variables.

(iv) A form of *self-consistency* is required: oblivious actions of individual zones reproduce the evolution of $\bar{T}$ as described by the aggregated model.

In the following section we develop the "oblivious" solution described in (iii). We then turn to the self-consistent aggregated model in (i) that defines the approximate interaction (7.10) in (ii). Mathematically, we obtain a fixed-point problem.

7.3.1 Local Optimal Control of a Single Zone

Suppose the interaction function $F(t)$ is given, possibly in a time-dependent form for $t \in [t_0, t_1]$. We consider the following dynamics for the single zone:

$$\dot{T}_i = \bar{l}_i(T_i; F) + b_i(T_i)u_i + d_i \tag{7.11}$$

where $\bar{l}_i$ is given by (7.10).

The control problem for single zone model is to choose the control law u_i so as to minimize the finite-horizon cost function

$$J_i(u_i; F) = \int_{t_0}^{t_1} c(T_i, u_i)dt. \tag{7.12}$$

The solution of the optimal control problem with the cost function $J_i(u_i; F)$ is standard. It is given in terms of the *optimal cost-to-go function* or *value function*:

$$J_i^*(T_i, t) = \min_{u_i} \left\{ \int_t^{t_1} c_i(T_i, u_i)dt \right\}.$$

The value function J_i^* is known to satisfy the Hamilton–Jacobi–Bellman (HJB) equation

$$\frac{\partial J_i^*}{\partial t} + \min_{u_i} \left\{ H_i \left(T_i, u_i, \frac{\partial J_i^*}{\partial T_i} \right) \right\} = 0 \tag{7.13}$$

with the boundary condition $J_i^*(T_i, t_1) = 0$. The *Hamiltonian* in (7.13) is defined for $\lambda \in \mathbb{R}$

$$H_i(T_i, u_i, \lambda) := c_i(T_i, u_i) + \lambda \left(l_i(T_i; F) + b_i(T_i) u_i \right)$$

with

$$l_i(T_i; F) := \bar{l}_i(T_i; F) + d_i.$$

The optimal control in (7.13) is explicitly obtained as

$$u_i^*(T_i; F) = -\frac{b_i(T_i)}{r} \left(\frac{\partial J_i^*}{\partial T_i}(T_i; F) \right). \tag{7.14}$$

Substituting (7.14) into (7.13), we obtain the HJB equation for $J_i^*(T_i, t)$:

$$\frac{\partial J_i^*}{\partial t} = \frac{1}{2} \frac{b_i^2(T_i)}{r} \left(\frac{\partial J_i^*}{\partial T_i} \right)^2 - l_i(T_i; F) \left(\frac{\partial J_i^*}{\partial T_i} \right) - \frac{1}{2} \Delta T_i^2. \tag{7.15}$$

7.3.2 Coupled Model

We now provide a complete description of the *coupled model* that is intended to approximate the game model for large N. This model is based on the interaction function $F(t)$ introduced in the preceding section. A value function $J^*(T, t; \omega)$ for the large N model is defined by the following differential equation identical to the HJB equation (7.15) for the single zone model.

$$\frac{\partial J^*}{\partial t} = \frac{1}{2} \frac{b^2(T)}{r} \left(\frac{\partial J^*}{\partial T} \right)^2 - l(T; F) \left(\frac{\partial J^*}{\partial T} \right) - \frac{1}{2} \Delta T^2.$$

The associated optimal feedback control law is then defined by

$$u^*(T; F) = -\frac{b(T)}{r} \left(\frac{\partial J^*}{\partial T}(T; F) \right). \tag{7.16}$$

Given the feedback control law (7.16), the differential equation that defines the evolution of the super-temperature $\bar{T}$ is given by

$$\bar{C} \dot{\bar{T}}(t) = (T_0(t) - \bar{T}(t))/\bar{R}_0 + \bar{U}(t) \tag{7.17}$$

where

$$\bar{U}(t) = N \int (\dot{Q}(t;\omega) + C_{\text{pa}} u^*(T(t;\omega);F)(T^s - T(t;\omega)))\rho(\omega)d\omega.$$

The only difference thus far is notational: $J_i^*(T,t)$ is the value function for a single zone with parameter ω_i, and $J^*(T,t;\omega)$ is the value function for a large number (continuum) of zones, distinguished by their own ω. Such is the case because we have *assumed* $F(t)$ is a known deterministic function that is furthermore consistent across the population.

All that remains is to specify $F(t)$ in a self-consistent manner. The consistency enforced here is inspired by the approximation given in (7.10). The two PDEs are coupled through this integral that defines the relationship between the interaction function F and the mean temperature $\bar{T}$:

$$F(t) = \bar{T}(t).$$

In summary, the coupled PDE model is given by: for $t \in [t_0, t_1]$,

$$\frac{\partial J^*}{\partial t} = \frac{1}{2}\frac{b^2(T)}{r}\left(\frac{\partial J^*}{\partial T}\right)^2 - l(T;F)\left(\frac{\partial J^*}{\partial T}\right) - \frac{1}{2}\Delta T^2 \tag{7.18}$$

$$\bar{C}\dot{\bar{T}}(t) = (T_0(t) - \bar{T}(t))/\bar{R}_0 + \bar{U}(t) \tag{7.19}$$

$$F(t) = \bar{T}(t) \tag{7.20}$$

with boundary conditions

$$J^*(T,t_1;\omega) = 0, \quad \bar{T}(t_0) = \sum_{i=1}^{n}(C_i/\bar{C})T_i(t_0).$$

Numerically, the optimal control may be obtained by iteratively solving the backward–forward equations (7.18) and (7.19) over a given (sufficiently long) time-horizon. A waveform relaxation algorithm for solving such equations appears in our earlier paper [14]. In the following, we describe an approximate solution based on the observation that the value function is known to approximately become a constant for large terminating times [15]. One of the attractive features of the proposed algorithm is that it yields a simple *state-feedback* law.

7.3.3 Approximate Local Optimal Control

In this section, we propose an approximation approach to the solution of coupled PDE (7.18)–(7.20) by considering the *equilibrium solutions*.

By setting $\partial J^*/\partial t \approx 0$ and letting $F = \bar{T}$ in (7.18), we consider the equilibrium solution to (7.18):

$$k(T)\left(\frac{\partial J^*}{\partial T}\right)^2 - 2m(T,\bar{T})\left(\frac{\partial J^*}{\partial T}\right) - n(\Delta T) = 0 \tag{7.21}$$

where we define

$$k(T) := b^2(T),\ m(T,\bar{T}) := rl(T;\bar{T}),\ n(\Delta T) := r\Delta T^2.$$

Since T^s (the temperature of supplied air) is always strictly less/more than T (the temperature of zone) when cooling/heating, then we always have

$$k(T) = (C_{\text{pa}}(T^s - T)/C)^2 > 0.$$

Thus (7.21) is always a second order equation, which can be solved with two well-defined solutions:

$$\left(\frac{\partial J^*}{\partial T}\right)_{\pm} = \frac{m(T,\bar{T})}{k(T)} \pm \frac{\sqrt{m^2(T,\bar{T}) + k(T)n(\Delta T)}}{k(T)}.$$

For any T, ΔT, and $\bar{T}$, we can check

$$\left(\frac{\partial J^*}{\partial T}\right)_{+} \geq 0, \quad \left(\frac{\partial J^*}{\partial T}\right)_{-} \leq 0.$$

We would like to construct a "value function" $\widehat{J}^*$ such that it is approximately convex with respect to T with minimum achieved at $\Delta T = T - T^{\text{set}} = 0$. One possible choice is

$$\frac{\partial \widehat{J}^*}{\partial T} = \begin{cases} (\partial J^*/\partial T)_+, & \text{if } \Delta T \geq 0 \\ (\partial J^*/\partial T)_-, & \text{if } \Delta T < 0. \end{cases} \tag{7.22}$$

However, such a choice of $(\partial \widehat{J}^*/\partial T)$ is not a smooth function of T, and neither is the associated control law (7.16). But the mass-flow rate (the control) is usually varied continuously to regulate the zone temperature for building system. To obtain a smooth control law, here we consider a smooth approximation to the sign function,

$$\text{sgn}(x) \approx \tanh(cx) = \frac{1 - e^{-2cx}}{1 + e^{-2cx}}, \quad \text{for} \quad c \gg 1. \tag{7.23}$$

Then we modify (7.22) to obtain the following smooth approximation:

$$\frac{\partial \widehat{J}^*}{\partial T} = \frac{m(T,\bar{T})}{k(T)} + \tanh(c\Delta T)\frac{\sqrt{m^2(T,\bar{T}) + k(T)n(\Delta T)}}{k(T)}$$

The approximate local optimal control law is chosen as

$$\hat{u}^*(T;\bar{T}) = -\frac{b(T)}{r}\left(\frac{\partial \widehat{J}^*}{\partial T}(T;\bar{T})\right). \tag{7.24}$$

By setting $\dot{\bar{T}} \approx 0$ in (7.19) and substituting (7.24) into (7.19), we can obtain the equilibrium solution $\bar{T}^s > 0$ by solving a second order equation (we omit the details here). Finally, the stationary local optimal control law is given by

$$\hat{u}^{*,s}(T) = -\frac{b(T)}{r}\left(\frac{\partial \widehat{J}^*}{\partial T}(T;\bar{T}^s)\right). \tag{7.25}$$

7.4 Mean-Field Control of Linearized System

In this section, we describe an optimal control law based on linearizing the building model along its nominal trajectory. Note that the nominal values of state (the zone temperatures) and control (the mass-flow rates) can be directly measured in practice.

By assuming the nominal state and the control values T^o and u^o, we linearize (7.11) and obtain the following linearized model: for $i = 1, \ldots, N$,

$$\dot{T}_i = \tilde{a}_i T_i + \tilde{b}_i u_i + \tilde{l}_i(F) + d_i$$

where we define the following quantities:

$$\tilde{a}_i := -1/\tau_i - C_{\mathrm{pa}} u_i^o / C_i, \quad \tilde{b}_i := C_{\mathrm{pa}}(T^s - T_i^o)/C_i, \quad \tilde{l}_i(F) := F/\tau_i + C_{\mathrm{pa}} T_i^o u_i^o / C_i.$$

We consider the same cost function (7.12) for each zone node. The local optimal control for the ith zone is explicitly obtained as:

$$u_i^*(T_i;F) = -\frac{\tilde{b}_i}{r_i}(\tilde{p}_i T_i - \tilde{g}_i)$$

where $\tilde{p}_i$ is the positive solution to the Ricatti differential equation

$$\dot{\tilde{p}}_i = -2\tilde{p}_i\tilde{a}_i + \tilde{b}_i^2\tilde{p}_i^2/r - 1$$

with the boundary condition $\tilde{p}_i(t_1) = 0$, and $\tilde{g}_i$ is the solution of the linear differential equation

$$\dot{\tilde{g}}_i = -(\tilde{a}_i - \tilde{b}_i^2\tilde{p}_i/r)\tilde{g}_i - T_i^{\mathrm{set}} + \tilde{p}_i(\tilde{l}_i(F) + d_i)$$

with the boundary condition $\tilde{g}_i(t_1) = 0$.

Similarly to Sect. 7.3.2, we can obtain the coupled PDE model by letting $F(t) \approx \bar{T}(t)$. We consider the case that zone parameters are drawn from certain distribution

$\rho(\omega)$ and consider the reduced model (7.17) to evolve $\bar{T}$. As before, we can also find the approximate local optimal control by considering the equilibrium solutions:

$$0 = -2\tilde{p}\tilde{a} + \tilde{b}^2\tilde{p}^2/r - 1,$$
$$0 = -(\tilde{a} - \tilde{b}^2\tilde{p}/r)\tilde{g} - T^{\text{set}} + \tilde{p}(\tilde{l}(\bar{T}) + d),$$

which leads to the following equilibrium solutions

$$\tilde{p}^s = \frac{r\tilde{a} + \sqrt{r^2\tilde{a}^2 + r\tilde{b}^2}}{\tilde{b}^2}, \quad \tilde{g}^s(\bar{T}) = \frac{\tilde{p}^s(\tilde{l}(\bar{T}) + d) - T^{\text{set}}}{\tilde{a} - \tilde{b}^2\tilde{p}^s/r}.$$

The approximate local optimal control is then chosen as:

$$\hat{u}^*(T; \bar{T}) = -\frac{\tilde{b}}{r}\left(\tilde{p}^s T - \tilde{g}^s(\bar{T})\right).$$

By substituting (7.26) into (7.19), we can obtain the equilibrium solution $\bar{T}^s$, and therefore the stationary local optimal control law $\hat{u}^{*,s}(T)$.

7.5 Simulation and Discussion

7.5.1 Basic Setup

Simulations are carried out for the four-zone building shown in Fig. 7.1: All four zones/rooms have an equal floor area of 5 m × 5 m and each wall is 3 m tall, which provides a volumetric area of 75 m^3 for each room. Room 1 has a small window (5 m^2) on the north facing wall, whereas rooms 2 and 4 have larger windows (7 m^2 each) on the east facing wall. Room 3 does not have a window.

The RC-network representation of the four-zone building has totally 36 building nodes plus 1 outside node [9]. Each building node is assigned with a thermal capacitance, two adjacent nodes are connected with a thermal resistance. The windows are modeled as single resistors since they have relatively little capacitance. The values of the capacitances and resistances are obtained from Carrier's Hourly Analysis Program [16]. The HVAC system used for simulation is designed to supply maximal mass flow rate of 0.25 kg/s per zone. The mass-flow rate m_i^{in} for $i = 1, \ldots, 4$ for four zones can be adjusted based on designed control laws. The supplied air temperature is fixed at $T^s = 12.8°\text{C}$. Here we assume there is no return air and 100 % of the outside air is sent to chiller. Number of people in each zone is uniformly generated as a random integer ranging between 0 and 4. Outside temperature and outside solar radiation data is obtained for a summer day (05/24/1996) of Gainesville, FL [17]. The outside temperature and the heat gain (due to solar radiation and people occupancy) of each zone are depicted in Fig. 7.3a, b, respectively.

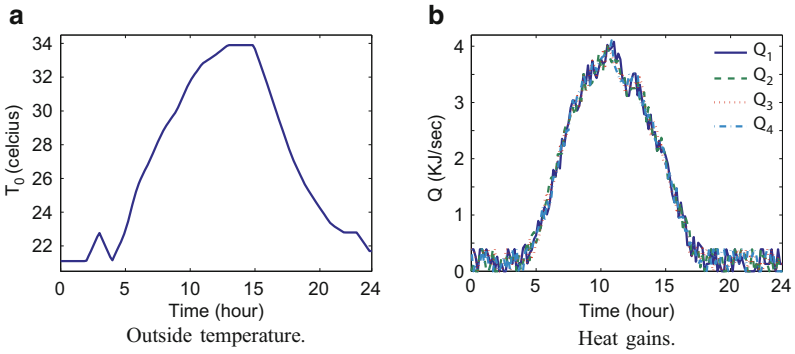

Fig. 7.3 Exogenous inputs for a 24-h period in Gainesville, FL: (**a**) outside temperature and (**b**) heat gains of each zone

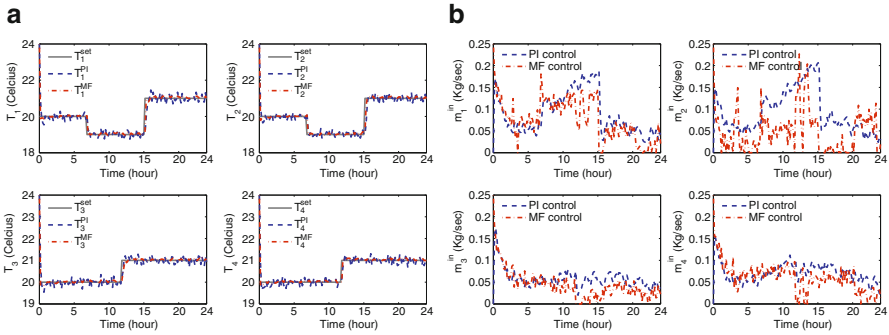

Fig. 7.4 Comparison results of (**a**) zone temperatures and (**b**) zone mass-flow rates for using PI control law and mean-field control law with $r = 10$

Numerical results presented in the following are obtained using ode45 function in Matlab for 24 h with the time step size chosen as 10 min. All temperatures of the building nodes are initialized at 24°C, respectively. The desired zone temperatures T_i^{set} for $i = 1, \ldots, 4$ are varying with time and are depicted as solid lines in Figs. 7.4 and 7.5. In the following, we apply the mean-field and PI control laws to regulate zone temperatures to track the desired values.

7.5.2 Simulation Results

To compare performance of the proposed controller with existing control algorithms commonly used in commercial buildings, we consider the following decentralized PI control law: for $i = 1, \ldots, 4$,

$$m_i^{\text{in}}(t) = K_p \Delta T_i(t) + K_i \int_0^t \Delta T_i(s) ds \tag{7.26}$$

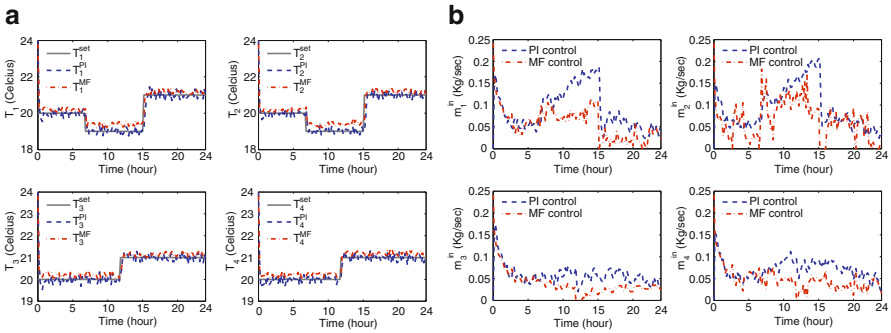

Fig. 7.5 Comparison results of (**a**) zone temperatures and (**b**) zone mass-flow rates for using PI control law and mean-field control law with $r = 60$

where the tuned proportional gain $K_p = -0.00005$, the tuned integration gain $K_i = 0.0001$, and the temperature tracking error $\Delta T_i := T_i^{\text{set}} - T_i$. We next compare the performance of the mean-field control law introduced in this chapter with that of the PI controller.

The mean-field control is implemented based on the stationary nonlinear policy (7.25). For the four-room building, we only consider the one super-node reduced model (7.6). The control performance becomes slightly better by adding more super-nodes into the reduced model. One may expect larger performance improvement by considering more super-nodes for more complex building topologies.

First, we take $r = 10$ in the individual cost function (7.9). We take $c = 5$ for smooth approximation of sign function in (7.23). We apply stationary local control law (7.25) and PI control law (7.26) to each zone, respectively. The comparison results of simulated zone temperatures are depicted in Fig. 7.4a. The comparison results of mass-flow rates associated with two control laws are depicted in Fig. 7.4b. We observe that the mean-field control has better temperature tracking performance than that for PI control (see Fig. 7.4a).

The total energy consumption of each zone can be computed based on the mass-flow rate entering each zone [8]. Here the total energy consumption is the combination of fan power and the chiller power consumptions. For PI control law, the total energy consumption (kWh) for each zone is 69.3, 72.5, 45.2, and 55.9, and the total energy consumption for all four zones is 242.9; For mean-field control law, the total energy consumption for each zone is 59.6, 38.9, 34.0, and 47.7, and the total energy consumption for all four zones is 179.2. In this case, the mean-field control thus reduces total energy consumption by 25 % over the PI control.

Then, we take $r = 60$ in the cost function (7.9). The comparison results of simulated zone temperatures are depicted in Fig. 7.5a. The comparison results of mass-flow rates associated two control laws are depicted in Fig. 7.5b. For mean-field control law, the total energy consumption (kWh) for each zone is 45.9, 52.1, 30.0, and 37.7, and the total energy consumption for all four zones is 165.7. We observe

that the temperature tracking performance for mean-field control is slightly worse than that for PI control (see Fig. 7.5a). But in this case the mean-field control reduces energy consumption by 31 % over the PI control, larger than in the previous case (compare Fig. 7.4b with Fig. 7.5b). This is due to a larger control penalty parameter r.

The simulation results for linearized control policy (7.26) are omitted in this chapter on account of space. In simulations, the linearized policy consumes more energy while maintaining comparable temperature tracking performance, as compared to the nonlinear control policy (7.25). These inefficiencies may be due to the unmodeled nonlinearities. We plan to study this in our future work.

7.6 Conclusions and Future Directions

In this chapter, we develop the mean-field methodology as a means to mitigate complexity associated with large-scale control problems in buildings. Rather than solving the large-scale centralized problem, we explore distributed game-theoretic solution approaches that work by optimizing with respect to the mean-field. Simulation results show that the proposed mean-field scheme achieves comparable temperature tracking performance while reducing energy consumption in the operation of HVAC systems. Moreover, the tradeoff between tracking performance and the energy savings can be made by adjusting the control penalty parameter in the mean-field scheme.

To help deal with uncertainty and time variations in building dynamics, we plan to next develop adaptation schemes for mean-field control based on approximate dynamic programming principles [14, 15]. We also plan to incorporate effects of humidity and ventilation requirements in computing the optimal controls for the HVAC system. We are also working on accurate model of convection effects in building thermal dynamics [18]. By considering the stronger inter-zone interactions arising from convection, we could probably save even more energy for operating HVAC systems.

References

1. Energy Future: Think Efficiency, The American Physical Society, Technical Report, 2008
2. M.R. Brambley, D. Hansen, P. Haves, D.R. Holmberg, S.C. McDonald, K.W. Roth, P. Torcellini, Advanced Sensors and Controls for Building Applications: Market Assessment and Potential R&D Pathways. Report Number: PNNL-15149. Prepared for the U.S. Department of Energy under Contract DE-AC05-76RL01830. Pacific Northwest National Laboratory (PNNL), Richland, WA, USA. Apr 2005
3. F. Oldewurtel, A. Parisio, C. Jones, M. Morari, D. Gyalistras, M. Gwerder, V. Stauch, B. Lehmann, K. Wirth, Energy efficient building climate control using stochastic model predictive control and weather predictions, in *American Control Conference* (2010), pp. 5100–5105

4. P. Morosan, R. Bourdais, D. Dumur, A distributed MPC strategy based on benders decomposition applied to multi-source multi-zone temperature regulation. J. Process Control **21**, 729–737 (2011)
5. Y. Ma, G. Anderson, F. Borrelli, A distributed predictive control approach to building temperature regulation, in *Proceedings of American Control Conference* (San Francisco, 2011), pp. 2089–2094
6. T.X. Nghiem, G.J. Pappas, Receding-horizon supervisory control of green buildings, in *Proceedings of American Control Conference* (San Francisco, 2011), pp. 4416–4421
7. V. Chandan, A.G. Alleyne, Optimal control architecture selection for thermal control of buildings, in *Proceedings of American Control Conference* (San Francisco, 2011), pp. 2071–2076
8. S. Goyal, P. Barooah, A method for model-reduction of nonlinear building thermal dynamics, in *American Control Conference* (2011), pp. 2077–2082
9. K. Deng, P. Barooah, P.G. Mehta, S.P. Meyn, Building thermal model reduction via aggregation of states, in *Proceedings of American Control Conference* (Baltimore, 2010), pp. 5118–5123
10. J.M. Lasry, P.L. Lions, Mean field games. Jpn. J. Math. **2**, 229–260 (2007)
11. M. Huang, R. Malhame, P. Caines, Nash certainty equivalence in large population stochastic dynamic games: connections with the physics of interacting particle systems, in *Proceedings of IEEE Conference on Decision and Control* (2006), pp. 4921–4926
12. M.M. Gouda, S. Danaher, C. Underwood, Building thermal model reduction using nonlinear constrained optimization. Build. Environ. **37**(12), 1255–1265 (2002)
13. M. Huang, P.E. Caines, R.P. Malhame, Large-population cost-coupled LQG problems with nonuniform agents: individual-mass behavior and decentralized ε-Nash equilibria. IEEE Trans. Autom. Control **52**(9), 1560–1571 (2007)
14. H. Yin, P.G. Mehta, S.P. Meyn, U.V. Shanbhag, Synchronization of coupled oscillators is a game, in *American Control Conference* (2010), pp. 1783–1790
15. D.P. Bertsekas, J.N. Tsitsiklis, *Neuro-Dynamic Programming* (Athena Scientific, Belmont, 1996)
16. Carrier Corporation, *HAP Quick Reference Guide* (Carrier Corporation, Farmington, CT, 2003)
17. National Solar Radiation Data Base (NSRDB): 1991–2005 Update: Typical Meteorological Year 3 [Online]. Available: http://rredc.nrel.gov/solar/old_data/nsrdb/1991-2005/tmy3/
18. S. Goyal, C. Liao, P. Barooah, Identification of multi-zone building thermal interaction model from data, in *Proceedings of IEEE Conference on Decision and Control* (2011), pp. 181–186

Chapter 8
Pseudospectral Optimal Control of Constrained Nonlinear Systems

Shengbo Eben Li, Kun Deng, Xiaoxue Zhang, and Quansheng Zhang

Abstract This chapter presents a unified pseudospectral computational framework for accurately and efficiently solving optimal control problems (OCPs). Any continuous-time OCP is converted into a nonlinear programming (NLP) problem via pseudospectral transformation. Through using pseudospectral method, both states and controls are approximated by global Lagrange interpolating polynomials at Legendre–Gauss–Lobatto (LGL) collocation points. The mapping relationship between the costates of OCP and the KKT multipliers of NLP is derived for checking the optimality of solutions. Besides, a quasi-Newton iterative algorithm is integrated to accurately calculate the LGL points for engineering practice, and a multi-phase preprocessing strategy is proposed to handle non-smooth problems. We use a general solver called Pseudospectral Optimal control Problem Solver (POPS), which is developed in Matlab environment to implement the computational framework. The classic vehicle automation problem, i.e., optimal path planning in an overtaking scenario, is formulated to demonstrate the effectiveness of POPS.

Keywords Optimal control • Nonlinear system • Constrained system

8.1 Introduction

Nowadays, road vehicles have continuously developed in terms of automation, electrification, and hybridization, driven by the demands on comfort, safety, and efficiency [1]. And now one common question is how to design optimal strategies to maximally enhance some performances of road vehicles. But there are some

S.E. Li • X. Zhang
State Key Laboratory of Automotive Safety and Energy, Department of Automotive Engineering, Tsinghua University, Beijing 10084, China
e-mail: lishbo@tsinghua.edu.cn

K. Deng (✉)
Coordinated Science Laboratory, University of Illinois at Urbana-Champaign, Urbana, IL 61801, USA
e-mail: kundeng2@illinois.edu

Q. Zhang
Center for Automotive Research, The Ohio State University, Bloomfield Hills, MI, USA

Q. Zhang et al., *Automotive Air Conditioning*, DOI 10.1007/978-3-319-33590-2_8

difficulties such as the nonlinearity and uncertainty of vehicle dynamics, limited computing resources of control units, and time-varying road/traffic conditions, and so on. Because of existing these difficulties, this question becomes more challenging. In automotive engineering, typical optimal control examples include power management for HEVs/EVs [2], optimal control for active suspensions [3], trajectory optimization for automated vehicles [4], and fuel optimized eco-driving assistance [5], etc.

The power management for HEV is to optimize the power distributions between thermal and electrical paths dynamically to achieve energy-saving for vehicle driving. Active suspensions are aimed at obtaining optimal performance of ride and handling through dynamically manipulating stiffness and damping of suspensions in response to vehicle motions and road conditions. The trajectory planning for automated vehicles is focused on the real-time optimization of vehicle routes to achieve the assigned driving tasks [4]. The fuel optimized eco-driving assistance is to reduce the fuel consumption by dynamically adjusting throttle angle, transmission gear ratio, and brake pressure in accordance with constraints on traffic conditions, road conditions, and the ability of vehicles [5].

Essentially, the aforementioned optimal strategies need to structure corresponding optimal control problems (OCPs). That is, it intends to minimize the given performance index of a dynamic system by manipulating control inputs. The main methods to obtain optimal strategies for both ICE-based and e-Powertrain-based road vehicles consist of traditional direct method (TDM), Pontryagin's minimum principle, and dynamic programming [6–8].

Pontryagin's minimum principle falls into the category of indirect methods. It gives the first-order necessary condition in the form of boundary value problems. But this method is unable to acquire the optimal solutions, when dealing with nonlinearities and complex constraints [9]. Dynamic programming is widely used in OCPs that are difficult to get the analytical solution, however this method exists the curse of dimensionality and has low computational efficiency [8]. The TDMs, such as shooting methods and collocation methods, are also widely applied to address complex problems in automation, hybridization, and electrification of road vehicles.

Compared to the TDMs, the pseudospectral (PS) method is more attractive due to its merits on high accuracy, lower sensitivity to initial value, and faster convergence [10]. Over the last few years, PS methods, in particular the Legendre PS method, have been extensively used to solve a broad class of OCPs arising in the trajectory optimization and real-time control of systems governed by ordinary differential equations. In 1995, Elnagar et al. first introduced the concept of PS method into optimal control community [11]. Since 2000, Fahroo, Ross, Gong, Rao et al. intensively studied the PS method, and obtained a series of important achievements, e.g., the existence of optimal solution, covector mapping theorem, convergence rate theorem, and principles for choosing the consistency parameter and the interpolation weight function [12–14]. The PS method is to approximate state and control variables via a finite order of global interpolating polynomials and convert the OCP into a nonlinear programming (NLP) problem at orthogonal collocation points [10, 11]. The formulated NLP problem has been shown to

converge to the original OCP in spectral accuracy. For any infinitely differentiable function, the spectral accuracy is $O(N^{-m})$ for every $m \in Z^+$, where N denotes Nth order approximation. For any analytic function, the convergence will be faster at the rate of (c^N) for some constant $0 < c < 1$ [15].

In recent years, the PS method has been successfully applied to problems in aerospace engineering. Some PS-based OCP solvers are also commercially, e.g., DIDO by Ross et al. [16], GPOPS by Rao et al. [17], PSOPT by Becerra et al. [18], and PROPT by Tomlab Optimization [19]. There are several commonly used PS methods: Chebyshev pseudospectral method (CPM), Legendre pseudospectral method (LPM), Gauss pseudospectral method (GPM), and Radau pseudospectral method (RPM). The CPM employs Chebyshev–Gauss–Lobatto points to discretize states/inputs and uses Chebyshev polynomials to approximate the state and control, and adopts Clenshaw–Curtis quadrature for numerical integration. Other three methods, i.e., the LPM, GPM, and RPM, use Lagrange interpolating polynomials to approximate states and control variables and Gaussian integral to calculate cost functions. The selection process of collocation points is the major difference among the three methods, but all three kinds of points are calculated based on Legendre polynomial [11, 20]. According to these studies, we know the performance of LPM, RPM, and GPM. Gauss and Radau methods have similar computational accuracy, and they have better costate estimation capabilities than Legendre method. However, the Legendre method has better performance for OCPs with fixed boundary conditions, while Gauss and Radau methods may not converge in some situations [10].

In this chapter, we develop a unified computational framework and software package aiming to efficiently calculate different types of OCPs arising from automotive engineering. The computational framework is based on LPM and three new improvements:

1. Performing the costate estimation for a more general OCP with a Bolza-type performance index and both equality and inequality constraints;
2. Adopting a quasi-Newton iterative algorithm to efficiently calculate collocation points;
3. Proposing a method to segment and transform non-smooth problems.

8.2 Computational Framework of Legendre Pseudospectral Method

In automotive engineering, we need to find an optimal control law $\boldsymbol{u}(t) \in \mathbb{R}^{N_u}$ to obtain the minimum designed performance index. For example, we usually choose the engine torque or acceleration as the control inputs and seek for an optimal solution to minimize fuel consumption for a specific driving task in economical automation systems. Other similar problems include the charging/discharging management of batteries, energy distributions for HEVs, optimizations of the stiffness and resistance for active suspensions, and path planning for automated vehicles.

8.2.1 General Bolza-Type OCP

The problem considered here can be expressed as a general Bolza-type OCP with terminal constraints, equality and inequality path constraints:

$$\min_{\boldsymbol{u}(t)} J = \varnothing\left(\boldsymbol{x}\left(t_f\right), t_f\right) + \int_{t_0}^{t_f} G\left(\boldsymbol{x}(t), \boldsymbol{u}(t), t\right) \mathrm{d}t$$

subject to

$$\begin{aligned} \dot{\boldsymbol{x}}(t) &= \boldsymbol{f}\left(\boldsymbol{x}(t), \boldsymbol{u}(t), t\right), \\ \boldsymbol{\varphi}\left(\boldsymbol{x}\left(t_0\right), \boldsymbol{x}\left(t_f\right), t_0, t_f\right) &= 0, \\ \boldsymbol{C}_{\mathrm{eq}}\left(\boldsymbol{x}(t), \boldsymbol{u}(t), t\right) &= 0, \\ \boldsymbol{C}_{\mathrm{inq}}\left(\boldsymbol{x}(t), \boldsymbol{u}(t), t\right) &\leq 0, \end{aligned} \tag{8.1}$$

where $t \in \mathbb{R}$ denotes the time, $\boldsymbol{x} \in \mathbb{R}^{N_x}$ denotes the state vector, $\boldsymbol{u} \in \mathbb{R}^{N_u}$ denotes the control vector, $\boldsymbol{f}(\cdot)$ denotes the state space function, $\varnothing(\cdot)$ denotes the Mayer performance index, $G(\cdot)$ denotes the Lagrange performance index, $\boldsymbol{\varphi}(\cdot)$ denotes the initial and terminal constraints, and $\boldsymbol{C}_{\mathrm{eq}}(\cdot)$ and $\boldsymbol{C}_{\mathrm{inq}}(\cdot)$ denote the equality and inequality path constraints, respectively.

8.2.1.1 Calculation Steps by LPM

Using the pseudospectral transformation, we approximate both state and control variables by Lagrange interpolating polynomials at the LGL points. The state space equations are represented as equality constraints. The integral of cost function is calculated by the Gauss–Lobatto quadrature rule. Then, the OCP is converted into an NLP problem, which can be solved by available optimization solvers. The detailed framework is described below.

Step 1: Time-Domain Transformation

To simplify the problem, we first transform the time domain $[t_0, t_f]$ to the canonical interval $[-1, 1]$:

$$\tau = \left(2t - t_f - t_0\right) / \left(t_f - t_0\right), \ \tau \in [-1, 1] \tag{8.2}$$

Step 2: Collocation and Discretization

For pseudospectral methods, the collocation points often come from the roots of orthogonal polynomials, which help avoid the Runge phenomenon. Let $P_N(\tau)$ denote the N-order Legendre polynomials [11], defined as

$$P_N(\tau) = \frac{1}{2^N N!}\frac{d^N}{d\tau^N}\left(\tau^2 - 1\right)^N \tag{8.3}$$

The LGL points are defined as $\tau_0 = -1$, $\tau_N = +1$, and τ_k being the roots of $\dot{P}_N(\tau)$ for $k = 1, 2, \ldots, N-1$. Clearly, these $(N+1)$ LGL points are also the roots of $\left(1-\tau^2\right)\dot{P}_N(\tau)$. Accurate calculation of LGL points is important to successfully implement the pseudospectral transformation. However, there is no explicit formula to compute the roots of $\dot{P}_N(\tau)$.

The state vector $\boldsymbol{x}(\tau)$ and control vector $\boldsymbol{u}(\tau)$ are discretized at points $\{\tau_0, \tau_1, \ldots, \tau_N\}$. The discretized state vectors are denoted by $\{\boldsymbol{X}_0, \boldsymbol{X}_1, \ldots, \boldsymbol{X}_N\}$ and the discretized control vectors are denoted by $\{\boldsymbol{U}_0, \boldsymbol{U}_1, \ldots, \boldsymbol{U}_N\}$, where $\boldsymbol{X}_i = \boldsymbol{x}(\tau_i)$ and $\boldsymbol{U}_i = \boldsymbol{u}(\tau_i)$. Then we approximate $\boldsymbol{x}(\tau)$ and $\boldsymbol{u}(\tau)$ by

$$\begin{aligned}
\boldsymbol{x}(\tau) &\approx \boldsymbol{X}(\tau) = \sum_{i=0}^{N} L_i(\tau)\boldsymbol{X}_i, \\
\boldsymbol{u}(\tau) &\approx \boldsymbol{U}(\tau) = \sum_{i=0}^{N} L_i(\tau)\boldsymbol{U}_i,
\end{aligned} \tag{8.4}$$

where $L_i(\tau)$ denotes the Lagrange interpolating basis function

$$L_i(\tau) = \prod_{j=0, j\neq i}^{N} \left(\tau - \tau_j\right) / \left(\tau_i - \tau_j\right) \tag{8.5}$$

Step 3: Transformation of State Space Equation

The states are approximated by interpolating polynomials. Then, the differential operation of states is approximated by the differential operation on Lagrange bases, denoted as

$$\dot{\boldsymbol{x}}(\tau_k) \approx \dot{\boldsymbol{X}}(\tau_k) = \sum_{i=0}^{N} \dot{L}_i(\tau_k)\boldsymbol{X}_i = \sum_{i=0}^{N} D_{ki}\boldsymbol{X}_i, \tag{8.6}$$

where $k = 0, 1, 2, \ldots, N$ and $\boldsymbol{D} = \{D_{ki}\} \in \mathbb{R}^{(N+1)\times(N+1)}$ denote the differentiation matrix [10], defined as

$$D_{ki} = \begin{cases} \frac{P_N(\tau_k)}{P_N(\tau_i)(\tau_k - \tau_i)}, & i \neq k \\ -N(N+1)/4, & i = k = 0 \\ N(N+1)/4, & i = k = N \\ 0, & \text{otherwise} \end{cases}. \tag{8.7}$$

Then the state space equation can be converted as the following $(N+1)$ equality constraints at LGL points,

$$\sum_{i=0}^{N} D_{ki} \boldsymbol{X}_i - \frac{t_f - t_0}{2} \boldsymbol{f}\left[\boldsymbol{X}_k, \boldsymbol{U}_k, \tau_k\right] = 0 \tag{8.8}$$

Step 4: Transformation of Performance Index

The performance index is transformed using the Gauss–Lobatto quadrature rule,

$$J = \varnothing\left(\boldsymbol{X}_N, \tau_N\right) + \frac{t_f - t_0}{2} \sum_{k=0}^{N} w_k G\left(\boldsymbol{X}_k, \boldsymbol{U}_k, \tau_k\right), \tag{8.9}$$

where $\boldsymbol{w}$ denotes the integration weight, defined as

$$w_k = \int_{-1}^{1} l_k(\tau) \mathrm{d}\tau = \frac{2}{N(N+1) P_N^2(\tau_k)} \tag{8.10}$$

The Gauss–Lobatto quadrature is critical to the accuracy of transforming the integral. The residual in Gauss–Lobatto quadrature is [21]

$$R_{N+1} = \frac{-(N+1) N^3 2^{2N+1} ((N-1)!)^4}{(2N+1)((2N)!)^3} G^{2N}(\xi) \tag{8.11}$$

Thus, by using $(N+1)$ LGL points, the quadrature residual is equal to zero for any polynomials with order less than $(2N-1)$.

Step 5: OCP to NLP Problem Conversion

Using the aforementioned steps, we can convert the OCP to the following NLP problem, i.e.,

$$\min_{\boldsymbol{X}_k, \boldsymbol{U}_k} J = \varnothing\left(\boldsymbol{X}_N, \tau_N\right) + \frac{t_f - t_0}{2} \sum_{k=0}^{N} w_k G\left(\boldsymbol{X}_k, \boldsymbol{U}_k, \tau_k\right),$$

subject

$$\begin{gathered} \left\| \sum_{i=0}^{N} D_{ki} \boldsymbol{X}_i - \frac{t_f - t_0}{2} \boldsymbol{f}\left(\boldsymbol{X}_k, \boldsymbol{U}_k, \tau_k\right) \right\|_{\infty} \leq \delta, \\ \left\| \boldsymbol{\varphi}\left(\boldsymbol{X}_0, \boldsymbol{X}_N, \tau_0, \tau_N\right) \right\|_{\infty} \leq \delta, \\ \left\| \boldsymbol{C}_{\mathrm{eq}}\left(\boldsymbol{X}_k, \boldsymbol{U}_k, \tau_k\right) \right\|_{\infty} \leq \delta, \\ \boldsymbol{C}_{\mathrm{inq}}\left(\boldsymbol{X}_k, \boldsymbol{U}_k, \tau_k\right) \leq 0, \end{gathered} \tag{8.12}$$

where $k,\ i = 0, \ldots, N$. The equality constraints are imposed at all points including two endpoints. A scalar δ is used to relax the equality constraints to avoid infeasibility. The scalar δ can be selected as [13]

$$\delta = (N-1)^{\alpha - m}, \tag{8.13}$$

where m implies that the optimal state variable has continuous $(m-1)$ th order classical derivatives, α is usually set as 3/2 [13]. There are $(N_x + N_u) \times N$ variables to be optimized in the NLP problem Eq. (8.12). For non-fixed terminal time t_f, we can also take t_f as an additional variable to be optimized. The converted NLP is a high-dimensional and sparse problem. Some known sparse NLP solvers can be used to solve this kind of problem, like SNOPT used here.

8.3 Implementation of Pseudospectral Method

We present the costate estimation with both equality and inequality constraints for the defined Bolza-type OCP. Because the computation of LGL points has no explicit expression, here we propose to adopt the quasi-Newton iterative algorithm to numerically calculate the collocation points. For non-smooth problems, we use a multi-phase preprocessing strategy to improve the approximation accuracy of the pseudospectral method. In addition, we build a Matlab environment-based solver, i.e., Pseudospectral Optimal control Problem Solver (POPS) to solve the problem.

8.3.1 Costate Estimation

The costate of OCPs is important to evaluate the optimality of solutions. But direct methods cannot provide explicit expressions of costate variables. Ross et al. suggested that there is a mapping relationship between costate variables of the original OCP and KKT multipliers of the associated NLP [12]. This mapping relationship can be used to compute the costate variables indirectly from the KKT multipliers. In the following, we will derive the mapping relationship for Bolza-type OCP as shown in Eq. (8.1).

First, we construct the Hamiltonian for the OCP:

$$H = \frac{t_f - t_0}{2}\left(G + \boldsymbol{\lambda}^{\mathrm{T}} \boldsymbol{f}\right) + \boldsymbol{\mu}_{\mathrm{eq}}^{\mathrm{T}} \boldsymbol{C}_{\mathrm{eq}} + \boldsymbol{\mu}_{\mathrm{inq}}^{\mathrm{T}} \boldsymbol{C}_{\mathrm{inq}}, \tag{8.14}$$

where $\boldsymbol{\lambda} \in \mathbb{R}^{N_x}, \boldsymbol{\mu}_{\mathrm{eq}} \in \mathbb{R}^{N_{C\mathrm{eq}}}, \boldsymbol{\mu}_{\mathrm{inq}} \in \mathbb{R}^{N_{C\mathrm{inq}}}$ are costate variables of the OCP corresponding to the state space model, equality path constraints, and inequality path constraints. According to the first-order optimality condition, we have the following differential equation:

$$\dot{\boldsymbol{\lambda}}\left(\tau_k\right) = -\left(\frac{\partial H}{\partial \boldsymbol{x}}\right)\left(\tau_k\right) = 0. \tag{8.15}$$

Since $\dot{\boldsymbol{\lambda}}$ satisfies $\dot{\boldsymbol{\lambda}}\left(\tau_k\right) = \sum_{i=0}^{N} D_{ki}\boldsymbol{\lambda}\left(\tau_i\right)$, then

$$\frac{t_f - t_0}{2}\left[\frac{\partial G}{\partial \boldsymbol{x}} + \left(\frac{\partial \boldsymbol{f}}{\partial \boldsymbol{x}}\right)^{\mathrm{T}}\boldsymbol{\lambda}\left(\tau_k\right)\right] + \left(\frac{\partial \boldsymbol{C}_{\mathrm{eq}}}{\partial \boldsymbol{x}}\right)^{\mathrm{T}}\boldsymbol{\mu}_{\mathrm{eq}} + \left(\frac{\partial \boldsymbol{C}_{\mathrm{inq}}}{\partial \boldsymbol{x}}\right)^{\mathrm{T}}\boldsymbol{\mu}_{\mathrm{inq}} = -\sum_{i=0}^{N} D_{ki}\boldsymbol{\lambda}\left(\tau_i\right) \tag{8.16}$$

After applying the pseudospectral transformation, the Lagrangian function of associated NLP is given by

$$\begin{aligned}\tilde{J} = \varnothing + \frac{t_f - t_0}{2}\sum_{i=0}^{N} w_i G_i + \tilde{v}^{\mathrm{T}}\varphi \\ + \sum_{i=0}^{N}\left[\tilde{\lambda}_i^T\left(\frac{t_f - t_0}{2} f_i - \dot{X}_i\right) + \tilde{\mu}_{\mathrm{eq},i}^T C_{\mathrm{eq},i} + \tilde{\mu}_{\mathrm{inq},i}^T C_{\mathrm{inq},i}\right]\end{aligned} \tag{8.17}$$

where $\tilde{\boldsymbol{\lambda}}$, $\tilde{\boldsymbol{\mu}}_{\mathrm{eq}}, \tilde{\boldsymbol{\mu}}_{\mathrm{inq}}, \tilde{\boldsymbol{v}}$ are the KKT multipliers of the NLP. According to the KKT conditions for a generic NLP, we have

$$\frac{\partial \tilde{J}}{\partial \boldsymbol{X}_k} = 0, \quad \frac{\partial \tilde{J}}{\partial \boldsymbol{U}_k} = 0, \quad \boldsymbol{C}_{\mathrm{eq},k} = 0, \quad \tilde{\boldsymbol{\mu}}_{\mathrm{inq},k}^T \boldsymbol{C}_{\mathrm{inq},k} = 0 \tag{8.18}$$

The partial derivatives of $\tilde{J}$ with respect to X_k are given below for $k = 1, \ldots, N-1$:

$$\begin{aligned}\frac{\partial \tilde{J}}{\partial \boldsymbol{X}_k} = \frac{t_f - t_0}{2}\left(\frac{\partial G_k}{\partial \boldsymbol{X}_k} w_k + \left(\frac{\partial \boldsymbol{f}_k}{\partial \boldsymbol{X}_k}\right)^{\mathrm{T}}\tilde{\boldsymbol{\lambda}}_k\right) + \left(\frac{\partial \boldsymbol{C}_{\mathrm{eq},k}}{\partial \boldsymbol{X}_k}\right)^{\mathrm{T}}\tilde{\boldsymbol{\mu}}_{\mathrm{eq},k} \\ + \left(\frac{\partial \boldsymbol{C}_{\mathrm{inq},k}}{\partial \boldsymbol{X}_k}\right)^{T}\tilde{\boldsymbol{\mu}}_{\mathrm{inq},k} - \frac{\partial}{\partial \boldsymbol{X}_k}\sum_{i=0}^{N}\tilde{\boldsymbol{\lambda}}_i^T \dot{\boldsymbol{X}}_i = 0\end{aligned} \tag{8.19}$$

Where

$$\frac{\partial}{\partial \boldsymbol{X}_k}\sum_{i=0}^{N}\tilde{\boldsymbol{\lambda}}_i^{\mathrm{T}}\dot{\boldsymbol{X}}_i = \sum_{i=0}^{N}\tilde{\boldsymbol{\lambda}}_i^{\mathrm{T}}\left(\frac{\partial}{\partial \boldsymbol{X}_k}\sum_{n=0}^{N} D_{in}\boldsymbol{X}_n\right) = \sum_{i=0}^{N} D_{ik}\tilde{\boldsymbol{\lambda}}_i \tag{8.20}$$

On the other hand, by considering

$$\begin{aligned} w_i D_{ik} &= -w_k D_{ki}, \quad i \neq k \\ D_{ik} &= D_{ki} = 0, \quad i = k \end{aligned} \tag{8.21}$$

We have

$$\frac{t_f - t_0}{2}\left[\frac{\partial G_k}{\partial \boldsymbol{X}_k} + \left(\frac{\partial \boldsymbol{f}_k}{\partial \boldsymbol{X}_k}\right)^{\mathrm{T}} \frac{\tilde{\boldsymbol{\lambda}}_k}{w_k}\right] + \left(\frac{\partial \boldsymbol{C}_{\mathrm{eq},k}}{\partial \boldsymbol{X}_k}\right)^{\mathrm{T}} \frac{\tilde{\boldsymbol{\mu}}_{\mathrm{eq},k}}{w_k} + \left(\frac{\partial \boldsymbol{C}_{\mathrm{inq},k}}{\partial \boldsymbol{X}_k}\right)^{T} \frac{\tilde{\boldsymbol{\mu}}_{\mathrm{inq},k}}{w_k} = -\sum_{i=0}^{N} D_{ki} \frac{\tilde{\boldsymbol{\lambda}}_i}{w_i} \tag{8.22}$$

By comparing Eq. (8.22) with Eq. (8.16), we know that if two equations are equivalent, we must have

$$\boldsymbol{\lambda}(\tau_k) = \frac{\tilde{\boldsymbol{\lambda}}_k}{w_k}, \quad k = 1, \cdots, N-1. \tag{8.23}$$

Eq. (8.23) provides the mapping relations between $\boldsymbol{\lambda}(\tau_k)$ and $\tilde{\boldsymbol{\lambda}}_k$ for k=1, . . . , N−1. For $k = 0, N$, we need to consider the effects of Mayer function $\varnothing$ and constraint $\boldsymbol{\varphi}$ to derive mapping relations for $\boldsymbol{\lambda}(t_0)$ and $\boldsymbol{\lambda}(t_N)$. The partial derivative of $\tilde{J}$ with respect to X_0 is given by:

$$\frac{t_f - t_0}{2}\left[\frac{\partial G_0}{\partial \boldsymbol{X}_0} w_0 + \left(\frac{\partial \boldsymbol{f}_0}{\partial \boldsymbol{X}_0}\right)^{\mathrm{T}} \tilde{\boldsymbol{\lambda}}_0\right] + \left(\frac{\partial \boldsymbol{C}_{\mathrm{eq},0}}{\partial \boldsymbol{X}_0}\right)^{\mathrm{T}} \tilde{\boldsymbol{\mu}}_{\mathrm{eq},0} + \left(\frac{\partial \boldsymbol{C}_{\mathrm{inq},0}}{\partial \boldsymbol{X}_0}\right)^{T} \tilde{\boldsymbol{\mu}}_{\mathrm{inq},0} + \left(\frac{\partial \boldsymbol{\varphi}}{\partial \boldsymbol{X}_0}\right)^{T} \tilde{\boldsymbol{v}} - \sum_{i=0}^{N} D_{i0} \tilde{\boldsymbol{\lambda}}_i = 0 \tag{8.24}$$

Since

$$\begin{aligned} w_i D_{i0} &= -w_0 D_{0i} \quad i \neq 0, \\ D_{00} &= -1/(2w_0) \quad i = 0. \end{aligned} \tag{8.25}$$

Then

$$\sum_{i=0}^{N} D_{i0} \tilde{\boldsymbol{\lambda}}_i = -w_0 \sum_{i=0}^{N} D_{0i} \frac{\tilde{\boldsymbol{\lambda}}_i}{w_i} - \frac{\tilde{\boldsymbol{\lambda}}_0}{w_0} \tag{8.26}$$

Thus, we have

$$\frac{t_f - t_0}{2}\left[\frac{\partial G_0}{\partial \boldsymbol{X}_0} + \left(\frac{\partial \boldsymbol{f}_0}{\partial \boldsymbol{X}_0}\right)^{\mathrm{T}} \frac{\tilde{\boldsymbol{\lambda}}_0}{w_0}\right] + \left(\frac{\partial \boldsymbol{C}_{\mathrm{eq},0}}{\partial \boldsymbol{X}_0}\right)^{\mathrm{T}} \frac{\tilde{\boldsymbol{\mu}}_{\mathrm{eq},0}}{w_0} + \left(\frac{\partial \boldsymbol{C}_{\mathrm{inq},0}}{\partial \boldsymbol{X}_0}\right)^{T} \frac{\tilde{\boldsymbol{\mu}}_{\mathrm{inq},0}}{w_0} = -\sum_{i=0}^{N} D_{0i} \frac{\tilde{\boldsymbol{\lambda}}_i}{w_i} - \frac{1}{w_0}\left(\frac{\tilde{\boldsymbol{\lambda}}_0}{w_0} + \left(\frac{\partial \boldsymbol{\varphi}}{\partial \boldsymbol{X}_0}\right)^{T} \tilde{\boldsymbol{v}}_0\right) \tag{8.27}$$

Similar arguments hold when considering the partial derivative of $\tilde{J}$ with respect to X_N:

$$\frac{t_f - t_0}{2}\left[\frac{\partial G_N}{\partial \boldsymbol{X}_N} + \left(\frac{\partial \boldsymbol{f}_N}{\partial \boldsymbol{X}_N}\right)^{\mathrm{T}} \frac{\tilde{\boldsymbol{\lambda}}_N}{w_N}\right] + \left(\frac{\partial \boldsymbol{C}_{\mathrm{eq},N}}{\partial \boldsymbol{X}_N}\right)^{\mathrm{T}} \frac{\tilde{\boldsymbol{\mu}}_{\mathrm{eq},N}}{w_N} + \left(\frac{\partial \boldsymbol{C}_{\mathrm{inq},N}}{\partial \boldsymbol{X}_N}\right)^{T} \frac{\tilde{\boldsymbol{\mu}}_{\mathrm{inq},N}}{w_N}$$
$$= -\sum_{i=0}^{N} D_{Ni} \frac{\tilde{\boldsymbol{\lambda}}_i}{w_i} + \frac{1}{w_N}\left(\frac{\tilde{\boldsymbol{\lambda}}_N}{w_N} - \frac{\partial \varnothing}{\partial \boldsymbol{X}_N} - \left(\frac{\partial \boldsymbol{\varphi}}{\partial \boldsymbol{X}_N}\right)^{T} \tilde{\boldsymbol{v}}_N\right) \tag{8.28}$$

By comparing Eq. (8.27) with Eq. (8.16), we know that if two equations are equivalent, the term containing $\boldsymbol{\lambda}(t_0)$ in Eq. (8.16) must be equal to the term containing $\tilde{\boldsymbol{v}}_0$ and $\tilde{\boldsymbol{\lambda}}_0$ in Eq. (8.27), i.e., $\boldsymbol{\lambda}(t_0)$ depends on both $\tilde{\boldsymbol{v}}_0$ and $\tilde{\boldsymbol{\lambda}}_0$. Thus, we cannot establish the mapping relation between $\boldsymbol{\lambda}(t_0)$ and $\tilde{\boldsymbol{\lambda}}_0$ without additional imposed conditions. Similar arguments also hold true for the mapping relation between $\boldsymbol{\lambda}(t_N)$ and $\tilde{\boldsymbol{\lambda}}_N$. However, there is a feasible solution when closure conditions with feasibility tolerance are added [22]. Here we add a set of closure conditions to establish the mapping relationship for $\boldsymbol{\lambda}(\tau_0)$ with respect to $\tilde{\boldsymbol{\lambda}}_0$, $\tilde{\boldsymbol{v}}_0$, and $\boldsymbol{\lambda}(\tau_N)$ with respect to $\tilde{\boldsymbol{\lambda}}_N$, $\tilde{\boldsymbol{v}}_f$. Equations (8.29) and (8.30) are newly added closure conditions:

$$\frac{\tilde{\boldsymbol{\lambda}}_0}{w_0} + \left(\frac{\partial \boldsymbol{\varphi}}{\partial \boldsymbol{X}_N}\right)^{\mathrm{T}} \tilde{\boldsymbol{v}}_0 = 0, \tag{8.29}$$

$$\frac{\tilde{\boldsymbol{\lambda}}_N}{w_N} - \frac{\partial \varnothing}{\partial \boldsymbol{X}_N} - \left(\frac{\partial \boldsymbol{\varphi}}{\partial \boldsymbol{X}_N}\right)^{T} \tilde{\boldsymbol{v}}_f = 0. \tag{8.30}$$

Then we obtain the relation mapping for $k = 0, N$:

$$\boldsymbol{\lambda}\,(t_0) = \frac{\tilde{\boldsymbol{\lambda}}_0}{w_0}, \quad \boldsymbol{\lambda}\,(t_N) = \frac{\tilde{\boldsymbol{\lambda}}_N}{w_N} \tag{8.31}$$

By considering the partial derivatives of $\tilde{J}$ with respect to $\boldsymbol{U}_k$ for $k = 0, \cdots, N$, we can similarly derive the following conditions:

$$\begin{aligned} \boldsymbol{\mu}_{\mathrm{eq}}\,(t_k) &= \tilde{\boldsymbol{\mu}}_{\mathrm{eq},k}/w_k, \\ \boldsymbol{\mu}_{\mathrm{inq}}\,(t_k) &= \tilde{\boldsymbol{\mu}}_{\mathrm{inq},k}/w_k. \end{aligned} \tag{8.32}$$

In summary, Eqs. (8.23), (8.31), and (8.32) establish the mapping relations between the costate variables of OCP and the KKT multipliers of the associated NLP, which provides an indirect way to examine the optimality of optimal solutions.

8.3.2 Numerical Calculation of Collocation Points

Due to implicit expression for the roots of $\dot{P}_N(\tau)$, the accuracy of directly solving $\dot{P}_N(\tau)$ through Legendre polynomials is very low. So, here we adopt the quasi-Newton algorithm to iteratively compute the roots of $\dot{P}_N(\tau)$. The quasi-Newton method includes two main parts: choosing an initial guess and designing an updating law. We chose the initial guess for iteration as the poles of N-order Chebyshev polynomial that has explicit mathematical representation to efficiently compute the roots of $(N+1)$ order polynomial $g(z) = \left(1-z^2\right)\dot{P}_N(z)$,

$$z_0 = \left\{\theta_k \middle| \ \theta_k = \cos(\pi k/N)\right\} \tag{8.33}$$

where $k = 0, 1, \ldots, N$. The updating law is designed as

$$z_{n+1} = z_n - \Delta z_n \tag{8.34}$$

where n denotes the step index, Δz_n is the length of each iteration. The Legendre polynomial satisfies the following recursive relation:

$$z_n \dot{P}_N(z_n) - \dot{P}_{N-1}(z_n) = N P_N(z_n) \tag{8.35}$$

Then, Δz_n can be mathematically expressed as

$$\Delta z_n = \frac{z_n P_N(z_n) - P_{N-1}(z_n)}{z_n \dot{P}_N(z_n) - \dot{P}_{N-1}(z_n)} = \frac{z_n P_N(z_n) - P_{N-1}(z_n)}{N P_N(z_n)}. \tag{8.36}$$

Note that Eq. (8.36) needs to compute the values of $P_N(z_n)$ and $P_{N-1}(z_n)$, which can be calculated by the recursive relation of Legendre polynomial [21], i.e.,

$$P_{m+1}(z_n) = \frac{2m+1}{m+1} z_n P_m(z_n) - \frac{m}{m+1} P_{m-1}(z_n), \tag{8.37}$$

where m=3, 4, ..., N. In summary, the computation algorithm for LGL collocation points is given below:

1. Initial points are determined using Eq. (8.33).
2. For step n,
   (a) Recursively compute $P_N(z_n)$ using Eq. (8.37) with initial conditions
   $P_1(z_n) = 1$;
   $P_2(z_n) = z_n$;
   (b) Use Eq. (8.34) and Eq. (8.36) to iteratively compute z_{n+1}.
3. Stop if $e = \|z_{n+1} - z_n\|_\infty < \varepsilon$.

We run this computation algorithm in [25] with 3.2 GHz CPU, and set $\varepsilon = 10^{-16}$. The computing time for choosing 40, 70, or 500 collocation points is 22, 31, or 35 ms, respectively. The solution efficiency satisfies the common requirements of computing resources.

The differentiation matrices and integration weights can be calculated by Eq. (8.7) and Eq. (8.10), respectively, with accurate calculated LGL points z and $P_N(z)$.

8.3.3 Multi-Phase Problems

The PS method has high accuracy for solving smooth problem, but it's weak for non-smooth problems. With the number of collocation points increasing, the solving accuracy can be improved to a certain extent, but the computational efficiency can significantly reduce. In order to address non-smooth problems, we employ a multi-phase strategy to apply the PS method. To be specific, it divides the original problem into multiple phases and applies the PS method at each phase, respectively. Besides, we also need to add some additional connectivity between different phases. For the OCP with known phase-division locations, the multi-phase processing strategy is straightforward. In particular, we let $\{T_1, T_2, \ldots, T_{P-1}\}$ denote the phase-division locations of a problem with P phases. Then the original non-smooth problem is converted into P-phase smooth OCPs. And we can set different performance indices, state equations, and path constraints for each phase. The total performance index is the summation of all phases:

$$J = \varnothing + \sum_{p=1}^{P} \frac{t_f^p - t_0^p}{2} \sum_{k=0}^{N^p} w_k^p G^p \left(\boldsymbol{X}_k^p, \boldsymbol{U}_k^p, \tau_k^p \right) \tag{8.38}$$

We add the connectivity constraints between two phases based on specific requirements. For example of a bang-bang control problem, the state variables between two phases must be continuous and the control variables are allowed to have break points. The connectivity constraints can be denoted as

$$C_{\text{phase}} \left[\boldsymbol{X}_f^i, \boldsymbol{U}_f^i, t_f^i, \boldsymbol{X}_0^j, \boldsymbol{U}_0^j, t_0^j \right] = 0 \quad 1 \le i, j \le P. \tag{8.39}$$

However, the phase-division locations are usually unknown in advance for researchers. There are two strategies to deal with such issues. The first strategy is to regard phase-division locations as additional optimization variables. This strategy increases the computational complexity but is easy to implement. The second strategy is to obtain initial optimization results first by roughly applying the PS method to the original problem, then find out the fast-changing regions of the state and control inputs, finally form a multi-phase problem by taking the fast-changing regions as a new phase. The basic idea is to increase the density of the collocation

points in the fast-changing regions, thus increasing the approximation accuracy. Based on the second strategy, we develop the following algorithm:

1. Obtain initial optimization results by roughly applying the PS method to the original problem.
2. Compute the changing rate of control input $\dot{\boldsymbol{U}} = \boldsymbol{DU}$ using differentiation matrix and initial computation results.
3. Set a threshold vector $\boldsymbol{H}$ for the changing rates. For any $j = 1, 2, \cdots, N_u$ and $i \in [m_1, m_2] \in (0, N)$, if $\dot{U}_{ji} > H_j$, we set time domain $[\tau_{m_1-1}, \tau_{m_2+1}]$ as a fast-changing region and set this region as a new single phase.
4. Increase the number of collocation points in the fast-changing region to improve the computational accuracy of the constructed multi-phase problem. Properly decrease the number of collocation points in the smooth region to improve the computational efficiency. Then we can obtain the optimal solution by solving the constructed multi-phase problem.

In fact, this method chooses different densities of collocation points for different regions. For a smooth region, good computational efficiency can be achieved by choosing sparse collocation points. For a non-smooth region, we can also choose dense collocation points to help improve the computational accuracy.

8.3.4 Pseudospectral Optimal Control Problem Solver

We develop a Matlab-environment-based software package, called POPS, to numerically calculate the solution of general OCPs. It includes four modules:

1. User configuration module including the OCP description and solver parameter setup;
2. Module for converting OCP into NLP;
3. Module to solve NLP;
4. Module for interacting with users, including data saving, figure drawing, etc.

The POPS is applicable to solve OCPs with:

1. Linear and/or nonlinear functions;
2. Smooth and/or non-smooth functions;
3. Free, fixed, and constrained states (both initial and terminal);
4. Equality and/or inequality constraints; differentiation-typed and/or integration-typed constraints;
5. Mayer-, Lagrange-, and Bolza-typed performance indices.

The POPS is compatible with other Matlab toolboxes. Users can call POPS in other Matlab applications. It also provides a large amount of flexibility for users to configure their own problems.

8.4 Application to Autonomous Vehicles

This case presents a trajectory planning problem for automated vehicles to overtake another vehicle under mild conditions, i.e., dry road and non-aggressive driving. As shown in Fig. 8.1, a vehicle is required to fulfill the task of overtaking the vehicle ahead following the optimal path within the predefined trajectory region, along with the guarantee to minimize the weighted sum of squares of the steering angle and the lateral acceleration.

8.4.1 Model for Control

The system state equations can be obtained through the kinematic model and the lateral dynamic model of vehicles with two degrees of freedom, as shown in Fig. 8.1. Under the assumption that the lateral tire force is proportional to the slip angle and the influence of longitudinal tire force, suspension, and slip angle on slip angle are ignored [23], the dynamics of vehicles in coordinate system *xoy* is derived as:

$$\begin{aligned} \dot{v} &= \frac{k_f+k_r}{mu}v + \left(\frac{ak_f-bk_r}{mu} - u\right)w_r - \frac{k_f}{mi}\delta_w, \\ \dot{w}_r &= \frac{ak_f-bk_r}{I_z u}v + \frac{a^2k_f+b^2k_r}{I_z u}w_r - \frac{ak_f}{I_z i}\delta_w, \\ \dot{\varphi} &= w_r, \end{aligned} \tag{8.40}$$

where v denotes the lateral velocity, k_f and k_r denote the cornering stiffness of two front tires and two rear tires, a and b denote the distances of the front tire and the rear tire from the center of vehicle gravity, respectively, m denotes the mass of a vehicle, u denotes the longitudinal velocity, w_r denotes yaw rate of vehicle, i denotes the transmission ratio of steering system, δ_w denotes the steering angle, I_z denotes the yaw moment of inertia of vehicle, and φ denotes yaw angle of vehicle in global axes.

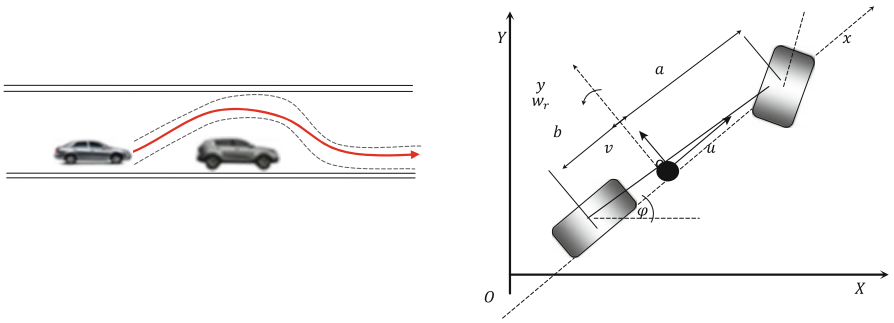

Fig. 8.1 Vehicle model with two degrees of freedom

To illustrate the trajectory of a vehicle, an earth coordinate system XOY is constructed, where the vehicle is located in X, Y. The relationship between moving trajectory and the states of vehicle can be presented as

$$\begin{aligned} \dot{X} &= u\cos\varphi - v\sin\varphi, \\ \dot{Y} &= u\sin\varphi + v\cos\varphi. \end{aligned} \tag{8.41}$$

During the overtaking task, reducing the steering angle and the lateral acceleration can increase the performance of vehicle ride and handling. The performance function is designed as:

$$\begin{aligned} J &= \int_0^{t_f} k_1 a_y^2 + k_2 \delta_w^2 \mathrm{d}t, \\ a_y &= u w_r + \dot{v}, \end{aligned} \tag{8.42}$$

where a_y denotes as the lateral acceleration and k_1, k_2 denote the weighting coefficients of performance index. The region of overtaking trajectory T_v is demonstrated in Fig. 8.2, following the definitions:

$$\begin{aligned} T_v &= \left\{ y \middle| \ |y - \tilde{y}| \le \varepsilon/2 \right\}, \\ \tilde{y} &= A_r / \left(1 + e^{-k_3(x-x_1)}\right) - A_r / \left(1 + e^{-k_4(x-x_2)}\right), \end{aligned} \tag{8.43}$$

where $\tilde{y}$ denotes the center line of the designed trajectory region, ε denotes the width of a trajectory region, and A_r, k_3, k_4, x_1, x_2 denote the coefficients of the center line.

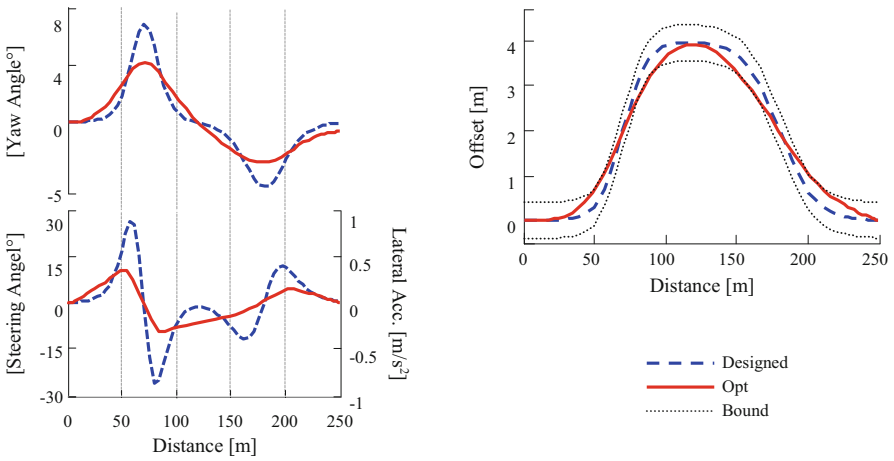

Fig. 8.2 POPS optimization results

8.4.2 The Formulation of OCP

The OCP for trajectory optimization is formulated as:

$$\min J = \int_0^{t_f} k_1 a_y^2 + k_2 \delta_w^2 \mathrm{d}t,$$

subject to

$$\begin{aligned}
\dot{v} &= \tfrac{k_f + k_r}{mu} v + \left(\tfrac{ak_f - bk_r}{mu} - u \right) w_r - \tfrac{k_f}{mi} \delta_w, \\
\dot{w}_r &= \tfrac{ak_f - bk_r}{I_z u} v + \tfrac{a^2 k_f + b^2 k_r}{I_z u} w_r - \tfrac{ak_f}{I_z i} \delta_w, \\
\dot{\varphi} &= w_r, \\
\dot{x} &= u \cos\varphi - v \sin\varphi, \\
\dot{y} &= u \sin\varphi + v \cos\varphi, \\
y - \tilde{y} &\le \varepsilon/2, \\
t_{f\min} &\le t_f \le t_{f\max}.
\end{aligned} \tag{8.44}$$

The parameters used for simulation are listed in Table 8.1.

8.4.3 Optimization Results

We explicitly use the developed solver POPS to compute the numerical solutions. The number of collocation points is set to 60. The optimal performance index is 0.0143, and the results are illustrated in Fig. 8.2. As shown in Fig. 8.2, the optimized trajectory via POPS has a relatively smoother trajectory and satisfies the boundary constraints precisely. We note that the maximum fluctuations of the steering angle decrease by more than 50 %, no rapid fluctuations in the process, and the lateral acceleration of the vehicle is significantly reduced.

Table 8.1 Simulation parameters

Parameter	Value	Parameter	Value
m	1450 kg	k_1	1
a	1.2 m	k_2	0.25
b	1.5 m	E	0.8 m
I_z	1550 kg $\cdot$ m^2	A_r	3.5 m
k_f	$-52,000$ N/rad	k_3	0.12
k_r	$-116,000$ N/rad	k_4	0.08
u	12.5 m/s	x_1	70 m
i	20	x_2	180 m
$t_{f\max}$	30 s	ε	0.8 m
$t_{f\min}$	10 s		

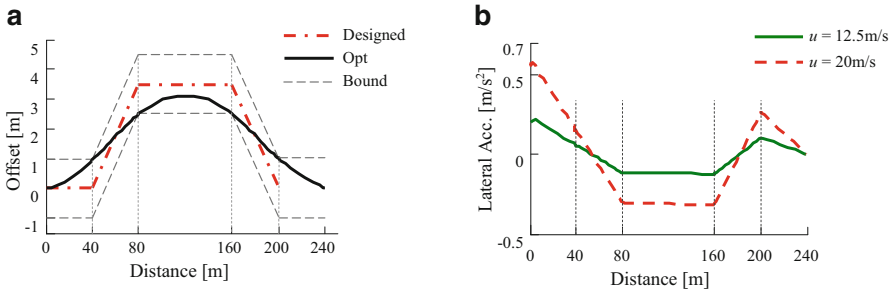

Fig. 8.3 POPS results for multiple phase problem (a) vehicle trajectory; (b) lateral acceleration

However, if the pre-designed center line of trajectory is not smooth but can only be described roughly by non-smooth functions, the POPS can still be applied to solve this problem via the multi-phase preprocessing strategy. The center line of non-smooth trajectory is described as

$$\tilde{y} = \begin{cases} 0, & x \in [0, 40] \\ 3.5/40 * (x - 40), & x \in [40, 80] \\ 3.5, & x \in [80, 160] \\ 3.5 - 3.5/40 * (x - 160), & x \in [160, 200] \\ 0, & x \in [200, 240] \end{cases}, \tag{8.45}$$

which consists of five sections shown in Fig. 8.3a, and ε is set to 2 m. The control variables and state variables are set to be continuous at the break points. The optimized trajectory is shown in Fig. 8.3a. The optimized lateral acceleration is shown in Fig. 8.3b, where u is set to 12.5 and 20 m/s. This new example can illustrate the idea of multi-phase strategy that dividing the original non-smooth problem into multiple smooth problems. Actually, this kind of trajectory optimization in overtaking task is highly nonlinear. It will be much more complicated if employing the strategy to numerically solve the first-order optimality conditions.

8.4.4 Comparison with Other Methods

In order to illustrate the advantages of the PS method compared to direct methods, we also use one TDM to solve the aforementioned problem. The TDM has following characteristics:

(a) Using equidistant points instead of orthogonal collocation in discretization;
(b) Using composite trapezoidal quadrature rule for the integral of cost function.

Finally, the convergence rate of both LPM and TDM is shown in Fig. 8.4. From Fig. 8.4, we can see the following things:

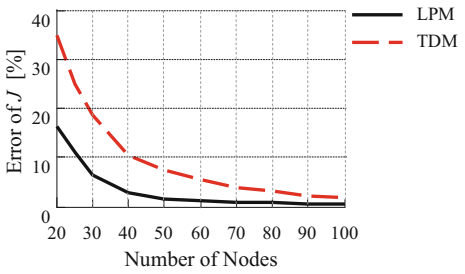

Fig. 8.4 Comparison of conversion rate of LPM and TD

1. The error of performance index compared to theoretical optimal solution.
   The error of performance index is less than 1 % of LPM with 60 collocation points, while the error of TDM with 60 collocation points is greater than 5.5 %. Actually, other similar comparison of PS method and TDM can reach the same conclusion that the pseudospectral method is more accurate than the traditional collocation methods [24].
2. The computional speed and accuracy compared to the theoretical optimal solution.
   The LPM converges faster and possesses higher accuracy than TDM with the same number of collocation points does. In fact, the computational load is determined by the number of collocation points, initial values, and the complexity of the OCPs, e.g., the number and types of constraints. This computational framework and the developed Matlab solver can solve most complex problems with better accuracy, but it is usually applied for offline calculation. For example, the time consumption is 2.69 s and 17.04 s at 20 and 40 collocation points when initial values are set to be zero vector (in Matlab with 3.2 GHz CPU). Greater than 95 % of time is consumed to solve the converted NLP problem by a large number of iterations, which is a common issue for most optimization methods.

8.5 Conclusions and Remarks

In this chapter, we developed a unified computational framework based on LPM for the purpose of accurately and efficiently calculating optimal control strategies. The mapping relationship between the costate variables of OCP and the KKT multipliers of NLP is derived for the sake of checking the optimality of solutions. For engineering implementation, a quasi-Newton iterative algorithm was designed to accurately calculate the LGL points and a multi-phase preprocessing strategy was proposed to handle non-smooth problems. The case study, i.e., optimal path planning of road vehicle, was used to demonstrate the effectiveness of the developed solver. The results show that the developed framework can effectively solve complex vehicle OCPs with linear and/or nonlinear dynamics, complex constraints, and different typed performance index.

References

1. A. Balachandran, J.C. Gerdes, Designing steering feel for steer-by-wire vehicles using objective measures. IEEE/ASME Trans. Mechatron. **20**(1), 373–383 (2014)
2. X. Hu, N. Murgovski, L.M. Johannesson, B. Egardt, Optimal dimensioning and power management of a fuel cell/battery hybrid bus via convex programming. IEEE/ASME Trans. Mechatron. **20**(1), 457–468 (2015)
3. W. Sun, Y. Zhao, J. Li, L. Zhang, H. Gao, Active suspension control with frequency band constraints and actuator input delay. IEEE Trans. Ind. Electron. **59**(1), 530–537 (2012)
4. S.J. Anderson, S.C. Peters, T.E. Pilutti et al., An optimal control based framework for trajectory planning, threat assessment, and semi- autonomous control of passenger vehicles in hazard avoidance scenarios. Int. J. Veh. Auton. Syst. **8**(2), 190–216 (2010)
5. S.E. Li, H. Peng, K. Li, J. Wang, Minimum fuel control strategy in automated car-following scenarios. IEEE Trans. Veh. Technol. **61**(3), 998–1007 (2012)
6. M. Kuriyama, S. Yamamoto, and M. Miyatake, Theoretical study on eco-driving technique for an electric vehicle with dynamic programming, in 2010 IEEE International Conference Electrical Machines and Systems (ICEMS), Incheon, pp. 2026–2030 (2010)
7. M.A.S. Kamal, M. Mukai, J. Murata, T. Kawabe, Ecological vehicle control on roads with up-down slopes. IEEE Trans. Intell. Transp. Syst. **12**(3), 783–794 (2011)
8. F. Mensing, R. Trigui, E. Bideaux, Vehicle trajectory optimization for application in ECO-driving, in *Vehicle Power and Propulsion Conference (VPPC)*, *IEEE* (2011), pp. 1–6
9. R.F. Hartl, S.P. Sethi, R.G. Vickson, A survey of the maximum principles for optimal control problems with state constraints. SIAM Rev. **37**(2), 181–218 (1995)
10. F. Fahroo, I.M. Ross, Advances in pseudospectral methods for optimal control, in *Proceedings of the AIAA Guidance, Navigation and Control Conference and Exhibit*, Honolulu, Hawaii, August 2008, pp. 18–21
11. G. Elnagar, M.A. Kazemi, M. Razzaghi, The pseudospectral Legendre method for discretizing optimal control problems. IEEE Trans. Autom. Control **40**(10), 1793–1796 (1995)
12. F. Fahroo, I.M. Ross, Costate estimation by a Legendre pseudospectral method. J. Guid. Control. Dyn. **24**(2), 270–277 (2001)
13. Q. Gong, I.M. Ross, W. Kang et al., Connections between the covector mapping theorem and convergence of pseudospectral methods for optimal control. Comput. Optim. Appl. **41**(3), 307–335 (2008)
14. D. Garg, W.W. Hager, A.V. Rao, Pseudospectral methods for solving infinite-horizon optimal control problems. Automatica **47**(4), 829–837 (2011)
15. L.N. Trefethen, *Spectral Methods in MATLAB* (SIAM, Philadelphia, 2000), pp. 7–40
16. I.M. Ross, *User's Manual for DIDO: A MATLAB Application Package for Solving Optimal Control Problems* (Tomlab Optimization, Sweden, 2004)
17. A.V. Rao, D.A. Benson, C. Darby, at al., Algorithm 902: A MATLAB software for solving multiple-phase optimal control problems using the gauss pseudospectral method, ACM Trans. Math. Softw. **37**(2), 22:1–39 (2010)
18. V.M. Becerra, *PSOPT Optimal Control Solver User Manual* (University of Reading, Reading, 2010)
19. P.E. Rutquist, M.M. Edvall, *PROPT-Matlab Optimal Control Software* (Tomlab Optimization Inc, Arcata, 2009), p. 260
20. D. Garg, M.A. Patterson, C. Francolin et al., Direct trajectory optimization and costate estimation of finite horizon and infinite horizon optimal control problems using a Radau pseudospectral method. Comput. Optim. Appl. **49**(2), 335–358 (2011)
21. P.G. Ciarlet, J.L. Lions, *Handbook of Numerical Analysis*, vol. 8 (Gulf Professional Publishing, Houston, 2002)

22. Q. Gong, I.M. Ross, W. Kang et al., On the pseudospectral covector mapping theorem for nonlinear optimal control, in *45th IEEE Conference on Decision and Control, December 13–15, 2006, San Diego, CA, USA* (2006), pp. 2679–2686
23. J. Huang, M. Tomizuka, LTV controller design for vehicle lateral control under fault in rear sensors. IEEE/ASME Trans. Mechatron. **10**(1), 1–7 (2005)
24. G.N. Elnagar, M.A. Kazemi, Pseudospectral Chebyshev optimal control of constrained nonlinear dynamical systems. Comput. Optim. Appl. **11**(2), 195–217 (1998)
25. Matlab (2009a). http://cn.mathworks.com/products/pfo/

Part III
Optimization

Chapter 9
Multi-Objective Supervisory Controller for Hybrid Electric Vehicles

Stefano Marelli and Simona Onori

Abstract In this article, we address the problem of energy management control design in hybrid electric vehicles (HEVs) to achieve minimum fuel consumption while optimally limiting battery degradation. We use Pontryagin's minimum principle (PMP) to solve the optimal control problem. To the end of controlling battery aging to guarantee battery performances over 150,000 miles, a battery capacity loss reference trajectory is defined and a battery aging model is used by the optimizer. The resulting optimal supervisory control strategy is able to regulate both state of charge and capacity loss to their reference values. Simulation results conducted on a pre-transmission HEV show that the battery capacity loss can be regulated to achieve the long-term objective without sacrificing much fuel economy.

Keywords Electric vehicles • Supervisory control • Multi-objective

9.1 Introduction

Battery aging plays an important role in hybrid electric vehicles (HEVs) performance: if not properly controlled, faster battery degradation leads to lower energy recovery and lower power output capacity, requiring the battery early replacement and causing a reduction in the HEV monetary saving. A hybrid vehicle has two (or more) sources of energy on-board, whose operation is coordinated by an energy management system (EMS) typically in a way that minimum fuel consumption is achieved [1–3]. Realistic figures of achievable improvement in fuel economy in HEVs range from 10 % for mild hybrids to more than 30 % for highly hybridized vehicles. This potential can be realized only with a sophisticated control system that optimizes energy flows within the vehicle. This consideration has spurred a considerable amount of research in the last 15 years towards *model-based optimal supervisory control techniques* moving away from heuristic or rule-based methods. Systematic model-optimization methods such as dynamic programming (DP) and

S. Marelli • S. Onori (✉)
Department of Automotive Engineering, Clemson University, International Center for Automotive Research, Greenville, SC 29607, USA
e-mail: stefano.marelli.engineer@gmail.com; sonori@clemson.edu

Q. Zhang et al., *Automotive Air Conditioning*, DOI 10.1007/978-3-319-33590-2_9

Pontryagin's minimum principle (PMP) have been successfully adopted to design controllers to improve the energy management in HEVs using meaningful objective functions [4–9].

These optimal control techniques are referred to as *non-causal*, in that their solution relies on a perfect knowledge of the driving cycle, and as such not implementable in real-time. Nonetheless, they are useful for two reasons: (i) they can be used to understand how an optimal solution works, from which rules can be extracted to design real-time implementable control strategies [10], (ii) they can be used to benchmark realizable strategies. For a more comprehensive overview of different control methods developed for HEVs, the reader can refer to [5].

Traditionally, the HEV energy management problem was formulated with the aim of minimizing fuel consumption (or emissions, [11]) while trying to guarantee a charge-sustaining operation of the battery. No considerations about battery use (or misuse) were included in the original problem formulation. Only recently, though, industry has become more concerned about efficiently managing the energy on-board HEVs and, at the same time, monitoring and controlling the battery degradation. If a model-based optimization approach has to be taken to this regards in order to systematically include battery deterioration concerns within the problem formulation, an aging model of the battery is needed. In fact, the study conducted at Argonne National Laboratory [12] showed that the best monetary savings in HEVs are obtained when the battery life matches the vehicle life. Battery End Of Life (EOL) is generally defined as the point in time when battery capacity reduces to 80 % of its initial value [12]. If the goal is to make the vehicle life (usually 150, 000 mi or 15 years) match the battery life, this translates into achieving a 20 % capacity degradation over 150, 000 mi, thus avoiding battery early replacement.

Only over the past few years, optimal supervisory control methods have included aging considerations. One of the first works in this vein is [13] that proposes a cost function that is a convex combination of instantaneous energy (fuel and electricity) and aging costs (given in terms of solid electrolyte interphase layer growth) and solves the problem via stochastic dynamic programming (SDP) for plug-in hybrid electric vehicles (PHEVs). In [14] a PMP-based solution is proposed where a convex combination of fuel and aging cost is used in the cost function; in this case, the capacity loss in HEV is being minimized. A weighting coefficient was used in the cost function to generate a family of Pareto front solutions. A similar approach is followed in [15], where the cost function proposed by [14] is normalized to simplify the physical interpretation of the control parameters.

These latter works tried to minimize the battery deterioration without any explicit goal on battery life duration. The first attempt to achieve such an objective is found in [16]. A battery aging model from [17] is used in the problem formulation, and a PMP-based solution is presented based on a two-state model (state of charge and capacity loss). A solution of the PMP problem was not given, rather an approximate solution based on extending the adaptation law, used in [10], to the two costates was presented, based on the simplistic assumption that the capacity loss trend over the

vehicle life span is linear. In [18] an adaptive version of PMP is proposed as well, to minimize fuel consumption and battery aging, while limiting battery temperature. Qualitative results were presented for rather limited conditions of operation.

The objective of this paper is to use an experimentally validated battery aging model into the EMS, to systematically control capacity degradation during the operational life of the vehicle, with a minimum impact on the vehicle performances. The problem of fuel consumption minimization and battery degradation limitation for HEVs is inherently a *two-time scale* control problem in that nominally the two objectives have to be reached over two different time horizons: driving cycle and battery life, respectively. In fact, we normally test vehicles performance over standard driving cycles while battery life is measured in terms of total ampere-hours throughput. The proposed optimal supervisory control strategy is able to reduce the two-time scale problem to a one-time scale problem, by minimizing an instantaneous cost function and guaranteeing a predefined battery degradation trend on a short-time horizon, leading to 20 % cumulative capacity loss over 150, 000 mi.

In this manuscript, we first use an experimentally validated battery aging model from [19] to monitor and control degradation within the multi-objective optimal control framework. We then express the costate dynamics of PMP, including the dependence of the mass fuel flow rate of the engine from the state of charge of the battery. Third, we formulate an aging limiting control problem with two states which requires a capacity loss reference trajectory to be defined. In this way, the multi-objective supervisory control problem (hereinafter referred to as "aging-limiting PMP" problem) is solved as a regulation problem on the two states (state of charge and capacity). The aging-limiting PMP (AL-PMP) problem is finally solved by proposing a novel analytic/numerical methodology along with a tuning algorithm. An analytic comparison between the newly proposed AL-PMP problem and the optimization presented in [1] is shown, and a new interpretation of the well-known ECMS strategy, extended to the case with battery aging, is proposed.

The paper is organized as follows: in Sect. 9.2 the adopted aging model is presented, and the capacity loss reference trajectory is defined; in Sect. 9.3 the vehicle simulator is presented, and a focus is put on the battery cell and pack model including aging; in Sect. 9.4 the meaningfulness of the control problem is explained and two situations are defined; in Sect. 9.5 the aging-limiting optimal control problem is formulated, and it is solved with AL-PMP in Sect. 9.6; in Sect. 9.7 the novel control strategy is compared with other two different approaches, which show to be equivalent to AL-PMP, but more problematic in the implementation; in Sect. 9.8 the penalty function on battery capacity loss is shown and analyzed; in Sect. 9.9 AL-PMP is optimally tuned and simulation results are shown in Sect. 9.10; finally, conclusions are given in Sect. 9.11.

9.2 Battery Aging Model and Capacity Loss Reference Trajectory

Aging is an irreversible process caused by parasitic chemical reactions that take place inside the battery. Batteries can undergo two types of aging: *calendar aging* [20, 21] and *cycle-life aging* [17, 19, 22]. In this paper only cycle-life aging is being addressed, and an empirical capacity degradation model is used in the control strategy.

The factors responsible for battery aging are usually referred to as *severity factors* [23]. In HEV applications, those are typically: state of charge, SOC, C-rate, defined as $I_c = I/Q$ (where I is the battery current in $[A]$ and Q is the actual capacity in $[Ah]$), and battery internal temperature, θ. The capacity loss model, from [19], is identified on real HEV battery data with a complete dependence on severity factors by means of a *severity factor function*, σ_{funct}. The following functional relationship exists between σ_{funct} and Q_{loss}:

$$Q_{\text{loss}}(SOC, I_c, \theta, Ah) = \sigma_{\text{funct}}(SOC, I_c, \theta) \cdot Ah^z \tag{9.1}$$

where Q_{loss} is the percent capacity loss, defined as $Q_{\text{loss}} = (1 - Q/Q_0) \cdot 100$, where Q_0 is the initial capacity in $[Ah]$; z is an empirical power exponent; and Ah is the accumulated ampere-hour throughput of the battery, given by $Ah = \int_0^t \frac{|I|}{3600} d\tau$. SOC is expressed as a fraction, I_c is in $[1/h]$ and θ is in [°C]. The severity factor function assumes the following form:

$$\sigma_{\text{funct}}(SOC, I_c, \theta) = (\alpha\, SOC + \beta) \cdot exp\left(\frac{-E_a + \eta\ |I_c|}{R_g\,(273.15 + \theta)}\right) \tag{9.2}$$

where α, β and η are model parameters (identified in [19]), E_a is the activation energy in $[J/mol]$ and R_g is the universal gas constant in $[J/mol/K]$.

In this work, the control-oriented severity factor map, σ_{map}, originally defined in [14] for PHEVs and then further refined for HEV batteries in [19], is considered. It is defined as the ratio of the total Ah-throughput under nominal conditions until EOL is reached (i.e., Γ) to the total Ah-throughput under actual operating conditions (i.e., γ):

$$\begin{aligned} \sigma_{\text{map}}(SOC, I_c, \theta) &= \frac{\Gamma\,(SOC_{\text{nom}}, I_{c,\text{nom}}, \theta_{\text{nom}})}{\gamma\,(SOC, I_c, \theta)} \\ &= \frac{\int_0^{t_{\text{EOL}}} |I_{\text{nom}}|\, d\tau}{\int_0^{t_{\text{EOL}}} |I|\, d\tau} \end{aligned} \tag{9.3}$$

where SOC_{nom}, $I_{c,\text{nom}}$, θ_{nom}, and I_{nom} represent predefined nominal operating conditions and t_{EOL} is the time at EOL. The severity factor map is a measure of the relative aging effect on the battery at a given operating condition with respect to

the nominal operation. It can be used the same way as an engine fuel consumption map, in that it allows to select the battery operating points in the domain (SOC, I_c, θ) to ensure lower capacity degradation. The capacity loss model (9.1), together with the severity factor function (9.2) is used in the following to capture battery aging dynamics and estimate the actual capacity, as described in Sect. 9.3.1.3. The severity factor map, on the other hand, is used in the EMS by the optimizer to select the optimal battery operating points to limit its aging, as described in Sect. 9.6.

9.2.1 Capacity Loss Reference for Cycle-Life

Since the electrochemical aging processes that take place inside the battery are irreversible, the capacity loss is a monotonically increasing function of *Ah*-throughput, as it can only increase if the battery is being used (or stay constant if the battery is not being used). In this paper, we define a capacity loss reference trajectory, with the purpose of limiting capacity loss over each day of driving. In particular, the capacity loss reference is expressed as a function of the driven distance d (expressed in miles, $[mi]$), and average severity factor values are used in σ_{funct} for (9.1). Simulations performed over US06 and FUDS driving cycles at ambient temperatures of $\theta_{\text{amb}} = 20$, 30 and 40°C produce the average values reported in Table 9.1. In addition, a scaling factor, K, is introduced, resulting in:

$$Q_{\text{loss,ref}}(d) = K \cdot \sigma_{\text{funct}}\left(\overline{SOC}, \overline{I}_c, \overline{\theta}\right) \cdot d^z \tag{9.4}$$

where z is from (9.1). K is selected to ensure that 20 % capacity loss is reached after 150, 000 mi, as follows:

$$K = \frac{Q_{\text{loss,EOL}}}{\sigma_{\text{funct}}\left(\overline{SOC}, \overline{I}_c, \overline{\theta}\right) \cdot d_{\text{EOL}}^z} \tag{9.5}$$

where the EOL capacity loss and traveled distance are $Q_{\text{loss,EOL}} = 20\,\%$ and $d_{\text{EOL}} = 150,000mi$, respectively, resulting in $K = 0.6837$. Figure 9.1 shows the capacity loss reference as a function of the driven distance until the distance d_{EOL} is reached.

The *two-time scale* optimal control problem is reduced to a single time scale problem by means of breaking up d_{EOL} into intervals of single days of driving, over which a daily capacity loss reference value is defined. Statistics shows that a typical

Table 9.1 Average severity factor values used in the capacity loss reference

Parameter	Value
$\overline{SOC}[-]$	0.446
$\overline{I}_c[1/h]$	2.43
$\overline{\theta}[°C]$	36.1

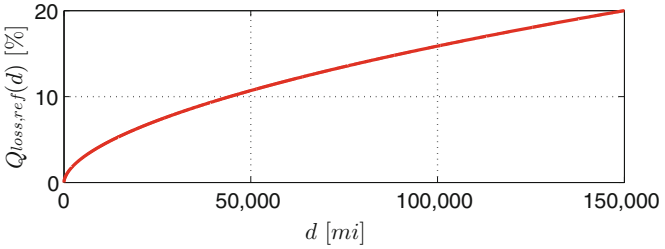

Fig. 9.1 Capacity loss reference based on driven distance

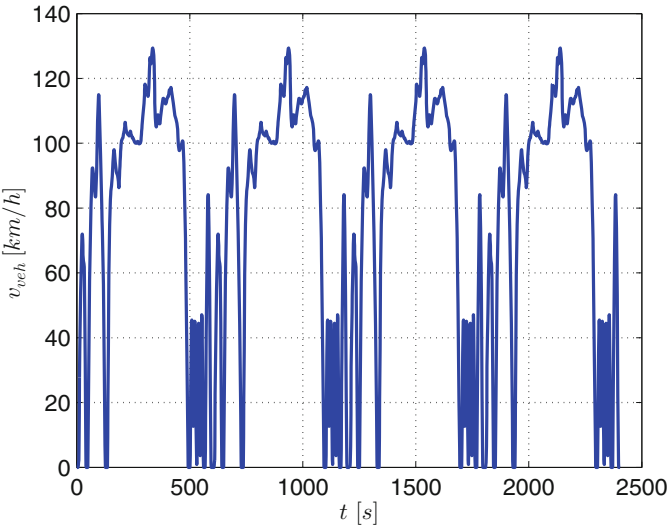

Fig. 9.2 Vehicle speed profile resulting from linking 4 US06 driving cycles

daily trip for a US car driver is estimated to be 28.97*mi* [24]. To account for this statistics, in this work, one day of driving is defined as the concatenation of four US06 or four FUDS driving cycles, resulting in a total distance driven in one day of $d_f = 32.14mi$ and $d_f = 30.02mi$, respectively. The two one-day speed profiles are shown in Figs. 9.2 and 9.3.

The daily Q_{loss} reference is computed from the overall capacity reference trajectory (9.4), over the daily distance traveled. The target value of capacity loss at the end of a generic day k (with $k \in \mathbb{N},\ k \leq k_{\text{EOL}}$, where k_{EOL} is the last day before battery EOL is reached) is obtained evaluating $Q_{\text{loss,ref}}(d)$ at $d = kd_f$. Figure 9.4 shows the quantity just defined, for the first three days of US06 driving cycles.

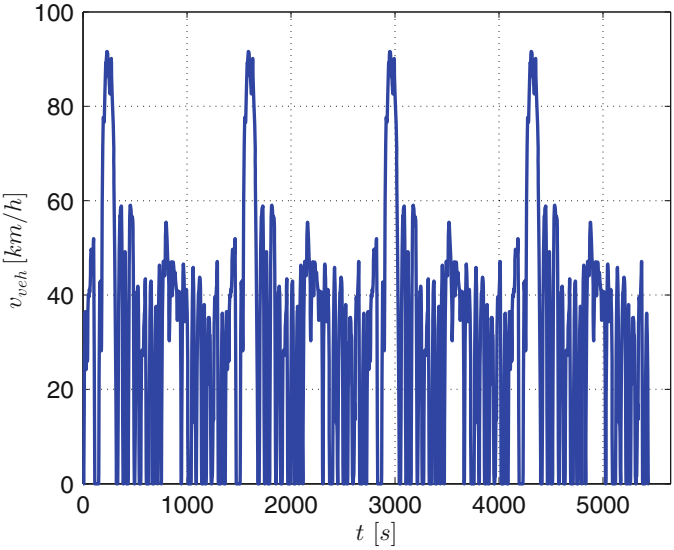

Fig. 9.3 Vehicle speed profile resulting from linking 4 FUDS driving cycles

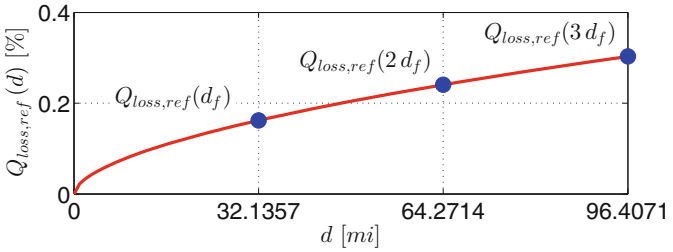

Fig. 9.4 Daily capacity loss reference points calculated from US06 driving cycles, for which $d_f = 32.1357mi$

9.3 Vehicle Simulator

The vehicle simulator used in this work is an improved version of the one developed in [15] that models the parallel pre-transmission Hybrid Honda Civic. The main characteristics of the vehicle are listed in Table 9.2 and its layout is shown in Fig. 9.5. It comprises an integrated motor assist (IMA) where the electric motor (EM) is mounted on the same shaft of the internal combustion engine (ICE). A continuous variable transmission (CVT) allows the vehicle to operate in (i) conventional, (ii) full-electric, (iii) power-assist, or (iv) recuperation mode. In the first mode of operation, only the ICE is running and supplies all the power requested by the driver. In the second mode, only the EM is running, and the engine is switched off. In power-assist mode, the EM and the ICE are running in parallel and the power

Table 9.2 Hybrid Honda Civic vehicle model characteristics used in the simulator

Component	Specifications
Vehicle mass	$1294kg$
ICE	$1.6l$, 85kW
	In-line 4-cylinders
	Gasoline
EM	Maximum peak power $30kW$
	Maximum continuous power $15kW$
CVT	Ratio 0.529–3.172
	Final drive 3.94
Battery pack	$LiFePO_4$
	Nominal capacity $4.6Ah$ ($803Wh$)
	Maximum power $20kW$

Fig. 9.5 Vehicle layout

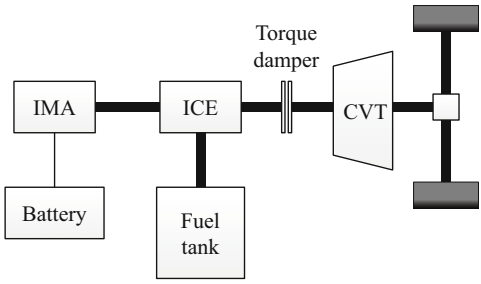

is split between the two, according to the supervisory control strategy. Finally, in recuperation mode, the EM is used to send all the braking power into the battery for energy recuperation; if the saturation limits of the EM or of the battery are reached, the remaining part of the braking power is transferred to the friction brakes, according to a series braking control strategy [25]. The CVT allows a smooth transition between the four modes of operation.

A quasi-static energy-based forward modeling approach is used to simulate the longitudinal dynamics of the hybrid vehicle [1], whose structure is shown in Fig. 9.6. A driver model converts the error between the driving cycle desired speed and the actual vehicle speed into the requested power P_{req}, which is sent to the Supervisory controller, along with ICE speed, ω_{ice}, EM speed ω_{em}, and SOC to generate the optimal actuators set points used in the Powertrain module. The actual vehicle velocity is obtained in the Vehicle dynamics block by integration of the longitudinal vehicle dynamics equation. The vehicle components, ICE and EM are modeled by means of their efficiency maps [15].

The improvements introduced in the simulator for the scope of the present work are related to the battery model, both in the Powertrain and in the Supervisory controller modules. Battery aging dynamics are modeled in the Powertrain model, whereas the formulation of a new instantaneous cost inside the Supervisory controller makes use of the severity factor map, as described in Sect. 9.6.

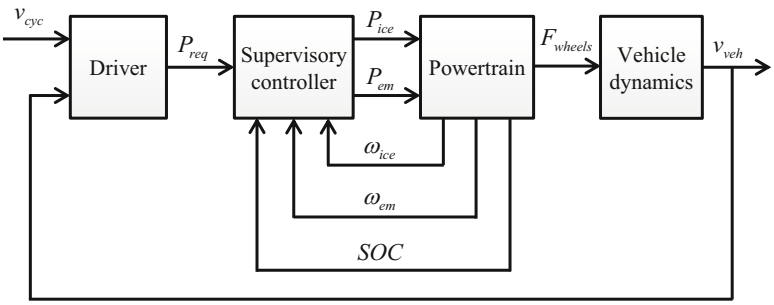

Fig. 9.6 Vehicle simulator block diagram

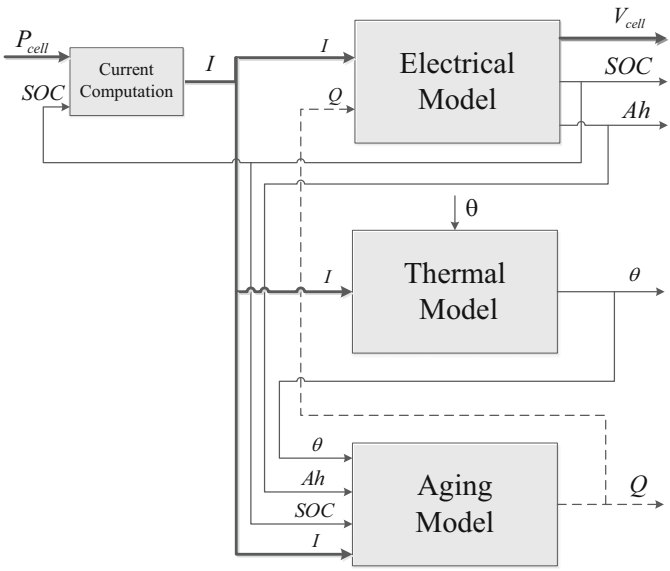

Fig. 9.7 Battery model layout: electrical, thermal, and aging dynamics and their interconnections

9.3.1 Battery Cell Model

In this work an ANR26650 $LiFePO_4$ battery system from A123 is considered, which has a nominal capacity of $2.3Ah$ and a nominal voltage of $3.3V$. The battery cell model is composed of three components: electrical, thermal, and aging, as depicted in Fig. 9.7. For each of these components, all the dynamics involved and their mutual effects are analyzed in the following. The battery pack model is then obtained by scaling up the cell parameters at pack level, according to the topology of the pack used.

9.3.1.1 Electrical Model

The electrical battery cell behavior is modeled with a 0th-order Randle's model. The input to the battery cell is the power, P_{cell}. The corresponding current is computed through the non-linear algebraic function [26]:

$$I = \frac{V_{\text{oc}}(SOC) - \sqrt{V_{\text{oc}}^2(SOC) - 4R_0(SOC,\theta)P_{\text{cell}}}}{2R_0(SOC,\theta)} \tag{9.6}$$

where I is positive in discharge, V_{oc} in $[V]$ is the cell open circuit voltage, which is a non-linear function of SOC, and R_0, in general a function of SOC and θ, is the cell internal resistance at the Beginning Of Life BOL. Figure 9.8 shows a typical trend of the resistance as a function of SOC parameterized for different values of temperature θ [27].
The SOC cell dynamics are defined by the equation:

$$\dot{SOC} = -\frac{I}{3600\, Q_0(\theta)} \tag{9.7}$$

where Q_0, the BOL capacity, is a function of θ as shown in Fig. 9.9.

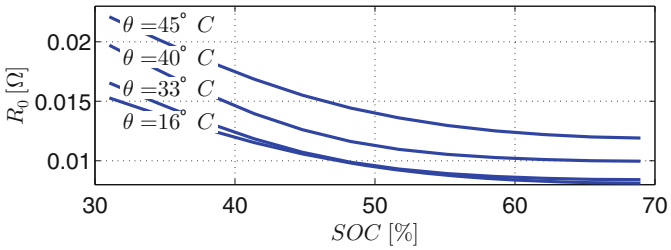

Fig. 9.8 Experimental characterization of R_0 as a function of SOC and θ for A123 ANR26650 battery cell

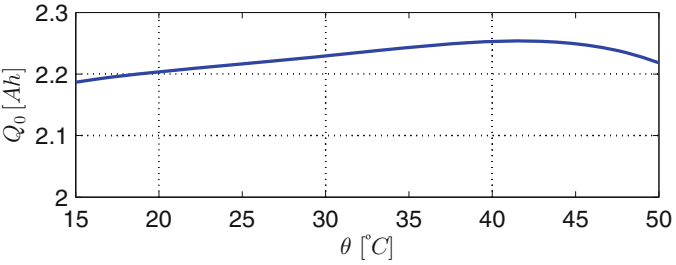

Fig. 9.9 Experimental characterization of Q_0 as a function of θ for A123 ANR26650 battery cell

As the battery is used, it ages. For, Q_0 must be updated with its actual value Q during vehicle operation. The increase in internal resistance due to aging is neglected in this work, and left as a future work.

The terminal voltage V_{cell} is given by

$$V_{\text{cell}} = V_{\text{oc}}(SOC) - R_0(SOC, \theta)\, I \tag{9.8}$$

and the cell power input is given by $P_{\text{cell}} = V_{\text{cell}}\, I$.

9.3.1.2 Thermal Model

The cell thermal model describes the cell temperature dynamics, taking into account the internal heat generation due to the current flowing inside the cell and the heat exchanged with the environment. The dynamics of the cell core temperature θ are described by the equation:

$$\dot{\theta} = \frac{1}{M_c C_p}\left[R_0(SOC, \theta)\, I^2 - \frac{\theta - \theta_{\text{amb}}}{R_u}\right] \tag{9.9}$$

where $R_0\, I^2$ in $[W]$ is the thermal power generated by Joule effect, $M_c C_p$ in $[J/°\text{C}]$ is the effective cell heat capacity, considered constant, θ_{amb} in $[°\text{C}]$ is the ambient temperature, and R_u is the thermal resistance to model the cell heat exchange with the environment. The parameter values of the first-order model used to simulate (9.9) are given in [28].

9.3.1.3 Aging Model

In order to define the capacity loss dynamics, we take the derivative of (9.1) with respect to time. Since the data used for the model identification are collected from tests conducted under SOC, I_c, and θ constant conditions, when computing the time derivative of Q_{loss}, σ_{funct} is considered as a constant. Thus $\frac{dQ_{\text{loss}}}{dt} = \frac{\partial Q_{\text{loss}}}{\partial Ah}\frac{\partial Ah}{\partial t}$, which leads to

$$\dot{Q}_{\text{loss}} = \sigma_{\text{funct}}(SOC, I_c, \theta)\, z \cdot Ah^{z-1} \cdot \dot{Ah} \tag{9.10}$$

The aging model (9.10) is integrated in the powertrain module to obtain the actual value of Q_{loss}. This is then used in the EMS to solve the multi-objective optimal control problem.

9.3.2 Battery Pack Model

The battery pack used in the vehicle is composed of $N_p = 2$ modules in parallel with $N_s = 54$ cells in series for each module. The battery pack quantities are computed, for the sake of simplicity, under the assumption that all the cells are equal and balanced, leading to a pack current of

$$I_{\text{batt}} = N_p\, I \tag{9.11}$$

a pack open circuit voltage of

$$V_{\text{oc,batt}} = N_s\, V_{\text{oc}} \tag{9.12}$$

and a terminal voltage of

$$V_{\text{batt}} = N_s\, V_{\text{cell}} \tag{9.13}$$

The battery pack power is given by

$$P_{\text{batt}} = N_p\, N_s\, P_{\text{cell}} \tag{9.14}$$

and the pack resistance by

$$R_{0,batt} = \frac{N_s}{N_p}\, R_0 \tag{9.15}$$

Moreover, the initial and actual pack capacities are:

$$Q_{0,batt} = N_p\, Q_0, \tag{9.16}$$

$$Q_{\text{batt}} = N_p\, Q \tag{9.17}$$

respectively.

9.4 Well-Posedness of Multi-Objective Control Problem

The aim of the multi-objective optimal control problem is to obtain minimum fuel consumption, while guaranteeing charge-sustainability and limited capacity degradation over a day of driving.

Because of the diverse nature of driving cycles (due to different terrains, drivers, weather conditions, etc.) the multi-objective optimal control problem is well defined (and meaningful) only for those cases where the driving conditions (in terms of severity factors: SOC and I_c) and/or ambient conditions (θ_{amb}) would lead to a

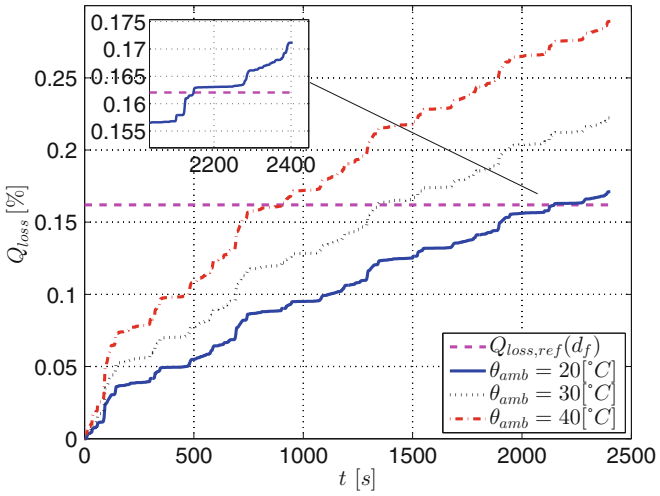

Fig. 9.10 Capacity loss over the first day (combination of 4 US06) of aggressive cycle for different ambient temperatures. Simulation results are obtained by controlling fuel consumption only (using the PMP method): capacity loss always exceeds the $Q_{\text{loss,ref}}(d_f)$ limit. If only fuel is minimized in the vehicle EMS, the battery will degrade (reaching EOL) prematurely

degradation of the battery beyond the acceptable target $Q_{\text{loss,ref}}(d_f)$. In this case, battery aging must be controlled. The US06 is one of such cycle, as shown in Fig. 9.10. In other cases, driving scenarios are inherently mild from an aging standpoint, in that they would never lead to a battery degradation close to the daily target value, as shown in Fig. 9.11 for the case of FUDS. Obviously, in such cases, battery aging does not have to be controlled, and the traditional fuel minimization problem can be employed.

Under aggressive cycles the EMS must monitor and limit the aging to meet the long-term goal of 20 % capacity loss over the vehicle life span to prevent anticipated battery degradation. Inclusion of a battery aging cost in the optimization problem is needed, at the price of slightly worsening in fuel economy. Under mild driving, operating in only fuel consumption minimization mode would be sufficient to guarantee a capacity loss below the target threshold.

The multi-objective optimal control problem is *well-posed* if the capacity degradation resulting from fuel consumption minimization exceeds its daily target limit. In this case, a multi-objective EMS is needed to optimally weigh fuel economy and battery aging.

The novel control strategy proposed in this work, referred to as *aging-limiting*, has the aim to control (limit) Q_{loss} (along with minimizing fuel consumption) to its daily target value $Q_{\text{loss,ref}}(d_f)$. Ideally, in a real-world scenario, a vehicle driving predictor would be used to interact with EMS. The EMS will then decide whether to switch to battery saving mode by activating the aging-limiting strategy or stay in the

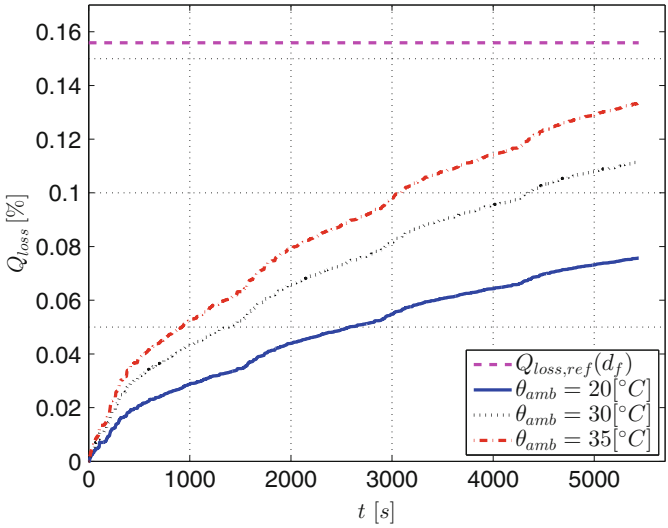

Fig. 9.11 Capacity loss over the first day (combination of 4 FUDS) of mild cycle for different ambient temperatures. Simulation results are obtained by controlling fuel consumption only (using the PMP method): capacity loss never exceeds the $Q_{\text{loss,ref}}(d_f)$ limit. In this specific cases, battery aging control is not needed

default fuel-consumption mode. The actual online strategy implementation is out of scope and will be investigated in the future.

In this work, we focus on the development of the new aging-limiting approach using US06 driving cycles as driving scenarios, for which the multi-objective control problem is well-posed.

9.5 Aging-Limiting Energy Management Problem Formulation

The aging-limiting control problem is formulated using the integral of the fuel power as cost function, as follows:

$$J(u, P_{\text{req}}) = \int_0^{t_f} \dot{m}_f(u, P_{\text{req}})\, Q_{\text{lhv}}\, dt \tag{9.18}$$

where u is the control input, i.e. the battery power $P_{\text{batt}} = I_{\text{batt}}\, V_{\text{batt}}$ in $[W]$ (positive in discharge); $\dot{m}_f$ is the mass fuel flow rate of the engine, in $[g/s]$; Q_{lhv} is the fuel lower heating value in $[J/g]$; and t_f is the final time instant in $[s]$, i.e. the duration of the driving day.

The goal of the aging-limiting supervisory controller is to find the optimal control sequence u^*, that minimizes (9.18) while (i) keeping SOC at the same reference value SOC_{ref} at the beginning and at the end of the driving day (9.19a), (ii) limiting the SOC excursion between fixed minimum and maximum values, respectively, $SOC_{\min}$ and $SOC_{\max}$ (9.19b), and (iii) controlling capacity loss to not exceed the target value (9.19c):

$$SOC(0) = SOC(t_f) = SOC_{\text{ref}} \tag{9.19a}$$

$$SOC_{\min} \leq SOC \leq SOC_{\max} \tag{9.19b}$$

$$0 \leq Q_{\text{loss}} \leq Q_{\text{loss,ref}}(d_f) \tag{9.19c}$$

The use of *power-based* cost function makes the choice of *depletion energy*, E_{dep} in $[J]$, to describe the battery dynamics, and the *effective energy-throughput*, E_{eff} in $[J]$, to describe battery aging dynamics, more practical as opposed to the traditionally used SOC and Q_{loss}. These quantities are defined as follows:

1. Depletion energy[1]:

$$\begin{aligned} x_1 = E_{\text{dep}} = \\ = E_{\text{dep}}(0) + \int_0^t I_{\text{batt}}(SOC, P_{\text{batt}}, \theta)\, V_{\text{oc,batt}}(SOC)\, d\tau \end{aligned} \tag{9.20}$$

   This state represents the amount of energy extracted from the battery pack and is equivalent to SOC in the control problem. Considering a negligible dependence of $V_{\text{oc,batt}}$ on SOC (typical in a charge-sustaining HEV), and a negligible variation of Q_{batt} over one day of driving, then the state of charge can be written as a function of E_{dep}[2]:

$$SOC = SOC(0) + \frac{E_{\text{dep}}(0) - E_{\text{dep}}}{3600\, Q_{\text{batt}}\, V_{\text{oc,batt}}} \tag{9.21}$$

2. Effective energy-throughput:

$$\begin{aligned} x_2 = E_{\text{eff}} = \int_0^t \sigma_{\text{map}}(SOC, I_c, \theta) \\ \cdot |I_{\text{batt}}(SOC, P_{\text{batt}}, \theta)|\, V_{\text{oc,batt}}(SOC)\, d\tau \end{aligned} \tag{9.22}$$

[1] The dependence on time will be left implicit in this paper, for simplicity.

[2] Under this assumption, it is possible to write (9.20) as $E_{\text{dep}} = E_{\text{dep}}(0) + V_{\text{oc,batt}} \int_0^t I_{\text{batt}}(SOC, P_{\text{batt}}, \theta)\, d\tau$ and the state of charge as $SOC = SOC(0) - \frac{1}{3600\, Q_{\text{batt}}} \int_0^t I_{\text{batt}}(SOC, P_{\text{batt}}, \theta)\, d\tau$. These two equations are then combined into (9.21).

It is equivalent in terms of energy to the *effective Ah-throughput*, Ah_{eff}, introduced in [14]. In the control problem this state is equivalent to Q_{loss}, in that it represents a measure of the degradation of the battery: any loss in capacity registered through an increase in Q_{loss} corresponds to an increase in E_{eff} of a commensurate magnitude.

Owing to the above definitions of the system states, the variables used in the control problem are rewritten as follows.

- Because SOC is a function of both E_{dep} (i.e., x_1) and Q_{batt} (or x_2), from (9.21), the battery current is also a function of the states x_1 and x_2:

$$I_{\text{batt}} = I_{\text{batt}}(SOC, P_{\text{batt}}, \theta) = I_{\text{batt}}(x_1, x_2, u, \theta) \tag{9.23}$$

- Similarly, the severity factor map is a function of both states:

$$\sigma_{\text{map}}(SOC, I_c, \theta) = \sigma_{\text{map}}\,(x_1, x_2, I_{\text{batt}}, \theta) \tag{9.24}$$

recalling that $I_c = I_{\text{batt}}/Q_{\text{batt}}$.

Thus, the state dynamics are as follows:

$$\dot{x}_1 = \dot{E}_{\text{dep}} = I_{\text{batt}}(x_1, x_2, u, \theta)\, V_{\text{oc,batt}}(x_1) \tag{9.25}$$

$$\dot{x}_2 = \dot{E}_{\text{eff}} = \sigma_{\text{map}}\,(x_1, x_2, I_{\text{batt}}, \theta)\ |I_{\text{batt}}(x_1, x_2, u, \theta)|\ V_{\text{oc,batt}}(x_1) \tag{9.26}$$

Finally, the following constraints are imposed to make the powertrain actuators operate within their physical limits (9.27a,9.27b,9.27c) and meet the total power request (9.27d):

$$0 \leq P_{\text{ice}} \leq P_{\text{ice,max}}(\omega_{\text{ice}}) \tag{9.27a}$$

$$P_{\text{em,min}}(\omega_{\text{em}}) \leq P_{\text{em}} \leq P_{\text{em,max}}(\omega_{\text{em}}) \tag{9.27b}$$

$$P_{\text{batt,min}} \leq P_{\text{batt}} \leq P_{\text{batt,max}} \tag{9.27c}$$

$$P_{\text{req}} = P_{\text{ice}} + P_{\text{em}} \tag{9.27d}$$

where $P_{\text{ice,max}}$ is the maximum engine power and it depends on ω_{ice} (in $[rpm]$); $P_{\text{em,min}}$ and $P_{\text{em,max}}$ are the minimum and maximum limits for the EM power, P_{em}, and they depend on the motor angular speed ω_{em} (in $[rpm]$); $P_{\text{batt,min}}$ and $P_{\text{batt,max}}$ are the constant minimum and maximum limits for the battery power. For the sake of simplicity, it is assumed that $P_{\text{em}} = P_{\text{batt}}$, which implies that the losses between the battery power output and the EM input are neglected.

Problem 1 (AL-EMP). The aging-limiting energy management problem (AL-EMP) consists in finding the optimal control sequence u^* which minimizes the cost function (9.18) under the dynamic constraints (9.25) and (9.26) and the global and local constraints (9.19) and (9.27).

In the standard energy management problem, battery aging is not accounted for and fuel consumption is the only cost being minimized; thus the constraint (9.19c) is not defined, as well as state (9.26) is not considered. The standard energy management problem is thus reduced to Problem 2.

Problem 2 (S-EMP). The standard energy management problem (S-EMP) consists in finding the optimal control sequence u^* which minimizes the cost function (9.18) under the dynamic constraint (9.25) and the global and local constraints (9.19a,9.19b) and (9.27).

9.6 Aging-Limiting Pontryagin's Minimum Principle Problem Solution

The Pontryagin's minimum principle (PMP) is used in this work to solve the AL-EMP. We refer to the solution of the AL-EMP through PMP as aging-limiting PMP (AL-PMP). To account for battery aging, an additional state (and, consequently, an additional costate) is added, as proposed in [16]. The Hamiltonian function for the AL-PMP is given by

$$H(u, P_{\text{req}}) = \dot{m}_f(u, P_{\text{req}})\, Q_{\text{lhv}} + \lambda_1 \dot{x}_1 + \lambda_2 \dot{x}_2 \tag{9.28}$$

where λ_1 is the first costate variable, relative to the depletion energy, and λ_2 is the second costate, relative to the effective energy-throughput; the state dynamics are defined in (9.25) and (9.26). If u^* is the optimal control input which minimizes (9.18) under the specified dynamic and global/local constraints, the following necessary conditions must hold true:

- u^* must minimize the Hamiltonian function H instantaneously;
- the governing equations of the optimal costates are given by

$$\begin{aligned} \dot{\lambda}_1^* &= -\frac{\partial H}{\partial x_1} \\ &= -\frac{\partial \dot{m}_f(u^*, P_{\text{req}})}{\partial x_1} Q_{\text{lhv}} - \lambda_1^* \frac{\partial \dot{x}_1}{\partial x_1} - \lambda_2^* \frac{\partial \dot{x}_2}{\partial x_1} \end{aligned} \tag{9.29}$$

$$\begin{aligned} \dot{\lambda}_2^* &= -\frac{\partial H}{\partial x_2} \\ &= -\frac{\partial \dot{m}_f(u^*, P_{\text{req}})}{\partial x_2} Q_{\text{lhv}} - \lambda_1^* \frac{\partial \dot{x}_1}{\partial x_2} - \lambda_2^* \frac{\partial \dot{x}_2}{\partial x_2} \end{aligned} \tag{9.30}$$

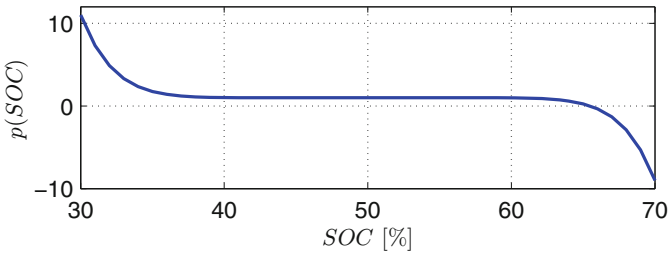

Fig. 9.12 Multiplicative penalty function for $SOC_{\text{ref}} = 50\,\%$, $SOC_{\text{min}} = 30\,\%$, $SOC_{\text{max}} = 70\,\%$, $a = 10$ and $b = 9$

The Hamiltonian (9.28) is modified by introducing a *penalty function*, $p(SOC)$, to limit the excursion of SOC during vehicle operation, thus enforcing the local state constraint (9.19b):

$$H(u, P_{\text{req}}) = \dot{m}_f(u, P_{\text{req}})\, Q_{\text{lhv}} + \lambda_1\, p(SOC)\, \dot{x}_1 + \lambda_2\, \dot{x}_2 \tag{9.31}$$

The penalty function on state of charge can be either additive or multiplicative, [1], and in this work the latter is chosen. Mathematically, a multiplicative penalty function is expressed as

$$p(SOC) = 1 - a \left(\frac{SOC - SOC_{\text{ref}}}{(SOC_{\text{min}} - SOC_{\text{max}})/2} \right)^b \tag{9.32}$$

This function acts modifying the cost of battery depletion in H according to the deviation of SOC from its target value SOC_{ref}. For positive a and odd b, $p = 1$ when $SOC = SOC_{\text{ref}}$; when $SOC < SOC_{\text{ref}}$, $p > 1$, resulting in an increase in the battery depleting cost in H; when $SOC > SOC_{\text{ref}}$, $p < 1$, thus decreasing the battery depleting cost in H. The penalty function, for the parameters values chosen in this work of $a = 10$ and $b = 9$, is shown in Fig. 9.12.

The choice of the initial costate values is referred to as *tuning* of the AL-PMP control strategy, and is discussed in Sect. 9.9.

Because $\dot{m}_f$ does not depend (at least in first approximation) on the second state, (9.29) and (9.30) can be expressed as

$$\dot{\lambda}_1^* = -\frac{\partial \dot{m}_f(P_{\text{batt}}, P_{\text{req}})}{\partial E_{\text{dep}}}\, Q_{\text{lhv}} - \lambda_1^* \frac{\partial \dot{E}_{\text{dep}}}{\partial E_{\text{dep}}} - \lambda_2^* \frac{\partial \dot{E}_{\text{eff}}}{\partial E_{\text{dep}}} \tag{9.33}$$

$$\dot{\lambda}_2^* = -\lambda_1^* \frac{\partial \dot{E}_{\text{dep}}}{\partial E_{\text{eff}}} - \lambda_2^* \frac{\partial \dot{E}_{\text{eff}}}{\partial E_{\text{eff}}} \tag{9.34}$$

The infinitesimal variation of E_{dep} upon an infinitesimal variation of SOC is obtained from (9.21). Thus, by means of using the following relations:

$$\begin{cases} \partial E_{\text{dep}} = -3600\, Q_{\text{batt}}\, V_{\text{oc,batt}}\, \partial SOC \\ \partial \dot{E}_{\text{dep}} = -3600\, Q_{\text{batt}}\, V_{\text{oc,batt}}\, \partial \dot{SOC} \end{cases} \tag{9.35}$$

the partial derivatives in (9.33) and (9.34) can be easily calculated from maps available in the powertrain model.

Thus (9.33) can be written as follows:

$$\begin{aligned} \dot{\lambda}_1^* = & \frac{\partial \dot{m}_f(P_{\text{batt}}, P_{\text{req}})}{\partial SOC} \frac{Q_{\text{lhv}}}{3600\, Q_{\text{batt}}\, V_{\text{oc,batt}}} - \lambda_1^* \frac{\partial \dot{SOC}}{\partial SOC} \\ & + \lambda_2^* \frac{\partial \dot{E}_{\text{eff}}}{\partial SOC} \frac{1}{3600\, Q_{\text{batt}}\, V_{\text{oc,batt}}} \end{aligned} \tag{9.36}$$

The term $\frac{\partial \dot{m}_f}{\partial SOC}$ is expressed as

$$\frac{\partial \dot{m}_f(P_{\text{batt}}, P_{\text{req}})}{\partial SOC} = \frac{\partial \dot{m}_f(P_{\text{batt}}, P_{\text{req}})}{\partial P_{\text{batt}}} \frac{\partial P_{\text{batt}}(SOC)}{\partial SOC} \tag{9.37}$$

where the first contribution is computed as

$$\frac{\partial \dot{m}_f(P_{\text{batt}}, P_{\text{req}})}{\partial P_{\text{batt}}} = -\frac{\partial \dot{m}_f(P_{\text{ice}}, P_{\text{req}})}{\partial P_{\text{ice}}} \tag{9.38}$$

since $P_{\text{batt}} = P_{\text{req}} - P_{\text{ice}}$. The term $\frac{\partial \dot{m}_f}{\partial P_{\text{ice}}}$ is the engine map, used in the vehicle simulator. The term $\frac{\partial \dot{m}_f}{\partial P_{\text{batt}}}$, on the other hand, is shown in Fig. 9.13.

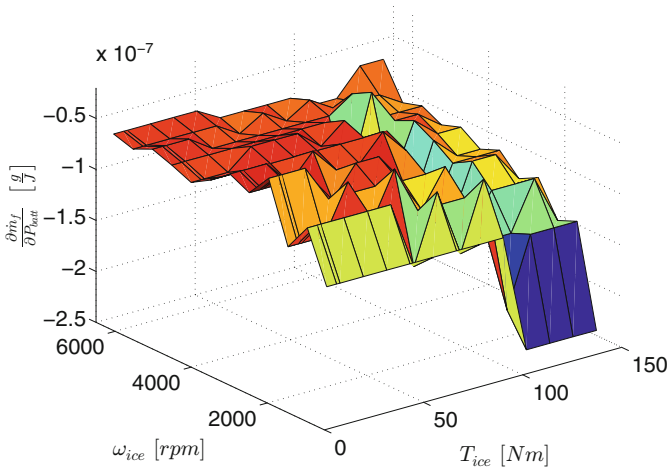

Fig. 9.13 Map depicting $\frac{\partial \dot{m}_f}{\partial P_{\text{batt}}}$ on the T_{ice}–ω_{ice} plane

From (9.14):

$$\frac{\partial P_{\text{batt}}(SOC)}{\partial SOC} = N_s N_p \frac{\partial P_{\text{cell}}(SOC)}{\partial SOC} \tag{9.39}$$

where $\frac{\partial P_{\text{cell}}}{\partial SOC}$ is available from the battery model. The resulting $\frac{\partial P_{\text{batt}}}{\partial SOC}$ map is shown in Fig. 9.14.
The term $\frac{\partial \dot{SOC}}{\partial SOC}$ is also extracted from the battery model and is shown in Fig. 9.15.

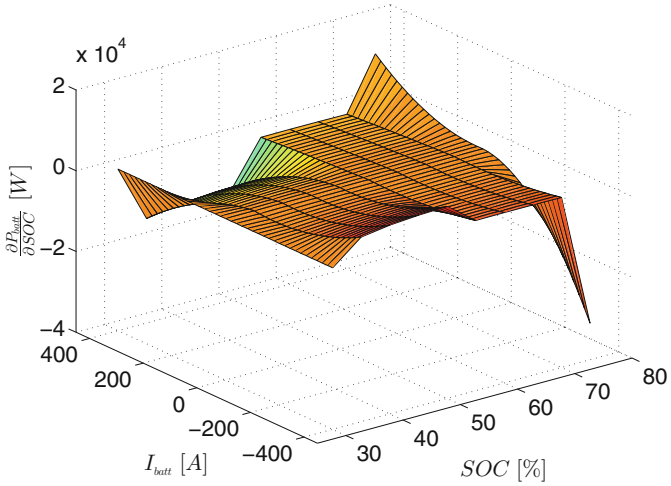

Fig. 9.14 Map depicting $\frac{\partial P_{\text{batt}}}{\partial SOC}$ on the SOC–I_{batt} plane

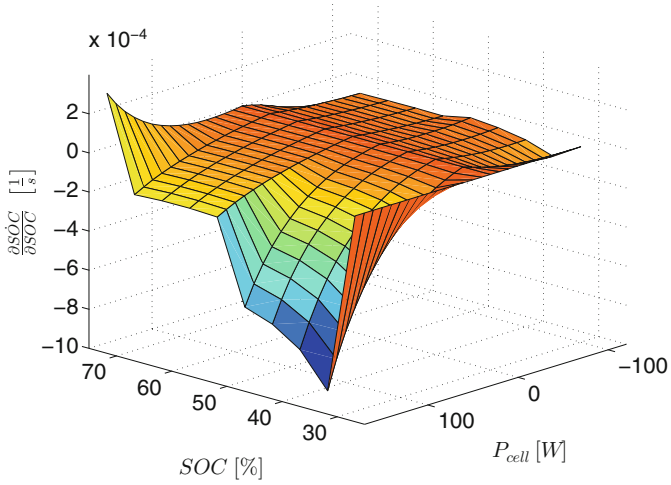

Fig. 9.15 Map depicting $\frac{\partial \dot{SOC}}{\partial SOC}$ on the P_{cell}-SOC plane

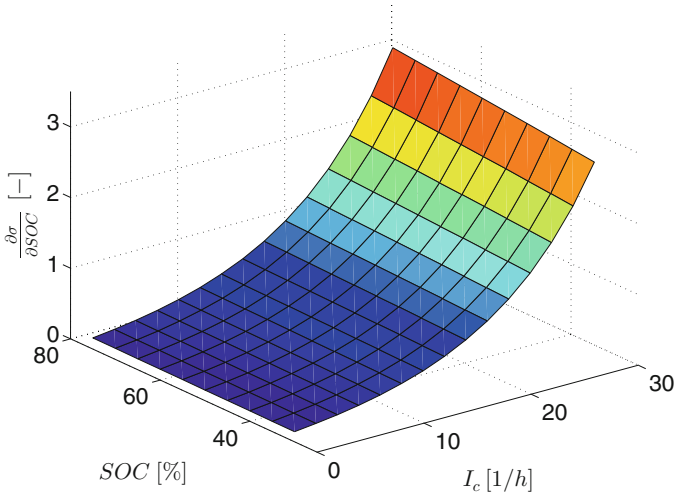

Fig. 9.16 Map depicting $\frac{\partial \sigma_{\text{map}}}{\partial SOC}$ on the I_c–SOC plane, for $\theta = 30°\text{C}$

Finally, $\frac{\partial \dot{E}_{\text{eff}}}{\partial SOC}$ is computed from (9.26) as

$$\begin{aligned}\frac{\partial \dot{E}_{\text{eff}}}{\partial SOC} =& \frac{\partial \sigma_{\text{map}}\left(E_{\text{dep}}, E_{\text{eff}}, I_{\text{batt}}, \theta\right)}{\partial SOC} \\ & \cdot \left|I_{\text{batt}}(E_{\text{dep}}, E_{\text{eff}}, P_{\text{batt}}, \theta)\right| V_{\text{oc,batt}} \\ & + \frac{\partial \left|I_{\text{batt}}(E_{\text{dep}}, E_{\text{eff}}, P_{\text{batt}}, \theta)\right|}{\partial SOC} \\ & \cdot \sigma_{\text{map}}\left(E_{\text{dep}}, E_{\text{eff}}, I_{\text{batt}}, \theta\right)\ V_{\text{oc,batt}}\end{aligned} \tag{9.40}$$

where the terms $\frac{\partial \sigma_{\text{map}}}{\partial SOC}$ and $\frac{\partial |I_{\text{batt}}|}{\partial SOC}$ are shown in Figs. 9.16 and 9.17, respectively.

The dynamics of the first costate can be numerically computed from the maps just shown.

The second costate dynamics, (9.34), can be written (from (9.25) and (9.26)) as

$$\begin{aligned}\dot{\lambda}_2^* =& -\lambda_1^* \frac{\partial I_{\text{batt}}(E_{\text{dep}}, E_{\text{eff}}, P_{\text{batt}}, \theta)}{\partial E_{\text{eff}}} V_{\text{oc,batt}}(E_{\text{dep}}) \\ & -\lambda_2^* \frac{\partial \left[\sigma_{\text{map}}\left(E_{\text{dep}}, E_{\text{eff}}, I_{\text{batt}}, \theta\right)\ \left|I_{\text{batt}}(E_{\text{dep}}, E_{\text{eff}}, P_{\text{batt}}, \theta)\right|\right]}{\partial E_{\text{eff}}} \\ & \cdot V_{\text{oc,batt}}(E_{\text{dep}})\end{aligned} \tag{9.41}$$

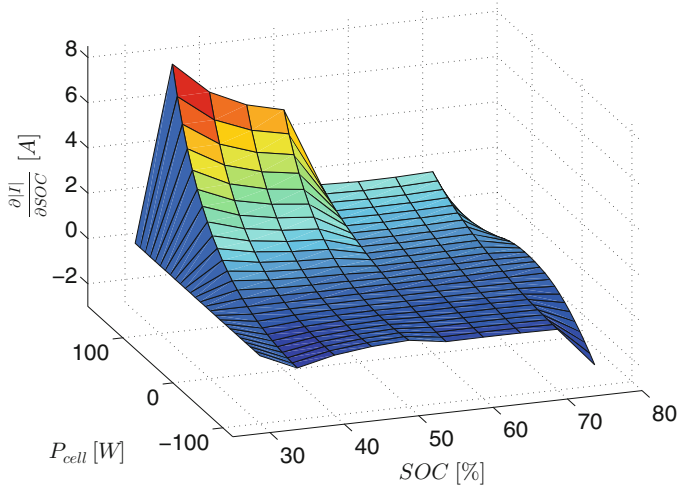

Fig. 9.17 Map depicting $\frac{\partial |I_{\text{batt}}|}{\partial SOC}$ on the SOC–P_{cell} plane

The partial derivatives in (9.41) are expressed as

$$\frac{\partial I_{\text{batt}}(E_{\text{dep}}, E_{\text{eff}}, P_{\text{batt}}, \theta)}{\partial E_{\text{eff}}} = \frac{\partial I_{\text{batt}}(SOC, P_{\text{batt}}, \theta)}{\partial SOC} \cdot \frac{\partial SOC(E_{\text{dep}}, E_{\text{eff}})}{\partial E_{\text{eff}}} \tag{9.42}$$

and

$$\begin{aligned} &\frac{\partial \left[\sigma_{\text{map}}(E_{\text{dep}}, E_{\text{eff}}, I_{\text{batt}}, \theta) \left|I_{\text{batt}}(E_{\text{dep}}, E_{\text{eff}}, P_{\text{batt}}, \theta)\right|\right]}{\partial E_{\text{eff}}} \\ &= \left[\frac{\partial \sigma_{\text{map}}(E_{\text{dep}}, E_{\text{eff}}, I_{\text{batt}}, \theta)}{\partial SOC} \left|I_{\text{batt}}(E_{\text{dep}}, E_{\text{eff}}, P_{\text{batt}}, \theta)\right| \right. \\ &\left. + \frac{\partial \left|I_{\text{batt}}(E_{\text{dep}}, E_{\text{eff}}, P_{\text{batt}}, \theta)\right|}{\partial SOC} \sigma_{\text{map}}(E_{\text{dep}}, E_{\text{eff}}, I_{\text{batt}}, \theta) \right] \\ &\cdot \frac{\partial SOC(E_{\text{dep}}, E_{\text{eff}})}{\partial E_{\text{eff}}} \end{aligned} \tag{9.43}$$

respectively. The term $\frac{\partial SOC}{\partial E_{\text{eff}}}$, appearing in both (9.42) and (9.43), was found to be negligible in simulation when compared to all the other costates dynamics terms (order of magnitude 10^{-8}), thus leading to the second costate dynamics to be approximated to $\dot{\lambda}_2^* \approx 0$, *i.e.* λ_2^* approximately constant:

$$\lambda_2^* \approx \lambda_{02}^* = const. \tag{9.44}$$

9.6.1 Comparison with Standard PMP Solution

The standard PMP solution is computed by minimizing the Hamiltonian function [1]:

$$H(u, P_{\text{req}}) = \dot{m}_f(u, P_{\text{req}})\, Q_{\text{lhv}} + \lambda\, \dot{x} \tag{9.45}$$

where the state x is the SOC, the costate is indicated with λ and its dynamics are

$$\dot{\lambda}^* = -\frac{\partial H}{\partial x} = -\lambda^* \frac{\partial \dot{x}}{\partial x} \tag{9.46}$$

When including battery aging consideration, the costate dynamics for the first state, as introduced in the present work, are

$$\dot{\lambda}^* = -\frac{\partial H}{\partial x} = \underbrace{-\frac{\partial \dot{m}_f(u^*, P_{\text{req}})}{\partial x} Q_{\text{lhv}}}_{\lambda_a} \underbrace{- \lambda^* \frac{\partial \dot{x}}{\partial x}}_{\lambda_b} \tag{9.47}$$

When comparing (9.46) and (9.47), one can see that the first term of (9.47), labeled as λ_a, is usually neglected in the standard PMP solution [14]. Simulation results (Fig. 9.18) show that this term gives a contribution to the costate dynamics which is of the same order of magnitude of the second term, labeled as λ_b. When the

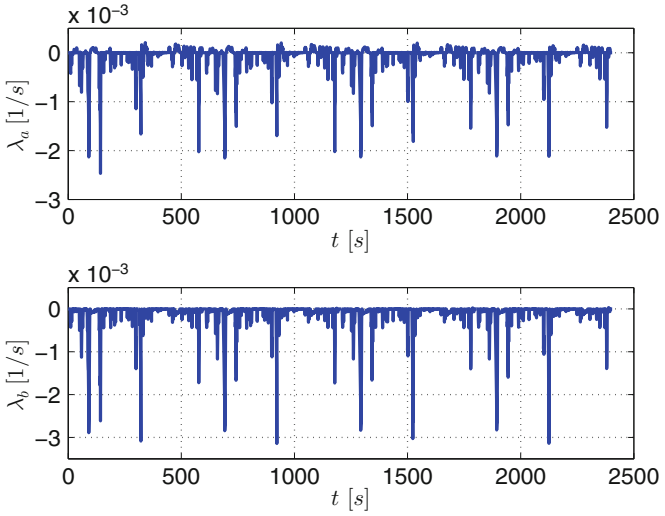

Fig. 9.18 Comparison of terms in $\dot{\lambda}^*$: $\lambda_a = -\frac{\partial \dot{m}_f}{\partial SOC} \frac{Q_{\text{lhv}}}{V_{\text{oc,batt}}\, Q_{\text{batt}}}$ (*top*) and $\lambda_b = -\lambda \frac{\partial \dot{SOC}}{\partial SOC}$ (*bottom*)

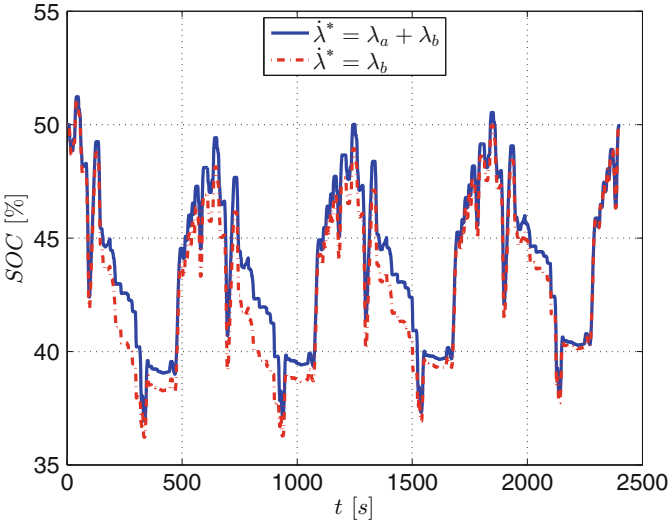

Fig. 9.19 Comparison of state of charge with and without the term $\lambda_a = -\frac{\partial \dot{m}_f}{\partial SOC} \frac{Q_{\text{lhv}}}{V_{\text{oc,batt}} Q_{\text{batt}}}$ in $\dot{\lambda}^*$

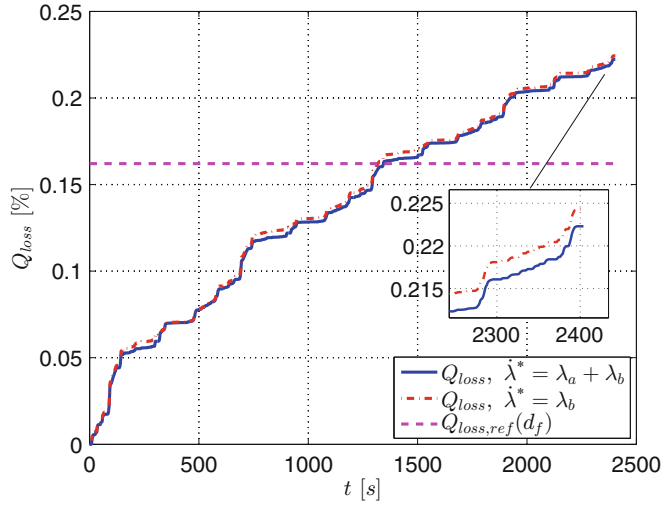

Fig. 9.20 Comparison of capacity loss with and without the term $\lambda_a = -\frac{\partial \dot{m}_f}{\partial SOC} \frac{Q_{\text{lhv}}}{V_{\text{oc,batt}} Q_{\text{batt}}}$ in $\dot{\lambda}^*$

term λ_a is kept in the overall solution, a slightly smaller *SOC* swing is observed, from Fig. 9.19, as well as a slight reduction of Q_{loss}, Fig. 9.20. The fuel economy is also slightly improved, 37.3206 *MPG* from 37.3048 *MPG* obtained when λ_a is not accounted for.

9.7 Remarks on Multi-Objective Optimal Control Formulation

In this section we show that the formulation of AL-PMP, as proposed in this paper, is equivalent to two other optimal control approaches, namely a multi-objective PMP and ECMS including aging consideration.

9.7.1 Multi-Objective PMP Problem

In this section, we show that the approach proposed in [14], i.e. a multi-objective optimal control formulation including fuel consumption and battery capacity degradation costs is equivalent to the method proposed in this paper. It is shown, though, that the AL-PMP gives some substantial advantages in terms of reduced tuning effort.

In [14] the cost function to be minimized is defined as the convex combination of two competing costs, i.e. fuel cost and aging cost, as follows:

$$J = \int_0^{t_f} (1-\alpha)\,\dot{m}_f + \frac{1}{3600}\,\alpha\,\frac{c_a}{\Gamma}\,\sigma_{\text{map}}\,|I_{\text{batt}}|\,dt \tag{9.48}$$

where α is a scalar parameter used to weight the two costs, c_a is a scalar, measured in $[g]$, which translates battery wear into equivalent fuel consumption, and $\Gamma = \frac{1}{3600}\int_0^{\text{EOL}} |I_{\text{batt,nom}}|\ dt$ is the total Ah-throughput under nominal cycling conditions. In [14], the dynamics of Ah_{eff} are given by

$$\dot{Ah}_{\text{eff}} = \frac{1}{3600}\,\sigma_{\text{map}}\,|I_{\text{batt}}| \tag{9.49}$$

and the Hamiltonian is written as

$$H = (1-\alpha)\,\dot{m}_f + \frac{1}{3600}\,\alpha\,\frac{c_a}{\Gamma}\,\sigma_{\text{map}}\,|I_{\text{batt}}| + \lambda\,\dot{SOC} \tag{9.50}$$

from which a PMP solution is computed, with dynamic constraints (9.7) and (9.49) and static constraints (9.19a, 9.19b) and optimal initial value of the costate λ_0^* found through the *shooting method*. The challenges with this formulation are that i) the choice of parameter value c_a is arbitrary and not necessarily trivial, and ii) a family of Pareto solutions is obtained as α is varied between 0 (only fuel consumption is considered in J) and 1 (only battery aging is considered in J), generating a trade-off between fuel and aging costs.

If we now normalize (9.50) (by $1-\alpha$ division and Q_{lhv} multiplication), we obtain

$$\begin{aligned}\bar{H} = \frac{Q_{\text{lhv}}}{1-\alpha} H =& \dot{m}_f\, Q_{\text{lhv}} + \frac{Q_{\text{lhv}}}{3600}\frac{\alpha}{1-\alpha}\frac{c_a}{\Gamma}\,\sigma_{\text{map}}\,|I_{\text{batt}}| \\ &+ Q_{\text{lhv}}\,\frac{\lambda}{1-\alpha}\left(-\frac{1}{3600\,Q_{\text{batt}}}\,I_{\text{batt}}\right)\end{aligned} \tag{9.51}$$

Defining $\bar{\lambda}_1 = Q_{\text{lhv}}\,\frac{\lambda}{\alpha-1}\,\frac{1}{3600\,Q_{\text{batt}}}$ and $\bar{\lambda}_2 = \frac{Q_{\text{lhv}}}{3600}\,\frac{\alpha}{1-\alpha}\,\frac{c_a}{\Gamma}$, the Hamiltonian is rewritten as

$$\bar{H} = \dot{m}_f\, Q_{\text{lhv}} + \bar{\lambda}_1\, I_{\text{batt}} + \bar{\lambda}_2\,\sigma_{\text{map}}\,|I_{\text{batt}}| \tag{9.52}$$

We can consider (9.52) as the Hamiltonian function associated with a control problem with a single objective cost function:

$$\bar{J} = \int_0^{t_f} \dot{m}_f\, dt \tag{9.53}$$

and the state dynamics given by (9.7), to account for battery depleting cost, with associate costate $\bar{\lambda}_1$, and (9.49) to account for battery aging with corresponding costate $\bar{\lambda}_2$.

Ultimately, the *two degrees of freedom* given by the choice of α and c_a are being translated into the costates $\bar{\lambda}_1$ and $\bar{\lambda}_2$.

The Hamiltonian of the AL-PMP solution, (9.28), can be written expressing explicitly the states dynamics as

$$H = \dot{m}_f\, Q_{\text{lhv}} + \lambda_1\, V_{\text{oc,batt}}\, I_{\text{batt}} + \lambda_2\, V_{\text{oc,batt}}\,\sigma_{\text{map}}\,|I_{\text{batt}}| \tag{9.54}$$

Comparing (9.54) and (9.52), one can clearly see the equivalence of the two problem formulations (same costs, (9.53) and (9.18), equivalent states, E_{dep} and E_{eff} and SOC and Ah_{eff}, respectively, as discussed in Sect. 9.5). In particular, the Hamiltonians (9.52) and (9.54) are identical under the conditions:

$$\begin{cases}\bar{\lambda}_1 = \lambda_1\, V_{\text{oc,batt}} \\ \bar{\lambda}_2 = \lambda_2\, V_{\text{oc,batt}}\end{cases} \tag{9.55}$$

or:

$$\begin{cases}\lambda_1 = \frac{Q_{\text{lhv}}}{3600\;Q_{\text{batt}}\,V_{\text{oc,batt}}}\,\frac{\lambda}{\alpha-1} \\ \lambda_2 = \frac{c_a\,Q_{\text{lhv}}}{3600\;\Gamma\,V_{\text{oc,batt}}}\,\frac{\alpha}{1-\alpha}\end{cases} \tag{9.56}$$

The advantages of using AL-PMP, though, is in that the challenge of selecting c_a and α is translated into optimally tuning the two costates λ_1, λ_2, which, in turn, boils down to solving Problem 1 with the AL-PMP algorithm presented in Sect. 9.9.

9.7.2 ECMS with Aging

In [26] it was shown that the PMP solution (of the S-EMP) is equivalent to the one given by ECMS. In this section, we want to show that a similar equivalence exists in the case of aging inclusion.

Under system dynamics:

$$\dot{E}_{\text{batt}} = I_{\text{batt}}(x_1, x_2, u, \theta)\, V_{\text{batt}}(x_1) \tag{9.57}$$

$$\dot{E}_{\text{eff}} = \sigma_{\text{map}}\,(x_1, x_2, I_{\text{batt}}, \theta)\;\; |I_{\text{batt}}(x_1, x_2, u, \theta)|\;\; V_{\text{oc,batt}}(x_1) \tag{9.58}$$

we want to instantaneously minimize the *equivalent fuel power*, $P_{f,\text{eqv}}$, given by the sum of the actual fuel power, P_f, and P_{dep} and P_{agn}:

$$P_{f,\text{eqv}} = P_f + P_{\text{dep}} + P_{\text{agn}} \tag{9.59}$$

where P_{dep} is the virtual fuel power associated with battery depletion and P_{agn} is the virtual fuel power associated with battery aging.

In particular, P_{dep} is defined as follows:

$$P_{\text{dep}} = s_1\, \dot{E}_{\text{batt}} \tag{9.60}$$

where s_1 is the *equivalency factor* which translates the battery depletion power into equivalent fuel power.

Usually, a value for s_1 when the battery is being charged, $s_{1,\text{chg}}$, and one when the battery is being discharged, $s_{1,\text{dis}}$ are used.

P_{agn} is defined as follows:

$$P_{\text{agn}} = s_2\, \dot{E}_{\text{eff}} \tag{9.61}$$

where s_2 is the equivalency factor associated with the battery aging power. This term introduces an additional equivalent fuel power when the battery is irreversibly aged.

Substituting equations (9.60) and (9.61) into the equivalent fuel power (9.59), yields to

$$P_{f,\text{eqv}} = \dot{m}_f\, Q_{\text{lhv}} + s_1\, V_{\text{batt}}\, I_{\text{batt}} + s_2\;\, V_{\text{oc,batt}}\, \sigma_{\text{map}}\, |I_{\text{batt}}| \tag{9.62}$$

The relation between the battery open circuit voltage and terminal voltage is by means of battery efficiency η_{batt}:

$$V_{\text{batt}} = \begin{cases} \eta_{\text{batt}}\, V_{\text{oc,batt}} & \text{if } I_{\text{batt}} \geq 0 \\ \frac{1}{\eta_{\text{batt}}} V_{\text{oc,batt}} & \text{if } I_{\text{batt}} < 0 \end{cases} \tag{9.63}$$

Defining:

$$\bar{s}_1 = \begin{cases} \bar{s}_{1,\text{dis}} = s_{1,\text{dis}}\, \eta_{\text{batt}} & \text{if } I_{\text{batt}} \geq 0 \\ \bar{s}_{1,\text{chg}} = \frac{s_{1,\text{chg}}}{\eta_{\text{batt}}} & \text{if } I_{\text{batt}} < 0 \end{cases} \tag{9.64}$$

(9.62) is written as follows:

$$P_{f,\text{eqv}} = \dot{m}_f\, Q_{\text{lhv}} + \bar{s}_1\, V_{\text{oc,batt}}\, I_{\text{batt}} + s_2\, V_{\text{oc,batt}}\, \sigma_{\text{map}}\, |I_{\text{batt}}| \tag{9.65}$$

which simply shows that ECMS with aging consideration and AL-PMP are equivalent. In addition,

$$\begin{cases} \lambda_1 = \bar{s}_1 \\ \lambda_2 = s_2 \end{cases} \tag{9.66}$$

hence:

$$s_1 = \begin{cases} \frac{\lambda_1}{\eta_{\text{batt}}} & \text{if } I_{\text{batt}} \geq 0 \\ \lambda_1\, \eta_{\text{batt}} & \text{if } I_{\text{batt}} < 0 \end{cases} \tag{9.67}$$

9.8 Penalty Function on Capacity Loss

A penalty function on capacity loss, $q(Q_{\text{loss}}, d)$, is introduced in the AL-PMP formulation to guarantee the targeted loss of capacity over each single day of driving. The Hamiltonian (9.31) becomes as follows:

$$H(u, P_{\text{req}}) = \dot{m}_f(u, P_{\text{req}})\, Q_{\text{lhv}} + \lambda_1\, p(SOC)\, \dot{x}_1 + \lambda_2\, q(Q_{\text{loss}}, d)\, \dot{x}_2 \tag{9.68}$$

where $p(SOC)$ enforces the local constraint on the state of charge. Contrary to the state of charge, for which positive and negative variations are allowed, the capacity loss (or effective energy-throughput) is a monotonically increasing function. To account for this characteristic, the proposed penalty function, $q(Q_{\text{loss}}, d)$, is a function of the driven distance.

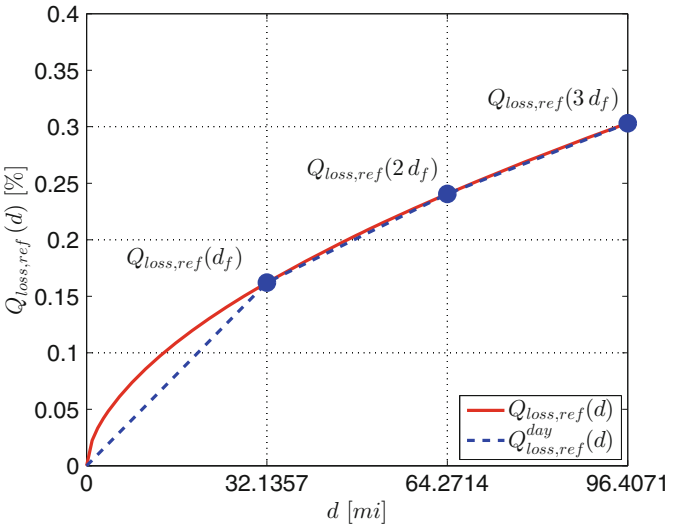

Fig. 9.21 $Q_{\text{loss,ref}}(d)$, $Q^{\text{day}}_{\text{loss,ref}}(d)$, and $Q_{\text{loss,ref}}(kd_f)$ over the first three days of US06 driving cycles, with $d_f = 32.1357mi$

We indicate as $Q^{\text{day}}_{\text{loss,ref}}(d)$ the reference capacity loss trajectory on a given day, d, with $d \in \left[(k-1)d_f,\, kd_f\right]$, in between the capacity loss of the previous day, $Q_{\text{loss,ref}}((k-1)d_f)$, and the following day $Q_{\text{loss,ref}}(kd_f)$:

$$Q^{\text{day}}_{\text{loss,ref}}(d) = \frac{Q_{\text{loss,ref}}(kd_f) - Q_{\text{loss,ref}}((k-1)d_f)}{d_f} \cdot d \tag{9.69}$$

In Fig. 9.21, $Q^{\text{day}}_{\text{loss,ref}}(d)$ is shown along with $Q_{\text{loss,ref}}(d)$ for the case of three days of US06 driving.

The linear reference $Q^{\text{day}}_{\text{loss,ref}}$ represents the maximum achievable capacity loss trajectory over one day of driving and its purpose is to *control* fast capacity loss at the beginning of each the driving day.

For implementation reasons, we define the maximum daily capacity loss to be equal to the daily reference loss plus a tolerance value (in the positive direction only, indicated as $Q^{+}_{\text{loss,tol}}$; this is assumed of the same value as the one used in Sect. 9.9 for the tolerance on ΔQ_{loss}, *i.e.* final state deviation from the daily target, namely $= 0.00324\,\%$):

$$Q_{\text{loss,max}}(d) = Q^{\text{day}}_{\text{loss,ref}}(d) + Q^{+}_{\text{loss,tol}} \tag{9.70}$$

The penalty function assumes then the following expression:

$$\begin{cases} q(Q_{\text{loss}}, d) = 1 + g \left(\frac{Q_{\text{loss}} - Q^{\text{day}}_{\text{loss,ref}}(d)}{Q^{+}_{\text{loss,tol}}} \right)^{h} \\ \qquad \text{for } Q^{\text{day}}_{\text{loss,ref}}(d) < Q_{\text{loss}} \leq Q_{\text{loss,max}}(d) \\ q(Q_{\text{loss}}, d) = 1 \qquad \text{for } Q_{\text{loss}} \leq Q^{\text{day}}_{\text{loss,ref}}(d) \end{cases} \tag{9.71}$$

It is worth noting that the $q(Q_{\text{loss}}, d)$ function is asymmetrical with respect to Q_{loss}. The parameter g is the gain of the penalty function, and increasing its value will result in an increase of the overall function value, as shown in Fig. 9.22; the parameter h is the exponent of the penalty function, and its effect is to change the function shape, as shown in Fig. 9.23. The ultimate effect of this change in shape is in a delayed intervention of the function (as h increases) on the aging cost in the instantaneous optimization. For large values of h the aging is weighted more and more only for large values of $Q_{\text{loss}} - Q^{\text{day}}_{\text{loss,ref}}(d)$, whereas smaller values of h are used when a more conservative approach on the aging is needed. In Fig. 9.24 the three-dimensional shape of the penalty function on capacity loss is presented when driven distance is included as well.

In the following section, the tuning of AL-PMP is presented, which, ultimately, consists in finding the optimal pair of initial values for the two costates $(\lambda^{*}_{01}, \lambda^{*}_{02})$.

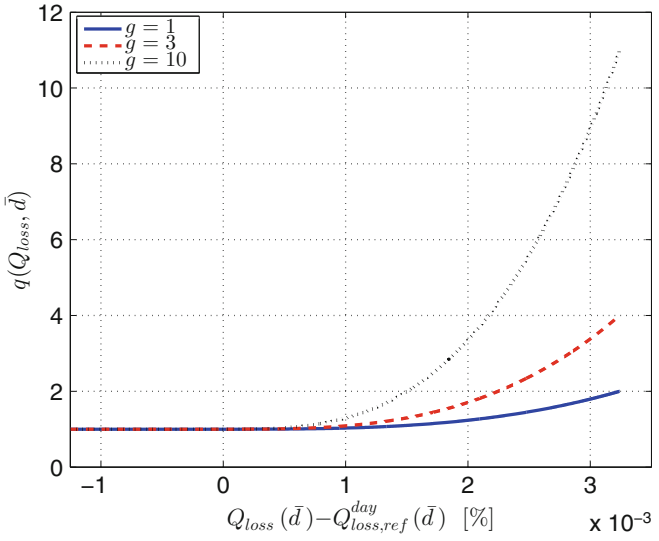

Fig. 9.22 Shape of the penalty function on Q_{loss} for different values of g and for a fixed value of $d = \bar{d}$. Negative values on the abscissa indicate that the battery can age less than its target daily value

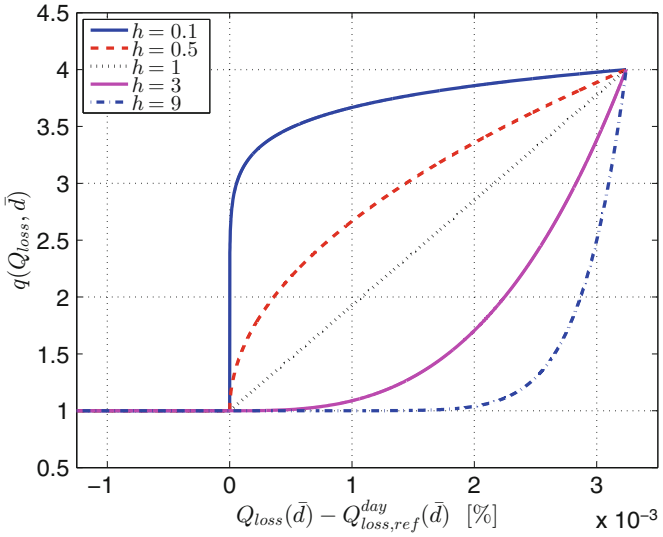

Fig. 9.23 Shape of the penalty function on Q_{loss} for different values of h, for a fixed value of $d = \bar{d}$

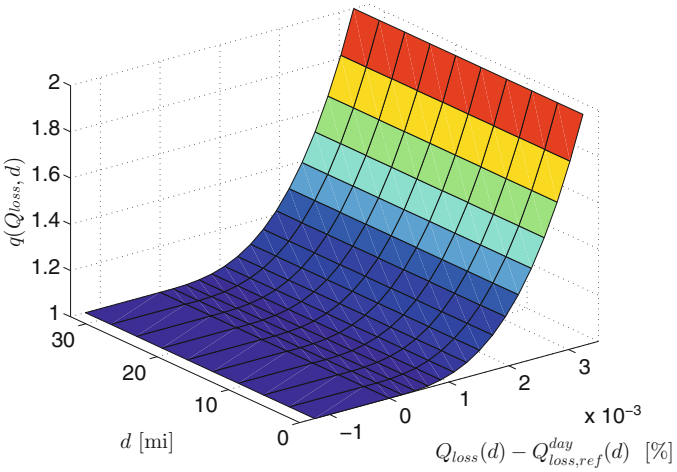

Fig. 9.24 Shape of the penalty function $q(Q_{\text{loss},d})$, as a function of Q_{loss} and d, with $g = 1$ and $h = 3$

9.9 AL-PMP Solution via Map-Based Tuning

In this section, the problem of finding the optimal pair of values $(\lambda_{01}^*, \lambda_{02}^*)$ in the AL-PMP strategy, that gives minimum fuel consumption m_f in $[kg]$ over the first day of driving with both state of charge and capacity loss regulated to their target values, is solved.

In the standard PMP solution, *shooting method* is used to iteratively tune λ_0 in order to obtain charge-sustainability [5]. This is possible given the bijective relationship between λ_0 and $SOC(d_f)$. In the AL-PMP the two costate dynamics are highly non-linear and coupled with no clear relation among them. For this reason, a new approach is proposed to tune the optimal supervisory controller.

An initial guess value for both costates is defined through the set Λ_0:

$$\Lambda_0 = \{(\lambda_{01}, \lambda_{02}) \mid \lambda_{01} \in \Lambda_{01}, \lambda_{02} \in \Lambda_{02}\} \tag{9.72}$$

where the vectors Λ_{01} and Λ_{02} are given by

$$\begin{aligned} \Lambda_{01} &= [\lambda_{01,\min} : \lambda_{01,\text{incr}} : \lambda_{01,\max}] \\ \Lambda_{02} &= [\lambda_{02,\min} : \lambda_{02,\text{incr}} : \lambda_{02,\max}] \end{aligned} \tag{9.73}$$

where the subscripts *max* and *min* are the maximum and minimum value for each costate and the subscript *incr* stands for the increment selected for the costates within that interval. Starting from each pair of initial values within the set Λ_0 AL-PMP is solved (state and costate dynamics are integrated forward in time) and three values are stored, namely:

- m_f,
- $\Delta SOC = SOC(d_f) - SOC_{\text{ref}}$,
- $\Delta Q_{\text{loss}} = Q_{\text{loss}}(d_f) - Q_{\text{loss,ref}}(d_f)$,

where ΔSOC and ΔQ_{loss} are the deviation of SOC and Q_{loss} from their target values at the end of the driving horizon, SOC_{ref} for the state of charge and $Q_{\text{loss,ref}}(d_f)$ for the capacity loss, respectively. Three matrices are built registering those final values for each pair of initial costates. These *maps* are easily plotted as function of λ_{01} and λ_{02}. From the generation of the three maps the optimal pair of costate is found as

$$(\lambda_{01}^*, \lambda_{02}^*) = \{(\lambda_{01}, \lambda_{02}) \mid \Delta SOC = 0 \wedge \Delta Q_{\text{loss}} = 0\} \tag{9.74}$$

The numerical value is found by means of the tuning algorithm presented next.

9.9.1 Tuning Algorithm Flowchart

The tuning procedure, summarized in the flowchart of Fig. 9.25, is composed of the following steps.[3]

[3] An important aspect of the tuning algorithm concerns the tolerances on the final state values. The approach followed in this work is as follows. Regarding SOC, a tolerance interval $SOC_{\text{tol}} = \pm 1\,\%$ is accepted for the charge-sustainability target. This means that all the values $\Delta SOC \in [-1, 1]\%$ are considered within the tolerance, and as such they are defined *sub-optimal* values. The *optimal* value is only one, i.e. $\Delta SOC^* = 0$, and it falls inside the tolerance interval. For Q_{loss} a similar

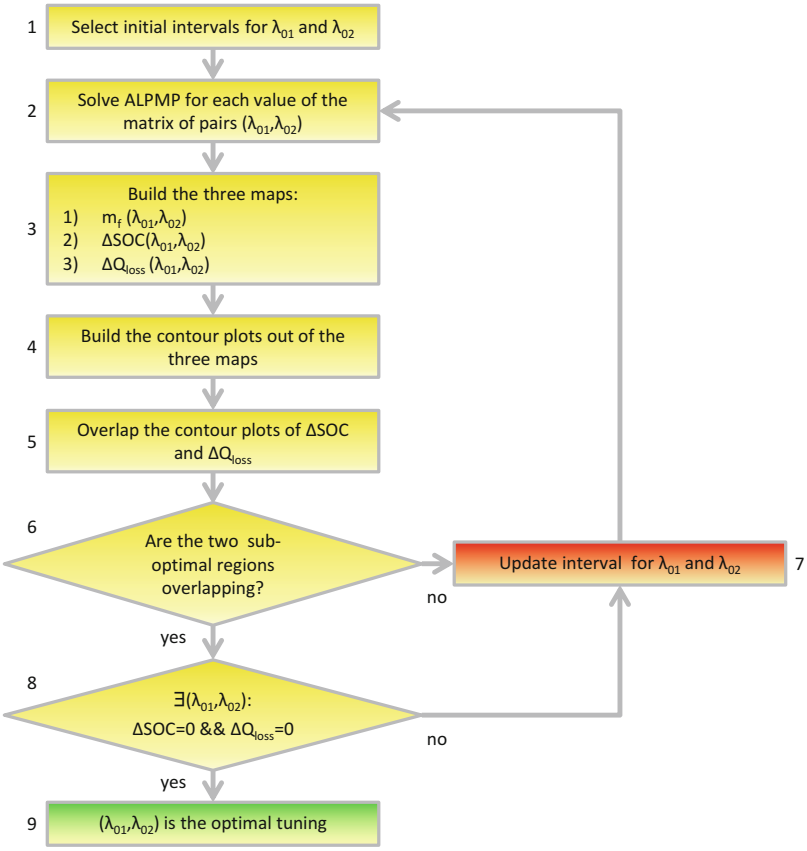

Fig. 9.25 AL-PMP tuning algorithm flowchart

1. The initial intervals for λ_{01} and λ_{02} are selected, thus vectors Λ_{01} and Λ_{02} and set Λ_0 are defined.
2. For each point of the set Λ_0, *i.e.* pairs $(\lambda_{01}, \lambda_{02})$, Problem 1 is solved.
3. m_f, ΔSOC, and ΔQ_{loss} are stored for each pair in Λ_0 and the corresponding maps are built.
4. The iso-value curves are plotted from the maps obtained in Step 3.
5. The contour plots of ΔSOC and ΔQ_{loss} intersect.

relative tolerance is considered and computed as follows. Given an $SOC_{\text{tol}} = \pm 1\,\%$ and a state of charge target of $SOC_{\text{ref}} = 50\,\%$, the relative tolerance for SOC is given by $SOC^{\text{rel}}_{\text{tol}} = \frac{\pm 1[\%]}{50\,\%}\,100 = \pm 2\,\%$; the relative tolerance for Q_{loss} is then $Q^{\text{rel}}_{\text{loss,tol}} = SOC^{\text{rel}}_{\text{tol}} = \pm 2\,\%$. The target for capacity loss, as explained in Sect. 9.2.1, for 4 US06 driving cycles ($d_f = 32.14mi$) is $Q_{\text{loss,ref}}(d_f) = 0.16205\,\%$, which leads to $Q_{\text{loss,tol}} = \frac{0.16205\,\%}{100}\,(\pm 2\,\%) = \pm 0.00324\,\%$. The *sub-optimal* values of capacity loss deviation are $\Delta Q_{\text{loss}} \in [-0.00324, 0.00324]\%$ and the *optimal* value is $\Delta Q^*_{\text{loss}} = 0$.

6. If the sets where both $SOC(d_f)$ and $Q_{\text{loss}}(d_f)$ are within the tolerance, i.e. $\Delta SOC \in SOC_{\text{tol}}$ and $\Delta Q_{\text{loss}} \in Q_{\text{loss,tol}}$ exists, go to Step 8, otherwise go to Step 7.
7. The solution is not found within the originally defined initial guess values for the costates, and the vectors Λ_{01} and Λ_{02} are updated.
8. The subset of Λ_0 for which both $SOC(d_f)$ and $Q_{\text{loss}}(d_f)$ lie on their respective target value, i.e. $\Delta SOC = 0$ and $\Delta Q_{\text{loss}} = 0$, is found.
9. The point $(\lambda_{01}^*, \lambda_{02}^*)$ in the set Λ_0 such that Step 8 is verified is the optimal tuning.

9.10 Simulation Results

Simulation results are shown in this section that implements the algorithm of Fig. 9.25. Four US06 driving cycles are simulated at an external temperature $\theta_{\text{amb}} = 30°\text{C}$, where it is imposed $SOC_{\text{ref}} = 50\,\%$, $SOC_{\text{min}} = 30\,\%$ and $SOC_{\text{max}} = 70\,\%$.

First, the initial intervals for the costates, as defined in (9.73), are chosen (Step 1):

$$\begin{aligned} \Lambda_{01} &= [2.00 : 0.04 : 2.60] \\ \Lambda_{02} &= [0.080 : 0.004 : 0.140] \end{aligned} \tag{9.75}$$

Note that the values of the initial costates are in general different from each other, and that the resolutions are selected in order to have vectors of length not more than 20; in this way Λ_0 contains not more than 400 points and the simulations take around $2.5h$ as the most, on a machine with an Intel i7 quad-core processor @2GHz and 6GB RAM. If better accuracy is required, a narrower and finer interval can be defined around the optimal point. The AL-PMP is solved for each pair in Λ_0 (Step 2), and the output maps are obtained (Step 3) and depicted in Fig. 9.26.

The contour plots shown in Fig. 9.27 are obtained from the maps of Fig. 9.26 (Step 4). Next, the contour plots relative to ΔSOC and ΔQ_{loss} are intersected (Step 5) and their intersection is shown in the dark grey area of Fig. 9.28 (Step 6). Within the shaded region of Fig. 9.28, the optimal tuning (the magenta dot on the right-hand side of the figure) of AL-PMP is found (Step 8), and the optimal pair of initial costates (Step 9) is

$$\begin{cases} \lambda_{01}^* = 2.3257 \\ \lambda_{02}^* = 0.113 \end{cases} \tag{9.76}$$

When using the proposed tuning to execute the AL-PMP, the variation of the final states from their reference is found to be practically zero: $\Delta SOC = -0.036763\,\%$ and $\Delta Q_{\text{loss}} = -0.000046505\,\%$. When applying the standard PMP (nominally, solving Problem 2), a similar performance is obtained for SOC, as from Fig. 9.29,

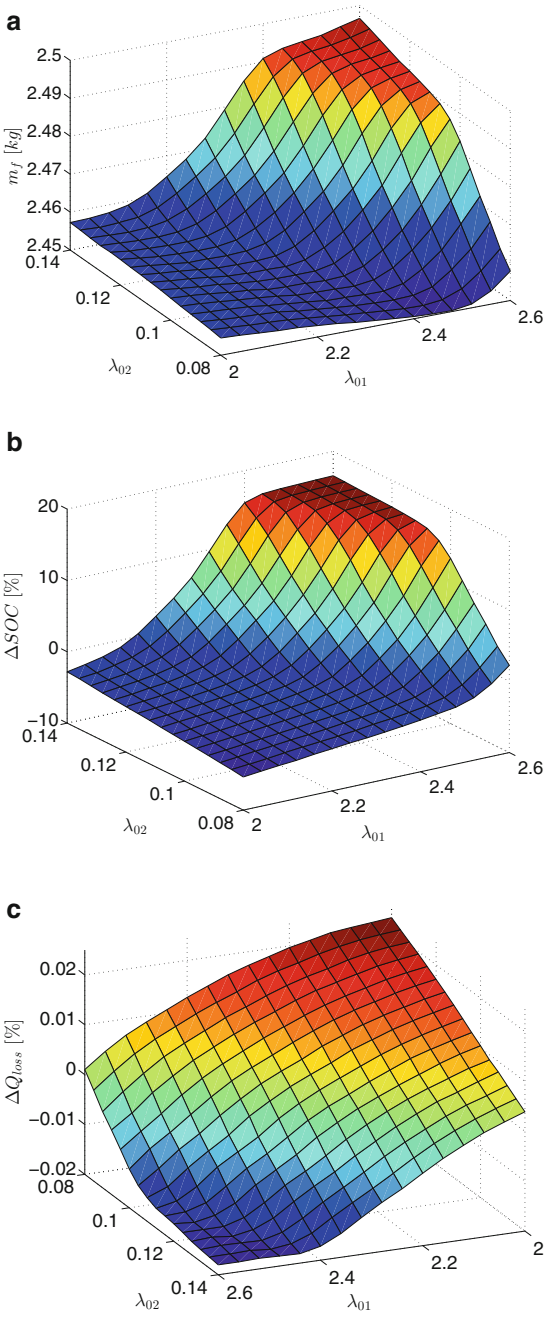

Fig. 9.26 Maps obtained for 4 US06 driving cycles at $\theta_{\text{amb}} = 30°\text{C}$, with the choice of initial costates from (9.75). (**a**) Fuel consumption. (**b**) Final state of charge variation with respect to target. (**c**) Final capacity loss variation with respect to target

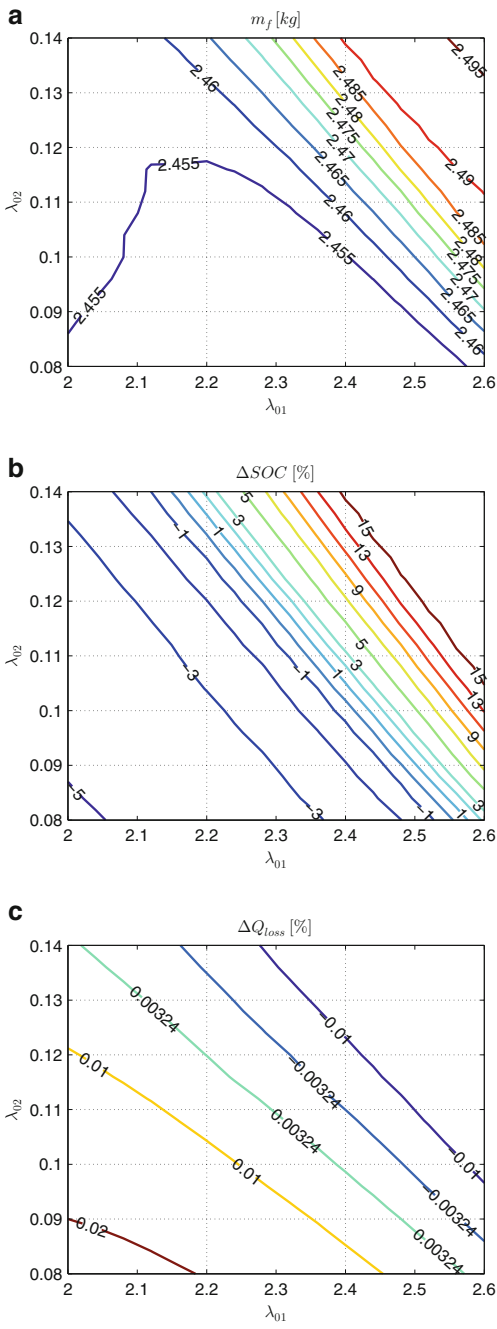

Fig. 9.27 Contour plots obtained for 4 US06 driving cycles at $\theta_{\text{amb}} = 30°\text{C}$, with the choice of initial costates as in (9.75). (**a**) Fuel consumption. (**b**) Final state of charge variation with respect to target. (**c**) Final capacity loss variation with respect to target

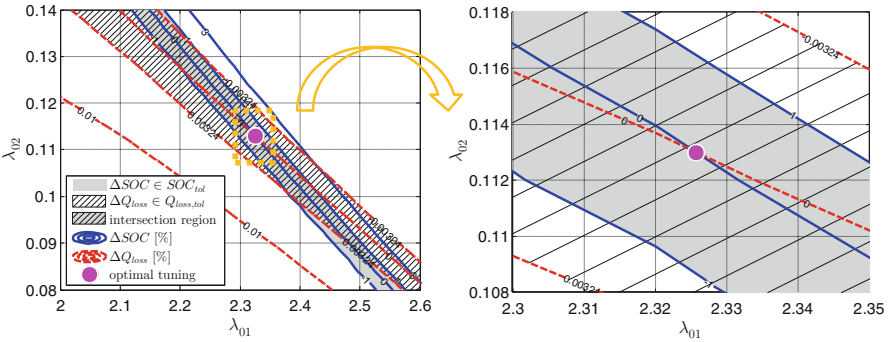

Fig. 9.28 Intersection of contour plots of Figs. 9.27b and c (*left plot*). The optimal solution (i.e.,, tuning) is found by the intersection of the 0-contour levels of ΔSOC and ΔQ_{loss} (as shown on the *right-hand side plot*)

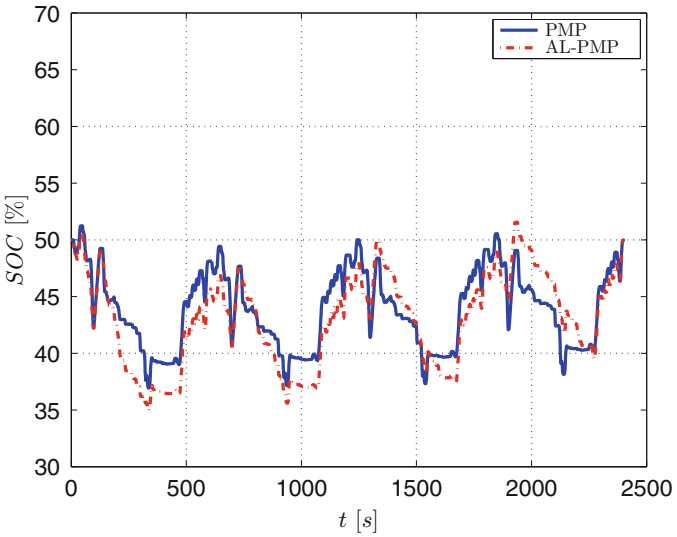

Fig. 9.29 Comparison of state of charge over the first day of driving for PMP and AL-PMP: both the strategies are able to regulate *SOC* to its reference value at the end of the day of driving

but Q_{loss} is not limited, as shown in Fig. 9.30: the capacity loss is more than 40 % higher than the target value (over the first day of driving). As a result, the target EOL will not be met, leading to a prematurely aged battery (when compared to vehicle life). From a fuel economy standpoint, on the other hand, only a slight difference is observed between PMP and AL-PMP, with just 0.56 % loss in terms of *MPG* for the latter (37.3206 for PMP and 37.1115 for AL-PMP).

Hence, significant reduction in battery aging at the price of a little worse fuel consumption is achieved when applying AL-PMP.

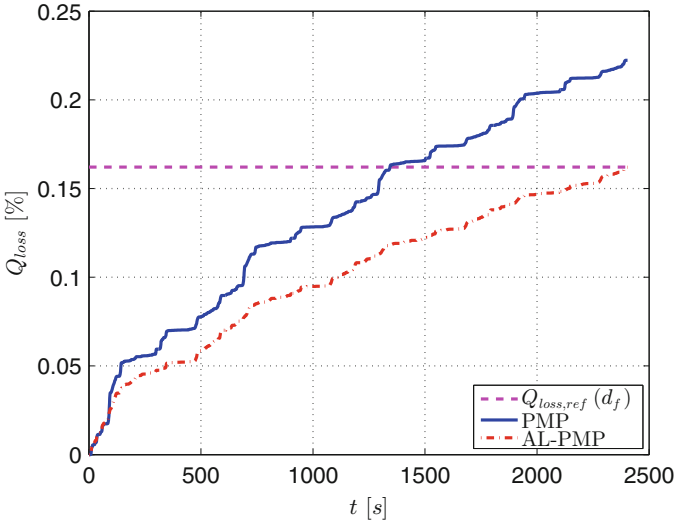

Fig. 9.30 Comparison of capacity loss over the first day of driving for PMP and AL-PMP: only AL-PMP is able to regulate Q_{loss} to its reference value at the end of the day of driving

Table 9.3 Comparison of optimal initial costate pairs $(\lambda_{01}^*, \lambda_{02}^*)$ in AL-PMP for different external temperatures over 4 US06 driving cycles

$\boldsymbol{\theta}_{\text{amb}}$ [°C]	$\boldsymbol{\lambda}_{01}^*$	$\boldsymbol{\lambda}_{02}^*$
20	3.1964	0.005954
25	3.0811	0.019333
29	2.565	0.082397
30	2.3257	0.113
31	1.8185	0.18396
32	1.0068	0.30417

In the following, AL-PMP solution is presented for different temperature scenarios.

9.10.1 Results for Different Ambient Temperatures

Simulation results are presented for different external ambient temperatures, over four US06 driving cycles. For each value of temperature considered, AL-PMP is tuned as described in Sect. 9.9. The optimal initial values of the costates are reported in Table 9.3 and shown in Fig. 9.31.

The optimal initial value of the first costate decreases with increasing temperature, while the optimal second costate is increasing. This can be explained thinking that higher temperatures represent more harmful conditions for the battery capacity loss. Given that, the aging term in the Hamiltonian (9.28), multiplied by λ_2, needs

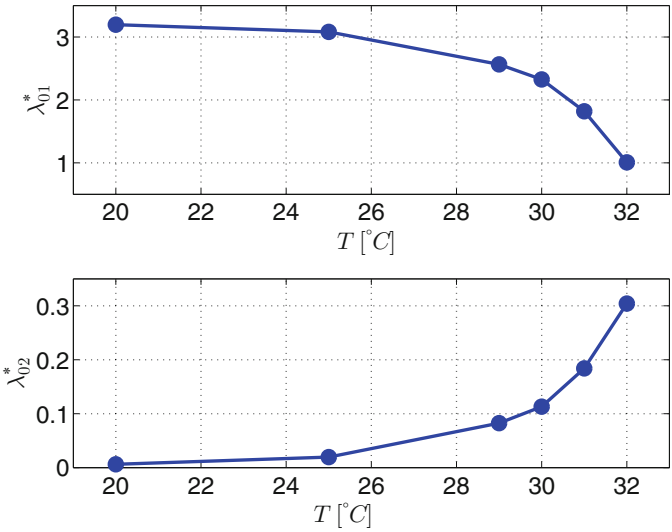

Fig. 9.31 Graphical representation of optimal initial costate values in AL-PMP for different external temperatures

to be weighted more in the optimization strategy than the fuel consumption and the battery charging/discharging term, the latter multiplied by λ_1.

The activation of the aging penalty function on capacity loss is not required when ambient temperature is below 33°C. For temperatures equal or above 33°C, the penalty function needs to be activated to obtain optimal capacity loss regulation, i.e. to find the optimal pair $(\lambda_{01}^*, \lambda_{02}^*)$ so that both ΔSOC and ΔQ_{loss} are exactly zero.

Nevertheless, simulation study shows that when the aging penalty function is *not* used in high temperature conditions, sub-optimal solutions are found. Namely, two ways are proposed to tune AL-PMP, which are presented in the following.

1. Tuning 1: optimal tuning is done for ΔSOC, and only sub-optimality is guaranteed for ΔQ_{loss}; this means that $\Delta SOC = 0$, while ΔQ_{loss} is chosen to be as close as possible to 0: the first condition selects the points on the plane that lie on the optimal *SOC* line, which is also within Q_{loss} tolerance.
2. Tuning 2: optimal tuning is done for ΔQ_{loss}, and only sub-optimality is guaranteed for ΔSOC; the points lie on the optimal Q_{loss} line, i.e. $\Delta Q_{\text{loss}} = 0$, and *SOC* is within the allowable tolerance.

The initial costate values found for the simulations performed are

1. Tuning 1:

$$\begin{cases} \lambda_{01} = 0.01 \\ \lambda_{02} = 0.4640 \end{cases} \tag{9.77}$$

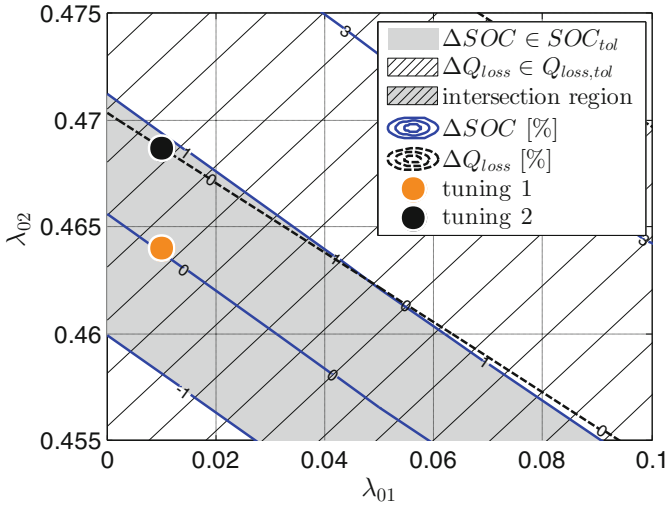

Fig. 9.32 Zoom on the intersection region of contour plots for 4 US06 driving cycles at $\theta_{\text{amb}} = 33°\text{C}$: the proposed tunings for AL-PMP are indicated with an orange spot (1—optimal for ΔSOC only) and a black spot (2—close-to-optimal for ΔQ_{loss} only)

Table 9.4 Results for the proposed tuning 1 and tuning 2 for $\theta_{\text{amb}} = 33°\text{C}$, in terms of relevant quantities: fuel consumption and final SOC and Q_{loss} deviations from targets

Tuning	m_f [kg]	ΔSOC [%]	ΔQ_{loss} [%]
1	2.4844	−0.031599	0.00084542
2	2.4862	0.87247	0.0000053273

2. Tuning 2:

$$\begin{cases} \lambda_{01} = 0.01 \\ \lambda_{02} = 0.4687 \end{cases} \tag{9.78}$$

as also shown in Fig. 9.32. Figures 9.33 and 9.34 show the results of the two tunings in terms of SOC and capacity loss profiles and Table 9.4 reports the numerical values of simulation outputs.

It is worth noting that the error on the target values for Q_{loss} in the tuning 1 and the error for SOC in the tuning 2 are very small. On the other hand, the capacity loss obtained from standard PMP is not even close to $Q_{\text{loss,ref}}(d_f)$: AL-PMP reduces Q_{loss} by more than 30 %, at the limited price of an increase of fuel consumption between 1.69 and 1.77 % ($m_f = 2.4430kg$ for PMP, see Table 9.4 for AL-PMP).

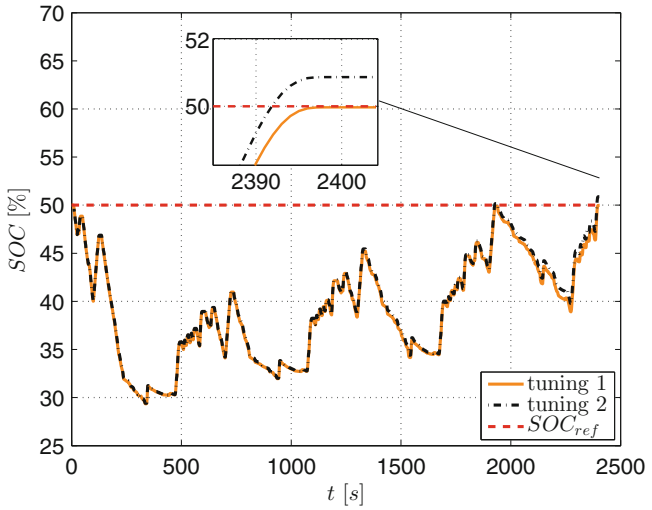

Fig. 9.33 State of charge profile for the proposed tuning 1 and tuning 2 for $\theta_{\text{amb}} = 33°\text{C}$. Note that *SOC* is below 30 % for a short time interval around $t = 300s$; this situation is penalized but allowed by the penalty function on *SOC*, which is a soft constraint in the optimization

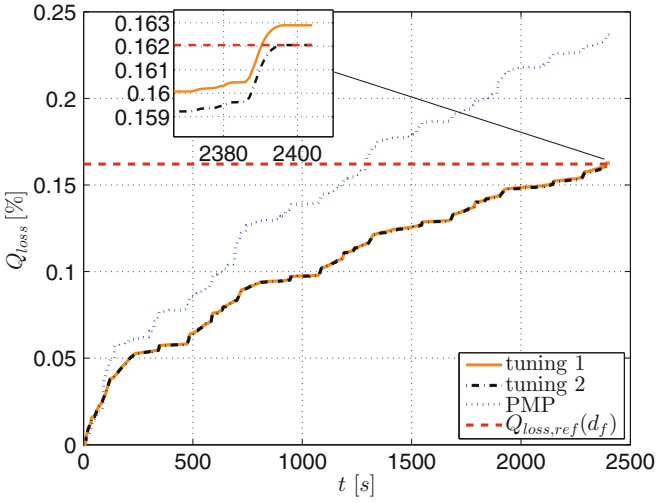

Fig. 9.34 Capacity loss profile for the proposed tuning 1 and tuning 2 for $\theta_{\text{amb}} = 33°\text{C}$. PMP solution is also reported

9.10.2 Results with Penalty Function

If the penalty function on aging dynamics is used, on the other hand, an optimal solution is found. From simulation results, at $\theta_{\text{amb}} = 33°\text{C}$, when using the

following calibration parameters for the aging penalty function:

$$\begin{cases} g = 3 \\ h = 1 \end{cases} \tag{9.79}$$

the optimal pair for the initial costate values is

$$\begin{cases} \lambda_{01}^* = 2.5859 \\ \lambda_{02}^* = 0.025833 \end{cases} \tag{9.80}$$

The resulting overlapped contour plots of ΔSOC and ΔQ_{loss} are shown in Fig. 9.35. In this case a well-defined intersection is obtained, hence the optimal solution is found.

Figure 9.36 shows the distribution of the operating points of the battery on the severity factor map contour plot, as a function of state of charge and C-rate, for a fixed battery temperature, both for PMP and AL-PMP. The distribution of points indicates that AL-PMP (b), compared to standard PMP (a), is effectively able to reduce the harshness of the battery operating conditions, since the maximum value reached in σ_{map} is less than 20 instead of almost 30, with lower C-rate of operation and larger state of charge range used. The engine efficiency map used by PMP and AL-PMP is shown in Fig. 9.37.

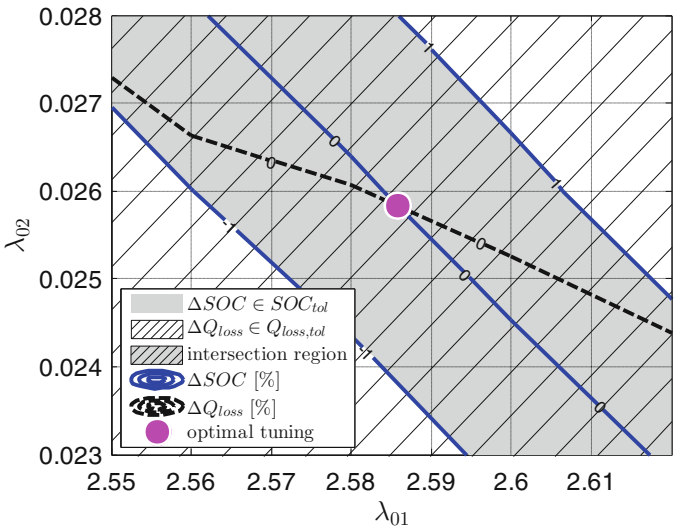

Fig. 9.35 Zoom on the intersection region of contour plots for 4 US06 driving cycles at $\theta_{\text{amb}} = 33°\text{C}$: the optimal tuning for AL-PMP with penalty function on Q_{loss} is indicated with a purple spot

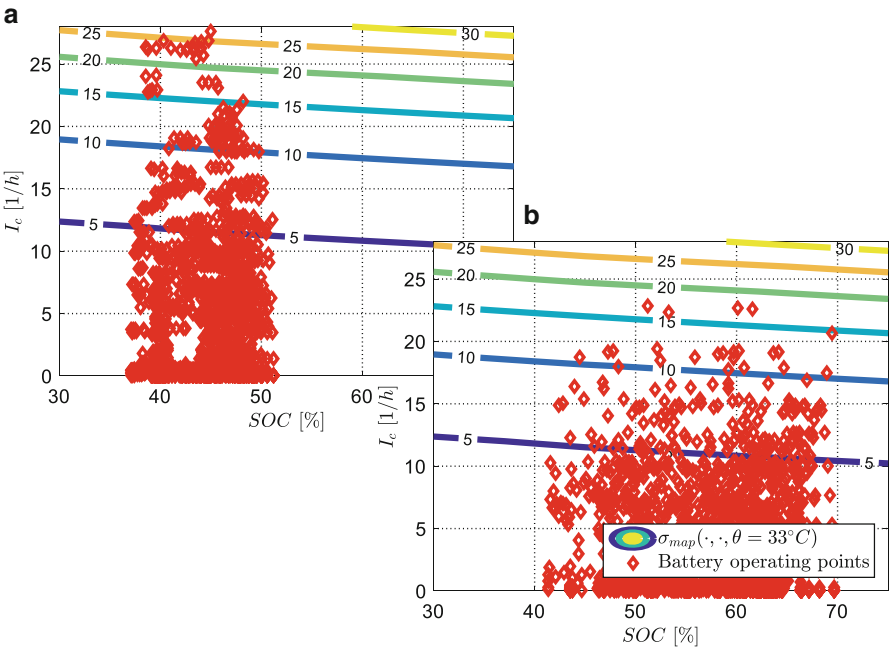

Fig. 9.36 Battery operating points on the severity factor map, for 4 US06 driving cycles at $\theta_{\text{amb}} = 33°\text{C}$: comparison between standard PMP (**a**) and AL-PMP (**b**)

Simulation results have shown that for extreme external temperatures combined with aggressive driving cycles like US06, AL-PMP cannot prevent the battery from aging more than the final daily target, even with the introduction of the penalty function. As an example, simulation results performed at $\theta_{\text{amb}} = 40°\text{C}$ and penalty function parameters

$$\begin{cases} g = 3 \\ h = 0.1 \end{cases} \tag{9.81}$$

are shown in Fig. 9.38 sub-optimal initial costates:

$$\begin{cases} \lambda_{01} = 0.1 \\ \lambda_{02} = 0.077 \end{cases} \tag{9.82}$$

One can see that both with or without penalty function, AL-PMP is not able to control capacity loss to its daily target. Nonetheless, the capacity loss is reduced by approximately 35 % from the PMP solution, and by about 7.5 % with respect to the AL-PMP solution without penalty function; furthermore, the final value of Q_{loss}, although not equal to $Q_{\text{loss,ref}}(d_f)$, is quite close to the target value.

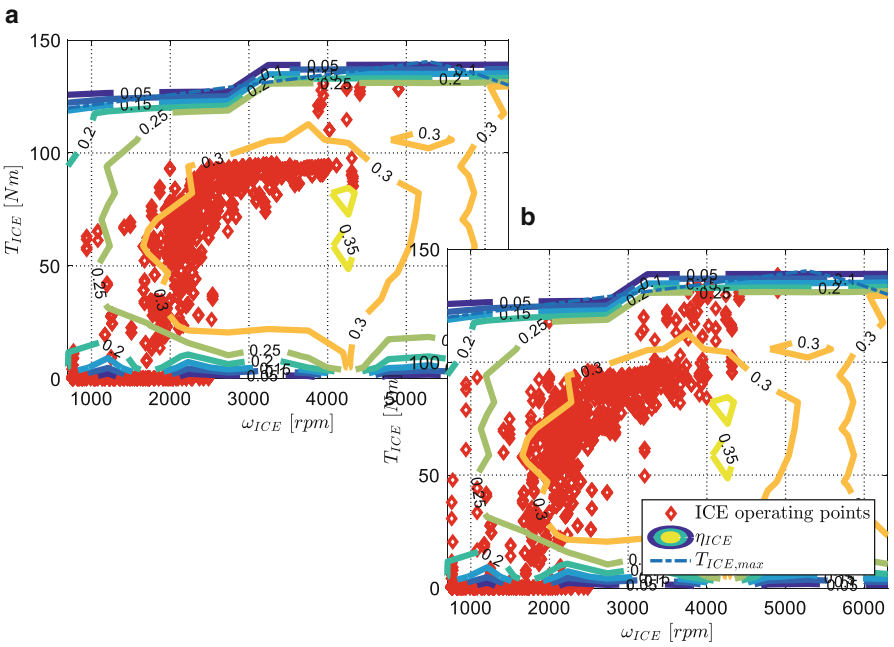

Fig. 9.37 Engine operating points for 4 US06 driving cycles at $\theta_{\text{amb}} = 33°\text{C}$: comparison between standard PMP (**a**) and AL-PMP (**b**)

Table 9.5 Simulation results for AL-PMP with penalty function ($g = 3, h = 0.1$) at $\theta_{\text{amb}} = 40°\text{C}$; comparison between discharge and charge phases

	Total	Discharge	Charge
Average I_c $[1/h]$	3.0257	1.9055	7.4036
Average θ [°C]	43.3322	43.2484	43.6600
Average σ_{map} $[-]$	4.5368	3.7351	7.6703
Extracted Ah	4.5472	2.2807	2.2665
Ah_{eff}	34.9286	10.1631	24.7655

In Table 9.5, discharge and charge battery events are compared for $\theta_{\text{amb}} = 40°\text{C}$. When using AL-PMP, only the discharge is being optimized. One can see that the C-rate in charge is on average almost four times larger than in discharge, with slightly higher temperature. Thus, on average the severity factor map is more than two times higher in charge, and so are the Ah_{eff}, which are directly related to aging, [14]. This means that the aging process takes place mostly during the charge phase (braking), which is not controlled with the present strategy. On the other hand, the extracted Ah are almost equal, as expected for a charge-sustaining HEV. This analysis emphasizes the importance to control battery charging, as also shown in Fig. 9.39, where the capacity loss profile is shown distinguishing between the discharge and charge phases. When Q_{loss} is controlled (discharge), it stays approximately constant, or increases at a small rate. When it is not controlled (charge), it undergoes important upwards steps that prevent to meet the daily target.

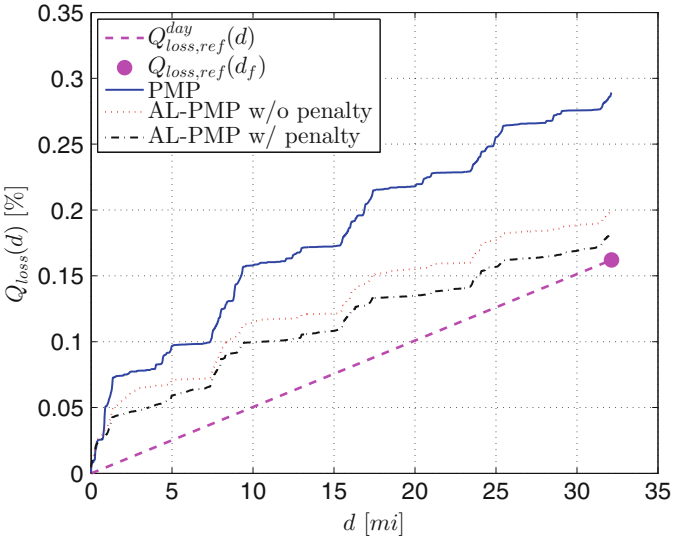

Fig. 9.38 Capacity loss results for $\theta_{\text{amb}} = 40°\text{C}$: comparison between PMP, AL-PMP with and without penalty function

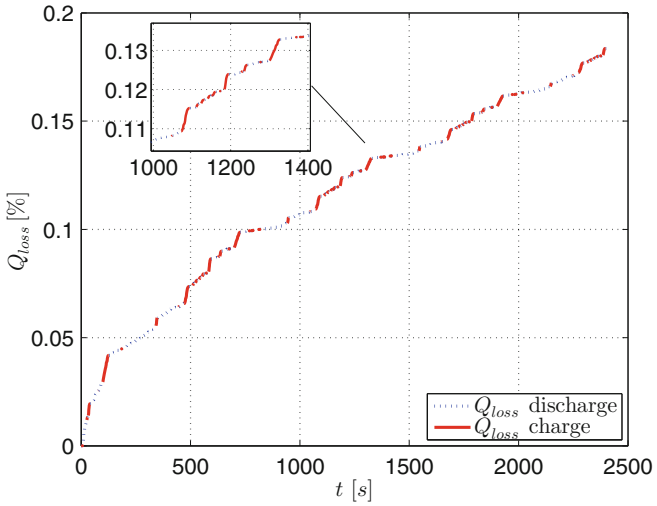

Fig. 9.39 Capacity loss profile for $\theta_{\text{amb}} = 40°\text{C}$ with the discharge and charge phases plotted separately

Simulations over a week of US06 driving (six days) are shown in Fig. 9.40, with $\theta_{\text{amb}} = 30°\text{C}$. The capacity loss reference values at the end of each day is tracked when using AL-PMP. Therefore, if battery degradation is not properly taken into account by the EMS, ultimately, the situation arises that an early replacement of

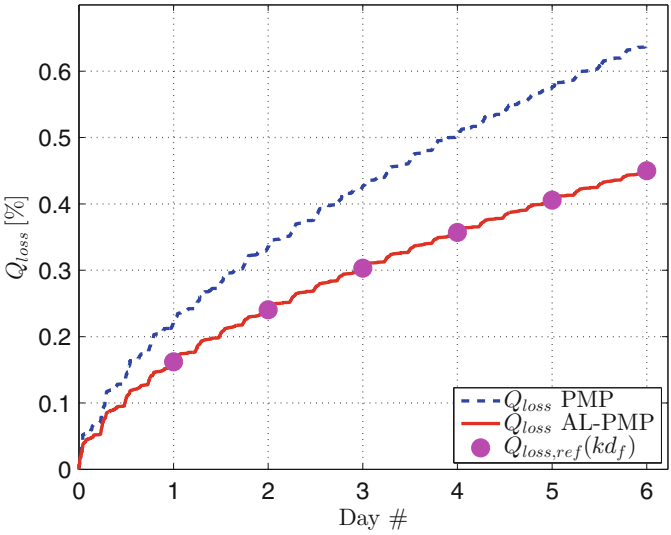

Fig. 9.40 Capacity loss profile over one week of simulation at $\theta_{\text{amb}} = 30°\text{C}$; comparison between reference values, results with standard PMP and with AL-PMP

the battery is needed. In Table 9.6 the results relative to the fuel consumption over the first week are shown. AL-PMP does not show a significant worsening in fuel economy when compared to PMP, showing that battery aging is much more sensitive to the choice of the control parameters than fuel consumption.

9.11 Conclusions

In this paper a new capacity loss model identified from real HEV data is adopted, from which a reference capacity loss profile is extracted and used in the multi-objective optimization strategy, referred to as AL-PMP. The AL-PMP is first formulated, and then solved with a new tuning algorithm. It is shown that both the state of charge and capacity loss are regulated to their respective reference values at the end of the first day of driving, at the price of a small increase in fuel consumption. For more severe driving conditions, a penalty function on capacity loss allows to obtain the same optimal results, but for extreme scenarios aging control is dominated by the uncontrolled charging phase. The same results obtained for the first day of driving are confirmed by simulations performed over an entire week of driving: both states are optimally controlled and the fuel consumption is comparable to that of a standard (i.e., that does not account for aging) control strategy.

Table 9.6 Fuel consumption obtained in simulation over the first week of driving at $\theta_{\text{amb}} = 30°\text{C}$: results for standard PMP and AL-PMP, and increase in fuel consumption of AL-PMP with respect to PMP

Day #	$m_f[kg]$ PMP	$m_f[kg]$ AL-PMP	Increase in $m_f[\%]$
1	2.4471	2.4573	0.417
2	2.4471	2.4696	0.922
3	2.4471	2.4717	1.008
4	2.4470	2.4721	1.022
5	2.4471	2.4724	1.036
6	2.4470	2.4727	1.050

As a possible future development of this work, in order to overcome the limitations of AL-PMP, two paths are proposed, to be integrated within the present solution:

- A simple approach is to apply a *rule-based* braking strategy, to limit the maximum braking power when temperature is above a certain safety threshold; in this way a milder aging effect will be obtained in charging and this will be sufficient to optimally meet the daily goal $Q_{\text{loss,ref}}(d_f)$, while maintaining charge-sustainability.
- Series braking, as implemented in this work, could be replaced by a more *ad hoc* parallel braking strategy with the purpose of optimizing recuperation as proposed in [25], and, at the same time, accounting for battery aging.

Acknowledgements The authors would like to acknowledge the support received from Honda R&D co., Ltd., Japan and they would also like to thank Girish Suri for the help in improving the vehicle simulator.

References

1. S. Onori, L. Serrao, G. Rizzoni, *Hybrid Electric Vehicles Energy Management Strategies* (Springer, Berlin/Heidelberg, 2016)
2. L. Guzzella, A. Sciarretta, *Vehicle Propulsion Systems: Introduction to Modeling and Optimization* (Springer, Berlin, 2007)
3. C. Chan, The state of the art of electric, hybrid, and fuel cell vehicles, Proc. IEEE **95**, 704–718 (2007)
4. F. Lewis, V. Syrmos, Dynamic programming, in *Optimal Control* (Wiley, New York, 1995), pp. 315–347
5. S. Onori, Model-based optimal energy management strategies for hybrid electric vehicles, in *Optimization and Optimal Control in Automotive Systems - Lect. Notes in Control Science*, ed. by H. Waschl, I. Kolmanovsky, M. Steinbuch, L. del Re (Springer, New York, 2014), pp. 199–218

6. R. Cipollone, A. Sciarretta, Analysis of the potential performance of a combined hybrid vehicle with optimal supervisory control, in *Computer Aided Control System Design, International Conference on Control Applications, International Symposium on Intelligent Control* (ASME, New York, 2006), pp. 2802–2807
7. R. Bellman, Dynamic programming and Lagrange multipliers, in *Proceedings of the National Academy of Sciences of the United States of America*, vol. 42, p. 767, 1956
8. L. Pontryagin, V. Boltyanskii, R. Gamkrelidze, E. Mischchenko, *The Mathematical Theory of Optimal Processes* (Interscience, New York, 1962)
9. A. Sciarretta, L. Guzzella, Control of hybrid electric vehicles - A survey of optimal energy-management strategies. IEEE Control Syst. Mag. 27, 60–70 (2007)
10. J. Kessels, M. Koot, P. Van den Bosch, D. Kok, Online energy management for hybrid electric vehicles. IEEE Trans. Veh. Technol. **57**, 3428–3440 (2008)
11. C. Musardo, B. Staccia, S. Midlam-Mohler, Y. Guezennec, G. Rizzoni, Supervisory control for NOx reduction of an HEV with a mixed-mode HCCI/CIDI engine, in *Proceedings of the American Control Conference*, vol. 6, 2005, pp. 3877–3881
12. N. Shidore, J. Kwon, A. Vyas, Trade-off between PHEV fuel efficiency and estimated battery cycle life with cost analysis, in *Vehicle Power and Propulsion Conference*. IEEE, 2009, pp. 669–677
13. S. Moura, J. Stein, H. Fathy, Battery health-conscious power management for plug-in hybrid electric vehicles via stochastic control, in *Dynamic Systems and Control Conference* (ASME, New York, 2010)
14. L. Serrao, S. Onori, A. Sciarretta, Y. Guezennec, G. Rizzoni, Optimal energy management of hybrid electric vehicles including battery aging, in *American Control Conference (ACC)*, 2011, pp. 2125–2130
15. L. Tang, S. Onori, G. Rizzoni, Optimal energy management of HEVs with consideration of battery aging, in *IEEE Transportation Electrification Conference and Expo (ITEC)*, 2014
16. S. Ebbesen, P. Elbert, L. Guzzella, Battery state-of-health perceptive energy management for hybrid electric vehicles. Trans. Veh. Technol. **61**, 2893–2900, 2012
17. J. Wang, P. Liu, J. Hicks-Garner, E. Sherman, S. Soukiazian, M. Verbrugge, H. Tataria, J. Musser, P. Finamore, Cycle-life model for graphite-$LiFePO_4$ cells. J. Power Sources, **196**, pp. 3942–3948, 2011
18. T. Pham, P. van den Bosch, J. Kessels, R. Huisman, Cost-effective energy management for hybrid electric heavy-duty truck including battery aging, in *Dynamic Systems and Control Conference (DSCC)*, 2013
19. G. Suri, S. Onori, A control-oriented cycle-life model for hybrid electric vehicle lithium-ion batteries. Energy **96**, 644–653 (2016)
20. M. Broussely, S. Herreyre, P. Biensan, P. Kasztejna, K. Nechev, R. Staniewicz, Aging mechanism in li ion cells and calendar life predictions. J. Power Sources **97–98**, 13–21 (2001)
21. S. Grolleau, A. Delaille, H. Gualous, P. Gyan, R. Revel, J. Bernard, E. Redondo-Iglesias, J. Peter, Calendar aging of commercial graphite/LiFePO4 cell - predicting capacity fade under time dependent storage conditions. J. Power Sources **255**, 450–458 (2014)
22. F. Todeschini, S. Onori, G. Rizzoni, An experimentally validated capacity degradation model for Li-ion batteries in PHEVs applications, in *8th IFAC International Symposium on Fault Detection, Supervision and Safety of Technical Processes* (2012)
23. S. Onori, P. Spagnol, V. Marano, Y. Guezennec, G. Rizzoni, A new life estimation method for lithium-ion batteries in plug-in hybrid electric vehicles applications, Int. J. Power Electron. **4**(3), 302–319 (2012)
24. 2009 National Household Travel Survey. Available: http://nhts.ornl.gov/2009/pub/stt.pdf [Online]
25. K. Bayar, R. Biasini, S. Onori, G. Rizzoni, Modelling and control of a brake system for an extended range electric vehicle equipped with axle motors. Int. J. Veh. Des. **58**, 399–426 (2012)

26. L. Serrao, S. Onori, G. Rizzoni, "ECMS as a realization of Pontryagin's Minimum Principle for HEV control, in *Proceedings of the American Control Conference* (IEEE Press, New York, 2009), pp. 3964–3969
27. A. Allam, S. Onori, S. Marelli, C. Taborelli, Battery health management system for automotive applications: a retroactivity-based aging propagation study, in *2015 American Control Conference (ACC)*, July 2015, pp. 703–716
28. A. Cordoba Arenas, S. Onori, Y. Guezzennec, G. Rizzoni, Capacity and power fade cycle-life model for plug-in hybrid electric vehicle lithium-ion battery cells containing blended spinel and layered-oxide positive electrodes J. Power Sources **278**, 473–483 (2015)

Chapter 10
Energy-Optimal Control of an Automotive Air Conditioning System for Ancillary Load Reduction

Quansheng Zhang, Stephanie Stockar, and Marcello Canova

Abstract The air conditioning system is currently the largest ancillary load in passenger cars, with a significant impact on fuel economy and CO_2 emissions. Considerable energy savings could be attained by simply adopting a supervisory energy management algorithm that operates the A/C system to reduce power consumption of the compressor, while maintaining the cabin comfort requirements.

This chapter proposes a model-based approach to the design of a supervisory energy management strategy for automotive air conditioning systems. Starting from an energy-based model of the A/C system that captures the complex dynamics of the refrigerant in the heat exchangers and the compressor power consumption, a constrained multi-objective optimal control problem is formulated to jointly account for fuel consumption, cabin comfort, and system durability.

The trade-off between fuel economy, performance, and durability is analyzed by performing a Pareto analysis of a family of solutions generated using dynamic programming. A forward-looking optimal compressor clutch policy is then obtained by developing an original formulation of the Pontryagin's minimum principle for hybrid dynamical systems. The simulation results demonstrate that the proposed control strategy allows for fuel economy improvement while retaining system performance and driver comfort.

Keywords Automotive air conditioning systems • Energy management • Optimal control

10.1 Introduction

In response to the increasing sustainability issues in transportation, the automotive industry is striving to improve fuel economy. While several improvements have been made to engines and transmissions for enhanced efficiency, considerable benefits

Reprinted from Zhang et al. (2016), with permission from IEEE.

Q. Zhang • S. Stockar (✉) • M. Canova
Center for Automotive Research, The Ohio State University, Columbus, OH 43212, USA
e-mail: zhang.777@osu.edu; stockar.1@osu.edu; canova.1@osu.edu

Q. Zhang et al., *Automotive Air Conditioning*, DOI 10.1007/978-3-319-33590-2_10

could can be attained at relatively low cost by reducing the energy consumption caused by the vehicle ancillary loads [1–3].

In particular, the air conditioning (A/C) system is one of the largest ancillary loads in passenger car, with profound impact on fuel consumption. According to [4], automotive A/C systems consume 5.5 % of the total annual automotive fuel demand, corresponding to an average fuel economy drop of about 18 %. Similar results were shown in [1], where the air conditioning compressor consumes up to 9 % of the engine power available at the crankshaft.

Significant research activity has focused on mitigating the energy consumption of vehicle A/C systems, for instance, by introducing variable displacement compressors, or electrically driven compressors and expansion valves [5, 6]. More recently, storage evaporators have been introduced to improve the cooling capacity when the vehicle stops in traffic [7].

Reduction in the energy consumption can also be achieved through the use of control strategies. This concept was, for instance, explored in [8], where a heuristic control was proposed to coordinate the compressor clutch engagement strategy with vehicle coasting and braking operations, hence utilizing vehicle waste energy to power the compressor. The results proposed show that up to 85 % of compressor operations could be powered by vehicle brake energy in urban drive conditions.

On the other hand, the design of more formal, model-based supervisory control strategies for A/C systems is particularly challenging due to the complex and nonlinear system dynamics determined by the mass and energy storage of the refrigerant in the heat exchangers, which affects the cooling load of the evaporator and the power consumption of the compressor. The control design is further complicated by the strong influence of the engine speed on the compressor flow rate and efficiency, as well as by the fact that the system typically operates intermittently by engaging and disengaging the clutch connecting the compressor to the engine crankshaft.

Few attempts have been made to solve the energy management of A/C systems as a hybrid optimal control problem (HOCP). For instance, hybrid model predictive control (HMPC) has been adopted for the optimization of residential and industrial refrigeration systems [9–11]. However, in industrial refrigeration systems the focus is on stabilizing the temperature of the storage space, while the short-term pressure fluctuations of the refrigerant in the evaporator and condenser are neglected. This represents a significant difference in comparison with automotive systems, where the duty cycle of the compressor clutch is typically quite short, causing rapid variations in the system pressures [12].

In this scenario, this chapter proposes a systematic approach to the design of a supervisory energy management strategy for automotive air conditioning systems. The approach is based on an energy-based, physics-based model of the A/C system that captures the refrigerant dynamics, heat transfer at the evaporator, and compressor power consumption caused by the clutch duty cycle and variations in the boundary conditions (air flow at condenser and evaporator). The model was validated on experimental data collected from the A/C system of a passenger car.

The A/C system energy optimization is studied next, focusing on fuel consumption, cooling performance (formulated through the tracking of a desired evaporator pressure), and clutch durability. This allows one to cast a constrained multi-objective optimal control problem for a nonlinear dynamical system, which is approached by applying dynamic programming (DP) to generate a family of solutions that determine a Pareto-optimal front.

A control strategy for the compressor clutch is then obtained through a novel approach, which combines the embedding method for hybrid dynamical systems and the Pontryagin's minimum principle (PMP), resulting into a control algorithm in forward-looking form.

The solution approach presented in this chapter for the energy optimization of the A/C system indicates a general framework for solving optimal hybrid control problem of vapor compression cycles, and could be extended to different classes of vehicle ancillary loads (for instance, the vehicle electrical loads, or the powertrain thermal management system).

This chapter is organized as follows. First, the energy-based A/C model considered in this study and its validation on vehicle data are described. Next, the A/C system control problem is qualitatively introduced and formalized as a multi-objective optimal control problem. The following section illustrates the dynamic programming solution and Pareto analysis. Then, the methodology followed to generate a forward-looking control policy is described, and a comparison with dynamic programming is made.

10.2 Description of the A/C System Model

The air conditioning system of a passenger car is generally based on the simple vapor compression cycle shown in Fig. 10.1. The compressor is engaged to the engine crankshaft through a magnetic clutch, determining the mass flow rate of refrigerant that circulates the system and, ultimately, the heat transfer rate at the

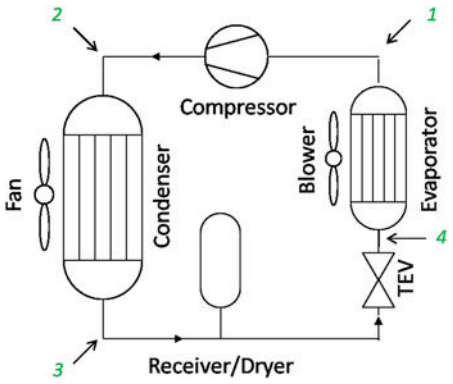

Fig. 10.1 Plant diagram of the A/C system

evaporator and condenser. In order to better understand the notation used in the following sections, Fig. 10.1 indicates the relevant thermodynamic states.

Since the A/C system typically operates in highly transient conditions due to the on/off clutch control strategy, the thermodynamic states may change significantly [13]. This poses a significant modeling challenge due to the different time scales induced by the mass and energy transport, which become challenging due of the phase changes.

10.2.1 Compressor Model

The flow and power consumption of the compressor are typically described through a quasi-static model [14, 15]. When the compressor is clutched to the engine, the flow rate and enthalpy are modeled based upon the characteristic maps expressed in terms of volumetric efficiency and isentropic efficiency [16]:

$$\dot{m}_c = \pi \cdot \tau \eta_v V_d \rho_1 \frac{N_e}{6 \cdot 10^4}, \qquad h_2 = h_1 + \frac{h_{2s} - h_1}{\eta_s} \tag{10.1}$$

where $\pi = [0, 1]$ is the compressor clutch command, τ the pulley ratio, N_e the engine speed, V_d the compressor displacement ($\mathrm{cm}^3/\mathrm{rev}$), and h_{2s} the enthalpy corresponding to the isentropic compression $1 \rightarrow 2s$.

The volumetric and isentropic efficiency are modeled as empirical functions of the compressor speed and the pressure ratio PR$= p_2/p_1$ [15]:

$$\begin{aligned} \eta_v &= \frac{\eta_{v0} - \epsilon(\mathrm{PR}^{1/\gamma} - 1)}{1 + C_1 Z^2} \\ \eta_s &= \eta_{s0} - C_2\,(\mathrm{PR} - 1) - Z\,(C_3 - C_4\,(\mathrm{PR} - 1)) \end{aligned} \tag{10.2}$$

where the Mach index Z is defined as:

$$Z = \frac{V_d^{1/3} \rho_1 N_c}{6 \cdot 10^4 \sqrt{p_1}} \tag{10.3}$$

and in this equation $N_c = \tau \cdot N_e$ is the compressor rotational speed, which is scaled with respect to the engine speed N_e by a constant pulley ratio τ.

The enthalpy rise corresponding to the isentropic compression $1 \rightarrow 2s$ is expressed as a function of the pressure ratio and thermodynamic condition at the suction side:

$$(h_{2s} - h_1) = h_1\,(p_1, T_1) \cdot \left(\mathrm{PR}^{\frac{\gamma-1}{\gamma}} - 1\right) \tag{10.4}$$

where γ is the specific heat ratio for the refrigerant.

The power output P_c and torque demand τ_c are computed by combining the previous equations:

$$\begin{aligned} P_c &= \frac{\eta_v}{\eta_s} V_d \rho_1 \frac{N_c}{6 \cdot 10^4} h_1 (p_1, T_1) \cdot \left(\mathrm{PR}^{\frac{\gamma-1}{\gamma}} - 1 \right) \\ \tau_c &= \frac{1}{2\pi \cdot 10^3} \frac{\eta_v}{\eta_s} V_d \rho_1 h_1 (p_1, T_1) \cdot \left(\mathrm{PR}^{\frac{\gamma-1}{\gamma}} - 1 \right) \end{aligned} \tag{10.5}$$

The parameters of the above model, η_{v0}, ϵ, C_1, η_{s0}, C_2, C_3, C_4 are identified on the compressor performance maps provided by the supplier.

Finally, the total torque required at the engine is obtained by adding the compressor torque load to the baseline engine torque profile acquired from the experimental data collected on the vehicle:

$$\tau_{\mathrm{tot}} = \tau_e + \tau_c \tag{10.6}$$

The total torque is used with the engine speed to calculate the instantaneous engine fuel consumption through a look-up table generated from engine experimental data.

10.2.2 Heat Exchangers Models

The energy-based modeling approach proposed in [17] is applied here to obtain models for the condenser and evaporator heat exchangers. The model is based upon the following assumptions:

1. Each heat exchanger is modeled as a lumped thermal mass with two control volumes representing, respectively, the volume occupied by the refrigerant circulating in the tubes and the metal mass (walls);
2. The compliance effects relative to the variations in mass flow rate in or out of the heat exchangers are negligible, hence the refrigerant mass flow rate predicted by the compressor model is uniform throughout the system. This assumption preserves the low-frequency dynamics, driven mainly by the heat transfer [18, 19].
3. The refrigerant within each heat exchanger is assumed present only in two-phase, hence neglecting phase changes. While this represents a drastic simplification of the physical behavior, the contribution of superheat or subcooled regions to the heat transfer is in practice limited [20];
4. The heat transfer dynamics is typically dominated by the fluid with the lowest convective heat transfer coefficient, namely the external air [21]. Therefore, the heat transfer from the refrigerant to the walls is assumed infinitely fast [20].

Considering the schematic of a simple cross-flow heat exchanger, for instance, the one shown in Fig. 10.2, the spatially averaged refrigerant temperature T and wall temperature T_w are determined by the refrigerant mass flow rate, $\dot{m}$, inlet

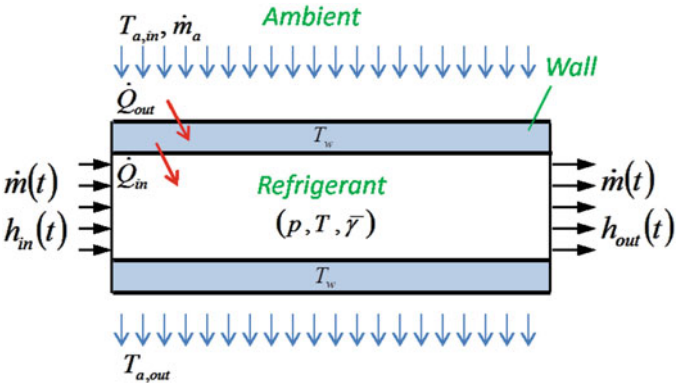

Fig. 10.2 Schematic of heat exchanger for the energy-based model

enthalpy, h_{in}, and by the air mass flow rate $\dot{m}_a$ and inlet temperature $T_{a,\text{in}}$. Under the above assumptions, an energy balance can be formulated for the refrigerant control volume:

$$V\frac{d}{dt}(\rho u) = \dot{Q}_{\text{in}} + \dot{m}\,(h_{\text{in}} - h_{\text{out}}) \tag{10.7}$$

where ρ is the average refrigerant density and u the specific internal energy.

Similarly, an energy balance applied to the wall thermal mass leads to:

$$M_w c\frac{dT_w}{dt} = \dot{Q}_{\text{out}} - \dot{Q}_{\text{in}} \tag{10.8}$$

where M is the metal mass of the heat exchanger, and c the specific heat.

Expressing the internal energy as a function of the average refrigerant enthalpy h, and applying the definition of averaged refrigerant property, the following equation is obtained:

$$\begin{aligned} u &= h - \frac{p}{\rho} \\ \rho h &= (1-\bar{\gamma})\rho_l h_l + \bar{\gamma}\rho_g h_g \end{aligned} \tag{10.9}$$

where γ represents the mean void fraction of the refrigerant, and ρ_g, h_g, ρ_l, h_l are the refrigerant thermodynamic properties calculated at saturated vapor and saturated liquid state. All of these properties depend only on the refrigerant pressure [22, 23].

Substituting Eq. (10.9) into the left-hand side of Eq. (10.7):

$$\frac{d(\rho u)}{dt} = \left[(1-\bar{\gamma})\frac{\partial \rho_l h_l}{\partial p} + \bar{\gamma}\frac{\partial \rho_g h_g}{\partial p} + \left(\rho_g h_g - \rho_l h_l\right)\frac{\partial \bar{\gamma}}{\partial p} - 1\right]\frac{dp}{dt} \tag{10.10}$$

where the term $[\cdot]$ is only a function of the refrigerant pressure and can be pre-computed analytically or through look-up tables from the R134a thermodynamic tables.

Note that the high thermal conductivity of the heat exchanger walls material and the high convective heat transfer coefficient of the refrigerant in the two-phase state typically result into a wall temperature that closely follows the refrigerant temperature. This makes it possible to introduce a further approximation, namely lumping the wall thermal mass into the refrigerant thermal mass:

$$M_w c \frac{dT_w}{dt} \approx M_w c \frac{dT}{dt} = \dot{Q}_{\text{out}} - \dot{Q}_{\text{in}} \tag{10.11}$$

Since the refrigerant within the heat exchanger is approximated to a two-phase system, the temperature is equal to the saturation temperature at the refrigerant pressure, hence:

$$M_w c \left(\frac{\partial T}{\partial p}\right) \frac{dp}{dt} = \dot{Q}_{\text{out}} - \dot{Q}_{\text{in}} \tag{10.12}$$

Substituting to Eq. (10.8), the energy balance equation for the entire heat exchanger (considering the refrigerant and the wall thermal mass) results:

$$\begin{aligned} V \Bigg[(1-\bar{\gamma}) \frac{\partial \rho_l h_l}{\partial p} + \bar{\gamma} \frac{\partial \rho_g h_g}{\partial p} + \left(\rho_g h_g - \rho_l h_l\right) \frac{\partial \bar{\gamma}}{\partial p} - 1 \\ + \frac{M_w c}{V} \left(\frac{\partial T}{\partial p}\right) \Bigg] \frac{dp}{dt} = \dot{Q}_{\text{out}} + \dot{m} \left(h_{\text{in}} - h_{\text{out}}\right) \end{aligned} \tag{10.13}$$

Equation (10.13) is the final form of the energy balance for a heat exchanger with predominant two-phase flow, under the assumptions described above. Applying to the evaporator and the condenser, Eq. (10.14) is obtained, where the subscripts e and c indicate the evaporator and condenser heat exchanger, respectively. In obtaining the equation, the following assumptions are made for simplicity:

1. The condenser inlet enthalpy h_2 is given by the compressor model;
2. The evaporator inlet enthalpy h_4 is the same as the condenser outlet enthalpy h_3, and approximated as equal to the saturated liquid enthalpy $h_l\,(p_2)$;
3. The temperature at the exit of the evaporator is regulated by the expansion valve, which is assumed to set a constant superheat temperature $\Delta T_{\text{SH}} = T_1 - T_g\,(p_1) = 10\,^{\circ}\text{C}$;
4. The evaporator outlet enthalpy h_1 is calculated assuming that thermodynamic state 1 is defined by the state $(p_1,\ T_1$;

$$
\begin{aligned}
&V_e\left[(1-\bar{\gamma}_e)\frac{\partial\left(\rho_l h_l\right)_e}{\partial p_1}+\bar{\gamma}_1\frac{\partial\left(\rho_g h_g\right)_e}{\partial p_1}+\left(\rho_g h_g-\rho_l h_l\right)_e\frac{\partial\bar{\gamma}_e}{\partial p_1}-1+\frac{M_{we}c_e}{V_e}\left(\frac{\partial T_1}{\partial p_1}\right)\right]\\
&\frac{dp_1}{dt}=\dot{Q}_e+\dot{m}_c\left(h_4-h_1\right)\\
&V_c\left[(1-\bar{\gamma}_c)\frac{\partial\left(\rho_l h_l\right)_c}{\partial p_2}+\bar{\gamma}_c\frac{\partial\left(\rho_g h_g\right)_c}{\partial p_2}+\left(\rho_g h_g-\rho_l h_l\right)_c\frac{\partial\bar{\gamma}_c}{\partial p_2}-1+\frac{M_{wc}c_c}{V_c}\left(\frac{\partial T_2}{\partial p_2}\right)\right]\\
&\frac{dp_2}{dt}=-\dot{Q}_c+\dot{m}_c\left(h_2-h_3\right)
\end{aligned}
\tag{10.14}
$$

The heat transfer rates in Eq. (10.14) are relative to the external heat exchange between the walls and the ambient air, and given by:

$$
\begin{aligned}
\dot{Q}_e&=\dot{m}_{a,e}c_{p,a}\left(T_{a,\text{in},e}-T_{a,\text{out},e}\right)\\
\dot{Q}_c&=\dot{m}_{a,c}c_{p,a}\left(T_{a,\text{out},c}-T_{a,\text{in},c}\right)
\end{aligned}
\tag{10.15}
$$

Neglecting the thermal mass of the air, the outlet air temperatures can be calculated in quasi-steady conditions by applying the $\epsilon-\text{NTU}$ method [24]. Note that the model considered in this study assumes two-phase flow within the two heat exchangers, leading to a special case where the heat exchangers behavior is independent of the flow arrangement. Therefore the effectiveness is given by:

$$
\epsilon=1-\exp\left(-\text{NTU}\right) \tag{10.16}
$$

and applying the definition of effectiveness:

$$
\begin{aligned}
T_{a,\text{out},e}&=T_e+\left(T_{a,\text{in},e}-T_e\right)\exp\left(-\text{NTU}_e\right)\\
T_{a,\text{out},c}&=T_c+\left(T_{a,\text{in},c}-T_c\right)\exp\left(-\text{NTU}_c\right)
\end{aligned}
\tag{10.17}
$$

For compact heat exchangers, the number of transfer units is generally defined as [21, 25]

$$
\text{NTU}=\frac{\alpha A_s[1-F_{\text{fin}}(1-\eta_{\text{FA}})]}{\dot{m}_a c_{p,a}} \tag{10.18}
$$

where α is the air heat transfer coefficient, A_S is the heat exchanger external surface area, F_{fin} is the fraction of air-to-structure surface area on fins, and η_{FA} is the air side fin efficiency. The numerical values for the above parameters are typically available from the heat exchanger manufacturer.

10.2.3 Final Form of the A/C System Model

The energy-based A/C model equations characterize a two-state nonlinear system that can be expressed in descriptor form:

$$\begin{aligned} D(x)\,\dot{x} &= f(x,u,v) \\ y &= g(x,u,v) \end{aligned} \tag{10.19}$$

where the states are the pressures in the evaporator and condenser:

$$x(t) = \begin{bmatrix} p_1(t) \\ p_2(t) \end{bmatrix} \tag{10.20}$$

and the output is the torque absorbed by the A/C compressor:

$$y(t) = [\tau_c(t)] \tag{10.21}$$

The controlled input to the A/C model is the compressor clutch command:

$$u(t) = [\pi(t)] \qquad s.t. \quad \pi = (0,1) \tag{10.22}$$

and, finally, the external input is represented by the rotational speed of the compressor shaft:

$$v(t) = [N_c(t)] \tag{10.23}$$

Note that, for simplicity, the flow rate and inlet temperature of the air at the evaporator and condenser are assumed constant and will be treated as parameters.

Based on Eq. (10.14), the system matrix results:

$$D(x) = \begin{bmatrix} d_{1,1} & 0 \\ 0 & d_{2,2} \end{bmatrix} \tag{10.24}$$

where:

$$\begin{aligned} d_{1,1} =& V_e \Bigg[(1-\bar{\gamma}_1)\frac{\partial(\rho_l h_l)_e}{\partial p_1} + \bar{\gamma}_1 \frac{\partial(\rho_g h_g)_e}{\partial p_1} + \\ &+ \left(\rho_g h_g - \rho_l h_l\right)_e \frac{\partial \bar{\gamma}_1}{\partial p_1} - 1 + \frac{M_{we} c_e}{V_e}\left(\frac{\partial T_1}{\partial p_1}\right) \Bigg] \\ d_{2,2} =& V_c \Bigg[(1-\bar{\gamma}_2)\frac{\partial(\rho_l h_l)_c}{\partial p_2} + \bar{\gamma}_2 \frac{\partial(\rho_g h_g)_c}{\partial p_2} + \\ &+ \left(\rho_g h_g - \rho_l h_l\right)_c \frac{\partial \bar{\gamma}_2}{\partial p_2} - 1 + \frac{M_{wc} c_c}{V_c}\left(\frac{\partial T_2}{\partial p_2}\right) \Bigg] \end{aligned} \tag{10.25}$$

The resulting D matrix is diagonal, indicating that the refrigerant dynamics in the two heat exchangers are partially independent.

The coupling between the evaporator and condenser heat exchangers is evident in the right-hand side of the governing equations, and is due to the refrigerant flow rate circulating in the A/C loop:

$$f(x,u,v) = \begin{bmatrix} \dot{m}_{a,e} c_{p,a} \left(T_{a,\text{in},e} - T_{a,\text{out},e}\right) + \dot{m}_c \left(h_4 - h_1\right) \\ \dot{m}_{a,c} c_{p,a} \left(T_{a,\text{out},c} - T_{a,\text{in},c}\right) + \dot{m}_c \left(h_2 - h_3\right) \end{bmatrix} \tag{10.26}$$

The control input to the A/C model is the compressor clutch command. When the clutch is connected ($\pi = 1$), the compressor rotates at a multiple of the engine speed (the two differ by a constant pulley ratio). The clutch command π enters implicitly in Eq. (10.26), through the dependence of the refrigerant flow rate $\dot{m}$ from the compressor shaft speed. On the other hand, when the clutch is disconnected, the A/C system is decoupled from the engine crankshaft and the refrigerant flow rate $\dot{m}$ is zeros.

10.2.4 Model Calibration and Validation

Most of the parameters of the energy-based model can be easily related to design and geometric data of the heat exchangers, as well as to the properties of the fluids.

In addition, since the heat transfer coefficients on the refrigerant side have been neglected due to their high value, only the air side is considered in the model. The correlations to calculate the heat transfer coefficients adopted in this work are specific to cross-flow compact heat exchangers with louvers and fins, and have been proposed by Chang and Wang [26] and Kim and Bullard [27].

This simplifies the calibration process to identifying two multipliers, $k_{\alpha_{e,a}}$ and $k_{\alpha_{c,a}}$, which correct the heat transfer correlations for the air side of the two heat exchangers. The calibration procedure is qualitatively described in Fig. 10.3 [12].

The identification was conducted on the complete A/C system model, starting from experimental data collected from a test vehicle. Experimental tests were conducted by running the vehicle at constant speed on a chassis dynamometer, to maintain engine speed values of 700, 1500, and 2500 rpm, respectively. The boundary conditions at the heat exchangers (air temperature and flow rate) were monitored but not actively controlled, hence leaving the cabin blower and condenser fan to operate according to the A/C system settings. The recorded engine speed N_e and clutch signal π are input to the model to calculate the pressure traces in the condenser and evaporators, which were then compared against the corresponding measured data.

The heat transfer multipliers were calibrated at a single speed (700 rpm), to minimize the RMS error on the condenser and evaporator pressure, ultimately

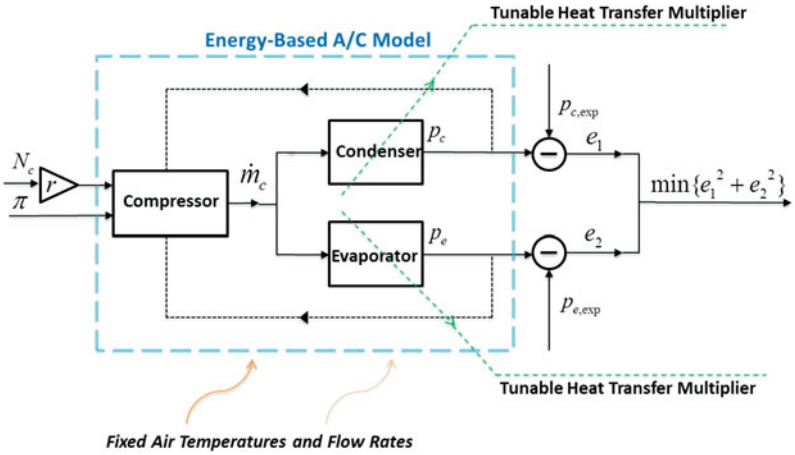

Fig. 10.3 Calibration procedure for the energy-based A/C model

Table 10.1 RMS error for the calibration and validation

Engine speed	700 rpm	1500 rpm	2500 rpm
RMS evaporator	21.47 kPa (3.5 %)	22.67 kPa (3.7 %)	25.59 kPa (3.5 %)
RMS condenser	20.19 kPa (3.3 %)	35.94 kPa (5.9 %)	75.51 kPa (12.5 %)

finding $k_{\alpha_{e,a}} = 0.4$ and $k_{\alpha_{c,a}} = 0.25$. The model was then validated by comparing the prediction to the experimental data at the other two engine speed conditions.

A summary of the results of the calibration procedure is shown in Table 10.1, reporting the RMS errors calculated on the condenser and evaporator pressures for the three cases considered. It is clear that the prediction error on the condenser pressure p_2 increases with the engine speed. This is mainly a consequence of neglecting the presence of the receiver/dryer shown in Fig. 10.1, whose filling-and-emptying dynamics affects the condenser pressure fluctuation amplitude. On the other hand, the error on the evaporator pressure p_1 remains limited for all cases, and is mainly driven by the simplifying assumptions adopted for deriving the energy-based model.

If more accuracy is desired, the above discrepancies could be mitigated by scheduling the heat transfer multipliers based on the engine speed and boundary conditions at the two heat exchangers.

Finally, a final test was conducted to verify the ability of the model to predict the energy consumption of the A/C system during transients. To this extent, a comparison was conducted against experimental data collected on the SC03 air conditioning test cycle.

Figure 10.4a reports the vehicle speed profile and the clutch command to the compressor. These two signals are inputs to the model, and the simulated evaporator pressure and fuel consumption are compared to the test data.

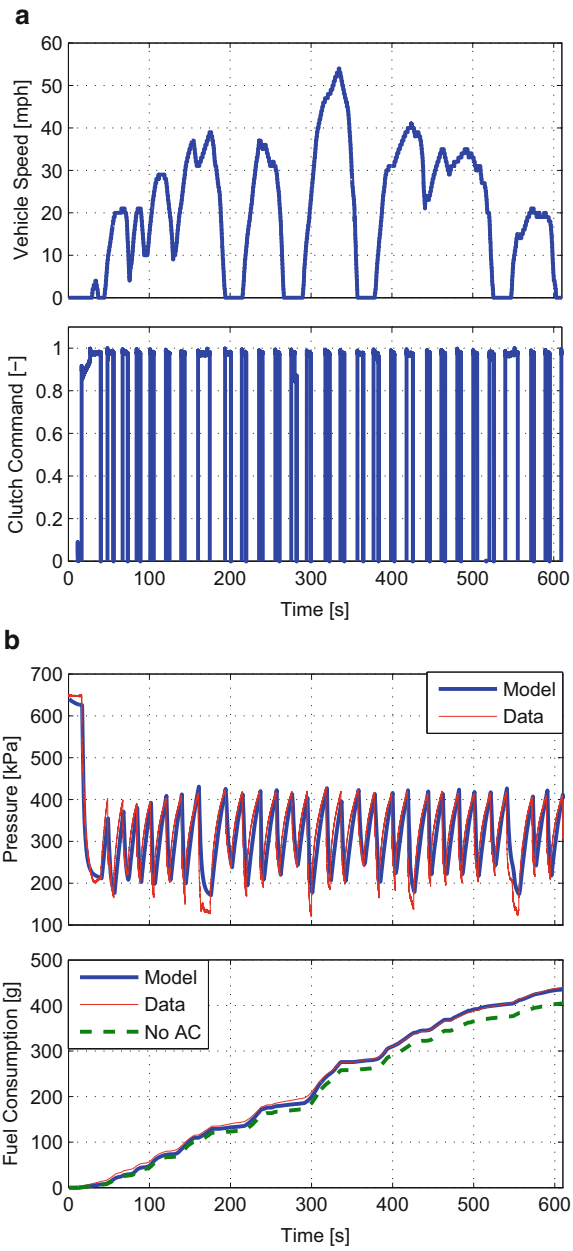

Fig. 10.4 Verification of the energy-based model on the SC03 driving cycle. (**a**) Engine speed and clutch profiles. (**b**) Evaporator pressure and cumulative fuel consumption

The results in Fig. 10.4b show that the model retains sufficient accuracy in predicting both outputs. In particular, the RMS error on the evaporator pressure remains below 5 %, while the model predicts the effects of the A/C system on the cumulative fuel consumption with less than 1.2 % error.

10.3 Formulation of the Energy Optimization Problem

The objective of a supervisory controller for the automotive A/C system is to operate the system in a way that reduces the compressor parasitic load in relation with the vehicle and engine operations, while maintaining the cabin comfort requirements and ensuring the reliability of the compressor clutch.

As a preliminary step towards control design, an optimization study is done to evaluate how to prioritize the aforementioned objectives. The first term considered is the total fuel consumption over a driving profile:

$$J_1 = \int_0^T \dot{m}_{\text{fuel}}(t)dt \tag{10.27}$$

where $\dot{m}_{\text{fuel}}(t)$ is the instantaneous fuel consumption of the engine. This term is obtained from the steady-state engine fuel consumption map implemented in the model, as a function of the engine speed and input torque. The effects of the ancillary loads are accounted for by adding the compressor torque to the engine torque, which is a time-varying external input dependent on the specific driving profile.

While optimizing for fuel economy, the controller must also maintain a level of comfort in the vehicle cabin. Without this objective, the solution of above optimal control problem would be trivial. Since modeling the thermal dynamics of the cabin, and the relative forms of heat rejection is overly complex and outside the scope of this work, the cabin comfort requirement is translated into a target pressure at the evaporator. This simplification is acceptable because the cooling load at the evaporator is largely a function of the refrigerant pressure (since the refrigerant is predominantly present in two-phase form). For this reason, a second term of the objective function represents a tracking error:

$$J_2 = \int_0^T (p_1(t) - p_{1,0})^2 dt \tag{10.28}$$

where p_1 is the actual evaporator pressure and $p_{1,0}$ is a reference value for the evaporator pressure. The solution of this optimal control problem will represent a trade-off between potential fuel savings and the temperature in the vehicle cabin.

Finally, to address both drivability issues and potential durability problems, an additional cost function is considered to prevent high frequency switching in the clutch signal:

$$J_3 = \int_{\Delta t}^T (\pi(t) - \pi(t - \Delta t))^2 dt \tag{10.29}$$

where $\pi(t)$ is the current clutch position, $\pi(t-1)$ is the clutch position at the previous time step, and Δt is the discretization time.

In summary, the objective function for the A/C system optimization problem is given by:

$$J = \alpha J_1 + \beta J_2 + \gamma J_3 \tag{10.30}$$

where α, β, and γ are the weighting factors. Moreover, the evaporator and the evaporator pressures are subject to state constraints:

$$p_2 \leq p_{2,\max} \tag{10.31}$$

$$p_1 \geq p_{1,\min} \tag{10.32}$$

From the above definition, it is clear that multiple conflicting objectives are present, which lead to the presence of non-dominated optimal solutions dependent upon the choice of the weighting factors.

10.3.1 Solution and Analysis

The dynamic programming (DP) algorithm is chosen as an off-line optimization method for solving the optimal control problem formulated above [28]. The plant model is discretized using the Euler forward scheme and the method developed in [29] is applied.

In order to remove the influence of the units and scales, the three objective functions J_1, J_2, and J_3 are normalized against the total fuel consumption over the SC03 drive cycle, the maximum RMS error on the evaporator pressure, and a maximum number of clutch switching events for the SC03 cycle.

Since the energy optimization problem consists of multiple objective functions with conflicting goals, the solution of the optimal control problem for different weighting factors consists in a set of non-dominated solutions. The Pareto analysis becomes a useful tool to provide a graphical representation of a trade-off between at least two performance variables in a system and to investigate how the weighting factors α, β, and γ affect the A/C system performance in terms of fuel consumption, evaporator pressure tracking, and clutch on–off operations. A large number of simulations were conducted to explore the parameter space $\alpha \times \beta \times \gamma$ in the range $[0 \quad 1] \times [0 \quad 1] \times [0 \quad 1]$.

The results of the simulation are represented in Fig. 10.5, in the space defined by the three objective functions. Since each simulation was generated using dynamic programming, each solution found corresponds to the result of an optimal clutch engagement policy for a specific combination of weights. A clear trade-off behavior among the three objective functions can be readily observed.

In addition to the results from the dynamic programming, the point corresponding to a simulation conducted by imposing the clutch profile measured on the vehicle for the SC03 cycle is represented. This point will be henceforth indicated as the *Baseline Condition*, and will be used as a benchmark for comparing the performance offered by different optimization solutions.

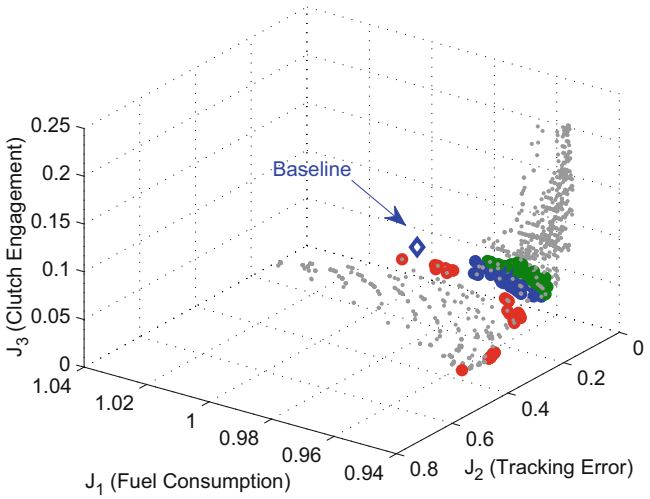

Fig. 10.5 Pareto-optimal surface resulting from dynamic programming

To better understand the trade-offs between objective functions, the results were sorted into three different groups, based on similar values of the objective function J_3, and then projected onto a 2D plane in the variables J_1 and J_2. The results are summarized in Fig. 10.6. The figures clearly illustrate the existence of a Pareto front among the three objective functions. Of particular interest is the trade-off between J_1 and J_2, which indicates the complexity of jointly optimize the A/C system for cabin comfort and for fuel economy.

Moreover, Fig. 10.6 shows that there is an opportunity to jointly optimize all of the three performance outputs from the baseline condition through optimal control, as the baseline point is not located on the Pareto-optimal front. In this case, it is necessary to evaluate which objective function should be prioritized for the system optimization. In particular, results show that it is possible to achieve a 2 % improvement in the fuel consumption over the SC03 cycle, without penalizing the tracking performance. This can be obtained by moving horizontally from the baseline point towards the Pareto front.

To illustrate the effect of the weighting factors on the state evolution and the control policy, the three scenarios summarized in Table 10.2 have been selected for comparison against the baseline controller. The values reported below correspond to the solution obtained with the backward-looking simulator.

The clutch profile and resulting evaporator pressure are shown in Fig. 10.7 for the baseline case and for the three optimized scenarios.

Scenario 1 represents a case where the target evaporator pressure is prioritized over the other two objectives. From Table 10.2, this strategy results into the lowest tracking error, but significant chattering of the A/C compressor clutch occurs. Note that, even in this limit case, the fuel consumption calculated on the SC03

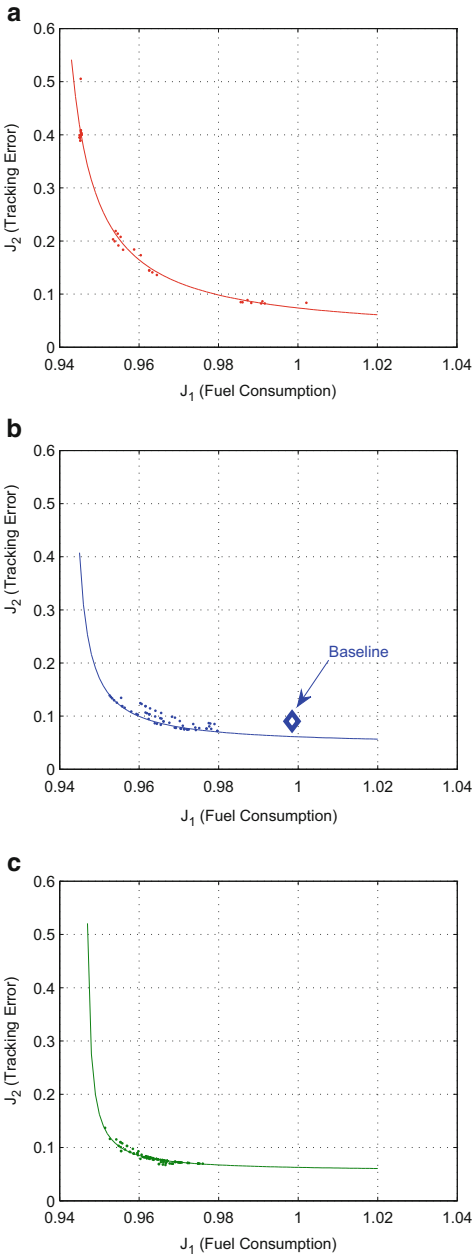

Fig. 10.6 Pareto-optimal fronts obtained from the surface in Fig. 10.5 at three different values of J_3. (**a**) Pareto curve for $0.03 \leq J_3 \leq 0.4$. (**b**) Pareto curve for $0.04 \leq J_3 \leq 0.05$. (**c**) Pareto curve for $0.04 \leq J_3 \leq 0.05$

Table 10.2 Comparison between optimal scenarios and baseline

	α	β	γ	J_1	J_2	J_3	M_{fuel} (g)	RMS_p (%)	n_{clutch}
Baseline	–	–	–	0.9985	0.0702	0.0474	415.9	31 %	29
Scenario 1	0.1	0.8	0.1	0.9579	0.0136	0.1920	399.1	14	105
Scenario 2	−1.0	0.1	0.2	0.9496	0.110	0.0645	395.6	37	37
Scenario 3	−0.1	0.4	0.4	0.9654	0.0353	0.1005	402.2	21	61

cycle is still lower than in the baseline case. *Scenario 2* relaxes the weight on the evaporator pressure tracking and achieves the best fuel economy, without significant deterioration of the system performance and clutch usage. Finally, *Scenario 3* attempts at striking a balance between the previous two scenarios. As Fig. 10.7 shows, this choice of weights leads to a more precise tracking of the pressure target at the evaporator, when compared to *Scenario 2*. On the other hand, this is achieved at the expense of the fuel consumption, which results higher than the other two scenarios.

For the derivation of the forward-looking energy management strategy, the weight combinations of *Scenario 2* have been selected and will be used in the next section.

10.4 Control Design for A/C System Energy Management

The analysis conducted above indicates that the A/C system is characterized by a short-term thermal energy storage capacity, which could be leveraged to save energy when the vehicle is decelerating or braking and reuse it during acceleration.

To this extent, the PMP is a technique that has been successfully applied in the past to solve fuel-optimal control problems for hybrid vehicles [30]. While this method provides only a set of *necessary conditions* for optimality, in some cases simple adaptive control schemes can be designed by exploiting information on the co-state dynamics [31].

On the other hand, the A/C system energy optimization is a considerably different problem, due to the highly nonlinear dynamics of the system and the presence of a penalty on switching in the objective function.

To this extent, a novel approach is here adopted, based on the hybrid optimal control theory. Specifically, the A/C system energy management, namely an optimal control problem with switching inputs and cost of switching, is transformed into a conventional, continuous-time optimal control by embedding the discrete inputs, then projecting the so-obtained equivalent control into the discrete domain. The approach adopted in this chapter is based on the work proposed by [32], presenting a unified approach to obtain optimal control policies for switching systems.

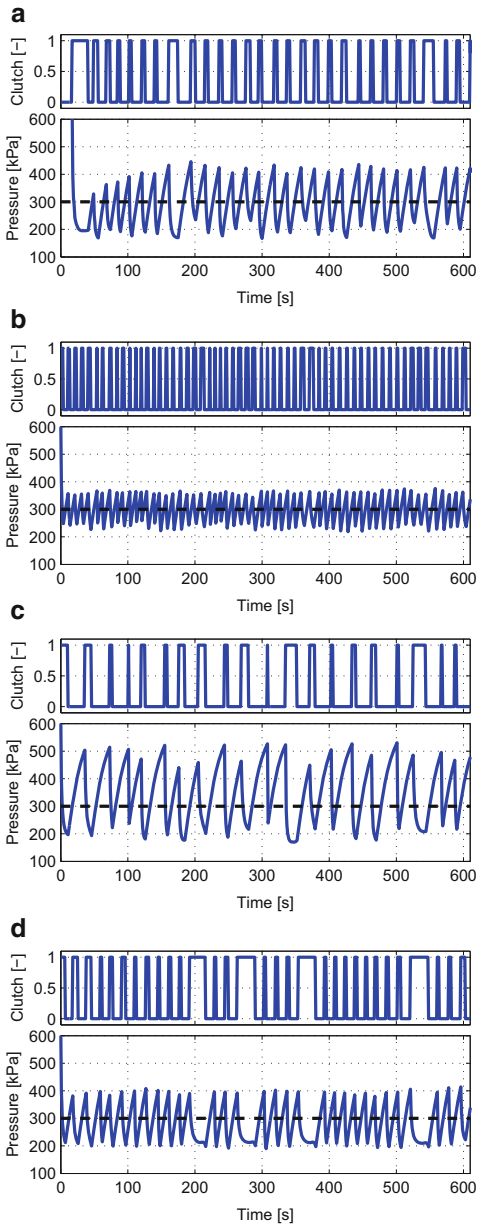

Fig. 10.7 Comparison of clutch profile and evaporator pressure during SC03 cycle for different optimization scenarios. (**a**) Baseline scenario (Production control). (**b**) Optimized scenario 1 (Priority on tracking). (**c**) Optimized scenario 2 (Priority on fuel economy). (**d**) Optimized scenario 3 (Balanced tracking and fuel economy)

The procedure was originally derived for a general switched system, formulating sufficient and necessary conditions for the optimality of the solution for a two-switched system, where the dynamic of the system for $x(t) \in \mathbb{R}^n$ is described by:

$$\dot{x}(t) = f_{s(t)}(t, x(t), u(t)), \quad x(t_0) = x_0 \tag{10.33}$$

where at each $t \geq_0$, $s(t) \in \{0, 1\}$ is the switching control, $u(t) \in \Omega \subset \mathbb{R}^m$ is the constrained control input constraint in the compact set $\Omega, f_0, f_1 : \mathbb{R} \times \mathbb{R}^n \times \mathbb{R}^m \longrightarrow \mathbb{R}^n$ are real vector-valued functions of class $\mathcal{C}^1$.

For finding the optimal solution, the problem is embedded into a larger family of systems and the optimal control problem is reformulated for the new system. It has been demonstrated that the set of optimal trajectories of the switching system is dense in the set of the optimal trajectories of the embedded system. Therefore, it is always possible to approximate the solution of the embedded control with an appropriate switching control [32].

The governing equations for the A/C system model are first rewritten as a class of hybrid systems:

$$\begin{aligned} \frac{dp_1}{dt} &= \frac{1}{d_{11}} \cdot f_1^{\pi}(p_1, p_2, t) \\ \frac{dp_2}{dt} &= \frac{1}{d_{22}} \cdot f_2^{\pi}(p_1, p_2, t) \end{aligned} \tag{10.34}$$

where the functions f_1^{π} and f_2^{π} are defined as:

$$f_1^{\pi}(p_1, p_2, t) = \begin{cases} -\dot{Q}_e + \dot{m}_c(h_4 - h_1) & \text{if} \quad \pi = 1 \\ -\dot{Q}_e & \text{if} \quad \pi = 0. \end{cases} \tag{10.35}$$

and

$$f_2^{\pi}(p_1, p_2, t) = \begin{cases} -\dot{Q}_c + \pi\dot{m}_c(h_2 - h_3) & \text{if} \quad \pi = 1 \\ -\dot{Q}_c & \text{if} \quad \pi = 0. \end{cases} \tag{10.36}$$

The objective function for this optimization problem is given by:

$$J = \int_0^{T_{\text{cycle}}} \frac{\alpha}{\bar{m}}\dot{m}_{\text{fuel}}(t) + \frac{\beta}{\bar{p}}(p_1(t) - p_{e,\text{ref}})^2 dt \tag{10.37}$$

and omitting the penalty on the switching.

This switching optimal control problem is solved by applying the PMP to the embedded system. Given the dynamics of the switching system, the embedded dynamics for the A/C system is

$$\begin{aligned} \frac{d\tilde{p}_1}{dt} &= \frac{1}{d_{11}} \cdot \left[(1 - \tilde{s}(t))f_1^0(p_1, p_2, t) + \tilde{s}(t)f_1^1(p_1, p_2, t)\right] \\ &= -\dot{Q}_e + \dot{m}\tilde{s}(t)(h_4 - h_1) \\ \frac{d\tilde{p}_2}{dt} &= \frac{1}{d_{22}} \cdot \left[(1 - \tilde{s}(t))f_2^0(p_1, p_2, t) + \tilde{s}(t)f_2^1(p_1, p_2, t)\right] \\ &= -\dot{Q}_c + \dot{m}\tilde{s}(t)(h_2 - h_3) \end{aligned} \tag{10.38}$$

where $\tilde{s}(t) \in [0, 1]$ is called *embedding factor*. Accordingly, the two Hamiltonians for the "clutch-on" and "clutch-off" case are

$$\begin{aligned} H_{\pi=1} &= L + \lambda_1 \frac{f_1^1}{d_{11}} + \lambda_2 \frac{f_2^1}{d_{22}} \\ &= L + \lambda_1 \frac{-\dot{Q}_e + \dot{m}_c(h_4 - h_1)}{d_{11}} \\ &\quad + \lambda_2 \frac{-\dot{Q}_c + \dot{m}_c(h_2 - h_3)}{d_{22}} \\ H_{\pi=0} &= L + \lambda_1 \frac{f_1^0}{d_{11}} + \lambda_2 \frac{f_2^1}{d_{22}} \\ &= L + \lambda_1 \frac{-\dot{Q}_e}{d_{11}} + \lambda_2 \frac{-\dot{Q}_c}{d_{22}} \end{aligned} \tag{10.39}$$

The associated Hamiltonian for the embedded problem is therefore obtained as:

$$\tilde{H} = \tilde{s}(t) H_{\pi=1} + (1 - \tilde{s}(t)) H_{\pi=0} \tag{10.40}$$

which, after some manipulation and substitutions, becomes

$$\begin{aligned} \tilde{H}(x(t), \tilde{s}(t), \lambda_1(t), \lambda_2(t), t) = L &+ \lambda_1 \left[\frac{-\dot{Q}_e}{d_{11}} + \tilde{s}(t) \frac{\dot{m}_c}{d_{11}} (h_4 - h_1) \right] \\ &+ \lambda_2 \left[\frac{-\dot{Q}_c}{d_{22}} + \tilde{s}(t) \frac{\dot{m}_c}{d_{22}} (h_3 - h_2) \right] \end{aligned} \tag{10.41}$$

Finally, the co-state dynamics for the two Lagrange multipliers are defined as:

$$\begin{aligned} \frac{d\lambda_1(t)}{dt} &= -\frac{\partial \tilde{H}}{\partial \tilde{p}_1} \\ \frac{d\lambda_2(t)}{dt} &= -\frac{\tilde{\partial} H}{\partial \tilde{p}_2} \end{aligned} \tag{10.42}$$

The optimal solution $\tilde{s} \in [0, 1]$ is found, such that

$$\tilde{s}^* = \text{argmin}_{\tilde{s}(t) \in [0,1]} \{ \tilde{H}(x(t), \lambda_1(t), \lambda_2(t), \tilde{s}, t) \} \tag{10.43}$$

10.4.1 Solution of the Embedded Optimal Control Problem

The optimization of the clutch command has been performed on the SCO3 driving cycle. The solution of the embedded problem is found using the shooting method to determine the initial condition of the two Lagrange multipliers λ_1 and λ_2. Figure 10.8 shows the results of the shooting method for the overall performance index J as well as for J_1 that represents the fuel consumption and J_2 which evaluate the tracking performance of the system.

Depending upon the selection of the initial conditions of the co-state dynamics, different clutch behaviors can be observed. For example, for $\lambda_{2,0} = -1e-4$ and any $\lambda_{1,0}$, the fuel consumption increases dramatically. This indicates that the controller is aggressive in turning on the A/C. This behavior is extremely sub-optimal, as too much clutching results in a pressure in the evaporator well below the desired set point, hence resulting in a worsen $J2$.

The opposite response can be observed for $\lambda_{2,0} = 1e-4$. In this case, the fuel consumption is very low, but the tracking performance is poor. This represents a case for which the controller prioritizes the fuel savings and neglects the comfort in the vehicle cabin. The clutch profile, state transition as well as the co-state dynamics of optimal solution for the selected combination of weight are shown in Fig. 10.9.

By comparing the clutching events with the speed profile of Fig. 10.9, it is clear that the embedded control inputs attempt at utilizing all the braking events to store energy in the A/C evaporator. Except for the control decision at the beginning of the cycle, which is influenced by the initial condition for the A/C clutch $\tilde{s}(t=0) = 1$, all the control decisions for which $\tilde{s}(t) = 1$ are coinciding with the deceleration of the vehicle.

Moreover, the amount of energy that can be stored in the A/C system by clutching on the compressor when coasting is very limited. A very short period of time—in the order of a few seconds—is enough to bring the evaporator pressure to its lower bound, as shown in Fig. 10.9. The faster dynamic of the A/C system compared to the vehicle acceleration and deceleration transients suggest an intrinsically low sensitivity of the co-state dynamics to the initial conditions.

To further clarify the impact of the initial condition (λ_{10}, λ_{20}) on the optimal solution, a sensitivity study was performed where the two initial conditions for the co-state dynamics where increased by a factor of 10. The results are shown in Fig. 10.10. Results show that, after few seconds, the co-states of the sub-optimal controller converge to the optimal trajectories and, after that, the two control policies are the same. This is justified by the fact that the dynamic of the A/C system is much faster than the dynamic of the vehicle and that the amount of energy available to be stored in form of lower pressure in the evaporator is also much smaller thanthe energy in play for any coasting or breaking events.

In addition to the marginal changes in control sequence and the pressure dynamics, the sub-optimal initial conditions result only into a marginal degradation of the overall performance, as reported in Table 10.3. Here, a sub-optimal estimation of the initial conditions results in a marginal increase of the fuel consumption by 0.01 %, while performing slightly better in the tracking of the desired pressure.

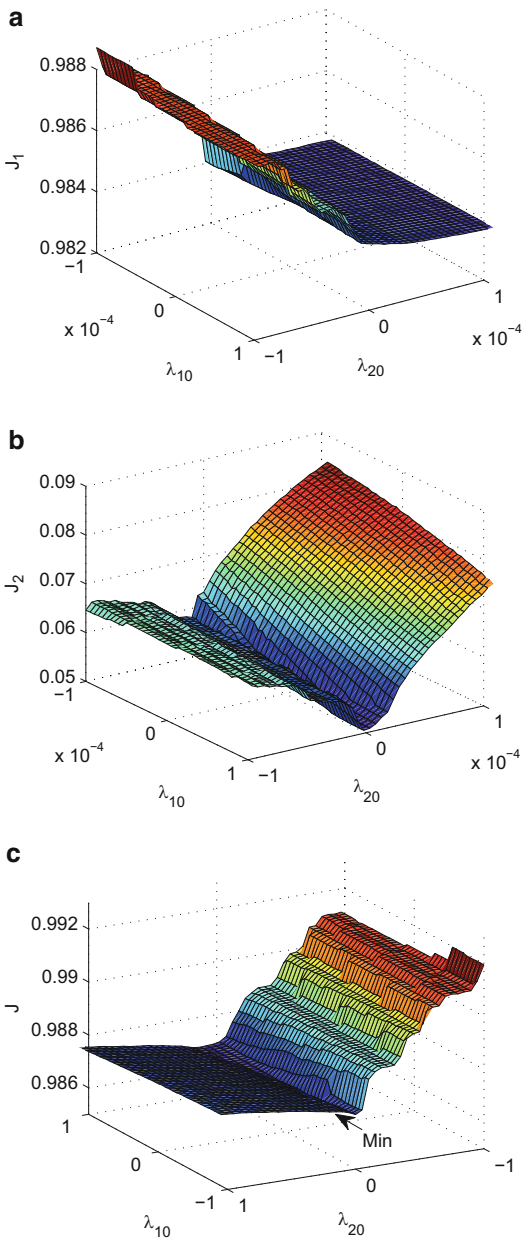

Fig. 10.8 Results of shooting method for equivalent control. (**a**) Objective function J_1. (**b**) Objective function J_2. (**c**) Objective function J

This result is of particular interest, and could be leveraged for the derivation of a practical algorithm for the energy management of the A/C system that does not depend upon the off-line solution of a two-points boundary value problem.

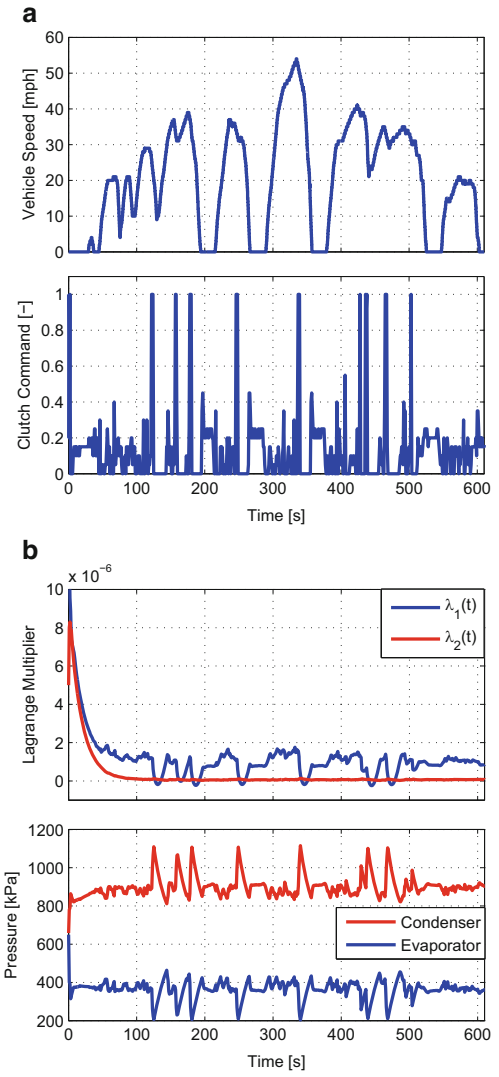

Fig. 10.9 Simulation results for optimal equivalent control (SC03 cycle). (**a**) Vehicle speed and optimal clutch command. (**b**) Co-states and A/C system pressures

10.4.2 Projection Results and Comparison with Dynamic Programming

Since the solution of the embedded control problem is continuous, the solution of the original switching control problem is found by projecting the embedded solution such that $\pi(t) \in \{0, 1\}$ [32]. It is clear, however, that the projected solution leads to a sub-optimal control policy.

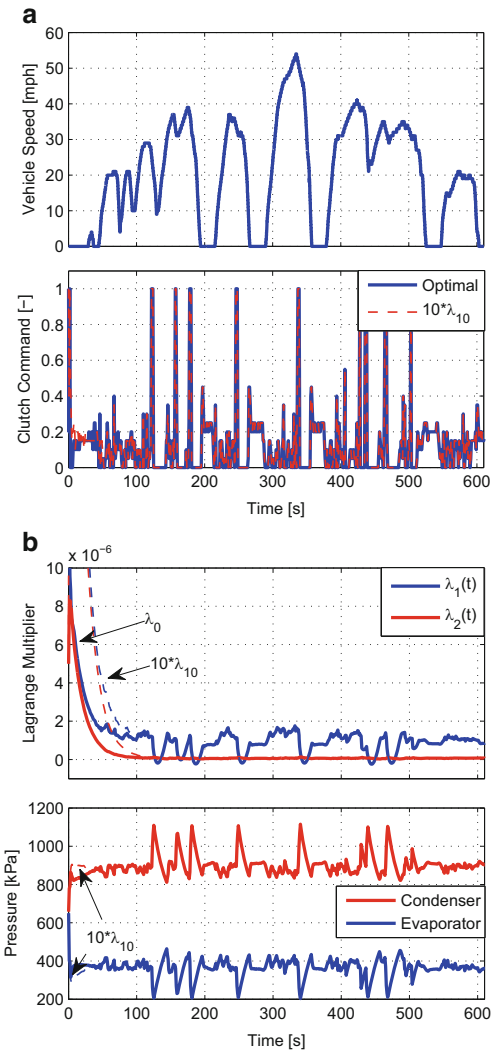

Fig. 10.10 Influence of initial conditions on the co-state dynamics. (**a**) Vehicle speed and optimal clutch command. (**b**) Co-states and a/c system pressures

Table 10.3 Sensitivity of the optimal solution to initial conditions of co-state dynamics

	J_1	J_2	J
Optimal	0.9842	0.0537	0.9868
Sub-optimal	0.9843	0.0523	0.9869

For this application, a solution in the form of a duty cycle command was defined to approximate a general continuous control input $u(.)$, as shown in Fig. 10.11. For each time interval T, which corresponds to the duration of the duty cycle, the following relation must hold:

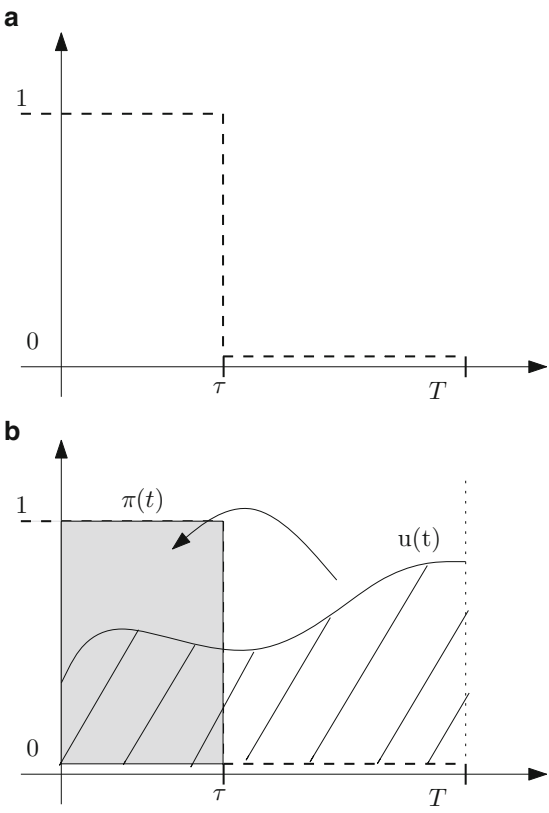

Fig. 10.11 Illustration of the method for projection of the equivalent control. (**a**) General form and parameters of duty cycle command. (**b**) Determination of duty cycle command τ

$$\int_0^T u(t)dt = \int_0^T \pi(t)dt = \int_0^\tau 1dt + \int_\tau^T 0dt = \tau \tag{10.44}$$

To determine the duration T of the duty cycle, the DP solution obtained for the original problem (switched system with cost of switching) was analyzed. Figure 10.12 shows the distribution of the times between two "clutch-on" events. The maximum time for the SCO3 cycle has been found to be about 45 s, while the average time is 35 s. Different duty cycle durations have been tested for the projection and a good compromise between number of clutching events, tracking performance, and fuel consumption has been found using the minimum time between two *on*.

The results obtained with the equivalent control are shown in Fig. 10.13 compared to the global optimal solution. The projected control presents a similar behavior compared to the DP in terms of evolution of the evaporator pressure as well as control actuation, but presents differences in the condenser pressure. The overall metrics for both, the DP and equivalent controller, are summarized in Table 10.4.

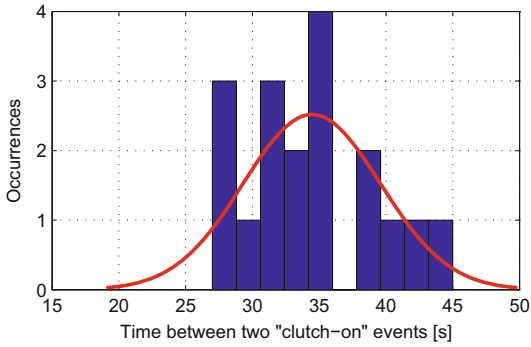

Fig. 10.12 Statistical analysis of the clutch switching frequency predicted by the DP solution

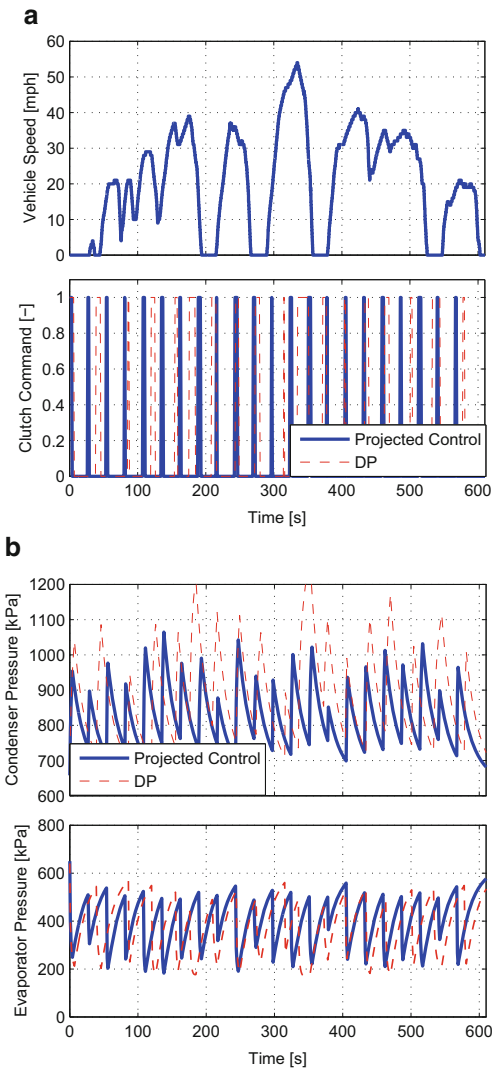

Fig. 10.13 Simulation results for the projected control and comparison with dynamic programming solution. (**a**) Vehicle speed and clutch command. (**b**) A/C condenser and evaporator pressure

Table 10.4 Comparison of the projected controller and DP solution

	J_1	J_2	J_3	J	M_{fuel} (g)	RMS_p (%)	n_{clutch}
Baseline	0.9985	0.0702	0.0474	1.0129	415.9	31	29
DP	0.9838	0.1485	0.0278	0.9961	409.9	25	37
Projected Control	0.9848	0.157	0.0686	1.0047	410.3	33	39

The projected controller was successfully design to limit the number of switchings: 39 occurrences against 37, which is the global optimal for the complete control problem. While the controller is sub-optimal with respect to fuel economy and tracking performance when compared to the DP result, the performance loss is only marginal, and still represents a significant improvement over the baseline control strategy.

An online implementation of the proposed controller could be easily achieved through simple considerations.

First, the sensitivity study on the initial conditions for the co-states could resolve the issue of solving a two-points boundary value problem, hence facilitating the implementation as a forward-looking strategy.

Furthermore, the projection required to define the switched control could be performed either completely off-line, as presented above, or performed partially online. For example, the solution of the embedded optimal control problem could be calculated for the time period T and then projected into an equivalent control by computing the duty cycle through Eq. (10.44). However, it is clear that this method would introduce a significant time delay in the control loop.

In this sense, model-predictive control could be a more suited approach to solve the embedded control problem and perform the projection online. This method appears particularly suited for this system due to its very fast dynamic compared to the time variation of the exogenous inputs. Moreover, a receding horizon technique can substantially limit the time delay introduced by the controller. Preliminary studies [33, 34] have shown promising results when combining the control of hybrid systems through embedding and the control projection.

References

1. M. Lyu, B. Doo, Y. Ku, A study of vehicle fuel economy improvement potential by optimization of the cooling and ancillary systems of a heavy duty engine. SAE Technical Paper No. 2007-01-1772 (2007)
2. C. Silva, R. Marc, T. Farias, Analysis and simulation of "low-cost" strategies to reduce fuel consumption and emissions in conventional gasoline light-duty vehicles. Energy Convers. Manag. **50**(2), 215–222 (2009)
3. F. Chiara, M. Canova, A review of energy consumption, management and recovery in automotive systems with considerations on future trends. Proc. Inst. Mech. Eng. Part D J. Automob. Eng. (2012)

4. J. Rugh, V. Hovland, S. Anderson, Significant fuel savings and emission reductions by improving vehicle air conditioning, in *15th Annual Earth Technologies Forum and Mobile Air Conditioning Summit, Washington, DC* (2004)
5. T. Qureshi, S. Tassou, Variable-speed capacity control in refrigeration systems. Appl. Therm. Eng. **16**(2), 103–113 (1996)
6. X. He, S. Liu, H. Asada, H. Itoh, Multivariable control of vapor compression systems. HVAC&R Res. **4**(3), 205–230 (1998)
7. R. Manski, T. Strauss, M. Kohl, M. Weinbrenner, Storage evaporators innovative ac concept for micro hybrid vehicles. SAE Technical Paper No. 2006-01-0268 (2006)
8. T. Harrison, Air conditioning system utilizing vehicle waste energy. SAE Technical Paper No. 2009-01-0543 (2009)
9. L.F. Larsen, T. Geyer, M. Morari, Hybrid model predictive control in supermarket refrigeration systems. *Proceedings of 2005 IFAC World Congress Praha* (2005)
10. D. Sarabia, F. Capraro, L.F. Larsen, C. de Prada, Hybrid control of a supermarket refrigeration systems, in *American Control Conference, 2007 (ACC'07)* (IEEE, 2007), pp. 4178–4185
11. C. Sonntag, A. Devanathan, S. Engell, O. Stursberg, Hybrid nonlinear model-predictive control of a supermarket refrigeration system, in *IEEE International Conference on Control Applications, 2007 (CCA 2007)* (IEEE, 2007), pp. 1432–1437
12. Q. Zhang, M. Canova, Lumped-parameter modeling of an automotive air conditioning system for energy optimization and management, in *Dynamic Systems and Control Conference (DSCC)* (ASME, 2013)
13. B. Li, A. Alleyne, A dynamic model of a vapor compression cycle with shut-down and start-up operations. Int. J. Refrig. **33**(3), 538–552 (2010)
14. G. Davis, F. Chianese, T. Scott, Computer simulation of automotive air conditioning-components, system, and vehicle. SAE Technical Paper 720077 (1972)
15. T. Scott, S. Sundaram, Robust compressor model for ac system simulation. SAE Technical Paper 2007-01-0596 (2007)
16. V. Chlumsky, *Reciprocating and Rotary Compressors* (E & F Spon Ltd, London, 1965)
17. M.C.Q. Zhang, Lumped-parameter modeling of an automotive air conditioning system for energy optimization and management, in ASME Dynamic Systems and Control Conference (2013)
18. M. Browne, P. Bansal, Transient simulation of vapour-compression packaged liquid chillers. Int. J. Refrig. **25**(5), 597–610 (2002)
19. M. Kumar, I. Kar, A. Ray, State space based modeling and performance evaluation of an air-conditioning system. HVAC&R Res. **14**(5), 797–816 (2008)
20. J. Jensen, Dynamic modeling of thermo-fluid systems. Ph.D. Dissertation, Department of Energy Engineering Institute for Energiteknik, Technical University of Denmark (Danmarks Tekniske Universitet) (2003)
21. K.S. Ramesh, P.S. Dusan, *Fundamentals of Heat Exchanger Design* (Wiley, New York, 2003)
22. L. Tong, Y. Tang, *Boiling Heat Transfer and Two-Phase Flow* (Taylor & Francis, London, 1997)
23. R. Sonntag, C. Borgnakke, G. Van Wylen, *Fundamentals of Thermodynamics* (Wiley, New York, 1998)
24. F.P. Incropera, *Introduction to Heat Transfer* (Wiley, New York, 2011)
25. W.M. Kays, A.L. London., *Compact Heat Exchangers* (McGraw Hill, New York, 1984)
26. Y. Chang, C. Wang, A generalized heat transfer correlation for Iouver fin geometry. Int. J. Heat Mass Transf. **40**(3), 533–544 (1997)
27. M. Kim, C. Bullard, Air-side thermal hydraulic performance of multi-louvered fin aluminum heat exchangers. Int. J. Refrig. **25**(3), 390–400 (2002)
28. D.P. Bertsekas, *Dynamic Programming and Optimal Control*, vol. 1, no. 2 (Athena Scientific, Belmont, 1995)
29. O. Sundstrom, L. Guzzella, A generic dynamic programming matlab function, in *IEEE International Conference on Control Applications, (CCA) & Intelligent Control, (ISIC)* (IEEE, 2009), pp. 1625–1630

30. L. Serrao, S. Onori, G. Rizzoni, ECMS as a realization of Pontryagin's minimum principle for HEV control, in *American Control Conference, 2009 (ACC'09)* (IEEE, 2009), pp. 3964–3969
31. C. Zhang, A. Vahidi, Route preview in energy management of plug-in hybrid vehicles. IEEE Trans. Control Syst. Technol. **20**(2), 546–553 (2012)
32. S.C. Bengea, R.A. DeCarlo, Optimal control of switching systems. Automatica **41**(1), 11–27 (2005)
33. R. Meyer, R.A. DeCarlo, P.H. Meckl, C. Doktorcik, S. Pekarek, Hybrid model predictive power flow control of a fuel cell-battery vehicle, in *American Control Conference (ACC), 2011* (IEEE, 2011), pp. 2725–2731
34. J. Neely, S. Pekarek, R. DeCarlo, N. Vaks, Real-time hybrid model predictive control of a boost converter with constant power load, in *Twenty-Fifth Annual IEEE Applied Power Electronics Conference and Exposition (APEC), 2010* (IEEE, 2010), pp. 480–490
35. Q. Zhang, S. Stockar, M. Canova, Energy-optimal control AQ1 of an automotive air conditioning system for ancillary load reduction. IEEE Trans. Control Syst. Technol. **24**(1), 67–80 (2016)

Chapter 11
Modeling Air Conditioning System with Storage Evaporator for Vehicle Energy Management

Quansheng Zhang and Marcello Canova

Abstract Automotive air conditioning (A/C) system significantly affects fuel consumption and emission. Thus, phase change material (PCM) is exploited in an innovative storage evaporator to improve the A/C system performance. Due to hybrid features introduced by mode switching when PCM changes its status between liquid and solid, the task of control-oriented modeling is particularly challenging. Upon the energy-based model built, optimal control of an advanced A/C system with a storage evaporator is formulated as to find an optimal clutch command sequence balancing fuel consumption, cabin comfort, and drivability constraints. In the scope of vehicle energy management, dynamic programming (DP) algorithm usually serves as a tool of obtaining benchmark optimal solution against which results from other optimal algorithms are compared. However, a direct application of DP algorithm to the optimization problem faces unexpected difficulty, because the discretization of state space is not feasible for an irregular multi-dimensional subspace formed by the multi-mode model. Alternatively, hybrid optimal control theory is pursued and a preliminary study is conducted to illustrate its promising application.

Keywords Air conditioning system • Storage evaporator • Phase change material • Dynamic programming • Hybrid optimal control

Nomenclature

TP	Two Phase
SH	Superheated
SC	Subcooled
N	Compressor Speed
T	Temperature

Reprinted from Zhang and Canova (2015), with permission from Elsevier.

Q. Zhang (✉) • M. Canova
Center for Automotive Research, The Ohio State University, 930 Kinnear Road, Columbus, OH 43212, USA
e-mail: zhang.777@osu.edu

Q. Zhang et al., *Automotive Air Conditioning*, DOI 10.1007/978-3-319-33590-2_11

a air
c Condenser
cmp Compressor
e Evaporator
g gas
h Enthalpy
l liquid
p Pressure
v Valve
$\dot{m}$ Mass Flow Rate
$\dot{Q}$ Heat Transfer Rate
α Valve Position
γ Void Fraction
δ uncertainty
ρ Density

11.1 Introduction

Automotive A/C system has profound effects on the vehicle fuel economy. The majority of A/C system is still heuristically controlled and operates in an inefficient way. An analysis conducted in NREL [1] showed that the use of systems is equivalent to 5.5 % of the domestic light duty vehicle fuel consumption. Two directions are mainly pursued in order to reduce fuel consumption of A/C system, namely model-based optimization and control design as well as hardware upgrades. The mass migration and heat transfer inside refrigerant loop are usually modeled using energy-based method [2], and its energy management is a typical multi-objective optimization problem balancing fuel consumption, cooling requirement, and mechanical weariness [3]. In [4–8], the optimal compressor clutch sequence is found using online implementable model predictive control (MPC) method. Recently, storage evaporator [9] is introduced to improve A/C system performance, because it increases thermal inertia and expands energy storage capability when the PCM changes its status between liquid and solid.

PCM has been widely applied in industrial areas, such as solar power plants, electronic devices, and transport [10, 11]. Depending on the specific application, different models have been developed to characterize the heat transfer and phase change dynamics. Generally, these models belong to two model categories, namely distributed-parameter model and lumped-parameter model. In [12–14], the phase change material (PCM) is treated as a one dimensional heat transfer model, a partial differential equation with boundary conditions specified. In [15], a simplified dynamic model is developed for predicting the energy impact due to the addition of the PCM. Usually, these models are tailored for performance analysis at design stage, helping the designers determine appropriate geometric parameters or material

types. However, little attention has been paid to the optimal operation of the PCM after the design stage.

This chapter is aimed to apply optimal control theory on automotive A/C system with storage evaporator. This work is challenging as it requires the modeling of phase change dynamics and choice of appropriate control methods. The A/C loop dynamics changes significantly over PCM status, such as completely frozen, freezing/melting, and completely melt. In other words, hybrid system dynamics exists and should be captured by the control-oriented model developed. The hybrid feature also affects the optimization process, as optimization algorithms applicable only in continuous domain might fail. Therefore, hybrid optimal control theory specifically developed for hybrid system is pursued herein. Different versions of hybrid minimum principle (HMP) exist. A general version of the HMP is presented by Sussmann [16] based on a set of needle variations and a Boltyanski approximation cone. Two versions of HMPs are introduced by Riedinger et al. [17, 18] and Shaikh and Caines [19] for hybrid systems with autonomous and controlled switching. Although the above HMPs have solid theoretical foundation, it has hardly been applied to a practical problem before, like the energy management of A/C system. Therefore, this chapter is aimed to illustrate the benefit of storage evaporator and the potential application of hybrid optimal theory on the A/C system energy management.

The chapter is organized as follows. Section 11.2 models the A/C system dynamics using a lumped-parameter approach and resulted system equations are in descriptor form. Section 11.3 compares the performances between storage evaporator and conventional evaporator, and identifies the benefits of enhanced thermal inertia. Section 11.4 fits the problem of optimal control of A/C system into the field of vehicle energy management, and tests two common optimization algorithms for a specific driving scenario.

11.2 Modeling A/C System with Storage Evaporator

As shown in Fig. 11.1, the A/C system of a passenger car is generally based on a simple vapor compression cycle realized through a fixed-displacement rotary piston compressor, a condenser heat exchanger with a fan, a receiver/drier, an evaporator with a blower, and a thermal expansion valve. The compressor is clutched on/off to remove heat from the air flowing through the evaporator and reject heat into the air flowing through the condenser, determined by the blower and fan rotation speed, respectively.

In an innovative A/C loop, the conventional evaporator is replaced with a storage evaporator with PCM added [9]. Physically, PCM in the outer tube is assembled around an inner tube which the refrigerant flows through. When the compressor is turned on, the refrigerant evaporates to solidify PCM that further cools down air flowing fins; when the compressor stops, the PCM starts to melt to prevent the air temperature rising up quickly until it is completely melted.

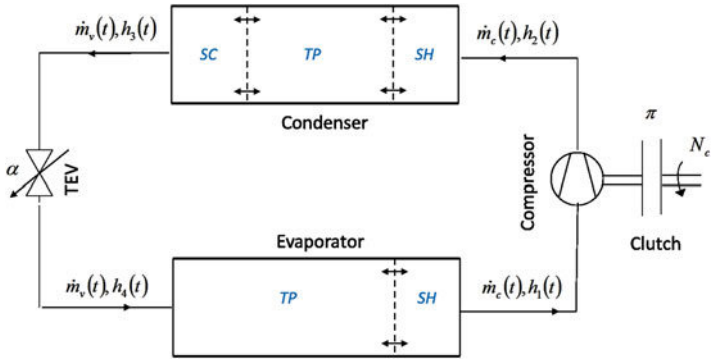

Fig. 11.1 Conventional A/C loop with refrigerant phase change

In addition to the refrigerant phase change between vapor and liquid, another phase change happens in the storage evaporator is the PCM melting or freezing between liquid and solid, both of which need to be captured in order to fully characterize the dynamics of the storage evaporator. In order to develop a supervisory controller, it is necessary to build suitable control-oriented A/C models balancing model accuracy and simulation time. Therefore, an energy-based model for the A/C system with storage evaporator is developed herein with major assumptions introduced sequentially to minimize the model complexity, since the computation burdens of optimization algorithms later developed strongly rely on the total number of states within the A/C model.

11.2.1 Lumped-Parameter Modeling Approach

The methodology of building a high-fidelity A/C model is generally classified into two categories, namely finite-volume method and moving-boundary method. However, the total number of system states in both cases is much more than the level that can be tolerated by those optimization algorithms commonly adopted in vehicle energy management. The main drawback of both methods is that the physical properties are treated as distributed parameters, meaning that a group of thermodynamic variables are required to characterize the thermo-fluid dynamics inside individual control volume. Therefore, a lumped-parameter modeling approach is adopted to facilitate future optimization algorithms development.

Assumption 1. The temperature spatial distribution of refrigerant, wall and PCM is uniform along the tube length direction.

Hence, the condenser is modeled as a lumped thermal mass with two control volumes representing, respectively, the volume occupied by the refrigerant circulating in the tubes and the metal mass (walls). Similarly, the evaporator consists of four

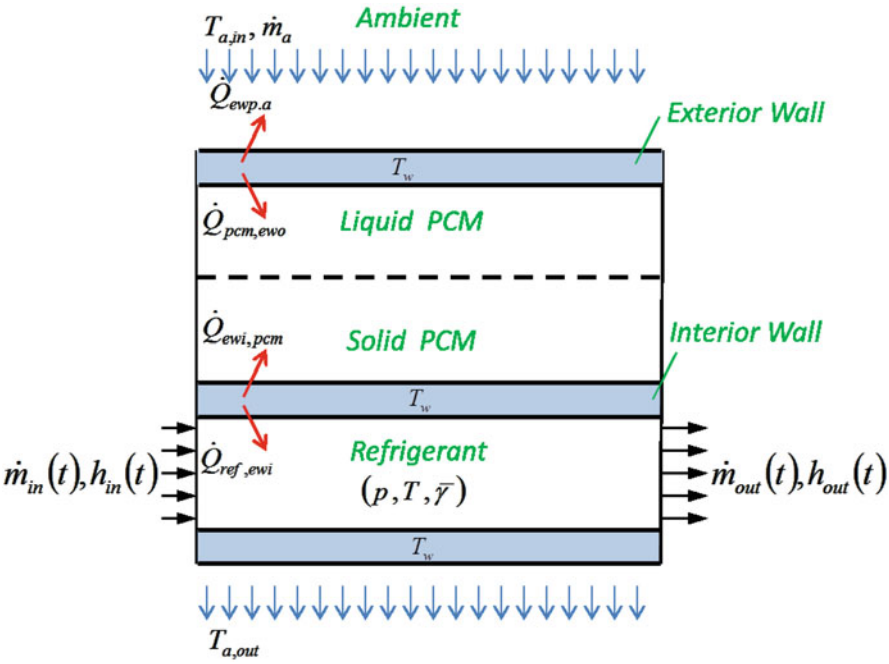

Fig. 11.2 Schematic of heat exchanger with PCM included (PCM in lower part is not drawn)

control volumes, two of which are closely related to PCM dynamics. Considering the schematic of a storage evaporator with refrigerant flowing in the inner tube and PCM stored in the outer tube, as shown in Fig. 11.2, the spatially average PCM temperature T_{pcm} and exterior wall temperature T_{ewo} are determined by the heat transfer rates between refrigerant, PCM, and air.

Following the assumption, an energy balance can be formulated for the PCM control volume:

$$\frac{d}{dt}(V\rho u) = \dot{Q}_{\text{ewi,pcm}} + \dot{Q}_{\text{pcm,ewo}} \tag{11.1}$$

where $\dot{Q}_{\text{ewi,pcm}}$ is heat transfer rate between the interior tube wall and the PCM, and $\dot{Q}_{\text{pcm,ewo}}$ is the heat transfer rate between the PCM and the exterior tube wall.

The energy balance equation for the exterior tube wall is

$$M_{\text{ewo}} c_{p,\text{ewo}} \frac{dT_{\text{ewo}}}{dt} = -\dot{Q}_{\text{pcm,ewo}} - \dot{Q}_{\text{ewo},a} \tag{11.2}$$

where M_{ewo} is the exterior wall mass, $c_{p,\text{ewo}}$ is the exterior wall specific heat, and $\dot{Q}_{\text{ewo},a}$ is the heat transfer rate between the exterior wall and air.

The heat transfer rate from the lumped PCM and exterior wall to the air, $\dot{Q}_{\text{pcm},a}$, is defined similar to $\dot{Q}_c$, and the heat transfer rate from the refrigerant to the lumped PCM and exterior wall, $\dot{Q}_{e,\text{pcm}}$, is determined mainly by their temperature difference.

$$\begin{aligned} \dot{Q}_{\text{pcm},a} &= \dot{m}_{a,e} c_{p,a} \left(T_{a,\text{out},e} - T_{a,\text{in},e}\right) \\ \dot{Q}_{e,\text{pcm}} &= K_{\text{pcm}} A \left(T_e - T_{\text{pcm}}\right) \end{aligned} \tag{11.3}$$

in which the heat transfer coefficient K_{pcm} is a piecewise function defined for each mode [15].

11.2.2 Refrigerant Dynamics

The dynamics on the refrigerant side involves both mass migration and heat transfer. Since the energy-based A/C model is tailored for vehicle energy management, the faster mass migration dynamics is simplified according to

Assumption 2. The compliance effects relative to the variations in mass flow rate in or out of the heat exchangers are negligible [20, 21].

This assumption preserves the low-frequency dynamics, driven mainly by the heat transfer process. Hence the refrigerant mass flow rate predicted by the compressor model is uniform throughout the system. When the clutch is engaged, the mass flow rate within the A/C loop is equal to the one calculated by the compressor model; when the clutch is disengaged, the mass flow rate within the A/C loop is null.

The compressor is treated as an algebraic element that outputs the refrigerant flow rate and enthalpy at the exit, as function of the thermodynamic conditions at the inlet, the condenser pressure, and the rotational speed:

$$\dot{m}_c = V_d \rho_1 \omega_c \eta_v, \qquad h_2 = h_1 + \frac{h_{2s} - h_1}{\eta_s} \tag{11.4}$$

where ω_c is the compressor rotation speed, V_d the compressor displacement, and h_{2s} the isentropic enthalpy.

As for the heat transfer process, the pressures inside the evaporator and condenser are of interest for the high-level controller managing vehicle energy, since the mechanical power entering the A/C loop through the compressor is stored in the pressurized refrigerant. In contrast, the variation of refrigerant temperature in different phase regions is out of scope, because it is only relevant to the low-level controller that regulates superheat temperature for safety consideration. Therefore, the refrigerant dynamics can be further simplified.

Assumption 3. The refrigerant within each heat exchanger is assumed present only in two-phase.

Although this represents a drastic simplification of the physical behavior, the contribution of superheat or subcooled regions to the heat transfer is in practice limited [22]. Their influences might be compensated by the calibration parameters in the energy-based A/C model, namely the tuning factors multiplying the heat transfer coefficients.

After mathematical derivations detailed in [2], the final energy balance equations for the refrigerant inside both evaporator and condenser are

$$\begin{aligned} V_e \Bigg[& (1-\bar{\gamma_1}) \frac{\partial \left(\rho_l h_l\right)_e}{\partial p_1} + \bar{\gamma_1} \frac{\partial \left(\rho_g h_g\right)_e}{\partial p_1} + \left(\rho_g h_g - \rho_l h_l\right)_e \frac{\partial \bar{\gamma_1}}{\partial p_1} - 1 \\ & + \frac{M_{we} c_e}{V_e} \left(\frac{\partial T_1}{\partial p_1}\right) \Bigg] \frac{dp_1}{dt} = \dot{Q}_e + \pi \dot{m} \left(h_4 - h_1\right) \\ V_c \Bigg[& (1-\bar{\gamma_2}) \frac{\partial \left(\rho_l h_l\right)_c}{\partial p_2} + \bar{\gamma_2} \frac{\partial \left(\rho_g h_g\right)_c}{\partial p_2} + \left(\rho_g h_g - \rho_l h_l\right)_c \frac{\partial \bar{\gamma_2}}{\partial p_2} - 1 \\ & + \frac{M_{wc} c_c}{V_c} \left(\frac{\partial T_2}{\partial p_2}\right) \Bigg] \frac{dp_2}{dt} = -\dot{Q}_c + \pi \dot{m} \left(h_2 - h_3\right) \end{aligned} \tag{11.5}$$

where the subscripts e and c indicate the evaporator and condenser heat exchanger, respectively.

Most of the parameters of the energy-based model can be easily related to design and geometric data of the heat exchangers, as well as to the properties of the fluids. In the single phase regions, the heat transfer correlation includes two parts [23]. For evaporation, the correlation proposed in [24] combines the nucleating boiling and convective boiling effects, $\alpha_{\text{tp}} = S\alpha_{\text{nb}} + F\alpha_{\text{sp}}$. For condensation, the correlation given by Koyama et al. [25] combines the influences of the forced convection Nu_F and gravity controlled convection Nu_B using an asymptotic expression $Nu = (Nu_F^2 + Nu_B^2)^{1/2}$. In addition, since the heat transfer coefficients on the refrigerant side have been neglected due to their high value, only the air side is considered in the model. The correlations to calculate the heat transfer coefficients adopted in this work are specific to cross-flow compact heat exchangers with louvers and fins, and have been proposed by Chang and Wang [26] and Kim and Bullard [27]. This simplifies the calibration process to identifying two multipliers, $k_{\alpha_{e,a}}$ and $k_{\alpha_{c,a}}$, which correct the heat transfer correlations for the air side of the two heat exchangers. Its ability to predict the energy consumption of the A/C system during transients was conducted against experimental data collected on the SC03 air conditioning test cycle [2].

11.2.3 PCM Mode Switching

The dynamics on PCM side involves only heat transfer. One main assumption proposed in [15] is adopted to facilitate the derivation of mathematical model for the PCM.

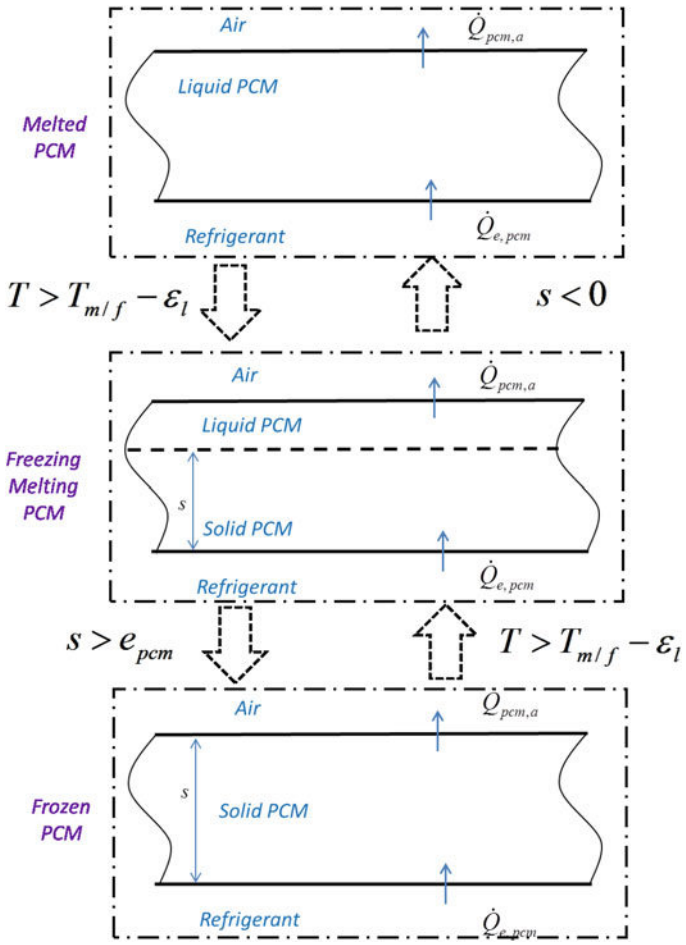

Fig. 11.3 Modes and mode switching condition

Assumption 4. The phase change process is slow enough to consider that heat transfer in the growing phase is in the steady state, and to assume a linear temperature profile in this phase.

In other words, the sensible heat in the growing phase is negligible compared to the latent heat involved, which is justified by the small Stefan number defined as $\text{Ste} = c_p(T_{\text{ewo}} - T_{\text{pcm}})/L_f = 2.59 \times 3/280 = 0.0267$.

The PCM in the storage evaporator undergoes three modes shown in Fig. 11.3 [15], namely freezing/melting mode, frozen mode, and melted mode. Depending on the modes, the left-hand side of Eq. (11.1) can be expressed in different ways.

At the freezing and melting modes, the PCM temperature T_{pcm} is fixed, and is equal to the phase change temperature T_{freezing} or T_{melting}. The latent heat caused by

phase change of the PCM between solid and liquid is used to store net heat transfer, resulting the solid PCM depth s varying. Hence, its energy balance equation using the solid PCM depth s as a state variable is written as.

$$\begin{cases} -\rho_{\text{pcm}} L_f A_c \frac{ds}{dt} = \dot{Q}_{e,\text{pcm}} + \dot{Q}_{\text{pcm,ewo}} \\ T_{\text{pcm}} = T_{\text{freezing}} = T_{\text{melting}} \end{cases} \tag{11.6}$$

where ρ_{pcm} is almost constant, L_f is the latent heat, and A_c is the cross sectional area of the PCM. The solid PCM depth s decreases if it absorbs heat and melts, and increases if it rejects heat and freezes. When the solid PCM depth s comes to zero, it switches into the completely melted mode; when the solid PCM depth s approaches the total PCM depth e_{pcm}, it switches into the completely frozen mode.

At the completely melted and completely frozen modes, the solid PCM depth s becomes 0 or e_{pcm}, respectively, and the PCM is in pure liquid or solid form. Its temperature T_{pcm} is determined by the heat transferred through the interior and exterior tube walls. The energy balance equations is

$$\begin{cases} s = \text{constant} \\ M_{\text{pcm}} C^s_{\text{pcm}} \frac{dT_{\text{pcm}}}{dt} = \dot{Q}_{e,\text{pcm}} + \dot{Q}_{\text{pcm,ewo}} \end{cases} \tag{11.7}$$

where M_{pcm} is PCM mass, C^s_{pcm} is PCM specific heat. At completely melted mode, when the PCM temperature T_{pcm} falls down to the freezing temperature T_{freezing}, it switches from melted mode to freezing mode. At completely frozen mode, when the PCM temperature T_{pcm} rises up to the melting temperature T_{melting}, it switches from the frozen mode to melting mode.

11.2.4 Descriptor Form

So far, the dynamics of the PCM and the exterior wall are separated. From the observation that the heat transfer dynamics is typically dominated by the fluid with the lowest convective heat transfer coefficient (the external air side), we propose the last assumption

Assumption 5. The heat transfer from the PCM to the walls is assumed infinitely fast [22].

In order to transform the system into a state space form with minimum number of states, the exterior wall temperature is eliminated by lumping the wall thermal capacitance into the PCM side, because the heat transfer coefficient between the PCM and the exterior wall is much bigger than the one between the exterior wall and the air.

$$M_{\text{ewo}} c_{p,\text{ewo}} \frac{dT_{\text{pcm}}}{dt} \approx M_{\text{ewo}} c_{p,\text{ewo}} \frac{dT_{\text{ewo}}}{dt} = -\dot{Q}_{\text{pcm,ewo}} - \dot{Q}_{\text{ewo},a} \tag{11.8}$$

When PCM is in melting/freezing mode, the PCM temperature T_{pcm} is not changed, indicating the variation of the exterior wall temperature T_{ewo} is negligible; When PCM is in melted or frozen modes, the PCM temperature T_{pcm} is changing, meaning that the thermal capacitance of the exterior wall should be considered.

Substitute Eq. (11.8) into Eq. (11.6), we get the differential equations describing the variation of PCM depth when it is in freezing and melting modes, as follows:

$$\begin{cases} -\rho_{\text{pcm}} L_f A_c \frac{ds}{dt} = \dot{Q}_{e,\text{pcm}} - \dot{Q}_{\text{pcm},a} \\ T_{\text{pcm}} = T_{\text{freezing}} = T_{\text{melting}} \end{cases} \tag{11.9}$$

Substitute Eq. (11.8) into Eq. (11.7), we get the differential equations describing the variation of PCM temperature when it is melted and frozen modes, as follows:

$$\begin{cases} s = \text{constant} \\ \left(M_{\text{pcm}} C^s_{\text{pcm}} + M_{\text{ewo}} c_{P,\text{ewo}} \right) \frac{dT_{\text{pcm}}}{dt} = \dot{Q}_{e,\text{pcm}} - \dot{Q}_{\text{pcm},a} \end{cases} \tag{11.10}$$

In order to merge Eqs. (11.9) and (11.10) into one set of differential equations, logic statement is incorporated into system dynamics as suggested in Eq. (11.11). The two forms are mathematically equivalent if a logic statement on PCM temperature is incorporated in depth dynamics and a logic statement on PCM depth is incorporated in temperature dynamics.

$$\begin{aligned} -\rho_{\text{pcm}} L_f A_{\text{pcm}} \frac{ds}{dt} &= [T \in (T_{m/f} - \epsilon_l, T_{m/f} + \epsilon_u)] \cdot (\dot{Q}_{e,\text{pcm}} - \dot{Q}_{\text{pcm},a}) \\ \left(M_{\text{pcm}} C^s_{\text{pcm}} + M_{\text{ewo}} c_{p,\text{ewo}} \right) \frac{dT_{\text{pcm}}}{dt} &= [s \notin (0, e_{\text{pcm}})] \cdot (\dot{Q}_{e,\text{pcm}} - \dot{Q}_{\text{pcm},a}) \end{aligned} \tag{11.11}$$

The energy-based A/C model with a storage evaporator can be expressed in descriptor form to facilitate its implementation and its use for control design. Note that the aforementioned model combining Eqs. (11.5) and (11.11) representative of a four-state nonlinear system and can be formulated as:

$$\begin{aligned} D(x)\dot{x} &= f(x, u, v) \\ y &= g(x, u, v) \end{aligned} \tag{11.12}$$

11.3 On/Off Cycle Evaluation of Storage Evaporator

The above storage evaporator model is implemented in Matlab/StateFlow with switching conditions labeled in Fig. 11.3. The completely frozen and melt modes change to each other through an intermediate mode named melting/freezing mode.

The condition indicating leaving the intermediate mode is that the solid PCM depth reach its physical limits, and the condition indicating entering the intermediate mode is that the PCM temperature T_{pcm} approaches the fixed phase change temperature specified by the PCM property.

Two major benefits exist if the evaporator thermal inertia is increased by adding PCM. Firstly, the increase of discharge temperature of the storage evaporator, compared to the standard evaporator, is significantly delayed, resulting in prolonged idle-stop time of the compressor. Secondly, the losses due to the refrigerant displacement during on/off cycles are reduced since the on/off cycle period become much longer than before. Simulation results supporting the possibility of both benefits are available using thermophysical properties of a eutectic aqueous solution provided in [15] and summarized in Table 11.1. Various phase change temperature, PCM thickness, and thermal loads can affect the simulation results. In current simulation, all relevant parameters are chosen intentionally so that a complete melting/freezing process exists when enough on/off time period is provided (Fig. 11.4).

A complete on/off cycle is shown in Fig. 11.5 with refrigerant temperature, PCM temperature, and discharge air temperature recorded. At the beginning of the cycle, all three temperatures are set to ambient temperature (here 20 °C). When

Table 11.1 Thermophysical properties of PCM

Symbol	Unit	Value	Explanation
L_f	kJ kg^{-1}	280	Latent heat
λ_s	$\text{W m}^{-1}\text{K}^{-1}$	1.8	Solid PCM thermal conductivity
λ_l	$\text{W m}^{-1}\text{K}^{-1}$	0.6	Liquid PCM thermal conductivity
ρ_s	kg m^{-3}	1042	Solid PCM density
ρ_l	kg m^{-3}	1115	Liquid PCM density
C_p	$\text{J kg}^{-1}\text{K}^{-1}$	2592	Specific heat

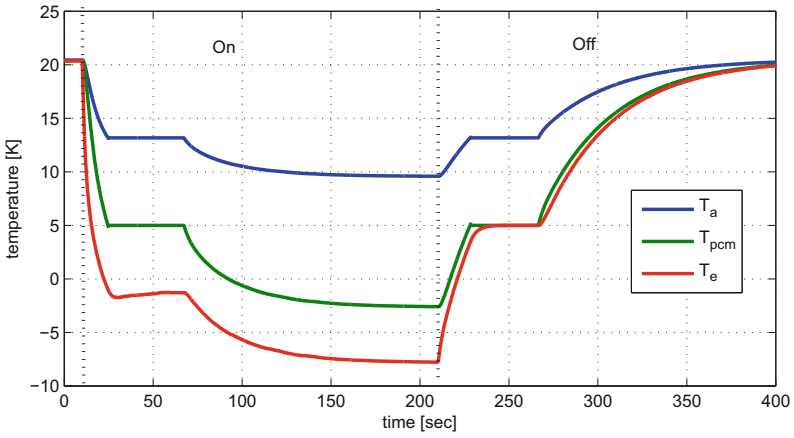

Fig. 11.4 Temperature profiles of evaporator with phase change material

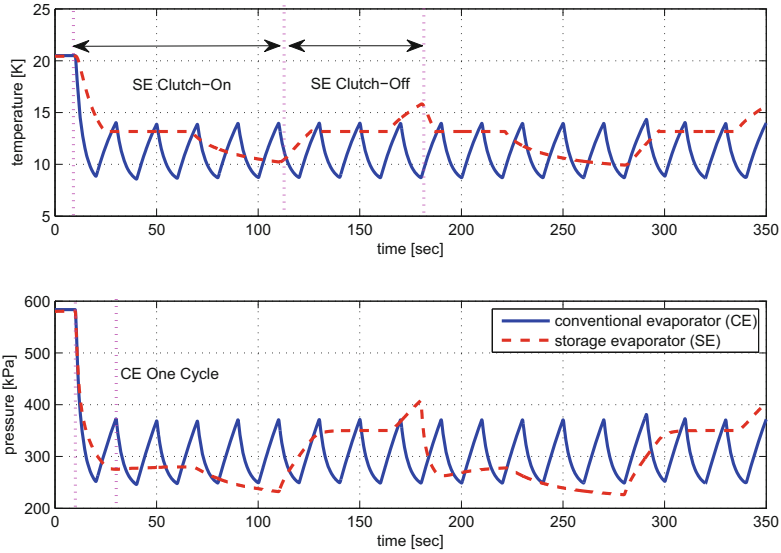

Fig. 11.5 Evolution of discharge temperature and evaporator pressure with and without PCM

clutch is engaged, refrigerant is propelled by the compressor into condenser and the evaporator pressure falls down, causing all three temperatures reduced. Since the melting/freezing temperature is set as 5 °C, the PCM temperature does not stop dropping until it reaches this physical limit. As soon as the freezing temperature is reached, PCM starts to freeze, maintaining the three temperatures fixed for around 40 s. After the PCM is completely frozen, all three temperatures fall down again till an energy balance is established among refrigerant, PCM and air. A similar analysis might be conducted duping the clutch disengagement, expect that PCM suppress the rapid increase of evaporator pressure. From the profile of discharge temperature, it is obvious that 40 s delay helps impeding fast variation of discharge temperature and narrowing down its amplitude.

The addition of PCM has also an impact on the on/off periods of the A/C system. Two complete on/off cycles are presented for an advanced A/C system with storage evaporator in Fig. 11.5 with discharge air temperature and evaporator pressure recorded. As a comparison, the on/off period of the clutch command of an ordinary A/C system without storage evaporator is modulated so that the average discharge air temperatures of both cases are comparable to each other. Similarly, the average evaporator pressure of both cases are maintained almost the same. From simulation results, the periodic variation of conventional evaporator pressure is more frequent the storage evaporator pressure. The on cycle of the A/C system with PCM is five times longer and the off cycle is three time longer than the convectional A/C system. Hence, the cooling and efficiency losses caused temporary charges of the heat exchangers during on/off cycle is significantly reduced, besides compressor mechanical weariness.

11.4 Energy Management Strategy

The objective of a supervisory controller for the automotive A/C system is to operate the system in a way that reduces the compressor parasitic load in relation with the vehicle and engine operations, while maintaining the cabin comfort requirements and ensuring the reliability of the compressor clutch. Therefore the objective function for optimization problem is given by:

$$J = \alpha J_1 + \beta J_2 + \gamma J_3 \tag{11.13}$$

where α, β, and γ are the weighting factors.

$$\begin{cases} J_1 = \int_0^T \dot{m}_{\text{fuel}}(t)dt \\ J_2 = \int_0^T (T_1(t) - T_{1,0})^2 dt \\ J_3 = \int_{\Delta t}^T (\pi(t) - \pi(t-\tau))^2 dt \end{cases} \tag{11.14}$$

The first term considered is the total fuel consumption over a driving profile, with $\dot{m}_{\text{fuel}}(t)$ the instantaneous fuel consumption of the engine. The cabin comfort requirement is translated into a discharge temperature at the evaporator. Hence, a second term of the objective function represents a tracking error, where T_1 is the actual discharge temperature and $T_{1,0}$ is a reference value for the discharge temperature. Finally, to address both drivability issues and potential durability problems, an additional cost function is considered to prevent high frequency switching in the clutch signal, where $\pi(t)$ is the current clutch position, $\pi(t-\tau)$ is the clutch position at the previous time step and τ is the discretization time. The control objective is to find the optimal trajectories of the compressor clutch command that minimizes the overall objective function.

11.4.1 Difficulties Faced by DP Algorithm

DP is widely used in vehicle energy management. However, DP algorithm implemented in [28, 29] cannot be directly applied to the optimization problem, because it is impossible to discretize the feasible subspace over a storage evaporator model in hybrid format as explained below.

From the simulation results, it is found that the possible optimal solution, if projected from the global space $(p_1, p_2, s, T_{\text{pcm}})$ into a subspace confined by (s, T_{pcm}), always moves along the blue fold line in Fig. 11.6. When the PCM is completely melted, $s = 0$ and T_{pcm} changes between a lower threshold T_l and the phase changing temperature $T_{\text{freezing/melting}}$; when the PCM is either freezing or melting, $T = T_{\text{freezing}} = T_{\text{melting}}$ and s changes between zero and the maximum depth e_{pcm}; when the PCM is completely frozen, $s = s_{\text{pcm}}$, and T_{pcm} changes between the phase changing temperature $T_{\text{freezing/melting}}$ and a upper threshold T_h. Hence, any feasible solution cannot move out of the "Z" shape domain.

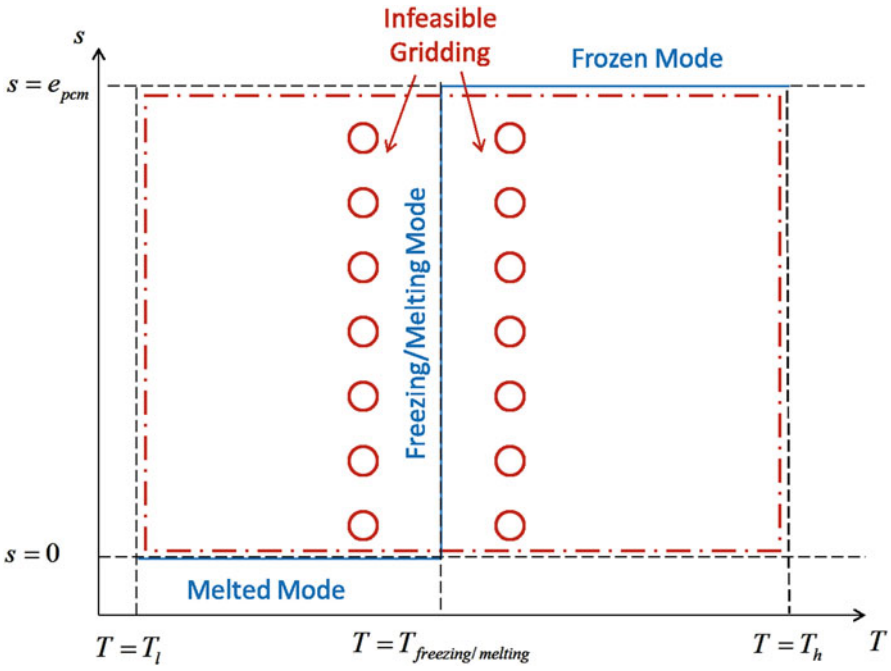

Fig. 11.6 DP failure due to discretization difficulty

In contrast, DP algorithm assumes that the feasible region is within a rectangular region outlined by $(s, T_{\text{pcm}}) = [0, e_{\text{pcm}}] \times [T_l, T_u]$. The numerical DP solver seeks to discretize the state space evenly, as depicted by the columns of red dots in Fig. 11.6. Obviously, a PCM during freezing or melting cannot have a temperature different from phase change temperature $T_{\text{freezing/melting}}$, since it is a hard constraint imposed by its physical property. Therefore, the DP algorithm implemented in [28, 29] fails at the very first step when the irregular subspace (s, T_{pcm}) needs gridding.

11.4.2 Hybrid Minimum Principle

Hybrid systems are systems whose dynamics are given by a coupling of continuous variables and modes in finite sets. A switched system, as a specific type of hybrid system, consists of several subsystems and a switching law, which takes places when a certain event signal is received. An event signal may be an external signal or an internal signal generated when an internal condition for the states, inputs, and/or time evolution is satisfied. An autonomous transition occurs if a switch manifold $m_{q_{j-1},q_j}(x) = 0$ is hit. A controlled transition occurs if there exists a discrete control input $\sigma_{q_{j-1},q_j} \in \Sigma_c$ such that $\Gamma(q_{j-1}, \sigma_{q_{j-1},q_j}(t_j)) \equiv \Gamma(q_{j-1}, \sigma_{q_{j-1},q_j}) = q_j$.

Table 11.2 Necessary conditions when objective functions defined with penalty terms

	Necessary conditions	
	Autonomous switching	Controlled switching
Costate dynamics	$\dot{\lambda} = -\frac{\partial H_q(x,\lambda,u)}{\partial x}$	
Hamiltonian minimization	$H_{q^0}(x^0, \lambda^0, u^0) \leq H_{q^0}(x^0, \lambda^0, v)$	
Costate continuity	$\lambda(t_j^-) = \lambda(t_j^+) + \nabla_x m_{j,j+1} + \nabla_x c$	$\lambda(t_j^-) = \lambda(t_j^+) + \nabla_x c$
Hamiltonian continuity	$H(t_j^-) = H(t_j^+) + \nabla_x m_{j,j+1} + \nabla_t c$	$H(t_j^-) = H(t_j^+) + \nabla_t c$

The energy management of A/C systems with storage evaporator is inherently a hybrid optimal control problem. The on/off operation sequence of the compressor clutch command is a controlled transition altering the dynamics of storing/releasing energy in the pressurized refrigerant. Besides, the mode switches among melted, melting, frozen, and freezing are triggered by either hitting the physical depth of the PCM or reaching the melting/freezing temperature. Upon these hybrid features, the problem is further complicated when the continuous actuators such as evaporator blower and condenser fan function.

For a hybrid system, its hybrid optimal problem is usually formulated using a hybrid objective function defined as:

$$\Sigma_{i=0}^{L} \int_{t_i}^{t_{i+1}} l_{q_i}(x_{q_i}(s), u(s))ds + g(x_{q_L}(t_f)) + c(x,t) \tag{11.15}$$

where $c(x,t)$ is a penalty on switching event. Necessary conditions for the above formulation are proposed in [30] and are summarized in detail in Table 11.2. Note that the Hamiltonian minimization condition over mode is no longer held. Instead, while all the continuity conditions are changed with gradients of penalty on switching events. In other words, switch might occur when the two Hamiltonians are matched, regardless of their relative values.

11.4.3 Preliminary Application to A/C System

An attempt is made to apply the HMP to the energy-optimal control of the A/C system. Some approximations are introduced at this point to simplify the mathematical complexity of the problem, with the objective of verifying the feasibility of the method to the optimal control of the A/C system. Specifically, the following assumptions are adopted to reduce the complexity while not causing significant changes to the A/C system dynamics and its hybrid optimal control formulation:

- The engine is assumed operating at constant speed and torque;

- The compressor torque is considered constant and independent of the evaporator and condenser pressure.

Based on the above, an attempt was made to apply the HMP to the energy-optimal control of the A/C system. If the A/C system model is written in hybrid form, the optimization problem is now characterized by the presence of two discrete inputs, namely ON when $\pi = 1$ and OFF when $\pi = 0$. In order to determine the mode selection, only two Hamiltonian functions corresponding to the ON/OFF inputs are required:

$$\begin{aligned} H_{\pi=1} &= L + \lambda_1 \frac{f_{1\text{on}}}{d_{11}} + \lambda_2 \frac{f_{2\text{on}}}{d_{22}} \\ H_{\pi=0} &= L + \lambda_1 \frac{f_{1\text{off}}}{d_{11}} + \lambda_2 \frac{f_{2\text{off}}}{d_{22}} \end{aligned} \tag{11.16}$$

where the Lagrangian function is the same as the one defined above, for the PMP application.

For simplicity of notation, define:

$$f_1 = \begin{cases} f_{1on} = -\dot{Q}_e + \dot{m}\,(h_4 - h_1)\,, & \text{if } \pi = 1; \\ f_{1off} = -\dot{Q}_e, & \text{if } \pi = 0. \end{cases} \tag{11.17}$$

$$f_2 = \begin{cases} f_{2on} = -\dot{Q}_c + \dot{m}\,(h_2 - h_3)\,, & \text{if } \pi = 1; \\ f_{2off} = -\dot{Q}_c, & \text{if } \pi = 0. \end{cases} \tag{11.18}$$

hence, the unified form of the Hamiltonian is

$$H = L + \lambda_1 \frac{f_1}{d_{11}} + \lambda_2 \frac{f_2}{d_{22}} \tag{11.19}$$

The costate dynamics is the partial differentiation of the Hamiltonian H over p_1 and p_2, respectively:

$$\begin{aligned} \tfrac{d\lambda_1(t)}{dt} &= -\bigtriangledown_{x_1} H = -(\tfrac{\partial L}{\partial p_1} + \lambda_1 \tfrac{\partial F_1}{\partial p_1} + \lambda_2 \tfrac{\partial F_2}{\partial p_1}) \\ \tfrac{d\lambda_2(t)}{dt} &= -\bigtriangledown_{x_2} H = -(\tfrac{\partial L}{\partial p_2} + \lambda_1 \tfrac{\partial F_1}{\partial p_2} + \lambda_2 \tfrac{\partial F_2}{\partial p_2}) \end{aligned} \tag{11.20}$$

The differentiation of L is trivial because only the quadratic tracking error includes two states explicitly. However, the analytical differentiation of F_i (defined as $d_{ii}^{-1} f$) is not straightforward and involves differentiation of the parameter d_{ii} and of the right-hand side term f, respectively.

$$\frac{\partial F_i}{\partial p_i} = -\frac{1}{d_{ii}^2} \frac{\partial d_{ii}}{\partial p_i} f_i + \frac{1}{d_{ii}} \frac{\partial f_i}{\partial p_i} \tag{11.21}$$

Note that the second order derivatives of the refrigerant properties with respect to the system pressures is mandatory to solve $\partial d_{ii}/\partial p_i$ analytically:

$$\frac{\partial d_{ii}}{\partial p_i} = (1-\bar{\gamma})\frac{d^2\rho_l h_l}{dp_i^2} + \bar{\gamma}\frac{d^2\rho_g h_g}{dp_i^2} + (\rho_g h_g - \rho_l h_l)\frac{d^2\bar{\gamma}_i}{dp_i^2} + \frac{\rho_w V_w c_{p,w}}{V_R}\frac{d^2 T_i}{dp_i^2} \quad (11.22)$$

On the other hand, $\partial f_i/\partial p_i$ is a piecewise function defined, respectively, for the cases of clutch engagement and disengagement:

$$\frac{\partial f_i}{\partial p_i} = \begin{cases} -\frac{\partial Q_i}{\partial p_i} + \dot{m}\frac{\partial \Delta h}{\partial p_i} + \Delta h\frac{\partial \dot{m}}{\partial p_i}, & \pi = 1; \\ -\frac{\partial Q_i}{\partial p_i}, & \pi = 0. \end{cases} \quad (11.23)$$

where the calculation of $\partial \dot{m}/\partial p_i$ requires analytical differentiation of the compressor model, including the complex correlations for the isentropic efficiency and the volumetric efficiency.

In order to avoid the significant complexity of conducting analytical differentiation of the above terms, look-up tables were generated off-line for the function F_i over different compressor speed, condenser pressure, and evaporator pressure, from

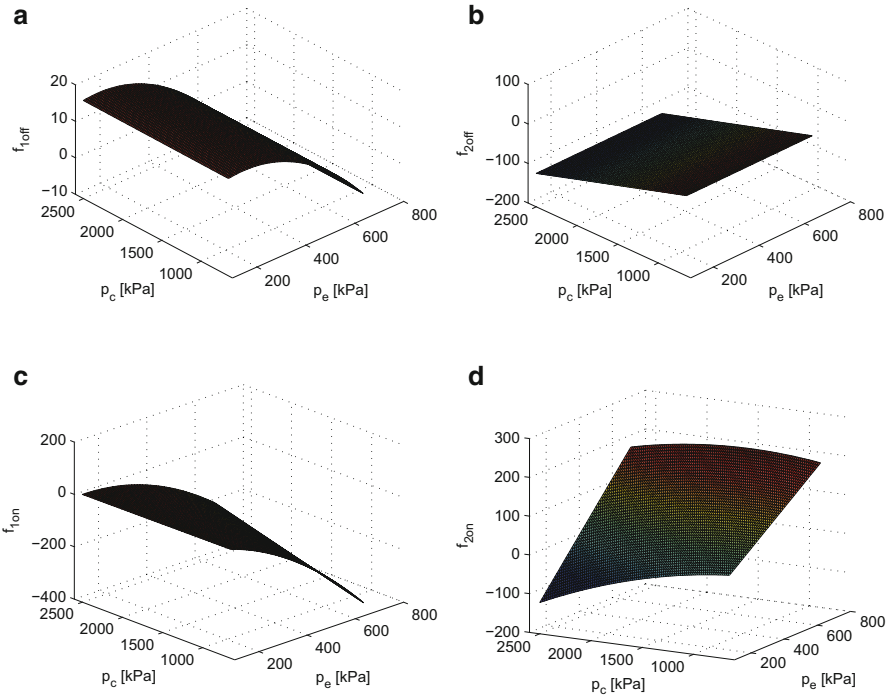

Fig. 11.7 Example of Mapping the Nonlinear Functions of the A/C Model. (**a**) Function $f_{1,\text{off}}$. (**b**) Function $f_{2,\text{off}}$. (**c**) Function $f_{1,\text{on}}$. (**d**) Function $f_{2,\text{on}}$

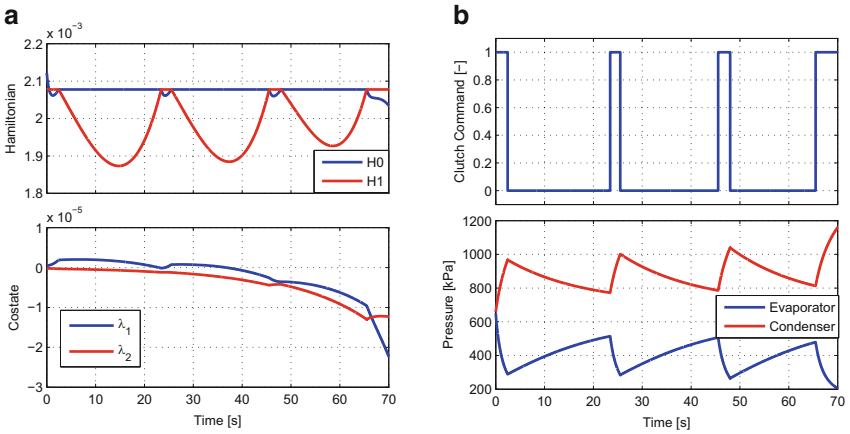

Fig. 11.8 Optimal Solution of the Simplified A/C System Using HMP-IDP. (**a**) Hamiltonian and costate. (**b**) Clutch command and pressures

which $\partial F_i/\partial p_i$ are then calculated through numerical differentiation and smoothing techniques. An example of the surfaces obtained for these functions is given in Fig. 11.7 for engine speed $N_e = 1300$ rpm.

In order to apply the hybrid optimal control theory, the shooting method is required to determine the optimal value for the initial conditions of the Lagrange multipliers, $(\lambda_{10}, \lambda_{20})$. A close observation to the optimal solution is shown in Fig. 11.8, limited to the first 60 s of simulation. The clutch command does not change the first time the two Hamiltonian functions intersect (around 5 s), but begins switching starting from the following intersection event, until the final time is reached. This is consistent with the HMP stating that the Hamiltonian matching is only a necessary conditions for the clutch command to switch.

References

1. J. Rugh, V. Hovland, S. Anderson, Significant fuel savings and emission reductions by improving vehicle air conditioning. *15th Annual Earth Technologies Forum and Mobile Air Conditioning Summit, Washington, DC* (2004)
2. Q. Zhang, M. Canova, Lumped-parameter modeling of an automotive air conditioning system for energy optimization and management, in *American Society of Mechanical Engineers (ASME) Dynamic Systems and Control Conference* (2013), pp. V001T04A003–V001T04A003
3. Q. Zhang, S. Stockar, M. Canova, Energy-optimal control of an automotive air conditioning system for ancillary load reduction. IEEE Trans. Control Syst. Technol. **24**(1), 67–80 (2016)
4. L.F. Larsen, T. Geyer, M. Morari, Hybrid model predictive control in supermarket refrigeration systems, in *Proceedings of 2005 IFAC World Congress Praha* (2005)
5. D. Sarabia, F. Capraro, L.F. Larsen, C. de Prada, Hybrid NMPC of supermarket display cases. Control Eng. Pract. **17**(4), 428–441 (2009)

6. C. Sonntag, A. Devanathan, S. Engell, O. Stursberg, Hybrid nonlinear model-predictive control of a supermarket refrigeration system, in IEEE International Conference on Control Applications (CCA) (IEEE, 2007), pp. 1432–1437
7. B. Solberg, P. Andersen, J.M. Maciejowski, J. Stoustrup, Optimal switching control of burner setting for a compact marine boiler design. Control Eng. Pract. **18**(6), 665–675 (2010)
8. T.G. Hovgaard, S. Boyd, L.F. Larsen, J.B. Jørgensen, Nonconvex model predictive control for commercial refrigeration. Int. J. Control **86**(8), 1349–1366 (2013)
9. R. Manski, T. Strauss, M. Kohl, M. Weinbrenner, Storage evaporators innovative ac concept for micro hybrid vehicles. SAE Technical Paper No. 2006-01-0268 (2006)
10. B. Zalba, J.M. Marın, L.F. Cabeza, H. Mehling, Review on thermal energy storage with phase change: materials, heat transfer analysis and applications. Appl. Therm. Eng. **23**(3), 251–283 (2003)
11. M.M. Farid, A.M. Khudhair, S.A.K. Razack, S. Al-Hallaj, A review on phase change energy storage: materials and applications. Energy Convers. Manag. **45**(9), 1597–1615 (2004)
12. F. Wang, G. Maidment, J. Missenden, R. Tozer, The novel use of phase change materials in refrigeration plant. part 1: experimental investigation. Appl. Therm. Eng. **27**(17), 2893–2901 (2007)
13. F. Wang, G. Maidment, J. Missenden, R. Tozer, The novel use of phase change materials in refrigeration plant. part 2: dynamic simulation model for the combined system. Appl. Therm. Eng. **27**(17), 2902–2910 (2007)
14. F. Wang, G. Maidment, J. Missenden, R. Tozer, The novel use of phase change materials in refrigeration plant. part 3: PCM for control and energy savings. Appl. Therm. Eng. **27**(17), 2911–2918 (2007)
15. K. Azzouz, D. Leducq, D. Gobin, Performance enhancement of a household refrigerator by addition of latent heat storage. Int. J. Refrig. **31**(5), 892–901 (2008)
16. H.J. Sussmann, A maximum principle for hybrid optimal control problems, in *Proceedings of the 38th IEEE Conference on Decision and Control*, vol. 1 (IEEE, 1999), pp. 425–430
17. P. Riedinger, F. Kratz, C. Iung, C. Zanne, Linear quadratic optimization for hybrid systems, in *Proceedings of the 38th IEEE Conference on Decision and Control*, vol. 3 (IEEE, 1999), pp. 3059–3064
18. P. Riedinger, C. Zanne, F. Kratz, Time optimal control of hybrid systems, in *Proceedings of the 1999 American Control Conference*, vol. 4 (IEEE, 1999), pp. 2466–2470
19. M.S. Shaikh, P. Caines, On the hybrid optimal control problem: theory and algorithms. IEEE Trans. Autom. Control **52**(9), 1587–1603 (2007)
20. M. Browne, P. Bansal, Transient simulation of vapour-compression packaged liquid chillers. Int. J. Refrig. **25**(5), 597–610 (2002)
21. M. Kumar, I. Kar, A. Ray, State space based modeling and performance evaluation of an air-conditioning system. HVAC&R Res. **14**(5), 797–816 (2008)
22. J. Jensen, Dynamic modeling of thermo-fluid systems. Ph.D. Thesis, Department of Energy Engineering Institute for Energiteknik, Technical University of Denmark (Danmarks Tekniske Universitet) (2003)
23. M. Steinke, S. Kandlikar, Single-phase liquid heat transfer in microchannels, in *International Conference on Microchannels and Minichannels* (2005)
24. W. Zhang, T. Hibiki, K. Mishima, Correlation for flow boiling heat transfer in mini-channels. Int. J. Heat Mass Transf. **47**(26), 5749–5763 (2004)
25. S. Koyama, K. Kuwahara, K. Nakashita, K. Yamamoto, An experimental study on condensation of refrigerant r134a in a multi-port extruded tube. Int. J. Refrig. **26**(4), 425–432 (2003)
26. Y. Chang, C. Wang, A generalized heat transfer correlation for Iouver fin geometry. Int. J. Heat Mass Transf. **40**(3), 533–544 (1997)
27. M. Kim, C. Bullard, Air-side thermal hydraulic performance of multi-louvered fin aluminum heat exchangers. Int. J. Refrig. **25**(3), 390–400 (2002)
28. O. Sundstrom, L. Guzzella, A generic dynamic programming Matlab function, in *IEEE International Conference on Control Applications (CCA) & Intelligent Control (ISIC)* (IEEE, 2009), pp. 1625–1630

29. O. Sundström, D. Ambühl, L. Guzzella, On implementation of dynamic programming for optimal control problems with final state constraints. Oil Gas Sci. Technol. Revue de l'Institut Français du Pétrole **65**(1), 91–102 (2010)
30. A. Pakniyat, P.E. Caines, The hybrid minimum principle in the presence of switching costs, in *Proceedings of the 52nd IEEE Conference on Decision and Control* (2013)
31. Q. Zhang, M. Canova, Modeling air conditioning system with storage evaporator for vehicle energy management. Appl. Therm. Eng. 87, 779–787 (2015)

Chapter 12
Cruising Control of Hybridized Powertrain for Minimized Fuel Consumption

Shengbo Eben Li, Shaobing Xu, Kun Deng, and Quansheng Zhang

Abstract This chapter studies the fuel-optimal cruising strategies of parallel hybrid electric vehicles and their underlying mechanisms. We formulate a discontinuous nonlinear optimal control problem to achieve fuel-optimal operations, and solve this problem using the Legendre pseudospectral method and knotting technique. Besides, three optimal cruising strategies in free/fixed-speed cruising scenarios are proposed: vehicle speed pulse-and-glide strategy (Speed-PnG), SOC pulse-and-glide strategy (SOC-PnG), and constant speed strategy (CS). Then we compare the performance and optimal behaviors of their engine and motor operations, and study their fuel-saving mechanisms. Finally, two principles to compromise between fuel economy and ride comfort are proposed and studied.

Keywords Electric vehicles • Energy management • Cruise control

12.1 Introduction

Due to the fuel economy standards and environmental concerns, the automotive industry needs to be more focused on improving the fuel economy of road vehicles [1]. Some technologies such as intelligent transportation systems, car body light-weighting, hybrid powertrains, and clean combustion have been developed and deployed [2, 3]. Hybrid electric vehicles (HEVs) have been widely used in our daily life, and many HEVs from Toyota, Ford, Honda, and GM have demonstrated significant potentials for fuel-savings [4]. HEVs are equipped with an energy buffer such

S.E. Li • S. Xu
State Key Laboratory of Automotive Safety and Energy, Department of Automotive Engineering, Tsinghua University, Beijing 10084, China
e-mail: lishbo@tsinghua.edu.cn

K. Deng (✉)
Coordinated Science Laboratory, University of Illinois at Urbana-Champaign, Urbana, IL 61801, USA
e-mail: kundeng2@illinois.edu

Q. Zhang
Center for Automotive Research, The Ohio State University, Bloomfield Hills, MI, USA
e-mail: zhang.777@buckeyemail.osu.edu

Q. Zhang et al., *Automotive Air Conditioning*, DOI 10.1007/978-3-319-33590-2_12

as a battery or super capacitor [5, 6]. Hybrid powertrains contribute to downsize the engine, avoid inefficient engine operation, and execute braking energy recuperation, leading to a better fuel economy compared to conventional vehicles [6].

The fuel economy of HEVs depends on many factors, including its powertrain configuration, component sizing, and control strategy [5, 6]. Many optimization-based and rule-based control rules have been developed to improve the fuel economy of HEVs in diverse riving scenarios and cycles [7]. In this chapter, we focus on designing fuel-optimal control strategies in cruising scenarios for parallel HEVs since parallel hybrid powertrains are commonly used in Honda, Hyundai, and many European hybrid vehicle models.

Cruising, as the most common maneuver, consumes a significant portion of the total energy, 35 % in urban conditions [8], and even higher on the highways. A survey showed that coach buses spent 65–78 % of their total driving time cruising on the freeways in Beijing [9]. Therefore, fuel-efficient cruising strategy is important to save the fuel usage. Specifically, about 1 % fuel-savings can cut down 20 million barrels of oil per year over the world in cruising scenarios [10].

In cruising scenarios, the frequently used cruising strategy is the constant speed (CS) operation, which means operating the engine and transmission at a constant state and traveling at a fixed speed. Besides, there is another cruising strategy, which is pulse and glide (PnG) cruising strategy, a strategy widely used in super-mileage competition vehicles [11]. It has been proven that the PnG strategy can be more fuel-efficient than the CS operation, with up to 20 % fuel-savings [11, 12]. Lee and Nelson also validated the fuel-saving performance in experiments.

For non-hybrid vehicles with a continuously variable transmission (CVT), Li and Peng formulated an optimal control framework and provide analytical optimal results of how PnG strategy works [11, 12]. The study showed that the vehicle inertia acts as a kinetic "energy buffer," which allows the engine to operate efficiently and intermittently. Due to this "energy buffer," PnG results in a higher average efficiency than the CS operation [11]. In spite of the better fuel economy, riding comfort is reduced due to the fluctuating speed of the PnG strategy [11, 12]. Parallel HEVs have two kinds of "energy buffer." The one is electric "energy buffer" (i.e., battery) and mechanical "energy buffer" (i.e., vehicle inertia). And the additional energy buffer enlarges the freedom in power management. More than just "swinging the vehicle speed high and low," the battery SOC also can be fluctuated to improve ride comfort. In fact, both vehicle kinetic energy and battery energy can be rocked back and forth to obtain optimal fuel economy or better trade-off between fuel economy and ride comfort. This chapter systematically studies how the dual-energy-storage system can be used for optimal fuel economy and its trade-off against ride comfort.

12.2 HEV Model and Problem Statement

12.2.1 HEV Model for Control

The parallel HEV we studied includes a mechanical powertrain and an electric powertrain, and its structure chart is shown in Fig. 12.1. The main components

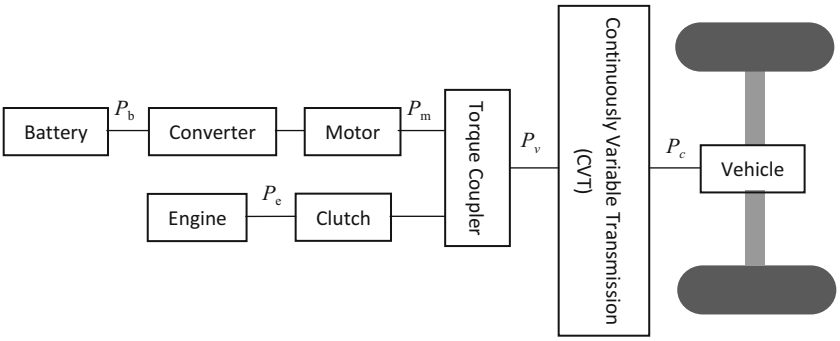

Fig. 12.1 Powertrain topology of the parallel HEV

in this parallel HEV are the battery, converter, motor, internal combustion engine (ICE), clutch, torque coupler, CVT, vehicle, and so on. The power generated by the engine can be used to propel the car and also can be used to charge the battery. Both engine and motor can drive the vehicle individually or together.

In order to obtain the optimal control rules of the engine and motor to minimize fuel consumption, we naturally fit the problem into an optimal control framework, using the engine power and motor power as control inputs. The performance index, plant dynamics, and constraints of this fuel-optimal control problem (OCP) are described below.

For simplicity, the following assumptions are made:

1. The dynamics of the fly-wheel, clutch, CVT, and motor are ignored;
2. The engine always operates on the best brake-specific-fuel-consumption (BSFC) line by using the CVT.

12.2.1.1 Vehicle Longitudinal Dynamics

In the parallel HEV, the engine and the motor can drive the vehicle together or separately. Based on the force balance equations, the distance s and velocity v satisfy:

$$\begin{aligned} \dot{s} &= v, \\ \dot{v} &= \frac{\eta_C P_e + P_m - F_r(v)v}{Mv}, \\ F_r(v) &= 0.5 C_D \rho_a A_v v^2 + Mgf, \end{aligned} \tag{12.1}$$

where M and g represent the vehicle mass and the gravity constant, η_C is the efficiency of the CVT, P_e is the engine power, P_m is the motor power, C_D is the aerodynamic drag coefficient, ρ_a is the air density, A_v is the frontal area of the vehicle, f is the rolling resistance coefficient, and F_r is aerodynamic drag and rolling resistance. It's worth mentioning that if the engine is off, the clutch can be disen-

gaged to avoid engine drag, that is, $P_e = 0$. And the motor power P_m can be either negative or positive, corresponding to charge mode or discharge mode, respectively.

The relationship of the speed ratio i_C of the CVT, the vehicle speed and the engine speed can be explained using Eq. (12.2):

$$i_C = w_e r_w / (i_0 v), \tag{12.2}$$

where w_e is the engine speed, $r_w$is the tire radius, and i_0 is the speed ratio of the final drive.

The mechanical efficiency of the CVT is nonlinear and depends on its speed ratio and load. For push-belt CVT, under high speed ratio or high power conditions the efficiency is high (about 85–90 %); otherwise it will rapidly deteriorate to about 70 % [13]. For hybrid vehicles, as the engine can eliminate low-power operations, the CVT can avoid some inefficient operations. Based on this assumption, we simplify the CVT efficiency to a constant η_C.

12.2.1.2 Battery and Motor Model

In addition to the above vehicle dynamics, the battery dynamic is expressed as [14]

$$\dot{\text{SOC}} = -\frac{V_{\text{oc}} - \sqrt{V_{\text{oc}}^2 - 4P_b \times R_{\text{int}}}}{2R_{\text{int}} \times C}, \tag{12.3}$$

where SOC denotes the state of charge of battery, V_{oc} is the battery voltage, R_{int} is the internal resistance, C is the battery capacity, and P_b is the battery power.

According to the structure chart of HEV (Fig. 12.1), there is the specific correlation between the battery power P_b and the motor power P_m. During charging, the motor is the equation of a generator and charges the battery. In this situation, both P_b and P_m are negative with the relationship below:

$$P_b = P_m \eta_m, \quad P_m < 0, \tag{12.4}$$

In the discharge mode, P_b and P_m are both positive, and governed by the relationship:

$$P_b = P_m / \eta_m, \quad P_m \geq 0, \tag{12.5}$$

where η_m (the efficiency of the motor) relies on the motor speed w_m and torque T_m, as shown in Fig. 12.2.

In this powertrain topology, the motor speed w_m is related to the vehicle speed, as shown in below,

$$w_m = i_m i_0 v / r_w, \tag{12.6}$$

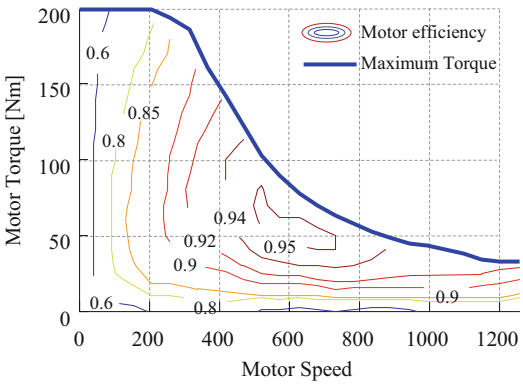

Fig. 12.2 Motor efficiency as a function of motor speed and torque

where i_m is the gear ratio of the torque coupler. The motor torque T_m is obtained from:

$$T_m = P_m / w_m. \tag{12.7}$$

We assume that the generator efficiency map is identical to the motor efficiency map, i.e.,

$$\eta_m (w_m, T_m) = \eta_m (w_m, -T_m), \tag{12.8}$$

12.2.2 Performance Index for Fuel Economy

For the purpose of measuring the fuel economy, the index "fuel consumption per 100 km" is proposed, which is defined as

$$J = \frac{\int_0^{t_f} \mathcal{F}_e dt}{s_f}, \tag{12.9}$$

where t_f, $\mathcal{F}_e$, and s_f denote the terminal time, engine fuel injection rate, and terminal distance, respectively.

The BSFC map is shown in Fig. 12.3a, where the blue sweet spot is positioned in maximum efficiency (power 18.9 kW, efficiency 38.3 %).

The Eco-line, collection of the most efficient points for varying power level, is shown in Fig. 12.3a. And Fig. 12.3b presents the fitting result of the Eco-line, whose efficiency η_e is fitted by:

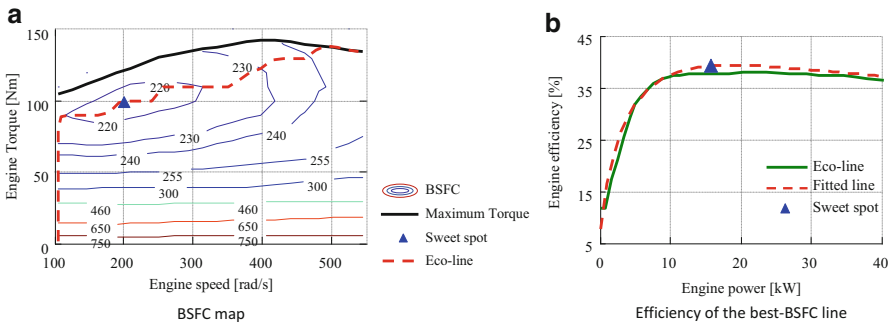

Fig. 12.3 Engine model. (**a**) BSFC map. (**b**) Efficiency of the best-BSFC line

$$\eta_e = \eta_0 + \sum_{i=1}^{3} k_i (P_e - P_0)^{1/(2i)}, \tag{12.10}$$

where η_0 and k_i are the fitting coefficients, P_e is engine power, and P_0 is a constant. Since the engine always operates on the Eco-line, the engine fuel injection rate $\mathcal{F}_e$ is obtained by

$$\mathcal{F}_e = \frac{P_e}{c_g \times \eta_e (P_e)}, \tag{12.11}$$

where c_g is the calorific value of gasoline. If the engine is shut off, then $\mathcal{F}_e = 0$.

In fact, the energy stored in the battery is derived from the engine, which means that the battery acts as an energy buffer rather than an original source. The initial and terminal states of SOC are constrained to be the same in this fuel-optimal cruising problem to ensure charge sustenance.

12.2.3 Constraints for Inputs and States

Due to the physical limits of the engine, CVT, battery, and motor, there are some equality and inequality constraints, as follows:

$$\begin{aligned} &P_{e,\min} \le P_{\mathrm{e}} \le P_{e,\max}, i_{C,\min} \le i_C \le i_{C,\max}, \mathrm{SOC}_{\min} \le \mathrm{SOC} \le \mathrm{SOC}_{\max}, \\ &T_{m,\min} \le T_m \le T_{m,\max}, w_{m,\min} \le w_m \le w_{m,\max}. \end{aligned} \tag{12.12}$$

In the cruising problem, the initial velocity v_0 and terminal velocity v_f are set to be equal, i.e.,

$$v_0 = v_f. \tag{12.13}$$

Similarly, the initial and terminal states of SOC are also constrained by:

$$\mathrm{SOC}_0 = \mathrm{SOC}_f. \tag{12.14}$$

12.2.4 Optimal Control Problem

The OCP for the parallel HEV is formulated as follows:

$$\min\ J = \frac{\int_0^{t_f} \mathcal{F}_e dt}{s_f},$$

Subject to

$$\begin{aligned}
&\dot{s} = v, \dot{v} = \tfrac{\eta_C P_e + P_m - F_r(v)v}{Mv}, \dot{\mathrm{SOC}} = -\tfrac{V_{\mathrm{oc}} - \sqrt{V_{\mathrm{oc}}^2 - 4P_b \times R_{\mathrm{int}}}}{2R_{\mathrm{int}} \times C},\\
&P_b = \begin{cases} \frac{P_m}{\eta_m} P_m \geq 0 \\ P_m \eta_m \, | P_m < 0 \end{cases},\\
&v_0 = v_f, \mathrm{SOC}_0 = \mathrm{SOC}_f, P_{e,\min} \leq P_e \leq P_{e,\max}, i_{C,\min} \leq i_C \leq i_{C,\max},\\
&\quad \mathrm{SOC}_{\min} \leq \mathrm{SOC} \leq \mathrm{SOC}_{\max}, T_{m,\min} \leq T_m \leq T_{m,\max}, w_{m,\min} \leq w_m \leq w_{m,\max}.
\end{aligned} \tag{12.15}$$

In fact, the state vectors are the distance s, velocity v, and SOC, denoted as $\boldsymbol{x} = (s, v, \mathrm{SOC})^T$. The control inputs consist of the engine power P_e and motor power P_m, denoted as $\boldsymbol{u} = (P_e, P_m)^T$. Other parameters not mentioned are listed in Table 12.1.

This OCP has strong nonlinearity in dynamics and discontinuity in switching between charge and discharge modes, so it is really a great challenge to solve. To address this discontinuous nonlinear problem, we use the Legendre pseudospectral method and knotting technique to convert the optical control problem (OCP) into a nonlinear programming (NLP) problem for more accurate numerical computation.

12.3 Legendre Pseudospectral Method and Knotting Technique

Since we assume the initial and terminal states of SOC must be the same, there are two possible cases: (a) both the engine and battery are used with no net change in battery energy, or (b) only the engine is used, which is a special case of (a) with the battery power always equal to zero. In a long riding, there may be many charge and discharge events, whose optimal profile is difficult to obtain by this strong nonlinear and nonconvex OCP.

Therefore, we focus on only one charge/discharge event over a shorter period of time.

12.3.1 Legendre Pseudospectral Method

The Legendre pseudospectral method (LPM) is a global collocation method for converting OCP into NLP [15–17]. In order to convert the OCP into an NLP problem, LPM discretizes the OCP at orthogonal collocation points and then employs global interpolating polynomials, rather than local interpolating polynomial, to approximate states and control inputs.

Compared to conventional methods (e.g., shooting method), LPM has higher accuracy and convergence speed [15]. But LPM is highly accurate only for smooth problems, which means that LPM is difficult to solve the non-smooth OCP that involves switching between different modes [16], like Eq. (12.15).

Here, we first simplify the switching rule and then apply the knotting technique to convert the OCP.

12.3.2 Knotting Technique

Under this simplification, the knotting technique is then utilized to convert the non-smooth problem. Its basis is to divide the original OCP into two smooth sub-stages, corresponding to the charge and discharge modes, and then each of the sub-stages is converted to an NLP problem by using LPM. Besides, the connection constraints need to be added between the consecutive stages to ensure continuity of the state vector (e.g., vehicle speed and SOC), and thus relink the two local trajectories into an integrated continuous one. Finally, the optimal results are obtained by the collaborative optimization of the two sub-stages.

Table 12.1 Key parameters of the vehicle dynamics

Parameters	Value	Parameters	Value
M	1450 kg	η_0	−10.06
C_D	0.28	P_0	3 kW
A_v	2.52 m^2	$P_{e,\max}$	60 kW
ρ_a	1.2 kg/m^3	$P_{e,\min}$	0
f	0.015	$i_{C,\max}$	0.4
r_w	0.287 m	$i_{C,\min}$	4.2
i_0	3.3	$w_{m,\max}$	1200 rad/s
i_m	2.63	$w_{m,\min}$	0
η_C	0.88	$\mathrm{SOC}_{\max}$	80 %
C	1.35 kWh	$\mathrm{SOC}_{\min}$	30 %
k_0, k_1, k_2	0.0253, −2.94922, 8.0482		

This technique helps us avoid accuracy loss compared with using only one smoothing function to approximate discontinuous variables. The process of converting the OCP by LPM and the knotting technique is stated as follows. To be concise, the initial time is denoted as T_0, and the terminal time of the two sub-stages are denoted as T_1 and T_2.

12.3.2.1 Step1: Conversion of Time Interval

The two stages are transformed into a canonical interval $[-1, 1]$ by

$$\tau = \frac{2t - \left(T_q + T_{q-1}\right)}{T_q - T_{q-1}}, \tag{12.16}$$

where q is 1 or 2.

12.3.2.2 Step2: Collocation Points and Approximation

The LPM employs Legendre–Gauss–Lobatto collocation points, which are the roots of the derivative of an Nth order Legendre polynomial, together with two end points: -1 and 1. Each phase can have a different number of collocation points, denoted as $N_q + 1$. The collocation points at the qth phase are denoted as $\tau_{q,i}$, where $i = 0, 1, \cdots, N_q$. The states s, v, and SOC are discretized to

$$\boldsymbol{X}_q = \begin{bmatrix} \mathbb{S}_{q,0} & \mathbb{S}_{q,1} & \cdots & \mathbb{S}_{q,N_q} \\ \mathbb{V}_{q,0} & \mathbb{V}_{q,1} & \cdots & \mathbb{V}_{q,N_q} \\ \mathcal{S}_{q,0} & \mathcal{S}_{q,1} & \cdots & \mathcal{S}_{q,N_q} \end{bmatrix}. \tag{12.17}$$

The engine power P_e and motor power P_m are also discretized to $\mathbb{P}_{eq,i}$ and $\mathbb{P}_{mq,i}$. Note that we only optimize the discretized states and control inputs; the dynamics $\boldsymbol{x}_q(\tau)$ and $\boldsymbol{u}_q(\tau)$ are obtained by Lagrange interpolation at collocations points, i.e.,

$$\begin{aligned} \boldsymbol{x}_q(\tau) &\approx \sum\nolimits_{i=0}^{N_q} L_{q,i}(\tau)\, \boldsymbol{X}_{q,i}, \\ \boldsymbol{u}_q(\tau) &\approx \sum\nolimits_{i=0}^{N_q} L_{q,i}(\tau)\, \boldsymbol{U}_{q,i}, \end{aligned} \tag{12.18}$$

where $L_{q,i}(\tau)$ are the Lagrange basis polynomials.

12.3.2.3 Step3: Conversion of the State Space Equations

The differential state equations can be approximated by the differential operation on the Lagrange basis polynomials, i.e.,

$$\dot{x}_q\left(\tau_{q,k}\right) = \sum\nolimits_{i=0}^{N_q} \dot{L}_{q,i}\left(\tau_{q,k}\right) X_{q,i} = \sum\nolimits_{i=0}^{N_q} D_{ki}^q X_{q,i}. \tag{12.19}$$

where $k = 0, 1, 2, \cdots, N_q$, and $\boldsymbol{D}^q$ is the differentiation matrix with explicit expression [15]. Then the vehicle dynamics Eq. (12.1) and battery dynamics Eq. (12.3) are converted to a series of equality constraints at the collocation points:

$$\begin{aligned}
&\sum\nolimits_{i=0}^{N_q} D_{ki}^q \mathbb{S}_{q,i} = \Delta T_q \times \mathbb{V}_{q,k}, \\
&\sum\nolimits_{i=0}^{N_q} D_{ki}^q \mathbb{V}_{q,i} = \Delta T_q \frac{\eta_{\mathrm{C}}\, \mathbb{P}_{eq,k} + \mathbb{P}_{mq,k} - F_r\left(\mathbb{V}_{q,k}\right) \mathbb{V}_{q,k}}{M \mathbb{V}_{q,k}}, \\
&\sum\nolimits_{i=0}^{N_q} D_{ki}^q \mathcal{S}_{q,i} = -\Delta T_q \frac{V_{\mathrm{oc}} - \sqrt{V_{\mathrm{oc}}^2 - 4\, \mathbb{P}_{bq,k} \times R_{\mathrm{int}}}}{2 R_{\mathrm{int}} \times C},
\end{aligned} \tag{12.20}$$

where $\Delta T_q = \left(T_q - T_{q-1}\right)/2$.

12.3.2.4 Step 4: Conversion of the Cost Function

The integral part of the cost function is calculated by Gaussian–Lobatto quadrature, so the performance index is computed by:

$$J = \sum\nolimits_{q=1}^{2} \frac{\Delta T_q \sum\nolimits_{k=0}^{N_q} w_{q,k} \mathcal{F}_e\left(\mathbb{P}_{eq,k}\right)}{\mathbb{S}_{2,N_2}}. \tag{12.21}$$

where $w_{q,k}$ are the weighting coefficients of the Gaussian–Lobatto quadrature, defined as [15]

$$w_{q,k} = \int_{-1}^{1} L_{q,k}(\tau)\, d\tau = \frac{2}{N_q\left(N_q + 1\right) P_{N_q}^2\left(\tau_{q,k}\right)}. \tag{12.22}$$

12.3.2.5 Step 5: Connection Constraints

Since the distance, velocity, and SOC are continuous between the two stages, the following constraints are added:

$$\mathbb{S}_{1,N_1} - \mathbb{S}_{2,0} = 0, \mathbb{V}_{1,N_1} - \mathbb{V}_{2,0} = 0, \mathcal{S}_{1,N_1} - \mathcal{S}_{2,0} = 0. \tag{12.23}$$

After these steps, the OCP Eq. (12.15) is converted into the following NLP problem:

$$J = \sum_{q=1}^{2} \frac{\Delta T_q \sum_{k=0}^{N_q} w_{q,k} \mathcal{F}_e\left(\mathbb{P}_{eq,k}\right)}{\mathbb{S}_{2,N_2}},$$

Subject to

$$\begin{aligned}
&\sum_{i=0}^{N_q} D_{ki}^{q} \mathbb{S}_{q,i} = \Delta T_q \times \mathbb{V}_{q,k},\\
&\sum_{i=0}^{N_q} D_{ki}^{q} \mathbb{V}_{q,i} = \Delta T_q \frac{\eta_{\mathrm{C}}\, \mathbb{P}_{eq,k} + \mathbb{P}_{mq,k} - F_r\left(\mathbb{V}_{q,k}\right) \mathbb{V}_{q,k}}{M \mathbb{V}_{q,k}},\\
&\sum_{i=0}^{N_q} D_{ki}^{q} \mathcal{S}_{q,i} = -\Delta T_q \frac{V_{\mathrm{oc}} - \sqrt{V_{\mathrm{oc}}^2 - 4\, \mathbb{P}_{bq,k} \times R_{\mathrm{int}}}}{2 R_{\mathrm{int}} \times C},\\
&\mathbb{P}_{bq,k} = \begin{cases} \frac{\mathbb{P}_{mq,k}}{\eta_m} & \mathbb{P}_{mq,k} \geq 0 \\ \mathbb{P}_{mq,k} \eta_m\, \mathbb{P}_{mq,k} & \mathbb{P}_{mq,k} < 0 \end{cases},\\
&\mathbb{V}_{1,0} = \mathbb{V}_{2,N_2},\\
&\mathcal{S}_{1,0} = \mathcal{S}_{2,N_2},\\
&0 = \mathbb{S}_{1,N_1} - \mathbb{S}_{2,0},\\
&0 = \mathbb{V}_{1,N_1} - \mathbb{V}_{2,0},\\
&0 = \mathcal{S}_{1,N_1} - \mathcal{S}_{2,0},\\
&P_{e,\min} \leq \mathbb{P}_{eq,k} \leq P_{e,\max},\\
&i_{C,\min} \leq i_C \leq i_{C,\max}.
\end{aligned} \tag{12.24}$$

where $k, i = 0, 1, 2, \cdots, N_q$; $q = 1, 2$.

The variables to be optimized include the traveling distance $\mathbb{S}_{q,k}$, vehicle speed $\mathbb{V}_{q,k}$, SOC of battery $\mathcal{S}_{q,k}$, engine power $\mathbb{P}_{eq,k}$, and motor power $\mathbb{P}_{mq,k}$. In essence, this NLP is a high-dimensional sparse constrained problem, and is solved by the sequential quadratic programming (SQP) algorithm [18].

12.4 Optimization Results

12.4.1 Speed-PnG Cruising Operation

12.4.1.1 Setting Conditions

Given that the vehicle is expected to cruise in a constant average speed, we focus on the general case, in which the vehicle speed is free. In this case, the average speed $\overline{v}$ must be equal to the expected speed v_{e}, i.e.,

$$\overline{v} = s_f / t_f = v_e. \tag{12.25}$$

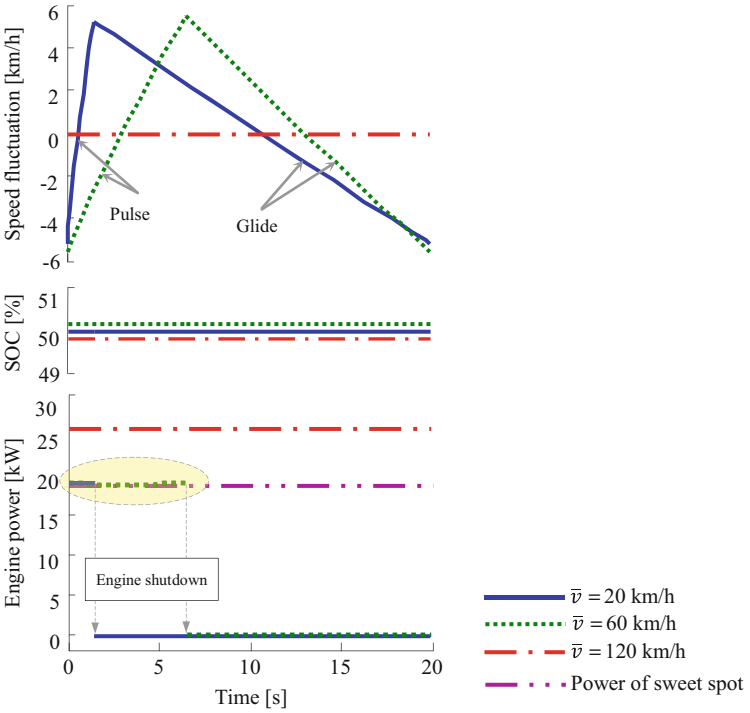

Fig. 12.4 Optimization results: Speed-PnG strategy at 20 and 60 km/h and CS strategy at 120 km/h

Both the initial and final SOC are set to 50 %, the terminal time is fixed to 20 s. The number of collocation points in each phase is set to 15. We select the three cases, in which this car cruises at 20, 60, and 120 km/h, respectively.

12.4.1.2 Solving Results

By using LPM and the knotting technique, their optimal profiles of speed fluctuation, SOC, and engine power are obtained and shown in Fig. 12.4. We can see that:

1. In the cases of 20 and 60 km/h,
   (a) As shown in Fig. 12.4, the fuel-optimal operation is to accelerate the vehicle to a higher speed first and then coast down to a lower speed. We called this variation of vehicle speed the speed fluctuation. And the speed fluctuations of the two cases are ±26 and ±9 %, respectively.
   (b) In Fig. 12.4, the SOC is constant for the whole duration of the two cases, which means no energy is converted to the battery and the battery/motor system is not used.

(c) In Fig. 12.4, the engine first runs at a high power, which approximately coincides with the power of the sweet spot, and then switches to shutdown with zero power output. So we know this optimal strategy is called "Speed-PnG" operation, consisting of pulse phase and glide phase under the influence of the fixed SOC and fluctuating speed, which is the vehicle speed *pulses* first and then *glides*.

2. In the case of 120 km/h

From Fig. 12.4, the states, such as the vehicle speed, SOC, and engine power, keep all constant. In this situation, the optimal operation is to cruise at a fixed speed driven by the engine only. And this optimal strategy is called "CS" (constant speed) operation.

In addition, this optimal strategy shows that:

(a) Actually, the optimal result is Speed-PnG operation rather than cruising at a fixed speed
(b) During cruising at low speeds (e.g., 20 km/h), the battery and motor are not utilized, and the optimal control rule of engine is to switch between the sweet spot and shutdown, corresponding to the pulse/glide phases.

12.4.1.3 Explication the Fuel Economy of Speed-PnG

In order to explicit the fuel economy of Speed-PnG, we set the CS operation as the benchmark. In the cases of 20 and 60 km/h, the fuel consumption of using CS is 4.30 and 3.47 L/100 km, respectively, dropping to 2.03 and 2.97 L/100 km if using Speed-PnG. Therefore, Speed-PnG achieves a fuel-savings of 52.7 and 14.45 % compared to CS, with fuel-saving rate $\eta_{\mathcal{F}}$ defined as

$$\eta_{\mathcal{F}} = \frac{J_{\mathrm{CS}} - J_{\mathrm{PnG}}}{J_{\mathrm{CS}}} \times 100\%, \tag{12.26}$$

where J_{CS} and J_{PnG} are fuel consumed by CS and PnG.

With expanding the above three examples to various average cruising speeds, the fuel-saving rate of Speed-PnG and corresponding average optimal engine power to pulse are shown in Fig. 12.5. When $\overline{v} \in [20, 104]$ km/h, the Speed-PnG strategy achieves better fuel economy than CS, and the optimal operating engine power approximately equals the power of the sweet spot.

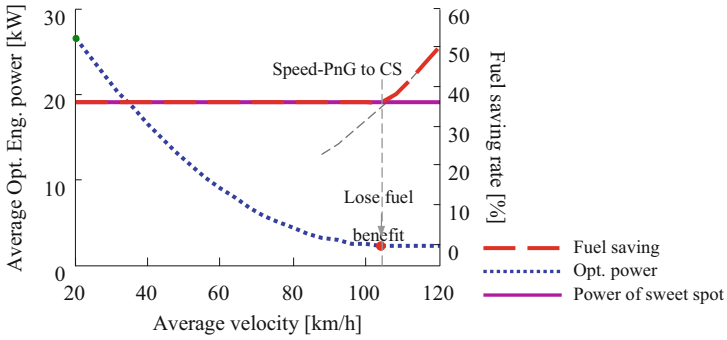

Fig. 12.5 Optimal fuel-saving rate and average engine power in the pulse phase of Speed-PnG

12.4.2 SOC-PnG Cruising Operation

12.4.2.1 Setting Conditions

In the Speed-PnG operation, the fluctuating speed is less acceptable for human drivers. So here we change the constraint on vehicle speed into cruising at a fixed speed; That is to say the vehicle maintains the constant speed rather than PnG:

$$v \equiv v_{\mathrm{e}}. \tag{12.27}$$

Under the limits, we set the terminal time to 100 s, and the initial and final SOC are set to 50 %. Three cases, cruising at 20, 40, and 60 km/h, are selected.

12.4.2.2 Solving Results

The optimization results are shown in Fig. 12.6, which shows that:

1. In the cases of 20 and 40 km/h, the engine begins to operate at a high power to maintain the vehicle cruising and charge the battery, with SOC rising; then the engine is shutdown and only the battery is used to drive the vehicle, with SOC dropping to initial value. So, the optimal result in this situation is that "SOC-PnG" operation which means the SOC *pulses* first and then *glides*, similar to the Speed-PnG.
2. In addition, we can also see that the optimal engine power in the pulse phase is 12.65 and 11.44 kW at 20 and 40 km/h, respectively. They are not in the position of the sweet spot (18.9 kW), which is generally considered to be optimal.
3. When cruising at 60 km/h, the SOC is constant (50 %) and the engine keeps operating at 6.13 kW, indicating that the vehicle is driven by engine only. Therefore, the optimal operation is CS rather than SOC-PnG.

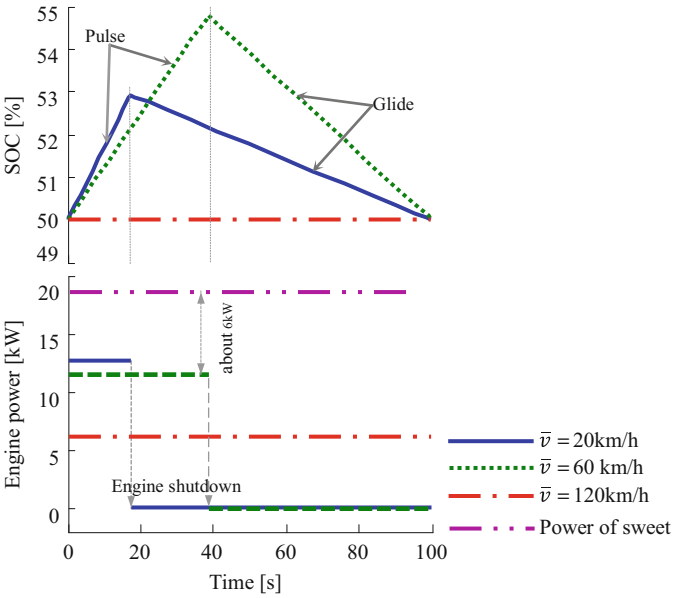

Fig. 12.6 Optimization results: SOC-PnG strategy at 20 and 40 km/h and CS strategy at 60 km/h

12.4.2.3 Explication the Fuel Economy of SOC-PnG

In the first two cases, the fuel consumption using the SOC-PnG strategies is 3.22 and 3.30 L/100 km, rising to 4.30 and 3.45 L/100 km if using CS, respectively. Thus, SOC-PnG achieves a fuel-savings of 25.1 and 4.3 % compared to CS. With individually optimizing the problems at different cruising speeds, the fuel-saving rate and optimal engine power to pulse are shown in Fig. 12.7. When $v \leq 48$ km/h, SOC-PnG can save fuel and its optimal engine power is around 12 kW. Therefore, with the cruising speed increasing, the fuel-saving rate decreases continuously and eventually CS becomes optimal.

From Fig. 12.7, we can see the optimal engine power straying from the sweet spot and the fuel-saving rate in the case of keeping the engine operating at the sweet spot (18.9 kW) to pulse. And the fuel-saving rate drops about 3 percentage points compared to the SOC-PnG optimum. As a simplification, keeping running the engine at fixed 12 kW only leads to less than 1 percentage reduction. Overall, in the SOC-PnG operation selecting a proper lower engine power to pulse can achieve better fuel performance than using the sweet spot.

12.4.3 Comparison Between Speed-PnG and SOC-PnG

As mentioned in the above, we know that both Speed-PnG and SOC-PnG can save fuel compared to CS in a particular speed interval. According to their optimal

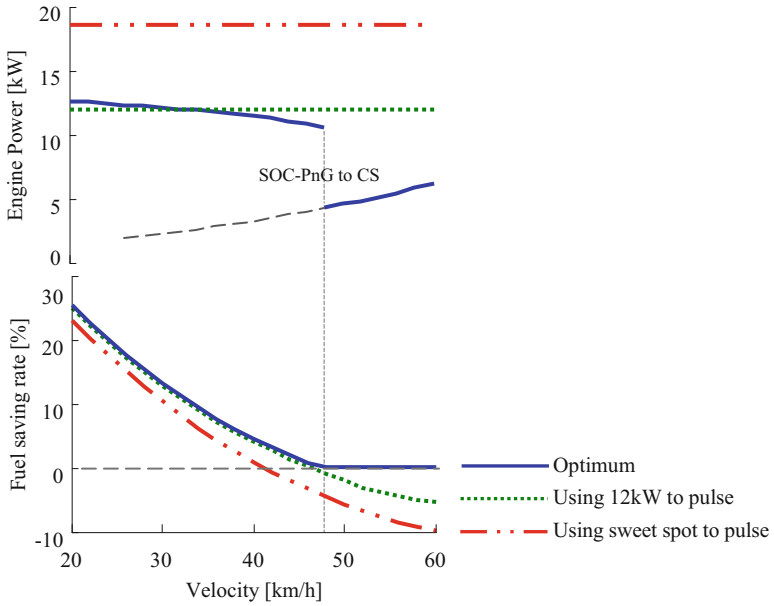

Fig. 12.7 Optimal average engine power and fuel-saving rate of SOC-PnG at different cruising speeds

fuel-saving rates in Fig. 12.8a, it's obvious that the Speed-PnG strategy has better fuel economy than SOC-PnG. And as the average speed increases, the fuel-saving capacity of both operations decreases and eventually vanishes.

For the SOC-PnG strategy, if the battery and motor are ideal (i.e., with 100 % efficiency), we call it as SOC-PnG (ideal), then we can operate the engine at the sweet spot to charge the battery with no conversion losing. So it should have the highest system efficiency, theoretically. In Fig. 12.8a, the fuel-saving rate of the Speed-PnG strategy is very close to that of SOC-PnG (ideal), which shows that Speed-PnG is the most efficient mode of operation. Considering riding comfort, the Speed-PnG strategy is less applicable due to the fluctuating speed.

The average optimal accelerations of Speed-PnG and SOC-PnG at various average cruising speeds are shown in Fig. 12.8b. In practice, a trade-off between fuel economy and ride comfort is possible.

12.5 Fuel-Saving Mechanisms

In this section, we study the underlying mechanisms of Speed-PnG and SOC-PnG by addressing the following questions.

But we need to introduce a key figure (i.e., Fig. 12.9) for understanding the mechanisms and answering the questions. In Fig. 12.9, the abscissa is power, the

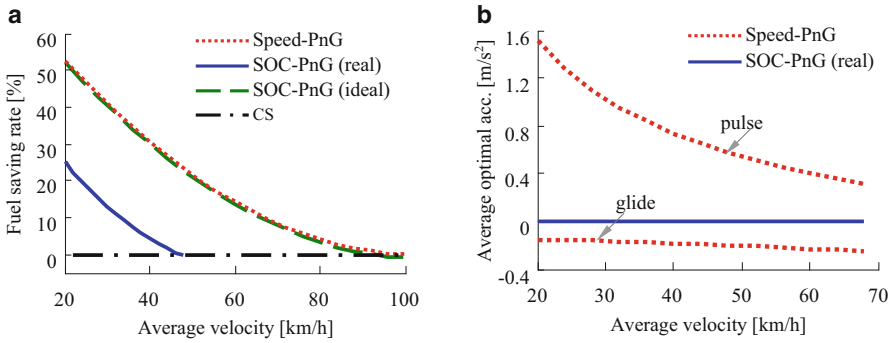

Fig. 12.8 Comparison of Speed-PnG and SOC-PnG (real/ideal). (**a**) Fuel-saving rate; (**b**) average optimal acceleration

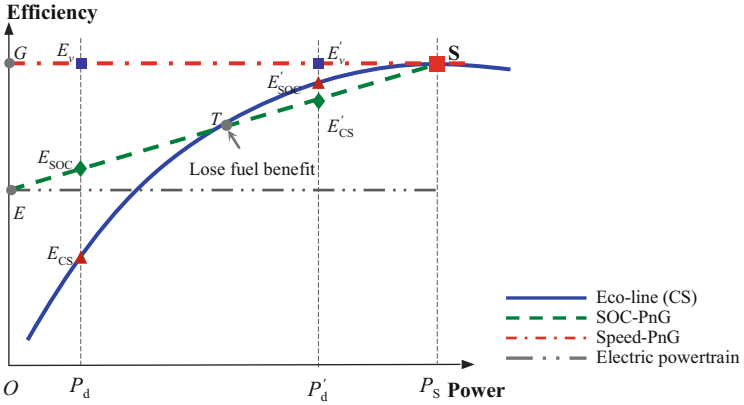

Fig. 12.9 Mechanism of Speed-PnG and SOC-PnG

ordinate is efficiency. If the vehicle cruises at a fixed speed v, the demanded engine power is recorded as P_d. Since the engine always operates on the Eco-line, point E_{CS} stands for the corresponding engine efficiency of using CS strategy.

Question 1 Why Speed-PnG saves fuel at a certain speed interval and is the most efficient operation?

Solution For this question, in Speed-PnG, the engine operates at the sweet spot S with highest efficiency η_{S} in pulse phase. In the glide phase, the engine is shutdown and the vehicle coasts, dissipating the stored kinetic energy, which is generated in the pulse phase with efficiency η_{S}. Therefore, points S/G stand for the pulse/glide phases, respectively. Ignoring the tiny difference of total aerodynamic drag in Speed-PnG and CS, the average engine power of Speed-PnG is equal to P_d, so point E_v indicates the average efficiency of Speed-PnG.

It is clear that the average efficiency (point E_v) of Speed-PnG is higher than that of CS (point E_{CS}). As the average cruising speed increases (e.g., point P_d moves to $P_d^{'}$), the efficiency of Speed-PnG (point $E_v^{'}$) remains fixed, while the efficiency of CS (point $E_{CS}^{'}$) increases. As a consequence, the fuel-saving rate decreases. When point P_d moves to P_S, the two strategies have the same efficiency, at which point Speed-PnG loses its fuel benefit and CS becomes the optimal operation.

In Speed-PnG, the vehicle body actually plays the role of an energy buffer with variable kinetic energy, and the kinetic energy can be "charged/discharged" with 100 % efficiency, thus making Speed-PnG the most efficient operation.

Question 2 Why SOC-PnG can save fuel and its fuel-saving capacity is lower than that of Speed-PnG?

Solution In order to answer this question, here we make some assumptions to simplify the problem, as below:

(a) The motor efficiency η_{m}, discharge/charge efficiency $\eta_{\mathrm{dis}}/\eta_{\mathrm{chg}}$/of the battery, are fixed;
(b) In pulse phase, the engine operates at sweet spot S to charge the battery and drive the vehicle, though it is not the optimum, as shown in Fig. 12.7.

In glide phase, the engine is shutdown and the motor drives the vehicle using the stored energy in pulse phase. The motor output energy originates from the engine with the following conversion steps: engine $\eta_{\mathrm{S}} \rightarrow$ motor $\eta_{\mathrm{m}} \rightarrow \eta_{\mathrm{chg}}$ battery $\eta_{\mathrm{dis}} \rightarrow$ motor $\eta_{\mathrm{m}} \rightarrow$ vehicle, where $\eta_{\#}$ is the efficiency. The overall efficiency is recorded as $\eta_E = \eta_S \eta_m \eta_{\mathrm{chg}} \eta_{\mathrm{dis}} \eta_m$. It is called the efficiency of electric powertrain, as shown in Fig. 12.9.

Here we argue that the efficiency of SOC-PnG is on the line ES; the proof is given below:

Record the duration of pulse phase as t_P, the total fuel consumption $\mathcal{F}_c$ is

$$\mathcal{F}_c = \frac{t_P P_S}{c_g \eta_S}, \tag{12.28}$$

where c_g is the calorific value of gasoline. Energy E_b charged to the battery is

$$E_b = t_P \left(P_S - P_d\right) \eta_m \eta_{\mathrm{chg}}. \tag{12.29}$$

In glide phase, the stored energy is consumed and the duration t_G is

$$t_G = \frac{E_b \eta_{\mathrm{dis}} \eta_m}{P_d}, \tag{12.30}$$

Thus, the average efficiency η_{SOC} of SOC-PnG is

$$\eta_{\mathrm{SOC}} = \frac{P_d \left(t_P + t_G\right)}{c_g \mathcal{F}_c} = \eta_E + \frac{P_d}{P_S} \left(\eta_S - \eta_E\right) \tag{12.31}$$

This formula shows that η_{SOC} is a linear function of P_d, with $\eta_{\mathrm{SOC}} = \eta_E$ when $P_d = 0$, and $\eta_{\mathrm{SOC}} = \eta_S$ when $P_d = P_S$. Point E_{SOC} thus stands for the average efficiency of SOC-PnG when the demanded power is P_d.

In Fig. 12.9, point E_{SOC} is higher than point E_{CS} at low speed, allowing SOC-PnG to save fuel when $\overline{v} < 48$ km/h, as shown in Fig. 12.7. As the demanded power increases, point E_{SOC} rises linearly and the point E_{CS} increases nonlinearly. At point T, the two strategies have the same efficiency, at where the optimal strategy changes from SOC-PnG to CS.

In SOC-PnG, the battery acts as the energy buffer to adjust the engine status. Compared to the vehicle body, the battery suffers an about 10 % conversion loss, along with the motor. Thus, SOC-PnG has lower fuel economy than Speed-PnG. If the battery/motor system is ideal with 100 % efficiency, point E coincides with G, and then point E_{SOC} coincides with E_v, which explains the similar fuel economy of SOC-PnG (ideal) and Speed-PnG (see Fig. 12.8).

Question 3 In Speed-PnG, why the optimal control is to operate the engine between the sweet spot and shutdown without using the battery/motor system?

Solution For question 3, in Speed-PnG, letting the engine switch only between the sweet spot and shutdown, we can then obtain the highest average efficiency (line GS) and best fuel economy. To avoid the conversion loss of the battery/motor system, the extra energy generated in the pulse phase is preferentially transferred to the vehicle body, thus the battery/motor is not used.

Question 4 In SOC-PnG, why the engine does not operate at the sweet spot to minimize the fuel consumption?

Solution For the question, if the engine operates at a random point with power P and efficiency η, Eq. (12.31) can be varied as

$$\max_P \eta_{\mathrm{SOC}} = \eta(P) \times \left(\beta_1 + \beta_2 \frac{P_d}{P}\right), \tag{12.32}$$

where $\beta_1 = \eta_{\mathrm{chg}}\eta_m\eta_{\mathrm{dis}}\eta_m$ and $\beta_2 = 1 - \beta_1$ are constants. Operating the engine at point S maximizes the engine efficiency $\eta(P)$ but makes the last term $1/P$ deviate from the optimal. We can further convert Eq. (12.32) to Eq. (12.33), i.e.,

$$\max_P \eta_{\mathrm{SOC}} = \eta(P) \times \left(1 - \beta_2 \frac{P - P_d}{P}\right), \tag{12.33}$$

where $\beta_2 = 1 - \eta_{\mathrm{chg}}\eta_m\eta_{\mathrm{dis}}\eta_m$ is the efficiency loss, and $(P - P_d)$ is the power converted to the battery. The last term reflects the conversion loss, and the higher P leads to a greater loss. Therefore, the optimal engine power P is the trade-off between engine efficiency and conversion loss. Note that for the real battery and motor, β_2 is related to P_{d} and P, the optimal power (see Fig. 12.7) is determined by a more complex nonlinear optimization problem.

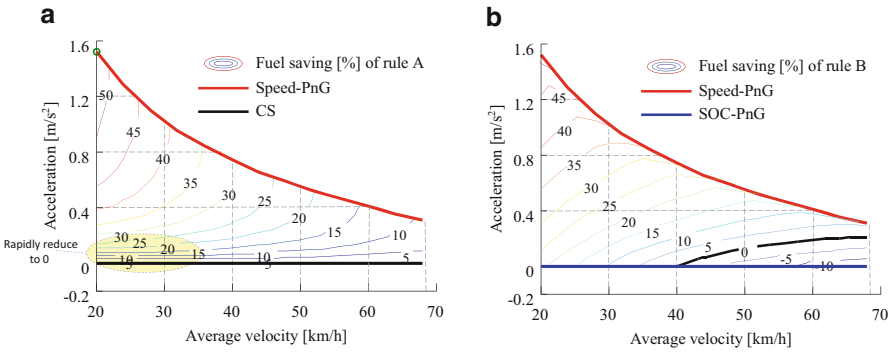

Fig. 12.10 Fuel economy of the two compromise strategies of rule A and rule B. (**a**) fuel-saving map of rule A; (**b**) fuel saving map of rule B

12.6 Compromised Rules and Performance

Even though having the highest fuel-saving rate, the Speed-PnG strategy suffers from poor ride comfort due to the fluctuating speed, as shown in Fig. 12.8. So in this section we present the principles to compromise between fuel economy and ride comfort, that is, to limit the acceleration in the pulse phase by sacrificing fuel-saving.

Based on Fig. 12.9, two rules are proposed to achieve the goal:

Rule A In the pulse phase, for a given lower acceleration, the battery and motor are not used; the engine operates at a lower power (lower efficiency) to accelerate rather than at the sweet spot (best efficiency), for example, using point T to replace the sweet spot S, as shown in Fig. 12.9.

Rule B In the pulse phase, for a given lower acceleration, the engine always operates at the sweet spot, but only part of the power is used to accelerate; the extra power is absorbed by the battery and later dissipated in the glide phase. In this case, both vehicle speed and SOC fluctuate periodically.

The fuel-saving rate of Rule A and Rule B at different acceleration and average speed is shown in Fig. 12.10a, b.

In rule A, the fuel-saving rate drops from the optimum (Speed-PnG) to that of the CS strategy as the acceleration decreases. Due to the nonlinear engine efficiency, the fuel-saving rate drops slowly at first and then quickly descends to zero. It can be explained by Fig. 12.9: as point S moves left, line GS moves down, and then point E_v goes down nonlinearly, depending on the profile of the best BSFC line. This rule can be regarded as a weighted sum of Speed-PnG and CS.

In rule B, as the acceleration decreases, we can gain better ride comfort and a loss of more fuel benefit. Figure 12.10b shows that the fuel-saving rate drops from the optimum (Speed-PnG) to that of SOC-PnG, at a roughly linear rate. In effect,

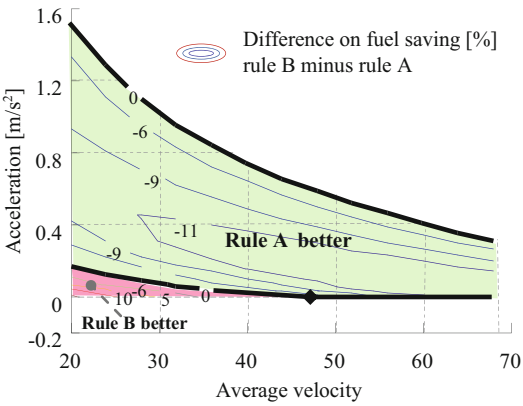

Fig. 12.11 Comparison of rule B and rule A (B minus A)

the lower the acceleration, the more power converted to the battery, thus leading to a greater conversion loss. This compromise rule can be regarded as a weighted sum of Speed-PnG and SOC-PnG. Designers can determine the weights based on their relative demand for fuel economy and comfort.

We can see the difference of rule B and rule A from Fig. 12.11. Under high speed and high acceleration, rule A achieves better fuel-saving than rule B. Otherwise, rule B is more economical. In practice, drivers or the control system can choose an acceptable acceleration level based on their preference for fuel economy or ride comfort, and then determine the proper compromising control rule using Fig. 12.11.

12.7 Conclusions and Remarks

In this chapter, we studied the fuel-optimal cruising strategies for parallel HEVs. And battery-motor system and inertia of vehicle body could form a dual-energy-storage system. The vehicle inertia has higher energy conversion efficiency; its utilization can further improve the fuel efficiency but incur penalty on ride comfort. Therefore, their coordination enables better trade-off between fuel economy and ride comfort. The detailed findings include:

1. Three fuel-optimal cruising strategies are proposed: Speed-PnG with fluctuating speed and fixed SOC, SOC-PnG with fluctuating SOC and fixed speed, and CS at a constant speed driven by the engine only.

   (a) In free cruising scenarios with a limited average speed, the optimal operation is Speed-PnG at medium speed, and then changes to CS at high speed. In Speed-PnG, the optimal control of the engine is to switch between the sweet spot and shutdown; the battery/motor system is not used to avoid conversion loss.

(b) In fixed-speed cruising scenarios, the optimal operation changes from SOC-PnG to CS at increasing speeds. In SOC-PnG, the engine does not operate at the sweet spot but at a lower power (e.g., about 12 kW for the studied HEV), which is a trade-off between engine efficiency and conversion loss.

2. Speed-PnG is the most efficient operation. It achieves better fuel economy than SOC-PnG, arising from the fact that vehicle inertia suffers from less conversion loss than battery. Due to the two energy buffers, the engine can operate at efficient region intermittently and avoid inefficient operation, thus both Speed-PnG and SOC-PnG strategies have better fuel economy than CS strategy.
3. In application, using both vehicle inertia and battery simultaneously can achieve better balance between fuel economy and ride comfort. For a limited acceleration, "decreasing the engine power without using the battery" is more efficient than "using the battery to absorb the extra energy with the engine operating at the sweet spot" under most conditions, except for the low speed low-acceleration condition.

Generally speaking, Speed-PnG strategy with fluctuating kinetic energy could only be implemented in sparse traffic flow. To implement the proposed strategies, more issues such as coordinating with driver operation, executing in car-following scenarios, and its effect on the fuel economy and smoothness of whole traffic flow should be further studied.

References

1. M. Kloess, A. Müller, Simulating the impact of policy, energy prices and technological progress on the passenger car fleet in Austria—a model based analysis 2010–2050. Energy Policy **39**(9), 5045–5062 (2011)
2. R.D. Reitz, Directions in internal combustion engine research. Combust. Flame **160**(1), 1–8 (2013)
3. Y.-L. Kang, Lightweight vehicle, advanced high strength steel and energy-saving and emission reduction. Chin J. Iron Steel **43**(6), 1 (2008)
4. B.G. Pollet, I. Staffell, J.L. Shang, Current status of hybrid, battery and fuel cell electric vehicles: from electrochemistry to market prospects. Electrochim. Acta **84**, 235–249 (2012)
5. D. Kum, H. Peng, N.K. Bucknor, Supervisory control of parallel hybrid electric vehicles for fuel and emission reduction. J. Dyn. Syst. Meas. Control. **133**(6), 061010(1)–061010(10) (2011)
6. K.Ç. Bayindir, M.A. Gözüküçük, A. Teke, A comprehensive overview of hybrid electric vehicle: powertrain configurations, powertrain control techniques and electronic control units. Energy Convers. Manag. **52**(2), 1305–1313 (2011)
7. K. Van Berkel, T. Hofman, B. Vroemen, M. Steinbuch, Optimal control of a mechanical hybrid powertrain. IEEE Trans. Veh. Technol. **61**(2), 485–497 (2012)
8. H.Y. Tong, W.T. Hung, C.S. Cheung, On-road motor vehicle emissions and fuel consumption in urban driving conditions. J. Air Waste Manage. Assoc. **50**(4), 543–554 (2000)
9. A. Wang, Y. Ge, J. Tan, M. Fu, A.N. Shah, Y. Ding, B. Liang, On-road pollutant emission and fuel consumption characteristics of buses in Beijing. J. Environ. Sci. **23**(3), 419–426 (2011)
10. A.E. Atabani, I.A. Badruddin, S. Mekhilef, A.S. Silitonga, A review on global fuel economy standards, labels and technologies in the transportation sector. Renew. Sust. Energ. Rev. **15**(9), 4586–4610 (2011)

11. S.E. Li, H. Peng, Strategies to minimize the fuel consumption of passenger cars during car-following scenarios. Proc. Inst. Mech. Eng. D J. Automob. Eng. **226**(3), 419–429 (2012)
12. S.E. Li, H. Peng et al., Minimum fuel control strategy in automated car-following scenarios. IEEE Trans. Veh. Technol. **61**(3), 998–1007 (2012)
13. T. Hofman, M. Steinbuch, R. van Druten, A.F. Serrarens, Design of CVT-based hybrid passenger cars. IEEE Trans. Veh. Technol. **58**(2), 572–587 (2009)
14. J. Liu, H. Peng, Modeling and control of a power-split hybrid vehicle. IEEE Trans. Control Syst. Technol. **16**(6), 1242–1251 (2008)
15. G. Elnagar, M.A. Kazemi, M. Razzaghi, The pseudospectral Legendre method for discretizing optimal control problems. IEEE Trans. Autom. Control **40**(10), 1793–1796 (1995)
16. I.M. Ross, F. Fahroo, Pseudospectral knotting methods for solving non-smooth optimal control problems. J. Guid. Control. Dyn. **27**(3), 397–405 (2004)
17. S. Xu, S.E. Li, K. Deng, S. Li, B. Cheng, A unified pseudospectral computational framework for optimal control of road vehicles. IEEE/ASME Trans. Mechatron. **20**, 1499–1510 (2014)
18. P.E. Gill, W. Murray, M.A. Saunders, SNOPT: an SQP algorithm for large-scale constrained optimization. SIAM Rev. **47**(1), 99–131 (2005)

Part IV
Fault Diagnosis

Chapter 13
Fault Detection and Isolation with Applications to Vehicle Systems

Pierluigi Pisu

Abstract This chapter provides solutions to the fault detection and isolation (FDI) problem when the model describing the system behavior is a deterministic continuous-variable system and faults can be modeled as additive signals acting on the process. The solution to this problem leads to a diagnostic system that consists of two parts: a residual generation module and a residual evaluation module. The chapter focuses on two FDI approaches: the observer design method and the nonlinear parity equation method. Illustrative examples on fault diagnosis for a brake-by-wire system and a battery demonstrate the efficacy of the methods.

Keywords Fault Detection • Fault Isolation • Automotive

13.1 Introduction to Fault Detection and Isolation

Any complex system or process is subject to the occurrence of faults. These systems may be mechanical, chemical, electrical, or some combination of these and may or may not be controlled by a computer. Faults include the complete or partial failure of actuators, sensors, or other components of the system, or the occurrence of events external to the system (disturbances) that prevent its normal functioning. The ability to detect the occurrence of any fault and identify its cause is critical for a number of reasons. In some cases faults can lead to great loss of life and property (e.g., aircraft, nuclear power plants, etc.) [22, 40]. Further, early detection of faults can allow timely corrective action which in many cases will greatly reduce the incidence of expensive, unexpected breakdowns (e.g., machinery in factories). Environmental considerations are also of importance such as systems for monitoring automobile engine emissions.

One of the simplest methods of fault detection and isolation (FDI) is to utilize hardware redundancy [4], usually in conjunction with a voting scheme [41]. For example, a computer may be used to monitor the outputs of a number of sensors

P. Pisu (✉)
Clemson University, Department of Automotive Engineering and International Center for Automotive Research, 4 Research Dr., Greenville, SC 29680
e-mail: pisup@clemson.edu

Q. Zhang et al., *Automotive Air Conditioning*, DOI 10.1007/978-3-319-33590-2_13

all of which measure the same physical variable. The reading that occurs most often among the sensors is then taken as the correct one. More sophisticated schemes may assign different weights to different sensors based upon their reliability and then use some decision-making scheme to estimate the correct measurement. The hardware redundancy approach is obviously expensive and is used only in systems where the higher cost is justified by the potential benefits in terms of safety and performance. With the increasing application of computers to the control of systems and processes, the use of computer-based approaches to FDI, i.e. those that use software or analytical redundancy, have become feasible [1, 2, 4, 14, 15, 20, 31, 32, 36]. In these approaches, data gathered from the system are analyzed by the computer in order to detect the presence of faults. The computer makes use of a priori knowledge about the system—usually embodied in a knowledge base or physical model—to make inferences about the presence or absence of faults from the data gathered. The focus of this discussion will be on model-based approaches to FDI.

Model-based FDI strategies use either a phenomenological model (which may be linear or nonlinear) or an empirical, input–output data-based model (again linear or nonlinear) to predict the outputs of the system that is being monitored, from a knowledge of its inputs. The difference between the measured and predicted output is called a residual. Under ideal conditions, i.e. when there are no faults, no noise corrupting the measurements, no uncertainty in the model, all the residuals will be zero. If a fault is present the residual is non-zero, allowing detection of the fault. When a fault is detected the residuals are further processed to isolate the location of the fault in the system.

The software algorithm that generates the residuals is called the residual generator. In the absence of faults the generator produces zero residuals, while in the presence of faults the generator is so constructed that the presence of specific faults give rises to unique signatures that allow the identification of the particular fault. The field of FDI has seen significant progress with respect to model-based algorithmic approaches to residual generation, and in many respects this subject area can be considered relatively mature [1–4, 15, 20, 23, 31, 32, 36, 39]. Recently, progress has also been made in the development of hierarchical approaches that permit the decomposition of a complex diagnostic process into a structure that can greatly simplify and systematize the development of structured FDI algorithms [33].

Faults that can occur in dynamic systems can almost always be classified into one of three types:

Input or actuator faults These are faults that arise due to failures in actuators, causing the actual inputs acting on a system to be different from the known or nominal values. Unmeasured disturbances are also most naturally modeled as input faults though in the FDI literature an artificial distinction is often made between disturbances and actuator failures.

Output or sensor faults Output faults arise due to faulty measurements and result in the measured values of the output variables being different from the true values. It should be noted that in any measurement system the true value of a variable is never known because there always is some amount of noise, sensor mis-calibration

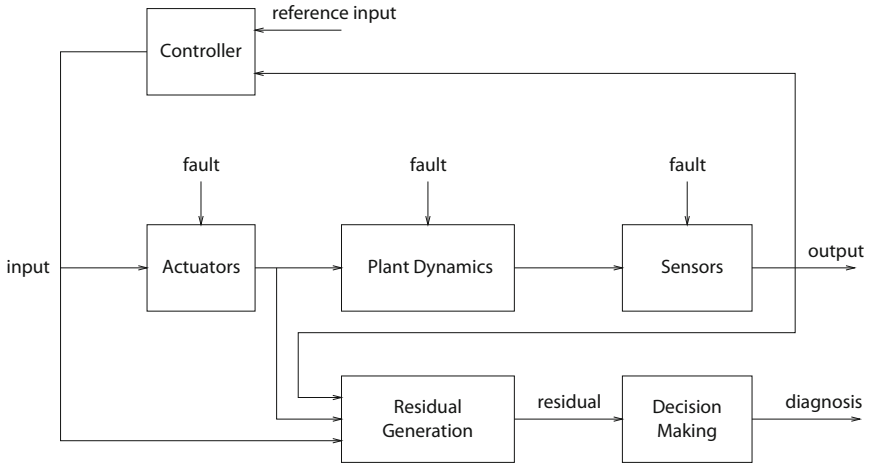

Fig. 13.1 General structure of a model-based FDI scheme with faults

and other factors that affect the accuracy of the measurement. However, when the discrepancies become unacceptably large, a sensor fault is considered to have occurred [8].

Parameter or component faults These are faults that can be represented as changes in system parameters, either due to failures in system components or due to natural changes in the system such as aging and wear. Component faults differ from input and output faults in an important way—they often enter the system equation nonlinearly, making it impossible to diagnose using linear diagnostic techniques. In nonlinear system, practically there is no difference between parameter faults and input faults, since a parametric fault can be modeled as an unknown input. In the following, therefore, no explicit distinction is made between parametric and input faults.

The general representation of a plant with possible faults is shown in Fig. 13.1

13.2 Observer Design Methods for FDI

Observer-based approaches reconstruct the outputs of the system from the input vector and sensor measurements by using observers [28–30]. Kalman filters, an optimal observer technique, can be used to optimize the outputs if sensor and process noise are considered. The errors between the actual outputs and the estimated outputs are then used as a residual for fault detection and fault isolation. If all of the sensors were error free, all of the residuals (the difference between the actual sensor outputs and the estimated sensor outputs) would be near zero. This assumes the plant is modeled correctly, there are no disturbances and the noise is negligible. Clark published several early papers [5–7] using observer-based schemes

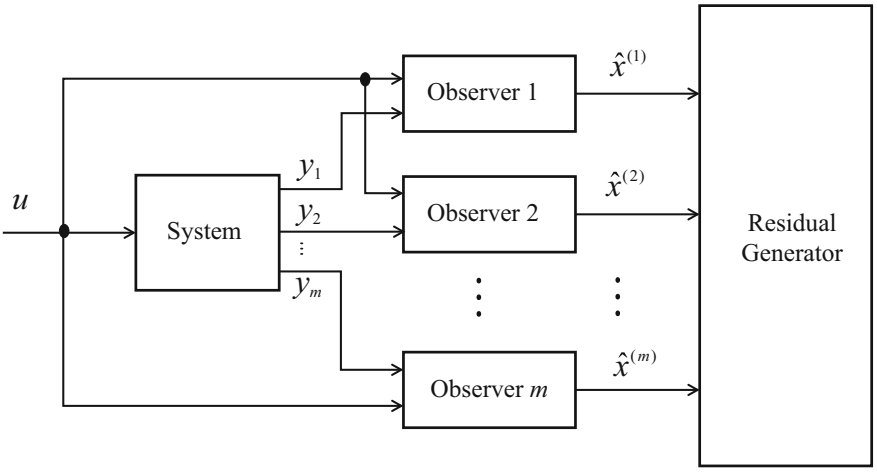

Fig. 13.2 General structure of a dedicated observer scheme

for instrument failure detection (IFD). His original work includes the single observer scheme [7] and the dedicated observer scheme [6].

In the following we are going to consider a dynamic system described by

$$\dot{x} = g(x, u) \tag{13.1}$$

$$y = h(x, u) \tag{13.2}$$

where $x = [x_1, \ldots, x_n]^T \in \mathbb{R}^n$, $y = [y_1, \ldots y_m]^T \in \mathbb{R}^m$, $u = [u_1, \ldots, u_p]^T \in \mathbb{R}^p$, with $g(\cdot, \cdot) : \mathbb{R}^{n \times p} \rightarrow \mathbb{R}^n, h(\cdot, \cdot) : \mathbb{R}^{n \times p} \rightarrow \mathbb{R}^m$ smooth functions, and $g(0, 0) = h(0, 0) = 0$.

13.2.1 Dedicated Observer Scheme

The dedicated observer scheme for sensor fault detection is represented in Fig. 13.2. The scheme utilizes an observer for each sensor measurement to estimate the output of the system.

Given the system (13.1)–(13.2) observable from each output, consider the set of observers described by

$$\dot{\hat{x}}^{(1)} = g_1(\hat{x}^{(1)}, u, y, \hat{y}_1) \tag{13.3}$$

$$\hat{y}_1 = h_1(\hat{x}^{(1)}, u) \tag{13.4}$$

$$\vdots \quad \vdots$$

$$\dot{\hat{x}}^{(m)} = g_m(\hat{x}^{(m)}, u, y, \hat{y}_m) \tag{13.5}$$

$$\hat{y}_m = h_m(\hat{x}^{(m)}, u) \tag{13.6}$$

where $\hat{x}^{(j)} \in \mathbb{R}^n, h_j : \mathbb{R}^{n\times p} \to \mathbb{R}, j = 1, \ldots, m$.

In absence of faults the state of each observer will converge to the system state, i.e., $\hat{x}^{(j)} = x$ for $j = 1 \ldots m$. If the sensor k is faulty, then $\hat{x}^{(k)} \neq x$, and $\hat{x}^{(j)} = x$ for $j \neq k$. In the case of single sensor fault, the faulty sensor can be isolated by comparing $\hat{x}^{(1)}, \ldots, \hat{x}^{(m)}$. By defining the primary residuals as

$$\hat{r}^{(1)} = \hat{x}^{(1)} - \hat{x}^{(2)} \tag{13.7}$$

$$\hat{r}^{(2)} = \hat{x}^{(2)} - \hat{x}^{(3)} \tag{13.8}$$

$$\vdots \quad \vdots$$

$$\hat{r}^{(m)} = \hat{x}^{(m)} - \hat{x}^{(1)} \tag{13.9}$$

and considering a row vector of normalizing weights $w^{(j)} = [w_1^{(j)}, \ldots, w_n^{(j)}], j = 1, \ldots, m$, secondary residuals $e_j \in \mathbb{R}$ can be defined as

$$e_j = w^{(j)} \cdot \hat{r}^{(j)}, j = 1, \ldots, m \tag{13.10}$$

During the decision making or residual evaluation phase, the secondary residuals are compared with thresholds. Threshold values are selected based on the sensor and system noise, and unmodeled dynamics to avoid the occurrence of false alarms [21]. A residual mismatch above a threshold value is indicated by a 1, while a residual below the threshold is indicated by 0. The error signatures in Table 13.1 can therefore be utilized to detect and isolate the fault.

13.2.2 Generalized Observer Scheme

The generalized observer scheme for sensor fault detection is represented in Fig. 13.3. Similarly to the previous approach, the scheme utilizes an observer for each sensor. In this scheme, each observer uses all measurements but the one corresponding to the sensor to be diagnosed.

Table 13.1 Error signature for single fault of dedicated observer scheme

Fault	e_1	e_2	$\cdots$	e_{m-1}	e_m
None	0	0	$\cdots$	0	0
Sensor y_1	1	0	$\cdots$	0	1
Sensor y_2	1	1	$\cdots$	0	0
$\vdots$	$\vdots$	$\vdots$	$\vdots$	$\vdots$	$\vdots$
Sensor y_{m-1}	0	0	$\cdots$	1	0
Sensor y_m	0	0	$\cdots$	1	1

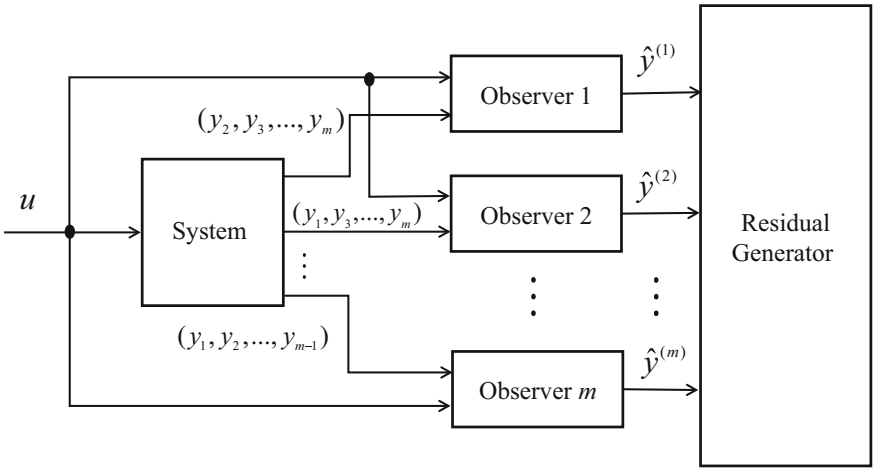

Fig. 13.3 General structure of a generalized observer scheme.

Given the system (13.1)–(13.2) observable from each set of $m-1$ outputs, define $y^{(1)} = [y_2, y_3, \ldots, y_m]^T, y^{(2)} = [y_1, y_3, \ldots, y_m]^T, \ldots, y^{(m)} = [y_1, y_2, \ldots, y_{m-1}]^T$ as vectors in R^{m-1}. Consider the set of observers described by

$$\dot{\hat{x}}^{(1)} = \hat{g}_1(\hat{x}^{(1)}, u, y, \hat{y}^{(1)}) \tag{13.11}$$

$$\hat{y}^{(1)} = h^{(1)}(\hat{x}^{(1)}, u) \tag{13.12}$$

$$\vdots \quad \vdots$$

$$\dot{\hat{x}}^{(m)} = \hat{g}_m(\hat{x}^{(m)}, u, y, \hat{y}^{(m)}) \tag{13.13}$$

$$\hat{y}^{(m)} = h^{(m)}(\hat{x}^{(m)}, u) \tag{13.14}$$

where $\hat{x}^{(j)} \in \mathbb{R}^n, h^{(j)} : \mathbb{R}^{n \times p} \to \mathbb{R}^{m-1}, j = 1, \ldots, m$.

In absence of faults the state of each observer will converge to the system state, i.e., $\hat{x}^{(j)} = x$ for $j = 1 \ldots m$. If the sensor k is faulty, then $\hat{x}^{(k)} = x$, and $\hat{x}^{(j)} \neq x, \forall j \neq k$. In the case of single sensor fault, the faulty sensor can be isolated by comparing $\hat{y}^{(1)}, \ldots, \hat{y}^{(m)}$ with the corresponding sensor measurements. By defining the primary residuals as

$$\hat{r}^{(1)} = y^{(1)} - \hat{y}^{(1)} \tag{13.15}$$

$$\hat{r}^{(2)} = y^{(2)} - \hat{y}^{(2)} \tag{13.16}$$

$$\vdots \quad \vdots$$

$$\dot{\hat{r}}^{(m)} = y^{(m)} - \hat{y}^{(m)} \tag{13.17}$$

Table 13.2 Error signature for single fault of generalized observer scheme.

Fault	e_1	e_2	$\cdots$	e_{m-1}	e_m
None	0	0	$\cdots$	0	0
Sensor y_1	0	1	$\cdots$	1	1
Sensor y_2	1	0	$\cdots$	1	1
$\vdots$	$\vdots$	$\vdots$	$\vdots$	$\vdots$	$\vdots$
Sensor y_m	1	1	$\cdots$	1	0

and considering a row vector of normalizing weights $w^{(j)} = [w_1^{(j)}, \ldots, w_{m-1}^{(j)}], j = 1, \ldots, m$, secondary residuals $e_j \in \mathbb{R}$ can be defined as

$$e_j = w^{(j)} \cdot \hat{r}^{(j)}, j = 1, \ldots, m \tag{13.18}$$

During the decision making or residual evaluation phase, the secondary residuals are compared with thresholds. A residual crossing a threshold is indicated by a 1, while a residual not crossing a threshold is indicated by 0. The error signatures in Table 13.2 can therefore be utilized to detect and isolate the fault.

13.2.3 Example of FDI for Brake-by-Wire System

In this section, an example of application of the generalized observer scheme to the problem of fault diagnosis in a brake-by-wire (BBW) system is presented. BBW refers to the technology in which mechanical and hydraulic components of traditional braking systems are replaced by electronic sensors and actuators to carry out the function of braking in a vehicle. BBW is a combination of electronic control systems coupled with a set of electromechanical actuators and the brake pedal. Details about the hazard analysis, fault tree analysis, and failure mode effect analysis can be found in [35], while in [18, 19, 33] different approaches are presented to deal with the problem of single and multiple fault detection for a BBW system. In the following, the problem of single fault detection and identification in sensors is obtained by means of observers using Luenberger observer design while converge can be demonstrated using Lyapunov approach.

A one-wheel brake model is considered here consisting of an electric dc motor, a ball screw that converts rotary motion into linear motion, and a caliper, which is modeled as a nonlinear spring. The motor shaft position θ is controlled by the input voltage V, which is the output of a controller whose purpose is to make the caliper force, F_{cal}, track the desired force u_j derived from the measured brake pedal force.

The dynamic equations for the one-wheel brake model are given by

$$\dot{\theta} = \omega \tag{13.19}$$

$$\dot{\omega} = K_i\, i - K_f\, F_{cal} \tag{13.20}$$

$$\frac{di}{dt} = \frac{1}{L}(-K_e\,\omega - R\,i + V) \tag{13.21}$$

$$F_{cal} = f(\theta) \tag{13.22}$$

where K_i, K_f, R, L, K_e are known parameters, i is the dc motor current, ω is the dc motor angular velocity, $f(\theta)$ is convex on the interval $I(\theta) = [0, \theta_{max}]$ of interest, and $f'(\theta) > \gamma_0$ with γ_0 positive constant.

In the development of the diagnostic scheme the motor current sensor, caliper force sensor, and motor position sensor faults are considered.

13.2.3.1 Caliper Force Observer Design

To design an observer for the caliper force sensor, it is assumed that the caliper force F_{cal} and the motor current i are known but they may be affected by an additive fault. Since the motor voltage V is not readily available only (13.19)–(13.20) are needed for the observer design.

Defining state variables as

$$x_1 = \theta$$
$$x_2 = \dot{x}_1 = \omega$$

and the system inputs as $u_1 = i$, $u_2 = F_{cal}$, the state equations can be written as

$$\dot{x}_1 = x_2 \tag{13.23}$$

$$\dot{x}_2 = K_i\,u_1 - K_f\,u_2 \tag{13.24}$$

$$y_1 = u_1 \tag{13.25}$$

$$y_2 = u_2 = f(x_1) \tag{13.26}$$

Notice that this system is a function of the inputs F_{cal} and i, both coming from available sensors. F_{cal} is also an output of the system so it can also be calculated from x_1. The observer for the caliper force is defined by the following equations:

$$\dot{\hat{x}}_1 = \hat{x}_2 + l_1(y_2 - \hat{F}_{cal}) \tag{13.27}$$

$$\dot{\hat{x}}_2 = K_i\,y_1 - K_f\,y_2 + l_2(y_2 - \hat{F}_{cal}) \tag{13.28}$$

$$\hat{F}_{cal} = f(\hat{x}_1) \tag{13.29}$$

where l_1 and l_2 are the observer gains. Defining the errors $e_1 = x_1 - \hat{x}_1$ and $e_2 = x_2 - \hat{x}_2$, in absence of faults the error dynamics are

$$\dot{e}_1 = e_2 - l_1(y_2 - \hat{F}_{cal}) = e_2 - l_1(f(x_1) - f(\hat{x}_1)) \tag{13.30}$$

$$\dot{e}_2 = -l_2(y_2 - \hat{F}_{cal}) = -l_2(f(x_1) - f(\hat{x}_1)) \tag{13.31}$$

Define $\xi = \dfrac{f(x_1) - f(\hat{x}_1)}{e_1}$, then

$$\dot{e}_1 = e_2 - l_1 e_1 \xi(x_1, \hat{x}_1) \tag{13.32}$$

$$\dot{e}_2 = -l_2 e_1 \xi(x_1, \hat{x}_1) \tag{13.33}$$

From $f'(x_1) > \gamma_0 > 0$ and the convexity property of $f(x_1)$, it follows that $\xi > \gamma_0 > 0$. It can be shown [33] by Lyapunov analysis that it is possible to determine l_1 and l_2 so that the error dynamics (13.32)–(13.33) are exponentially stable at the origin. The following residual is generated and can be compared to a threshold to signify a sensor fault

$$r_{F_{\text{cal}}} = y_2 - \hat{F}_{\text{cal}} = y_2 - f(\hat{x}_1)$$

In absence of faults, sensor noise or modeling errors the residual $r_{F_{\text{cal}}}$ is zero. It is easy to verify that the residual will be non-zero in the presence of a sensor fault in y_1 or y_2.

13.2.3.2 Motor Position Observer Design

In this case, the motor position θ and the current i are assumed to be available through sensors but eventually affected by additive fault. Starting from (13.19)–(13.20) with $u_1 = i$, the system equations can be written as

$$\dot{x}_1 = x_2 \tag{13.34}$$

$$\dot{x}_2 = K_i u_1 - K_f f(x_1) \tag{13.35}$$

$$y_1 = i \tag{13.36}$$

$$y_3 = x_1 \tag{13.37}$$

The observer is defined as

$$\dot{\hat{x}}_1 = \hat{x}_2 + l_3(y_3 - \hat{x}_1) \tag{13.38}$$

$$\dot{\hat{x}}_2 = K_{\text{i}}\, y_1 - K_f f(y_3) + l_4(y_3 - \hat{x}_1) \tag{13.39}$$

The residual in this case is given by

$$r_\theta = y_3 - \hat{x}_1 \tag{13.40}$$

Convergence of the observer depends on the selection of the gains l_3, l_4. Analysis of stability can be conducted via Lyapunov approach [33].

Table 13.3 Error signature for BBW System.

Fault in sensor	r_θ	$r_{F_{\text{cal}}}$
None	0	0
F_{cal}	0	1
θ	1	0
i	1	1

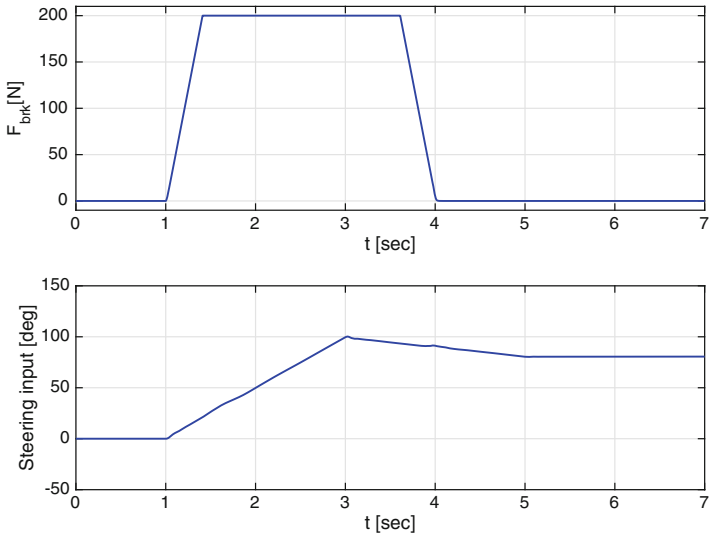

Fig. 13.4 Driver inputs.

13.2.3.3 Fault Detection and Isolation

In the case of single faults, the associated residuals fault signature can be generated as shown in Table 13.3. A non-zero residual above a threshold value, whose selection depends on the noise and unmodeled dynamics for the system, is indicated by 1, while a residual within the threshold bounds is indicated by 0.

This signature table can be generated by observing that $r_{F_{\text{cal}}}$ does not depend on the position sensor measurement fault by construction because the observer (13.27)–(13.29) uses only information from current sensor and caliper force sensor. Similarly, r_θ does not depend on the caliper sensor fault because the observer (13.38)–(13.39) utilizes only information from the current sensor and the position sensor.

In Fig. 13.5 the residuals for the caliper force and the motor position sensors in absence of faults are depicted. A braking force and steering angle are applied as shown in Fig. 13.4, and an initial vehicle speed of 115 Km/h is considered.

The thresholds for residual evaluation must be tuned to have a zero error signature with healthy conditions and to guarantee a certain robustness to uncertain dynamics.

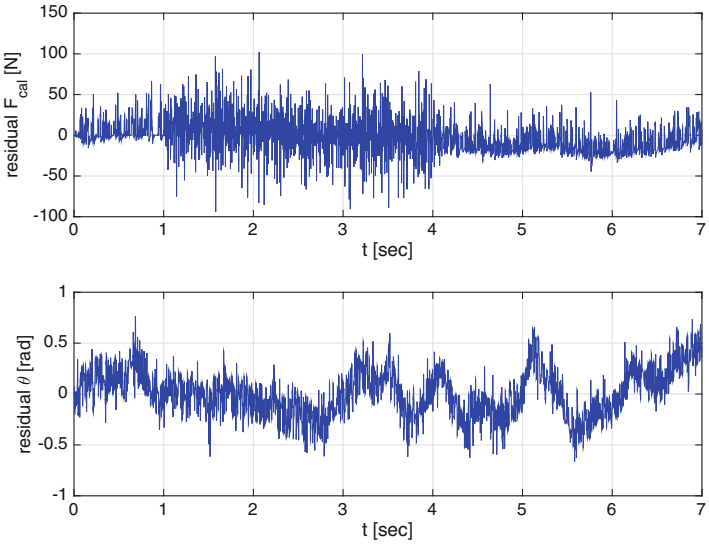

Fig. 13.5 Residuals in absence of faults.

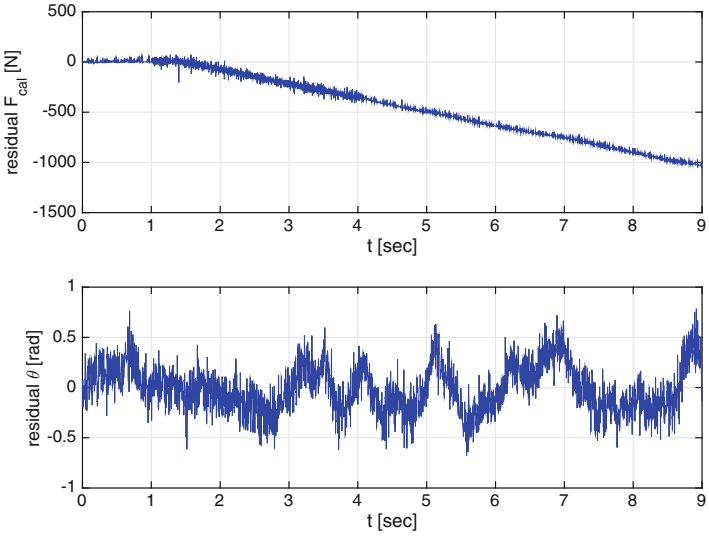

Fig. 13.6 Residuals with caliper force sensor faulty.

In Fig. 13.6, the residuals and error signature for caliper force and motor position, in the case of faulty caliper force sensor, are presented. The fault is represented by a step of -200 N injected in the caliper force sensor at $1.4s$. In the second test, a fault of $\pi/5$ rad in the motor position sensor is injected at $2s$. The measured position is shown in Fig. 13.7 where the effect of the fault is clearly visible.

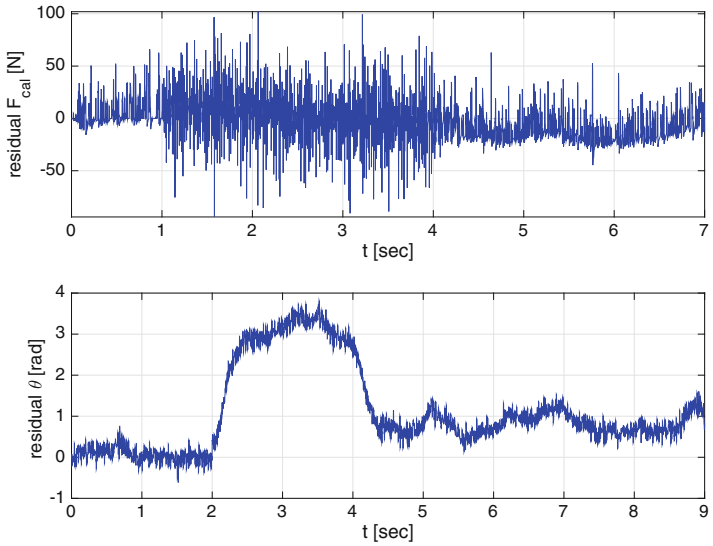

Fig. 13.7 Residuals with motor position sensor faulty.

13.3 NPERG Method

The nonlinear parity equation residual generator (NPERG) method is the most general approach for fault diagnosis when dealing with nonlinear systems [34]. The NPERG approach was introduced in 1994 by Krishnaswami and Rizzoni [24, 25] in the contest of fault diagnosis for internal combustion engines, and then extended to the general case of continuous time nonlinear systems by Krishnaswami [26] in 1996. Zhirabok extended the approach to the case of discrete time nonlinear systems [43], while Zhang et al. [42] provided results in the case of systems modeled by polynomial differential-algebraic equations.

The scheme utilizes input and state observers to provide FDI using nonlinear dynamic models of a system. The observers are configured in such a way that sensor faults are detected and isolated using nonlinear output estimators, while input and plant parameter faults are isolated using nonlinear input estimators.

The main idea behind the approach resides in the fact that any FDI scheme is a map that acts upon the measurements obtained from the system under study and produces an output that is unique for each combination of faults that can occur in the system. Thus an FDI scheme can be represented as the map $W : \mathbb{R}^m \rightarrow \mathbb{R}^q$

$$W(y) = s \tag{13.41}$$

where $s \in \mathbb{R}^q$ is the output vector produced by the FDI scheme. It should be noted that $rank(W) \leq m$. Now, assume

$$x(t) = \Phi(t, u(t)) \tag{13.42}$$

where $\Phi(\cdot,\cdot)$ is a nonlinear function of the input and time, solution of the dynamic system (13.1). From (13.2) and (13.42), the measured output in presence of actuator and sensor faults can be expressed as

$$y = h(\Phi(t, u(t) + \Delta u), u(t) + \Delta u) + \Delta y = H(t, u(t) + \Delta u) + \Delta y \tag{13.43}$$

where $H : \mathbb{R}^p \to \mathbb{R}^m$, and $rank(H) = m$ from uniqueness of solution. From (13.43) the internal form of the residual generator (13.41) can be written as

$$s = W(H(t, u(t) + \Delta u) + \Delta y) = Q(f(t)) \tag{13.44}$$

where Q is the composition of the two maps H and W, and $f(t) = [\Delta y, \Delta u]^T$ is the faults vector.

Definition 1 (FDI Scheme). An FDI scheme is a function or operator acting on the system's measurements to produce a unique output for each combination of faults that can occur in the system. The scheme is said to be *strongly isolating* if the elements of the vector s also track the time histories of the values of the faulty variables.

13.3.1 Conditions and Capabilities of a Diagnostic System

This section is intended to serves as a compilation of definitions, theorems, and basic properties related to diagnosability in nonlinear systems. Detailed description of these results can be found in [26].

13.3.1.1 Diagnosis of a Single Fault

Let f_j represent the j^{th} element of the fault vector $f(t)$. The j^{th} fault is said to exist if $f_j \neq 0$. A fault can be detected if it is *observable* from the measured outputs of the system. A fault can be isolated if it has a unique non-zero effect on the available measurements. The following theorem states this in more precise mathematical terms.

Theorem 1 (Strong Isolability of a single fault). *A fault f_j can be strongly isolated only if $\frac{\partial y}{\partial f_j} \neq 0$.*

Proof. Note that from Definition 1, f_j is strongly isolable for $t \in [t_0, t_1]$, if the following function can be constructed

$$w_j(y(t)) = s_j(t) = f_j \tag{13.45}$$

From (13.43), by defining $G(t, f(t)) = H(t, u(t) + \Delta u) + \Delta y$, it follows

$$y(t) = G(t, f(t)) = G(t, [f_1(t), f_2(t), \ldots, f_j(t), \ldots f_{m+p}(t)]) \tag{13.46}$$

From the implicit function theorem, local invertibility follows and therefore

$$\frac{\partial G}{\partial f_j} \neq 0 \ \forall y(t), f_j(t), t \in [t_0, t_1] \tag{13.47}$$

if and only if

$$f_j = s_j(t) = w_j(y(t)) \tag{13.48}$$

which is the condition for strong isolability. □

From Theorem 1 it follows that single output faults are always isolable because $\frac{\partial G}{\partial \Delta y} = I_{m \times m}$, where $I_{m \times m}$ is the identity matrix of dimension m.

13.3.1.2 Diagnosis of Multiple Faults

Consider now the case of k simultaneous faults. Indicate with f_{faulty} a vector that contains the k non-zero components of $f(t)$, and with $f_{nofaulty}$ a vector of the remaining zero components of $f(t)$. Defining $G(t, f(t)) = H(t, u(t) + \Delta u) + \Delta y$, the following theorem holds:

Theorem 2. *A set of k simultaneously occurring faults can be strongly isolated if and only if there exists some subset J of $k + 1$ components of the output vector*

$$y(t) = G(t, f_{faulty}(t), f_{nofaulty}) = G(t, f_{faulty}(t), [0, 0, \ldots 0]) \tag{13.49}$$

which taken k at a time and denoted as

$$y^i = G^{(i)}(t, f_{faulty}(t), [0, 0, \ldots 0]), \quad i = 1, \ldots, k, \quad y^i \in J \tag{13.50}$$

satisfies

$$rank\left(\frac{\partial G^{(i)}}{\partial f_{faulty}}\right) = k, \quad i = 1, \ldots, k \tag{13.51}$$

Corollary 1 (Maximum Simultaneous multiple faults isolation). *Given m available measurements a maximum of $k \leq m - 1$ multiple faults that occur simultaneously can be strongly isolated.*

Proof. This follows from Theorem 2 and the fact that since there are m measurements a maximum of m independent equations are available. Hence $k + 1 \leq m \Leftrightarrow k \leq m - 1$. □

Corollary 2. *Multiple simultaneous output faults that satisfy Corollary 1 are always strongly isolable.*

Proof. This may be seen from the fact that if a combination of any k output faults, $k < m$ is denoted by $\Delta y^i \in \mathbb{R}^k$ then

$$\frac{\partial G^{(i)}}{\partial \Delta y^i} = I_{k\times k} \tag{13.52}$$

13.3.2 FDI Algorithm Design for Nonlinear Dynamic Systems

The previous section provides necessary and sufficient condition for the existence of a solution to the FDI problem under the assumption that the output of the systems is algebraically related to the inputs. Theorems 1 and 2 and their associated corollaries all depend upon the existence of unique solutions to the system of equations relating the fault variables to the available measurements. Dynamic systems in which the inputs can be solved for uniquely from available outputs are said to be invertible. Thus the requirement of obtaining unique solutions may simply be stated as the system be invertible with respect to the given set of measurements and faults. This is defined more precisely by the following Lemma [26].

Lemma 1. *Given ν input faults and r output faults, the total number of occurring simultaneous faults $k = \nu + r$ can be strongly isolated if and only if $k = \nu + r \leq m - 1$ and there exists at least $k + 1$ measurements such that the given set of faults are invertible with respect to any set of these measurements taken k at a time.*

Proof. The proof follows directly from Theorem 2 condition for the existence of unique solutions to the fault variables and the relationship between invertibility and unique solvability [16]. □

This result is extremely significant since it allows results from inversion of nonlinear systems to be utilized for the solution of FDI problems.

Corollary 3. *A set of ν simultaneously occurring input faults can be strongly isolated if and only if the total number of simultaneous faults satisfies $k = \nu + r \leq m - 1$ and the faulty inputs are invertible with respect to at least some $\nu + 1$ of the available non-faulty outputs taken ν at a time.*

Proof. From (13.43) it is seen that output faults enter the measurement equation algebraically. Therefore these faults are always invertible [16]. Now eliminating the measurement equations in which the output fault terms appear from the set of available measurement equations, the remaining equations arise from non-faulty output measurements and from Lemma 1 the input faults must be invertible with respect to some $\nu + 1$ of the available non-faulty outputs taken ν at a time. □

13.3.2.1 The Nonlinear Parity Equation Residual Generation Scheme

For the majority of nonlinear dynamic systems a closed form solution cannot be derived, therefore the fault variables can only be numerically determined. In this case, to solve the FDI problem, a design procedure known as the Nonlinear Parity Equation Residual Generation (NPERG) scheme can be employed [26]. Consider the system represented by

$$\dot{x} = f(x, u + \Delta u) \tag{13.53}$$

$$y = h(x, u + \Delta u) + \Delta y \tag{13.54}$$

where ν inputs and r outputs can simultaneously be faulty and $\nu + r = k \leq m - 1$.

Based on Theorem 2 and Lemma 1, the NPERG algorithm can be defined as follows:

NPERG Algorithm [26]
Step 1 [Estimate faults under faulty set assumption] Assume that r elements of the output vector and ν elements of the input vector are faulty. Then the other $m-r$ elements are not faulty. Referring back to Corollary 3 these outputs can be used to estimate the inputs that are suspected of being faulty. Construct an inverse model that estimates the ν input elements, from a suitable set of ν elements of the m-r outputs that are assumed to be non-faulty. Now, using the estimated values of the assumed faulty inputs and the nominal values of the other inputs construct a forward model to estimate all the other measured outputs, including the r outputs that are assumed faulty.
Step 2 [Consistency check] If the assumed set of faults and the actual set of faults match, the measured and the estimated values of the assumed non-faulty outputs of the forward model should match (within measurement and modeling errors). In this case faults have been isolated and estimates obtained in step 1 are also the correct estimates of the faulty variables. If the values do not match, proceed to step 3.
Step 3 [Correct and repeat] If the consistency check fails it is necessary to assume a different combination of faulty elements and repeat step 1 and 2.

The consistency check described in step 2 of the above procedure is known in fault detection literature as *residual evaluation* and each set of inverse and forward models from step 1 is referred to as a *residual generator*. The implementation of the algorithm leads to constructing estimator and forward model for each possible combination of faults. Figure 13.8 shows the schematic of the residual generator for a particular combination of faults. In Fig. 13.8, the subscript *nf* identifies the set of variables that are assumed to be without faults for that particular residual generator and the subscript *f* indicates the set of variables that are assumed to be faulty.

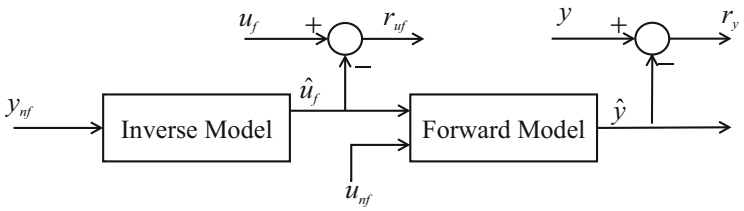

Fig. 13.8 Single element of an NPERG scheme.

13.4 Inverse Models Using Sliding Modes

The sliding mode approach can be used to design asymptotic observers which are dynamic systems for estimating all the components of a state vector using the measured components directly. In addition, using the equivalent control approach [38], an implicit model inversion can be realized and unknown inputs can be estimated from the measured outputs [13, 37]. To illustrate the idea, first the observer design using sliding modes is briefly introduced and second the approach for input fault estimation is presented. For a detailed explanation on sliding mode control theory the reader should refer to [38].

13.4.1 Design of State Estimator for Linear Systems

Consider a linear time invariant system described in state space as follows

$$\dot{x} = Ax + Bu, \quad x \in \mathbb{R}^n, \quad u \in \mathbb{R}^p \tag{13.55}$$

$$y = Cx, \qquad y \in \mathbb{R}^m, \quad rank(C) = m < n \tag{13.56}$$

It is assumed that the matrices A, B, and C are known, and that the pair (A, C) is observable. Since the $rank(C) = m < n$ the observed vector can be represented as

$$y = C_1 x_1 + C_2 x_2, \quad x_1 \in \mathbb{R}^{n-m}, \quad x_2 \in \mathbb{R}^m, \quad det(C_2) \neq 0 \tag{13.57}$$

By solving with respect to x_2

$$x_2 = C_2^{-1}(y - C_1 x_1) \tag{13.58}$$

By mean of the nonsingular coordinate transformation matrix

$$T = \begin{bmatrix} I_{n-m} & 0 \\ C_1 & C_2 \end{bmatrix} \tag{13.59}$$

the system can be rewritten in the new variables x_1 and y as

$$\dot{x}_1 = A_{11}x_1 + A_{12}y + B_1u \tag{13.60}$$

$$\dot{y} = A_{21}x_1 + A_{22}y + B_2u \tag{13.61}$$

where

$$TAT^{-1} = \begin{bmatrix} A_{11} & A_{12} \\ A_{21} & A_{22} \end{bmatrix}, \; TB = \begin{bmatrix} B_1 \\ B_2 \end{bmatrix} \tag{13.62}$$

An observer to estimate x_1 and y in the system can be written as

$$\dot{\hat{x}}_1 = A_{11}\hat{x}_1 + A_{12}\hat{y} + B_1u - L_v\nu \tag{13.63}$$

$$\dot{\hat{y}} = A_{21}\hat{x}_1 + A_{22}\hat{y} + B_2u + \nu \tag{13.64}$$

$$\nu = Msgn(y - \hat{y}) \tag{13.65}$$

$$[sgn(y - \hat{y})]^T = [sgn(y_1 - \hat{y}_1), \cdots, sgn(y_m - \hat{y}_m)] \tag{13.66}$$

where L_v is the observer gain matrix and the estimation error is defined as $e_y = y - \hat{y}$ and $e_1 = x_1 - \hat{x}_1$. The vector y is measured, hence e_y is available. The discontinuous vector function ν is chosen such that the sliding mode is enforced in the manifold $e_y = y - \hat{y} = 0$ and the mismatch between y and $\hat{y}$ is reduced to zero. From the previous equations, the error dynamics can be written as

$$\dot{e}_1 = A_{11}e_1 + A_{12}e_y + L_v\nu \tag{13.67}$$

$$\dot{e}_y = A_{21}e_1 + A_{22}e_y - \nu \tag{13.68}$$

For $M > ||A_{21}e_1 + A_{22}e_y||$, after a short transient, sliding motion will begin on the sliding manifold $e_y = 0$, and the equivalent control becomes $\nu_{eq} = A_{21}e_1$. Substituting the equivalent control ν_{eq} into (13.67), the sliding motion equation can be derived as

$$\dot{e}_1 = (A_{11} + L_vA_{21})e_1 \tag{13.69}$$

which is of order $(n-m)$ and a Luenberger estimator design can be utilized to define the dynamics of e_1 by selecting the design variable L_v. Note that observability of the pair (A_{11}, A_{21}) follows from observability of the pair (A, C).

13.4.2 Input Fault Estimation

Consider the system described by

$$\dot{x} = Ax + B(u + \Delta u), \quad x \in \mathbb{R}^n, \quad u \in \mathbb{R}^p \tag{13.70}$$

$$y = Cx, \qquad y \in \mathbb{R}^m, \quad rank(C) = m,\ m \geq p \tag{13.71}$$

With the change of coordinates (13.59), the system can be written as

$$\dot{x}_1 = A_{11}x_1 + A_{12}y + B_1(u + \Delta u) \tag{13.72}$$

$$\dot{y} = A_{21}x_1 + A_{22}y + B_2(u + \Delta u) \tag{13.73}$$

Considering the observer (13.63)–(13.66), the error dynamics become

$$\dot{e}_1 = A_{11}e_1 + A_{12}e_y + B_1\Delta u + L_v v \tag{13.74}$$

$$\dot{e}_y = A_{21}e_1 + A_{22}e_y + B_2\Delta u - v \tag{13.75}$$

with $e_y = y - \hat{y}$ and $e_1 = x_1 - \hat{x}_1$. For $M > ||A_{21}e_1 + A_{22}e_y + B_2\Delta u||$ sliding mode on the manifold $e_y = 0$ is enforced. Applying the equivalent control method

$$\dot{e}_1 = (A_{11} + L_v A_{21})e_1 + (B_1 + L_v B_2)\Delta u \tag{13.76}$$

$$v_{eq} = -(A_{21}e_1 + B_2\Delta u) \tag{13.77}$$

So, the equivalent control is function of the input fault. If L_v can be designed such that $A_{11} + L_v A_{21}$ is stable and $B_1 + L_v B_2 = 0$, then $e_1 \to 0$ as $t \to \infty$ and $v_{eq} = -B_2\Delta u$. In this case, if the $rank(B_2) = p$, it is always possible to rearrange the rows of $v_{eq} = -B_2\Delta u$ such that the last p equations form a system of independent equations that can be solved with respect to Δu. The equivalent values v_{eq} can be extracted from the switching signal v using a set of first order filters of the form [38]

$$\tau\dot{z} + z = v, \quad z \approx v_{eq} \tag{13.78}$$

13.5 Fault Diagnosis of Li-Ion Batteries

In the following, we illustrate the NPERG solution to the problem of fault diagnosis of Li-Ion batteries in the case of single sensor fault utilizing sliding mode observer design.

13.5.1 Battery Model

Several approaches have been considered in existing literature for modeling the Li-ion battery cells. The first kind of models are derived from electrochemical principles [11]. However, these electrochemical models are generally computationally expensive and too complex for real-time designs. Another type of model, which is most prevalent in Li-ion battery literature, is the electrical equivalent circuit

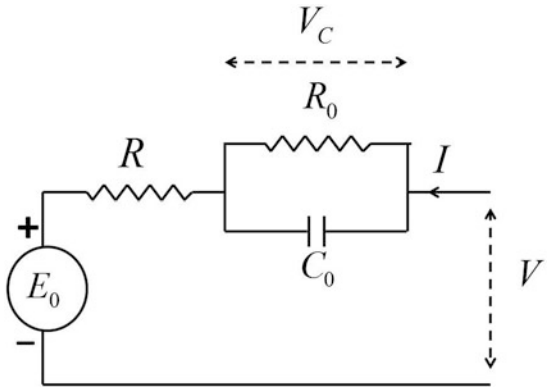

Fig. 13.9 Battery equivalent circuit.

model [12, 17, 27]. The advantage of this model is that it is simple in construction and suitable for real-time computations. In this study, an electrical circuit model (Fig. 13.9) and a lumped thermal dynamics model are adopted.

The electrical dynamics of the battery cell can be written using Kirchhoff's law, and with a usual definition of SOC:

$$\dot{V}_c = -\frac{V_c}{R_0 C_0} + \frac{I}{C_0} \tag{13.79}$$

$$S\dot{O}C = -\frac{I}{Q} \tag{13.80}$$

$$V = E_0 - RI - V_c \tag{13.81}$$

where V is the terminal voltage, I is the input current, R, R_0, and C_0 are the resistance and capacitance of the electrical circuit, V_c is the voltage across the capacitor C_0, E_0 is the open-circuit voltage, and Q is the charge capacity of the battery cell. In this example, some of these parameters are assumed to follow quadratic dependency on SOC and linear dependency on core temperature T_c as given by

$$E_0 = \alpha_0 + \alpha_1 SOC + \alpha_2 SOC^2 + \alpha_3 T_c \tag{13.82}$$

$$R = \beta_0 + \beta_1 SOC + \beta_2 T_c \tag{13.83}$$

while R_0,C_0 are constant.

A radial thermal model similar to the one presented in [10] is chosen for the cylindrical Li-ion battery cell. It models a heat source at the core of the battery and two temperature states (the core temperature and the surface temperature) given as

$$C_c \dot{T}_c = \frac{T_s - T_c}{R_c} + RI^2 + \frac{V_c^2}{R_0} \tag{13.84}$$

$$C_s \dot{T}_s = -\frac{T_s - T_c}{R_c} + \frac{T_{amb} - T_s}{R_u} \tag{13.85}$$

where R_c is the thermal resistance between the battery core and battery surface, R_u is the convective resistance between the battery surface and the surrounding air, C_c is the heat capacity of internal battery material, C_s is the heat capacity of the battery material at the surface, and T_{amb} is the surrounding air temperature.

13.5.2 Diagnostic Problem

In this example, the case of single faults for the battery system is explored. The possible sensors faults in a Li-ion cell can be current sensor, voltage sensor, and temperature sensor (surface) faults. In the presence of the sensor faults, the system outputs can be modeled by

$$I_{meas} = I + \Delta_I \tag{13.86}$$

$$V_{meas} = V + \Delta_V \tag{13.87}$$

$$T_{meas} = T_s + \Delta_T \tag{13.88}$$

Other faults of interested are thermal runaway fault can be modeled by representing an additional heat generation term θ_1, whereas a convection coefficient fault (cooling system fault) can be represented by θ_2

$$C_c \dot{T}_c = \frac{T_s - T_c}{R_c} + RI^2 + \frac{V_c^2}{R_0} + \theta_1 \tag{13.89}$$

$$C_s \dot{T}_s = -\frac{T_s - T_c}{R_c} + \frac{T_{amb} - T_s}{R_u} + \theta_2 \tag{13.90}$$

Considering the nominal battery model in (13.79)–(13.85), the state-space representation can be written as

$$\dot{x}_1 = a_{11}x_1 + a_{12}x_2 + a_{13}x_3^2 + b_{11}f_R(SOC, x_1)u_1^2 \tag{13.91}$$

$$\dot{x}_2 = a_{21}x_1 + a_{22}x_2 + b_{22}u_2 \tag{13.92}$$

$$\dot{x}_3 = a_{33}x_3 + b_{33}u_1 \tag{13.93}$$

where $x_1 = T_c$, $x_2 = T_s$, $x_3 = V_c$, $u_1 = I$, $u_2 = T_{amb}$, $a_{11} = -a_{12} = -\frac{1}{R_c C_c}$, $a_{13} = \frac{1}{R_0}$, $a_{21} = \frac{1}{R_c C_s}$, $a_{22} = -\frac{1}{R_u C_s} - \frac{1}{R_c C_s}$, $a_{33} = -\frac{1}{R_0 C_0}$, $b_{11} = \frac{1}{C_c}$, $b_{22} = \frac{1}{R_u C_s}$, $b_{33} = \frac{1}{C_0}$, $f_R(SOC, x_1) = R = \beta_0 + \beta_1 SOC + \beta_2 x_1$.

From (13.81)–(13.83), the measured voltage of the battery can be written as

$$V = \alpha_0 + \alpha_1 SOC + \alpha_2 SOC^2 - \beta_0 u_1 - \beta_1 SOC\, u_1 + (\alpha_3 - \beta_2 u_1)x_1 - x_3 \tag{13.94}$$

With the available measurements of current and voltage, and assuming that the *SOC* is available via Coulomb counting from (13.80), a new output y_1 can therefore be defined as

$$y_1 = V - \left(\alpha_0 + \alpha_1 SOC + \alpha_2 SOC^2 - \beta_0 u_1 - \beta_1 SOC\, u_1\right) = (\alpha_3 - \beta_2 u_1)x_1 - x_3 \tag{13.95}$$

while $y_2 = x_2$.

13.5.3 Fault Diagnosis Scheme

By considering the occurrence of a single fault, the NPERG method described in section 13.3.2.1 can be applied to solve the fault diagnosis problem. A schematic representation of the diagnostic scheme is given in Fig. 13.10. Alternative FDI scheme can be found in [9]. In the following paragraphs, the elements and the working of the scheme are described in detail.

13.5.3.1 Core Temperature Estimation

In the development of the diagnostic scheme, the first assumption is that the voltage sensor is faulty, while all other sensors are not faulty. A first step is therefore to build an inverse model utilizing the non-faulty output y_2 to estimate the unknown state x_1.

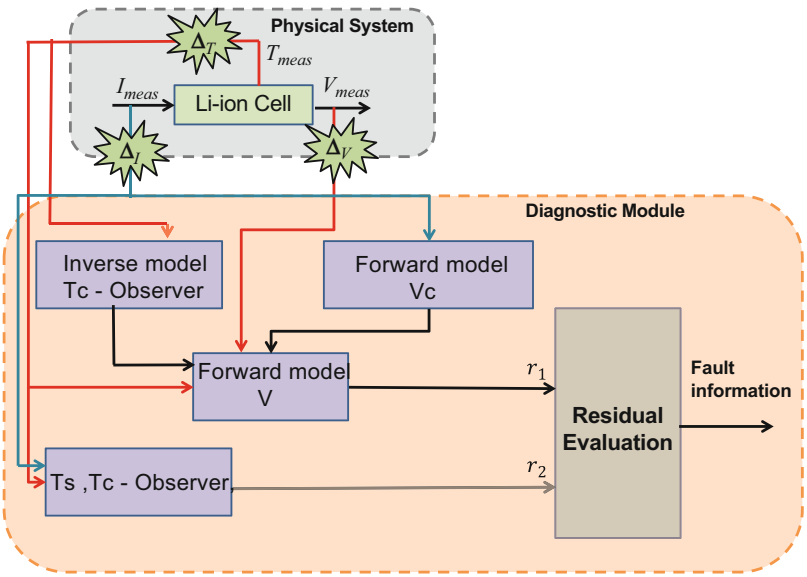

Fig. 13.10 Diagnostic scheme for the battery system.

This can be achieved by the sliding mode observer

$$\dot{\hat{x}}_2 = a_{22}\hat{x}_2 + b_{22}u_2 + L\,sgn(y_2 - \hat{x}_2) \tag{13.96}$$

Indicating with $e_2 = x_2 - \hat{x}_2$ the error between surface temperature and the observer state, the error dynamics are given by

$$\dot{e}_2 = a_{21}x_1 + a_{22}e_2 - L\,sgn(e_2) \tag{13.97}$$

If L is selected such that $L > a_{21}x_1 + a_{22}e_2(0) > 0$, then, by simple Lyapunov analysis, it is possible to show that $e_2 \to 0$ in finite time. Therefore, from the equivalent control method [13, 37], it follows that the equivalent output error injection ϑ_2, which is a continuous approximation of the switching error injection term $L\,sgn(e_2)$ in the sliding mode observer, satisfies the condition

$$\vartheta_2 = a_{21}x_1 \tag{13.98}$$

The equivalent output error injection ϑ_2 can be extracted from the $L\,sgn(e_2)$ by means of an appropriate low pass filter [38]

$$\tau\dot{\vartheta}_2 + \vartheta_2 = L\,sgn(e_2) \tag{13.99}$$

and the estimate of x_1

$$\hat{x}_1 = \frac{\vartheta_2}{a_{21}} \tag{13.100}$$

13.5.3.2 Capacitor Voltage Forward Model

Utilizing the available current input u_1, the following forward model reconstructs the voltage V_c

$$\dot{\hat{x}}_3 = a_{33}\hat{x}_3 + b_{33}u_1 \tag{13.101}$$

From (13.95) a residual can be generated as

$$r_1 = y_1 - (\alpha_3 - \beta_2 u_1)\hat{x}_1 + \hat{x}_3 \tag{13.102}$$

In presence of a voltage sensor fault

$$r_1 = \Delta_V \tag{13.103}$$

13.5.3.3 Temperature Observer

Utilizing u_1 and y_2, a temperature observer can be designed as follows:

$$\dot{\hat{x}}_1 = a_{11}\hat{x}_1 + a_{12}\hat{x}_2 + a_{13}\hat{x}_3^2 + b_{11}f_R(SOC, \hat{x}_1)u_1^2 - k_1 L_1 sgn(y_2 - \hat{x}_2) \quad (13.104)$$

$$\dot{\hat{x}}_2 = a_{21}\hat{x}_1 + a_{22}\hat{x}_2 + b_{22}u_2 + L_1 sgn(y_2 - \hat{x}_2) \quad (13.105)$$

$$\dot{\hat{x}}_3 = a_{33}\hat{x}_3 + b_{33}u_1 - k_2 L_1 sgn(y_2 - \hat{x}_2) \quad (13.106)$$

Define $\tilde{x}_1 = x_1 - \hat{x}_1$ and $\tilde{x}_2 = x_2 - \hat{x}_2$, then the error dynamics are

$$\dot{\tilde{x}}_1 = a_{11}\tilde{x}_1 + a_{12}\tilde{x}_2 + a_{13}(x_3^2 - \hat{x}_3^2) + b_{11}\beta_2\tilde{x}_1 u_1^2 + k_1 L_1 sgn(\tilde{x}_2) \quad (13.107)$$

$$\dot{\tilde{x}}_2 = a_{21}\tilde{x}_1 + a_{22}\tilde{x}_2 - L_1 sgn(\tilde{x}_2) \quad (13.108)$$

$$\dot{\tilde{x}}_3 = a_{33}\tilde{x}_3 + k_2 L_1 sgn(\tilde{x}_2) \quad (13.109)$$

From (13.108), if $L_1 > a_{21}\tilde{x}_1 + a_{22}\tilde{x}_2$, then $\tilde{x}_2 \to 0$ in finite time and $\vartheta_1 = [L_1 sgn(\tilde{x}_2)]_{eq} = a_{21}\tilde{x}_1$. Replacing in (13.107)

$$\dot{\tilde{x}}_1 = (a_{11} + k_1 a_{21})\tilde{x}_1 + a_{13}\tilde{x}_3(x_3 + \hat{x}_3) + b_{11}\beta_2\tilde{x}_1 u_1^2 \quad (13.110)$$

$$\dot{\tilde{x}}_3 = a_{33}\tilde{x}_3 + k_2 a_{21}\tilde{x}_1 \quad (13.111)$$

To analyze the convergence of the observer error, consider the Lyapunov function candidate

$$V = \frac{1}{2}(\tilde{x}_1^2 + \tilde{x}_3^2) \quad (13.112)$$

Therefore, the following can be written:

$$\dot{V} = \tilde{x}_1\dot{\tilde{x}}_1 + \tilde{x}_3\dot{\tilde{x}}_3 \quad (13.113)$$

$$= (a_{11} + k_1 a_{21} + b_{11}\beta_2 u_1^2)\tilde{x}_1^2 + a_{13}\tilde{x}_1\tilde{x}_3(x_3 + \hat{x}_3) + a_{33}\tilde{x}_3^2 + k_2 a_{21}\tilde{x}_1\tilde{x}_3 \quad (13.114)$$

If k_1,k_2 can be selected such that $a_{11} + k_1 a_{21} + b_{11}\beta_2 u_1^2 < 0$, and $a_{33}(a_{11} + k_1 a_{21} + b_{11}\beta_2 u_1^2) - \frac{1}{4}(a_{13}(x_3 + \hat{x}_3) + k_2 a_{21})^2 < 0$, then $\dot{V} < 0$ and $\tilde{x}_1, \tilde{x}_3 \to 0$ as $t \to \infty$. A residual can be generated from the output error injection ϑ_1 as

$$r_2 = \vartheta_1 \quad (13.115)$$

In the case of voltage sensor fault this residual will be zero as the voltage does not affect the observer state estimation. The residual will be non-zero in the presence of either a current sensor fault or a temperature sensor fault.

Based on the previous analysis, the FDI logic is given by the fault signatures in Table 13.4.

Table 13.4 Fault signature for battery system.

Fault in sensor	r_1	r_2
None	0	0
Voltage	1	0
Temperature	0	1
Current	1	1

Table 13.5 Identified battery parameters.

Parameter	Value
α_0	2.28 V
α_1	2.2 V
α_2	0 V
α_3	0.001 V/K
β_0	2.205 Ω
β_1	0.01 Ω
β_2	0.007 Ω/K
C_c	18.6 J/K
C_s	0.1 J/K
R_c	150.6 K/W
R_u	200 K/W

13.5.3.4 Simulation Results

A LiCoO2/Graphite Li-ion battery (18650 cylindrical cell) was studied with two T-type thermocouples installed on it: one on the surface and the other inserted into the battery core. The core thermocouple was inserted after discharging the battery and drilling through the center of the positive electrode side. The parameters of the battery model (13.79)–(13.85) were identified using nonlinear optimization technique that fits the two-state thermal model simulated data with the experimental data. The experimental data was collected in the *SOC* range of 50–80%, temperature range of 15–40 °C, and current range up to $2C$. Current profiles include constant currents, pulse discharge, and ramp currents. The parameters identified are listed in Table 13.5.

In this section, the simulation studies are presented to show the effectiveness of the proposed scheme. The current profile is a scaled and modified urban dynamometer drive cycle shown in Fig. 13.11, together with the corresponding temperature and voltage responses under no fault condition.

To test the effectiveness of the diagnostic scheme, three different faults (see Fig. 13.12) have been injected in three separate cases: (a) a -1°C temperature bias sensor fault is injected at $200s$ for $50s$; (b) a -4A current bias sensor fault is injected at $500s$ for $50s$; and (c) a -3V voltage bias sensor fault is injected at $800s$ for $50s$.

Figure 13.13 illustrates the residuals response to the three types of faults in presence of noise. The FDI scheme correctly detects and isolates the faults accordingly to the fault signatures in Table 13.4.

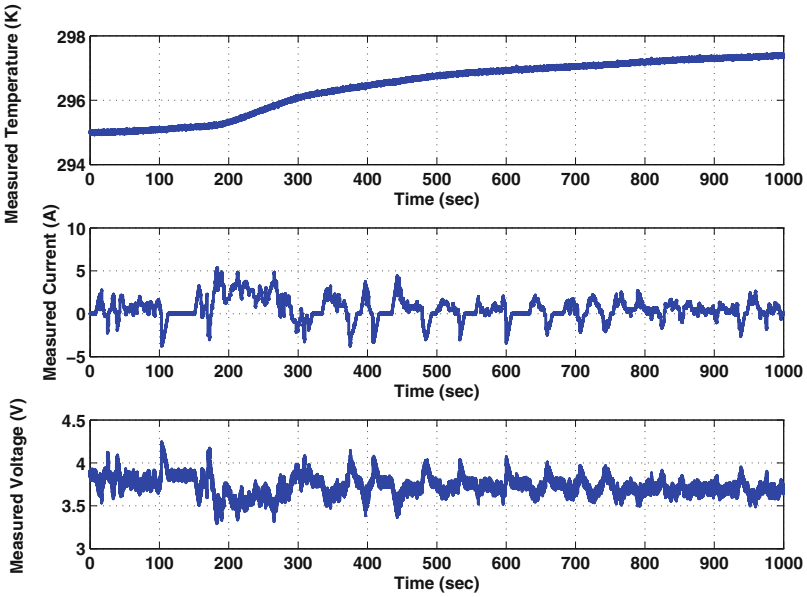

Fig. 13.11 Voltage, current, and temperature profiles in absence of faults.

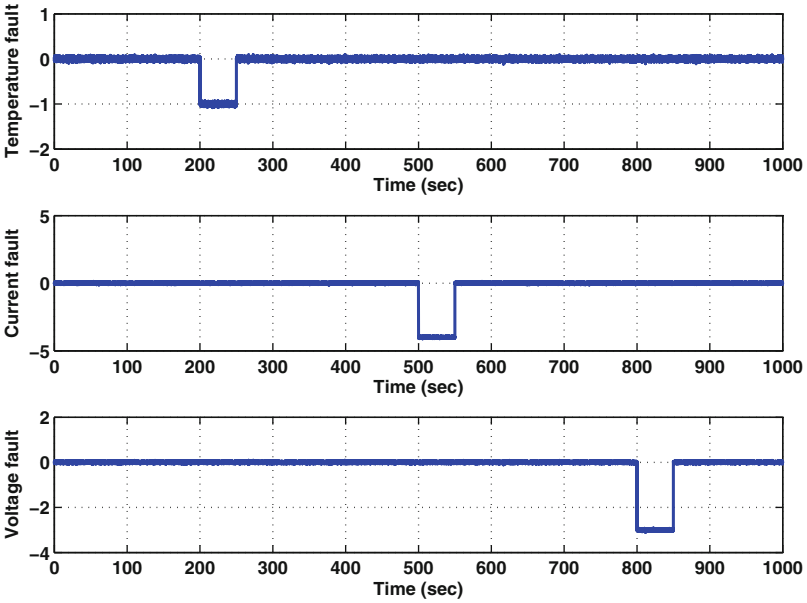

Fig. 13.12 Injected sensor faults at 200s, 500s, and 800s.

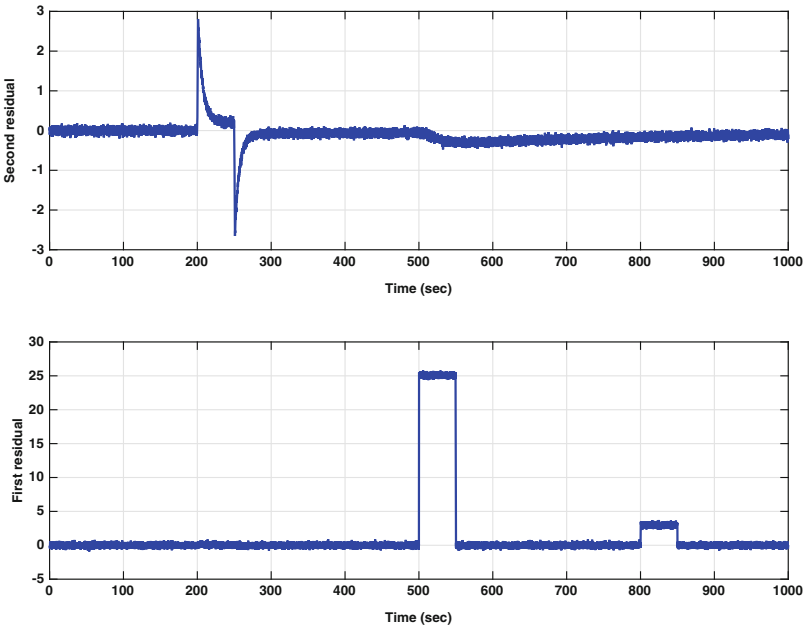

Fig. 13.13 Residuals response under abrupt faults.

References

1. Basseville M, Benveniste A (1986) Detection of abrupt changes in signals and dynamical systems. Springer-Verlag, Berlin.
2. Blanke M, Kinnaert M, Lunze J, Staroswiecki M (2006) Diagnosis and fault- tolerant control. Springer, New York.
3. Caccavale F, Villani L (2003) Fault diagnosis and fault tolerance for mechatronic systems: recent advances. Springer, New York.
4. Chen J, Patton RJ (1999) Robust model-based fault diagnosis for dynamic systems. Kluwer Academic Publishers, Boston.
5. Clark RN (1975) Detecting instrument malfunctions in control systems. IEEE Transactions on Aerospace and Electronic Systems, 11(4):465–473.
6. Clark RN (1978) Instrument fault detection. IEEE Transactions on Aerospace and Electronic Systems, 14:456–465.
7. Clark RN (1978) A simplified instrument failure detection scheme. IEEE Transactions on Aerospace and Electronic Systems, 14:558–563.
8. Clark RN, Setzer W (1980) Sensor fault detection in a system with random disturbances. IEEE Transactions on Aerospace and Electronic Systems, 16:468–473.
9. Dey S, Mohon S, Pisu P, Ayalew B (2016) Sensor Fault Detection, Isolation and Estimation in Lithium-ion Batteries. IEEE Transactions in Control Systems Technology, accepted.
10. Doughty DH, Butler PC, Jungst RG, Roth EP (2002) Lithium battery thermal models. Journal of Power Sources, 110(2):357–363.
11. Doyle M, Fuller TF, NewmanJ (1993) Modeling of galvanostatic charge and discharge of the lithium/polymer/insertion cell. Journal of the Electrochemical Society, 140(6):1526–1533.

12. Dubarry M, Vuillaume N, Liaw BY (2009) From single cell model to battery pack simulation for Li-ion batteries. Journal of Power Sources, 186(2):500–507.
13. Edwards C, Spurgeon SK, Patton RJ (2000) Sliding mode observers for fault detection and isolation. Automatica, 36(4):541–553.
14. Frank PM (1990) Fault diagnosis in dynamic systems using analytical and knowledge- based redundancy survey and some new results. Automatica, 26:459–474.
15. Gertler JJ (1998) Fault detection and diagnosis in engineering systems. Marcel Dekker, New York.
16. Hirschorn R M (1979) Invertibility of nonlinear control systems. Siam Journal of Control and Optimization, 17(2):289–297.
17. Hu Y, Yurkovich S, Guezennec Y, Yurkovich BJ (2011) Electro-thermal battery model identification for automotive applications. Journal of Power Sources, 196(1):449–457.
18. Hwang W, Hah K (2011) Model-based Sensor Fault Detection Algorithm Design for Electro-Mechanical Brake. Proceedings of the , 137(1),14th International IEEE CONFERENCE ON INTELLIGENT TRANSPORTATION SYSTEMS (ITSC)
19. Hwang W, Huh K (2015) Fault Detection and Estimation for Electromechanical Brake Systems Using Parity Space Approach. Journal of Dynamics system measurement and control-transaction Of the ASME, 137(1), doi: 10.1115/1.4028184.
20. Isermann R (2006) Fault-diagnosis systems: an introduction from fault detection to fault tolerance. Springer-Verlag, Berlin.
21. Johansson A, Bask M, Norlander T (2006) Dynamic threshold generators for robust fault detection in linear systems with parameter uncertainty. Automatica, 42:1095–1106.
22. Kapoor K, Jensen F (2015) Indonesia says faulty part, crew action factors in AirAsia crash. Reuters, Reuters Thompson, December 1st.
23. Korbicz, J, Koscielny J, Kowalczuk Z, Cholewa W (2004) Fault diagnosis: models, artificial intelligence, applications. Springer, New York.
24. Krishnaswami V, Rizzoni G (1994) Nonlinear parity equation residual generation for fault detection and Isolation. Proceedings of the IFAC/IMACS Symposium on Fault Detection, Supervision and Safety for Technical Processes-SAFEPROCESS '94, pp. 317–322, Espoo, Finland.
25. Krishnaswami V, Luh GC, Rizzoni G (1995) Nonlinear Parity Equation Based Residual Generation For Diagnosis of Automotive Engine faults. Control Engineering Practice, 3(10):1385–1392.
26. Krishnaswami V (1996) Model based fault detection and isolation in nonlinear dynamic systems. PhD Thesis, The Ohio State University, Columbus, OH.
27. Liaw BY, Nagasubramanian G, Jungst RG, Doughty DH (2004) Modeling of lithium ion cells:A simple equivalent-circuit model approach. Solid state ionics, 175(1):835–839.
28. Luenberger DG (1964) Observing the state of a linear system. IEEE Transactions on Military Electronics, 8(2):74–80.
29. Luenberger DG (1966) Observers for multivariable systems. IEEE Transactions on Automatic Control, 11:190–197.
30. Luenberger DG (1971) An introduction to observers IEEE Transactions on Automatic Control,16:596–602.
31. Patton RJ, Frank P, Clark R (1989) Fault diagnosis in dynamic systems: theory and application. Prentice-Hall, NY.
32. Patton RJ, Clark RN, Frank PM (2000) Issues of fault diagnosis for dynamic systems. Springer-Verlag, London.
33. Pisu P (2010) Hierarchical model-based fault diagnosis: theoretical results and applications to vehicle systems. VMD publishing, Berlin.
34. Puig V, Quevedo J (2002) Passive robust fault detection using fuzzy parity equations. Mathematics and Computers in Simulation, 60:193–207.
35. Roberts M, Chhaya T (2011) An Approach to the Safety Design and Development of a Brake-by-Wire Control System. SAE Technical Paper 2011-01-0212, doi:10.4271/2011-01-0212.

36. Simani S, Fantuzzi C, Patton R (2003)Model-based fault diagnosis in dynamic systems using identification techniques. Springer, New York.
37. Tan CP, Edwards C (2000) Sliding mode observers for detection and reconstruction of sensor faults. Automatica, 38(10):1815–1821.
38. Utkin V, Guldner J, Shi J (2009) Sliding Mode Control in Electromechanical Systems. CRC Press, Taylor and Francis, London.
39. Vachtsevanos G, Lewis F, Roemer M, Hess A, Wu B (2006) Intelligent fault diagnosis and prognosis for engineering systems. Wiley, Hoboken, N.J.
40. Walker JS (2004) Three Mile Island: A Nuclear Crisis in Historical Perspective. Berkeley: University of California Press. ISBN 0-520-23940-7.
41. Willsky AS (1976) A Survey of Design Methods for Failure Detection in Dynamic Systems. Automatica, 12:601–611, November.
42. Zhang, Basseville M, Beneviste A (1998) Fault Detection and Isolation in Nonlinear Dynamic Systems: A Combined Input-Output and Local Approach. Automatica, 34(11):1359–1373.
43. Zhirabok AN (1999) Parity space approach to fault diagnosis in nonlinear systems. 1999 European Control Conference (ECC), Karlsruhe, pp. 232–235.

Chapter 14
Fault Detection and Isolation of Automotive Air Conditioning Systems using First Principle Models

Quansheng Zhang and Marcello Canova

Abstract Although model-based fault detection and isolation (FDI) has become a common design tool in automotive fields, its application to automotive air conditioning (A/C) systems based upon vapor compression cycles is limited due to the lack of control-oriented models characterizing the refrigerant phase change. The emergence of moving boundary method (MBM) illuminates a promising way of assisting FDI scheme development, because common faults in automotive A/C systems, such as compressor fault, pressure transducer fault, and fouling fault, can be easily incorporated by the control-oriented model developed. Out of various observed-based FDI methods, the H_∞ filter technique, due to its robustness to model uncertainties and external disturbances, is chosen for designing FDI scheme over actuator/sensor/parameter faults. The model and the filter are connected closed-loop by an H_∞ controller gain-scheduled to meet different cooling loads. From the closed-loop analysis results, the H_∞ filter is capable of detecting and isolating actuator/sensor faults, as well as estimating parameter faults, even if external disturbances imposed on the air side of the evaporator exist.

Keywords Air Conditioning System • H Infinity Filter • Moving Boundary Method • Fault Detection and Isolation

Nomenclature

TP	Two Phase
SH	Superheated
SC	Subcooled
N	Compressor Speed

Reprinted from Zhang and Canova (2015), with permission from Elsevier.

Q. Zhang (✉) • M. Canova
Center for Automotive Research, The Ohio State University, 930 Kinnear Road, Columbus, OH 43212, United States
e-mail: zhang.777@osu.edu

Q. Zhang et al., *Automotive Air Conditioning*, DOI 10.1007/978-3-319-33590-2_14

T Temperature
a air
c Condenser
cmp Compressor
e Evaporator
g gas
h Enthalpy
l liquid
p Pressure
v Valve
$\dot{m}$ Mass Flow Rate
$\dot{Q}$ Heat Transfer Rate
α Valve Position
γ Void Fraction
δ uncertainty
ρ Density
ζ Normalized Phase Region Length
μ Structured Singular Value

14.1 Introduction

Timely detection and isolation of underlying faults is crucial for meeting stringent safety requirements in industry. Compared to hardware redundancy technique, model-based FDI method leads to significant cost savings. Various approaches have been applied to the residual generation problem, e.g., parity equation methods, observer-based methods, or frequency domain methods, [1–4]. In observer-based FDI methods [5, 6], actuator commands and sensor measurements are exploited to design filters for generating residuals that are compared to thresholds. In particular, H_∞ filters attract more interests due to their robustness to model uncertainties and external disturbances. An optimization problem is formulated to minimize the influences of measurement noises, external disturbances, and model uncertainties on the residuals and to maximize the effects of the faults on the residuals. A standard framework for the problem formulation and solution was proposed in [7, 8], with applications to aircraft longitudinal motion [9, 10].

Model-based FDI method has widespread applications in automotive engines, especially air path systems and fuel path systems [11, 12]. In contrast, its application to auxiliary loads, such as A/C systems, has not been addressed, with limited publications available. However, vapor compression cycle (VCC), the thermodynamic process obeyed by automotive A/C system, is widely applied in many industry fields, such as refrigerators, air conditioners, heat pumps, and chillers. Early works on VCC fault diagnosis heavily relied on simplified models, resulting into intense calibration efforts and poor performances during transient [13]. For instance, a simplified physical model of a small heat pump system was used to generate

predictions, whose differences from monitored observations were transformed into useful statistical quantities to be compared with predetermined thresholds [14]. A statistical rule-based fault detection and diagnostic method for A/C equipment was developed in [15], and demonstrated in limited testing with a roof-top air conditioner in [16] together with a fault evaluation method. Steady-state data representing normal operations were used to develop seven polynominal models characterizing the A/C performance and determine the statistical thresholds for fault detection, while transient data with faults were used to evaluate fault diagnosis performance [17]. However, since they lack control-oriented models describing the thermofluid dynamics of the phase-changing refrigerant in heat exchangers, it is difficult to achieve balances between physical accuracy and computation time of the designed FDI algorithms [18, 19].

A lumped-parameter modeling approach named MBM method of developing control-oriented models for heat exchangers with phase change changing fluid was proposed in [20–22], where the refrigerant is lumped according to its phase status, namely pure vapor, pure liquid, and mixture of vapor and liquid. Differential equations describing the mass and energy balances of the phase change process were developed. The MBM A/C model offers the advantage of capturing the transient behavior of the system, and reducing the simulation time without sacrificing physical accuracy.

In this chapter, a control-oriented model derived from first principles is used to design an FDI scheme on an automotive A/C system. A brief literature review is given in Section 14.2. Exemplary actuator/sensor/parameter faults are modeled and merged into the MBM A/C model in Section 14.3. The closed-loop system composed of the control-oriented model, the output-tracking controller, and the FDI filter is presented in Section 14.4. The closed-loop performances are evaluated over model uncertainties and external disturbances in Section 14.5, with both abrupt and incipient faults considered.

14.2 Recent Development of VCC Fault Diagnosis

According to a comprehensive literature in [23, 24], FDI method can be generally classified into two approaches, namely data-driven approaches and model-based approaches (quantitative or qualitative). Data-driven approaches need a large amount of training data representing both normal and faulty operation, as well as a thorough understanding of the system and expertise in statistics. The resulted models are specific to the system for which they are trained and cannot be extrapolate beyond the range of the tracing data. In contrast, strengths of FDI schemes based on quantitative models allow to model both normal and faulty operation based on first principles, such that the transient behavior of the systems is captured more precisely than any other modeling technique. In other words, they are

particularly important for capturing faults during transient operation. Model-based approaches range from empirical models, simplified models, and physics-based models. Following the above classification criterion, recent developments of FDI schemes on VCC applications during last decade are presented in the order of model complexity.

Empirical models are simplest, even sometimes static. In [25, 26], a gray box modeling approach is adopted to capture the influence of both operating conditions and faults on system performance. The steady-state heat exchangers are divided into regions according to the refrigerant phase, and each region is modeled with $\epsilon - NTU$ methods under a crossflow configuration. The static model describing the input–output relationship is useful for diagnosing multiple-simultaneous faults in VCC equipment with decoupling feature exploited and virtual sensor developed [27].

Simplified models neglect some dynamics under certain assumptions. A four-state nonlinear model of a supermarket refrigeration system is built using a lumped-parameter approach in [28]. A bank of extended Kalman filters (EKFs) is constructed for isolating two temperature sensor faults in the types of drift, offset, freeze, and hard-over, and a multi-model adaptive estimation method is employed to handle parametric fault caused by freeze-over or dirty built up in [29]. However, the isolation between sensor faults and parametric faults cannot be handled by the current scheme, and is compensated by a bank of unknown input observers (UIOs) constructed in [30], where one state variable is treated as a system unknown input. Unfortunately, the control-oriented model introduced [28] oversimplified the heat transfer process between the refrigerant and the air, as the refrigerant loop excluding the evaporator is not modeled and assumed as known boundary conditions.

The dynamic response of a chiller to the change of working conditions is captured using a lumped-parameter model is built in [31], in which four first-order differential equations are built to represent the dynamics of thermal storages at the inlet and outlet of the condenser and evaporator, respectively. A new semi-physical subcooling model is adopted to represent the condensing region and subcooling region in the heat exchanger [32]. By analyzing the changing trends of two proposed performance indexes, namely the normalized heat transfer coefficient and the fictitious subcooling temperature, the pattern in fault conditions can be obtained. Similarly, a strategy, in which six physical performance indices are used to describe the health conditions and thus indicate chiller faults, is validated against field data from a centrifugal chiller in a real building [33]. Although the model presents the effects of working conation changes on compressor load, it cannot describe the dynamic performance of chiller operation.

Physics-based models have been recently used for analyzing fault effects. In [34], the possibility of using more complex moving boundary models for FDI in subcritical VCC equipment is explored. A linearized form of the model is used to explore the sensitivity of each output to fault conditions of evaporator frosting, refrigerant, and valve leakages; however, no practical FDI algorithm is implemented. The static component-based fault detection method is also tested for a transcritical refrigeration system for faults such as over/undercharge, evaporator fouling, gas cooler fouling, and compressor valve leakage [35]. The method is also applicable to large transient of the refrigerant during start-up or shut-down process

[36]. However, physics-based models, as far as the authors know, have never been used for design FDI scheme during transient.

14.3 Fault Modeling Using MBM A/C Model

Commonly observed faults are labeled at corresponding locations in the A/C loop and incorporated into mathematical models describing thermofluid dynamics.

14.3.1 Overview of A/C System Faults

A basic automotive A/C system is composed of four primary components, namely evaporator, compressor, condenser, and expansion valve as illustrated in Figure 14.1. The VCC removes heat from the air flowing to the cabin through the evaporator, as the refrigerant evaporates from two-phase (TP) status into superheated (SH) status, and rejects heat to the air flowing through the condenser, as the refrigerant condenses from superheated (SH) status into subcooled (SC) status through two-phase (TP) status. The enthalpy, mass flow rate, and pressure, are exchanged by the four components. Basically, the two heat exchangers set the pressures of the system, while the compressor and expansion valve determine the mass flow rates at the inlet and outlet of the evaporator and condenser.

Typical faults occurring in vapor compression systems summarized in [13] are labeled in Figure 14.1. For instance, compressor faults can be caused by motor winding failure and unbalanced voltage, or by refrigerant contamination and liquid slugging. Stepper motor and electronic controller failures could make the expansion valve malfunction. Fouling and frosting are major concerns on the surface of the heat exchangers. Refrigeration leak may occur in the pipeline. In addition to system faults, the pressure transducers and thermocouples for experimental measurement are also possible fault sources. According to the terminology of the model-based FDI, the above faults are classified into three categories, namely actuator faults (e.g., compressor fault and valve fault), sensor faults (e.g., pressure transducer fault and thermocouple fault), and parametric faults (e.g., pipe leakage and fouling). From a fault observability standpoint, the number of simultaneously detectable faults is determined by the total number of sensors available. Due to hardware limitations, the faults of interest include one actuator fault (compressor fault), sensor fault (pressure transducer fault), as well as one parametric fault (evaporator fouling fault).

An in-depth analysis of the influences of the faults on the automotive A/C system performance can be done with a control-oriented model. In a well-established modeling framework, the compressor and valve are modeled as static components. The dynamics related to the heat and mass transfer inside the heat exchangers are described using the MBM method [20, 22], describing the mass and energy conservation for transient one-dimensional flow. After derivations detailed in [37]

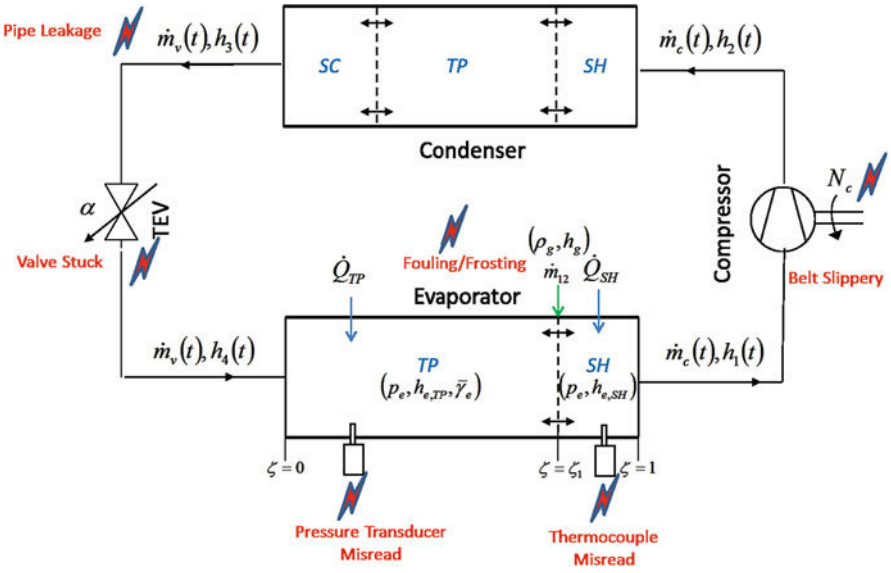

Fig. 14.1 A/C System Components and Possible Faults

and not included here for brevity, the final mathematical equations describing system dynamics , together with faults, are in the descriptor form,

$$\begin{aligned} Z(x, f_a)\frac{dx}{dt} &= f(x, f_a, u, v, f_N) \\ y &= g(x, f_a, f_p) \end{aligned} \tag{14.1}$$

The inputs are the compressor rotation speed and expansion valve opening percentage, $u = \left[N_c \ \alpha\right]^T$. The boundary conditions are the variables describing the air side of the heat exchangers, and could be treated as unknown disturbances, $v = \left[\dot{m}_{ea} \ T_{ea,in}\right]^T$. The state vector describing the evaporator status includes 5 variables as: $x_e = \left[\zeta_{e1} \ p_e \ h_{e2} \ T_{e1w} \ T_{e2w}\right]^T$. Finally, the outputs are the evaporator pressure and superheat temperature, $y = \left[p_e \ SH\right]^T$, which are only functions of refrigerant states. The Z matrix and f vector are complex expressions of refrigerant properties, heat transfer coefficients, and geometric parameters [37].

14.3.2 Actuator Fault

The compressor fault f_N belongs to actuator faults. In compressor, the mass flow rate $\dot{m}_c$ and outlet enthalpy h_2 are defined, respectively, as:

$$\dot{m}_c = \eta_v V_d \rho_1 \omega_c, \qquad h_2 = \frac{h_{2s} - h_1}{\eta_s} + h_1 \tag{14.2}$$

where V_d is the compressor displacement, ρ_1, h_1 the refrigerant density and enthalpy at the compressor inlet, ω_c the compressor speed in rad/sec, and $h_{2s} - h_1$ is the isentropic enthalpy difference. Thus, the mass flow rate and enthalpy change are mainly determined by the compressor rotation speed ω_c in rad/s or N_c in rpm. If the compressor fault f_N is modeled as an additive fault, the actual compressor speed N_{AC} is different from the commanded compressor speed N_{cmd} from the controller, $N_{AC} = N_{cmd} + f_N$. Note that although f_N is additive, it acts nonlinearly due to its influence on η_v and η_s.

14.3.3 Sensor Fault

Two sensors are installed into the evaporator for control purposes, namely one pressure transducer and one thermocouple. The thermocouple is installed at the outlet of the evaporator in order to measure the degree of superheated temperature. Obviously, both faults are closely related to the refrigerant dynamics involving of pressure and temperature. Hence, the mass balance equation and energy balance equation for the refrigerant in the superheated region of the evaporator are presented:

$$-\left(\frac{\rho_{e,SH} - \rho_g}{\rho_{e,SH}}\right)\frac{d\zeta_1}{dt} + \frac{1}{\rho_{e,SH}}\frac{\partial \rho_{e,SH}}{\partial p_e}\frac{dp_e}{dt}\cdot(1-\zeta_1) + \frac{1}{\rho_{e,SH}}\frac{\partial \rho_{e,SH}}{\partial h_{e,SH}}\frac{dh_{e,SH}}{dt}\cdot(1-\zeta_1) = \frac{\dot{m}_{12}}{\rho_{e,SH}V_e} - \frac{\dot{m}_c}{\rho_{e,SH}V_e} \tag{14.3a}$$

$$-\frac{\rho_g\left(h_g - h_{e,SH}\right)}{\rho_{e,SH}}\frac{d\zeta_1}{dt} + \frac{1}{\rho_{e,TP}}\frac{dp_e}{dt}\cdot(1-\zeta_1) - \frac{dh_{e,SH}}{dt}\cdot(1-\zeta_1) = \frac{\dot{m}_{12}}{\rho_{e,SH}V_e}\left(h_g - h_{e,SH}\right) - \frac{\dot{m}_c}{\rho_{e,SH}V_e}\left(h_1 - h_{e,SH}\right) + \frac{\dot{Q}_{SH}}{\rho_{e,SH}V_e} \tag{14.3b}$$

where p_e is the evaporator pressure, ζ_1 the two-phase region normalized tube length, $h_{e,SH}$ the enthalpy of the refrigerant at the tube exit, $\dot{m}$ mass flow rate, $\dot{Q}$ heat transfer rate, ρ density. All these variables have been labeled in Figure 14.1.

A high-level understanding of these differential equations is possible without diving into the mathematical details. The left-hand side (LHS) represents the variation of independent states of the refrigerant, $\zeta_1, p_e, h_{e,SH}$, and right-hand side (RHS) the exchanger of mass and enthalpy at the inlet and outlet of individual phase region, $\dot{m}, h$, as well as the heat transfer along the wall of corresponding region $\dot{Q}$. The terms multiplying the state variations depend on the refrigerant inherent thermodynamic properties, hence are state-dependent. The mass and energy bal-

ances for the subcooled, two-phase, and superheated region of the condenser are not shown here because of their indirect relationships to faults. The pressure transducer measurement is directly linked to one state of the differential equations, $p_m = p_e$ if no fault exists, or $p_m = p_e + f_p$ if a fault emerges.

14.3.4 Parameter Fault

The fouling on the tube exterior surface reduces heat transfer rates as a result of reduced heat transfer coefficient. The fouling dynamics is closely related to the wall temperature dynamics of the heat exchangers. A lumped thermal mass approach is adopted to describe the temperature of the walls separating the refrigerant control volume from the external air flow:

$$\rho_w A_w c_w \left[L\frac{dT_w}{dt} + T_w \left(v_{b2} - v_{b1}\right) \right] + \rho_w A_w c_w \left(T_{w1} v_{b1} - T_{w2} v_{b2}\right) = \dot{Q}_{in} - \dot{Q}_{out} \tag{14.4}$$

where A_w is a representative cross-sectional area. The internal and external heat transfer models assume pure convection occurring between the wall and the fluids in contact. In case of the external heat transfer (air to wall), the following equation is used:

$$\dot{Q}_{out} = \alpha_{out} \left(\pi D_{out} L\right) \left(T_a - T_w\right) \tag{14.5}$$

where D_{out} is the hydraulic diameter. The fouling fault is modeled as $\alpha_{out,act} = \alpha_{out} + f_\alpha$, where α_{out} is a theoretical value computed using heat transfer correlations for compact heat exchangers, and $\alpha_{out,act}$ is the actual heat transfer coefficient of the heat exchanger.

14.4 Experiment System

Provided that commands to compressor speed N_c and valve position α, as well as measurements of evaporator pressure p_e and superheat temperature SH, are available for the control module and the FDI module, as depicted in Figure 14.2, the instrumented test vehicle enables accomplishing tasks of

1. modeling and calibrating an MBM A/C model [37, 38];
2. designing an H_∞ controller for output tracking [37, 38];
3. developing FDI schemes in the closed-loop of plant, controller, and filter.

When the MBM A/C model is validated, the air mass flow rates and temperatures on the evaporator side $\dot{m}_{ea}$, T_{eo} and condenser side $\dot{m}_{ca}$, T_{co}, are either controllable or measurable. The output signals, such as air temperatures leaving the heat exchangers

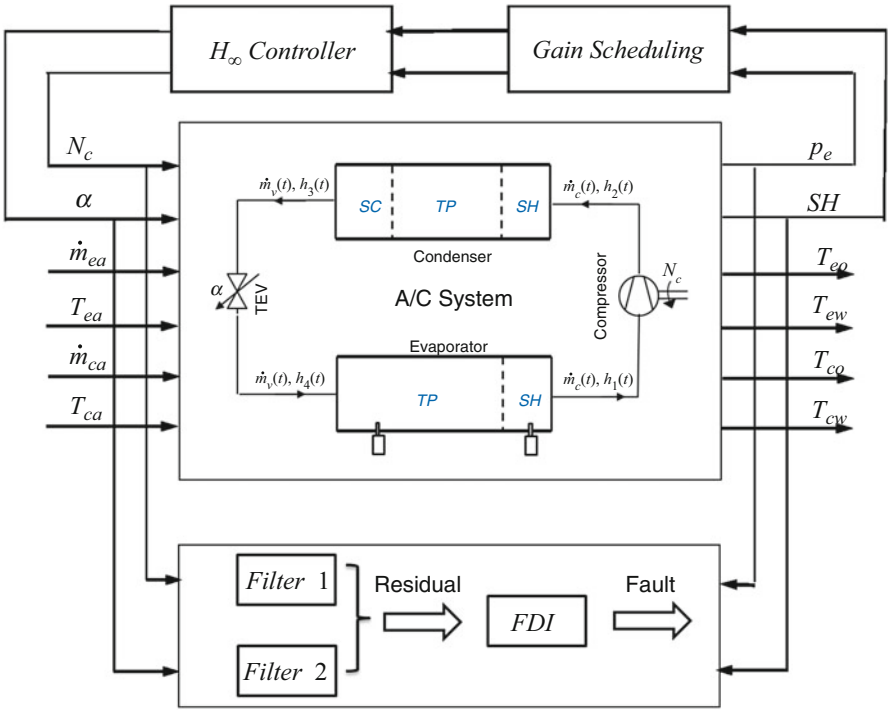

Fig. 14.2 Interconnections of Plant, Controller, and FDI

T_{eo}, T_{co} and tube wall temperatures T_{ew}, T_{cs}, are predicable using the MBM A/C model. Since the A/C system dynamics change significantly over working points, the H_∞ controller dynamics is supposed to be scheduled accordingly. Both the model validation and control design have been accomplished in [37], and the main results are summarized for the convenience of the H_∞ filter development.

An automotive A/C system in a Minivan is studied. The test vehicle was instrumented with an ETAS ES1000 system interfaced with the engine control unit (ECU) to allow for acquisition of engine torque and speed, and to control the radiator fan and cabin blower. The vehicle was installed on a chassis dynamometer, allowing for the characterization of the system both at steady-state conditions and during driving cycles.

Leveraging upon the available experimental setup, the model was calibrated using the data collected during the tests when vehicle/engine speeds are maintained at nominal steady state, and verified with reference to the SC03 air conditioning cycle whose vehicle speed trace for this regulatory driving cycle. After validation, the nonlinear A/C model is linearized at three operating conditions, corresponding to low, medium, and high cooling loads. The system matrices of the LTI A/C model are provided in [37, 38].

The robust H_∞ controller is designed to track prescribed trajectories of two output variables, namely the evaporator pressure p_e and the superheat temperature SH. Meanwhile, the controller should reject disturbances caused by air mass flow rate at the evaporator, $\dot{m}_{ea}$. The system matrices of the final H_∞ controller after model order reduction, together with its derivation process, are given in [37, 38].

The H_∞ fault diagnosis problem is to find a stable filter F such that 1) the performance error is minimized under all possible uncertainties Δ; 2) the faults effect on the residuals is maximized with disturbance effect minimized. The second objective is equivalent to minimization of the error between the residual and the weighted fault. Hence, a standard performance index can be given as follows:

$$\sup_{0<\|\Phi\|_2<\infty} \frac{\|res - T_{fid} f\|_2}{\|\Phi\|_2} \tag{14.6}$$

and the matrices T_{fid} and Φ vary depending on the type of problems. Please refer to [7, 8] for theoretical backgrounds and [9, 10] for application examples.

14.5 Results and Analysis

Following the general FDI schemes introduced, two separated H_∞ filters, namely an actuator/sensor FDI filter and a parameter FDI filter, will be designed to detect the compressor fault and the pressure transducer fault, as well as to estimate the fouling fault using the MBM A/C model.

14.5.1 Actuator and Sensor FDI

For the FDI scheme, the standard H_∞ synthesis, which requires selecting appropriate weighting functions for optimization problem formulation, enables that the generated residuals to follow the faulty signals dynamically. The reference fault weights $W_{fault,act}$, $W_{fault,sen}$ and estimation error weights $W_{err,act}$, $W_{err,sen}$ are selected in order to minimize the error at low frequencies and relax the constraints at higher frequencies. The H_∞ filter calculated based on the augmented plant model is inherently high-order. From the analysis of the singular values of system matrices of the H_∞ filter, three states dominate the system dynamics. Hence, the H_∞ filter after model order reduction is given below.

Table 14.1 Fault Signatures for A/C System

	res_1	res_2
No Fault	0	0
Sensor Fault	0	1
Actuator Fault	1	0
Both Faults	1	1

$$
\begin{aligned}
A_F &= \begin{pmatrix} -6.24e-6 & 0.004616 & -0.0006508 \\ -0.004895 & -0.08784 & 0.08659 \\ 0.0008169 & 0.08861 & -0.2091 \end{pmatrix} \\
B_F &= \begin{pmatrix} -4.152e-5 & -0.001717 & 0.0001151 & -0.2094 \\ -0.0004144 & -0.1061 & 0.004668 & -21.91 \\ -0.003091 & 0.2544 & -0.004444 & 12.53 \end{pmatrix} \\
C_F &= \begin{pmatrix} 0.1383 & -21.87 & 12.43 \\ -0.5172 & -1.187 & -1.66 \end{pmatrix}
\end{aligned}
\tag{14.7}
$$

Suitable thresholds are selected to allow for categorizing the fault signatures as 0 (no fault detected) and 1 (fault detected). Table 14.1 summarizes the FDI scenario for the actuator/sensor faults of the A/C plant. Theoretically, the selection criterion depends on the probability density function (PDF) of faulty and non-faulty signals. Because the faulty and non-faulty PDFs may have significant overlap, it might result in a certain probability of error either from false alarm or missed detections. Thus, an optimal threshold must be determined using hypothesis testing, such that the probability of error, as an integral of the overlapped region of the PDF, is minimized [39]. Given a nominal PDF and a maximum allowable probability of error, e.g., 5%, the minimum level of detectable fault can be calculated, e.g., 10 rpm for compressor fault and 1 kPa for pressure transducer fault. In order to reduce the complexity of thresholds selection, the differentiation between faulty and non-faulty residuals is enlarged intentionally by injecting more significant fault, e.g., 50 rpm for compressor fault and 10 kPa for pressure transducer fault.

14.5.1.1 Performance Evaluation

A test of the performance of the H_∞ filter designed is shown in Fig. 14.3, with the actual sensor measurements (p_e, SH), commands to actuators (N_c, α), and corresponding residuals (res_1, res_2) recorded. The robustness of the filter ensures that the residual generation process becomes less sensitive to some discrepancies between the actual A/C plant and the LTI model used during the filter design process. Hence, the working point is taken away from the design point corresponding to the medium cooling load, where inputs are set to $N_c = 1000$ rpm and $\alpha = 40\%$, and corresponding outputs are regulated to $p_e = 250$ kPa and $SH = 20\,^0C$. The A/C

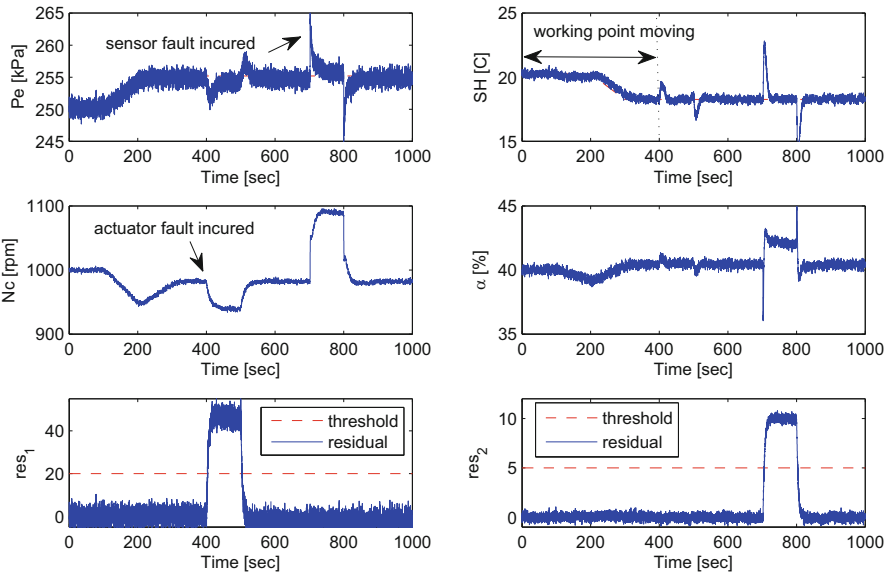

Fig. 14.3 Plant Outputs, Inputs, and Filter Residuals for Abrupt Fault

system settles down before $T = 400$ sec, resulting an increased evaporator pressure by 5 kpa and a reduced superheat temperature by 2.5 ^oC.

The actuator fault is a fixed value of positive 50 rpm in the compressor speed N_c injected at $T = 400s$ and removed at $T = 500s$. As seen from Fig. 14.3, the actuator fault causes the first residual res_1 to cross the threshold, while the second residual res_2 changes negligibly. Because the H_∞ controller is inherently a passive fault tolerant controller, the commanded compressor speed N_c sent to the actuator is reduced by around 50 rpm in order to compensate the actuator fault. The sensor fault is a fixed value of positive 10 kPa in the pressure transducer p_e injected at $T = 700s$ and removed at $T = 800s$. As seen from Fig. 14.3, the sensor fault causes the second residual res_2 to cross the threshold, while the first residual res_1 changes negligibly. Although the measured evaporator pressure jumps by 10 kPa abruptly, the robustness of the H_∞ controller forces the A/C plant to move to another working point by modulating the two actuators, in order to counteract the influence of the pressure transducer misreading and guarantee that it returns to $p_e = 255$ kPa.

Besides the scenario with an abrupt change of an actuator/sensor fault, the H_∞ filter is also capable of estimating the faulty actuator/sensor facing an incipient change. As before, the working point is moved from the one corresponding to the medium cooling load for the first 400 sec. A gradual deteriorated actuator, starting at healthy status at 400 sec and ending at 5% faulty signal at 1000 sec, is injected to represent an incipient actuator fault. Similarly, a gradual deteriorated sensor, starting at healthy status at 700 sec and ending at 4% faulty signal at 1000 sec, is injected to represent an incipient sensor fault. From fig. 14.4, the first residual res_1 estimates the

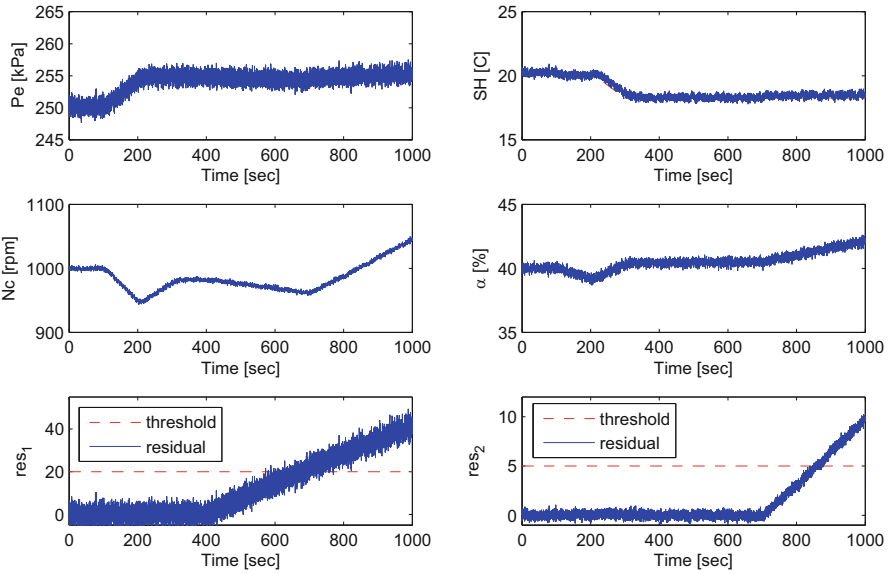

Fig. 14.4 Plant Outputs, Inputs, and Filter Residuals for Incipient Fault

actuator fault, and the second residual res_2 estimates the sensor fault very accurately. However, for the fixed thresholds specified, the H_∞ filter cannot detect the actuator fault with a delay of 200 sec, and the sensor fault with a delay of 100 sec. For instant fault detection, an H_∞ filter with an adaptive threshold is expected.

14.5.1.2 Limitations

The designed H_∞ filter suffers several limitations, from the forthcoming observations that the residuals generated are sensitive to boundary conditions and plant variations. In Figure 14.5, the air velocity through the evaporator deviates from the nominal value 4 m/sec sinusoidally after 400 sec, while both the actuator and sensor faults are injected as constant values at the beginning of the test. As expected, the residuals representing fault occurrences exceed the thresholds when the air velocity is constant for the first phase ($t < 400sec$). For the second phase ($t > 400sec$), however, as the air velocity oscillates, the residuals fall below thresholds despite that faults exist all the time, indicating that missed detection happens.

The influences of external disturbances on the residuals may be removed once additional thermocouples are installed on exterior surfaces of the heat exchangers in order to provide the wall temperatures at individual phase regions. Note that the choice of wall temperature signal is targeted for the specific disturbance coming from the air side, as the latter is independently observable from the former. Thus the control-oriented A/C system model for the H_∞ filter design has more outputs

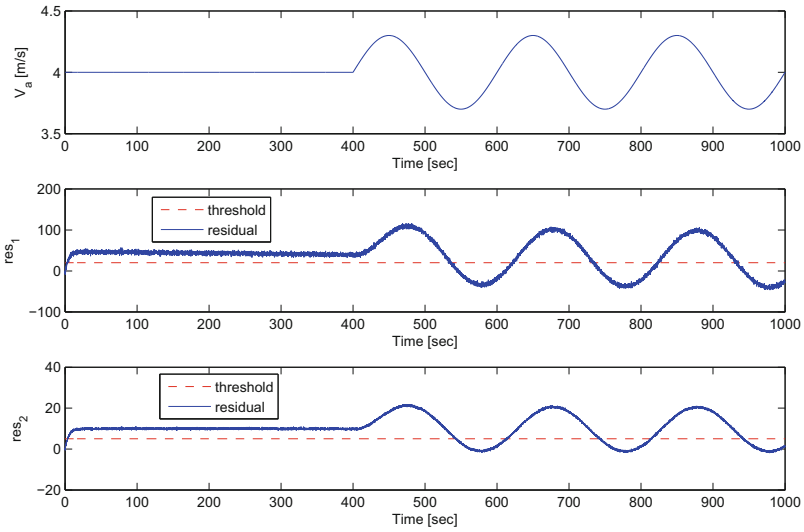

Fig. 14.5 Influence of External Disturbance on Residual Generation

available than before, allowing that the synthesis process has additional authority of rejecting external disturbances. After the new filter replaces the original one, the residuals for both actuator fault and sensor fault change in a similar manner to those in Figure 14.3, while extra actuator efforts are required to counteract the effects of external disturbances.

Plant variations also affect the filter performance, even if the H_∞ controller is gain-scheduled to the LTI A/C plants obtained at different linearization points. For instance, the working point corresponding to the low cooling load is selected, and the H_∞ filter is designed using the same weighing functions used for the medium cooling load scenario for consistency. As before, the working point is taken away from the design point, and actuator fault and sensor fault are injected sequentially in Figure 14.6. From the two figures in the third row, the two residuals generated are very noisy, such that false alarms and missing alarms happen frequently with respect to fixed thresholds, especially for the residual of sensor fault res_2. In order to distinguish residuals from noises, additional filters modulating the gains and frequency of the original filters are added in series of the original to remove noises. From the two figures in the fourth row, two residuals after filtering are capable of detecting and isolating actuator fault injected at 400 sec and sensor fault injected at 700 sec. In other words, the appropriate filters at low cooling load are a product of the additional filter and the original one corresponding to medium cooling load. The sensitivity of residuals to plant variables is removable if the H_∞ filter is designed using gain-scheduling technique, such as linear parameter varying (LPV) approach in [40].

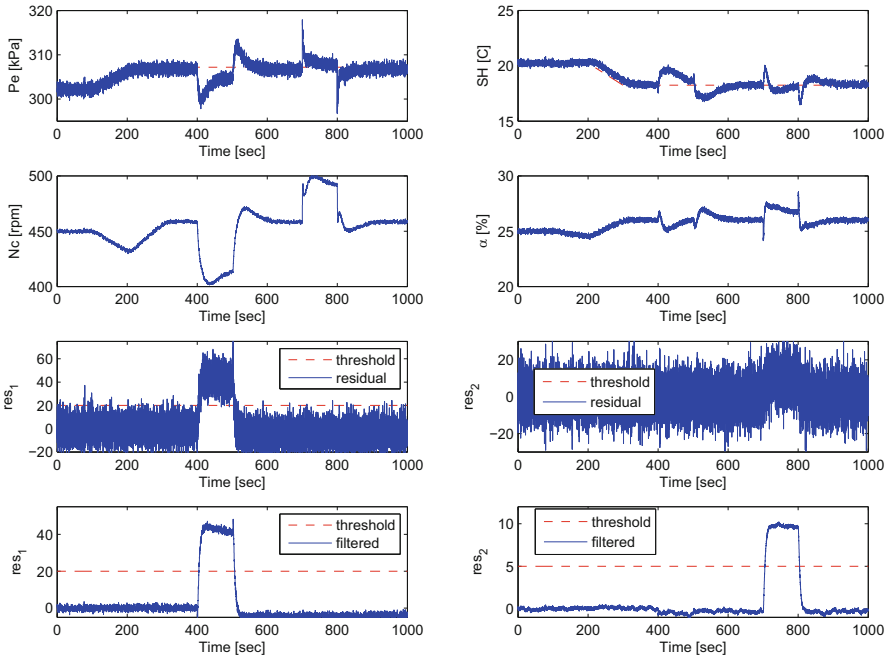

Fig. 14.6 Plant Variation Effect on Residual Generation.

14.5.2 Parametric FDI

In the scheme of the parameter FDI scheme, the standard μ synthesis, which requires structuring the uncertainty block for optimization problem formulation, enables the generated residual has the same amplitude of the parameter fault. The uncertainty block is constructed by perturbing the nominal system around equilibrium points. After appropriate weighting functions selected, the H_∞ filter calculated based on plant model with uncertainty block is inherently high-order. From the analysis of the singular values of the filter system matrices, three states dominate the system dynamics. Hence, the H_∞ filter after model order reduction is given below.

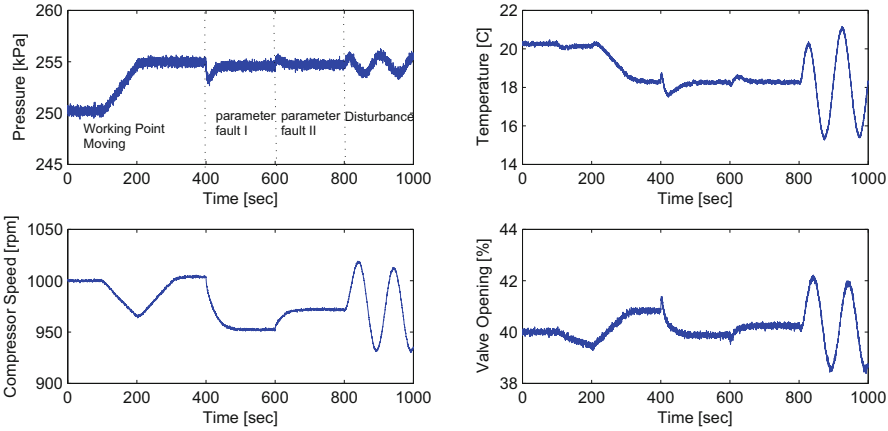

Fig. 14.7 Plant Output and Inputs for Parameter Fault

$$
\begin{aligned}
A_F &= \begin{pmatrix} -0.1535 & -0.3811 & 0.02074 \\ 0.3794 & -3.514 & 0.6827 \\ 0.02033 & -0.6843 & -0.03135 \end{pmatrix} \\
B_F &= \begin{pmatrix} 0.01559 & -0.08417 & 0.005109 & -16.82 \\ -0.2407 & -1.999 & -0.02167 & 19.56 \\ -0.03282 & -0.235 & -0.003236 & 1.142 \end{pmatrix} \\
C_F &= \begin{pmatrix} 16.82 & 19.65 & -1.162 \\ 1.549e-5 & -5.925e-5 & 0.0001626 \end{pmatrix}
\end{aligned}
\tag{14.8}
$$

The above H_∞ filter is incorporated into the closed-loop system for evaluating its performance when the corresponding parameter changes abruptly under external disturbances. As before, the working point is moved from the one corresponding to the medium cooling load for the first 400 sec. Then parameter faults, whose amplitudes are 5% and 3% of the nominal value, and time duration are 200 sec, are injected sequentially to check residual variations. Finally, a sinusoidal disturbance is added to the air velocity of the evaporator side for the ending 200 sec. The commands sent to the actuators and measurements from the sensors are recorded in Fig. 14.7.

In Fig. 14.8, the capability of the H_∞ filter is demonstrated by showing whether the residual *res*, calculated as the ratio of $\|\hat{f}_p\|/\|\hat{z}_p\|$, follows the actual parameter variation. It is clear that the amplitudes of the changing parameter fault (5% and 3% sequentially) are captured by the residual signal after transient. Although external disturbances cause the estimations of f_p and z_p change sinusoidally, the residual representing the faulty parameter amplitude is maintained constant after $T = 800$ sec. Hence, the designed H_∞ filter is capable of detecting the parameter fault under external disturbances.

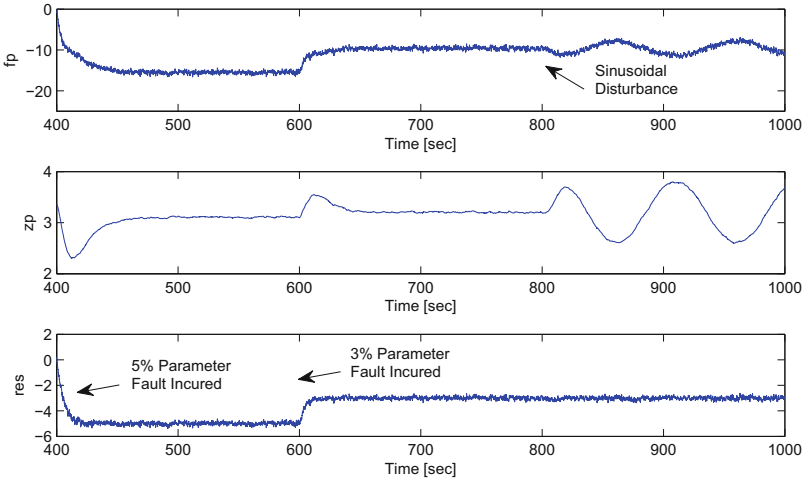

Fig. 14.8 Residual Calculation for Abrupt Parameter Fault

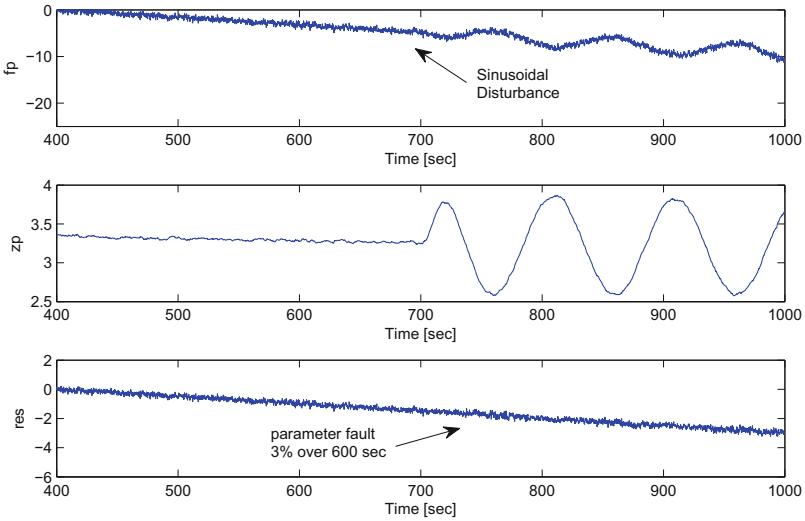

Fig. 14.9 Residual Calculation for Incipient Parameter Fault

Besides the scenario with an abrupt change of a parameter fault, the H_∞ filter is also capable of estimating the faulty parameter facing an incipient change. A gradual deteriorated parameter, starting as unfaulty status at 400 sec and ending as 3% faulty status at 1000 sec, is injected to represent an incipient parameter fault. From Figure 14.9, the residual estimates the parameter fault very accurately, no

matter whether the A/C plant is disturbance-free for the first 300 sec or affected by sinusoidal fault for the second 300 sec. Therefore, it is concluded that the H_∞ filter designed is capable of estimating both abrupt and incipient parameter faults.

References

1. Frank, P.M.. Fault diagnosis in dynamic systems using analytical and knowledge-based redundancy: A survey and some new results. *Automatica* 1990;26(3):459–474.
2. Isermann, R.. Model-based fault-detection and diagnosis–status and applications. *Annual Reviews in control* 2005;29(1):71–85.
3. Isermann, R.. Fault-diagnosis systems. Springer; 2006.
4. Ding, S.X.. Model-based fault diagnosis techniques; vol. 2013. Springer; 2008.
5. Frank, P.M., Ding, X.. Survey of robust residual generation and evaluation methods in observer-based fault detection systems. *Journal of process control* 1997;7(6):403–424.
6. Patton, R., Chen, J.. Observer-based fault detection and isolation: robustness and applications. *Control Engineering Practice* 1997;5(5):671–682.
7. Mangoubi, R.S.. Robust estimation and failure detection: A concise treatment. Springer Publishing Company, Incorporated; 2012.
8. Stoustrup, J., H Niemann, H.. Fault estimation standard problem approach. *International Journal of Robust and Nonlinear Control* 2002;12(8):649–673.
9. Marcos, A., Ganguli, S., Balas, G.J.. An application of h fault detection and isolation to a transport aircraft. *Control Engineering Practice* 2005;13(1):105–119.
10. Marcos, A., Balas, G.J.. A robust integrated controller/diagnosis aircraft application. *International Journal of Robust and Nonlinear Control* 2005;15(12):531–551.
11. Nyberg, M., Stutte, T.. Model based diagnosis of the air path of an automotive diesel engine. *Control Engineering Practice* 2004;12(5):513–525.
12. Kimmich, F., Schwarte, A., Isermann, R.. Fault detection for modern diesel engines using signal-and process model-based methods. *Control Engineering Practice* 2005;13(2):189–203.
13. Keir, M.C., Alleyne, A.G.. Dynamic modeling, control, and fault detection in vapor compression systems. Tech. Rep.; Air Conditioning and Refrigeration Center. College of Engineering. University of Illinois at Urbana-Champaign.; 2006a.
14. Wagner, J., Shoureshi, R.. Failure detection diagnostics for thermofluid systems. *Journal of dynamic systems, measurement, and control* 1992;114(4):699–706.
15. Rossi, T.M.. Detection, diagnosis, and evaluation of faults in vapor compression equipment 1995;.
16. Rossi, T.M., Braun, J.E.. A statistical, rule-based fault detection and diagnostic method for vapor compression air conditioners. *HVAC&R Research* 1997;3(1):19–37.
17. Breuker, M.S., Braun, J.E.. Evaluating the performance of a fault detection and diagnostic system for vapor compression equipment. *HVAC&R Research* 1998;4(4):401–425.
18. Katipamula, S., Brambley, M.R.. Review article: methods for fault detection, diagnostics, and prognostics for building systems a review, part i. *HVAC&R Research* 2005a;11(1):3–25.
19. Katipamula, S., Brambley, M.R.. Review article: methods for fault detection, diagnostics, and prognostics for building systemsa review, part ii. *HVAC&R Research* 2005b;11(1):3–25.
20. He, X.D., Liu, S., Asada, H.H.. Modeling of vapor compression cycles for multivariable feedback control of HVAC systems. *Journal of dynamic systems, measurement, and control* 1997;119(2):183–191.
21. He, X., Liu, S., Asada, H., Itoh, H.. Multivariable control of vapor compression systems. *HVAC&R Research* 1998;4(3):205–230.
22. Li, B., Alleyne, A.. A dynamic model of a vapor compression cycle with shut-down and start-up operations. *International Journal of refrigeration* 2010;33(3):538–552.

23. Katipamula, S., Brambley, M.R.. Review article: methods for fault detection, diagnostics, and prognostics for building systemsa review, part i. *HVAC&R Research* 2005c;11(1):3–25.
24. Katipamula, S., Brambley, M.R.. Review article: Methods for fault detection, diagnostics, and prognostics for building systemsa review, part ii. *HVAC&R Research* 2005d;11(2):169–187.
25. Cheung, H., Braun, J.E.. Simulation of fault impacts for vapor compression systems by inverse modeling. part i: Component modeling and validation. *HVAC&R Research* 2013a;19(7): 892–906.
26. Cheung, H., Braun, J.E.. Simulation of fault impacts for vapor compression systems by inverse modeling. part ii: System modeling and validation. *HVAC&R Research* 2013b;19(7):907–921.
27. Li, H., Braun, J.E.. Decoupling features and virtual sensors for diagnosis of faults in vapor compression air conditioners. *International Journal of Refrigeration* 2007;30(3):546–564.
28. Larsen, L.F., Izadi-Zamanabadi, R., Wisniewski, R.. Supermarket refrigeration system-benchmark for hybrid system control. *Proc of ECC07* 2007;.
29. Yang, Z., Rasmussen, K.B., Kieu, A.T., Izadi-Zamanabadi, R.. Fault detection and isolation for a supermarket refrigeration system-part one: Kalman-filter-based methods. In: *The 18th World Congress of the International Federation of Automatic Control (IFAC 2011)*. 2011a:13233–13238.
30. Yang, Z., Rasmussen, K., Kieu, A., Izadi-Zamanabadi, R.. Fault detection and isolation for a supermarket refrigeration system part two: Unknown-input-observer method and its extension. In: *18th IFAC World Congress*. 2011b:.
31. Wang, S.w., Wang, J., Burnett, J.. Mechanistic model of centrifugal chillers for HVAC system dynamics simulation. *Building services engineering research and technology* 2000;21(2): 73–83.
32. Zhao, Y., Wang, S., Xiao, F., Ma, Z.. A simplified physical model-based fault detection and diagnosis strategy and its customized tool for centrifugal chillers. *HVAC&R Research* 2013;19(3):283–294.
33. Wang, S., Cui, J.. A robust fault detection and diagnosis strategy for centrifugal chillers. *HVAC&R Research* 2006;12(3):407–428.
34. Keir, M.C., Alleyne, A.G.. Dynamic modeling, control, and fault detection in vapor compression systems. Tech. Rep.; Air Conditioning and Refrigeration Center. College of Engineering. University of Illinois at Urbana-Champaign.; 2006b.
35. Janecke, A.K.. A comparison of fault detection methods for a transcritical refrigeration system. Ph.D. thesis; Texas A&M University; 2011.
36. Ayyagari, B.. Simulation and validation of vapor compression system faults and start-up/shut-down transients. Ph.D. thesis; Texas A&M University; 2011.
37. Zhang, Q., Canova, M.. Modeling and output feedback control of automotive air conditioning systems. *Submitted to International Journal of Refrigeration* 2014;.
38. Zhang, Q., Fiorentini, L., Canova, M.. H robust control of an automotive air conditioning system. In: *American Control Conference (ACC), 2014*. IEEE; 2014:5675–5680.
39. Marcicki, J., Onori, S., Rizzoni, G.. Nonlinear fault detection and isolation for a lithium-ion battery management system. In: *ASME 2010 Dynamic Systems and Control Conference*. American Society of Mechanical Engineers; 2010:607–614.
40. Szászi, I., Marcos, A., Balas, G.J., Bokor, J.. Linear parameter-varying detection filter design for a boeing 747-100/200 aircraft. *Journal of guidance, control, and dynamics* 2005;28(3): 461–470.
41. Q. Zhang, M. Canova, Fault detection and isolation of automotive air conditioning systems using first principle models. Control Eng. Pract. **43**, 49–58 (2015)

Chapter 15
Evaluating the Performance of Automated Fault Detection and Diagnosis Tools

David Yuill

Abstract Automated fault detection and diagnosis (AFDD) has the potential to provide early warning of performance degradation faults before they might otherwise be apparent, and before they cause failure of the system. AFDD approaches have been developed in many industries, such as aerospace, process control, and air-conditioning. In air-conditioning applications the cost-sensitivity of the market requires that there is minimal cost premium for AFDD, so methods typically must be deployed with very few sensors to provide input and minimal engineering cost. In addition, because life safety is not a concern, less accurate methods can be tolerated. In this landscape, there are many methods that don't perform well, but until recently there has been no standardized method or metrics to test or describe performance of AFDD. This chapter describes a new methodology, and a specific method to test and characterize the performance of AFDD tools that are applied to air-conditioning systems, and illustrates the methods with a case study. The widely used AFDD approach tested in the case study shows poor performance, which underscores the importance of evaluating AFDD performance.

Keywords Fault detection • Fault isolation • Air-conditioning system • Building

15.1 Introduction

Many automated fault detection and diagnosis (AFDD) approaches have been developed over the past few decades in applications for process control, aerospace, and nuclear industries. In these applications there can be a very high cost associated with sustaining a fault, so early detection is of paramount importance. Consequently, a relatively high cost of implementation is often acceptable. When high implementation costs can be tolerated, a large number of sensors can be deployed to give the AFDD method a large number of redundant results to compare. Fundamentally, AFDD approaches compare a measured result with an expected result, and infer potential problems from the discrepancy.

D. Yuill (✉)
University of Nebraska – Lincoln, Omaha, NE, USA
e-mail: dyuill@unl.edu

Q. Zhang et al., *Automotive Air Conditioning*, DOI 10.1007/978-3-319-33590-2_15

In a competitive commercial industry, costs become more important. The automotive industry's OBD II requirements provide a mechanism to promote use of diagnostics by removing the first-cost disadvantage to manufacturers that include them in their automobiles. A regulated approach can be beneficial when the potential advantages are not well understood by consumers, and it can also stimulate research and development efforts to provide improved diagnostic methods.

AFDD for air-conditioning systems has been under development since the 1980s, but hasn't been very widely adopted until quite recently. There has been particular interest in AFDD for air-cooled unitary air-conditioning systems, such as the systems used to condition residential and light commercial buildings (referred to as "unitary systems" hereafter). The reasons for the focus on these systems are: (a) they are very widely adopted; (b) they are typically manufactured at low-cost due to market forces, and are therefore expected to have greater potential for developing faults or having manufacturing faults; (c) these systems typically receive maintenance less frequently and from technicians who have less equipment-specific training than other systems, such as large chillers or air-handling units.

The challenge for developers of AFDD for unitary systems is that although the behavior of real systems deployed in the field is quite complex, there is very little budget available for deploying AFDD tools. The reason is the same as in (b) above: the market is extremely cost-competitive, so the added cost from additional sensors will often price a model out of the market. Furthermore, the challenge is compounded by a marketing difficulty: faults and their impacts are not very well understood, particularly by typical consumers of unitary systems, and marketers don't like to tell potential customers that their products are likely to have problems. If consumers wish to select a higher-end system, they will typically select one with a higher efficiency rating, which is quantified with a standard test.

To address this challenge, developers of AFDD for unitary systems need to gain as much diagnostic capability as they can with a minimum of sensor data. Since the relative cost of microprocessors is low compared to sensors, this means that more sophisticated algorithms may be used in place of sensors. For example, one approach is to use the so-called virtual sensors to infer refrigerant pressure based on temperature measurements, because temperature is less costly to measure than pressure. Similarly, virtual flow sensors have been developed in place of airflow or refrigerant flow measurements. Another common approach is to bypass permanently installed sensors and processors, and use a portable device. Although the increasingly complex algorithms may reduce the monetary cost, they increase the uncertainly of the results and the robustness of the methods. For example, a portable device may work well on some models of air-conditioner, but not others; some methods may work well in one set of operating conditions and fault conditions, but not in others.

One problem with increasingly complex algorithms that use an increasing amount of inference is that they sometimes become increasingly likely to give erroneous results. Compounding this problem is that the complexity also makes the algorithms harder to test, both for the developer and for a potential adopter of the AFDD. Finally, this problem becomes still worse if there is no methodology for measuring the performance of AFDD, or any method for expressing or characteriz-

ing performance. As Vachtsevanos et al. [1] note, no such methodologies exist for diagnostics for any military or commercial applications.

Despite the unknown performance of AFDD for unitary systems, many tools and approaches have been developed by researchers and by commercial entities, and many are available in the marketplace. These tools have been widely deployed, and have even been included in codes, such as California's building energy code, Title 24–2013 [2], which contains a simple diagnostic that is required for residential air-conditioner installations.

This chapter provides some background on AFDD methods and lays out standard terminology, then describes the first standardized approach for evaluating the performance of AFDD algorithms in AFDD intended for application to unitary systems [3, 4].

15.2 AFDD Method Categorization

There are many ways to categorize AFDD methods. Some possible categorizations are described below. These categorizations are not exclusive; a single method may fall within several of these categories.

Steady-state or dynamic data inputs. Some methods require a system to be operating in a quasi-steady-state before the AFDD can be applied. This may require an automated method to have a steady-state detector, or a more manual method to use the operator's judgement to determine whether the system is operating steadily.

Model-based, rule-based, or data-driven. Model-based approaches may use mechanistic models or empirical models, or some combination of these (often called "gray-box models") to predict values for variables that will be compared to measured values. Some AFDD approaches use a set of expert rules to determine whether a variable is within a reasonable operating range. Finally, pure data-driven methods are gaining in popularity, such as machine learning approaches.

Instantaneous or time series. Instantaneous methods conduct diagnostics based upon a snapshot of the system's operation. These methods are necessary for AFDD tools that are not installed in the system. Time series data conversely compare performance over time, and trigger fault detection when a significant degradation in performance is sensed while accounting for variations in operating conditions.

On-board, online, or portable. On board AFDD refers to methods that use permanently installed sensors, and has diagnostic algorithms that are processed on site. Online AFDD methods use sensor data that are conveyed through internet protocol to a centralized offsite processing facility. Portable AFDD typically consists of handheld maintenance devices, which include sensors that are temporarily attached to the system to be diagnosed. Portable devices require more labor input and may have disadvantages with respect to the specificity of the internal models, but have the advantage of not requiring permanently installed sensors.

15.3 AFDD Performance Evaluation Terminology

There are several terms that should be used with a specific and consistent meaning when discussing AFDD performance evaluation for vapor compression cycle air-conditioner diagnostics. The definitions are mainly taken from Yuill [5], but some are derived from the literature on AFDD in general, including sources such as Braun [6], Isermann [7, 8], and Katipamula and Brambley [9].

Fault—A state of the system or equipment that causes a degradation in performance.
Fault Detection—Detection and reporting of a fault, without specification of the type or severity of the fault.
Fault Diagnosis—Specification of the fault, which consists of two processes: fault isolation and fault assessment.
Fault Isolation—The component of fault diagnosis in which the location or type of fault is identified.
Fault Assessment—The fault level expressed with reference to physical measurements.
Fault Tolerance—A decision to not address a fault, typically because it is not considered cost effective to currently address it.
Fault Intensity—The fault level expressed with reference to physical measurements.
Fault Impact Ratio (FIR)—A ratio that quantifies the effect of a fault on system performance. It is calculated as the capacity or COP divided by the capacity or COP that the system would give under the same conditions if no fault were present. FIR is calculated as:

$$\mathrm{FIR}_Q = \frac{\mathrm{capacity}_{\mathrm{faulted}}}{\mathrm{capacity}_{\mathrm{unfaulted}}} \qquad \mathrm{FIR}_{\mathrm{COP}} = \frac{\mathrm{COP}_{\mathrm{faulted}}}{\mathrm{COP}_{\mathrm{unfaulted}}}$$

AFDD Protocol—An algorithm to conduct the necessary calculations and comparisons to generate a diagnosis, and the data type and formatting that must be fed to the algorithm. An AFDD protocol does not include the hardware (e.g., sensors) in an AFDD tool.

In addition to these definitions, Yuill [5] provides a taxonomy for outcomes when an AFDD algorithm's performance is evaluated:

1. No Response—The AFDD cannot provide a response with respect to the presence of a fault, typically either because it can't be applied for a given set of conditions, or it has excessive uncertainty about its detection or diagnosis.
2. Correct—The AFDD correctly identifies the state of the system, whether faulted or unfaulted, and identifies the fault type if a significant fault is present.
3. False Alarm—A fault is detected, but no significant fault is actually present.
4. Misdiagnosis—A significant fault is correctly detected, but the wrong fault type is diagnosed.

5. Missed Detection—A significant fault is present, but the AFDD does not detect a fault.
6. No Diagnosis—A significant fault is correctly detected, but the AFDD does not provide a diagnosis of the type of fault.

15.4 AFDD Performance Evaluation Method

The method developed by Yuill and Braun [4] applies to handheld AFDD devices intended for unitary systems that are operating at steady state. The method addresses only air-conditioners that have a single fault or no fault; units with multiple simultaneous faults are not included in the performance test input data, nor are they considered in the application of the taxonomy provided above.

The approach to the evaluation of AFDD protocols is to feed a set of data to each protocol and observe the responses, collecting and categorizing them to develop summary statistics. The data represent typical conditions that an AFDD tool may encounter:

– Several different systems with different properties, such as configuration, refrigerant type, SEER rating, and expansion device type
– A range of ambient and indoor thermal conditions
– Different types of faults, or with no fault
– Different intensities of fault

For each test case (a single combination of the conditions above) the protocol gives a response. These responses are tallied and organized to give statistics that reflect the overall utility of the protocol. The evaluation process is summarized in Fig. 15.1.

The following subsections describe the components of the evaluation method in greater detail.

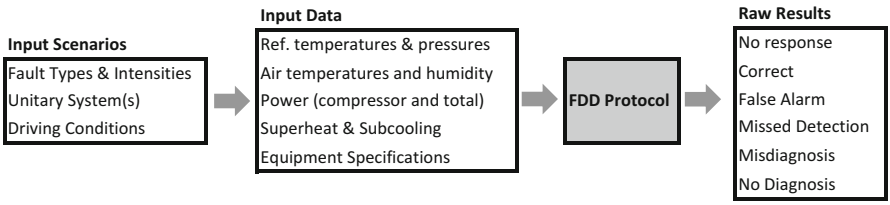

Fig. 15.1 General evaluation method

15.4.1 Faulted and Unfaulted Operation

Faults are conditions that affect performance negatively and they have some level of severity. We have developed two ways to characterize this level of severity. The first is fault intensity (FI), which is related to measurable quantities. For example, a 20 % undercharge. The second is FIR, which is related to equipment performance, and is tied to either capacity or coefficient of performance (COP). For example, when $FIR_{COP} = 95\,\%$, it says that the equipment is operating at 95 % of its maximum efficiency under a given set of operating conditions.

There is not a direct relationship between FI and FIR. This means that it is possible to have faults that have some FI, but with no measurable degradation of performance. This raises the question of how do we draw a distinction between faulted and unfaulted operation. The answer for the Yuill and Braun [4] method is that we consider FIR, because the equipment performance is generally what equipment operators and users of AFDD are concerned with. This leads to another question, which is: how much performance degradation constitutes faulted operation? Our approach is to leave this as a variable quantity, using FIR *thresholds* to draw the distinction between faulted and unfaulted. We evaluate each protocol at several thresholds so that a user of the results can choose the threshold he or she considers appropriate. If the FIR threshold is 99 %, it means that test cases with FIR above this threshold are considered to be unfaulted, regardless of the FI. This threshold concept is important in the consideration of False Alarms, described below.

15.4.2 Test Case Outcomes

When FDD is applied, there are six possible outcomes with respect to fault isolation, as listed in the taxonomy above. False Alarms is an important category, and has a special treatment. Specifically, a False Alarm is indicated when the protocol gives a response that a fault is present and:

1. the fault's impacts on capacity and efficiency are both below a given threshold (i.e., FIR_Q and FIR_{COP} are both above the threshold)
2. the system is not overcharged by 5 % or more
3. the suction superheat is within the range 1–36 °F

The special requirement in bullet b is included for the following reason. An overcharged system may have a significant fault, but no significant impact on capacity or COP. Consider the example case of a system that is 10 % overcharged, but has no significant degradation of capacity or COP. An equipment operator may want to know about the overcharge, since it can be associated with reduction of compressor life, even though it doesn't impact the current performance of the equipment. To address this situation, if the refrigerant is overcharged by more than 5 % the system is considered faulted, even if the fault impact is below the given threshold.

To evaluate an AFDD protocol using this taxonomy, one feeds it multiple input scenarios, each of which gives one of these test outcomes. Test outcomes for No Response, False Alarm, Misdiagnosis, Missed Detection, and No Diagnosis are gathered and expressed as rates, using percentages. Test outcome 2—Correct—is implied by the other outcomes.

15.4.3 Test Case Outcome Rate Calculations

In rate calculations, the numerator is the number of test cases that have a given test outcome (one of the six listed above). The denominator for each test outcome rate is described below. Each denominator is defined based on determining a meaningful rate. The denominators include only the cases that could apply to each type of outcome. For example, a Misdiagnosis can't be made on a test in which no fault is present, so only those cases determined to be faulted are included in the denominator for Misdiagnosis rate. (If a protocol indicates a fault when none is present, this is a False Alarm, not a Misdiagnosis). Thus, the potential range is from 0 to 100 % for each outcome rate. The details of the rate calculations are given in Table 15.1.

Table 15.1 Rate calculation method for evaluation outcomes

Rate	Numerator	Denominator
No Response	Number of cases that meet the "No Response" criteria	Total number of test cases
False Alarm	Number of cases that meet the "False Alarm" criteria described above	The number of cases in which the fault impacts are below a specified threshold, the unit is less than 5 % overcharged, the suction superheat is in the range 1–36 °F, and for which the protocol gives a response
Misdiagnosis	Number of cases for which a fault is present, and the protocol indicates a different fault is present	The number of cases in which the input data library indicates the presence and intensity of a fault, and the protocol indicates that the system has a fault
Missed Detection	Number of cases for which a fault is present, and the protocol indicates that no fault is present	The number of cases in which the input data library indicates the presence and intensity of a fault, and the protocol gives a response
No Diagnosis	Number of cases for which a fault is present, and the protocol indicates that no fault is present	The number of cases in which the input data library indicates the presence and intensity of a fault, and the protocol gives a response

15.4.4 Fault Types

The faults that are included in the scope of the AFDD evaluation methodology were selected based upon the availability of experimental data with faults imposed. Choosing this set of faults is not arbitrary, because the faults that have been tested experimentally generally correspond to those faults that have the greatest cost for system operators. This cost is a function of the likelihood of the fault arising and the penalty on operating costs that the fault imposes. Furthermore, the AFDD tools that currently exist also tend to focus on this set of faults. Table 15.2 lists the faults, describes how they are implemented in laboratory tests, and gives the abbreviations that refer to each fault type. The descriptions and formal definitions of fault intensity are proposed for standard usage by Yuill and Braun [4].

Table 15.2 Description of fault types and their fault intensity definitions

Fault type	Abbr.	Description	Fault intensity definition
Under- or over-charge	UCOC	A mass of refrigerant charge that is less or more than either (a) the manufacturer's recommended mass, or (b) the mass that gives the best system performance	$\mathrm{FI}_{\mathrm{charge}} = \frac{m_{\mathrm{actual}} - m_{\mathrm{nominal}}}{m_{\mathrm{nominal}}}$
Low-side heat transfer	EA	Evaporator faults; reduced evaporator airflow is used to implement this fault in a laboratory	$\mathrm{FI}_{\mathrm{EA}} = \frac{\dot{V}_{\mathrm{actual}} - \dot{V}_{\mathrm{nominal}}}{\dot{V}_{\mathrm{nominal}}}$
High-side heat transfer	CA	Condenser faults; reduced condenser airflow is used to implement this fault in a laboratory	$\mathrm{FI}_{\mathrm{CA}} = \frac{\dot{V}_{\mathrm{actual}} - \dot{V}_{\mathrm{nominal}}}{\dot{V}_{\mathrm{nominal}}}$
Liquid line restriction	LL	Flow restrictions in the liquid line. FI is pressure drop across restriction divided by pressure drop from condenser to evaporator	$\mathrm{FI}_{\mathrm{LL}} = \frac{\Delta P_{\mathrm{LL,faulted}} - \Delta P_{\mathrm{LL,unfaulted}}}{\Delta P_{\mathrm{LL,unfaulted}}}$
Non-condensables	NC	The presence of non-condensable gas in the refrigerant. FI is mass of N_2 divided by mass of N_2 that would fill the system at standard temperature and pressure	$\mathrm{FI}_{\mathrm{NC}} = \frac{m_{\mathrm{N_2,faulted}}}{m_{\mathrm{N_2,ref}}}$
Compressor leakage	VL	Leakage of refrigerant from high to low pressure regions in the compressor. Implemented in the laboratory with a metered hot-gas bypass	$\mathrm{FI}_{\mathrm{VL}} = \frac{\dot{m}_{\mathrm{faulted}} - \dot{m}_{\mathrm{unfaulted}}}{\dot{m}_{\mathrm{unfaulted}}}$

15.4.5 Input Data

The AFDD evaluation method described above requires a large and representative set of input data to be fed through the AFDD protocol that is being tested. Gathering such a set of data can be quite difficult. The data need to represent operation in the range of conditions in which the AFDD might be applied (combinations of indoor and outdoor temperatures and indoor humidity values), with and without faults of each fault type, at varying fault intensities for each fault type, and in combinations of fault and operating condition. Finally, if the AFDD is to be applied generally, i.e., not intended for a specific unitary system, then it needs to be tested with a representative range of systems.

Yuill and Braun [4] used a library of laboratory measurement data that was a combination of results from multiple experimenters at various laboratories. There are nine unitary systems represented in the data set. They carefully vetted the data for accuracy and realism, and compiled them into a standardized format. The library is summarized in Table 15.3. The table includes configuration (rooftop unit or split system), rated capacity, refrigerant type, expansion device type (fixed orifice or thermostatic expansion device), the number of tests for each fault type, and the range of ambient temperature over which the tests were conducted. The fault types are described below.

Case studies were carried out using this set of input data on the publicly available diagnostic protocol described in CEC [10]. The results were presented in Yuill and Braun [4], and were generally disappointing, including high False Alarm rates. In the public response to these results a discussion began about whether the conditions in the laboratory tests were representative of the actual conditions in which an AFDD tool may be deployed. A model developed by Cheung and Braun [11, 12] was subsequently used to provide a library of simulation data at a controlled set of input conditions. This model is a fault-enabled gray-box model that combines physics-based models wherever possible, and uses the experimental data described in Table 15.3 to train some portions of the model, such as parameters describing the heat exchanger performance. Yuill et al. [13] validated the model, and Yuill et al. [3] described a modified method of AFDD performance evaluation based upon simulation data.

Yuill and Braun [14] subsequently compared evaluation results for several AFDD protocols three different input data libraries. The first was the original measurement data, which were gathered by the original experimenters at an essentially arbitrary set of conditions; the second was modeled data for the exact same conditions and unitary systems as the measurement data; and the third library used simulation data from a set of realistic scenarios, including assumptions about fault prevalence and typical operating conditions when AFDD protocols are applied. The comparison showed that any differences in results when comparing the measurement-based results with simulation-based results are insignificant compared to the effects of using a realistic distribution of conditions. Therefore, it can be concluded that

Table 15.3 Measurement data input data library from Yuill and Braun [4]

No.	Type	Capacity (tons)	Refrig.	Exp. device	No fault	UC	OC	EA	Number of tests				Ambient temp.	
									CA	LL	NC	VL	Min. (°F)	Max. (°F)
1	RTU	3	R410A	FXO	24	25	12	21	6	0	0	0	67	125
2	RTU	3	R22	FXO	39	34	0	26	36	34	0	33	60	100
3	RTU	5	R407C	FXO	17	15	12	19	8	0	0	0	67	116
4	Split	3	R410A	FXO	1	29	1	0	0	0	0	0	82	127
5	Split	2.5	R410A	TXV	16	12	12	21	15	16	15	16	70	100
6	Split	3	R410A	TXV	2	30	7	0	0	0	0	0	83	127
7	Split	3	R410A	TXV	4	4	7	0	0	0	0	0	82	125
8	Split	3	R22	TXV	4	8	0	8	0	0	0	0	82	125
9	Split	3	R22	FXO	4	4	4	6	0	0	0	0	82	125
				Total	111	161	55	101	65	50	15	49		

meaningful evaluations must be conducted using data generated by reliable models, unless laboratory testing can be conducted for all combinations of operating and fault conditions and air-conditioner models of interest.

15.5 Case Study

To illustrate the usage of the protocol, a case study is presented here, showing the results of evaluating the diagnostic protocol that is part of the California 2013 building energy code [2]. The case study results here are from an evaluation using the measurement data library as inputs (described in Table 15.3). The protocol is publicly available, which is why it is presented here. However, it is limited in scope. It is intended only to check for refrigerant charge faults, although it also requires direct measurement of evaporator airflow. This presents two philosophical questions with respect to evaluating AFDD performance. The first is: how should the airflow measurement requirement be treated? We have assumed that the technician correctly measures airflow prior to applying the AFDD. In a practical sense, this means that we removed all cases in which there is an evaporator heat transfer fault (which is implemented in the laboratory as a reduction in evaporator airflow). This approach is conservative; in actual application, which includes the myriad problems with accurate airflow measurement in the field, the AFDD may not perform as well as indicated in this case study.

The second philosophical question is: should an AFDD protocol be tested with faults other than those faults it is intended to diagnose? Since other faults may be present when an AFDD protocol is applied, it is reasonable to include other faults in the input data when any AFDD protocol is tested, regardless of whether it is intended to diagnose those faults. For example, if an AFDD protocol is intended to diagnose only the presence of non-condensable gas in the refrigerant, but it flags this fault in cases in which the condenser is fouled or the system is overcharged, it may not be a very useful protocol. An effective evaluation of the performance of AFDD protocols should consider the importance of each fault type. This importance is a combination of the likelihood of the fault occurring at each fault intensity (a probability density function, which is referred to as "fault prevalence" in Yuill and Braun [14, 15]), and the cost of the fault at that intensity for the application of interest.

Clearly, the consideration of fault cost can be quite complex. Yuill and Braun [15] provide a methodology for calculating this cost and for considering fault prevalence in the total value calculation for a particular AFDD tool. In their analysis, the protocol presented in the case study below gives a negative value, overall. This is primarily driven by the additional service technician costs that are associated with False Alarms and Misdiagnoses. They found that the cost of Missed Detections is not very significant because many faults do not cause sufficient reductions in equipment life and efficiency to warrant the cost of addressing them.

15.6 Results

In Fig. 15.2 the False Alarm rates for the case study protocol are shown. The way to interpret these results is as follows. On the left side, the FIR threshold is 100 %. This means that any test case in which the capacity and COP of the unit are at (or above) the capacity and COP of the unit at the same conditions is considered unfaulted, regardless of whether the experimenter imposed a fault (with the exception of overcharge, as noted above). The rationale is that a fault that has no impact shouldn't be considered a fault. If the protocol flags such as case as faulted, it is considered a False Alarm. The protocol flags about 13 % of these cases as faulted.

Moving rightward the same logic is applied. If a fault is so minor that it reduces either capacity or COP by a maximum of 2.5 %, for example, it is considered unfaulted at the 97.5 % FIR threshold. This protocol flags about 40 % of cases that have no fault sufficient to reduce capacity or COP by 2.5 %. The results in Fig. 15.2 could be considered a set of individual results for which a user can choose the result that is meaningful to them. A user for whom any fault less than 5 % is considered insignificant uses the 95 % FIR threshold result, and ignores the other threshold's results.

The results for Misdiagnosis are different than for False Alarms. In a Misdiagnosis, there must be a fault present for it to be considered a Misdiagnosis. Therefore, the threshold concept used for False Alarms doesn't apply. Instead, we group the Misdiagnosis cases into bins with respect to the FIR. Since faults affect capacity and COP differently, some tests may be in different bins depending on whether capacity or COP is considered. Therefore, two data series are presented: one for the capacity FIR bins and one for the COP FIR bins (Fig. 15.3).

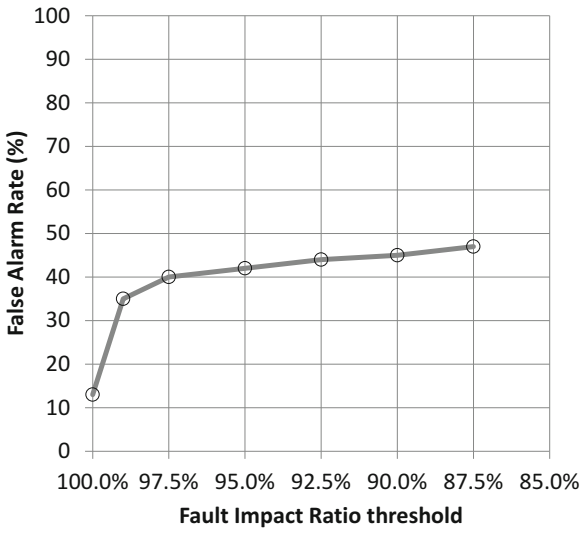

Fig. 15.2 False Alarm rates for case study AFDD protocol

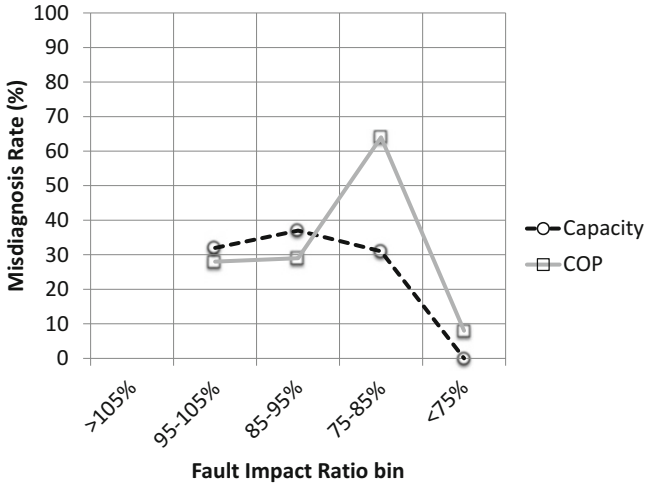

Fig. 15.3 Misdiagnosis results for case study AFDD protocol

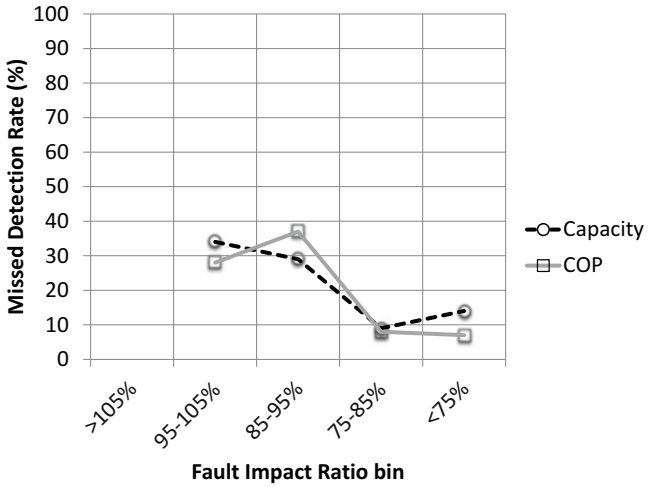

Fig. 15.4 Missed Detection results for case study AFDD protocol

Missed Detection results are presented in the same manner as Misdiagnosis results: the results are grouped into bins by FIR and presented in separate series for capacity and COP effects (Fig. 15.4).

15.6.1 Discussion of Case Study Results

As noted earlier, the performance of this protocol is disappointing. False Alarms are a particularly expensive problem for diagnostics to provide in most settings (automotive, buildings, aerospace, etc.). One might assume that since this protocol is intended to be applied only to charge faults, it would perform better if all other faults were eliminated. This is true; the protocol does perform better when it is only fed inputs that have charge faults or no fault. However, it is difficult to imagine scenarios in which a charge fault might be present, but no other faults could possibly be present. In fact the results above probably indicate better performance than this protocol might see in the field because the existing set of measurement data (described in Table 15.3) has a very large proportion of charge fault data. When the EA data are removed, 327 of the remaining 506 tests have either a charge fault or no fault. In fact, Yuill et al. [3] show that this system performs far worse when an even distribution of faults and conditions is used.

The Misdiagnosis results in Fig. 15.3 show an expected result: the rate of Misdiagnoses decreases as the fault's severity increases, with less than 10 % of the cases being Misdiagnosed from the bin with FIR less than 75 %. However, this result is caused by a related issue to the discussion regarding a heavy distribution of charge faults. The faults in a laboratory settings that cause the largest decrease in capacity and efficiency are undercharge faults, which is one that this protocol can diagnose. When Yuill et al. [3] used an even distribution of faults, the Misdiagnosis rates showed no clear relation to FIR. A similar result occurs with Missed Detection results.

One result type that is not presented here is the No Diagnosis results. This result represents the cases in which a protocol indicates the presence of a fault but cannot or does not diagnose what type of fault it is. The protocol in this case study always provides a diagnosis when it detects a fault, so the result would be zero in all ranges.

15.7 Conclusions

AFDD tools have potential to reduce operating costs in air-conditioners by giving early warning of faults that can degrade performance and reduce equipment life. However, there has been little scrutiny until recently on the effectiveness of the AFDD protocols to give accurate results. This is partly because there has been no metrics by which to describe the performance of AFDD, either in air-conditioners or in equipment in general. A methodology has now been developed to systematically evaluate the performance of AFDD tools for unitary air-conditioners. The methodology includes a taxonomy of performance outcomes with which performance can be quantified and measured. The AFDD evaluation method has been applied to several air-conditioners, and found that performance is often not as good as might

be expected. Results from one widely applied AFDD method have been shown in a case study, to demonstrate how the evaluation methodology is applied.

The results of evaluating existing methods showed that many currently existing tools don't perform very well. One conclusion from this result is that AFDD should be widely tested to ensure that they perform well enough to provide net benefits. It is hoped that the existence of an evaluation methodology will help developers of future methods to develop more effective methods. In addition, as methods are improved and as potential adopters of AFDD and developers of codes and standards are more able to quantify performance and benefits of AFDD, that it will become more widely adopted.

References

1. G.J. Vachtsevanos, F.L. Lewis, M.J. Roemer, A. Hess, B. Wu, *Intelligent Fault Diagnosis and Prognosis for Engineering Systems* (Wiley, Hoboken, NJ, 2006)
2. California Energy Commission (CEC), *2013 Building Energy Efficiency Standards for Residential and Nonresidential Buildings*. CEC-400-2012-004-CMF-REV2 (California Energy Commission, Sacramento, 2012)
3. D.P. Yuill, H. Cheung, J.E. Braun, Evaluation of fault detection and diagnostics tools by simulation results of multiple vapor compression systems, in *Proceedings of 15th International Refrigeration and Air Conditioning Conference*, Paper 2605, West Lafayette, July 2014
4. D.P. Yuill, J.E. Braun, Evaluating the performance of FDD protocols applied to air-cooled unitary air-conditioning equipment. HVAC&R Res. **19**(7), 882–891 (2013)
5. D.P. Yuill, Development of methodologies for evaluating performance of fault detection and diagnostics protocols applied to unitary air-conditioning equipment. Doctoral Dissertation, School of Mechanical Engineering, Purdue University, Lafayette, IN, 2014
6. J.E. Braun, Automated fault detection and diagnostics for the HVAC&R industry. HVAC&R Res. **5**(2), 85–98 (1999)
7. R. Isermann, Process fault detection based on modeling and estimation: A survey. Automatica **20**(4), 387–404 (1984)
8. R. Isermann, Supervision, fault-detection and fault-diagnosis methods: An introduction. Control. Eng. Pract. **5**(5), 639–652 (1997)
9. S. Katipamula, M.R. Brambley, Methods for fault detection, diagnostics, and prognostics for building systems: A review, Part I. HVAC&R Res. **11**(1), 3–25 (2005)
10. California Energy Commission (CEC), *2008 Building Energy Efficiency Standards for Residential and Nonresidential Buildings*. CEC-400-2008-001-CM (California Energy Commission, Sacramento, 2008)
11. H. Cheung, J.E. Braun, Simulation of fault impacts for vapor compression systems by inverse modeling. Part I: Component modeling and validation. HVAC&R Res. **19**(7) (2013)
12. H. Cheung, J.E. Braun, Simulation of fault impacts for vapor compression systems by inverse modeling. Part I: System modeling and validation. HVAC&R Res. **19**(7) (2013)
13. D.P. Yuill, H. Cheung, J.E. Braun, Validation of a fault-modeling equipped vapor compression system model using a fault detection and diagnostics evaluation tool, in *Proceedings of 15th International Refrigeration and Air Conditioning Conference*, Paper 2606, Purdue University, West Lafayette, July 2014
14. D.P. Yuill, J.E. Braun, Effect of the distribution of faults and operating conditions on AFDD performance evaluations. Appl. Therm. Eng. (2016). Accepted Dec 2015
15. D.P. Yuill, J.E. Braun, A figure of merit for overall performance and value of AFDD tools. In review (2016)

Index

Q. Zhang et al., *Automotive Air Conditioning*, DOI 10.1007/978-3-319-33590-2